Université de Toulouse

THÈSE

En vue de l'obtention du

DOCTORAT DE L'UNIVERSITÉ DE TOULOUSE

Délivré par :
Institut National Polytechnique de Toulouse (INP Toulouse)

Discipline ou spécialité :

Science et Génie des Matériaux

Présentée et soutenue par :
Thomas Gheno

le : vendredi 31 août 2012

Titre :

Oxydation et carburation d'alliages modèles chromino-formeurs dans le dioxyde de carbone

---

Ecole doctorale :
Sciences de la Matière (SDM)

Unité de recherche :
CIRIMAT

Directeur(s) de Thèse :
Daniel Monceau, Directeur de Recherche CNRS, CIRIMAT
David Young, Professeur Émérite, UNSW (Australie)

Rapporteurs :

Gerald H. Meier, Professeur des Universités, University of Pittsburgh (USA)
Willem J. Quadakkers, Directeur de Recherche, Forschungszentrum Jülich (Allemagne)

Membre(s) du jury :

Philippe Marcus, Directeur de Recherche CNRS, ENSCP
Fabien Rouillard, Ingénieur de Recherche CEA Saclay
Pascal Lamesle, Maître-Assistant Mines d'Albi, ICA

Oxidation and carburisation of model chromia-forming alloys in carbon dioxide

by

Thomas Gheno

A thesis prepared under the supervision of

Daniel Monceau, Directeur de Recherche au CNRS, CIRIMAT
David J. Young, Emeritus Professor, UNSW

as part of a cotutelle arrangement with

CIRIMAT
Institut National Polytechnique de Toulouse
Toulouse, France

School of Materials Science and Engineering
The University of New South Wales
Sydney, Australia

August 2012

Acknowledgements

I would like to thank Gerald Meier and Joe Quadakkers for accepting to examine this thesis, and for taking part in the oral defence in Toulouse.

I would like to express my deepest gratitude to my supervisor David Young. David's encyclopaedic yet intuitive knowledge of high temperature oxidation, his immense experience as an academic, have been invaluable. To have benefited from his patient teaching is a much appreciated privilege.

I have enjoyed help from a number of persons during my stay at the School of Materials Science and Engineering in Sydney. I want to thank Jianqiang Zhang and Rahmat Kartono for teaching me the art of making and oxidising metal specimens. May the EMU staff also be acknowledged for helping me with electron microscopy.

Getting paperwork right can be as difficult as rationalising nucleation-growth kinetics — and not quite as rewarding, but unavoidable. Many thanks to the School office staff for assistance with administrative matters. In particular, I feel most grateful to Lana Strizhevsky for being ever so kind and understanding.

I am indebted to my colleagues for exhorting me to get out of the office, thus keeping me more or less sane. Cheers Julian, Sam, Lois, Alex, Hugh. Likewise, my thoughts also go to my flatmates on Fitzgerald Ave, who made my stay in Sydney a great and diverse experience.

Remerciements

J'aimerais remercier Philippe Marcus pour avoir accepté de présider mon jury de thèse, ainsi que Fabien Rouillard et Pascal Lamesle pour avoir participé au jury lors de la soutenance à Toulouse.

J'adresse mes plus profonds remerciements à mon directeur de thèse Daniel Monceau. Sa contribution à ma formation va bien au delà des aspects scientifiques: source d'inspiration, de stimulation, d'encouragements, c'est aussi et surtout pour l'attention apportée aux aspects humains et pour le soucis de donner du sens à cette formation que je lui suis reconnaissant.

J'ai bénéficié de l'aide de nombre de personnes pendant mon séjour au CIRIMAT à Toulouse. J'aimerais remercier les virtuoses du MEB Yannick Thebault et Djar Oquab pour m'avoir appris un peu de leur art, et pour avoir été aussi impliqués dans l'aide qu'ils m'ont apportée à tirer le maximum du microscope. De la même manière, je remercie Cédric Charvillat pour les expériences ATG et Olivier Marsan pour les analyses Raman. Sans oublier Alexandre Freulon, tenancier du laboratoire de métallographie, où j'ai été un habitué.

J'ai eu la chance de profiter de l'atmosphère d'entraide règnant au CIRIMAT, encouragée par les chercheurs et enseignant-chercheurs. En particulier, je veux remercier Eric Andrieu et Dominique Poquillon pour avoir été disponibles et dévoués à partager leur expérience malgré des emplois du temps surchargés.

Qu'il soit manifesté dans des discussions scientifiques, de l'assistance mutuelle sur des difficultés pratiques ou du soutien moral, le sens de communauté existant entre les doctorants au CIRIMAT a grandement contribué à rendre mon séjour plus agréable. En particulier, mes pensées vont à Christophe, Serge, Pauline, Martin S., Bertrand, Damien, Vincent, John, Martin R., Céline, Mathilde, Guilhaume, Koenraad.

Finalement, c'est avec une grande affection que je dédie cette thèse à ma famille et à mes amis à Toulouse, Paris et ailleurs, qui me donnent plus que je ne peux exprimer par écrit.

Title

Oxidation and carburisation of model chromia-forming alloys in carbon dioxide.

Abstract

Materials to convey hot CO_2-rich gases are needed in carbon capture technologies currently being developed. This work is aimed at investigating the factors controlling the oxidation of chromia-forming alloys in these atmospheres. To do so, model Fe–Cr and Fe–Cr–Ni alloys were exposed to Ar–CO_2–H_2O gas mixtures at 650 and 800 °C, and the reaction products examined using conventional metallography techniques. Carbide precipitation beneath oxide scales reflects a carbon supersaturation at the metal/oxide interface relative to the external atmosphere: as a gradient of oxygen potential is established across the growing scale, an elevated carbon activity results at the interface if the scale transmits carbon. On the basis of a local equilibrium model, measured carburisation rates and precipitate volume fractions were used to evaluate the influence of oxide composition and of the presence of H_2O in the gas on carbon uptake/transport in the scales. Limited carburisation beneath Cr_2O_3 scales was shown by means of an analysis of subscale chromium depletion not to alter the oxide stability. The morphological evolution of Fe-rich oxide nodules formed as a result of localised Cr_2O_3 failure was studied in relation to the alloy ability to supply chromium to the metal/oxide interface. Application of nucleation-growth models to the kinetics of nodule development allowed the resistance of Cr_2O_3 scales to be evaluated in terms of nodule nucleation rates determined from experimental nodule surface coverages and specimen weight gains. The relative importance of nodule nucleation and growth in determining the overall alloy performance as a function of reaction temperature is discussed.

Keywords

Oxidation, carburisation, carbon dioxide, water vapour.

Titre

Oxydation et carburation d'alliages modèles chromino-formeurs dans le dioxyde de carbone.

Résumé

La capture du carbone de combustion implique le transport de gaz riches en CO_2 à haute température. Cette étude vise à préciser les facteurs contrôlant l'oxydation d'alliages chromino-formeurs dans ces environnements. Des alliages modèles Fe–Cr et Fe–Cr–Ni ont ainsi été exposés à des mélanges Ar–CO_2–H_2O à 650 et 800 °C, et les produits de réaction examinés à l'aide de techniques de métallographie conventionnelles. La précipitation de carbures sous des couches d'oxyde indique une sursaturation en carbone à l'interface métal/oxyde, par rapport à l'atmosphère extérieure. Sur la base d'un modèle d'équilibre thermodynamique local, les vitesses de carburation et fractions volumiques de précipités mesurées sont utilisées pour évaluer l'influence de la composition de l'oxyde et de la présence d'H_2O dans le gaz sur le transport du carbone. En analysant la déplétion en chrome dans l'alliage sous-jacent, nous montrons que la carburation limitée sous une couche de chromine n'altère pas la stabilité de l'oxyde. L'évolution morphologique des nodules d'oxydes riches en fer formés à la suite de la rupture localisée de la chromine est mise en relation avec la capacité de l'alliage à fournir du chrome à l'interface métal/oxyde. L'application de modèles de germination-croissance aux cinétiques de dévelopement de nodules permet d'évaluer la résistance des couches de chromine via des fréquences de germination déterminées à partir des taux de recouvrement de nodules et des gains de masse des échantillons. Nous examinons enfin l'importance relative de la germination et de la croissance des nodules dans le contrôle de la performance globale des alliages en fonction de la température de réaction.

Mots clés

Oxydation, carburation, dioxyde de carbone, vapeur d'eau.

Table of Contents

Introduction

While coal-fired power plants represent a main source of electricity for many countries, the low production costs associated with coal combustion are offset by carbon dioxide emission in the atmosphere, contributing to the greenhouse effect. Renewable energies constitute a promising alternative to the use of fossil fuels, but considerable development of these technologies is needed to meet the ever-growing demand for energy. In these conditions, coal is predicted to remain indispensable for energy generation in the next decades [1]. As a consequence, advanced power generation technologies are being developed to mitigate CO_2 emissions whilst preserving the economic advantages of coal combustion. Current innovation is focused on improved power plant efficiency, and CO_2 capture with a view to its geological sequestration. At the forefront of this global effort, countries involved include Germany [2] and the USA [3]. Australia is particularly concerned, because it relies heavily on coal for power supply, and also as a core element of its economy. In recent years, Australia has been fostering research and development for CO_2 capture and storage through various state and/or industry-based initiatives [4–7].

Oxyfuel combustion [8–10] is an emerging technology which consists of burning coal in a mixture of oxygen and recirculated exhaust gas rather than in air. Eliminating N_2 generates a flue gas mainly composed of CO_2 and H_2O, allowing easier CO_2 separation. However, the gas mixture, heated at temperatures of around 600 °C and above, raises concern as to the corrosion resistance of the steels employed as piping or heat exchanger materials. While alloy design is primarily concerned with mechanical properties, and, in particular, creep resistance, corrosion is of critical importance. Not only will metal loss reduce the effective load-bearing section of a component, but fast oxide scale growth can act as an insulating barrier, thereby affecting heat transfer and causing localised overheating. In addition, scale spallation can lead to erosion of components located downstream [11].

Ferritic, martensitic or austenitic chromium steels are used for various heat-resisting applications at moderate temperatures. Resistance of these alloys to corrosion relies on the formation of slow-growing, chromium-rich oxide scales. As chromium is oxidised preferentially over iron or any other alloy component, oxidation is defined as *selective*. This state of *protective* oxidation, thus named because of the low reaction rate, requires a minimum amount of chromium to be available at the metal/oxide interface. If the alloy fails to deliver a sufficient flux of chromium to its surface, rapid iron oxide grows results. Non-selective oxidation is associated with a rapid acceleration of the reaction rate, termed *breakaway*.

The oxidation behaviour of chromium steels in CO_2-based environments has been widely studied, in particular because carbon dioxide has been employed as a

coolant in nuclear power plants. Alloys which oxidise protectively in air have been shown to suffer breakaway oxidation in CO_2 [12–14]. Although carbon dioxide is expected to pose no threat in terms of carburisation, available information indicates that conventional materials can be attacked by carbon upon exposure to CO_2. Extensive internal precipitation of chromium-rich carbides has been shown [12] to hinder outward chromium diffusion, thereby inhibiting selective oxidation.

Corrosion by water vapour is also well documented, because many industrial processes involve steam, for example as a heat transfer medium in power plants or as a product/reactant in solid oxide fuel/electrolyser cells. The addition of H_2O to a gas mixture, or its substitution for oxygen, is known to trigger breakaway oxidation of Fe–Cr alloys [15–18]. Various explanations of this effect have been proposed, and are detailed subsequently.

While the mechanisms underlying the deleterious effects of CO_2 and H_2O might differ, maintaining protective oxidation in both of these gases requires relatively high chromium concentrations, and in particular, higher than in air. Essentially, as both CO_2- and H_2O-rich environments are highly corrosive, it is necessary to investigate the oxidation of alloys exposed to gas mixtures containing large amounts of both species, a situation which has so far received little attention.

The present work is concerned with fundamental aspects rather than applications in industrial service conditions. Model Fe–Cr and Fe–Cr–Ni alloys are considered in place of ferritic and austenitic chromium steels, respectively. Similarly, the gases employed are model Ar–CO_2–H_2O mixtures. Excluding minor alloying elements, which are necessary in terms of material manufacturing and mechanical properties, and additional gas components, which are unavoidable in actual service conditions, allows a simplified study of the combined effects of CO_2 and H_2O on selective oxidation of chromium.

The first Chapter of the present manuscript contains a review of relevant works available in the literature, first to provide a general framework of high temperature oxidation, and subsequently to define the issues specifically related to reaction in CO_2–H_2O. Experimental procedures and characterisation techniques are described in Chapter 2, and experimental results are gathered in Chapter 3. The discussion is organised in three parts of increasing complexity. Chapter 4 is concerned with determining how the growth of Fe-rich oxide scales is affected by alloy and gas composition. Chapter 5 addresses the issue of carburisation. Attention is focused on the thermodynamic conditions prevailing at the surface of oxidised alloys and on the mechanism of internal carbide formation, the ultimate aim being to examine the conditions under which carburisation can affect selective oxidation. The mechanism

and kinetics of breakaway oxidation are investigated in Chapter 6. The transition from protective oxidation to fast scaling is in essence a localised phenomenon, but its consequences are measured at the scale of a laboratory specimen. This final Chapter aims to analyse the factors controlling chromium selective oxidation in terms of both local reaction mechanisms and general alloy performance, and also to discuss the use of techniques employed to relate micro and macroscopic scale descriptions.

* * *

This thesis was prepared under a cotutelle arrangement with the University of New South Wales (UNSW) and the Institut National Polytechnique de Toulouse (INPT).

This work was conducted under the supervision of David J. Young and Daniel Monceau, at the School of Materials Science and Engineering, UNSW (Sydney, Australia), from February 2009 to December 2010 and from January 2012 to July 2012, and at the Centre Inter-universitaire de Recherche et d'Ingénierie des Matériaux, INPT (Toulouse, France), from January 2011 to December 2011. Financial support was provided by the Australian Research Council Discovery program. Additional funding was obtained through a Cotutelle Grant jointly provided by the French Embassy in Australia and the Australian Academy of Science, and through a Cotutelle Grant from the INPT.

Chapter 1

Literature review

The present literature survey is aimed at providing a scientific framework for this study. High temperature alloys are designed to withstand chemically aggressive environments, mostly by producing protective oxide scales. Exposure to multicomponent gas mixtures can lead to complex oxidation patterns, which result from interdependent reactions.

Section 1.1 addresses the reaction of pure metals with oxygen as a single oxidant, laying the foundations of high temperature oxidation. General principles pertaining to the oxidation of alloys are presented in Section 1.2, where, again, the reacting atmosphere contains no other oxidant than oxygen. The particular case of Fe–Cr alloys is treated in Section 1.3, while Section 1.4 briefly shows how the general principles of oxidation apply to the reaction of Fe–Cr alloys with carbon. The structure of these four general parts was inspired by Young's [19] and Birks and Meier's [20] textbooks on high temperature oxidation.

The combined effects of oxidation and carburisation are introduced in Section 1.5, in which results related to reaction in CO_2-rich atmospheres are reviewed. The oxidation behaviour of Fe–Cr alloys in H_2O-rich gases is discussed in Section 1.6, and the last Section briefly addresses the case where both CO_2 and H_2O are present at significant concentrations.

1.1 Oxidation of pure metals

This Section is aimed at defining general concepts related to high temperature oxidation; it is concerned with the reaction of pure metals with oxygen as a single oxidant. Thermodynamics and mechanistic aspects are first presented. Then, the cases of iron and chromium are briefly described. The last part deals with some aspects related to the mechanical integrity of oxide scales.

1.1.1 Thermodynamics of oxidation

The reaction of a metal M with O_2, leading to the formation of the oxide M_aO_b, is the result of both oxidation of the metal and reduction of O_2, which are described by the following half equations:

$$a\,\mathrm{M} = a\,\mathrm{M}^{\frac{2b}{a}+} + 2b\,\mathrm{e}^- \tag{1.1}$$

$$\frac{b}{2}\,\mathrm{O_2} + 2b\,\mathrm{e}^- = b\,\mathrm{O}^{2-} \tag{1.2}$$

The overall equation for this reaction is written

$$a\,\mathrm{M(s)} + \frac{b}{2}\,\mathrm{O_2\,(g)} = \mathrm{M_aO_b\,(s)} \tag{1.3}$$

An equilibrium constant $K_{1.3}$ is associated with this reaction, so that when the system is in thermodynamic equilibrium,

$$\frac{a_{\mathrm{M_aO_b}}}{a_{\mathrm{M}}^{\mathrm{a}} p_{\mathrm{O_2}}^{\mathrm{b/2}}} = K_{1.3} \tag{1.4}$$

where a_i is the activity of species i and $p_{\mathrm{O_2}}$ the oxygen partial pressure. The constant $K_{1.3}$ is defined by

$$K_{1.3} = \exp\left(-\frac{\Delta_{\mathrm{r}} G^0_{1.3}}{RT}\right) \tag{1.5}$$

where $\Delta_{\mathrm{r}} G^0_{1.3}$ is the standard free energy of reaction (1.3), R the ideal gas constant and T the temperature. When one considers the formation of 1 mol of product from reactants in their standard states, this variable is called the standard free energy of formation of the product and noted $\Delta_{\mathrm{f}} G^0$. The case of a pure metal leading to a single phase oxidation product is considered here, so that activities are equal to unity for the condensed phases. The oxygen pressure in the M–$\mathrm{M_aO_b}$–$\mathrm{O_2}$ system in thermodynamic equilibrium is then given by

$$\frac{1}{\left(p_{\mathrm{O_2,eq}}\right)^{b/2}} = \exp\left(-\frac{\Delta_{\mathrm{f}} G^0}{RT}\right) \tag{1.6}$$

The quantity $p_{\mathrm{O_2,eq}}$ is called the dissociation pressure of the oxide; this is the minimum value of $p_{\mathrm{O_2}}$ required to oxidise the metal. To predict the stability of the oxide, the oxygen partial pressure of the system has to be compared to $p_{\mathrm{O_2,eq}}$:

- if $p_{\mathrm{O_2}} < p_{\mathrm{O_2,eq}}$, the metal is stable and stays unoxidised;
- if $p_{\mathrm{O_2}} \geqslant p_{\mathrm{O_2,eq}}$, the oxide is stable and expected to grow on the metal.

The standard free energy of reaction, $\Delta_{\mathrm{r}} G^0$, results from the contribution of the standard enthalpy of reaction, $\Delta_{\mathrm{r}} H^0$, and the standard variation of internal entropy ΔS^0:

$$\Delta_{\mathrm{r}} G^0 = \Delta_{\mathrm{r}} H^0 - T\Delta S^0 \tag{1.7}$$

The Ellingham approximation assumes that $\Delta_{\mathrm{r}} H^0$ and ΔS^0 are independent of temperature. Table 1.1 gives values of these parameters, and of the corresponding $p_{\mathrm{O_2,eq}}$ at 800 °C for iron and chromium oxides. It is seen that $\mathrm{Cr_2O_3}$ is more stable than iron oxides (chromium is less noble than iron).

1.1.2 Mechanisms and kinetics of oxidation

1.1.2.1 Electrochemical reactions and mass transport

In ideal cases, the oxide formed as a result of high temperature oxidation is a solid phase, compact and adherent to the metal surface. Such an oxide scale acts as

Table 1.1 – Standard free energies for the formation of iron and chromium oxides [19] and corresponding dissociation pressures at 800 °C.

	$\Delta_r H^0$ ($kJ\,mol^{-1}$)	ΔS^0 ($J\,mol^{-1}\,K^{-1}$)	$p_{O_2,eq}$ at 800 °C (atm)
$Fe+\frac{1}{2}O_2=FeO$	-264.9	-65.4	1.1×10^{-19}
$3\,FeO+\frac{1}{2}O_2=Fe_3O_4$	-312.2	-125.1	4.7×10^{-18}
$2\,Fe_3O_4+\frac{1}{2}O_2=3\,Fe_2O_3$	-249.5	-140.7	2.6×10^{-10}
$\frac{2}{3}Cr+\frac{1}{2}O_2=\frac{1}{3}Cr_2O_3$	-373.4	-86	4.3×10^{-28}

a physical barrier between the metal and the gas, preventing direct contact. The metal is ionized at the metal/oxide interface and oxygen at the oxide/gas interface, but for the overall reaction (1.3) to proceed further, transport of one or both ions across the oxide scale is required. According to Wagner's theory of oxidation [21], mass transport results from two distinct driving forces, and is thus described in terms of charged species migrating in an electrical field and of chemical species diffusing along chemical potential gradients. Solid state diffusion is enabled by the presence of defects in the oxide phase, which can be point defects (vacancies and interstitials), 2D (dislocations) or 3D (grain boundaries) defects. In the latter two cases, the transport is called short-circuit diffusion. The relative contributions of lattice and grain boundary transport depend on temperature and oxide grain size.

The kinetics of oxidation are determined by the rate of the slowest step of the process. Rate laws associated with the most common rate-controlling steps are presented in the following paragraphs.

1.1.2.2 Rate laws

Linear kinetics

If the rate-controlling step proceeds at a constant rate, oxidation kinetics follow a linear law

$$X = k_\ell t \tag{1.8}$$

where X is the scale thickness, k_ℓ the linear rate constant and t the oxidation time. Linear kinetics may be observed in the early, transient stage of oxidation, as the thin oxide film supports very rapid diffusion, and oxidation is limited by the relatively slow interfacial processes. Porous or non adherent scales do not constitute a barrier separating the alloy from the atmosphere, and the condition of fast metal supply is fulfilled throughout the oxidation process, which results in continued linear kinetics. Linear kinetics may also be obtained when a fast-growing oxide is formed in a dilute

or otherwise slowly-reacting atmosphere, as oxygen supply by gas phase diffusion or adsorption at the oxide surface is rate-controlling.

Parabolic kinetics

Rate control by diffusion of one or both reactants across the oxide scale results in parabolic kinetics. This happens when the scale is compact and adherent, and sufficiently thick for chemical and electrical potential gradients to be established. The corresponding rate law is of the form

$$X^2 = 2\,k_\mathrm{p} t \tag{1.9}$$

where k_p is the parabolic rate constant. In practical cases, the extent of oxidation is commonly determined by measuring the weight gain of the specimen per unit of surface area, $\dfrac{\Delta m}{A}$. The parabolic law is then written

$$\left(\frac{\Delta m}{A}\right)^2 = 2\,k_\mathrm{pm} t \tag{1.10}$$

where k_pm is the gravimetric rate constant, usually with units $\mathrm{g^2\,cm^{-4}\,s^{-1}}$. The two parabolic rate constants are related, for an oxide $\mathrm{M_aO_b}$, via

$$k_\mathrm{pm} = \left(\frac{bM_\mathrm{O}}{V_{\mathrm{M_aO_b}}}\right)^2 k_\mathrm{p} \tag{1.11}$$

where M_O is the atomic mass of oxygen, 16 $\mathrm{g\,mol^{-1}}$, and $V_{\mathrm{M_aO_b}}$ the oxide molar volume.

Since initial oxide growth is not limited by diffusion, parabolic kinetics are more accurately described as

$$X^2 = 2\,k_\mathrm{p} t + k' \tag{1.12}$$

where k' reflects the contribution of the oxide formed before diffusion-controlled kinetics are reached.

Other rate laws

In situations where the oxide of interest grows from another preexisting oxide, and where both diffusion and surface reactions affect the oxidation kinetics, a general expression for the rate law is [22–24]

$$t = a + b\frac{\Delta m}{A} + c\left(\frac{\Delta m}{A}\right)^2 \tag{1.13}$$

where a and b are functions of the mass of the preexisting oxide and the linear and parabolic constants of the new oxide, and $c = (2k_\mathrm{pm})^{-1}$.

Finally, kinetics of oxidation at low temperatures have been described using logarithmic or other rate laws [25], which are not of interest to the present work.

1.1.2.3 Stages of the oxidation process

The main stages undergone by a pure metal exposed to an atmosphere containing oxygen as a single oxidant can be described in terms of metal activity across the growing oxidation product, as schematically represented in Fig. 1.1. Figure 1.2 shows the corresponding oxidation kinetics. Initially, the metal supply by diffusion through the thin oxide film is very rapid. In this state of virtual equilibrium, the metal activity is close to unity at the oxide surface (Fig. 1.1(a)). The oxidation rate is constant and controlled by the surface reaction. As the oxide thickens, the metal activity at the oxide/gas interface decreases and a metal activity gradient is established across the scale. Since the metal activity at the oxide surface cannot fall below a value of equilibrium with the atmosphere a^*_{M}, the gradient decreases as the scale thickens (Fig. 1.1(b)), and consequently the metal flux is reduced. As long as surface reactions are relatively slow, the oxygen supply cannot keep up with the metal flux, and interfacial equilibrium is not reached. Conversely, if surface reactions are fast enough, the metal activity will reach its limiting value, and the oxide/gas interface be at equilibrium. The reaction rate then decreases according to a parabolic law, and this stage is observed as long as a compact and adherent scale can be maintained. Ultimately this scale might suffer mechanical damage (cracks, spallation), possibly allowing gas access to the metal (Fig. 1.1(c)). Since diffusion-controlled oxidation rates decrease with increasing scale thickness, partial or total scale spallation, which represents a gross weight loss, results in accelerated reaction. The net weight change, which may be positive or negative, depends on the particular morphology and extent of damage encountered, and on the frequency at which it occurs. Similarly, if the oxide forms volatile compounds, the kinetics of combined growth and volatilisation will depend on the relative rates of the two processes, as shown schematically in Fig. 1.2.

When the kinetically limiting step is diffusion across the scale, as the oxidation rate continuously decreases, oxidation is sometimes called protective. In the literature, the word protective has thus been applied regardless of the value of the rate constant, including for relatively fast-growing oxides, such as Fe-rich oxides. The more recent use, favoured in the present document, is restricted to relatively slow-growing oxides (mainly Cr_2O_3 and Al_2O_3), such that fast formation of Fe-rich oxides is called non-protective, even though the oxidation rate may continually decrease as a result of diffusion control.

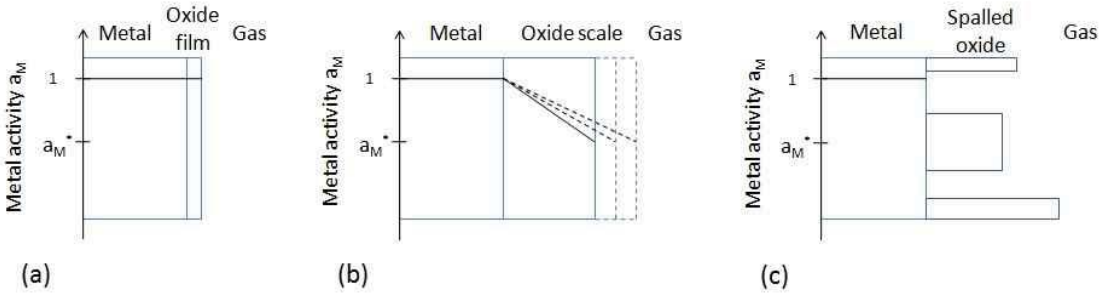

Figure 1.1 – Schematic representation of metal activity in a growing oxidation product. (a) thin oxide film; (b) compact and adherent oxide scale; (c) spalled oxide scale.

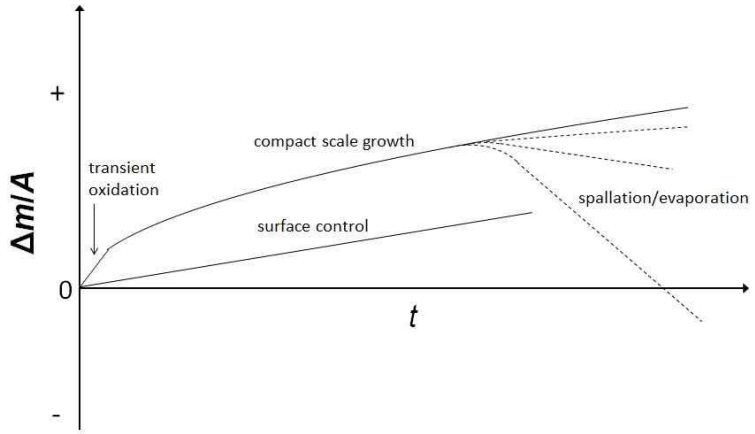

Figure 1.2 – Schematic representation of oxidation kinetics in various situations.

1.1.2.4 Factors affecting diffusion-controlled kinetics

During the steady-state, parabolic stage of oxidation, the value of the rate constant is a function of several parameters. The temperature and oxidant pressure, the oxide constitution and chemical composition, on the one hand, determine the chemical and electrical potential gradients across the scale. Other factors, such as the scale microstructure or mechanical state, may also affect oxidation kinetics. While no theoretical treatment may possibly take into account all effects, the Wagner theory of oxidation [21] is a rather complete mechanistic analysis of the process, which has proved useful to the quantitative prediction or rationalisation of oxidation rates, as well as for the fundamental understanding it provides. Based on the bulk transport properties of the scale and the driving forces for its formation, the theory leads to an expression of the parabolic rate constant as a function of physical parameters, which can be measured independently (e.g., diffusion coefficients and concentrations).

Assuming that cationic transport is rate-controlling and using Fick's first law, a simplified treatment enables parabolic kinetics to be derived. The outward cation flux, j_{M}, is opposite to the inward flux of cation defects (here taken as vacancies in the cation sublattice):

$$j_{\mathrm{M}} = -j_{\mathrm{V_M}} \tag{1.14}$$

$$j_{\mathrm{V_M}} = -\frac{(1+\alpha) D_{\mathrm{V_M}} \left([\mathrm{V_M}]^{(\mathrm{II})} - [\mathrm{V_M}]^{(\mathrm{I})} \right)}{X} \qquad \text{for } X > 0 \tag{1.15}$$

where α and $D_{\mathrm{V_M}}$ are the absolute charge and diffusion coefficient of the vacancies, and $[\mathrm{V_M}]^{(\mathrm{II})}$ and $[\mathrm{V_M}]^{(\mathrm{I})}$ the vacancy concentrations at the oxide/gas and metal/oxide interface, respectively. The evolution of the scale thickness with time, for an oxide $\mathrm{M_aO_b}$, follows the differential equation

$$\frac{dX}{dt} = \frac{V_{\mathrm{M_aO_b}}}{\mathrm{a}} j_{\mathrm{M}} \tag{1.16}$$

Assuming that the interfaces are at thermodynamic equilibrium, the boundary vacancy concentrations are taken to be constant. If, in addition, $D_{\mathrm{V_M}}$ is constant across the scale, Eq. (1.16) can be written

$$\frac{dX}{dt} = \frac{k_{\mathrm{p}}}{X} \qquad \text{for } X > 0 \tag{1.17}$$

with

$$k_{\mathrm{p}} = \frac{V_{\mathrm{M_aO_b}}}{\mathrm{a}} (1+\alpha) D_{\mathrm{V_M}} \left([\mathrm{V_M}]^{(\mathrm{II})} - [\mathrm{V_M}]^{(\mathrm{I})} \right) \tag{1.18}$$

Integrating with $X(t=0) = 0$, one obtains Eq. (1.9).

Temperature and oxygen partial affect the rate constant via the phase boundary defect concentrations and the defect diffusion coefficient. Point defect equilibrium will be illustrated here in the case of cation-deficient compounds, which form cation vacancies according to

$$\frac{1}{2}\,\mathrm{O_2} = \mathrm{O_O} + \alpha\,\mathrm{h^{\cdot}} + \mathrm{V_M^{\alpha\cdot}} \tag{1.19}$$

where the Kroger-Vink notation [26] hase been used: $\mathrm{S_M^X}$ represents the oxide lattice species, where the subscript designates the normal occupancy in a perfect crystal and the principal symbol designates the species actually occupying the site. The superscript indicates the effective charge of the defect, using prime, dot and cross for negative, positive and zero charge, respectively, and $\mathrm{h^{\cdot}}$ is an electron hole. The law of mass action is written

$$K_{1.19} = \frac{[\mathrm{V_M^{\alpha\cdot}}]\,[\mathrm{h^{\cdot}}]^{\alpha}}{p_{\mathrm{O_2}}^{1/2}} \tag{1.20}$$

The condition for lattice electroneutrality is

$$[\mathrm{h}^{\cdot}] = \alpha\,[\mathrm{V}_{\mathrm{M}}^{\alpha\cdot}] \tag{1.21}$$

and the law of mass action results in

$$[\mathrm{V}_{\mathrm{M}}^{\alpha\cdot}] \propto p_{\mathrm{O_2}}^{\frac{1}{2(\alpha+1)}} \tag{1.22}$$

It follows from Eq. (1.18) and (1.22) that k_{p} is proportional to $\left(p_{\mathrm{O_2}}^{1/n}\right)^{(\mathrm{II})} - \left(p_{\mathrm{O_2}}^{1/n}\right)^{(\mathrm{I})}$, with $n = 2(\alpha+1)$. Since the oxygen partial pressure at the metal/oxide interface is usually negligible in comparison to that at the oxide/gas interface (values such as those given in Table 1.1 are to be compared with the atmosphere $p_{\mathrm{O_2}}$), k_{p} varies with $\left(p_{\mathrm{O_2}}^{1/n}\right)^{(\mathrm{II})}$. Conversely, when oxide growth occurs predominantly by inward anionic diffusion, the rate constant is not affected by the ambient oxygen pressure.

The vacancy concentration is seen using Eqs. (1.20) and (1.21) to be proportional to the equilibrium constant for vacancy formation, $K_{1.19}$, which depends on temperature according to

$$K_{1.19} = \exp\left(-\frac{\Delta_{\mathrm{r}}H^0_{1.19} - T\Delta S^0_{1.19}}{RT}\right) \tag{1.23}$$

Similarly, the vacancy diffusion coefficient is thermally activated, which can be expressed by the Arrhenius equation

$$D_{\mathrm{V_M}} = D^0_{\mathrm{V_M}} \exp\left(-\frac{E_{\mathrm{a}}}{RT}\right) \tag{1.24}$$

where $D^0_{\mathrm{V_M}}$ is a constant and E_{a} the activation energy. Accordingly, k_{p} varies with $\exp\left(-\dfrac{E_{\mathrm{a}} + \Delta_{\mathrm{r}}H^0_{1.19}}{RT}\right)$.

1.1.3 Oxidation of iron and chromium

1.1.3.1 Iron

The Fe–O phase diagram presented in Fig. 1.3 shows that iron oxidises to form three oxide phases: wustite FeO (stable at temperatures above 570 °C), magnetite Fe_3O_4 and hematite Fe_2O_3. The blue and red lines are called diffusion paths and determine the local equilibrium state of the Fe–O system. In the presence of oxygen at a temperature higher than 570 °C, the blue diffusion path indicates that FeO will form on the iron surface, then Fe_3O_4 will grow on the wustite surface as a result of the oxidation of iron and wustite, and these phases are expected to oxidise into Fe_2O_3. Thus, providing that oxygen is available in a sufficient quantity, the final

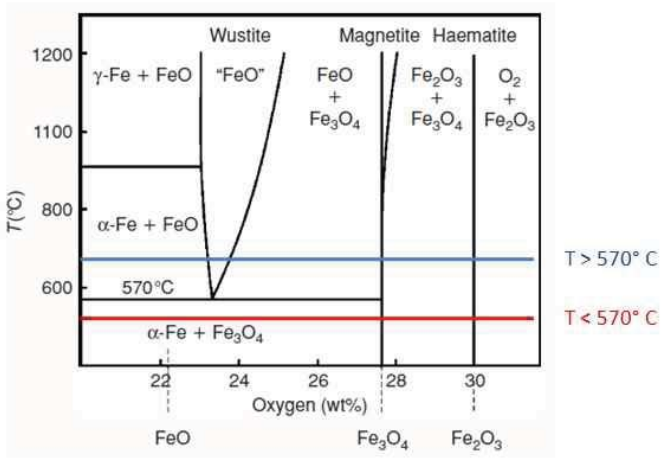

Figure 1.3 – Diffusion paths on the Fe–O phase diagram.

(and global) equilibrium state of the system initially formed of iron in oxygen is $Fe_2O_3 + O_2$.

However, the global thermodynamic description is not necessarily adapted to the experimental observation, mainly because mass transport by solid-state diffusion, which is critical when solid phases react, is not instantaneous in comparison to the experimental time scale. Thus the kinetics of the system are of great practical importance. The transport properties of oxide phases are determined by their defect structure. The defect structures of iron oxides are complex and will not be discussed here in detail. A quite extensive review of the defect structure and transport properties of the three iron oxides has been published by Gleitzer in Ref. [27].

The relationship between defect structure and transport properties will be illustrated here using the work of Dieckmann and Schmalzried [28,29] on iron diffusivity in Fe_3O_4. These authors measured the iron tracer diffusion coefficient at various p_{O_2}, in the whole stability range of Fe_3O_4. As shown in Fig. 1.4, the values are proportional to $p_{O_2}^{2/3}$ at high p_{O_2} and to $p_{O_2}^{-2/3}$ at low p_{O_2}. The predominant defects are identified as cation vacancies at high p_{O_2} and cation interstitials at low p_{O_2}. Describing magnetite as an inverse spinel, that is, $Fe^{3+}\left[Fe^{2+}Fe^{3+}\right]O_4$, where the first trivalent ion is in a tetrahedral site, and the brackets indicate octahedral sites, the corresponding defect equations are written

$$\frac{2}{3}\,O_2 + 3\,Fe_o^{2+} = V_o + 2\,Fe_o^{3+} + \frac{1}{3}\,Fe_3O_4 \tag{1.25}$$

$$Fe_o^{2+} = Fe_i^{2+} + V_o \tag{1.26}$$

where the subscripts o and i refer to octahedral and interstitial sites, respectively.

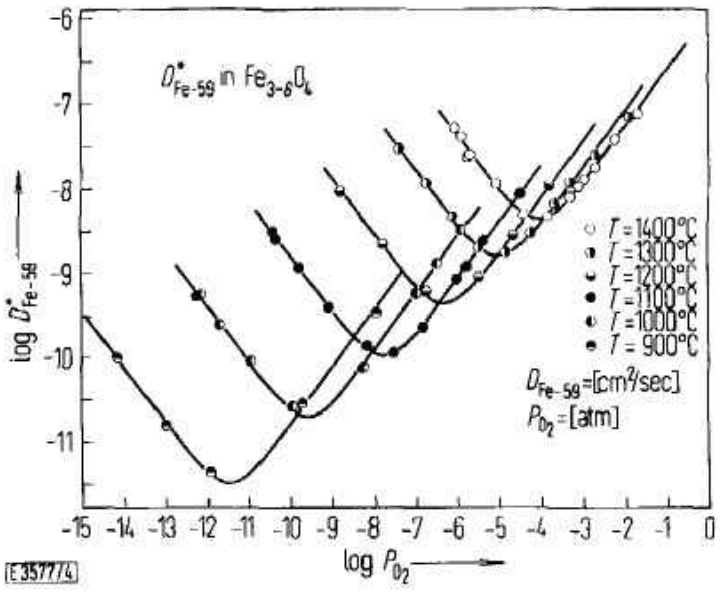

Figure 1.4 – Iron tracer diffusion in magnetite as a function of temperature and oxygen partial presure, after [28].

The corresponding laws of mass action are

$$K_{1.25} = \frac{[\mathrm{V_o}]\,[\mathrm{Fe_o^{3+}}]^2}{p_{\mathrm{O_2}}^{2/3}\,[\mathrm{Fe_o^{2+}}]^3} \tag{1.27}$$

$$K_{1.26} = \frac{[\mathrm{V_o}]\left[\mathrm{Fe_i^{2+}}\right]}{[\mathrm{Fe_o^{2+}}]} \tag{1.28}$$

Since divalent and trivalent cations on octahedral sites are present in the whole crystal, their concentration is equal to unity, and it follows that

$$[\mathrm{V_o}] \propto p_{\mathrm{O_2}}^{2/3} \tag{1.29}$$

$$\left[\mathrm{Fe_i^{2+}}\right] \propto p_{\mathrm{O_2}}^{-2/3} \tag{1.30}$$

The same $p_{\mathrm{O_2}}$ dependances are obtained for tetrahedral vacancies and trivalent interstitials.

Table 1.2 gives a simplified summary of the crystal structure, deviation from stoichiometry and associated defects for the three iron oxide phases. In the case of FeO, the possibility of having a high iron vacancy concentration (associated with a wide stability field in Fig. 1.3) leads to high cation mobility (see experimental data in Refs. [30] and [31]). As a consequence, FeO growth is relatively fast. Conversely, since Fe_2O_3 is highly stoichiometric, the defect concentration is low and so is cation mobility. Thus, Fe_2O_3 grows much slower than Fe_3O_4 and FeO.

Table 1.2 – Crystal structure, predominant defects and deviation from stoichiometry for iron oxides stable at high temperature, after Ref. [27].

Phase	Crystal structure	Predominant defects	Deviation from stoichiometry
FeO	halite	V''_{Fe}	$Fe_{1-x}O$ $0.055 \leqslant x \leqslant 0.155$
Fe_3O_4	inverse spinel	V''_{Fe}/V'''_{Fe} at high p_{O_2} $Fe_i^{\cdot\cdot}/Fe_i^{\cdot\cdot\cdot}$ at low p_{O_2}	$Fe_{3-x}O_4$
α-Fe_2O_3	corundum	$V_O^{\cdot\cdot}$, $Fe_i^{\cdot\cdot\cdot}$ and $Fe_i^{\cdot\cdot}$	$Fe_{2+y}O_{3-x}$ (small non-stoichiometry)

The large differences between the growth rates of iron oxides were evident in the work of Paidassi [32] on iron oxidation in air between 700 and 1250 °C. In this temperature range, the three oxides were formed in successive layers, from FeO in contact with the metal to Fe_2O_3 in contact with the atmosphere. The layers grew according to parabolic kinetics with steady-state relative thicknesses of 1, 4 and 95% for Fe_2O_3, Fe_3O_4 and FeO, respectively. An Arrhenius plot of the global parabolic constant is given in Fig. 1.5 [32], and is in good agreement with the results of Davies et al [33]. Paidassi [32] also provided parabolic rate constants for the three

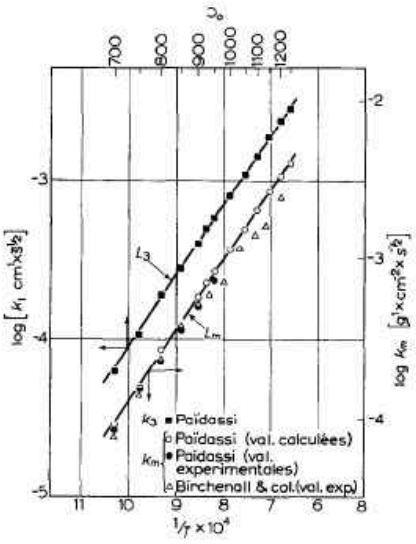

Figure 1.5 – Influence of the temperature on the growth rate of FeO, expressed as thickness increase (k_3) and weight gain (k_m). Empty circles represent values of k_m calculated from thickness measurements [32].

individual iron oxide layers, using the rate law

$$e_i = k_i\sqrt{t} + \epsilon_i \tag{1.31}$$

where e_i is the thickness, k_i is the rate constant ($k_i = \sqrt{2k_\mathrm{p}}$ with k_p defined in Eq. (1.9)), ϵ_i is a constant, and $i = 1, 2, 3$ for the Fe_2O_3, Fe_3O_4 and FeO layer, respectively. At 800 °C, the author thus obtained $k_1 = 1.41 \times 10^{-6}$ cm s$^{-1/2}$, $k_2 = 7.5 \times 10^{-6}$ cm s$^{-1/2}$, $k_3 = 1.93 \times 10^{-4}$ cm s$^{-1/2}$, and $k = 2.0 \times 10^{-4}$ cm s$^{-1/2}$ for the whole scale. These figures confirm that FeO grows much faster than the two other oxides, and is responsible for the main part of the overall scale growth. An extensive theoretical treatment of the problem of parabolic, multilayer scale formation, applied to the oxidation of iron, has been published by Gesmundo and Viani [34, 35].

1.1.3.2 Chromium

High temperature oxidation of chromium results in the formation of Cr_2O_3, which has the corundum structure. Although it has been the object of extensive investigation, the defect structure of Cr_2O_3 remains unclear [25]. After reviewing electrical conductivity and diffusion results, Kofstad [25] suggested that predominant defects are chromium interstitials at low oxygen partial pressure, with oxygen vacancies as minority defects, and oxygen interstitials or chromium vacancies at near-atmospheric oxygen partial pressure.

At temperatures higher than 700 °C, Cr_2O_3 growth kinetics on pure chromium are generally reported as parabolic, but rate constants values vary greatly between the different studies [36]. Specimen preparation, and in particular the initial surface state, has been shown [37] to be a determining factor in the value of the rate constant and even in the growth mechanism. Chromium and oxygen self-diffusion in Cr_2O_3, the role of grain boundary diffusion and the relationship between diffusivity and growth rate have been extensively studied by Sabioni et al [38–42].

At 1000 °C the average value of $k_\mathrm{pm} = 10^{-10}$–10^{-11} g^2 cm^{-4} s^{-1} can be compared with that for wustite growth on iron, 10^{-6} g^2 cm^{-4} s^{-1} (calculated from Ref. [32]). The fact that chromia grows several orders of magnitude slower than iron oxides is the reason behind the utilisation of chromia forming alloys in high temperature applications.

1.1.4 Mechanical failure of oxide scales

Slow-growing, compact and adherent oxide scales provide alloys with resistance to corrosion. As a result of chemical, mechanical or combined effects, scale failure can

lead to changes in oxidation mechanism and kinetics. This Section is concerned with mechanical failure of thermodynamically stable oxide scales; effects related to selective oxidation are dealt with subsequently.

Mechanical failure results from stress accumulation in an initially adherent scale. As long as metal and oxide are bound, their assemblage can be regarded as a composite material. In the hypothetical case of an external load parallel to the metal/oxide interface, the two phases undergo the same deformation. Since it is stiffer, higher stress will be generated in the ceramic phase. In addition, metals have lower yield strengths, and thus greater ability to relieve stress by plastic deformation. For these reasons, the mechanical integrity of the metal-oxide system is limited by those of the oxide and of the interface.

Specimen geometry is of practical importance, since stresses are amplified in zones of small curvature radius. Specimen edges are thus particularly prone to mechanical failure. The integrity of the scale is maintained as long as stress is accommodated by plastic deformation, which occurs by creep at high temperature.

Epitaxial stresses

In the very first stage of oxidation, oxide crystals grow in epitaxial relation with the metal substrate. As the phases have different lattice parameters, epitaxial stresses are generated, which will only affect thin oxide films.

Growth stresses

Oxide formation is associated with a volume change, as a result of the difference of molar volume between metal and oxide. This difference can be described by the Pilling and Bedworth ratio,

$$\rho_{\mathrm{PB}} = \frac{V_{\mathrm{M_aO_b}}}{aV_{\mathrm{M}}} \tag{1.32}$$

In most cases, the molar volume of the oxide is higher than that of the metal, and $\rho_{\mathrm{PB}} \geqslant 1$. For example $\rho_{\mathrm{PB}} \simeq 2$ for the Cr–Cr_2O_3 system, and 1.7, 2.1 and 2.14 for oxidation of iron into FeO, Fe_3O_4 and Fe_2O_3, respectively. Oxide growth at the metal/oxide interface by inward oxygen diffusion is limited in space, which induces compressive stress. In contrast, the oxide/gas interface is mechanically free, so that scales growing by outward cation diffusion are apparently not affected. However, stress can be generated in these scales if the outer surface is not flat, and if the strain accompanying the transformation is not entirely perpendicular to the interface. Furthermore, as the volume of the metal core decreases, scale adhesion to the metal results in compressive stress parallel to and tensile stress normal to the metal surface [43]. Oxide formation within the scale by counterdiffusion of

cations and anions generates large compressive stress, which have been analysed by Srolowitz and Ramanarayanan [44]. Various theories for growth stress generation and relief have been reviewed by Stringer [45].

Thermal stresses

Thermal stresses are generated during temperature variations as a result of the difference in thermal expansion coefficient between metal and oxide. In the case of temperature cycling, repeated scale spallation and reformation lead to drastic metal loss (see decreasing curve in Fig. 1.2).

Injection of metal lattice vacancies

When a metal atom is ionised and enters the scale at the metal/oxide interface, a vacancy is injected in the metal lattice. The vacancies thus generated during oxidation by outward cation diffusion can be annihilated via dislocation climb at the metal/oxide interface or precipitate out as voids in the metal phase, or as planar defects such as dislocation loops. These phenomena and their consequences have been studied by several authors, for example in Refs [46, 47]. Vacancy precipitation at the metal/oxide interface may induce adhesion loss and interfacial delamination.

Porosity due to divergence in the oxygen flux

Maruyama and co-workers [48,49] modelled the formation of voids within magnetite scales resulting from divergence in the oxygen flux. The mathematical treatment involves the determination of oxygen and metal ion activities across the scale. Then, the oxygen flux is calculated and its divergence, due to the variation of oxygen diffusivity across the scale, leads to the amount of oxygen in deficiency or excess. This information is used to predict the positions of void nucleation and the extent of their growth.

Impurities

Impurities such as sulfur are known to alter scale adhesion to the alloy by segregating at the metal/oxide interface. Many studies have experimentally highlighted the detrimental effect of sulfur [50–52], be it on alumina- or chromia-formers, on Ni or Fe based alloys, after isothermal or cyclic oxidation. Sulfur is thought to segregate to intact metal/oxide interfaces and directly alter their adhesion [53,54], or to segregate to the free surface of interfacial voids and lower their surface energy, which favours their growth [55, 56]. Many other impurities can be present in alloys and alter scale adhesion by various mechanisms. In particular, if they do not form a solid solution

with the oxide and precipitate at the metal/oxide interface in the initial stage of oxidation, full contact between the scale and the metal may be locally prevented [57].

1.2 Oxidation of alloys

Reaction products of various natures and morphologies are potentially formed during oxidation of alloys, including solid-solution oxides and multiphase scales. This complexity is of decisive practical importance, since pure metals are rarely used as engineering materials.

In this Section, the main features pertaining to the oxidation of alloys in atmospheres containing oxygen as a single oxidant are described, with emphasis on binary alloys. Alloys containing three or more components present a higher degree of complexity, but the general principles can be derived from the study of binary alloys. Thermodynamic aspects are first considered. Then, the concept of selective oxidation is presented, and various oxidation morphologies are described.

1.2.1 Phase diagrams and diffusion paths

Predicting or rationalising the oxidation behaviour of alloys requires knowledge of the thermodynamics and kinetics of the system. From the point of view of thermodynamics, the study differs from that of pure metals in that metal or oxide solid solutions may be formed, and activities vary in solid solutions. The dissolution of a metal M, for which the reference state is a pure solid phase, is described as

$$\mathrm{M\,(s)} = \underline{\mathrm{M}} \tag{1.33}$$

for which the law of mass action is written

$$K_{1.33} = \exp\left(\frac{-\Delta\bar{G}_{\mathrm{M}}^{\mathrm{xs}}}{RT}\right) = \frac{N_{\mathrm{M}}}{a_{\mathrm{M}}} \tag{1.34}$$

where $\Delta\bar{G}_{\mathrm{M}}^{\mathrm{xs}}$ is the excess free energy of mixing, and contains the contribution of the enthalpy of mixing and excess entropy of mixing: $\Delta\bar{G}_{\mathrm{M}}^{\mathrm{xs}} = \Delta\bar{H}_{\mathrm{M}}^{\mathrm{m}} - T\Delta\bar{S}_{\mathrm{M}}^{\mathrm{xs}}$. The relationship between mole fraction and activity is usually written

$$a_{\mathrm{M}} = \gamma_{\mathrm{M}} N_{\mathrm{M}} \tag{1.35}$$

where γ_{M} is the activity coefficient, defined by $RT\ln\gamma_{\mathrm{M}} = \Delta\bar{G}_{\mathrm{M}}^{\mathrm{xs}}$. The energies of mixing and the activity coefficient usually vary with temperature and composition, but are independent of the composition in the case of ideal or Henrian solutions. Simple problems, such as determining the dissociation pressure of a given oxide on a given alloy, can be resolved by using empirical activity coefficients, and for example assuming the value constant in a certain composition range. However, the thermodynamics of multicomponent systems are often dealt with using dedicated

softwares, such as ThermoCalc [58] or FactSage [59], which, on the basis of assessed solid solution models, compute phase equilibria.

The composition and morphology of the oxidation products are also determined by the kinetics of the system. Again, diffusion properties are made relatively complex because of compositional effects. From a practical point of view, an alloying element is added to produce an alloy with better oxidation resistance than the base metal. The concentration of the alloying element at the metal/oxide interface has a critical role in the evolution of the system.

Phase diagrams are a useful graphical representation of a system's thermodynamics. In a ternary system, the representation commonly used is an isothermal section under the form of a Gibbs triangle. Considering diffusion paths on a phase diagram, one might take into account thermodynamic equilibrium and diffusion kinetics so as to study the steady-state morphology of the oxidation products. Basic principles pertaining to the general constitution of ternary phase diagrams and to the interpretation of the diffusion paths in terms of diffusion structure will be described here. These subjects were discussed in details by Clark and Rhines [60] and Kirkaldy and Brown [61], respectively. Under isobaric and isothermal conditions, the phase rule is written

$$F = C - P \tag{1.36}$$

where F is the number of degrees of freedom, C the number of components and P the number of phases. Thus in a ternary system, a single phase is determined by the composition of two independent components, and may be represented by a 2D field in the phase diagram, if it is not strictly stoichiometric. A two-phase region (only one independent component) is defined by a continuum of tie-lines joining two single-phase regions. Along a tie-line, the activity of all constituents is fixed, the composition of the two phases is that of the two end points, and the composition of the system may only vary through the mole fraction of the two phases. Three-phase equilibria are invariant: the compositions of the three phases are fixed, and given by the three corners of the triangle.

A few rules concerning diffusion paths will be derived here from the construction of the diagrams, as summarised by Dalvi and Coates [62]. It is to be noted that the case of an oxide scale growing in a steady state, under diffusion-control, is particular: local thermodynamic equilibrium is achieved everywhere, but the system as a whole is not at equilibrium. Furthermore, the system is spatially oriented, in that the oxygen activity is monotonically decreasing from the gas to the metal (say, along a vertical axis), but fixed in the two directions parallel to the metal surface. Thus, diffusion paths are related to actual diffusion structure as illustrated in Fig. 1.6,

where A and B are metal components. A single-phase field corresponds to a single-

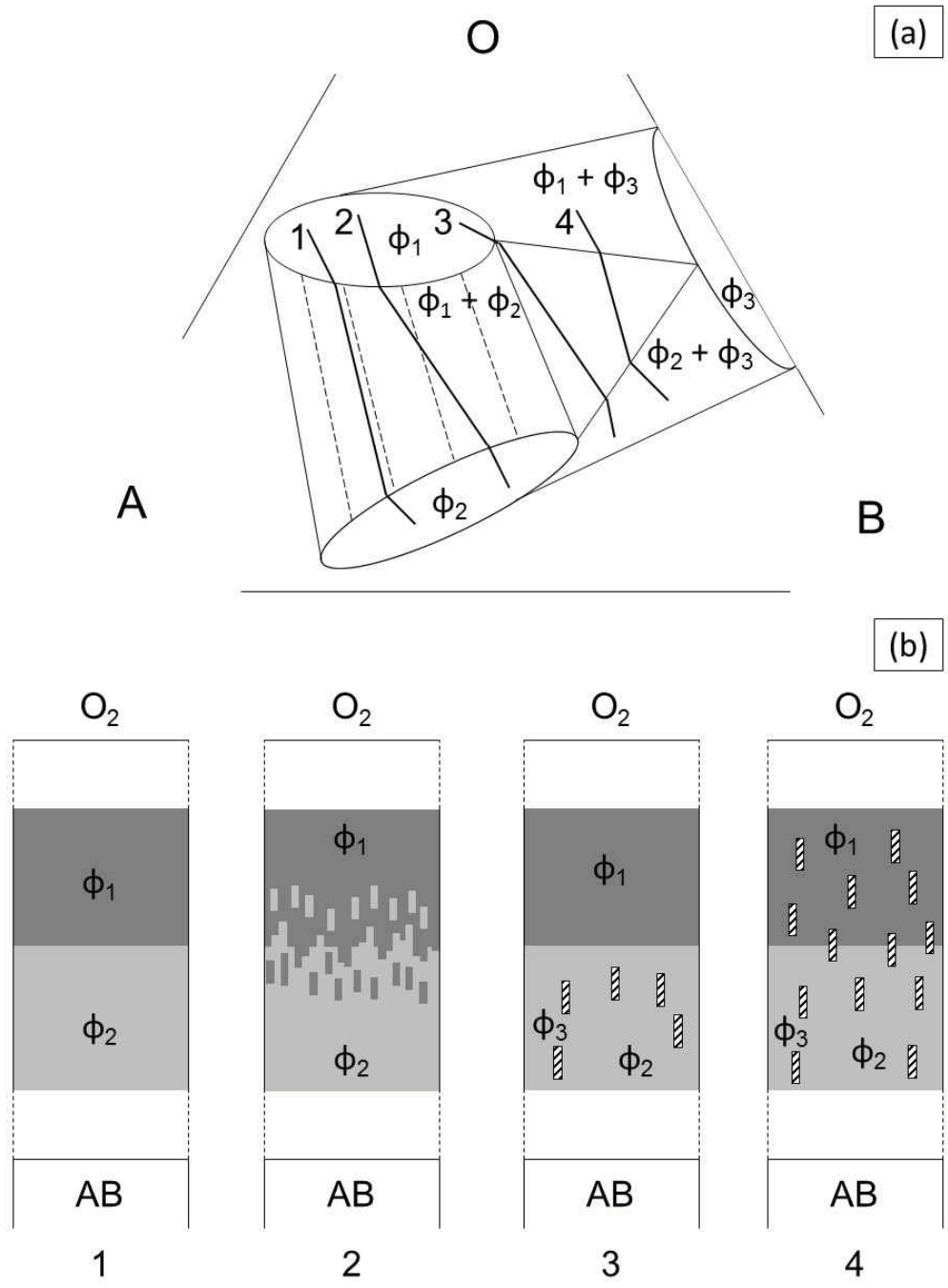

Figure 1.6 – Schematic representation of (a) diffusion paths and (b) corresponding diffusion structures.

phase layer. When traversing a two-phase field along a tie-line, all activities are fixed, and the interface is defined by a constant oxygen activity: this corresponds to a planar interface (parallel to the metal surface) between two single-phase regions

(path 1). Conversely, when cutting tie-lines, interfaces may exist with varying oxygen activity, and may therefore be unlocalised. This corresponds to a two-phase layer, that is, the precipitation of one phase into another (path 2). When traversing a three-phase triangle from a corner to a side, the diffusion structure is a planar interface between a single-phase layer and a two-phase layer (3 phases altogether, path 3). If the triangle is crossed from side to side, the planar interface is between two two-phase layers (3 phases altogether, path 4).

1.2.2 The concept of selective oxidation

A binary alloy AB is considered, where the base metal A and alloying element B react according to

$$\mathrm{A} + \frac{1}{2}\,\mathrm{O_2} = \mathrm{AO} \tag{1.37}$$

$$\mathrm{B} + \frac{1}{2}\,\mathrm{O_2} = \mathrm{BO} \tag{1.38}$$

We consider the case where the alloying element forms a more stable oxide than the base metal, such as in most engineering alloys. In terms of standard free energy of formation, this condition is expressed as

$$\Delta_\mathrm{f} G^0_{BO} < \Delta_\mathrm{f} G^0_{AO} \tag{1.39}$$

Oxide solid solutions and oxides of a metal element with various oxidation states are omitted here for simplicity.

When the alloy AB is placed under oxidising conditions, various steady-state scenarios may arise, depending on the initial concentration of the alloying element, N^0_B, and on the oxygen partial pressure in the atmosphere. Some of these possibilities have been summarised and schematically represented by Atkinson [63], as shown in Fig. 1.7. A more complete treatment of scale morphologies observed on binary alloys has been published by Bastow et al. [64], who closely investigated the thermodynamic stabilities and mass transport properties of the oxidation products to organise and describe various patterns.

If the oxygen partial pressure in the atmosphere is not high enough for A to oxidise (that is, if $p_{\mathrm{O_2}}$ is lower than the dissociation pressure of AO), then only BO may form. This can be the case in low pressure or diluted oxygen-containing atmospheres, or in other gas mixtures such as CO–$\mathrm{CO_2}$ or $\mathrm{H_2}$–$\mathrm{H_2O}$. Two types of critical B concentrations may be defined, as illustrated in Fig. 1.7(a). For low B concentrations, only internal oxidation is observed. With increasing B concentrations, an external scale is also formed, and finally internal oxidation is suppressed. For a given

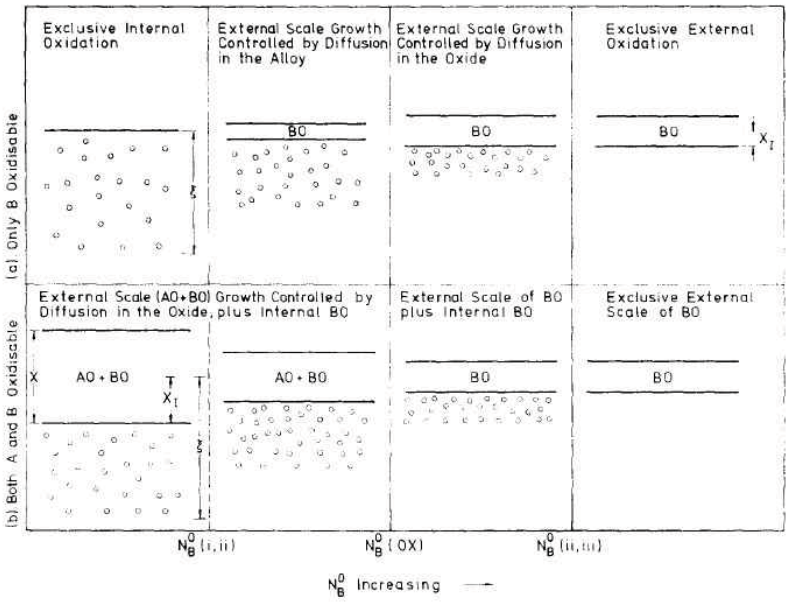

Figure 1.7 – Schematic steady-state microstructures resulting from the oxidation of an alloy AB for which the oxide of B is more stable than the oxide of A. (a) Under conditions such that only BO is stable; (b) under conditions such that both AO and BO are stable [63].

gas p_{O_2}, the influence of N_B^0 on the occurrence of internal and/or external oxidation is due to the competition between the inward flux of oxygen in the alloy and the outward flux of B. Internal oxidation will be discussed in more details subsequently. If the outward flux of B is high enough for external scaling but not high enough to counter B consumption by scale growth, not only will B oxidise internally, but growth of the external scale will be limited by B supply from the alloy. As oxidation is controlled by alloy diffusion, scale growth is slower than it would be on pure B, where it is controlled by diffusion in the oxide, as described earlier.

In most practical cases (oxidation in air for example), both AO and BO are thermodynamically stable (Fig. 1.7(b)). It is also common for the less stable oxide (AO) to be the fastest growing. For low B concentrations, BO particles will precipitate internally, and an external scale containing both oxides will be formed. With increasing B concentrations, AO formation, and eventually internal oxidation, are suppressed. Alternaltively, a two layer stack may form: AO–AO+BO or AO–BO. The AO layer can be a remant of the transient stage, and/or be formed by kinetic demixing: A is soluble in the original scale but segregation due to differential diffusion causes the solubility limit to be exceeded, and AO precipitates. The location of the AO layer is thus determined by the ions diffusivities in the original scale, as the faster diffusing species segregates in the outer part of the scale, and the slower in

the inner part. However, local thermodynamic equilibrium requires that the oxygen partial pressure decrease from the gas to the metal, which limits the possibilities of stacking sequence: as BO is more stable than AO, the dissociation pressure of BO is less than that of AO, and the oxygen flux underneath a BO layer is not high enough for A to oxidise.

Selective oxidation refers to the case where only BO forms. This situation is of great practical importance, since most high temperature resistant alloys are designed to form slow-growing alumina or chromia scale. Formation of a compact and adherent, slow-growing oxide with a constantly decreasing rate (e.g. parabolic kinetics) is termed "protective oxidation". Selective oxidation results in a depletion of B in the alloy. The shape of the depletion profile is determined by the relative scaling rate and diffusion coefficient of B in the alloy, as illustrated in Fig. 1.8: faster oxidation causes the depletion to be of greater amplitude (the interfacial B content is lower), and faster diffusion causes the depletion to extend to a larger depth, with a higher interfacial B content. In Fig. 1.8, the concentration of B for all profiles

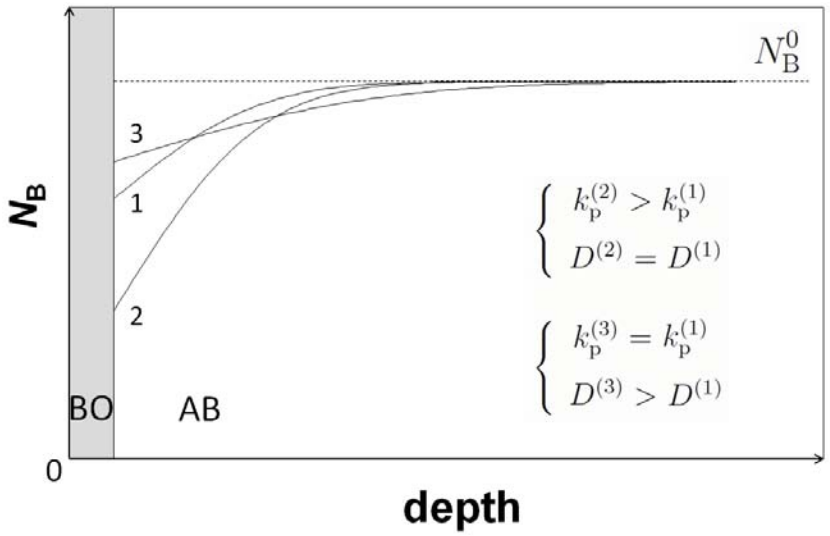

Figure 1.8 – Schematic representation of concentration profiles of alloying element B underneath a BO scale in the case of a semi-infinite specimen.

eventually reaches a constant value: this bulk concentration is that of the alloy before oxidation. As long as this is the case and scaling kinetics are parabolic, the interfacial concentration is constant. However, for a specimen of finite dimensions, the depletion profiles generated on the two opposed faces eventually overlap in the middle of the specimen. The whole profile is then gradually shifted downward, and in particular the interfacial concentration decreases.

Breakaway is the transition from protective oxidation to the fast growth of oxides containing the base metal. By extension, the expression "breakaway oxidation" is sometimes used in reference to the latter, non-protective stage. Breakaway is thought to occur by either of two mechanisms: intrinsic chemical failure or chemically-induced failure, as termed by Evans [65]. Failure of the protective scale is intrinsically chemical when the interfacial concentration of element B falls below the critical value for the thermodynamic stability of BO, and the base metal oxidises. Alternatively, if the protective oxide is physically damaged (by cracking or spallation), and the B-depleted alloy, directly exposed to the atmosphere, is unable to reform BO, failure is mechanically-induced. Depletion and breakaway will be discussed in more details in the case of Fe–Cr alloys in a subsequent Section.

1.2.3 Internal oxidation

Internal oxidation is the reaction of oxygen dissolved in a metal matrix with a solute element to form a dispersion of oxide precipitates. We consider a binary alloy AB, in which B is less noble than A and forms the oxide BO_ν (solid solution oxides are omitted). The equilibrium describing the stability of the internal precipitates is

$$\underline{\mathrm{B}} + \nu\,\underline{\mathrm{O}} = \mathrm{BO}_\nu\,(\mathrm{s}) \tag{1.40}$$

which is obtained by considering the oxidation reaction and the dissolution of oxygen and solute element in the metal matrix

$$\mathrm{B}\,(\mathrm{s}) + \frac{\nu}{2}\,\mathrm{O}_2\,(\mathrm{g}) = \mathrm{BO}_\nu\,(\mathrm{s}) \tag{1.41}$$

$$\frac{1}{2}\,\mathrm{O}_2\,(\mathrm{g}) = \underline{\mathrm{O}} \tag{1.42}$$

$$\mathrm{B}\,(\mathrm{s}) = \underline{\mathrm{B}} \tag{1.43}$$

The laws of mass action are written

$$K_{1.41} = \exp\left(\frac{-\Delta_\mathrm{f} G^0_{\mathrm{BO}_\nu}}{RT}\right) = \frac{1}{a_\mathrm{B} p^{\nu/2}_{\mathrm{O}_2}} \tag{1.44}$$

$$K_{1.42} = \exp\left(\frac{-\Delta \bar{G}^{\mathrm{xs}}_\mathrm{O}}{RT}\right) = \frac{1}{\gamma_\mathrm{O}} = \frac{N_\mathrm{O}}{p^{1/2}_{\mathrm{O}_2}} \tag{1.45}$$

$$K_{1.43} = \exp\left(\frac{-\Delta \bar{G}^{\mathrm{xs}}_\mathrm{B}}{RT}\right) = \frac{1}{\gamma_\mathrm{B}} = \frac{N_\mathrm{B}}{a_\mathrm{B}} \tag{1.46}$$

Recognising that (1.40) = (1.41) − ν (1.42) − (1.43), the law of mass action for the internal oxidation reaction is written

$$K_{1.40} = \exp\left(\frac{-\Delta_\mathrm{r} G^0_{1.40}}{RT}\right) = \frac{1}{N_\mathrm{B} N^\nu_\mathrm{O}} \tag{1.47}$$

with $\Delta_r G^0_{1.40} = \Delta_f G^0_{BO_\nu} - \nu\,\Delta\bar{G}^{xs}_O - \Delta\bar{G}^{xs}_B$.

It follows from the thermodynamic analysis that for internal oxidation to proceed, the concentrations of dissolved oxygen and element B in the alloy must be high enough for the the solubility product, defined as $K_{sp} = N_B N_O^\nu$, to be exceeded. The contribution of B is straightforward; as for oxygen, the solute concentration is related to p_{O_2} via Eq. (1.45), where p_{O_2} is the atmosphere oxygen partial pressure in the absence of external scaling, and the dissociation pressure of the oxide layer in contact with the metal if an external scale was formed. A second condition, related to the kinetics of the process, must be met: the concentration of B must be lower than that leading to exclusive external scaling. This will be detailed subsequently.

The mechanism of internal oxidation may be described as follows. Internal oxide particles are found below the alloy surface in a precipitation zone, whose depth is defined by the condition $N_B N_O^\nu \geqslant K_{sp}$. At the reaction front, parallel to the alloy surface, new BO_ν particles nucleate and grow. Reactant supply occurs by inward diffusion of oxygen from the alloy surface and outward diffusion of B from the bulk alloy. In most cases, the permeability of oxygen, defined as the product of the surface atom fraction and diffusion coefficient, $N_O^{(s)} D_O$, is much larger than that of B, $N_B^0 D_B$. As a consequence, B is immobile relative to oxygen: it is oxidised in situ. In these conditions, a new precipitate nucleates when a sufficient oxygen supersaturation is reached, and its growth is limited by the availability of B. Growth continues until local B depletion makes the oxidation front moves forward in the alloy.

If the oxide BO_ν is extremely stable, the reaction zone is assumed to consist of precipitates in a matrix of pure A. Further assuming that only oxygen diffuses ($N_O^{(s)} D_O \gg N_B^0 D_B$), a mass balance at the reaction front allows the kinetics of internal oxidation to be described by the rate equation

$$X_i^2 = 2\,k_i t \tag{1.48}$$

$$k_i = \frac{N_O^{(s)} D_O}{\nu\, N_B^0} \tag{1.49}$$

where X_i is the penetration depth and k_i the rate constant. The parabolic rate law reflects diffusion control.

Precipitation is termed incomplete when the stability of the oxide is not extermely high, and some B remains in solution in the reaction zone. This case was studied by Ohriner and Morral [66]. A treatment taking into account diffusion of B was established by Wagner [67] and discussed by Rapp [68]. In particular, Wagner [67] proposed a calculation of the critical value of N_B^0 for the transition from

internal to exclusive external oxidation. Given that oxygen diffuses in the metal but not in the oxide precipitates, the oxygen inward flux decreases with increasing BO_ν volume fraction. At some point, the flux of B will be high enough to stop the ingress of the reaction front in favour of the precipitates continued growth, which finally results in the formation of a continuous layer. On this basis, and assuming that the flux of B is now important ($\frac{N_O^{(s)}}{N_B^0} \ll \frac{D_B}{D_O} \ll 1$), the critical B content is found to be

$$N_B^0 = \left(\frac{\pi g*}{2\nu} \frac{V_{AB}}{V_{BO_\nu}} \frac{N_O^{(s)} D_O}{D_B} \right)^{1/2} \tag{1.50}$$

where $g*$ is the critical volume ratio necessary to form a continuous BO_ν layer (typically $g* = 0.3$) and V_{AB} and V_{BO_ν} the molar volumes of alloy and oxide.

The size of the precipitates results from the competition between nucleation and growth rates, and is controlled by the velocity of the reaction front: nucleation occurs as soon as the necessary degree of supersaturation is reached, and growth occurs until the next nucleation event. Therefore, the size of the precipitates is inversely proportional to the front velocity. When the oxidation front reaches a certain depth, the decreasing number of nucleation events enables the particles to grow elongated.

Oxide precipitation induces a volume change in the alloy, which is almost always an expansion. The compressive stress can be deleterious if not readily accommodated by creep of the metal matrix. In addition, the presence of internal oxides may cause an embrittlement of the alloy subsurface.

1.2.4 External multiphase scales

We again consider a binary alloy AB, where the metals form the oxides AO and BO, and $\Delta_f G^0_{BO} < \Delta_f G^0_{AO}$. When both oxides are thermodynamically stable, a large variety of oxide scales are potentially formed, depending on the gas p_{O_2}, the concentration of B in the alloy and the diffusivity of the metals in the oxide phases. Some of the possible reaction morphologies are schematically represented in Fig. 1.9, where internal oxidation has been omitted for clarity. Two limiting cases are straightforward: A-rich alloys will form only AO, and B-rich alloys will form only BO (Fig. 1.9(a) and (e)). For intermediate concentrations, scales containing both oxides are formed. A theoretical treatment of this situation was established by Wagner [69], and developed further by Gesmundo et al [70].

During a first stage, both oxides nucleate on the metal surface. Both types of nuclei thicken and grow laterally in a competitive process to cover the alloy

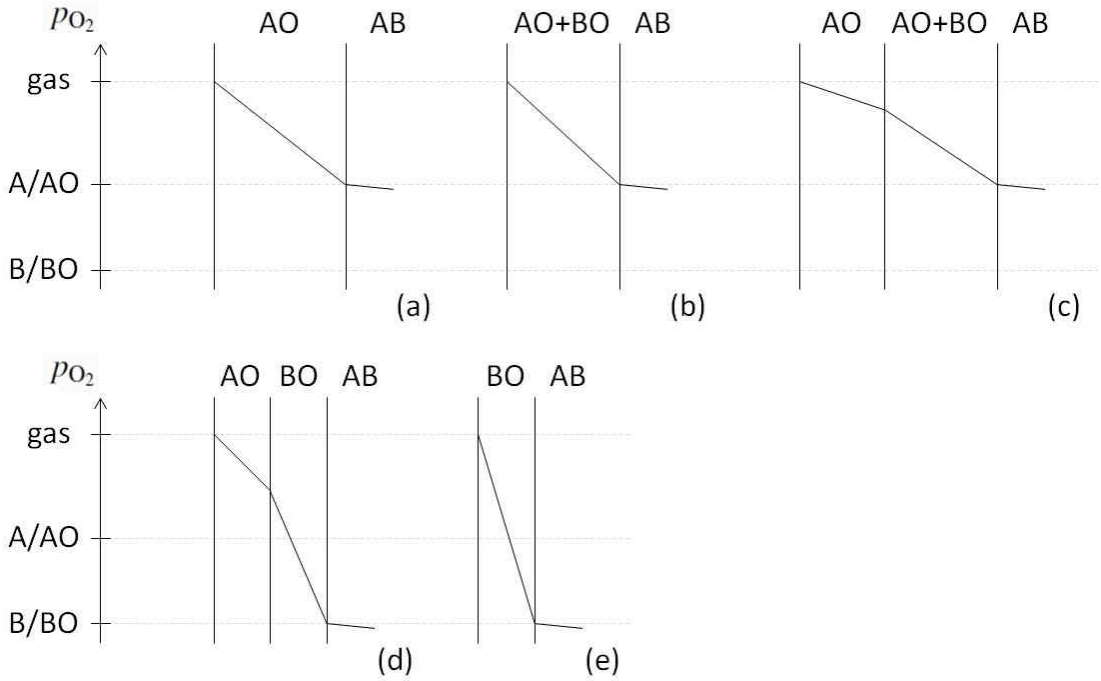

Figure 1.9 – Oxygen partial pressure across oxide scales formed in conditions where oxides of both A and B are thermodynamically stable.

surface. The concentration of B determines the spatial distribution of the oxides, which in turn controls the overall scaling rate. For relatively low B contents, the scale contains BO particles embedded in an AO matrix (Fig. 1.9(b)). The volume fraction of BO particles increases with increasing alloy B concentration. In many cases, the most stable oxide is also the slowest growing. Thus, the total ionic flux across the scale is all the more reduced when more BO islands are present: this is called diffusional blocking [19]. For higher B concentrations, BO may form a continuous layer (Fig. 1.9(d)). As the BO layer is continuously covering the alloy, the overall scaling rate is limited by diffusion in BO, and is therefore low. As discussed in Section 1.2.2, the formation of continuous layers of AO or BO may also result from demixing. For example in Fig. 1.9(c), faster diffusion of A through the AO+BO scale led to its segregation in the upper part of the scale, and eventually to the precipitation of AO into a continuous layer. This may also arise when the alloy forms only BO at first, but A diffuses faster than BO grows, and AO precipitates in an outer layer (Fig. 1.9(d)).

Figure 1.9 includes schematic representations of the p_{O_2} profiles across the various oxide scales. For scales of AO or AO+BO, the oxygen activity at the metal/oxide interface is determined by the A/AO equilibrium, and is therefore relatively high. Thus the oxygen permeability is high, and internal oxidation of B to form the sta-

ble BO could follow. Conversely, if the metal surface is covered by BO, the lower interfacial p_{O_2} will not favour internal oxidation of B.

1.3 Oxidation of Fe–Cr alloys

Binary Fe–Cr alloys are commonly used as structural materials. Their use is mainly limited to moderate temperatures (up to $\sim$ 600 °C) because the ferritic structure, stabilised by chromium, does not provide satisfactory creep resistance at higher temperatures. Resistance to oxidation is obtained by the formation of Cr_2O_3, but the variety of Fe–Cr solid solution oxides possibly results in more complex and less protective oxide scales. This Section aims at presenting the Fe–Cr–O system, describing the various oxidation morphologies which can be encountered, and most importantly, discussing the conditions for chromium selective oxidation.

1.3.1 The Fe–Cr–O system

A $\log p_{O_2} - N_{Cr}$ predominance diagram calculated at 627 °C [71] is shown in Fig. 1.10. Since Fe–Cr–O is a ternary system, the three-phase equilibria are invariant: when

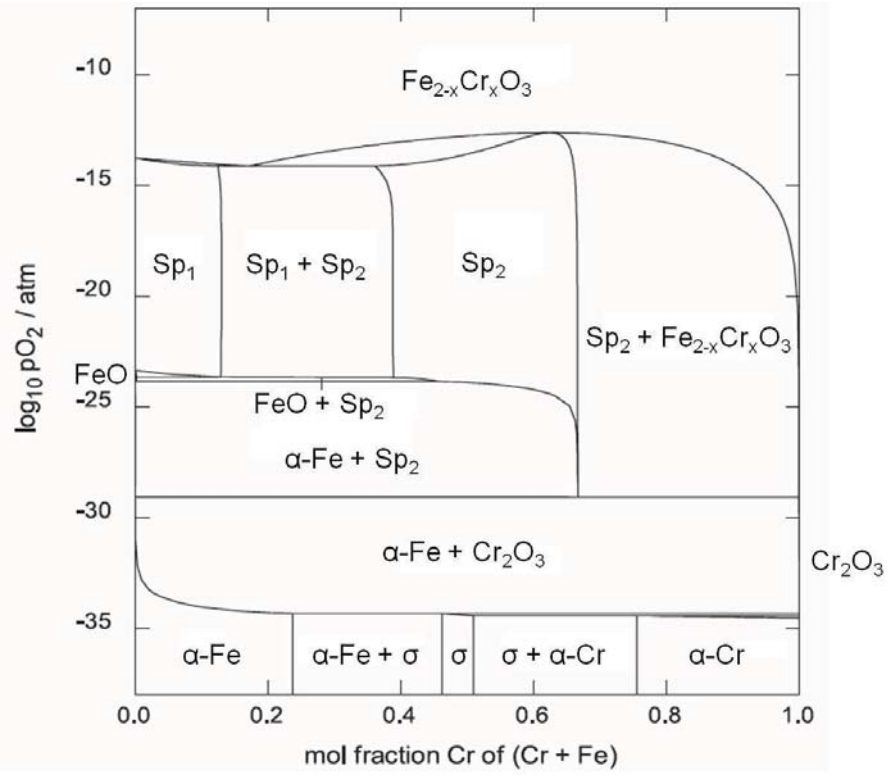

Figure 1.10 – Calculated log p_{O_2} – N_{Cr} predominance diagram in the Fe–Cr–O system at 900 K, after [71].

three phases coexist, their compositions are fixed, and the composition of the system varies only because the mole fractions of the phases vary. The activities of the three

components are also fixed, and the three-phase equilibria are thus represented by horizontal lines (constant p_{O_2}) in Fig. 1.10.

At low p_{O_2}, only metal phases are present: the Fe-rich and Cr-rich ferritic phases, and the brittle σ phase which contains about 50 at. % of each element. The corundum oxide phases, Fe_2O_3 and Cr_2O_3, form a continuous solution, $Fe_{2-x}Cr_xO_3$, with $0 \leqslant x \leqslant 2$. Chromia is the most stable oxide of the Fe–Cr–O system, but its dissociation pressure increases as it dissolves Fe. The solubility of chromium in the widely non-stoichiometric $Fe_{1-\delta}O$ is important, and varies with δ. The solubilities of Cr in Fe_3O_4 and of Fe in $FeCr_2O_4$ are significant but limited, since the two spinel phases are not completely miscible. Two solid solution spinels exist, with the general formula $Fe_{3-x}Cr_xO_4$: an Fe-rich phase with $0 \leqslant x \lesssim 0.38$ and a Cr-rich phase with $1.16 \lesssim x \leqslant 2$, noted Sp_1 and Sp_2, respectively, in Fig. 1.10.

1.3.2 Diffusivity in oxide phases

Wüstite

As discussed in Section 1.1.3.1, FeO is highly defective. The elevated growth rate due to this large non-stoichiometry is not affected by the dissolution of chromium [19,20].

Spinel phases

Töpfer et al [72] measured iron and chromium tracer diffusion coefficients in the spinel solid solution $Fe_{3-x}Cr_xO_4$ with $0 \leqslant x \leqslant 1.2$ at 1200 °C as a function of oxygen activity. For all spinel compositions, the curves of $\log D_{Fe}$ and $\log D_{Cr}$ versus a_{O_2} were V-shaped, as for iron diffusion in magnetite (see 1.1.3.1). The slopes at high and low oxygen activity were also 2/3 and -2/3, repectively, indicating that cation vacancies and cation interstitials, respectively, determine the diffusion of cations. The diffusion coefficient of chromium was three orders of magnitude lower than that of iron for all spinel compositions and oxygen activity. The diffusion coefficients of both iron and chromium were independent of spinel composition at high a_{O_2}, but decreased with x in $Fe_{3-x}Cr_xO_4$ at low a_{O_2}.

Corundum solid solution

Footner et al [73] measured the electrical conductivity of $Fe_{2-x}Cr_xO_3$ solid solutions between 600 and 1100 °C (see Fig. 1.11). As iron is dissolved in Cr_2O_3, the cation vacancy concentration is reduced until the p-type conductivity is suppressed. As the oxide iron content further increases, a transition to n-type conduction is observed, and the resistivity decreases. Although it is not specified in Ref. [73], the conductiv-

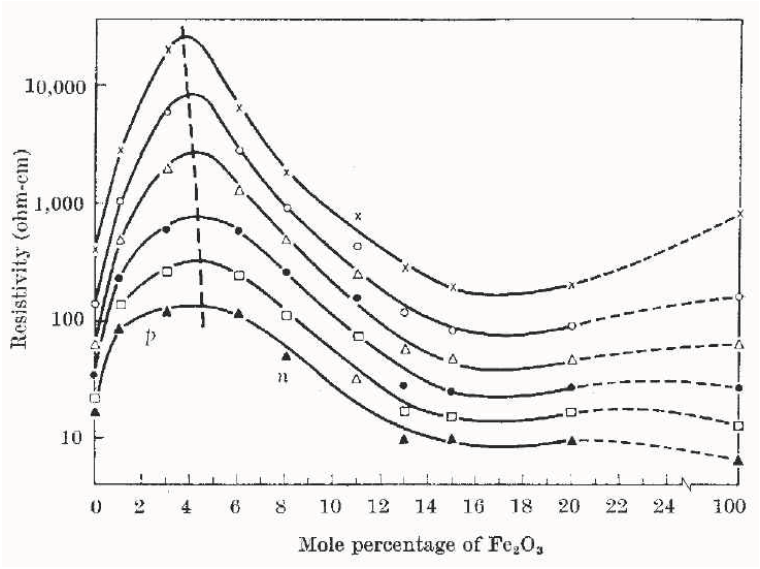

Figure 1.11 – Electrical resistivity of sintered Fe_2O_3–Cr_2O_3 compacts, after [73]. × 600 °C; ○ 700 °C; △ 800 °C; • 900 °C; □ 1000 °C; ▲ 1100 °C.

ity measurements were most likely done at ambient pressure, whereas diffusion in a thermally grown oxide occurs in a p_{O_2} gradient. However, the variations of electrical conductivity showed good correlation with the evolution of the oxidation rate as a function of alloy composition. In particular, the oxide composition of maximum resistivity corresponded to the alloy composition showing minimum oxidation rate, about 20 wt. % Cr.

1.3.3 Oxide morphology

Dalvi and Coates [62] applied the concept of diffusion path to the oxidation of Fe–Cr alloys using an isothermal section of the Fe–Cr–O phase diagram at 1000 °C shown in Fig. 1.12. For very dilute alloys, the oxide scale is the same as that formed on pure iron: FeO / Fe_3O_4 / Fe_2O_3, from the metal to the atmosphere. With increasing chromium content, $FeCr_2O_4$ precipitates in the FeO layer. The total scaling rate is still caracteristic of pure iron at first, but since iron diffusion is slower in $FeCr_2O_4$ than in FeO, as the volume fraction of $FeCr_2O_4$ increases, the diffusional cross-section decreases (diffusional blocking). Eventually FeO is supressed, and the scale consists of $Fe_{1.5}Cr_{1.5}O_4$+$FeCr_2O_4$, Fe_3O_4 and Fe_2O_3 layers. As the chromium content further increases, iron-rich spinels are supressed, and the growth rate of the resulting $FeCr_2O_4$ / $Fe_{2-x}Cr_xO_3$ scale is significantly reduced. Finally, higher chromium contents enable Cr_2O_3 to be formed.

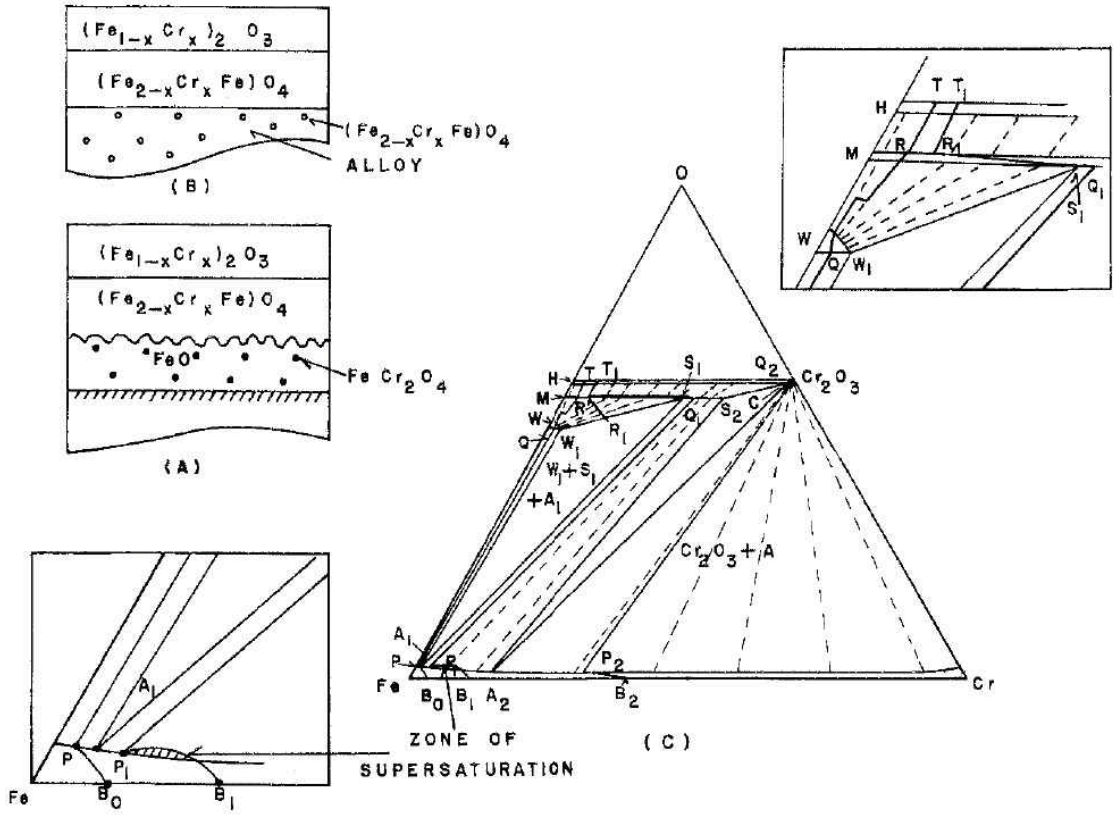

Figure 1.12 – Schematic representation of the scale structures corresponding to the oxidation of (a) very dilute and (b) dilute Fe–Cr alloys. (c) 1000 °C isotherm of the Fe–Cr–O system (at. %) and possible diffusion paths corresponding to the oxidation of Fe–Cr alloys. W_1–$Fe_{0.97}Cr_{0.02}O$; S_1–$Fe_{1.5}Cr_{1.5}O_4$; S_2–$FeCr_2O_4$; C–<1 at. % Fe; A_1–<1 at. % Cr; A_2–13.6 at. % Cr, 76.4 at. % Fe. Insert at the top right shows the oxide region on an expanded scale. (Figure published in Ref. [62]. References for (a), (b) and (c) given in [62].)

1.3.4 Selective oxidation of chromium and breakaway oxidation

The formation of Cr_2O_3 on Fe–Cr alloys is first examined by considering the thermodynamic equilibrium between the oxide and chromium in the alloy

$$2\,\underline{\mathrm{Cr}} + \frac{3}{2}\,\mathrm{O_2\,(g)} = \mathrm{Cr_2O_3\,(s)} \tag{1.51}$$

which is obtained from the formation of Cr_2O_3 from the pure components in their reference state and the dissolution of chromium in the alloy

$$2\,\mathrm{Cr\,(s)} + \frac{3}{2}\,\mathrm{O_2\,(g)} = \mathrm{Cr_2O_3\,(s)} \tag{1.52}$$

$$\mathrm{Cr\,(s)} = \underline{\mathrm{Cr}} \tag{1.53}$$

The equilibrium constants for reactions (1.52) and (1.53) are defined by

$$K_{1.52} = \exp\left(\frac{-\Delta_f G^0_{Cr_2O_3}}{RT}\right) = \frac{1}{a^2_{Cr} p^{3/2}_{O_2}} \tag{1.54}$$

$$K_{1.53} = \exp\left(\frac{-\Delta \bar{G}^{xs}_{Cr}}{RT}\right) = \frac{1}{\gamma_{Cr}} = \frac{N_{Cr}}{a_{Cr}} \tag{1.55}$$

Recognising that (1.51) = (1.52) − 2 (1.53), the law of mass action for Eq. (1.51) is written

$$K_{1.51} = \exp\left(\frac{-\Delta_f G^0_{Cr_2O_3} + 2\,\Delta \bar{G}^{xs}_{Cr}}{RT}\right) = \frac{1}{N^2_{Cr} p^{3/2}_{O_2}} \tag{1.56}$$

Using the standard free energy of formation given in Ref. [74], and the dissolution data in Ref. [75], one calculates $N_{Cr} = 9.1 \times 10^{-22}$ in 0.2 atm O_2 at 800 °C. However, the competitive oxidation of iron must also be considered. The next most stable oxide in the Fe–Cr–O system is $FeCr_2O_4$, formed according to

$$\underline{Fe} + \frac{1}{2}\,O_2\,(g) + Cr_2O_3\,(s) = FeCr_2O_4\,(s) \tag{1.57}$$

Thus the competition equilibrium is

$$\underline{Fe} + \frac{4}{3}\,Cr_2O_3\,(s) = \frac{2}{3}\,\underline{Cr} + FeCr_2O_4\,(s) \tag{1.58}$$

Since the chromium concentrations involved are small, the solvent iron is approximated as pure ($a_{Fe} = N_{Fe} = 1$), and the law of mass action of Eq. (1.58) defines the critical chromium concentration for thermodynamic stability of Cr_2O_3, N^*_{Cr}, as

$$K_{1.58} = \exp\left(\frac{-\Delta_f G^0_{FeCr_2O_4} + \frac{1}{3}\Delta_f G^0_{Cr_2O_3} - \frac{2}{3}\,\Delta \bar{G}^{xs}_{Cr}}{RT}\right) = \left(N^*_{Cr}\right)^{2/3} \tag{1.59}$$

Again using the data in Refs. [74, 75], one obtains $N^*_{Cr} = 8.3 \times 10^{-5}$ for $T = 800$ °C. Thus, on the basis of the thermodynamic analysis, any alloy containing more than 8.3×10^{-3} at. % chromium is expected to form Cr_2O_3 at this temperature.

Nevertheless, the possibility of protective Cr_2O_3 growth is also determined by the diffusion kinetics in the reacting system. First, the outward chromium flux must be high enough to compensate for the inward oxygen flux and prevent internal oxidation. This requires a minimum chromium concentration in the alloy, as discussed in Section 1.2.3.

When an external Cr_2O_3 scale is formed, chromium consumption at the metal/oxide interface causes a decrease of the chromium concentration in the subscale, because diffusion in the alloy is not instantaneous. The resulting depletion profile is determined by the relative diffusivities of chromium in the alloy and in the scale (the latter

being included in the scale growth rate), as shown in Section 1.2.2. For Cr_2O_3 formation to be maintained, the interfacial chromium concentration, N_{Cr}^{i}, must exceed the value defined by the thermodynamic stability of the oxide, N_{Cr}^{*}. The problem of depletion during initial (i.e. transient) external oxidation was studied by Whittle et al [76], in the case of an alloy AB forming a pure B oxide. The authors used a numerical method to solve Fick's second law

$$D_B \frac{\partial^2 C_B}{\partial x^2} = \frac{\partial C_B}{\partial t} \tag{1.60}$$

for diffusion in the alloy, with a boundary condition at the moving metal/oxide interface taking into account the flux of B departing the alloy and that entering the scale. In Eq. (1.60), $C_B(x,t)$ is the concentration of B, where x is the distance from the original alloy surface, and D_B is the diffusion coefficient of B in the alloy, assumed not to vary with composition. In calculating concentration profiles, the authors considered parabolic, cubic and logarithmic scaling kinetics. It is worth noting that parabolic kinetics must be described by a rate law of the type $X^2 = k_1 t + k_2$ with $k_2 > 0$. Indeed, a null value would require an infinite flux of B at $t = 0$ because the scale growth rate would then be infinite, which does not occur in actual systems (see Section 1.1.2.2). This numerical method was applied to the specific case of Fe–Cr alloys in Ref. [77]. In Fig. 1.13, the interfacial chromium content is seen to be minimum at the beginning of scale formation, and to increase subsequently until reaching a constant value.

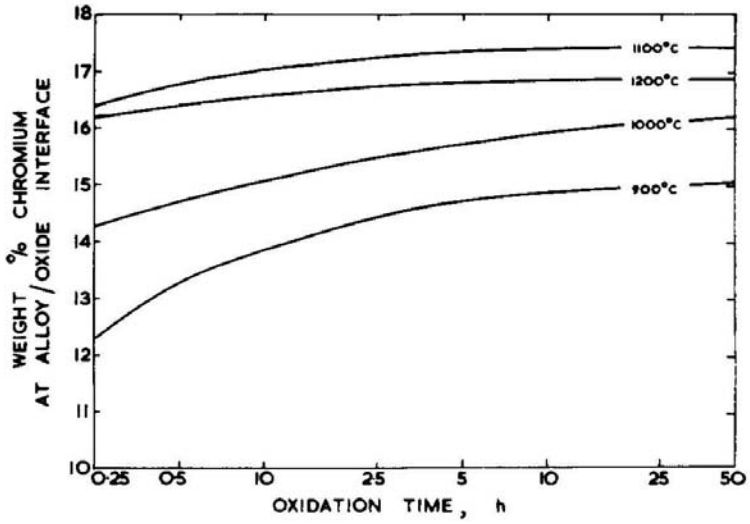

Figure 1.13 – Calculated wt.% chromium at the alloy/oxide interface as a function of time; Fe-27.4% Cr oxidised at 900-1200 °C [77].

The constant interfacial concentration reflects a steady-state situation, where the

flux of chromium departing the alloy at the moving metal/oxide interface compensates for the flux of chromium consumed by scale growth. The theoretical analysis of diffusion in the steady-state regime was first established by Wagner [78]. Describing Cr_2O_3 growth kinetics as Eq. (1.9), $X^2 = 2k_p t$, Wagner's original expression is adapted to calculate the mole fraction of chromium at a distance x from the initial alloy surface as

$$N_{Cr}(x,t) = N_{Cr}^{i} + \left(N_{Cr}^{0} - N_{Cr}^{i}\right) \frac{\operatorname{erf}\left(\dfrac{x}{2\sqrt{D_{Cr}t}}\right) - \operatorname{erf}\left(\dfrac{2V_a}{V_{ox}}\sqrt{\dfrac{k_p}{2D_{Cr}}}\right)}{1 - \operatorname{erf}\left(\dfrac{2V_a}{V_{ox}}\sqrt{\dfrac{k_p}{2D_{Cr}}}\right)} \tag{1.61}$$

where V_a and V_{ox} are the alloy and oxide molar volume, respectively, and D_{Cr} the chromium diffusion coefficient. Again one considers the formation of pure Cr_2O_3, and V_a and D_{Cr} are assumed not to vary with alloy composition. The interfacial chromium mole fraction is calculated using the expression

$$\frac{N_{Cr}^{0} - N_{Cr}^{i}}{1 - N_{Cr}^{i}} = F\left(\frac{2V_a}{V_{ox}}\sqrt{\frac{k_p}{2D_{Cr}}}\right) \tag{1.62}$$

where F is a function defined by $F(u) = \sqrt{\pi}u(1 - \operatorname{erf} u)\exp u^2$. Thus, if the small N_{Cr}^{*} value is neglected, the minimum chromium concentration for scale/alloy kinetic equilibrium is obtained by introducing $N_{Cr}^{i} = 0$ in Eq. (1.62) as $(N_{Cr}^{0})_I = F\left(\dfrac{2V_a}{V_{ox}}\sqrt{\dfrac{k_p}{2D_{Cr}}}\right)$.

In many cases, scale growth is considerably slower than diffusion in the alloy, i.e. $k_p \ll D_{Cr}$. Using the approximation $F(u) \simeq \sqrt{\pi}u$ for $u \ll 1$, the interfacial chromium mole fraction during the steady-state regime is written

$$N_{Cr}^{i} = \frac{N_{Cr}^{0} - \phi}{1 - \phi} \tag{1.63}$$

where $\phi = \dfrac{2V_a}{V_{ox}}\sqrt{\dfrac{\pi k_p}{2D_{Cr}}}$, which can be further approximated as

$$N_{Cr}^{i} = N_{Cr}^{0} - \phi \tag{1.64}$$

In both cases the criterion for the balance of chromium fluxes at the metal/oxide interface becomes $(N_{Cr}^{0})_I = \phi$.

In Wagner's treatment of diffusion kinetics expressed by Eq. (1.61), the oxidised alloy was considered as a semi-infinite specimen. However, in actual situations, specimens have finite dimensions, and the quantity of chromium in the alloy, called

the chromium reservoir, is also finite. Thus, the steady-state regime cannot last indefinitely, and after the depletion profiles generated on the two opposite faces overlap in the middle of the specimen, the interfacial concentration will decrease. This situation was treated by Whittle [79] in the case where the rate constant of Cr_2O_3 growth is small enough for the condition $\phi \ll 1$ to be met and the displacement of the metal/oxide to be neglected. Under the assumptions made so far (pure Cr_2O_3 is formed according to a simple parabolic law, Eq. (1.9), and V_a and D_{Cr} are independent of alloy composition) chromium concentration in the alloy is then calculated as[1]

$$N_{Cr}(x,t) = N^0_{Cr} - \phi \sum_{n=0}^{+\infty} \left[\text{erfc}\left(\frac{2nL + x}{2\sqrt{D_{Cr}t}}\right) + \text{erfc}\left(\frac{2(n+1)L - x}{2\sqrt{D_{Cr}t}}\right)\right] \tag{1.65}$$

where x is the distance in the alloy from the metal/oxide interface, and L the specimen half-thickness. Chromium depletion profiles for a 1 mm thick Fe-20Cr alloy at 800 °C were generated using Eq. (1.65), with the k_p value found in Ref. [73] and diffusion data in Ref. [81]. The curves in Fig. 1.14 were plotted for reaction times ranging from 10 to 5×10^5 h. After 10 h, depletion is limited to about 20

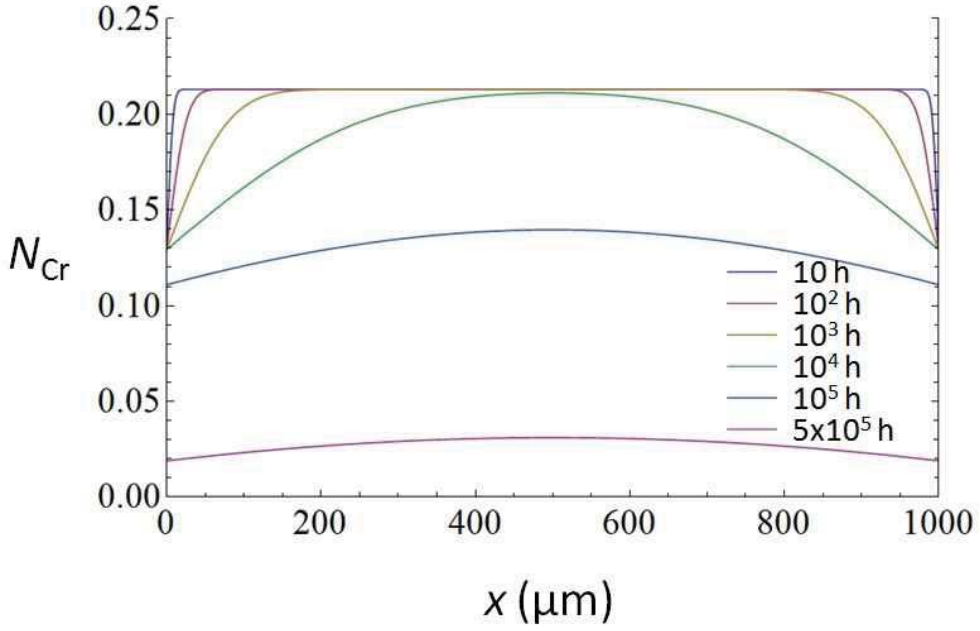

Figure 1.14 – Chromium concentration profiles calculated from Eq. (1.65) using Mathematica 8.0 [82]. Details given in text.

μm below the metal/oxide interface. As the reaction continues, depletion extends

[1]The equation in Ref. [79] is in error in omitting the 2 prior to the nL and $(n+1)L$ terms, as noted by Cowen and Webster [80].

into the alloy, and the steady-state regime is maintained up to about 10^4 h. During this stage, the interfacial concentration is constant, $N^{\mathrm{i}}_{\mathrm{Cr}} = N^{0}_{\mathrm{Cr}} - \phi$ as given by Eq. (1.64); the diffusion profile is that of a semi-infinite specimen, and can therefore be calculated using the appropriate solution to Fick's second law

$$\frac{N^{\mathrm{i}}_{\mathrm{Cr}} - N_{\mathrm{Cr}}(x,t)}{N^{\mathrm{i}}_{\mathrm{Cr}} - N^{0}_{\mathrm{Cr}}} = \mathrm{erf}\left(\frac{x}{2\sqrt{D_{\mathrm{Cr}}t}}\right) \tag{1.66}$$

Once depletion extends to the specimen mid-plane, however, the interfacial content decreases (see $t = 10^5$ and 5×10^5 h in Fig. 1.14).

It follows from the diffusional analysis of the system that if a Cr_2O_3 scale is formed during the transient stage, it is expected to stay thermodynamically stable during the steady-state regime, until the interfacial chromium concentration falls below the value defined by the scale/alloy thermodynamic equilibrium, N^{*}_{Cr}, because of through-specimen depletion. When this eventually occurs, iron oxidises and the scaling rate rapidly increases, marking the separation between protective and non-protective oxidation, called breakaway. Breakaway is thus due to Intrinsic Chemical Failure of the protective scale, according to the definition given by Evans et al [65].

The influence of specimen thickness on chromium depletion and subsequent scale failure as predicted by Eq. (1.65) was verified experimentally, for example by Cowen and Webster [80] in the case of 25Cr/20Ni steel foils at 700–750 °C in dry CO_2. However, for specimens of usual thickness, the time to breakaway predicted by Eq. (1.65) is unrealistically long: for example about 70 years in the conditions of Fig. 1.14. While thin foils may grow intact oxide scales within their predicted lifetime, and subsequently suffer pure chemical failure, scales formed on thicker specimens are likely to undergo mechanical failure while still thermodynamically stable. Scale cracking or spallation will expose the chromium depleted alloy to the corrosive atmosphere, and result in breakaway if the chromium concentration at the alloy surface is not high enough for Cr_2O_3 to reform. A theoretical analysis of alloy composition during scale spalling/rehealing was proposed by Whittle [83]. With the same assumptions as those used to establish Eq. (1.65), the chromium mole fraction in the alloy after Cr_2O_3 spalled at time t^*, and subsequently reformed, is obtained

by numerical approximation as[1]

$$N_{\mathrm{Cr}}(x,t) = N^0_{\mathrm{Cr}} - \frac{\phi}{1-\phi}\left[\operatorname{erfc}\left(\frac{x}{2\sqrt{D_{\mathrm{Cr}}(t-t^*)}}\right)\left(1+\frac{\phi}{1-\phi}\frac{2}{\pi}\arcsin\sqrt{\frac{t^*}{t}}\right) + \frac{2}{\pi}\int_0^{\sqrt{\frac{t^*}{t-t^*}}}\exp\left(-\frac{x^2(1+u^2)}{4D_{\mathrm{Cr}}t}\right)\frac{\mathrm{d}u}{1+u^2}\right], \quad \text{for } t > t^* \tag{1.67}$$

where again x is the distance from the metal/oxide interface. Thus, the interfacial concentration is given for $x = 0$ as[2]

$$\begin{aligned} N^{\mathrm{i}}_{\mathrm{Cr}}(t) &= N^0_{\mathrm{Cr}} - \frac{\phi}{1-\phi}\left[1+\frac{\phi}{1-\phi}\frac{2}{\pi}\arcsin\sqrt{\frac{t^*}{t}} + \frac{2}{\pi}\arctan\sqrt{\frac{t^*}{t-t^*}}\right] \\ &= \frac{1}{1-\phi}\left[N^0_{\mathrm{Cr}} - \phi - \frac{\phi}{1-\phi}(1-N^0_{\mathrm{Cr}})\frac{2}{\pi}\arcsin\sqrt{\frac{t^*}{t}}\right], \quad \text{for } t > t^* \end{aligned} \tag{1.68}$$

Keeping the experimental conditions used in Fig. 1.14, the interfacial concentration calculated from Eq. (1.68) is plotted in Fig. 1.15, with spallation occuring at $t^* = 1$ h. During the steady state regime, the constant interfacial concentration is defined by

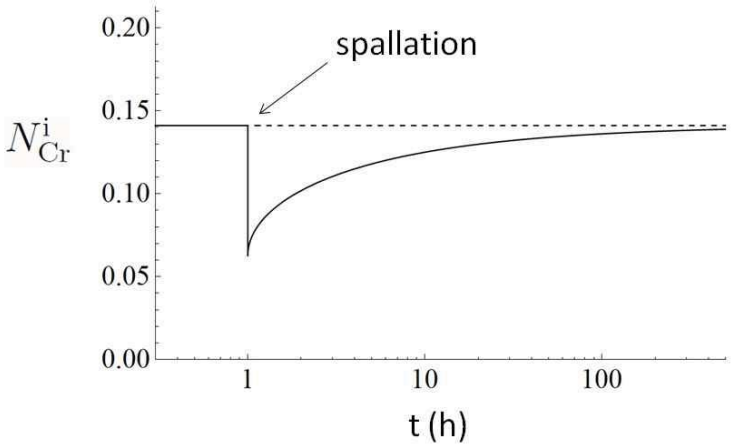

Figure 1.15 – Interfacial chromium concentration during Cr_2O_3 steady-state growth, spallation and reformation, calculated from Eq. (1.68) using Mathematica 8.0 [82]. Details given in text.

the scale/alloy kinetic equilibrium, and has the value given by Eq. (1.64), $N^{\mathrm{i}}_{\mathrm{Cr}} = \frac{N^0_{\mathrm{Cr}} - \phi}{1-\phi}$. After the initial scale spalls, the growth rate is maximum, as is the flux of

[1] In Ref. [83], Eq. (15) omits brackets. The correct form is given in the paper's appendix, Eq. (A.14).

[2] In Ref. [83], Eq. (16) is incorrect; Eq. (A.15) is the correct equation.

chromium departing the alloy at the interface, and the interfacial concentration is minimum, before progressively increasing to the steady-state value. The minimum value is obtained for $t \to t^*$ ($t > t^*$) as

$$N_{\mathrm{Cr}}^{\mathrm{i}} = \frac{N_{\mathrm{Cr}}^0 - \phi(2-\phi)}{(1-\phi)^2} \tag{1.69}$$

It is important to note that Eqs. (1.67–1.69) were obtained for a scaling rate law of the type $X^2 = 2k_{\mathrm{p}}t$, and therefore do not reflect the transient stage of oxidation as treated in Ref. [76, 77] (see Fig. 1.13). For the experimental conditions used in Fig. 1.15, the steady-state value is $\dfrac{N_{\mathrm{Cr}}^0 - \phi}{1-\phi} = 1.41 \times 10^{-1}$, and the minimum value $\dfrac{N_{\mathrm{Cr}}^0 - \phi(2-\phi)}{(1-\phi)^2} = 6.27 \times 10^{-2}$. The case of multiple spallation is treated in Ref. [83]. Here, it is simply noted that with the data used so far, an Fe–20Cr alloy oxidised at 800 °C would be capable of supporting Cr_2O_3 reformation after the initial layer spalled, since the minimum interfacial concentration is higher than N_{Cr}^*. If the latter value is taken as zero, the minimum initial chromium concentration to support Cr_2O_3 reformation is obtained for $N_{\mathrm{Cr}}^{\mathrm{i}} = 0$ in Eq. (1.69) as

$$\left(N_{\mathrm{Cr}}^0\right)_{\mathrm{II}} = \phi(2-\phi) \tag{1.70}$$

Thus, if $N_{\mathrm{Cr}}^0 < (N_{\mathrm{Cr}}^0)_{\mathrm{II}}$, spallation of the initial Cr_2O_3 layer will cause iron to oxidise. Evans et al [65] claimed that this Mechanically Induced Chemical Failure could only occur after depletion has extended to the whole specimen and the interfacial chromium content has fallen below the steady-state value, because after the bare alloy is exposed, the oxidation front enters the alloy so rapidly that depletion has no effect if it is localised. However, in Whittle and Wood's work [77, 84–86], breakaway oxidation of Fe–Cr alloys reacted in air was attributed to mechanical failure, because nodule formation was localised randomly on the specimens surface, and the interfacial chromium concentration measured elsewhere was too high for intrinsic chemical failure. Following breakaway, the scale constitution and growth rate depend on the chromium concentration left at the metal/oxide interface. Various scale morphologies may then be obtained (see Sections 1.2.4 and 1.3.3), from the fast-growing scale containing Fe_3O_4+$FeCr_2O_4$ as an inner layer and outer layers of pure iron oxides, to the more favourable situation where a Cr-rich "healing layer" is formed at the base of the scale.

1.4 Carburisation of Fe–Cr alloys

Most of the general principles described so far in the case of reaction with oxygen also apply to oxidation by carbon, which is briefly introduced in the present Section.

Carbonaceous gases present in reactive atmospheres produce carbon by the synthesis gas reaction

$$CO + H_2 = C + H_2O \tag{1.71}$$

the Boudouard reaction

$$2\,CO = C + CO_2 \tag{1.72}$$

and hydrocarbon cracking

$$C_xH_y = x\,C + \frac{y}{2}\,H_2 \tag{1.73}$$

Commercial carburising atmospheres often contain both C- and O-bearing gas species, and the oxygen partial pressure due to the presence of, for example, carbon dioxide or water vapour is enough to cause simultaneous oxidation and carburisation. The latter can be studied independently by using C_xH_y–H_2 mixtures at low p_{O_2}, in order to artificially prevent oxidation. Under many conditions, reactions (1.71), (1.72) and (1.73) are very slow and hardly reach equilibrium unless catalysed. Consequently, C-bearing gas mixtures can become supersaturated with respect to carbon, whose activity is then higher than unity. In such atmospheres, alloys act as catalysts for carbon deposition and undergo disruption and fragmentation, a phenomenon known as metal dusting.

Carburisation, which may occur for $a_C < 1$, is a form of oxidation, in that the degree of oxidation of metal species is increased when forming carbides. Carburisation is also very similar to oxide formation in terms of the thermodynamics, reaction mechanism and kinetics: it consists of either external carbide scale formation or carbon dissolution and diffusion into the metal phase, leading to internal carbide precipitation. Thus most of the principles given in the preceding Sections also apply to carburisation, and the present Section will briefly introduce some particulars of carburisation, focusing on Fe–Cr alloys.

1.4.1 Thermodynamics of carburisation

The carbon activity at an alloy surface can be calculated from the law of mass action corresponding to the reaction producing carbon, e.g. reactions (1.71), (1.72) and (1.73). In a gas mixture containing several C-bearing species, since gas phase equilibrium is often not reached, different values of a_C may be obtained depending on the reaction considered. In this case, a_C is commonly assumed to be established

by the most rapid reaction. The standard free energy of formation for pure Cr and Fe carbides are given in Table 1.3, together with the carbon activity at the metal/carbide equilibrium at 800 °C. Nickel does not form carbides under the con-

Table 1.3 – Standard free energy of formation of Cr and Fe carbides [19] and carbon activity for the metal/carbide equilibrium at 800 °C.

$\Delta_f G^0 = \Delta_f H^0 - T\Delta S^0$	$\Delta_f H^0$ (kJ mol^{-1})	ΔS^0 (J mol^{-1} K^{-1})	a_C at 800 °C
$Cr_{23}C_6$	-411.2	38.7	2.1×10^{-4}
Cr_7C_3	-174.5	25.5	5.3×10^{-4}
Cr_3C_2	-84.35	11.53	4.4×10^{-3}
Fe_3C	29.04	28.0	8.9×10^{-1}

dition of interest, and it is seen that chromium carbides are much more stable than iron carbides.

An isothermal section of the Fe–Cr–C phase diagram at 1000 °C [87] is presented in Fig. 1.16. The Fe–Cr–C system contains solid solution carbides, designated as

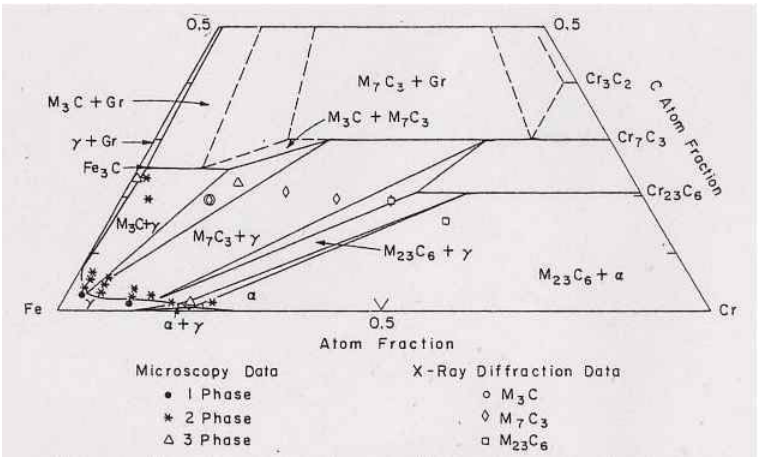

Figure 1.16 – Fe–Cr–C: isothermal section at 1000 °C [87]

$M_{23}C_6$, M_7C_3 and M_3C (M=Fe,Cr). The compounds are rather stoichiometric in terms of C fraction, but accept wide ranges of metal composition.

1.4.2 Kinetics of carburisation

As with oxidation, the morphology of carburisation is the result of a competition between internal precipitation and external scale formation, favoured by rapid carbon inward diffusion and chromium outward diffusion, respectively. The example

of an alloy forming pure chromium carbides is considered. Wagner's analysis [67] predicts the minimum initial mole fraction of chromium in the alloy N^0_{Cr} to form an external scale of the carbide CrC_ν:

$$N^0_{\mathrm{Cr}} = \left(\frac{\pi g^* }{2\nu} \frac{V_{\mathrm{alloy}}}{V_{\mathrm{CrC}_\nu}} \frac{N^{(\mathrm{s})}_{\mathrm{C}} D_{\mathrm{C}}}{D_{\mathrm{Cr}}} \right)^{1/2} \tag{1.74}$$

with the usual notations (see Eq. (1.50)). For materials of interest, the permeability of carbon $N^{(\mathrm{s})}_{\mathrm{C}} D_{\mathrm{C}}$ is very high, so that inward carbon diffusion prevails over outward chromium diffusion, and carbides precipitate internally. For example, in α-Fe at 800 °C, with $a_{\mathrm{C}} = 1$, $N^{(\mathrm{s})}_{\mathrm{C}} D_{\mathrm{C}} = 1.5 \times 10^{-9}$ cm^2 s^{-1} (from solubility data in Ref. [88], and diffusion data in Refs. [89, 90]), whereas $D_{\mathrm{Cr}} = 5.4 \times 10^{-12}$ cm^2 s^{-1} (from diffusion data in [81]).

Internal carburisation obeys the same kinetics as internal oxidation (Section 1.2.3), that is, parabolic kinetics, indicating diffusion control. In the case where carbon permeability is much higher than that of chromium, as illustrated above for α-Fe at 800 °C, the depth of carbon penetration X_{c} is given by [67]

$$X_{\mathrm{c}}^2 = 2\, k_{\mathrm{c}} t \tag{1.75}$$

$$k_{\mathrm{c}} = \frac{N^{(\mathrm{s})}_{\mathrm{C}} D_{\mathrm{C}}}{\nu N^0_{\mathrm{Cr}}} \tag{1.76}$$

where k_{c} is the rate constant. Young and Ahmed published experimental results confirming the parabolic rate law [91] and the influence of the N^0_{Cr} value [92] for Fe–Cr alloys at temperatures around 1000 °C.

As discussed earlier for internal oxidation, the morphology of the precipitates is the result of a competition between nucleation and growth. Depending on alloy microstructure, a more rapid carbon diffusion will lead to a quicker supersaturation and the nucleation will tend to be homogeneously distributed. On the other hand, the presence of grain boundaries will involve a rapid chromium supply to the precipitates and favour their continued growth [19].

Internal precipitation of carbides induces changes in alloys properties, such as increased superficial hardness. This is the desired object of carburisation used as an engineering process. However, the volume increase [93] associated with this phase transformation can be very deleterious to heat resisting alloys.

1.5 Reaction of Fe–Cr alloys in CO_2

A large number of studies have been carried out regarding Fe–Cr alloys reaction in CO_2. This is due to the practical importance of steel as a structural material, and in particular to the use of high pressure CO_2 as a coolant in nuclear power plants. Thus, research published in the 70's as part of the development of the British Magnox and AGR technologies [94, 95] is very useful to the purpose of the present work. For reasons related to both oxidation and mechanical resistance, various steel grades were used as a function of operating temperature. Results for mild steels (containing up to 0.5 wt. % Si and C) and low alloy steels (up to 2.5 wt. % Cr and 1.2 wt. % Mn) are available for low temperatures, typically 300–500 °C. Ferritic 9Cr-1Mo steels were studied at about 500–650 °C. At higher temperatures, typically 600–800 °C, austenitic stainless steels such as 18/8 (18Cr/8Ni, 304 and 316 series), 20/25 (904L) or 25/20 (310) were considered. Laboratory testing temperatures were often 100–200 °C higher than those corresponding to actual operating conditions at the time of the studies.

When used as a coolant in nuclear power plants, high pressure CO_2 contained low levels of H_2O, CO or H_2, which was reproduced in laboratory testing conditions. The present Section is focused on "dry CO_2", so that the experimental results concern gases with low concentrations of H_2O, typically a few ppm.

Because of the presence of both carbon and oxygen in the atmosphere, Fe–Cr alloys exposed to CO_2 may undergo carburisation and/or oxidation. In a first Section, gas phase thermodynamics are considered to determine the oxidising and carburising potentials of CO–CO_2 mixtures with respect to Fe–Cr alloys. As will be seen, pure CO_2 and CO_2-rich mixtures favour oxidation, such that external scales consist of oxides rather than carbides in these atmospheres. Section 1.5.2.1 addresses the reaction of low chromium materials in gas mixtures simulating nuclear power plant cooling atmospheres, that is, low temperature, high pressure gas containing up to a few percent CO. Subsequent Sections deal with reaction in almost pure CO_2 at higher temperatures and atmospheric pressure, including external scaling and internal attack. Reaction and mass transport mechanisms, as well as interactions between oxidation and carburisation, are finally discussed.

1.5.1 Thermodynamics of competitive oxidation and carburisation

Equilibrium between carbon monoxide and carbon dioxide is written

$$CO_2 = CO + \frac{1}{2} O_2 \tag{1.77}$$

$$K_{1.77} = \frac{p_{CO} p_{O_2}^{1/2}}{p_{CO_2}} \tag{1.78}$$

Carbon is produced by the Boudouard reaction, (1.72), for which the law of mass action is written

$$K_{1.72} = \frac{p_{CO_2} a_C}{p_{CO}^2} \tag{1.79}$$

In laboratory conditions, the oxygen partial pressure in flowing gas mixtures is often controlled via Eq. (1.78), by imposing the fluxes of CO and CO_2. Similarly, the carbon activity is controlled by imposing the composition and total pressure of the CO–CO_2 mixture, noting that Eq. (1.79) can be written

$$a_C = \frac{K_{1.79} b^2 p_T}{1 + b} \tag{1.80}$$

where $b = \dfrac{p_{CO}}{p_{CO_2}}$ and $p_T = p_{CO} + p_{CO_2}$. Figure 1.17 presents the carbon activity as a function of oxygen partial pressure for CO–CO_2 mixtures, both determined by the value of the p_{CO}/p_{CO_2} ratio. The values are calculated at 650 and 800 °C, for

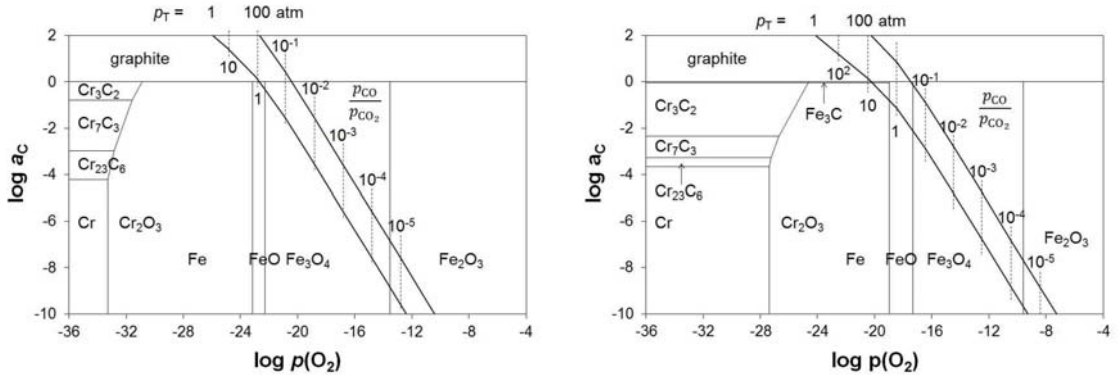

(a) 650 °C (b) 800 °C

Figure 1.17 – Oxygen and carbon activities in CO–CO_2 mixtures, and predominance diagrams for iron and chromium oxides and carbides.

total pressures of 1 and 100 atm, using thermodynamic data tabulated in Ref. [74]. The dashed lines are iso-p_{CO}/p_{CO_2} lines, with the corresponding ratios indicated.

The fact that they are vertical reflects the pressure dependance of reaction (1.72), and the absence of such dependance for reaction (1.77). At a given total pressure, the p_{CO}/p_{CO_2} ratio is an indicator of the oxidising and carburising potentials of the CO–CO_2 mixture. In Fig. 1.17 predominance diagrams for iron and chromium oxides and carbides, generated using thermodynamic data in Tabs. 1.1 and 1.3, are superimposed on the CO–CO_2 potentials graphs. Clearly, CO_2-rich mixtures are oxidising and decarburising with respect to iron and chromium. In the following paragraphs, the competitive reaction of oxygen and carbon with iron or chromium is discussed for CO–CO_2 mixtures in general.

1.5.1.1 Case of pure iron

Let us consider temperatures above 570 °C, so that the main reactions are the formation of FeO and cementite Fe_3C

$$\mathrm{Fe} + \frac{1}{2}\,\mathrm{O_2} = \mathrm{FeO} \tag{1.81}$$

$$(p_{\mathrm{O_2}})_{\mathrm{eq}}^{-1/2} = \exp\left(-\frac{\Delta_{\mathrm{f}} G^0_{\mathrm{FeO}}}{RT}\right) \tag{1.82}$$

$$3\,\mathrm{Fe} + \mathrm{C} = \mathrm{Fe_3C} \tag{1.83}$$

$$(a_{\mathrm{C}})_{\mathrm{eq}}^{-1} = \exp\left(-\frac{\Delta_{\mathrm{f}} G^0_{\mathrm{Fe_3C}}}{RT}\right) \tag{1.84}$$

The competition reaction is written

$$\mathrm{Fe_3C} + \frac{3}{2}\,\mathrm{O_2} = 3\,\mathrm{FeO} + \mathrm{C} \tag{1.85}$$

and, assuming that the solid phases are non-miscible, the equilibrium condition is

$$\left(\frac{a_{\mathrm{C}}}{p_{\mathrm{O_2}}^{3/2}}\right)_{\mathrm{eq}} = \exp\left(\frac{-3\Delta_{\mathrm{f}} G^0_{\mathrm{FeO}} + \Delta_{\mathrm{f}} G^0_{\mathrm{Fe_3C}}}{RT}\right) \tag{1.86}$$

When the actual gas $p_{\mathrm{O_2}}$ and a_C are compared to the equilibrium conditions expressed by Eq. (1.82), (1.84) and (1.86), four scenarios of external scaling may arise. This problem has been formalised by Pettit et al. [96]:

1. $(p_{\mathrm{O_2}})_{\mathrm{gas}} \geqslant (p_{\mathrm{O_2}})_{\mathrm{eq}}$ and $(a_{\mathrm{C}})_{\mathrm{gas}} < (a_{\mathrm{C}})_{\mathrm{eq}}$ — only FeO is stable;
2. $(p_{\mathrm{O_2}})_{\mathrm{gas}} < (p_{\mathrm{O_2}})_{\mathrm{eq}}$ and $(a_{\mathrm{C}})_{\mathrm{gas}} \geqslant (a_{\mathrm{C}})_{\mathrm{eq}}$ — only Fe_3C is stable;
3. $(p_{\mathrm{O_2}})_{\mathrm{gas}} \geqslant (p_{\mathrm{O_2}})_{\mathrm{eq}}$ and $(a_{\mathrm{C}})_{\mathrm{gas}} \geqslant (a_{\mathrm{C}})_{\mathrm{eq}}$ — the most stable phase is determined by Eq. (1.86) and one of the following occurs:
   a) $\left(\frac{a_{\mathrm{C}}}{p_{\mathrm{O_2}}^{3/2}}\right)_{\mathrm{gas}} > \left(\frac{a_{\mathrm{C}}}{p_{\mathrm{O_2}}^{3/2}}\right)_{\mathrm{eq}}$ — Fe_3C predominates;

b) $\left(\frac{a_C}{p_{O_2}^{3/2}}\right)_{gas} < \left(\frac{a_C}{p_{O_2}^{3/2}}\right)_{eq}$ — FeO predominates.

These thermodynamic conditions determine which phase is most stable as an external scale. If this scale is not compact and gas has continuous access to the metal, p_{O_2} and a_C remain those of the bulk atmosphere at the metal surface and these conditions remain valid. If, on the other hand, the scale is compact, chemical potential gradients are generated across it, and conditions at the metal/scale phase boundary differ from those considered above. Let us study the possibility of Fe_3C formation in the presence of a FeO scale (case 3b), assuming that a steady state has been reached where both metal/oxide and oxide/gas interfaces are in thermodynamic equilibrium. As a consequence of the oxygen activity gradient across the oxide, if carbon penetrates the scale, Fe_3C is expected to form where the $\frac{a_C}{p_{O_2}^{3/2}}$ ratio exceeds that defined by Eq. (1.86). In order to determine the depth at which condition 3 switches from 3b to 3a, the evolution of the carbon activity across the scale must be known, which depends on the thermodynamics of the interaction between CO–CO_2 and the oxide, and on the conditions of the C-bearing species transport in the oxide. Considering the equilibrium between CO and CO_2 via Eq. (1.77), it may be argued that the decrease in p_{O_2} across the oxide scale would correspond to an increase of the p_{CO}/p_{CO_2} ratio, which would favour carbide precipitation. This question will be treated in Chapter 5.

Finally, it should be emphasised that the value of $(a_C)_{eq}$ is relatively high, 1.5 and 0.89 at 650 and 800 °C, respectively. Consequently, at low temperatures, if a_C is high enough to stabilise Fe_3C, then $a_C \geqslant 1$ and graphite also is stable. The thermodynamics of the Boudouard reaction, (1.72), are such that graphite precipitation is favoured at low temperatures. The issue of carbon deposition in oxide scales is addressed in Section 1.5.2.1.

1.5.1.2 Case of Fe–Cr alloys

In the case of Fe–Cr alloys, oxidation itself may result in various situations, as discussed in Section 1.3, and only limiting cases can be studied using the argument of the previous paragraph. For instance, a very dilute alloy will tend to form only iron oxides and chromium carbides. The thermodynamics of the situation are straightforward, and the only interest lies in determining the variation in a_C across the oxide scale, or of p_{O_2} across the carbide scale. Competitive reaction of oxygen and carbon with chromium will arise for high chromium contents. The relative stabilities of Cr_2O_3 and $Cr_{23}C_6$ may then be compared using the following predominance

criterion

$$2\,Cr_{23}C_6 + \frac{69}{2}\,O_2 = 23\,Cr_2O_3 + 12\,C \tag{1.87}$$

$$\left(\frac{a_C^{12}}{p_{O_2}^{69/2}}\right)_{eq} = \exp\left(\frac{-23\Delta_f G^0_{Cr_2O_3} + 2\Delta_f G^0_{Cr_{23}C_6}}{RT}\right) \tag{1.88}$$

Let us consider CO_2-rich atmospheres, where Cr_2O_3 predominates, and forms a scale on the alloy surface. Provided that the carbon activity across the scale is known, the thermodynamic condition for carbide formation in the alloy is determined by taking into account chromium depletion. The value of the interfacial chromium mole fraction, N^i_{Cr}, is calculated from the rates of Cr_2O_3 growth and chromium diffusion in the alloy, as discussed in Section 1.3.4. Assuming that the alloy is an ideal solution of chromium in iron, the oxygen partial pressure at the interface between Cr_2O_3 and the depleted alloy is given by

$$(p_{O_2})^{-3/2}_{eq} = \left(N^i_{Cr}\right)^2 \exp\left(\frac{-\Delta_f G^0_{Cr_2O_3} + 2\Delta\bar{G}^{xs}_{Cr}}{RT}\right) \tag{1.89}$$

and the carbon activity required to form $Cr_{23}C_6$ at the metal/oxide interface is determined using

$$(a_C)^{-6}_{eq} = \left(N^i_{Cr}\right)^{23} \exp\left(\frac{-\Delta_f G^0_{Cr_{23}C_6} + 23\Delta\bar{G}^{xs}_{Cr}}{RT}\right) \tag{1.90}$$

Of course the equilibrium carbon activity can be calculated for any position in the alloy, using the variable $N_{Cr}(x,t)$ of Section 1.3.4. Severe chromium depletion would require a very high carbon activity to form the carbide, certainly above unity, entering the field of graphite stability.

As discussed in Section 1.3.4, for Cr_2O_3 to be thermodynamically and kinetically stable, a sufficient flux of chromium is required at the metal/oxide interface. Carbon ingress in the alloy and subsequent precipitation of chromium-rich carbides may possibly affect the outward flux of chromium. This concern will be addressed in Section 1.5.6.

1.5.2 Oxidation and carburisation products

1.5.2.1 Reaction at low temperature, high pressure

This Section is concerned with industrial-type CO_2-rich gas mixtures, containing up to several percent CO. The gas pressures in the works cited are in the range 1–53 bars.

At low temperatures (300–580 °C) and high pressure, pure iron and mild and low alloy steels initially form a scale of dense Fe_3O_4 [97–100]. The oxidation rate is relatively low and continuously decreasing. The duration of this "protective" stage varies with temperature, alloy and gas composition, from hundreds to tens of thousands of hours. In a subsequent stage, scale breakdowns occurs locally, and nodules of porous Fe_3O_4 spread until complete surface coverage is reached [97, 98, 101]. This non-protective stage was not observed during exposure at atmospheric pressure [100]. The non-protective scale contains significant amounts of carbon. In Ref. [97], the carbon content was measured as 6 wt. % by EPMA, which corresponds to an approximately equimolar carbon–Fe_3O_4 mixture. After the transition period, oxidation proceeds according to rapid, linear kinetics, showing that the scale no longer provides the relatively good protection associated with diffusion-controlled growth. Because the formation of the porous, carbon-containing oxide is associated with a transition from relatively slow, parabolic kinetics to more rapid, linear kinetics, it was termed "breakaway" in the literature, although it is not related to the concept of selective oxidation. This type of breakaway will be briefly discussed here.

Breakaway of mild and low alloy steels in low temperature (300–580 °C) CO_2 was seen to be favoured by increasing CO content [97] and gas pressure [100], and to be associated with carbon deposition in the oxide scale. Surman [102] used CO–CO_2 mixtures at atmospheric pressure to reproduce the reaction observed in high pressure CO_2 on pure iron at 500 °C. While oxidation was protective in gases containing up to 26% CO, breakaway was observed for a 40%CO–CO_2 mixture. In addition, the carbon content of the oxide drastically increased between 20% and 40% CO mixtures. From these observations, the author [102] concluded that breakaway oxidation of mild and low alloy steel in high pressure CO_2 could be caused by the generation of a high CO-containing atmosphere within the scale, leading to carbon deposition. Carbon would then prevent the oxide crystallites from sintering and promote a non-protective structure. Carbon deposition in scales is also thought to cause mechanical breakdown by generation of high stresses [103]. A mechanistic model for breakaway oxidation of mild steel in CO_2 in the temperature range 350–550 °C was proposed by Gibbs [104], which involves CO build-up in pores of the scale inner layer, carbon deposition by the Boudouard reaction and the generation of compressive stresses.

Reaction of Fe–9Cr alloys and 9Cr-1Mo steels in high pressure CO_2 at temperatures of 550–580 °C leads to the formation of iron-rich oxide scales. Initially, the scales are duplex, formed by an outer Fe_3O_4 layer and an inner Fe–Cr spinel layer [105–108]. The presence of an Fe_2O_3 layer at the scale/gas interface was also

reported [109]. During a protective stage the scale is dense and grows according to parabolic kinetics. A transition to non-protective behaviour is subsequently observed, marked by carbon deposition [105] and the development of multiple layers in the inner part of the scale [107,108], and a transition to fast linear kinetics [106]. The similarities between these observations and those reported for breakaway of mild and low alloy steel suggest a common reaction mechanism, although in the case of 9Cr alloys views on the role of carbon deposition disagree, some authors considering it to mark the onset of breakaway oxidation [95], and others observing it in protective scales [106].

In summary, a form of breakaway involving carbon deposition and mechanical breakdown of initially dense scales was seen to occur on iron and low chromium alloys. This type of non-protective behaviour was associated with relatively long reaction times at low temperatures, in high pressures atmospheres containing up to several percent CO.

1.5.2.2 Oxidation of pure iron

Smeltzer [110] investigated the oxidation of iron in pure CO_2 at atmospheric pressure in the temperature range 600–1100 °C. The scales consisted of a large proportion of FeO with an thin outer Fe_3O_4 layer below 910 °C, and only FeO at higher temperatures. The oxidation rate obeyed a linear law during an initial period, and a parabolic law for longer exposures. Linear kinetics were thought by the author to be due to rate control by the slow surface reaction (dissociation of CO_2 and incorporation of chemisorbed oxygen in the scale). As the scale grew thicker, cation diffusion became slower, resulting in parabolic kinetics. The parabolic rate constants were smaller for reaction in CO_2 than reaction in oxygen at the same pressure. According to the author, since the oxygen activity in CO_2 is smaller than that of oxygen gas, the oxygen concentration in FeO at the scale/gas interface is smaller in CO_2, therefore the gradient of iron vacancy concentration is also smaller and iron diffusion proceeds at a lower rate than in oxygen.

Rahmel and Tobolski [111] oxidised iron at 950 °C in O_2–CO_2 mixtures , with 11 to 84 % CO_2. Oxidation proceeded according to parabolic kinetics, with rate constants about 1.2 times higher in the O_2–CO_2 mixtures than in pure O_2. The addition of CO_2 resulted in increased scale porosity, and caused the displacement of inert markers from the metal/oxide interface outward in the FeO layer. On the basis of an oxide dissociation–reformation mechanism (see Section 1.5.4), the authors suggested that the presence of a CO–CO_2 mixture in pores enabled oxygen

transport inward, and mitigated the reduction in diffusional cross-section otherwise associated with porosity.

1.5.2.3 External scaling of Fe–Cr alloys and chromium steels

Exposure of alloys containing up to $\sim$ 15–18 wt. % chromium to pure CO_2 at atmospheric pressure and temperatures above 600 °C leads to the formation of external oxide scales of similar morphology to those described in Section 1.5.2.1 for reaction at lower temperatures. The scales are multilayered but separated in two parts, with the interface at the original alloy surface. The outer part is composed of iron oxides and is relatively compact, while the inner part contains both iron and chromium, and presents a significant porosity [96, 112]. Fujii and Meussner [112] studied the reaction of model Fe–Cr alloys containing 1 to 15 wt. % chromium at 700, 900 and 1100 °C. In all cases the inner layer consisted of a mixture of FeO and Fe–Cr spinel oxide. The outer part of the scale contained FeO, Fe_3O_4 and Fe_2O_3 layers at 700 °C, FeO and Fe_3O_4 at 900 °C and only FeO at 1100 °C. The absence of the higher iron oxides reflects the increase in the outward flux of iron at the scale/gas interface with increasing temperature. This multilayer morphology was also reported by other investigators [12,96] for Fe–15Cr alloys reacted at 900 °C, and for an 18/8 (type 304) steel in the temperature range 649–982 °C [113]. Thus, non-selective oxidation of low chromium alloys in pure CO_2 is seen to produce the same oxide scales as those formed during exposure to air, as was described in Section 1.3.3.

Cox et al [114] exposed model Fe–Cr alloys to a CO_2–1%CO mixture at 600 °C and atmospheric pressure. Alloys containing 5, 9 and 12 wt. % Cr grew Fe-rich multilayer oxide scales, while Fe–15Cr and Fe–20Cr first formed a Cr-rich, rhomboedral $(Fe, Cr)_2O_3$ scale before suffering breakaway. The duration of the protective stage varied, and the authors noted that it was sensitive to Cr content, surface preparation and crystal orientation of the metal substrate. However, variability in the time to breakaway was also observed between specimens of the same composition, surface state and microstructure [115]. Breakaway was described as follows [115]. Initially, a thin Cr-rich α-M_2O_3 film grows according to parabolic kinetics. During a transition stage, spinel oxide crystals are formed locally. The nuclei spread laterally and thicken, until complete surface coverage is reached and oxidation proceeds according to secondary parabolic kinetics. Fujii and Meussner [112] also reported that Fe–15Cr and Fe–20Cr alloys reacted at 1100 °C initially formed a protective Cr_2O_3 scale, before developing the multilayer oxide. The incubation time was longer in the case of the Fe–20Cr alloy, but no details on the breakaway reaction were given.

Giggins and Pettit [12] showed that reaction of an Fe–35Cr alloy at 600 and 900 °C resulted in exclusive Cr_2O_3 formation.

Information regarding reaction in industrial-like conditions is inconclusive, because commercial steels differ in many aspects other than the chromium content. Allan et al [116] tested various ferritic and austenitic steels in high pressure (14–41 bar) CO_2 with 2–5 % CO. At 650–700 °C, alloys containing 12 and 25 wt. % Cr formed only Cr_2O_3, while the 15Cr and 18Cr steels showed a wide range of behaviour, including local formation of duplex Fe-rich oxide, consisting of an outer Fe_3O_4 layer and an inner Fe–Cr spinel layer. At 750 °C, steels of types 18/8/Nb, 19/14/Nb, 20/20 and 20/25/Nb were tested, and only the 18/8/Nb steels suffered breakaway. Garrett et al [117] exposed austenitic stainless steels based on the compositions 18 wt. % Cr – 8 wt. % Ni (Type 316 and 321) and 25 wt. % Cr – 20 wt. % Ni (Type 310) to a 41 bar CO_2–2%CO mixture at 650 °C. All alloys produced both Cr_2O_3 and duplex iron-rich oxide nodules, the latter being found in small proportions on the 25/20 steels, but far more prevalent on the 18/8 steels. Nodules found on the 25/20 steels were relatively thin and contained about 35 wt. % Cr in the inner layer. The duplex oxide formed on the 18/8 steels was much thicker, and contained only 22 wt. % Cr in the inner layer. In most cases a "healing layer" containing 35 wt. % Cr was also observed at the base of the scale.

1.5.2.4 Internal attack

The work of Fujii and Meussner [112] on reaction of Fe–Cr alloys containing 1–15 wt. % Cr in pure CO_2 provides a detailed description of internal attack underneath the multilayer Fe-rich oxide. Internal oxidation occurred to a small extent at all temperatures, and the subscale reaction was mainly concerned with carbon. At 700 °C, all alloys were initially ferritic, and carbon entry in the substrate caused internal precipitation of Fe–Cr carbides, to an extent increasing with alloy chromium concentration. Intergranular carbides were found throughout the specimens, while intragranular ones were present only near the metal/oxide interface. The Fe–Cr spinel particles present in the inner layer were replicas of the carbides, which sometimes remained embedded in the oxide near the alloy surface, showing that in situ oxidation of the carbides occured within the inner oxide layer (that is, it was relatively slow compared to the rate at which the oxidation front advanced inward). Carbon dissolution was also seen to occur in pure iron, although no carbides were formed. At 900 °C, pure iron initially had the BCC ferrite structure, but carbon ingress resulted in the formation of an austenite band near the metal/oxide

interface. In the case of the initially ferritic Fe–1Cr alloy, the entire alloy was transformed to austenite, which formed pearlite on cooling, to an extent increasing with reaction time, reflecting the progressively increasing carbon uptake. For the 5 and 10Cr compositions, the austenitic alloy dissolved carbon at high temperature, and transformed to martensite on cooling. The initially ferritic Fe–15Cr alloy produced a $\gamma + M_{23}C_6$ mixture near the metal/oxide interface, and the lamellar austenite regions formed martensite on cooling.

McCoy [113] also reported that the extent of carbide precipitation underneath the multilayer oxide increased with chromium concentration in model alloys, but that it decreased when Cr_2O_3 was formed. Indeed, Giggins and Pettit [12] showed that Cr_2O_3 was a much more efficient barrier to carbon than is Fe-rich oxide: during reaction in pure CO_2 at 600 and 900 °C, carbide precipitation was scarce under Cr_2O_3 formed on Fe–35Cr, but extensive under the multilayer oxide formed on Fe–15Cr. The same observation was made after reaction of commercial steels in atmospheric [13] or high [116] pressure CO_2-rich atmospheres. Meier et al [118] studied the influence of Cr_2O_3 thermodynamic stability on its ability to exclude carbon. Their results confirmed that stable, growing Cr_2O_3 scales were effective barriers to carbon penetration, and that iron oxides were not.

1.5.3 Scaling mechanism

Iron-rich, multilayer oxide scales formed in CO_2-rich atmospheres as a result of non-selective oxidation of Fe–Cr model alloys or steels were seen in the preceding Sections to present similar morphologies, despite the variety of the experimental conditions. To a certain extent, a common view is held by various investigators as to the growth mechanism of these scales. The multilayer morphology was also observed during oxidation in other corrosive environments containing oxygen-bearing species such as SO_2, H_2O or (Pb–Bi)–O, which might suggest a common growth mechanism, as claimed by Rouillard et al [109].

Oxidation experiments on Fe–9Cr alloys using isotopic $C^{18}O_2$ tracers [107, 108, 119] showed that the outer layer was formed at the scale/gas interface, indicating that it grows by iron outward diffusion. As a result, vacancies are injected and condense in the underlying metal, eventually forming pores at the metal/oxide interface [114]. The inner layer is commonly thought to grow at this interface, in the so-called "available space", by inward oxygen transport [105, 109, 120]. However, on the basis of $C^{18}O_2$ experiments, Taylor et al [107] argued that the reaction sites were in fact distributed within the inner layer, although recognising that continued

growth within the oxide would lead to large compressive stresses and mechanical failure, which was not observed. Oxygen was shown by means of $C^{18}O_2$ tracers [119] to reach the inner layer by gas transport rather than solid-state diffusion. This observation is also supported by considering the fact that oxygen lattice diffusion in iron oxides is too slow to account for the observed growth rates, as noted in Refs. [103, 107, 120]. Pritchard and Truswell [106] studied the role of the inner and outer layers in the overall kinetics by oxidising a 9Cr steel in CO_2, removing part of the multilayer scale, and resuming oxidation. The authors noted that the removal of the outer part had no effect on the oxidation kinetics, while removal of part of the inner layer resulted in a rate increase, and concluded that diffusion in the inner layer was the rate-limiting step. Oxygen transport is thought to be fast, so that iron diffusion is rate-determining [120]. This is also reflected in the fact that scales with inner layers of different compositions grow at different rates [105].

1.5.4 Mass transport in oxide scales

In the same way that oxygen diffuses inward to form the inner oxide layer, carburisation of the metal substrate indicates that carbon traverses the scale. Carburisation was seen in Section 1.5.2.4 to occur underneath iron-rich multilayer and (to a lesser extent) Cr_2O_3 scales grown in pure CO_2. Evidence for carbon transport across Cr_2O_3 was also provided from oxidation experiments carried out in CO–CO_2 [12, 96] or other C-containing mixtures. For instance, pure chromium exposed to a CO–CO_2–N_2 mixture [121] formed a three-layer external scale, composed of chromium nitride in contact with the metal, chromium carbides in the middle and Cr_2O_3 at the scale/gas interface. Maintained growth of this structure indicates that the Cr_2O_3 scale was permeable to carbon. However, Wolf and Grabke [122] investigated carbon distribution in bulk oxides by detecting ^{14}C with a sensitivity of 0.01 ppm, and showed that there was no measurable solubility of carbon in FeO, Fe_3O_4 and Cr_2O_3. Carbon was only detected in cracks, pores or grain boundaries which had cracked open. As a consequence, carbon transport across scales of these oxides cannot be due to dissolution and lattice diffusion. Transport could occur instead by means of molecular CO_2, but the scale microstructures are reported [112] to appear impermeable to gas. Furthermore, these scales grow at rates controlled by solid-state diffusion, and continuous pathways for gas phase transport through the scale therefore cannot exist during steady-state oxidation.

The exact mechanism for transport of both carbon and oxygen by molecular diffusion is not clear, although many tentative explanations have been published.

As initially proposed by Rahmel and Tobolski [111], mass transport across pores has been suggested to occur by oxide dissociation–reformation [112]. As seen in Fig. 1.18, this mechanism involves oxygen generation by oxide dissociation at the top of a pore, its consumption by oxide reformation at the bottom of the pore, and its transport by means of a CO–CO_2 mixture. As a consequence no new oxide is

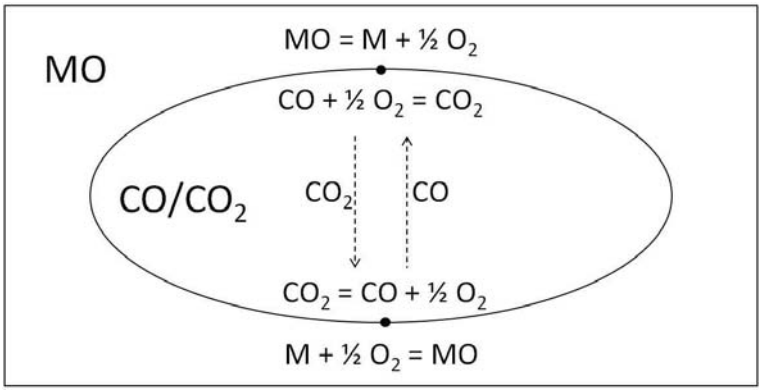

Figure 1.18 – Schematic representation of the dissociation/reformation mechanism.

formed, and the pore migrates upward. Oxygen transport by this means is thought to be significant only if the pore contains a gas mixture such as CO–CO_2 or H_2–H_2O, in which the total gas pressure is much higher than the oxygen pressure in equilibrium with the oxide.

Extending this concept, and in particular the early works of Mrowec [57] and Bruckmann et al [123, 124], Gibbs and Hales [46] proposed a model for continued growth of inner layers of duplex scales involving the generation of dissociation microchannels, through which molecular CO_2 could enter the scale. Such an open pore might be expected to heal by oxidation, but according to the authors [46] there is a critical value for the channel's diameter under which the oxygen activity gradient down the channel is the same as that in the scale. Since the outward cation flux follows iso-oxygen activity contours, cations are expected to migrate parallel to and not towards the channel (see Figure 1.19). However, the fact that the driving force for the cation flux is a gradient in the oxygen activity does not mean that cations cannot diffuse at all in directions other than that of the steepest gradient. In the situation represented in Figure 1.19(b), a minor part of the cation flux could in fact be directed towards the channel, causing its healing by oxidation. Furthermore, such microchannels have never been observed and their existence as a possible alternative to solid-state diffusion is only supported by the fact that molecular CO_2 must

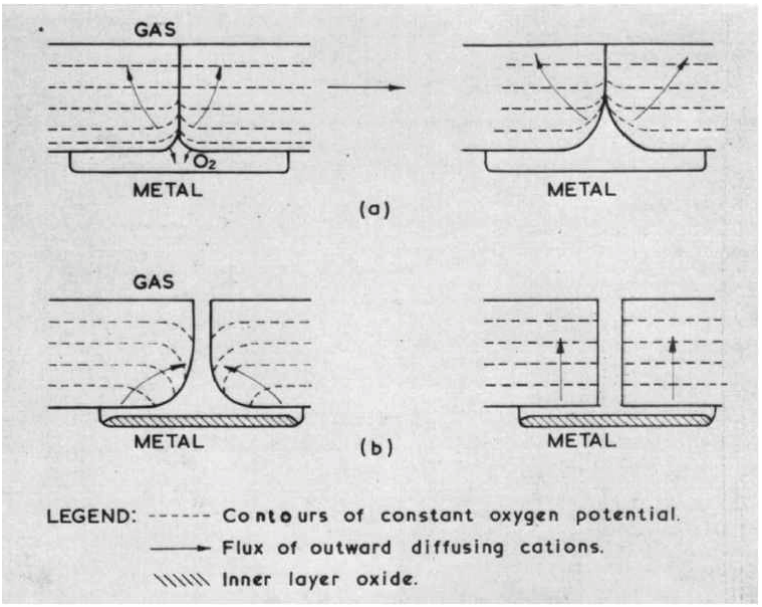

Figure 1.19 – The development of microchannels above interfacial voidage. (a) Anisotropic dissociation opens up channels. (b) Channel "heals" to equilibrium size. After Ref. [46].

enter the scale. Highlighting some shortcomings of the dissociation microchannels, Kofstad [43] proposed an alternative route for molecular transport, based on grain deformation and grain boundary sliding, and resulting in porosity along oxide grain boundaries. Other mechanisms have been proposed for the formation of nano- or microchannels, as summarised in Ref. [109]. In studies involving carburisation of chromia-forming materials [121, 125, 126], molecular transport via grain boundaries has been suggested to account for carbon transfer through the scale.

1.5.5 Carburisation mechanism

Whatever the means of carbon transport across oxide scales might be, the fact remains that it results in alloy carburisation. However, as discussed in Section 1.5.1, gas phase thermodynamics show that CO_2-rich atmospheres are expected to be decarburising with respect to iron and chromium at the relevant temperatures. A commonly held view is that reaction of iron with CO_2 constitutes a source of CO via

$$\mathrm{Fe} + \mathrm{CO_2} = \mathrm{FeO} + \mathrm{CO} \tag{1.91}$$

or

$$3\,\mathrm{Fe} + 4\,\mathrm{CO_2} = \mathrm{Fe_3O_4} + 4\,\mathrm{CO} \tag{1.92}$$

which builds up in pores at the metal/oxide interface and causes the local carburising potential of the gas to increase [102, 104, 112, 113, 116, 127]. A mechanistic and quantitative description has been proposed in a very recent model for carburisation of a 9Cr steel in CO_2 by Rouillard et al [128].

The term "build-up" often used in the works cited before suggests a non steady-state situation, and Rouillard's model [128] is explicitly based on a non-equilibrium description, disregarding the thermodynamics of the system. Nonetheless, the increase in p_{CO}/p_{CO_2} toward the metal/oxyde interface may be understood by considering the equilibrium between carbon dioxide and carbon monoxide, Eq. (1.77). Applying the law of mass action, Eq. (1.78), to scales growing at rates controlled by solid-state diffusion, where local thermodynamic equilibrium prevails, the p_{O_2} gradient along the scale is expected to result in an opposed p_{CO}/p_{CO_2} gradient [19,20,129], and the carburising potential to increase and reach a maximum at the metal/oxide interface, where p_{O_2} is minimum.

Thermodynamic aspects relevant to carburisation of Fe–Cr alloys in CO_2 will be specifically addressed as part of the present work in Chapter 5.

1.5.6 Influence of carbide formation on selective oxidation

Giggins and Pettit [12] studied the oxidation behaviour of an Fe–15Cr alloy in oxygen, CO_2 and CO–CO_2 mixtures at 900 °C. The alloy produced a Cr_2O_3 scale when reacted in O_2, but formed an iron-rich duplex scale and an extensive network of internal Cr-rich carbides when exposed to CO_2. The alloy was also precarburised in a graphite pack to obtain the same carbides, and subsequently oxidised in O_2, reacting with the same rate as it did in CO_2. The authors thus concluded that non-selective oxidation in CO_2 was due to the extensive internal carbide precipitation. When reacted in CO–CO_2 with $p_{CO}/p_{CO_2} = 3$, the Fe–15Cr alloy formed a Cr_2O_3 scale disrupted by areas of internal Cr_2O_3 and extensive carbide precipitation.

The association between non-protective oxidation and carburisation led the authors [12] to conclude that even though the carbides released chromium for outward diffusion, the flux of chromium was lower than in the absence of carbides, so that, given the inward oxygen flux, internal Cr_2O_3 formation could not be avoided. Using a CO–CO_2 mixture with $p_{CO}/p_{CO_2} = 23$, the inward oxygen flux was decreased, and Cr_2O_3 formed as an external scale. According to the authors [12], the interaction between oxidation and carburisation is two-fold: alloys containing moderate amounts of chromium, such as Fe–15Cr, oxidise faster than high chromium alloys, such as Fe–35Cr, before a protective steady-state is reached with the formation of a

continuous Cr_2O_3 scale. The faster oxidation leads, via the CO–CO_2 equilibrium, to higher carbon activity, which enhances carburisation, and in turn prevents selective oxidation of chromium.

Reacted at 550 °C, commercial steels containing 9–12Cr were seen to form protective oxide scales in air, but to undergo breakaway oxidation in Ar–CO_2 [13]. Meier et al [14] studied oxidation of model Fe–Cr alloys in various environments in the temperature range 550–650 °C. During exposure in air, alloys containing 13 and 22Cr formed only Cr_2O_3, while the Fe–10Cr alloy showed local Fe-rich nodule formation. In Ar–30CO_2, the Fe–22Cr alloy maintained its protective behaviour, but the 10 and 13Cr alloys underwent important breakaway oxidation. On the basis of the work of Ref. [12] (see previous paragraphs), the deleterious influence of CO_2 was attributed to extensive carbide precipitation. Meier et al [14] also confirmed the complex interaction between oxidation and carburisation first discussed in Ref. [12]. A P92 (9Cr) steel was exposed to Ar–50CO_2 and Ar–50CO_2 plus 1 and 3 % O_2 at 550 °C. While the steel formed a continuous iron-rich multilayer scale in Ar–50CO_2, O_2 additions resulted in the local formation of Cr_2O_3 regions, to an extent increasing with the gas oxygen content. According to the authors, oxygen consumed the CO produced by the oxidation reaction, thereby reducing the carburisation potential of the gas, and the adverse effects due to carburisation.

1.6 Reaction of Fe–Cr alloys in H_2O

Water vapour being present in most of the industrial atmospheres relevant to high temperature oxidation, either as an impurity or as a major constituent, its effect on oxidation has raised considerable interest, and a very large number of papers have been published on this subject. This is reflected, for example, in the recent review by Saunders et al [130]. The present Section is mostly limited to studies concerning Fe–Cr alloys.

Experimental findings relative to the oxidation of pure iron and Fe–Cr alloys in H_2O-rich atmospheres are first presented. Section 1.6.4 deals with the various effects of H_2O on oxidation, and their possible influence on selective oxidation of chromium.

1.6.1 Oxidation of pure iron

Oxidation kinetics of pure iron are little affected by the addition of H_2O to air or O_2. Investigating the case of iron at different temperatures, Rahmel and Tobolski [111] observed no kinetic effect at 750 °C, whereas oxidation rates rose by factors of 1.2 and 1.6 at 850 °C and 900 °C, respectively. The authors also noted that H_2O additions resulted in increased scale porosity, and caused the displacement of inert markers from the metal/oxide interface outward in the FeO layer, as CO_2 additions did. The changes in oxidation kinetics and morphology were explained by the authors on the basis of a mechanism involving oxide dissociation–reformation, as briefly described in the case of CO_2 in Section 1.5.2.2. Tuck et al [131] also observed a small increase in iron oxidation kinetics when adding 12 % H_2O to O_2 at 980 °C.

Rahmel and Tobolski [111] reported that when H_2O was added to O_2, FeO scales showed better adherence to iron substrates, which was attributed by the authors to increased scale plasticity. Tuck et al [131] suggested that dissolution of hydrogen in FeO would enhance the mobility of dislocations and thereby improving the ability of the scale to creep.

1.6.2 Oxidation products

Exposure of Fe–Cr alloys and steels containing up to $\sim$ 15–18 wt. % chromium to Ar–H_2O mixtures at atmospheric pressure results in non-selective oxidation, and the external oxide scales are very much like those formed during exposure to CO_2 (see Section 1.5.2.3).

Fujii and Meussner [132, 133] studied the reaction of iron and Fe–Cr alloys containing 1–25 wt. % chromium in Ar–10%H_2O at 700–1100 °C. Alloys containing 15 wt. % Cr or less produced thick Fe-rich multilayer scales, and in all conditions the inner part of the scale was a mixture of FeO and Fe–Cr spinel oxide. The outer layers contained FeO only at 900 °C and 1100 °C, while an outermost Fe_3O_4 layer was visible after reaction at 800 °C, and Fe_2O_3 also formed at the scale/gas interface during reaction at 700 °C. Iron and the Fe–Cr alloys with 15Cr or less reacted according to linear kinetics, all with a similar rate. In view of the scale morphology and oxidation kinetics, the authors concluded that the oxidation rate was determined by an oxide/gas interface reaction. The absence of the higher iron oxides at the higher test temperatures reflects the fast iron outward diffusion, relative to the interfacial process. Essuman et al [134] observed the same type of multilayer scale morphology after oxidation of Fe–10Cr and Fe–20Cr alloys in Ar–7%H_2O at 900 and 1050 °C, identifying the scale/gas interface process as rate-limiting.

Alloys forming iron-rich multilayer scales also undergo internal oxidation [132, 134]. The importance of internal oxidation will be discussed subsequently.

Alloys containing a sufficient chromium concentration initially form a protective Cr_2O_3 scale. After this incubation period, multilayer Fe-rich oxide nucleates and spreads on the alloy surface, until complete coverage is reached. Breakaway is identified by a change from slow, parabolic kinetics to fast, linear kinetics. Breakaway in wet atmospheres has been observed, for example, on a 9Cr steel reacted at 650 °C [17], 12–18Cr ferritic stainless steels reacted at 800–1000 °C [16, 135], model Fe–15Cr and Fe–20Cr alloys at 900–1000 °C [136], or model Fe–20Cr and Fe–25Cr in the temperature range 700–1100 °C [133]. The effects of gas and alloy composition are clear [133, 136]: the duration of the protective stage decreases with decreasing alloy chromium concentration and increasing gas H_2O content.

Meier et al [14] published a systematic study of the chromium concentration required for model Fe–Cr alloys to form Cr_2O_3 in Ar–30H_2O in the temperature range 550–650 °C. Alloys with 9 and 10Cr formed continuous iron-rich multilayer scales. Between 11 and 15Cr, the alloys formed both Cr_2O_3 and iron-rich nodules, the extent of breakaway oxidation decreasing with increasing chromium concentration. Protective oxidation was reached for 16 wt. % chromium. However, the authors also showed that minor alloying additions had a significant importance, since several commercial alloys all containing less than 9 wt. % chromium consistently had lower weight gains than the model alloys.

1.6.3 Scaling and mass transport mechanism

The growth mechanism of multilayer iron-rich scales resulting from non-selective oxidation of Fe–Cr alloys in H_2O-containing environments is thought to be quite similar to that operating in CO_2 (Section 1.5.3). Oxidations experiments in Ar–H_2O using inert markers [132] and in steam using ^{18}O tracers [137] indicated that the outer scale grows by outward cation diffusion, and the inner scale by oxygen transport inwards.

Measurements of the oxygen self-diffusion coefficient in Fe_3O_4 in water vapour at 300–550 °C [138] showed that oxygen solid-state diffusion was at least 5 orders of magnitude too slow to account for the observed growth rate of the inner layer formed on mild steels at these temperatures. As in the case of CO_2 (Section 1.5.4), alternative routes for oxygen transport must be considered.

Outward cation diffusion is thought to cause vacancy injection and condensation into interfacial pores [136,137]. Investigating the oxidation of pure iron, Rahmel and Tobolski [111] suggested that an H_2–H_2O mixture was formed in these pores, and that oxygen transport across the pores occurred by oxide dissocation–reformation (see Section 1.5.4). Fujii and Meussner [132, 133], and later other investigators [17, 103, 131, 137, 139] considered that this mechanism was operating in the case of Fe–Cr alloys. The size and number of pores was found to increase with p_{H_2O} [111], suggesting that water vapour not only enables oxygen transport, but also stabilises the porous structure. Oxide bridges are thought to provide a pathway for continued cation lattice diffusion outwards [111, 132].

The presence of an H_2–H_2O mixture in pores of the oxide scale requires these species to enter the oxide in the first place. Ehlers et al [17] noted that an oxygen activity gradient existed across the scale, as was evident from the stacking sequence of the oxide phases, indicating that transport of the O-bearing species across the scale was slower than gas phase diffusion; the authors suggested H_2O molecular diffusion along internal surfaces. In addition, the scaling rate was found [17] to depend on the p_{H_2O} to p_{O_2} ratio, rather than on p_{H_2O} itself. According to the authors [17], this indicates that a competitive adsorption step is rate-determining. In a review of water vapour effects on the oxidation of chromia-formers, Young [140] related different results obtained in complex atmospheres to the role of competitive adsorption of gas species on oxide surfaces and grain boundaries. In Ref. [121] for example, the addition of H_2O to the reacting gas suppressed the scale permeability to nitrogen.

1.6.4 Effects of H_2O on selective oxidation

The addition of H_2O to a gas mixture, or its substitution for O_2, is known to trigger breakaway oxidation. This effect has been documented in direct comparisons of dry and wet atmospheres, for example for

- 9–12Cr steels in air / Ar–H_2O at 500–700 °C [13];
- Fe–10Cr and Fe–13Cr in air / Ar–H_2O [14];
- a 9Cr steel in N_2–O_2 / N_2–O_2–H_2O at 650 °C [17];
- Fe–10Cr and Fe–20Cr in Ar–O_2 / Ar–H_2O at 900 °C [134];
- an Fe–13Cr alloy in dry and wet air at 680–980 °C [139];
- Fe–5Cr, Fe–10Cr, Fe–15Cr and Fe–20Cr in O_2 / O_2–H_2O at 750 and 900 °C [15];
- 12–18Cr ferritic stainless steels in Ar–O_2 / Ar–H_2O at 800–1000 °C [16, 135].

The critical content for Cr_2O_3 formation is seen to vary with temperature, as could be expected because of the temperature dependence of diffusion coefficients in both oxide and metal phases, but also with the concentration of other alloying elements (see for example Ref. [14]).

Various explanations have been put forward to account for the fact that selective oxidation requires higher chromium concentrations in wet gases than in dry gases. Possible reasons are listed in the following Sections.

1.6.4.1 Chromia growth kinetics and mechanism

Chromia growth on pure chromium was seen to be faster in pure H_2O [141], Ar–H_2O [142] or Ar–H_2–H_2O [143] than in dry oxygen. Accelerated Cr_2O_3 growth due to H_2O addition was also reported in the case of Fe–17Cr and Fe–25Cr alloys [18].

Norby [144] studied hydrogen dissolution in oxides and showed that the value of p_{H_2O}, controlling the lattice proton concentration, could exert an influence on cation and oxygen vacancy concentrations. Similarly, Young [140] related the gas composition dependance of Cr_2O_3 growth at low oxygen potentials to the equilibrium of H_2O with hydroxyl (OH^-) and proton defects.

According to Galerie et al. [145], hydroxyl ions, which are posssibly found in oxides as substitutional defects in oxygen sites or along grain boundaries, play an important role in growth kinetics of Cr_2O_3 formed in wet gases. Noting that OH^- exhibits a higher mobility than O^{2-}, the authors suggested that higher growth rates were expected in wet gases if oxidation is diffusion-controlled and proceeds according to an anionic mechanism (that is, anions diffuse faster than cations).

Zurek et al. [146] used ^{18}O and $H_2^{18}O$ tracers to study the growth mechanism of Cr_2O_3 on Ni-based alloys, and showed that the predominant transport process changed from cationic in Ar–O_2 to anionic in Ar–H_2–H_2O. However, the results of Hultquist et al. [141], obtained from an isotopic tracer study of oxidation of pure chromium, indicate that the situation is more complex. In short term exposures, oxide growth was seen to be more important at both metal/oxide and oxide/gas interfaces when proceeding in H_2O rather than O_2, but the proportions of inner and outer growth were not significantly affected by the gas composition. For longer exposures, the proportion of inner growth was found to be more important in H_2O than in O_2, but this tendency was reversed for chromium specimens whose hydrogen concentration was reduced from 5–7 wt. ppm to less than 1 wt. ppm before exposure.

However, a faster growing scale alone cannot account for accelerated breakaway: as discussed in Section 1.3.4, if a Cr_2O_3 scale is formed initially, the chromium flux entering the scale at the metal/oxide interface is expected to be balanced by an equal flux from the alloy, and the scale is expected to stay kinetically stable so long as depletion does not extend to the whole specimen, and, of course, providing that mechanical integrity is maintained.

Furthermore, the scale adherence to the metal substrate was seen to be improved when Cr_2O_3 was grown in a wet gas [141, 143, 146]. This was directly associated with a drastic reduction of scale spallation during cooling to room temperature, as compared with oxidation in dry oxygen [143]. The better adherence in the presence of H_2O is thought to be due to the important part of anionic growth in wet atmospheres, which reduces the extent of interfacial void formation by vacancy injection [141, 146]. In addition, the presence of a H_2–H_2O mixture in pores of the scale is thought to enable fast oxygen transport by a dissociation–reformation mechanism (see Section 1.5.4), which would result in a decrease of the number and size of interfacial pores, and in turn enhance scale adhesion [143, 146].

It should be noted, nevertheless, that Ikeda and Nii [15] defended an opposite view, observing that scale spallation from model Fe–Cr alloys occurred to a greater extent when H_2O was added to O_2. The authors used the "sulphur decoration" technique, which consists of a short (30 to 60 s) exposure to H_2S at the end of an oxidation experiment. Subsequent analysis of the sulphur distribution enables one to determine which parts of the scale were open to gas penetration during oxidation. According to the authors, exposure of Fe–Cr alloys containing 5 to 20 wt. % Cr to O_2–H_2O led to scale cracking and continued gas penetration to the scale/alloy interface, associated with fast growing Fe-rich oxides, namely breakaway oxidation. In contrast, when the same alloys were exposed to dry O_2, or in the case

of pure metals (Ni and Cr), Fe–30Cr and Fe–19Cr–5Al alloys in both dry and wet atmospheres, cracking was observed, but oxide formation filled up the cracks and prevented continued gas penetration. According to the authors, the effect of H_2O in triggering breakaway oxidation is to cause more frequent scale cracking, or to prevent crack healing. The authors suggested that the bond between oxide grains could be weakened by adsorbed H_2O molecules, making scales fragile.

1.6.4.2 Internal oxidation

Iron–chromium alloys exposed to H_2O-containing gases undergo internal oxidation [17, 132, 134, 147], precipitating Cr-rich oxides. While this is also true in dry O_2, internal attack is enhanced in the presence of H_2O [134, 147]. As discussed in Section 1.2.3, the fact that chromium is oxidised internally or externally is the result of a competition between the inward oxygen flux and the outward chromium flux at the alloy surface or metal/oxide interface. In this respect, the observation of Essuman et al. [134] that internal oxidation does not occur when a Cr_2O_3 layer is formed at the base of the iron-rich scale (after reaction in Ar–20%O_2), but occurs in the absence of Cr_2O_3 (in Ar–4%H_2–7%H_2O and Ar–7%H_2O), is to be expected (see Section 1.2.4). While they recognised this point, the authors claimed that the cause-and-effect relationship must be reversed, and that fast-growing, iron-rich oxides were formed in Ar–7%H_2O precisely because chromium was oxidised internally.

Two mechanisms were put forward in Ref. [134] to account for enhanced internal oxidation in H_2O-containing gases. As H_2O dissociates at the alloy surface to produce dissolved oxygen and hydrogen, rapid hydrogen diffusion inwards would shift the H–O–H_2O equilibrium and result in a metastable state of high oxygen activity, which in turn would enhance the oxygen flux, and the tendency for chromium to oxidise internally. However, the question remains whether the interfacial oxygen activity is controlled by the H–O–H_2O equilibrium or, rather, by the metal/oxide equilibrium. Alternatively, the authors proposed that the presence of hydrogen dissolved in the alloy would increase the oxygen diffusivity by lattice distortion.

In any case, it must be noted that an argument based on oxygen diffusivity, and consequently on the relative importance of internal oxidation, could only be formulated *at a given oxygen activity*, that is, in the present case, for external oxides of the same composition. In Ref. [134], even if one disregards the presence or otherwise of Cr_2O_3 at the base of the scale on the grounds that it results from the absence or not of internal oxides, the composition of the whole scale differs between the Ar–20%O_2 and Ar–7%H_2O reactions. Thus, a direct comparison cannot be

made, and the fast growth of iron-rich oxides in the H_2O-containing atmosphere could, in principle, also result from another H_2O-related effect.

Oxidation experiments of Fe–Cr alloys in dry and wet atmospheres at an oxygen activity set by an Fe/FeO buffer at 800 °C were carried out by Ani et al. [147]. The chromium concentration required for the transition from internal to external oxidation was increased in the presence of H_2O. Internal oxidation of an Fe–5Cr alloy, which produced no external oxide in both dry and wet atmospheres, was showed to proceed at faster rates in wet atmospheres. Furthermore, the authors showed that hydrogen dissolution did not significantly affect the kinetics of chromium diffusion in the metal. Instead, enhanced internal oxidation was attributed to an increase in oxygen permeability. This was associated with a transition in the shape of the internal oxide precipitates, from equiaxe in dry O_2 to spike-like in the presence of H_2O, thought to accelerate oxygen diffusion.

1.6.4.3 Chromium volatilisation

The formation of volatile chromium compounds from Cr_2O_3 scales and its effect on chromium consumption have been documented for many years [148]. It has been lately confirmed that the predominant species in the presence of both O_2 and H_2O is chromium oxy-hydroxide, $CrO_2(OH)_2$ [149], which forms according to

$$\frac{1}{2}\,Cr_2O_3 + H_2O + \frac{3}{4}\,O_2 = CrO_2(OH)_2 \tag{1.93}$$

Young and Pint [149] used the theory of gas transport in the viscous-flow regime to calculate the mass transfer coefficient of $CrO_2(OH)_2$ volatilisation, and estimated chromium loss rates from Cr_2O_3 scales in air + H_2O. The good agreement with chromium mass balance determined from the characterisation of oxidised samples showed that chromium depletion in chromia-forming alloys can be fully described by taking into account oxide formation and volatilisation.

Investigating the oxidation of 304L steel in O_2 and O_2–10%H_2O at 600 °C, Asteman et al. [150] reported that the addition of H_2O triggered $CrO_2(OH)_2$ volatilisation, which resulted in mass losses after long exposures, and in chromium depletion in the outer part of the scale and in the alloy directly below the metal/oxide interface. In a subsequent paper [151], the authors further showed that increasing the gas H_2O content and flow rate resulted in enhanced volatilisation, and in accelerated breakaway oxidation. Noting that iron diffused at least as fast as chromium in Cr_2O_3, and was completely soluble in it, the authors indicated that iron dissolution in Cr_2O_3 inevitably led to the formation of fast-growing iron-rich oxides, that is,

breakaway oxidation. The authors observed that in the presence of H_2O, $CrO_2(OH)_2$ volatilisation made the chromium to iron ratio in the oxide decrease faster than in dry oxygen, thereby accounting for accelerated breakaway.

The formation of volatile chromium compounds from Cr_2O_3 is also possible in dry atmospheres, but occurs to a much lesser extent, and is not significant at temperatures below ~ 1000 °C. For volatilisation to be important at lower temperatures, the presence of both H_2O and O_2 in the reacting atmopshere is required. Meier et al. [14] showed that an Fe–22Cr alloy reacted at 650 °C formed a protective Cr_2O_3 scale in Ar–30H_2O, but underwent breakaway oxidation when O_2 was added to the gas mixture. The presence of O_2 was thought by the authors to trigger $CrO_2(OH)_2$ volatilisation, and in turn result in non-selective oxidation.

1.7 Reaction of Fe–Cr alloys in CO_2–H_2O

Information as to the oxidation behaviour of Fe–Cr alloys in atmospheres containing large amounts of both CO_2 and H_2O is scarce. In two recent studies, the oxidation behaviour of chromium steels [13] and model Fe–Cr alloys [14] in CO_2–H_2O was seen to be very similar to that observed in Ar–CO_2 and Ar–H_2O mixtures, described in Sections 1.5 and 1.6, respectively.

Pirón Abellán et al. [13] showed that 9–Cr steels exposed to Ar–50CO_2, Ar–50H_2O and CO_2–30H_2O formed thick iron-rich multilayer scales, plus internal oxides, and internal carbides when CO_2 was present in the atmosphere. As was seen in previous Sections, these reaction products are typical of non-selective oxidation. At 550 °C, the scales consisted of an inner Fe_3O_4+$(Fe,Cr)_3O_4$ layer, and outer Fe_3O_4 and Fe_2O_3 layers. The weight gains measured in CO_2–H_2O and Ar–CO_2 were quite similar, and both higher than those measured in Ar–H_2O. The difference was attributed by the authors to internal carbide formation, which of course did not occur in Ar–H_2O. Particles consisting of a Cr-rich carbide core in a Cr-rich oxide shell were identified by TEM observations in the inner oxide layer of a P92 (9Cr) steel exposed to CO_2–H_2O. In terms of the oxidation mechanism, this observation confirms the findings of Fujii and Meussner [112], who first reported that the Cr-rich oxide particles in the scale inner layer resulted from in situ oxidation of the internal carbides, and that the conversion process was slow relative to the rate at which the oxidation front advanced, which caused carbides to remain partially present in the scale, near the metal/oxide interface (see Section 1.5.2.4).

Pirón Abellán et al. [13] also studied the influence of oxidation temperature. At 650 and 700 °C, the higher diffusivity of chromium in the alloy caused the scale inner layer to be richer in chromium than those grown at 550 °C, and the extents of both internal oxidation and carburisation were reduced.

As was also discussed in Section 1.5.5, Pirón Abellán et al. [13] pointed out that the equilibrium carbon activity in Ar–CO_2 and CO_2–H_2O was far lower (approximately 12 orders of magnitude) than that required to form chromium carbides, and that in the presence of CO_2, the low p_{O_2} value at the metal/oxide interface resulted in an elevated carbon activity. The authors concluded that the extent of carburisation was controlled by the scale permeability to CO_2 rather than by the carbon activity in the external atmosphere. Furthermore, the extent of carburisation was seen to be more important in Ar–CO_2 than in CO_2–H_2O. This observation was thought to result from a competitive adsorption process: H_2O adsorption would be favoured over that of CO_2, which would account for a reduction in the amount of

carbon transmitted from the gas to the metal in the case of the H_2O-containing atmosphere. This view is in agreement with earlier studies from Zheng and Young, who showed that nitridation and carburisation beneath Cr_2O_3 were hindered by SO_2 additions [125], and that the scale permeability to nitrogen was suppressed in the presence of H_2O [121].

Finally, the ability of an alloy to oxidise protectively or otherwise was shown in Refs. [13,14] to be the same in CO_2–H_2O as in Ar–CO_2 or Ar–H_2O (see Sections 1.5 and 1.6, respectively). In particular, the minimum chromium concentration required for Cr_2O_3 formation is higher in these mixtures than in air.

1.8 Summary

To conclude this literature survey, the main aspects relative to the oxidation of Fe–Cr alloys in CO_2- and/or H_2O-rich atmospheres are summarised.

When exposed to CO_2, H_2O or CO_2–H_2O gases, Fe–Cr alloys containing moderate amounts of chromium form iron-rich, multilayer oxide scales typical of non-selective oxidation. These scales are made of two parts: an outer region is located above the original metal surface and consists of iron oxides, while the inner part, below the original surface, also contains chromium (and other alloying elements if present in the alloy). At temperatures above 570 °C, the outer region comprises layers of the three iron oxides FeO, Fe_3O_4 and Fe_2O_3. With increasing temperature, the Fe_2O_3 and Fe_3O_4 layers are progressively suppressed at the oxide/gas interface, because of the slow surface reaction rate relative to iron outward diffusion. The inner layer is a mixture of FeO and $(Fe, Cr)_3O_4$, the fraction of spinel particles increasing with alloy chromium concentration. Internal oxides are found below the scale, consisting of Cr-rich spinel or rhombohedral oxide in a Cr-depleted metal matrix. Extensive precipitation of internal carbides occurs in CO_2-containing gases.

The multilayer structure is thought to result from iron diffusion outward to form the outer layers, and oxygen and carbon transport inward to form the inner regions. The high stability of chromium oxides and carbides, relative to iron compounds, together with the slow diffusivity of chromium in both metal and oxide phases, relative to the high mobility of iron, and to a greater extent oxygen and carbon, account for the fact that chromium is oxidised in situ as the carburisation and oxidation fronts advance in the alloy. The overall scaling rate is thought to be controlled by iron diffusion in the inner oxide layer, and decreases as the scale chromium content increases.

Alloys containing more than $\sim$ 20 wt. % chromium form a protective Cr_2O_3 scale. The actual figure for selective oxidation, which depends on temperature and secondary factors, is similar in CO_2, H_2O and CO_2–H_2O, and higher in these environments than in air. As was discussed in Sections 1.2 and 1.3, the occurrence of selective oxidation is determined by the availability of chromium at the metal/oxide interface, relative to the growth rate of Cr_2O_3 and to the diffusivity of oxygen in the alloy. While the outcome is quite similar in CO_2 and H_2O, the mechanisms underlying the relatively poor oxidation resistance are thought to be different when one considers either the C-bearing or the H-bearing molecule.

It is evident from the thermodynamics of the gas phase C–O system that CO_2-rich mixtures are oxidising but not carburising to either iron or chromium. However,

the formation of an external oxide scale enables internal carburisation of the alloys, since the p_{CO}/p_{CO_2} ratio increases as the oxygen activity decreases across the oxide scale. Internal precipitation of Cr-rich carbides is thought to trigger breakaway in CO_2, as it reduces the availability of chromium for oxide formation.

Despite (or because of) the fact that oxidation in H_2O-containing atmospheres has been subject to considerable interest, the reasons for accelerated breakaway in the presence of hydrogen remain obscure. Chromia scales have been shown to grow faster in the presence of H_2O, which has been attributed to hydrogen dissolution (in the form of OH^-) in the oxide. The dissolution of hydrogen in the metal matrix is thought to enhance the tendency for chromium to oxidise internally, by increasing the permeability of oxygen. In atmospheres containing significant amounts of both H_2O and O_2, the volatilisation of $CrO_2(OH)_2$, formed by the reaction of Cr_2O_3 with the gas species, is deleterious in that it accelerates the growth rate of the oxide, and the reduction of the Cr/Fe ratio in the oxide.

Chapter 2

Materials and experiments

2.1 Materials

This study is concerned with the reaction of model materials: pure iron, binary Fe–Cr and ternary Fe–Cr–Ni alloys, whose nominal composition is given in Table 2.1. The materials were prepared by argon arc-melting iron (99.99 % pure), chromium

Table 2.1 – Materials chemical composition (wt. %, balance = Fe) and phase constitution (wt. %).

Chemical composition		Phase constitution			
Cr	Ni	1150 °C[a]	as-annealed[b]	650 °C[a]	800 °C[a]
0	0	γ	α	α	α
2.25	0	γ	α	α	α
9	0	γ	α	α	α
9	10	γ	$\alpha - \gamma$	γ	γ
9	20	γ	γ	γ	γ
20	0	α	α	α	α
20	10	$\gamma - 6.8\alpha$	$\gamma - \alpha$	$\gamma - 14\sigma - 0.2\alpha$	$\gamma - 2.2\sigma$
20	20	γ	γ	$\gamma - 8.7\sigma$	γ
25	0	α	α	$\alpha - 6.5\sigma$	α
25	10	$\gamma - 49\alpha$	$\gamma - \alpha$	$\gamma - 32\sigma$	$\gamma - 24\sigma$
25	20	γ	γ	$\gamma - 25\sigma$	$\gamma - 13\sigma$

[a]calculated
[b]experimental

(99.995 % pure) and nickel (99.95 % pure). Ingots were annealed in Ar–5%H_2 at 1150 °C for 48 h, and slowly cooled inside the furnace. Using diffusion data [81] for chromium in α-Fe and γ-Fe, the characteristic diffusion length $\sqrt{4D_{\mathrm{Cr}}t}$ is calculated to be 610 µm and 60 µm for the ferritic and austenitic alloys, respectively, in the annealing conditions. These distances are sufficiently large for the cast ingots to be homogenised during annealing. Despite flushing the furnace with Ar–5%H_2 prior to annealing, oxygen was left in small quantities: pure iron did not oxidise, but the chromium-containing ingots formed Cr_2O_3. This had no effect on the chromium concentration of the specimens, however, since only the core of the half-spheroid ingots was subsequently used to cut specimens (about 6–8 one-gram specimens were obtained from each 25 g ingot).

Rectangular specimens were cut and ground to approximate dimensions 12–16 × 6–8 × 1–1.5 mm, and drilled to obtain suspension holes. Before reaction, the

specimens were mechanically ground to a 1200 grit finish using SiC paper, degreased, ultrasonically cleaned in ethanol, weighed and measured.

A large number of specimens were reacted in this study (421), and the as-annealed condition (microstructure and chemical composition) was characterised in only a limited number of cases. No particular emphasis was put on controlling the specimen microstructures. As–annealed materials had coarse and irregular grains, with sizes in the approximate range 50 – 1500 µm (see Fig. 2.1). The crystal struc-

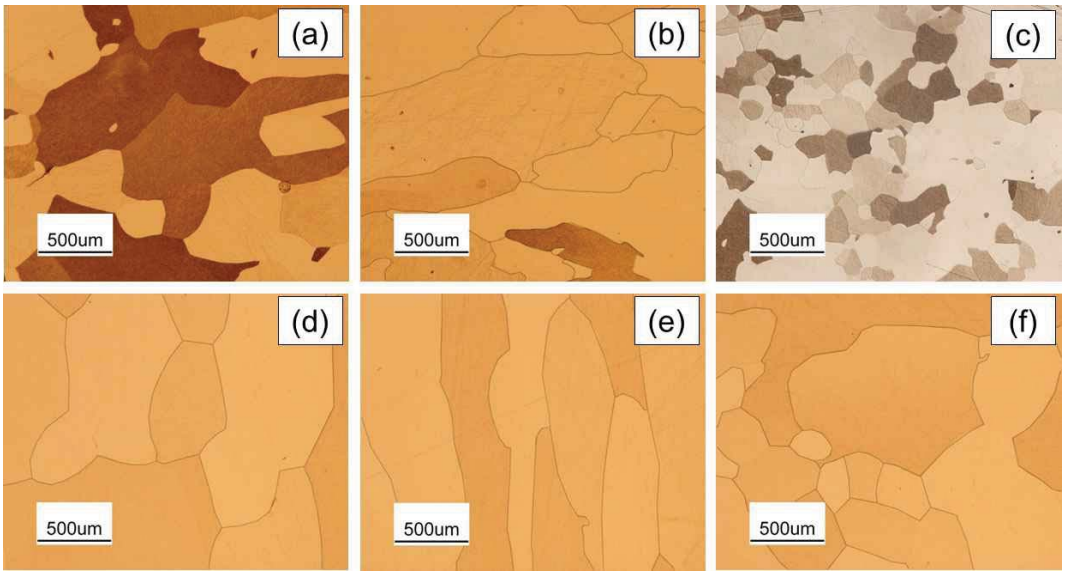

Figure 2.1 – Optical micrographs of as–annealed materials etched with Vilella's reagent. (a) Fe; (b) Fe–2.25Cr; (c) Fe–9Cr; (d–f) Fe–20Cr (same specimen).

ture was determined by X-ray diffraction, and the results are reported in Table 2.1. Iron and binary alloys were fully ferritic. Refering to the Fe–Cr phase diagram shown in Fig. 2.2, it may be inferred that during cooling from annealing to room temperature, the microstructures were fixed in the temperature range defined by the lower limit of the γ-loop, 853 °C, and the $\alpha/\alpha+\sigma$ phase boundary at wt. % Cr = 25, 667 °C. The alloys with 10Ni were shown by XRD to have a dual $\alpha-\gamma$ crystal structure, while those containing 20Ni were fully austenitic in the as-annealed condition. The thermodynamics of the Fe–Cr–Ni system were investigated for both reaction temperatures, 650 and 800 °C, using the Thermo-Calc [58] software, and the SSOL database as of 1992. It should be noted that since the 1992 SSOL database does not contain Fe–Cr–Ni as an assessed system, the calculations might be in error. Isothermal sections of the phase diagrams are shown in Fig. 2.3. Equilibrium activities of the metals, phase proportions and composition of the phases were also determined.

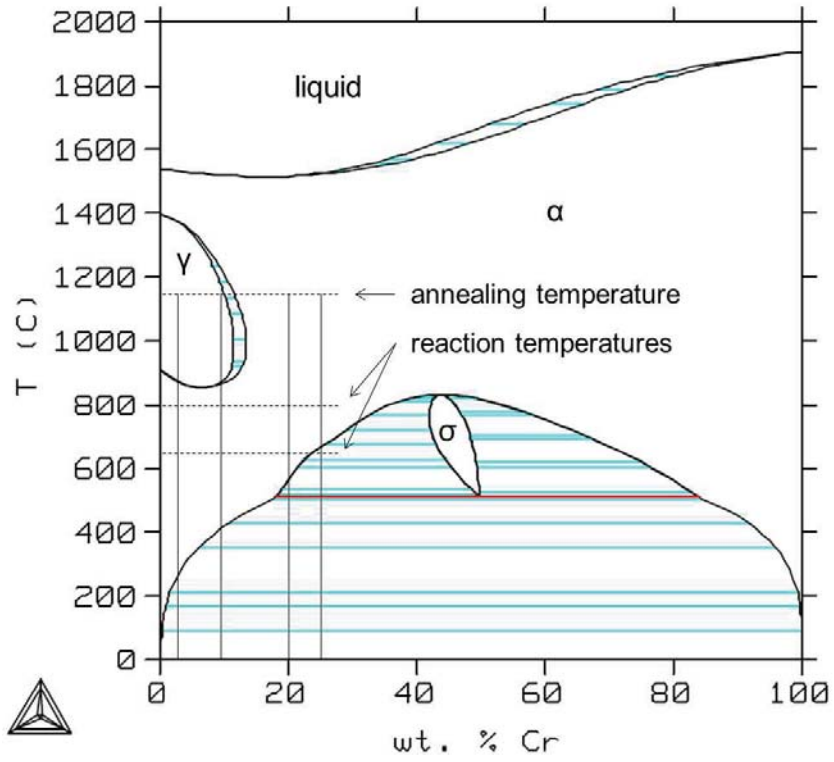

Figure 2.2 – Phase diagram of the Fe–Cr system, generated with Thermo-Calc [58], using the BIN97 database.

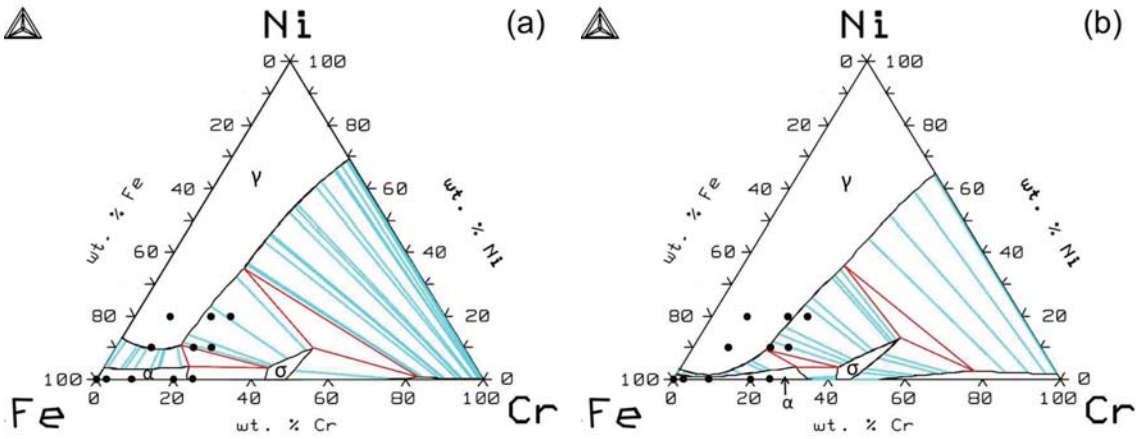

Figure 2.3 – Isothermal sections of the Fe–Cr–Ni phase diagram at (a) 650 °C and (b) 800 °C. Generated with Thermo-Calc [58], using the SSOL database (1992). The black dots indicate the compositions of the materials used in this study.

The phase constitution is reported in Table 2.1. However, the σ-phase, predicted to form in the 20Cr and 25Cr ternary alloys, was never detected by XRD or metallographic examination after reaction. The microstructures after reaction were in fact similar to that observed in the as annealed condition. For instance, after 100 h reaction of an Fe–25Cr–10Ni specimen in Ar–CO_2–H_2O at 800 °C, the metal substrate was shown by XRD to consist of γ and α (see optical micrograph in Fig. 2.4), and not γ and σ as predicted by thermodynamic equilibrium at 800 °C. The fact

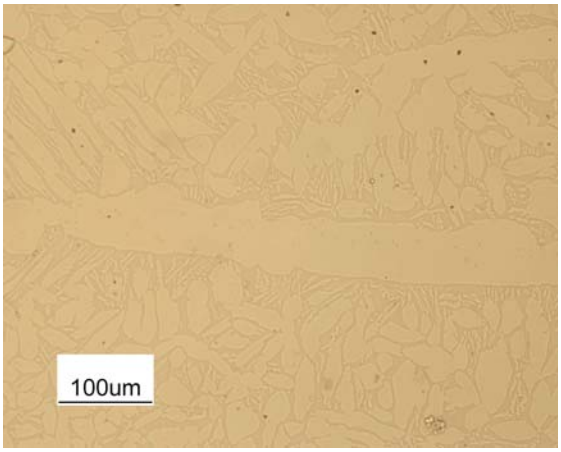

Figure 2.4 – Optical micrograph of an Fe–25Cr–10Ni specimen after 100 h exposure to Ar–20CO_2–20H_2O at 800 °C. The contrast between the α (dark) and γ (bright) phases was obtained by polishing with a basic (pH = 9.8) solution of 0.04 µm silica particles.

that the microstructure does not reach equilibrium during reaction is likely due to the fact that the diffusion length of chromium is quite short at the reaction temperatures and in the time scales considered. Using diffusion data [81] for chromium in α-Fe and γ-Fe, the characteristic diffusion length $\sqrt{4D_{\mathrm{Cr}}t}$ lies between 0.1 µm for austenitic alloys reacted 40 h at 650 °C and 30 µm for ferritic alloys reacted 100 h at 800 °C.

The composition of an Fe–9Cr ingot was verified by chemical analysis. The chromium content was measured as (9.2 ± 0.3) wt. % by inductively coupled plasma optical emission spectroscopy (ICP–OES), and no carbon could be detected after combustion in a LECO CS230 instrument, with a 4 ppm sensitivity. Analysis by SEM–EDS in the bulk, non-altered region of reacted alloys also confirmed that the actual compositions were very close to the nominal compositions given in Table 2.1.

2.2 Gas mixtures

Isothermal oxidation experiments were performed at 650 and 800 °C in flowing Ar–CO_2–H_2O gas mixtures, whose composition is given in Table 2.2. The Ar–CO_2 mixtures were obtained by mixing high purity argon and carbon dioxide (99.995 % pure, less than 5 molar ppm O_2 and H_2O). The individual gas flows were regulated using mass flow controllers. Wet gases were produced using distilled water according to the procedure described in Section 2.3. All experiments were run at near atmospheric pressure, with a total linear gas velocity of about 2 $cm\,s^{-1}$. The reaction temperature was controlled within ± 1 °C.

Table 2.2 – Gas composition (vol. %, balance = Ar), and equilibrium oxygen and carbon potential at P = 1 atm, T = 650 and 800 °C.

Gas composition (%)		650 °C		800 °C	
CO_2	H_2O	p_{O_2} (atm)	a_C	p_{O_2} (atm)	a_C
20	0	5.1×10^{-9}	1.6×10^{-15}	1.6×10^{-7}	6.9×10^{-14}
20	5	6.6×10^{-9}	1.2×10^{-15}	1.8×10^{-7}	5.9×10^{-14}
20	20	1.1×10^{-8}	7.7×10^{-16}	2.5×10^{-7}	4.2×10^{-14}
0	20	8.0×10^{-9}	n/a	1.6×10^{-7}	n/a

The equilibrium oxygen and carbon activities, calculated according to the method described in Appendix A, are also included. Given the values of p_{O_2} and a_C required to form iron and chromium oxides and carbides (see Tables 1.1 and 1.3), the gas mixtures used in the present study are oxidising and non-carburising with respect to the materials of interest, as discussed in the literature review.

It should be noted that for all atmospheres considered here, the oxygen impurity content in the Ar and CO_2 gas bottles was higher than the equilibrium p_{O_2} (the maximum O_2 volume fraction specified by the manufacturer was 5 ppm). This does not affect the relative stability of the oxides and carbides.

2.3 Oxidation experiments

Isothermal oxidation experiments were carried out using two different installations: a classic furnace where specimens of all 11 materials were reacted at the same time (time-lapse experiments), and a furnace equipped with a built-in microbalance, enabling continuous weight measurement of one specimen at a time (thermogravimetric analysis or TGA experiments).

The time lapse experiments were performed in Sydney, using a vertical tube furnace in a configuration where the specimens were mobile. A system of magnets enabled the specimen holder to be moved inside the gas-tight reactor. Before an experiment, the furnace temperature and reacting gas composition were stabilised. The specimens were inserted in the cold zone, and the chamber was flushed with the reacting gas for 30 minutes. Given the gas flow rate and the reactor volume, this is expected to allow the desired gas composition to be attained within the reactor. An experiment was started by lowering the specimens into the hot zone. At the end of an experiment, the reacting gas was stopped, the specimens were raised to the cold zone and cooled in argon. The specimens were weighed before and after reaction using a precision balance with a 0.1 mg accuracy. The procedure was repeated with varying reaction times in order to obtain weight change kinetics.

The TGA experiments at 800 °C were performed in Sydney using a MK2–M5 microbalance from CI Precision, in a configuration where the furnace was mobile. The accuracy given by the manufacturer was 0.1 µg, but the actual drift was not measured. The experimental procedure was the same as for the time-lapse experiments, except that prior to an experiment, the chamber was flushed with a dry Ar–CO_2 mixture, the wet gas being prepared but sent into a secondary line, bypassing the chamber. An experiment was started by raising the furnace so that the specimen was located in the hot zone, and, in the case of wet gases, simultaneously flowing the reacting gas into the chamber.

In these two configurations, wet gases of controlled p_{H_2O} were generated by passing mixtures of argon and carbon dioxide through a thermostated water saturator (see 2.5). The distilled water in contact with the gas mixture was set at a temperature about 20 °C higher than that required to produce the nominal p_{H_2O}. The excess water vapor was subsequently condensed by cooling the wet gas in a distillation column. The temperature difference between the two baths, between 15 and 25 °C depending on the total gas flow rate, was set so that the excess water vapour was entirely condensed in the distillation column, ensuring control over the gas p_{H_2O}. All downstream gas lines were wrapped with heating tape and maintained at a temperature higher than the dew point of the wet gas to avoid condensation.

The TGA experiments at 650 °C were carried out in Toulouse using a Setsys Evolution microbalance from Setaram, equipped with a Wetsys humidifying system. The drift was measured by running experiments with no specimen in gas flows corresponding to the experimental conditions, and values lower than 3 $\mu g\,h^{-1}$ were obtained. This thermobalance was not set to have a mobile part. The specimen was inserted in the chamber, which was maintained at 70 °C while flushing with

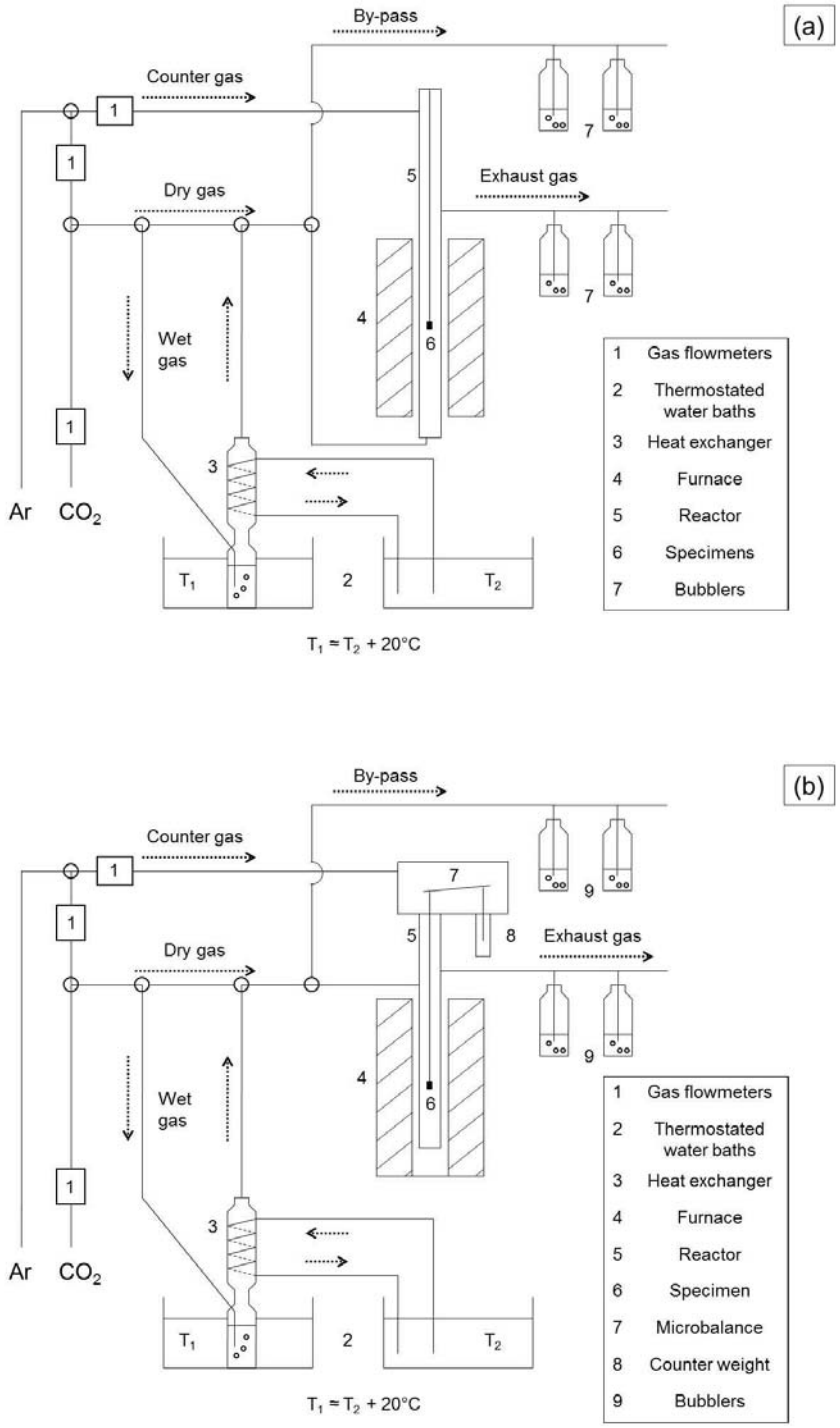

Figure 2.5 – Schematic representation of the gas lines in the (a) time-lapse and (b) TGA configurations.

the reacting gas. The furnace was subsequently turned on, and ran the following temperature profile:

- heating at 20 °C/min from 70 to 600 °C;
- heating at 5 °C/min from 600 to 650 °C;
- hold at 650 °C; and
- cooling in furnace to room temperature ($\sim$ 30 min).

The principle of the commercial humidifying system was slightly different from that of the "house-made" system described above, in that the water vapour concentration was set by mixing a fully saturated Ar–CO_2–H_2O mixture with a dry Ar–CO_2 gas in appropriate proportions.

2.4 Characterisation techniques

After reaction, all specimens were weighed and photographed. Metallographic cross-sections were prepared by cold mounting, sectioning and polishing with SiC paper, and diamond and silica solutions. Selected specimens were characterised using the following techniques:

X-ray diffraction (XRD) was carried out in Sydney using a Phillips X'pert Pro MPD diffractometer. In general, XRD was performed on as-reacted specimens and only the outermost oxide layers were analysed; in some cases, the reaction products were polished off using SiC paper. Alternative grinding and XRD enabled deeper regions to be analysed, across the oxide scale to the bulk alloy.

Etching was performed with the following solutions:

- Murakami's reagent (1 g $K_3Fe(CN)_6$, 1 g KOH, 10 mL H_2O) to reveal chromium carbides;
- 2 % HCl in ethanol to darken FeO;
- Vilella's reagent (7 mL saturated solution of picric acid in ethanol, 3 mL HCl, 40 mL ethanol) to reveal alloy grain structure, martensite laths and carbides.

Optical microscopy was carried out on specimen surfaces and cross-sections.

Scanning electron microscopy–energy dispersive spectroscopy (SEM–EDS) was used for high magnification imaging and chemical analysis of specimen surfaces and cross-sections. The models used were, in Sydney: Hitachi S3400; in Toulouse: LEO 435VP SEM with PGT IMIX EDS system. Most of the chemical analysis was done in Toulouse, using pure iron, chromium and nickel as standards. The probe current was measured using a Faraday cage connected to an external ammeter and maintained at the same value during analysis of standards and specimens. This way analysis of metal phases was quantitative, with an accuracy of about 1 wt. %. Analysis of light elements (carbon and oxygen) and of all elements in ceramic (carbide and oxide) phases was only qualitative. The spatial resolution (width of the beam–specimen interaction zone) was about 1 µm.

Electron probe microanalysis (EPMA) was carried out in Grenoble (France) on specimen cross-sections using a CAMECA SX50 model, equipped with four wavelength dispersive spectrometers (WDS), a liquid nitrogen trap and air leak to mitigate specimen contamination and improve light elements analysis.

Raman spectroscopy was performed in Toulouse using a Horiba Jobin–Yvon Labram HR 800 Raman microscope on specimen surfaces and cross-sections, with an argon laser (wavelength 532 nm, power 20 mW), yielding a 1 μm^3 spatial resolution.

Transmission electron microscopy (TEM) was performed in Sydney with a Phillips CM200 microscope equipped with a CCD camera and an EDS system. Selected area diffraction patterns (SADP) were recorded on photographic films. The thin sections for TEM analysis were prepared by focused ion beam (FIB) milling using a single gallium beam in an FEI XP200 microscope.

Chapter 3

Experimental results

The present Chapter consists of a description of the experimental results. Reactions at 650 and 800 °C are treated separately. For each temperature, a distinction is made between iron and alloys with 2.25 and 9 wt. % chromium, referred to as low chromium alloys, which oxidised rapidly and produced Fe-rich oxide scales, and high chromium materials (20Cr and 25Cr alloys) which contained enough chromium to form Cr_2O_3, at least initially.

3.1 Low chromium alloys at 650 °C

3.1.1 Weight gain kinetics

Weight change kinetics for reaction of the low chromium alloys in dry and wet CO_2 at 650 °C are shown in Fig. 3.1. Values of $\Delta m/A$ measured after 80 h exposure in Ar–20H_2O are also included. The variability observed between specimens of the same composition reacted in a given gas was important. Because of this lack of reproducibility, the reaction kinetics could not be analysed in an accurate way. An approximate use is made of standard (linear or parabolic) rate laws, for comparison purposes.

Reaction kinetics of iron were approximately parabolic, although an initial linear stage may have existed during exposure to dry CO_2. Additions of H_2O(g) led to increased weight gains, but no significative difference was seen between the Ar–20CO_2–5H_2O and Ar–20CO_2–20H_2O reactions. An average parabolic rate constant k_{pm}, as defined in

$$\left(\frac{\Delta m}{A}\right)^2 = 2k_{\mathrm{pm}}t \tag{3.1}$$

is given in Table 3.1. More precisely, k_{pm} was determined from a linear fit of the

Table 3.1 – Parabolic rate constants, as defined in Eq. (3.1), for reaction of low chromium alloys at 650 °C.

Alloy	k_{pm} (10^{-5} mg^2 cm^{-4} s^{-1})
Fe	70
Fe–2.25Cr	13
Fe–9Cr	18
Fe–9Cr–10Ni	8.1
Fe–9Cr–20Ni	3.1

data in a $\Delta m/A = \mathrm{f}\left(t^{1/2}\right)$ plot, using a least-squares method. It is recognised that

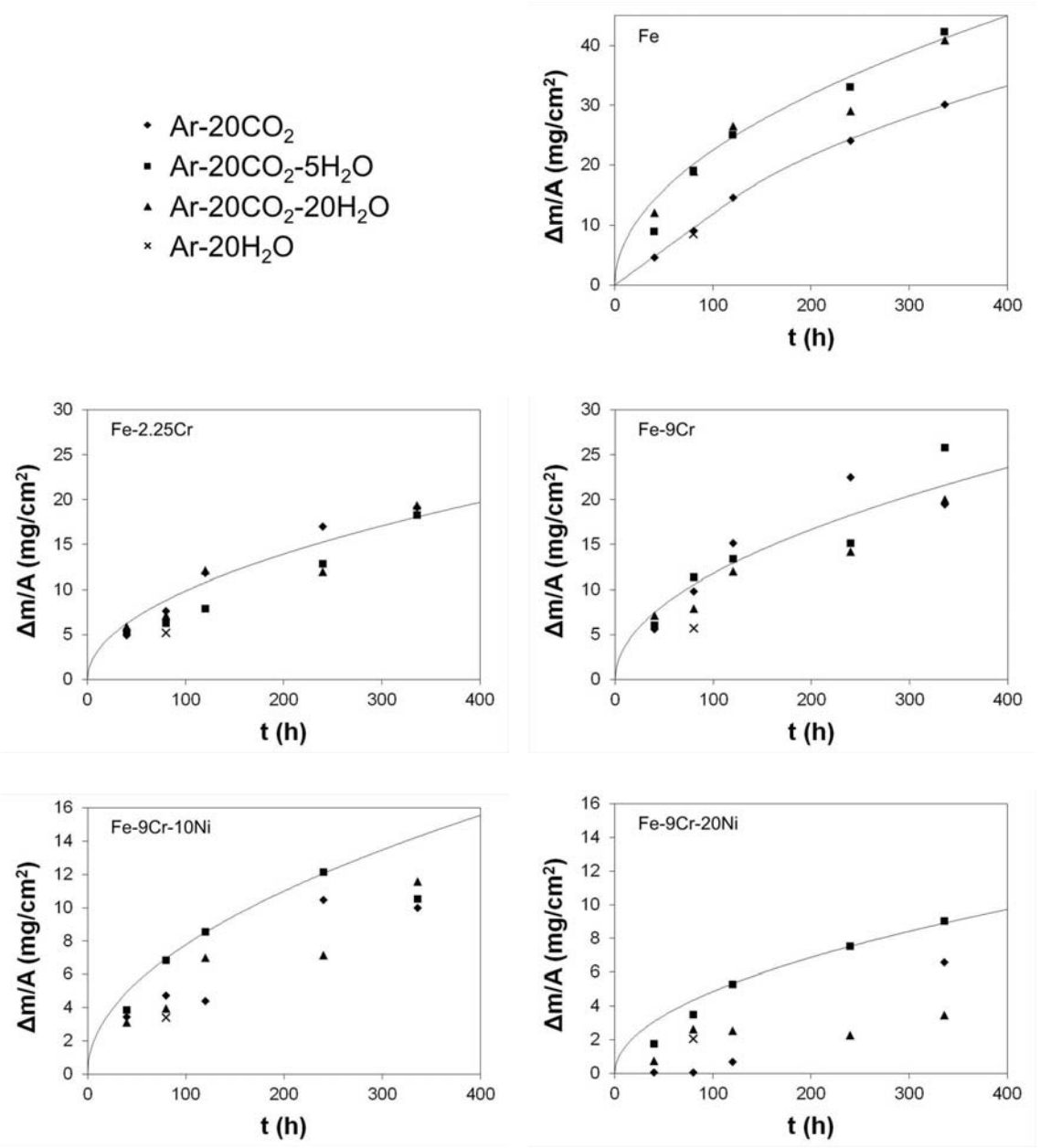

Figure 3.1 – Weight change kinetics of low chromium alloys at 650 °C. Solid lines are linear and parabolic fits of the data.

different gases might in principle yield different rate constants. Such a difference between reactions in Ar–20CO_2–5H_2O and in Ar–20CO_2–20H_2O could not be identified using the present data. Thus the single, average k_{pm} value given in Table 3.1 should be considered as approximate and is used only for the purpose of evaluating the influence of alloy composition.

The Fe–2.25Cr and Fe–9Cr alloys reacted according to approximately parabolic kinetics in both dry and wet CO_2, with no visible influence of the gas composition. Average k_{pm} values are given in Table 3.1.

In the case of the 9Cr ternary alloys, scale spallation was too important for reliable information to be obtained from $\Delta m/A$ measurements. For some unknown reason, spallation was less marked for these alloys in Ar–20CO_2–5H_2O than in the other gases. Assuming parabolic kinetics, the corresponding $\Delta m/A$ data for this gas were used to determine k_{pm} values (Table 3.1), for comparison purposes.

Changes in alloy composition affected the weight gain kinetics more than the gas composition did, as chromium and nickel additions caused significant reductions in weight uptake.

3.1.2 Surface appearance

The lack of reproducibility seen in $\Delta m/A$ measurements is related to the non-uniform appearance of the specimen surfaces. As is shown subsequently, the alloys formed oxide scales consisting of multiple layers. The outer layers, identified by XRD and local Raman analysis as iron oxides, did not develop uniform surface coverage. At the oxide/gas interface, an Fe_2O_3 layer (grey colour) and Fe_2O_3 whiskers (red colour) formed preferentially at the bottom of the specimens, that is, downstream in the gas flow. Figure 3.2(a) shows a typical example. However, the surface coverage by Fe_2O_3 varied from specimen to specimen, and even from one face to the other of a given specimen. The fact that the surface morphology was influenced by

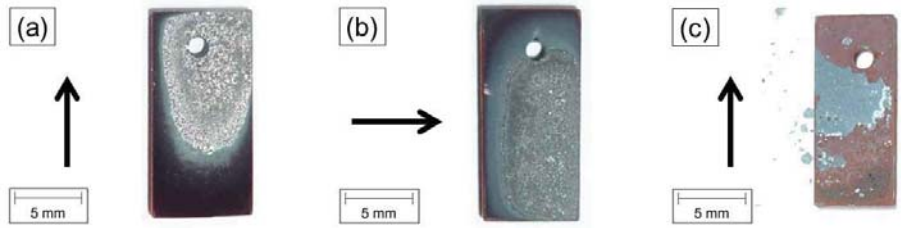

Figure 3.2 – Photographs showing specimen surface appearance after reaction at 650 °C. Fe–2.25Cr in Ar–20CO_2 for (a) 240 h and (b) 336 h; (c) Fe–9Cr–10Ni, 120 h in Ar–20CO_2–5H_2O. Black arrows indicate direction of gas flow.

the direction of the gas flow was confirmed by running an experiment in an horizontal furnace (see Fig. 3.2(b)). In addition, partial spallation of the external oxide layers (Fig. 3.2(c)) occurred to highly variable extents, in terms of both surface and thickness (number of layers) of spalled oxide. Spallation was most important in the case of the 9Cr ternaries.

The surface oxides had similar microstructures after reaction of all alloys in all gases. Typical surface micrographs are shown in Fig. 3.3. Oxide phases were identi-

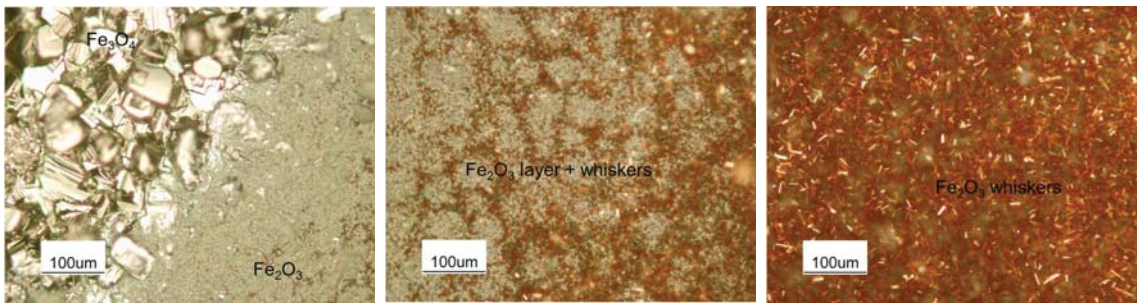

(a) Fe_3O_4 and Fe_2O_3 layers (b) Fe_2O_3 layer and whiskers (c) Fe_2O_3 whiskers

Figure 3.3 – Optical micrographs showing microstructure of surface oxides grown on Fe–9Cr after 120 h exposure to Ar–20CO_2 at 650 °C.

fied individually by local Raman analysis. The Fe_3O_4 layer consisted of large, faceted crystals (Fig. 3.3(a)). Hematite was present as a fine-grained layer (Fig. 3.3(b)), sometimes covered by whiskers (Fig. 3.3(c)).

3.1.3 Oxidation products

During exposure to dry and wet CO_2, the low chromium alloys produced external oxide scales consisting of multiple layers. Optical micrographs are shown in Fig. 3.4 in the case of the 9Cr alloys. All scales were separated in two parts. The outer part contained one or several single-phase layers; it was rather compact but presented signs of coarse mechanical fracture: large cracks both parallel and normal to the alloy surface, and large cavities. In some cases, part of the outer scale was not visible in cross-section, either because it was not formed at this location or because it spalled during cooling (see Fig. 3.2). The inner scale consisted of a fine grained multiphase layer, with a fine porosity. In the case of Fe–2.25Cr (Fig. 3.5) and Fe–9Cr (Fig. 3.4(a,d)), the inner scale porosity was extensive; pores were oriented in a direction parallel to the alloy surface and at times coalesced into one or several rows. The number of these rows increased with gas H_2O content. Porosity in the inner scale of the 9Cr ternary alloys was much less pronounced and more uniformly

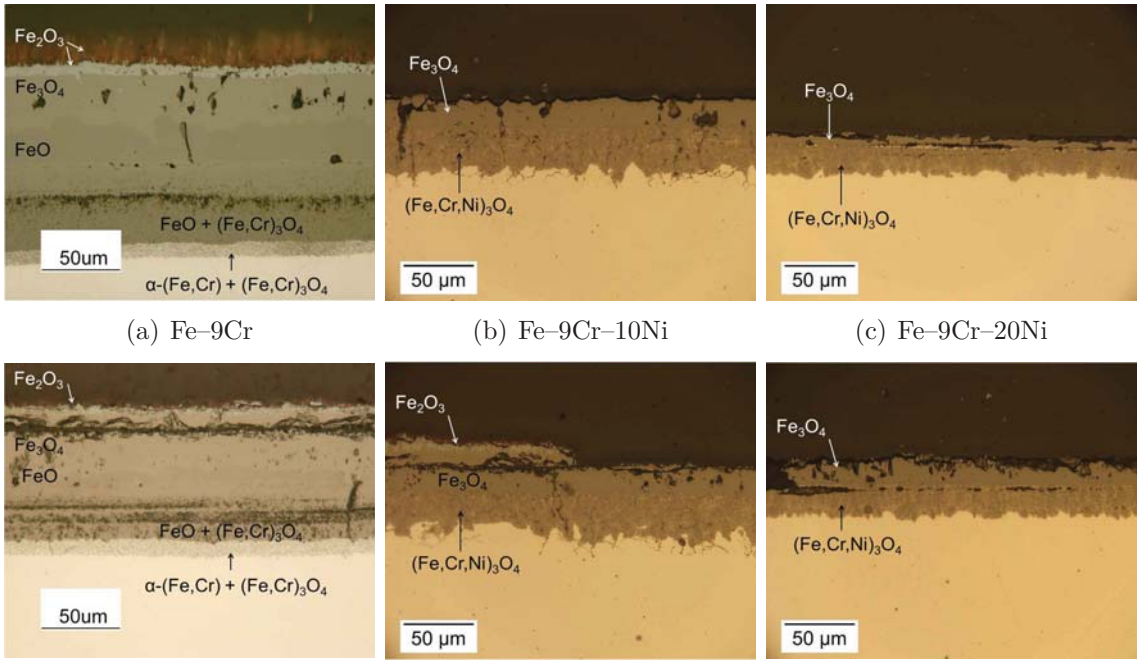

(a) Fe–9Cr (b) Fe–9Cr–10Ni (c) Fe–9Cr–20Ni

(d) Fe–9Cr (e) Fe–9Cr–10Ni (f) Fe–9Cr–20Ni

Figure 3.4 – Optical micrographs of oxide scales formed after 120 h reaction in (a-c) Ar–20CO_2 and (d-f) Ar–20CO_2–20H_2O at 650 °C.

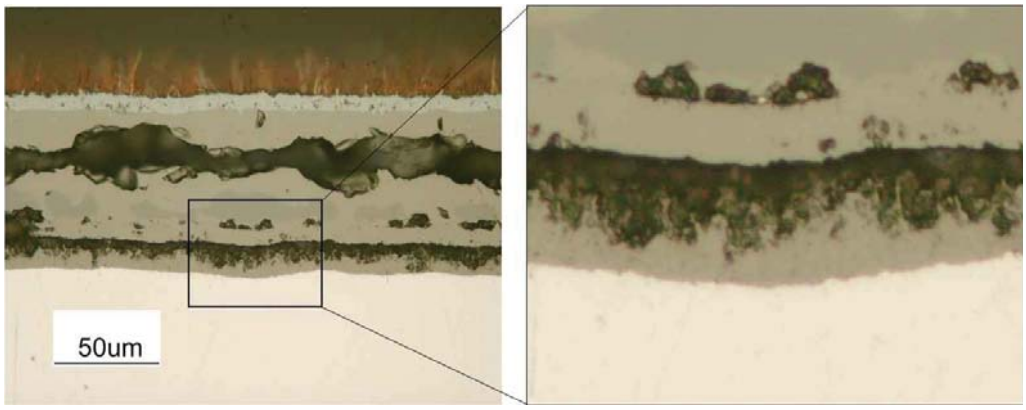

Figure 3.5 – Optical micrographs showing porosity in the inner layer of the scale formed on Fe–2.25Cr after 120 h exposure to Ar–20CO_2 at 650 °C.

dispersed, as seen in Fig. 3.4.

The inner layer of the scale grown on Fe–9Cr contained two phases, as is evident on the SEM view of the etched cross-section in Fig. 3.6(a). In the case of the 9Cr

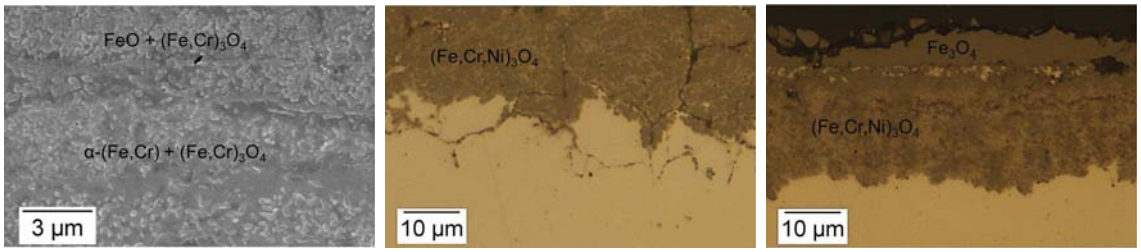

(a) Fe–9Cr (b) Fe–9Cr–10Ni (c) Fe–9Cr–20Ni

Figure 3.6 – Metal/oxide interface after 120 h reaction in Ar–20CO_2 at 650 °C. (a) SEM SE view of specimen etched with Murakami's reagent; (b) and (c) OM views of as-polished cross-sections.

ternaries, the inner layer contained two or more oxide phases, some metal islands and cracks normal to the alloy surface (Fig. 3.6(b,c)). Metal islands were concentrated near the interface between inner and outer scale of the Fe–9Cr–20Ni alloy. The Fe–9Cr alloy was prone to internal oxidation during exposure to dry and wet CO_2. The volume fraction of oxide precipitates was seen to be very large, but examination by SEM confirmed that a two-phase metal + oxide mixture was indeed formed (see for example Fig. 3.6(a)). Internal oxidation was observed in none of the other alloys. The Fe–9Cr–10Ni alloy did form oxide protrusions in the metal substrate (Fig. 3.6(b)), but these were more or less in contact with the oxide scale.

Chemical analysis by SEM–EDS of an oxide scale formed after reaction of Fe–9Cr in Ar–20CO_2 showed that the outer layers were iron oxides, while the inner layer also contained chromium. Diffractograms from a series of planes parallel to the alloy surface were obtained by alternately grinding off a controlled thickness of oxide and performing XRD analysis. Signals produced by different oxide layers were recorded on a given diffractogram, because neither the oxide layers nor the grinding planes were perfectly parallel to the alloy surface. However, all phases could be identified by examining the results of 7 diffractograms, given the depth at which they were recorded, and in light of the cross-section micrograph obtained from the opposite face of the specimen. Selected diffractograms obtained this way after exposure to Ar–20CO_2 are shown in Fig. 3.7. The procedure was repeated after reaction of Fe–9Cr in Ar–20CO_2–5H_2O, yielding the same results. The three layers composing the outer scale were, from the scale/gas interface, Fe_2O_3, Fe_3O_4 and FeO. The inner layer was identified as a mixture of FeO and mixed Fe–Cr spinel. The signal from

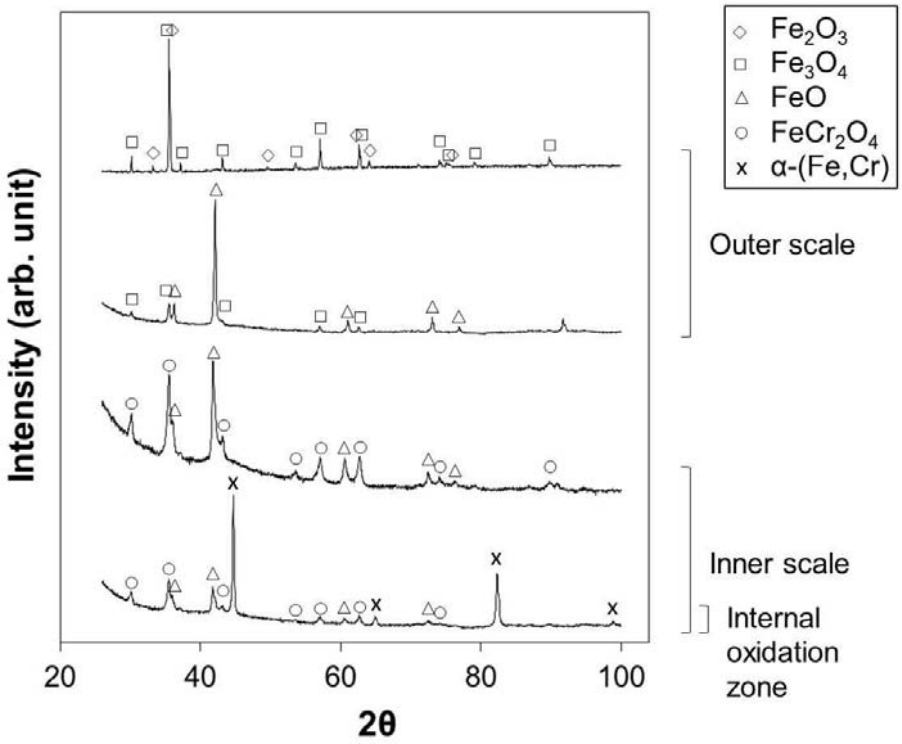

Figure 3.7 – Diffractograms recorded in the oxide scale grown on Fe–9Cr after 240 h reaction in Ar–20CO_2 at 650 °C.

the latter phase was seen to match $FeCr_2O_4$ reference patterns better than Fe_3O_4 ones; however, the exact composition could not be determined because the lattice parameter of the Fe-rich and Cr-rich spinel solid solutions vary only slightly with composition. Simarly, the internal oxidation zone was identified as an α-(Fe,Cr) + $(Fe, Cr)_3O_4$ mixture, with no further specification of the composition possible. Chromia was not detected at all.

The oxides formed after reaction of an Fe–9Cr–10Ni specimen in Ar–20CO_2–20H_2O were identified by local Raman analysis (Fig. 3.8). Comparison with the work of McCarty and Boehme [152] showed that the outer layers were Fe_2O_3 and Fe_3O_4. The Raman signal recorded in the inner layer did not enable the phases of this region to be distinguished from one another. Wustite is Raman active with main bands at ~ 280 and ~ 400 cm^{-1} [153]; these were not observed. The signal was characteristic of spinel oxides, with a main band at ~ 675 cm^{-1}. While this figure is too high to correspond to pure Fe_3O_4 [152], it is also too low for the $NiCr_2O_4$ and $NiFe_2O_4$ spinels, according to the data tabulated in Ref. [154]. Given that it contained at least two phases (see Fig. 3.6(b,c)) the inner layer may be described as a mixture of several spinel phases of general composition $(Fe, Cr, Ni)_3O_4$. As is seen in Fig. 3.4, the scales grown on Fe–9Cr–10Ni and Fe–9Cr–20Ni in Ar–20CO_2

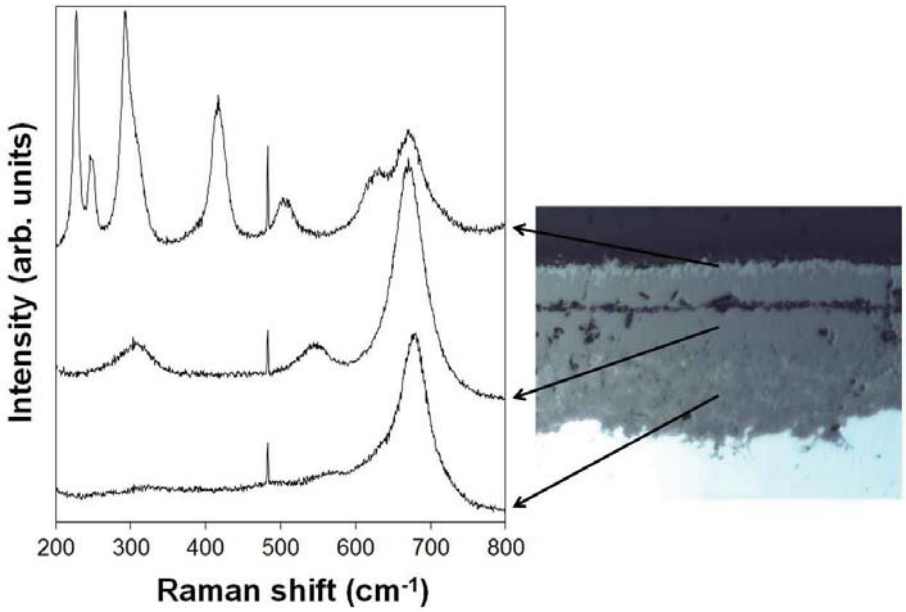

Figure 3.8 – Raman spectra recorded in the oxide scale grown on Fe–9Cr–10Ni after 120 h reaction in Ar–20CO_2–20H_2O at 650 °C.

and Ar–20CO_2–20H_2O all had a similar appearence. Thus the phase constitution derived from Raman analysis on one specimen is thought to be representative, to some degree, of the scales grown on both alloys in all gases.

3.1.4 Oxide growth kinetics

The thickness of the oxides formed on the Fe–9Cr alloy (external scale + internal oxidation zone) was measured after varying reaction times, as shown in Fig. 3.9(a). The standard deviation indicated by the error bars was always relatively small, reflecting the uniformity of the oxide scale in a given cross-section. However, the scale thickness varied along the specimen length (see Fig. 3.2). These variations were not investigated — all cross-sections were prepared from the middle of the specimens, approximately, in order to yield comparable results, representative of the average scale morphology. Nevertheless, the thickness data in Fig. 3.9 present some scatter. While the number of datapoints was too small, and the scatter too large for a rate law to be properly identified, the thickening kinetics may be described as approximately parabolic, for comparison purposes. Thus, the simple rate law

$$X^2 = 2k_\mathrm{p}t \tag{3.2}$$

was used to determine k_p values from fitting the data in Fig. 3.9(b). Values of k_p corresponding to Ar–20CO_2, Ar–20CO_2–5H_2O and Ar–20CO_2–20H_2O are seen in

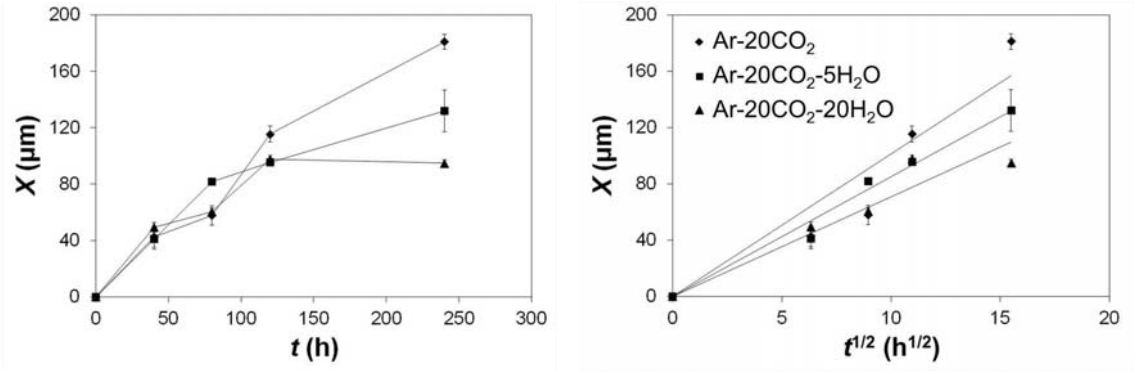

(a) Linear plot (b) Parabolic plot

Figure 3.9 – Oxide growth kinetics of Fe–9Cr at 650 °C. Mean values obtained from ∼ 10 measured values. Error bars indicate ($X \pm$ stdev), where stdev denotes standard deviation.

Table 3.2 to be quite similar. As for the gravimetric data (Fig. 3.1), the scatter was

Table 3.2 – Oxidation rate constants, k_p (10^{-11} cm^2 s^{-1}), measured after reaction at 650 °C.

	from X (Eq. (3.2))				from $\Delta m/A$ (Eq. (3.1))
Gas (Ar–20CO_2–)	0H_2O	5H_2O	20H_2O	average	average
Fe					39
Fe–2.25Cr	7.6			7.6	7.1
Fe–9Cr	14	10	6.9	10	10
Fe–9Cr–10Ni	6.6		5.3	6.0	4.0
Fe–9Cr–20Ni	0.97		2.0	1.5	1.5

too important for the influence of the gas composition to be distinguished.

Oxide thicknesses were measured after 120 h reaction of Fe–2.25Cr, Fe–9Cr–10Ni and Fe–9Cr–20Ni in Ar–20CO_2 and Ar–20CO_2–20H_2O. In view of the gravimetric data (Fig. 3.1), oxide growth kinetics may be described as parabolic, for comparison purposes. The thicknesses were thus used to determine k_p values from Eq. (3.2). These parabolic constants, obtained from one specimen only, are to be considered as rough estimates, and are included in Table 3.2 only as a basis for comparison.

Oxide growth rates were also estimated from gravimetric data. As is shown subsequently, the alloys also suffered carburisation, but the contribution of carbon uptake to the total weight gains were negligible (see Appendix D). Values of k_{pm} given in Table 3.1 were converted to k_p values using Eq. (1.11). On the basis of the results presented in Section 3.1.3, the oxides were assumed to be dense FeO in the

case of the binary alloys, and dense Fe_3O_4 for the ternary alloys. Again, this procedure does not constitute a proper analysis of the oxidation kinetics; in particular, the kinetics were not *demonstrated*, but rather *assumed* to be parabolic, and the k_p values obtained this way are included in Table 3.2 for comparison purposes.

In view of all the approximations involved, the agreement between rate constants obtained from thickness and $\Delta m/A$ data is surprisingly good. Both sets of data can be considered to be, to a certain extent, representative of the alloy reactions. A general observation is that chromium and nickel additions caused k_p values to decrease.

3.1.5 Carburisation products

Carburisation of low chromium alloys at 650 °C was investigated by etching cross-sections with Murakami's reagent. Analysis by SEM–EDS confirmed that the internal particles revealed this way were Cr-rich carbides. The Fe–2.25Cr alloy formed only intergranular carbides, as shown in Fig. 3.10. The precipitates were present

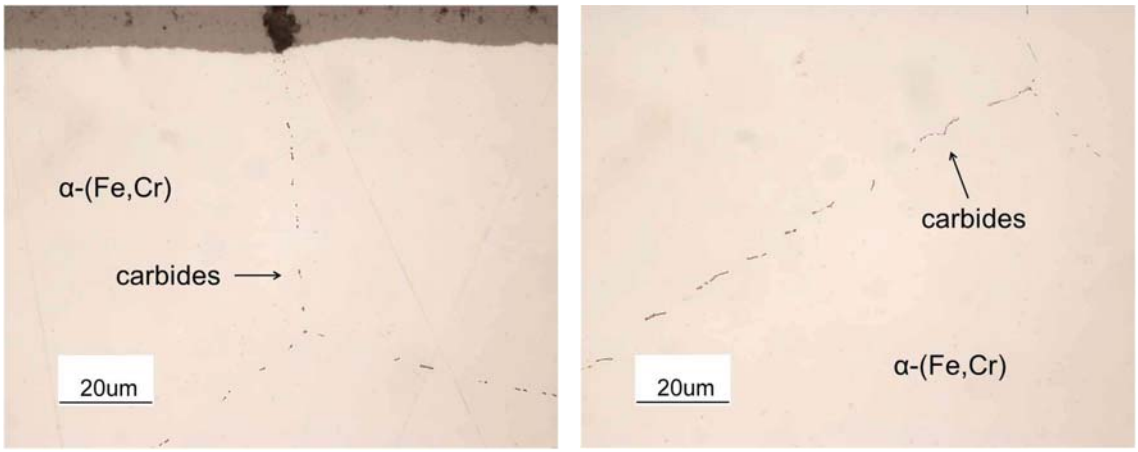

(a) Metal/oxide interface (b) Bulk alloy

Figure 3.10 – Optical micrographs showing intergranular carburisation in Fe–2.25Cr after 120 h exposure to Ar–20CO_2 at 650 °C. Specimen etched with Murakami's reagent.

throughout the cross-section after 120 h reaction in dry CO_2, but specimens reacted for other reaction times were not examined.

The Fe–9Cr alloy suffered extensive carburisation in dry and wet CO_2, forming both intragranular carbides throughout the specimens, and densely precipitated intragranular carbides in the subscale region (Fig. 3.11). Intergranular carburisation penetrated the entire specimen thickness after the shortest reaction time, 40 h. The

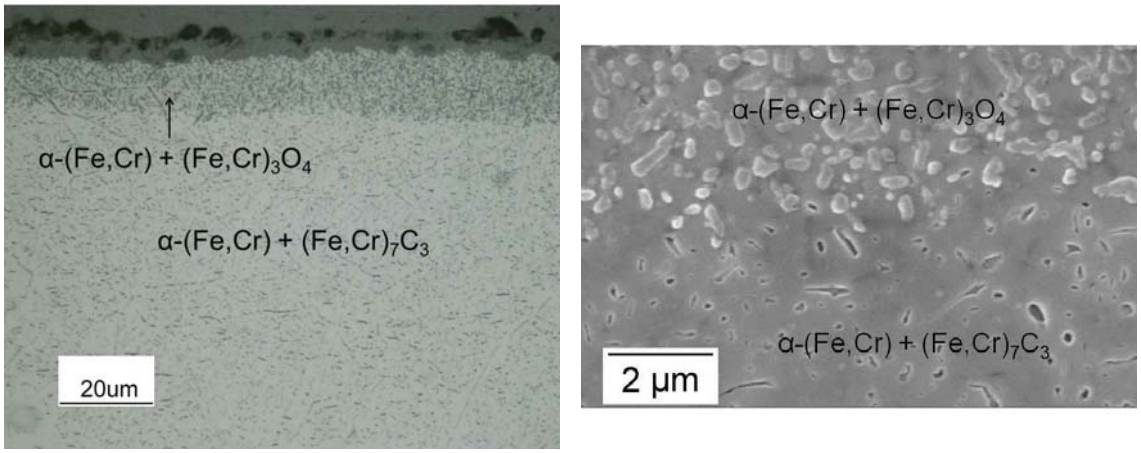

(a) Overview (b) Interface between IOZ and ICZ

Figure 3.11 – Intragranular carburisation in Fe–9Cr at 650 °C. (a) optical micrograph, 240 h in Ar–20CO_2–20H_2O; (b) SEM SE image of interface between internal oxidation zone (IOZ) and carburisation zone (ICZ), 120 h in Ar–20CO_2. Specimens etched with Murakami's reagent.

carburisation morphology was the same in dry and wet CO_2. One specimen was used for XRD analysis. The oxide scale and some reacted alloy were gradually polished off, and diffractograms were recorded near the metal/oxide interface and $\sim$ 36 µm beneath it. As is seen in Fig. 3.12, a peak could be attributed to $(Fe, Cr)_7C_3$, but it was very small despite analysing a surface of area $\sim$ 0.8 cm^2 and polished down to a 3 µm diamond solution. No peak corresponding to $M_{23}C_6$ was detected.

In the case of the 9Cr ternary alloys, particular care had to be taken in the metallographic preparation to determine the presence or absence of internal carbides. As shown in Fig. 3.13, carburisation of the Fe–9Cr–10Ni alloy was limited to a sparse intragranular precipitation in the subscale region after exposure to dry CO_2, and no carbides were found after reaction in Ar–20CO_2-20H_2O. The Fe–9Cr–20Ni alloy did not form any carbide when exposed to Ar–20CO_2 or Ar–20CO_2–20H_2O.

The kinetics of intragranular carburisation were investigated in the case of the Fe–9Cr alloy. Carbide penetration depths, X_c, were measured from the interface between the internal oxidation and internal carburisation zones. In both dry and wet CO_2, X_c increased according to a parabolic rate law (Fig. 3.14)

$$X_c^2 = 2k_c t \tag{3.3}$$

Values of k_c obtained from fitting data in $X_c = \mathrm{f}\left(t^{1/2}\right)$ plots are given in Table 3.3. The rate constant is seen to decrease with increasing H_2O concentration in the reacting gas. The volume fraction of carbides in the ferrite matrix, f_V, after reaction in Ar–20CO_2 and Ar–20CO_2-20H_2O was measured from optical micrographs such as

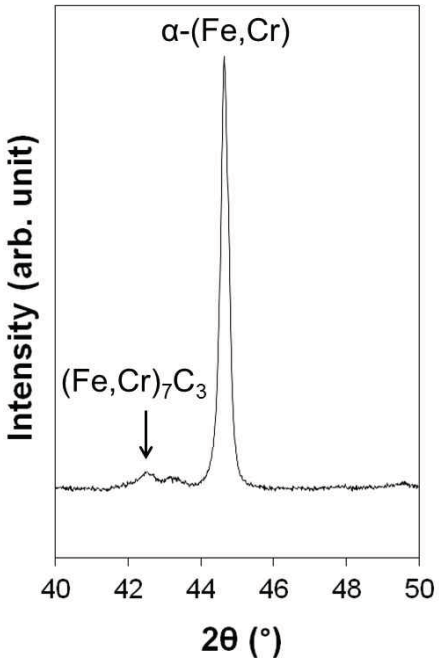

Figure 3.12 – Diffractogram recorded in the internal carburisation zone (36 µm beneath the metal/oxide interface) of Fe–9Cr after 240 h exposure to Ar–20CO_2–5H_2O at 650 °C.

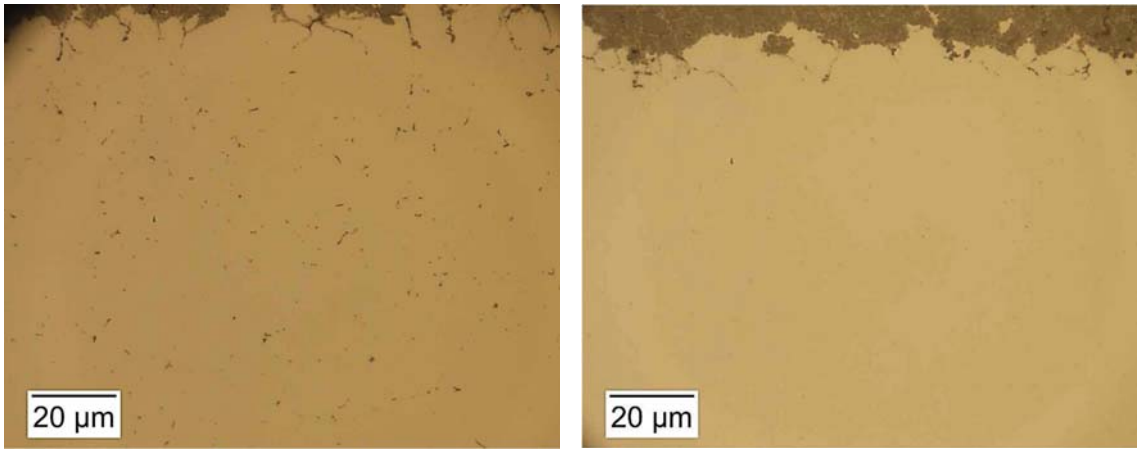

(a) Ar–20CO_2 (b) Ar–20CO_2–20H_2O

Figure 3.13 – Optical micrographs of subscale region in Fe–9Cr–10Ni after 120 h reaction at 650 °C. Specimens etched with Murakami's reagent.

Table 3.3 – Carburisation rates for Fe–9Cr at 650 °C, as defined in Eq. (3.3).

Gas	k_c (10^{-10} cm^2 s^{-1})
Ar–20CO_2	6.5
Ar–20CO_2–5H_2O	4.6
Ar–20CO_2–20H_2O	2.5

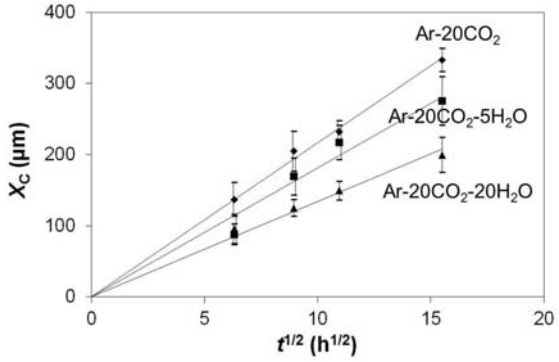

Figure 3.14 – Carburisation kinetics of Fe–9Cr at 650 °C. Mean values obtained from 10 or more measured values. Error bars indicate ($X_c \pm$ stdev), where stdev denotes standard deviation.

that shown in Fig. 3.11(a) using the ImageJ [155] software. As the precipitates are equiaxed, f_V is considered equal to the surface fraction measured on a cross-sectional view. The influence of the area of the analysed zone, image resolution and parameters of the analysis procedure (mainly contrast enhancement and thresholding) was investigated in order to reach a compromise between amount of data collected, depth resolution and precision of the measured values. Measurements were then made in 50 µm deep zones, with a precision of about 2%; that is, f_V at an absolute depth x from the interface between internal oxidation and internal carburisation corresponds to an average $(f_V \pm 1)$ % in the depth range $[x - 25; x + 25]$ µm. Results plotted against the relative depth x/X_c are shown in Fig. 3.15. The general shape of the

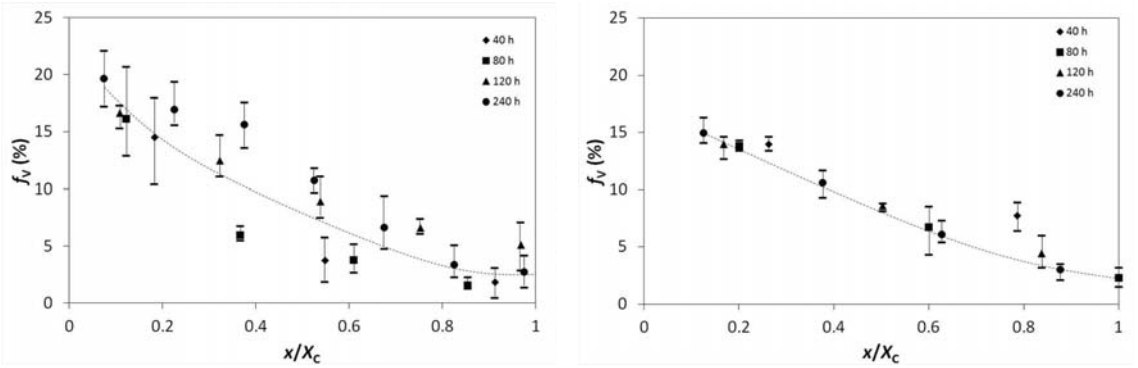

(a) Ar–20CO_2 (b) Ar–20CO_2–20H_2O

Figure 3.15 – Carbide volume fractions in Fe-–9Cr after reaction at 650 °C. Mean values obtained from 4 measured values at each depth, with minimum and maximum indicated by the error bars.

profiles is seen to be independent of reaction time or gas composition. However, on

average for the four reaction times, the value obtained near the alloy surface (in the [0;50] µm deep region) was higher in the dry gas, with $f_V = 0.17$ compared with $f_V = 0.14$ in Ar–20CO_2-20H_2O.

3.2 Low chromium alloys at 800 °C

3.2.1 Weight gain kinetics

Weight changes recorded after reaction of the low chromium alloys in Ar–20CO_2, Ar–20CO_2–5H_2O, Ar–20CO_2–20H_2O and Ar–20H_2O at 800 °C are shown in Fig. 3.16. Some variability is seen between specimens of the same composition reacted in a given gas, but to a lesser extent than was observed for reaction at 650 °C.

Oxidation kinetics of pure iron were linear in Ar–20CO_2 and Ar–20CO_2–5H_2O, with a higher rate constant in the wet gas. Reaction of iron in gases containing 20H_2O led to parabolic kinetics, with no significant effect of the presence of CO_2(g) on the rate constant. Reaction kinetics of Fe–2.25 and Fe–9Cr were linear in Ar–20CO_2, Ar–20CO_2–5H_2O and Ar–20H_2O, and as in the case of iron, the rate constants were higher in the wet gases. Both binary alloys reacted according to parabolic kinetics in Ar–20CO_2–20H_2O. Partial scale spallation was, after some of the experiments, very important in the case of the 9Cr ternary alloys, which reduced the amount of useful $\Delta m/A$ data. Oxidation kinetics of Fe–9Cr–10Ni were linear in dry CO_2, and approximately parabolic in the other atmospheres. The oxidation rate of Fe–9Cr–20Ni seemed to decrease with time in all atmospheres, which may be, in a very approximate way, associated with parabolic kinetics.

Gravimetric data corresponding to linear kinetics in Ar–20CO_2 were used to determine rate constants $k_{\ell m}$ defined by the rate law

$$\frac{\Delta m}{A} = k_{\ell m} t \tag{3.4}$$

The $k_{\ell m}$ values are seen in Table 3.4 to be quite close from one another. Similarly,

Table 3.4 – Linear and parabolic rate constants for reaction of low chromium alloys at 800 °C.

	$k_{\ell m}$ (10^{-4} mg cm^{-2} s^{-1}) in Ar–20CO_2 Eq. (3.4)	k_{pm} (10^{-3} mg^2 cm^{-4} s^{-1}) in Ar–20CO_2–20H_2O Eq. (3.1)
Fe (TGA)	1.2	28
Fe–2.25Cr	1.3	5.6
Fe–9Cr	1.4	4.3
Fe–9Cr–10Ni	1.1	0.80
Fe–9Cr–20Ni		0.32

rate constants k_{pm} defined by Eq. (3.1), and determined from fitting data obtained

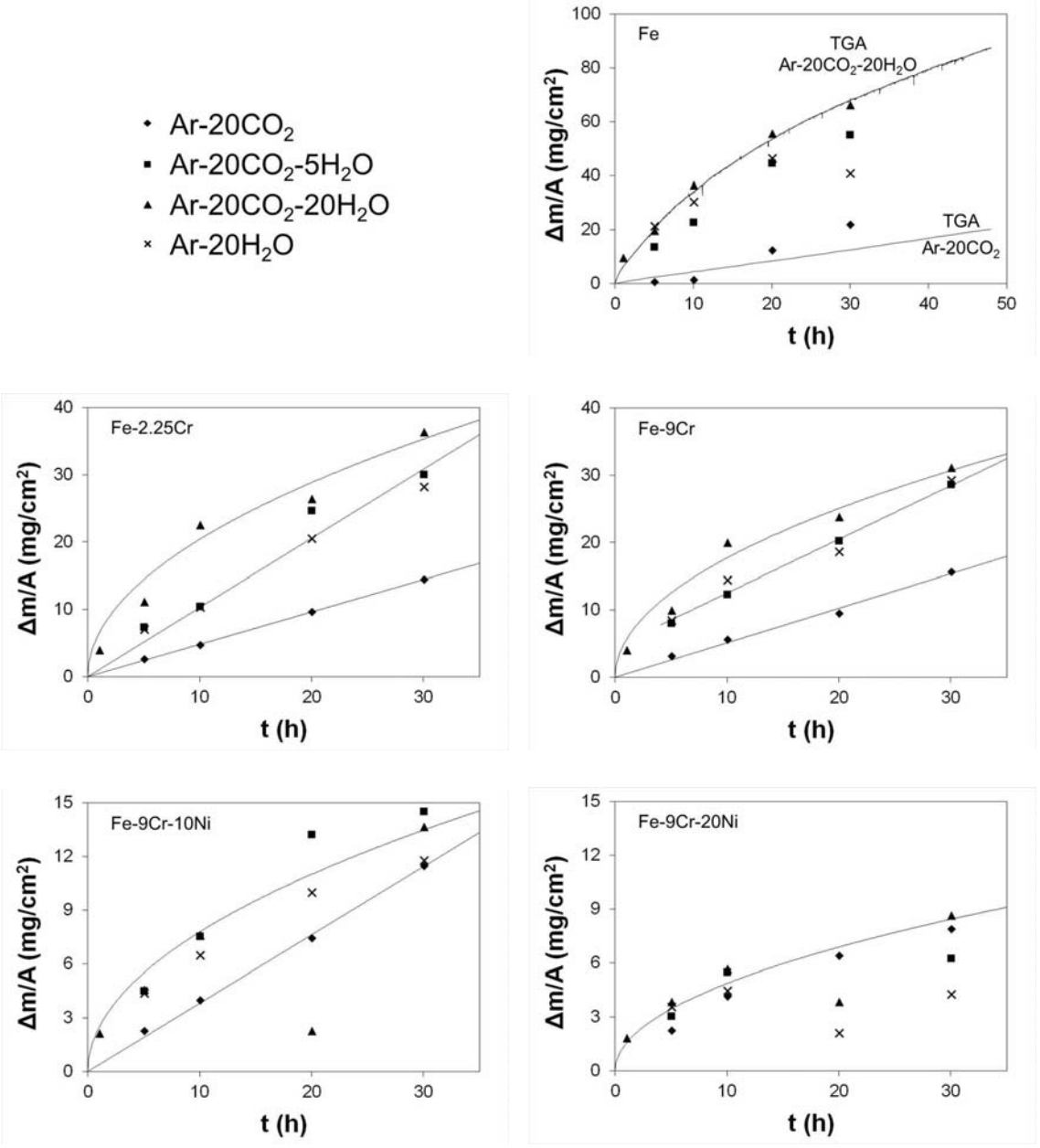

Figure 3.16 – Weight change kinetics of low chromium alloys at 800 °C. Solid lines are TGA data in the graph of Fe, and linear and parabolic fits of the data elsewhere.

after reaction in Ar–20CO_2–20H_2O using $\Delta m/A = \mathrm{f}\left(t^{1/2}\right)$ plots, are included in Table 3.4. No data from reaction in Ar–20H_2O or Ar–20CO_2–5H_2O were used to determine the rate constants showed in Table 3.4. In the case of pure iron, the use of TGA data allowed a more precise determination of k_{pm}. Early stage kinetics were in fact subparabolic, and the k_{pm} value was calculated by fitting an equation of the form $\Delta m/A = at^{1/2} + b$ to the data measured for $t > 10$ h ($a = \sqrt{2k_{\mathrm{pm}}}$). As mentioned earlier, in the case of Fe–9Cr–10Ni and Fe–9Cr–20Ni, kinetics were approximately parabolic in all H_2O-containing gases, but partial scale spallation limited the amount of available data. In order to improve the sampling volume used for determining rate constants, obviously unreliable results (representing weight loss) were dismissed, and k_{pm} values (Table 3.4) were determined as averages of values obtained from reaction in Ar–20CO_2–5H_2O, Ar–20CO_2–20H_2O and Ar–20H_2O (and Ar–20CO_2 in the case of Fe–9Cr–20Ni). Both chromium and nickel additions are seen in Table 3.4 to cause significant reductions in k_{pm} values.

3.2.2 Surface appearance

The appearance of the specimen surfaces after reaction at 800 °C was quite uniform, and similar for all low chromium alloys. Reaction in dry CO_2 and Ar–20CO_2–5H_2O produced faceted surfaces. A typical example is shown in Fig. 3.17(a). The

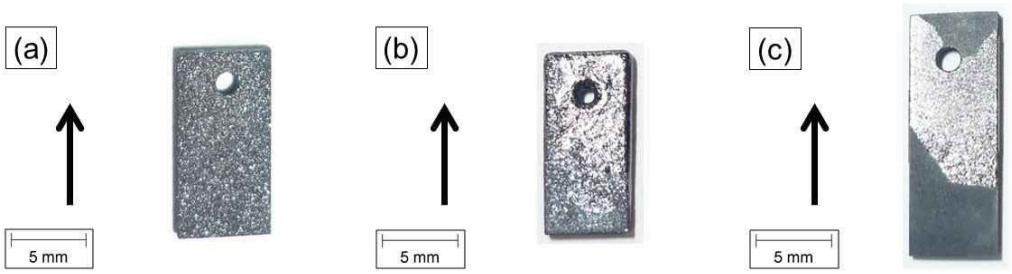

Figure 3.17 – Photographs showing specimen surface appearance after reaction at 800 °C. (a) Fe–9Cr, 10 h in Ar–20CO_2; (b) Fe–2.25Cr, 30 h in Ar–20CO_2–20H_2O; (c) Fe–9Cr–10Ni, 20 h in Ar–20CO_2–20H_2O. Black arrows indicate direction of gas flow.

surfaces were less rough after reaction in Ar–20CO_2–20H_2O. No variation of surface appearance was observed in relation to the direction of the gas flow, unless in rare cases after reaction in Ar–20CO_2–20H_2O, where the smoother type of surface did not extend to the bottom of the specimens (downstream), as shown in Fig. 3.17(b). Partial scale spallation was observed on rare occasions and to small extents in the

case of iron and the binary alloys, but was more significant for the 9Cr ternaries (Fig. 3.17(c)).

The surface oxides were identified as FeO and Fe_3O_4 by XRD analysis. For all alloys, the signal of FeO was the most important after reaction in dry CO_2, and that of Fe_3O_4 prevailed after reaction in wet CO_2.

Figure 3.18 presents SEM images of the surface morphology developed on iron, representative of reaction of all alloys, in Ar–20CO_2, Ar–20CO_2–5H_2O and Ar–20CO_2–20H_2O. Large, faceted oxide crystals are seen to form during reaction in dry

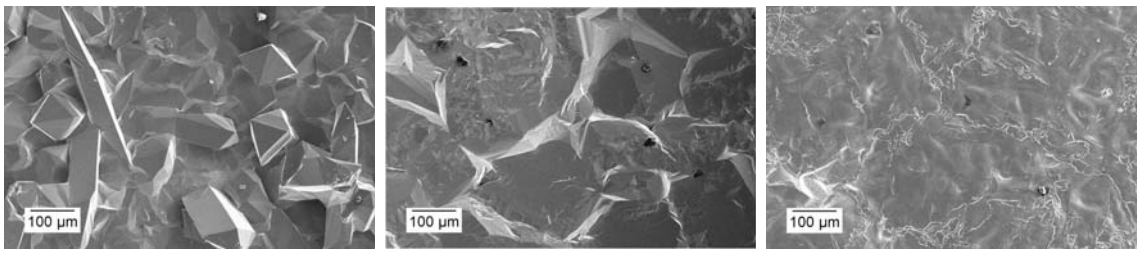

(a) Ar–20CO_2 (b) Ar–20CO_2–5H_2O (c) Ar–20CO_2–20H_2O

Figure 3.18 – Scanning electron micrographs (SE mode) showing surface morphology of oxide scales formed on iron after 48 h reaction at 800 °C.

CO_2. The addition of 5% H_2O(g) caused a decrease in the surface roughness, and the surfaces were quite flat after exposure to Ar–20CO_2–20H_2O.

3.2.3 Oxidation products

Reaction of iron in Ar–20CO_2 and Ar–20CO_2–5H_2O at 800 °C produced scales of FeO; Fe_3O_4 was occasionally formed at the scale surface, but mostly the scale was single-phase, as shown in Fig. 3.19(a). After reaction in Ar–20CO_2–20H_2O, magnetite was found to form a thin continuous layer at the oxide/gas interface (Fig. 3.19(b)). In Fig. 3.19, a 2% HCl solution in ethanol was used to etch FeO; the cube-shaped Fe_3O_4 particles found in the FeO layer after reaction in Ar–20CO_2–20H_2O precipitated during cooling, as a result of the non-stability of FeO below 570 °C [153]. Precipitation occured only in the outer part of the FeO layer, where the oxide was oxygen-rich.

Oxide scales produced by reaction of the low chromium alloys at 800 °C were morphologically similar to those formed at 650 °C. The optical micrographs shown in Figs. 3.20(a,c) are typical of the oxides grown on both Fe–2.25Cr and Fe–9Cr. In the same way, both the Fe–9Cr–10Ni and Fe–9Cr–20Ni alloys formed oxide scales as shown in Figs. 3.20(b,d).

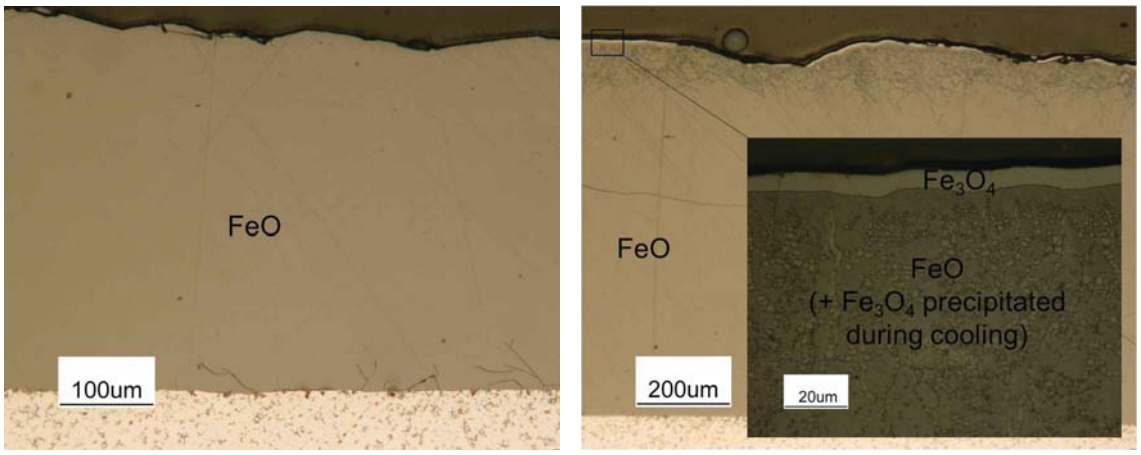

(a) Ar–20CO_2–5H_2O (b) Ar–20CO_2–20H_2O

Figure 3.19 – Optical micrographs of oxide scales formed on iron after 48 h reaction at 800 °C. Specimens etched with HCl solution.

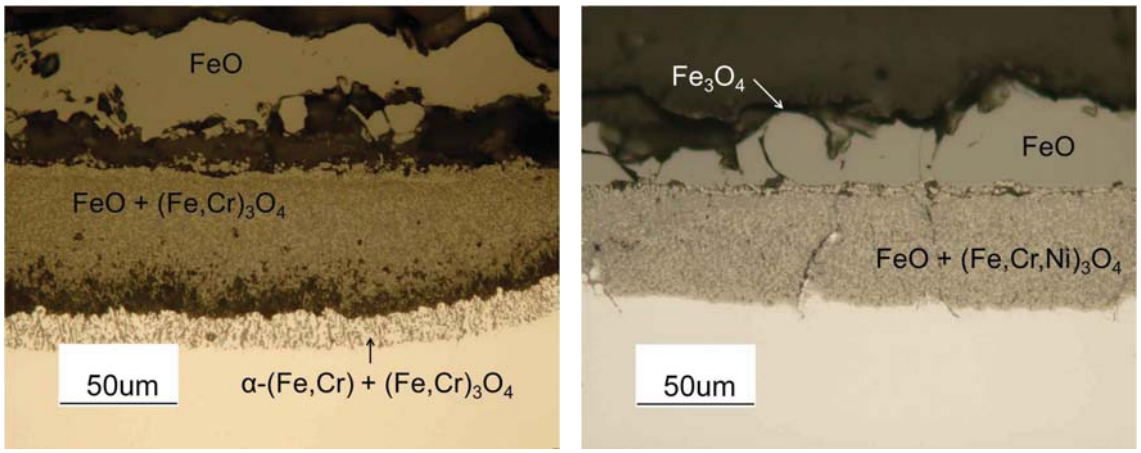

(a) Fe–9Cr, Ar–20CO_2 (b) Fe–9Cr–10Ni, Ar–20CO_2

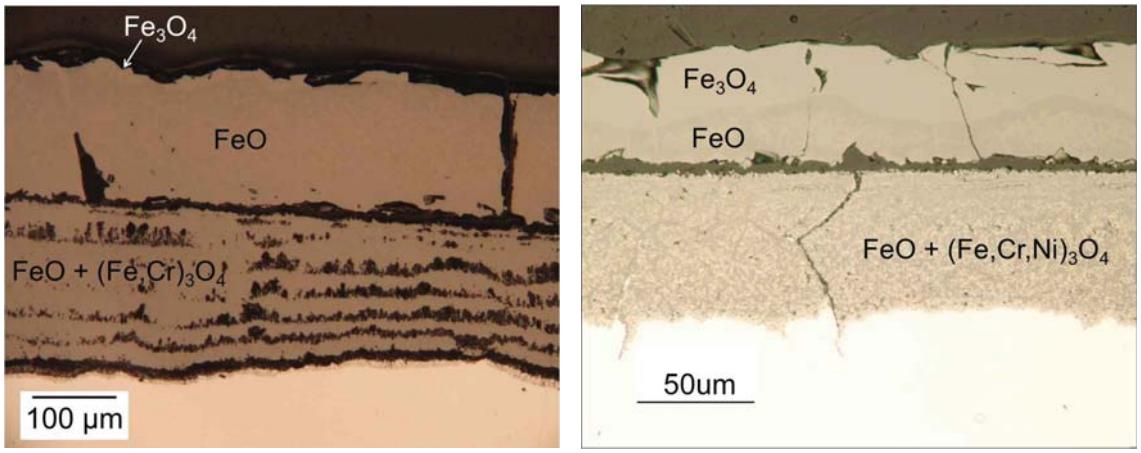

(c) Fe–9Cr, Ar–20CO_2–20H_2O (d) Fe–9Cr–10Ni, Ar–20CO_2–20H_2O

Figure 3.20 – Optical micrographs of oxide scales formed on 9Cr alloys in 30 h reaction at 800 °C.

All oxide scales can be divided in two parts. The outer part was relatively coarse-grained and rather compact, but contained large cracks and cavities. In contrast, the inner part was fine-grained and porous. This morphological difference is visible in the polished cross-sections of Fig. 3.20, but is best observed on fracture sections, such as those shown in Fig. 3.21. In the case of the binary alloys reacted

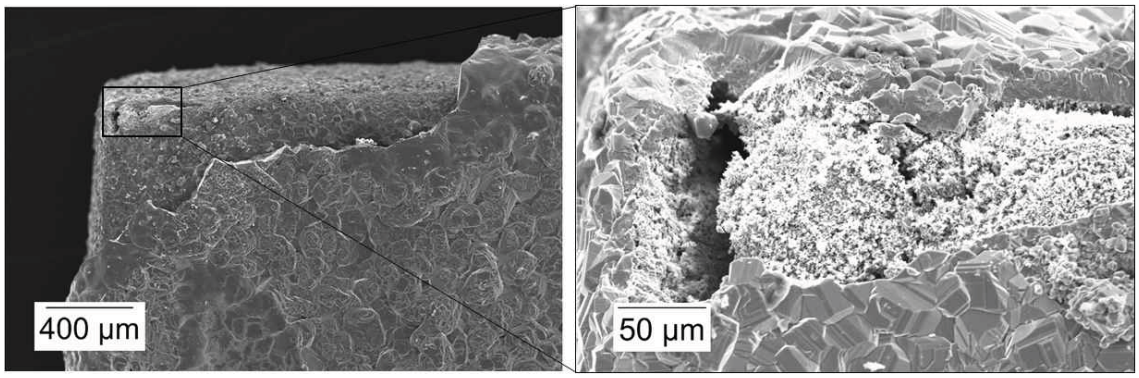

Figure 3.21 – Scanning electron micrographs (SE mode, surface view) showing microstructure of outer and inner layers of oxide scale formed on Fe–2.25Cr after 48 h reaction in Ar–20CO_2–5H_2O at 800 °C.

in dry CO_2, pores were found throughout the inner layer, but were particularly prevalent at the base of the scale, and coalesced in large cavities next to the metal surface (Fig. 3.20(a)). After exposure to both Ar–20CO_2–5H_2O and Ar–20CO_2–20H_2O, pores were concentrated in several rows of large cavities parallel to the metal surface (Fig. 3.20(c)). In the case of the 9Cr ternaries, however, porosity seemed to be uniformly distributed in the inner layer (Figs. 3.20(b,d)).

Analysis by SEM–EDS showed that the outer layers were iron oxides, while the inner layer also contained chromium, and nickel in the case of the ternary alloys. The oxide phases were identified by etching FeO with an HCl solution, and by means of XRD analysis. The outer scale formed during reaction in dry CO_2 consisted mainly of FeO. Some Fe_3O_4 was scattered at the surface of the scale formed on the binary alloys, and formed a continuous layer in the case of the 9Cr ternaries, as seen in Fig. 3.22. The amount of surface Fe_3O_4 observed on the binary alloys was greater after exposure to Ar–20CO_2–5H_2O, and a continuous layer was formed during reaction in Ar–20CO_2–20H_2O. Figure 3.23 shows the distribution of FeO and Fe_3O_4 in the outer layer after exposure of the 9Cr alloys to Ar–20CO_2–20H_2O. The relative thickness of the oxygen-rich Fe_3O_4 increased with increasing nickel concentration in the alloy.

The phase constitution of the scales grown on the 9Cr alloys was investigated by

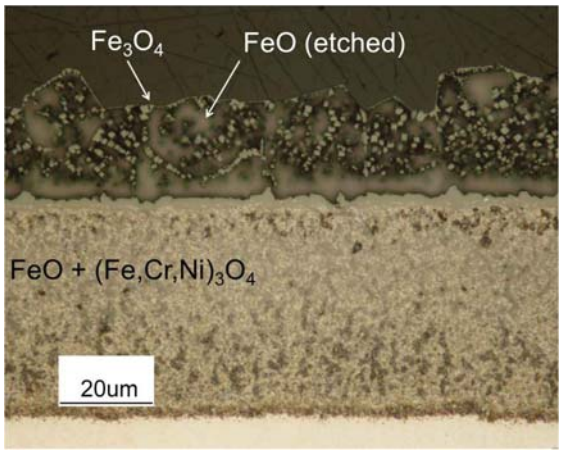

Figure 3.22 – Optical micrograph of oxide scale formed on Fe–9Cr–20Ni reacted 30 h in Ar–20CO_2 at 800 °C; specimen etched with HCl solution.

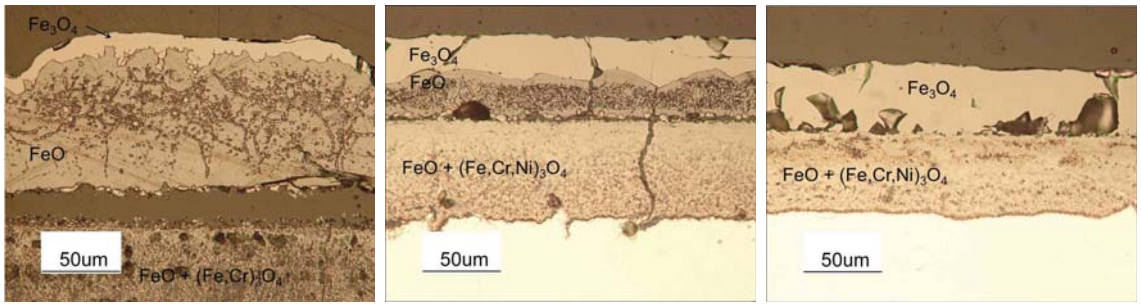

(a) Fe–9Cr (b) Fe–9Cr–10Ni (c) Fe–9Cr–20Ni

Figure 3.23 – Optical micrographs of outer layers of oxide scales formed after 30 h reaction in Ar–20CO_2–20H_2O at 800 °C. Specimens etched with Vilella's reagent.

means of the alternate XRD/grinding method; diffractograms were thus recorded throughout the scale to the metal substrate. For all three alloys, spectra of both FeO and spinel oxide were detected in the inner layer. Analysis by SEM–EDS of scales grown on Fe–2.25Cr and Fe–9Cr showed that the inner layer consisted of Cr-rich particles in an Fe-rich matrix (images are shown in Fig. 3.24 for Fe–9Cr); the two-phase mixture was thus identified as FeO + $(Fe, Cr)_3O_4$. Volume fractions of the spinel phase, $f_{V,sp}$, were measured from optical and scanning electron micrographs, with varying magnifications, and using two methods. In a few cases, $f_{V,sp}$ was determined by tracing a grid on an image, and measuring the length of horizontal and vertical lines crossing spinel precipitates. In this method, the sampling volume is determined by the dimensions of the grid, relative to the precipitate size. For grids fine enough, $f_{V,sp}$ depended neither on the grid's dimensions nor on the image selected. This good reproducibility was limited by the small number of images

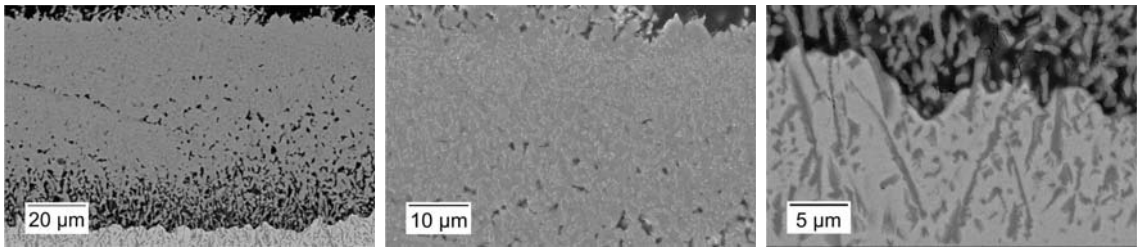

(a) Overview (b) Outer part (c) Scale/IOZ interface

Figure 3.24 – Scanning electron micrographs of inner scale formed in Fe–9Cr after 30 h reaction in Ar–20CO_2 at 800 °C. (a,c) BSE mode; (b) SE mode.

used. Alternatively, $f_{V,sp}$ measurements were made by conventional image analysis using ImageJ [155], which allowed a much larger number of images to be processed. However, the results were very sensitive to the parameters used in the analysis procedure — mainly contrast enhancement and binarisation by methods such as sharpening, thresholding, eroding, dilating. This procedure could not be automated because contrasts varied between the different images. Great care was taken in order to obtain results both comparable with one another and consistent with those obtained by the lengthy grid method. Average results ($f_{V,sp} \pm 3$) % are given in Table 3.5. Given the experimental uncertainty, the volume fraction is seen to be

Table 3.5 – Volume fractions of spinel oxide in inner scale, $f_{V,sp}$ (%), measured after reaction at 800 °C.

	Ar–20CO_2	Ar–20CO_2–5H_2O	Ar–20CO_2–20H_2O
Fe–2.25Cr	10.1	9.7	10.0
Fe–9Cr	33.5		30.5

independent of gas composition; however, a significant increase is seen between Fe–2.25Cr and Fe–9Cr.

Both binary alloys were prone to internal oxidation in dry and wet CO_2. The internal oxides were seen by EDS–SEM to be Cr-rich. Analysis by XRD showed, in the case of Fe–9Cr, that the internal oxidation zone consisted of a α + spinel mixture, and no Cr_2O_3 was detected. The internal particles had the same morphology as those formed in the inner oxide layer: small and equiaxed, with a very low volume fraction for Fe–2.25Cr; elongated and more densely precipitated for Fe–9Cr. In the latter case, a morphological continuity between the internal and inner layer precipitates was evident, as seen in Fig. 3.24(c).

Scanning electron micrographs of the inner oxide layer formed on the 9Cr ternar-

ies are shown in Figs. 3.25 and 3.26. In both cases the microstructure was par-

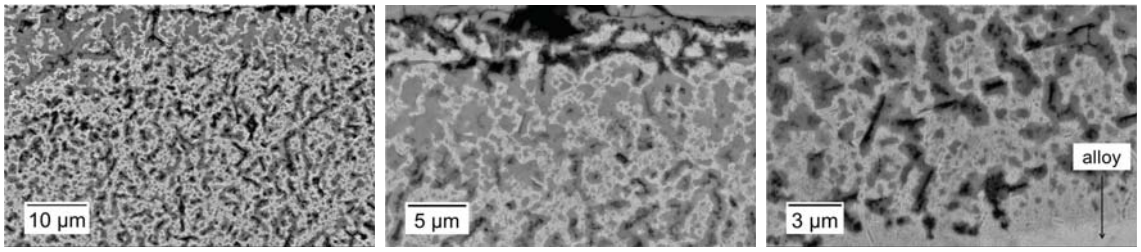

(a) Overview (b) Outer part (c) Metal/oxide interface

Figure 3.25 – Scanning electron micrographs (BSE mode) of inner scale formed in Fe–9Cr–10Ni after 30 h reaction in Ar–20CO_2 at 800 °C.

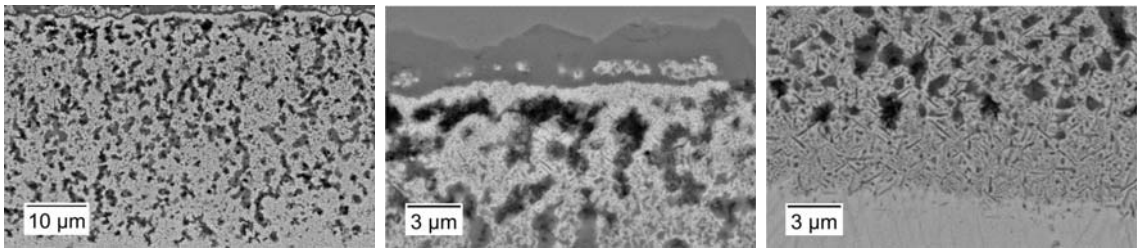

(a) Overview (b) Outer part (c) Metal/oxide interface

Figure 3.26 – Scanning electron micrographs (BSE mode) of inner scale formed in Fe–9Cr–20Ni after 30 h reaction in Ar–20CO_2 at 800 °C.

ticularly fine, and the number of phases could not be determined. A dark phase is preferentially observed on the edges of the numerous pores, and was seen by SEM–EDS to be Cr-rich, while iron and nickel were concentrated in the other phases. At least one type of acicular particle precipitated in the oxide matrix. The volume fraction of Cr-rich phase was measured by image analysis to be 55 % and 22 % for Fe–9Cr–10Ni and Fe–9Cr–20Ni, respectively, from images such as those shown in Figs. 3.25 and 3.26. Furthermore, a Cr-enriched zone was detected by SEM–EDS in the outermost part of the inner layer for both 9Cr ternaries. A compact and continuous layer was visible at this location in the case of Fe–9Cr–20Ni (Fig. 3.26(b)); this was not observed in scales formed on Fe–9Cr and Fe–9Cr–10Ni (Figs. 3.24(b) and Fig. 3.25(b), respectively). Finally, the 9Cr ternaries did not undergo internal oxidation to any significant extent: only a very sparse distribution of oxide precipitates was sometimes observed in the metal substrate, with a penetration depth lower than 1 µm.

3.2.4 Oxide growth kinetics

The thickness of the oxides formed on the Fe–9Cr alloy (external scale + internal oxidation zone) was measured after varying exposure times to Ar–20CO_2 and Ar–20CO_2–20H_2O. Oxide growth followed linear kinetics in Ar–20CO_2 and parabolic kinetics in Ar–20CO_2–20H_2O, in both cases to a good approximation (Fig. 3.27). These results are consistent with the gravimetric data (Fig. 3.16).

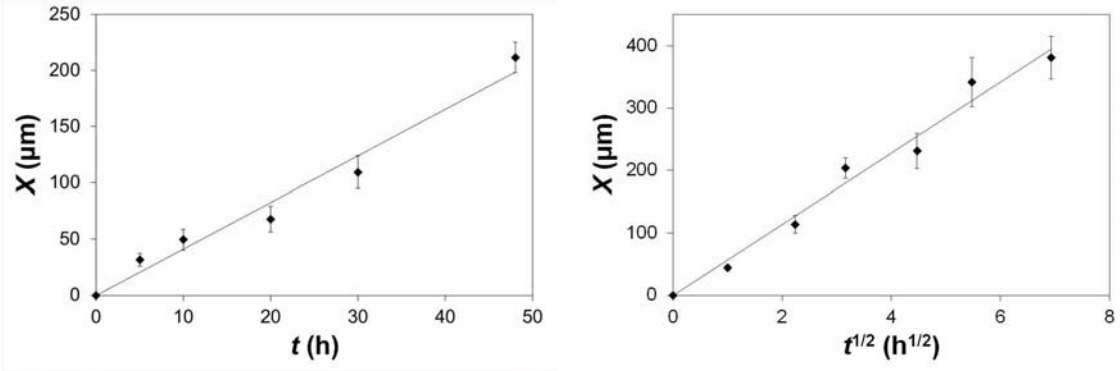

(a) Ar–20CO_2, linear plot (b) Ar–20CO_2–20H_2O, parabolic plot

Figure 3.27 – Oxide growth kinetics of Fe–9Cr at 800 °C. Mean values obtained from ∼ 10–30 measured values. Error bars indicate ($X \pm$ stdev), where stdev denotes standard deviation.

A linear rate law

$$X = k_\ell t \tag{3.5}$$

was fitted to the data of Fig. 3.27(a) to yield the rate constant k_ℓ given in Table 3.6. Also included are k_ℓ values for Fe, Fe–2.25Cr and Fe–9Cr–10Ni, determined from

Table 3.6 – Oxidation rate constants measured after reaction at 800 °C.

	k_ℓ (10^{-8} cm s^{-1}) in Ar–20CO_2		k_p (10^{-9} cm^2 s^{-1}) in Ar–20CO_2–20H_2O	
	from X Eq. (3.5)	from $\Delta m/A$ Eq. (3.4)	from X Eq. (3.2)	from $\Delta m/A$ Eq. (3.1)
Fe	7.9	8.7	18	16
Fe–2.25Cr	15	10	3.6	3.1
Fe–9Cr	12	11	4.5	2.4
Fe–9Cr–10Ni	8.3	7.9	0.53	0.45
Fe–9Cr–20Ni	n/a	n/a	0.39	0.18

thicknesses measured after either 30 or 48 h exposure to dry CO_2. Values obtained

from a single specimen should be considered as estimates only. The gravimetric constants $k_{\ell \mathrm{m}}$ given in Table 3.4 were converted to k_ℓ values via

$$k_{\ell \mathrm{m}} = \frac{bM_{\mathrm{O}}}{V_{\mathrm{M_aO_b}}} k_\ell \tag{3.6}$$

with the usual notations, assuming that the oxides were dense FeO, seen in Section 3.2.3 to be the predominant phase at this temperature. Values obtained from thickness and weight gain data are seen in Table 3.6 to be in reasonable agreement, except for Fe–2.25Cr where the difference is significant.

Similarly, a parabolic rate constant k_{p} (Eq. (3.2)) was determined for reaction of Fe–9Cr in Ar–20CO_2–20H_2O using the $X = \mathrm{f}\left(t^{1/2}\right)$ plot shown in Fig. 3.27(b), and k_{p} values were estimated from thicknesses measured on a single specimen of each of the other alloys. The values are compared in Table 3.6 with those obtained from the $\Delta m/A$ data given in Table 3.4, after conversion. Again, all scales were considered to be dense FeO in applying Eq. (1.11). The agreement between values obtained from thickness and gravimetric data is good, except for Fe–9Cr; the difference is unacceptable considering the evolution of k_{p} with alloy composition.

3.2.5 Carburisation products

Etching with Murakami's reagent did not reveal any carbide in the low chromium materials after reaction at 800 °C. Carburisation at this temperature was instead investigated using Vilella's reagent, which produced useful results.

No sign of carburisation was observed after reaction of iron and Fe–2.25Cr in any of the gases, whereas reaction of Fe–9Cr in both dry and wet CO_2 resulted in carbide and martensite precipitation. Intergranular carbides, visible on as-polished cross-sections (Fig. 3.28), were found at depths reaching about 150 µm after 1 h reaction, and throughout reacted specimens from 5 h.

Martensite was identified visually in etched cross-sections (Fig. 3.29), and its composition studied by means of EPMA and hardness testing. Internal precipitation was not uniform, as will be described subsequently. Microanalysis was carried out on an as-polished cross-section, where martensite had been previously marked using microhardness indents. The instrument was calibrated using pure iron and four Fe–C alloys containing 0.2 to 1 wt. % carbon; the sensitivity and resolution were estimated to be 0.1 wt. %. The carbon concentration thus obtained was (0.2 ± 0.04) wt. % (standard deviation for 7 point measurements) in martensite, and less than 0.1 wt. % in ferrite grains. Chromium was evenly distributed between transformed and untransformed grains, with (9.4 ± 0.1) wt. % in both phases. Vickers microhardness

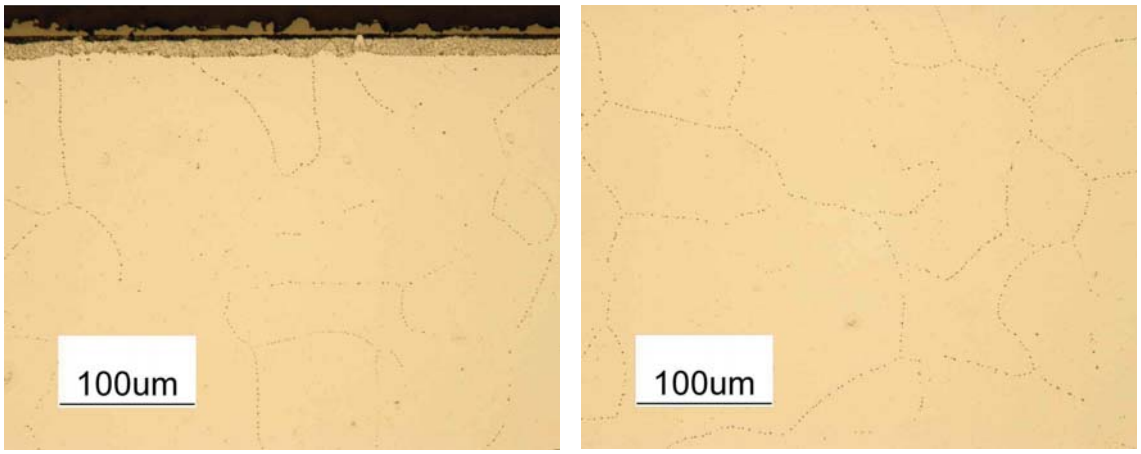

(a) Metal/oxide interface (b) Bulk alloy

Figure 3.28 – Optical micrographs showing intergranular carburisation in Fe–9Cr after 5 h exposure to Ar–20CO_2 at 800 °C (as polished).

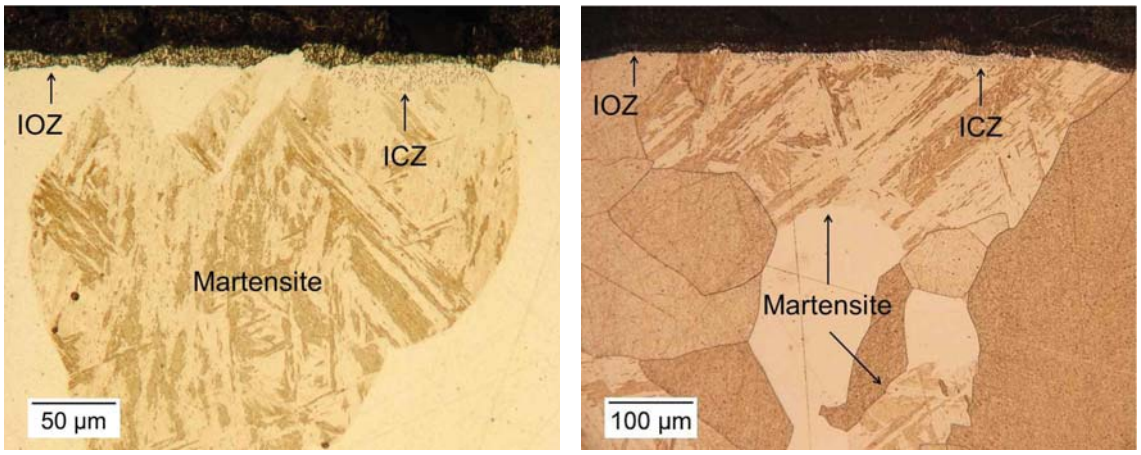

(a) Ar–20CO_2 (b) Ar–20CO_2–20H_2O

Figure 3.29 – Optical micrographs of martensite formed in Fe–9Cr after 20 h reaction at 800 °C. Specimens etched with Vilella's reagent.

tests with a 200 g load yielded HV values of about 100 and 400 for ferrite and martensite, respectively. Hardness data as a function of carbon concentration in Fe–C martensite can be found in Refs. [156,157] for example. Using the relationship corresponding to as-quenched martensite, an HV value of 400 is found to correspond to about 0.1–0.2 wt. % carbon. This result is to be considered with caution for several reasons: (i) the alloy of interest contained chromium, which could affect the hardness–composition relation; (ii) the experimental procedure in the present oxidation tests was not designed to reach fast cooling rates typical of quenching; (iii) self-tempering during cooling and ageing at room temperature may induce changes in alloy structure [158]. Nevertheless, in the absence of intended tempering, higher

carbon contents would lead to significantly higher HV values (for example HV 800 at 0.6 wt. % C [156,157]). Furthermore, the value of 0.2 wt. % is in agreement with the EPMA measurement.

Although the phase transformation affected entire grains, it did not occur in a uniform manner along the metal/oxide interface: some grains neighbouring the martensite remained untransformed, while some isolated martensite was found deep inside the alloy, surrounded by untransformed grains. The distibution of martensite in entire cross-sections is shown in Fig. 3.30. Precipitation occurred preferentially

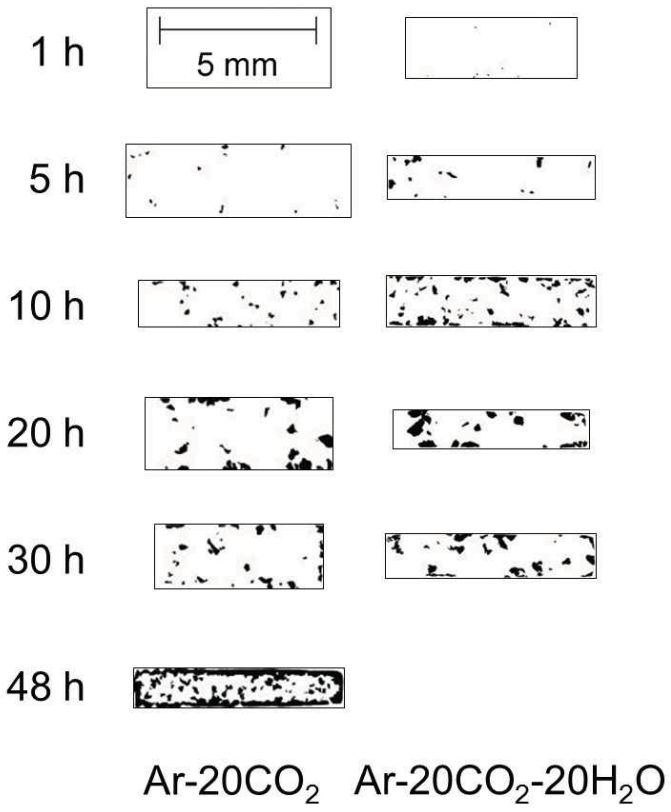

Figure 3.30 – Distribution of martensite (in black, obtained from binarisation of series of optical micrographs) in Fe–9Cr specimens after reaction at 800 °C.

near the metal/oxide interface after relatively long reaction times. This is particularly visible in Fig. 3.30 after 48 h exposure to Ar–20CO_2, and a very similar distribution was observed after reaction in Ar–20CO_2–5H_2O (but not Ar–20CO_2–20H_2O, as is shown subsequently).

Intragranular carbides were occasionally observed in a narrow 10 µm strip between the internal oxidation zone and the martensite, as seen in Figs. 3.29 and 3.31. However, in other regions where martensite formed near the alloy surface, no car-

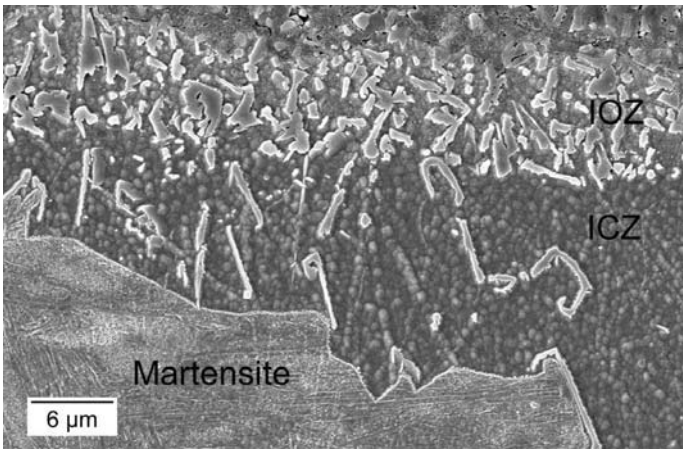

Figure 3.31 – Scanning electron micrograph of internal carburisation zone in Fe–9Cr after 20 h reaction at 800 °C. Specimen etched with Vilella's reagent.

bides were found. Carbides were never detected in the absence of martensite, i.e. at the internal oxide/ferrite interface. Foil specimens were prepared from the sample shown in Fig. 3.31, by FIB milling. The TEM—EDS results in Fig. 3.32(a) and (b) show that the α matrix was depleted in chromium, while the carbides and oxides were chromium-rich. Selected area diffraction patterns (SADP) were recorded and interpreted with the help of the CaRIne Crystallography software [159]. The patterns shown in Fig. 3.32(c) and (d) are characteristic of $(Fe, Cr)_{23}C_6$ and α-Fe, respectively.

The reaction pattern described in the preceding paragraphs (intergranular carbides, martensite, and occasionally intragranular carbides between martensite and the internal oxidation zone) was observed after reaction in Ar–20CO_2, Ar–20CO_2–5H_2O and Ar–20CO_2–20H_2O, with two exceptions. In the specimen reacted 30 h in Ar–20CO_2–20H_2O, intragranular carbides were observed around transformed grains, including away from the alloy surface, and to a larger extent than in the other specimens, as shown in Fig. 3.33(a). After 48 h exposure to Ar–20CO_2–20H_2O, no martensite was observed, but intragranular carbides were found throughout the specimen (Fig. 3.33(b)). The reason for these two exceptions to the carburisation pattern observed otherwise is unclear; a possible cause could be unintended and unnoticed changes in the cooling rate.

After reaction in both dry and wet CO_2, the Fe–9Cr–10Ni alloy was fully transformed to martensite (Fig. 3.34), while no carburisation product was found in Fe–9Cr–20Ni.

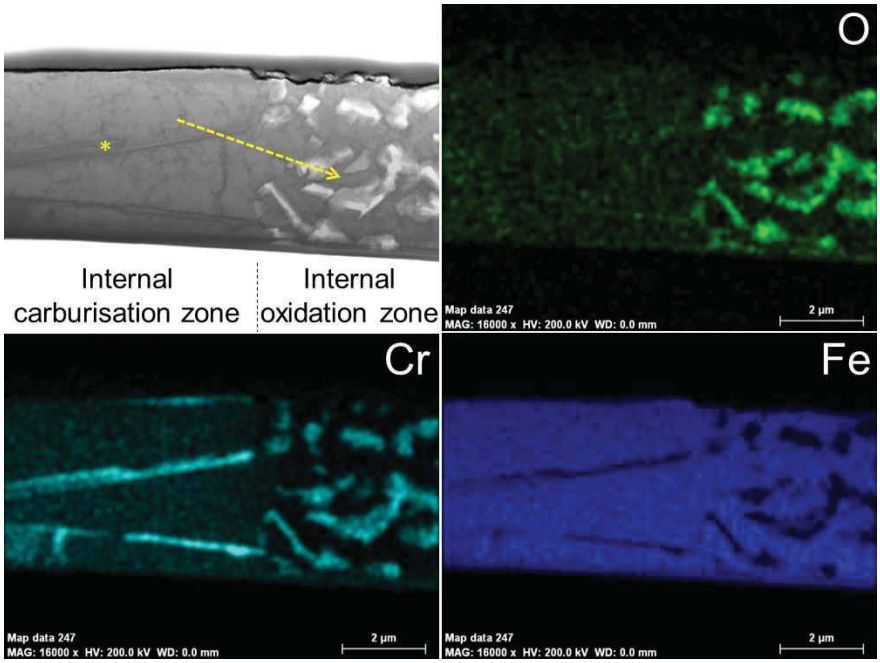

(a) Bright field image and elemental maps

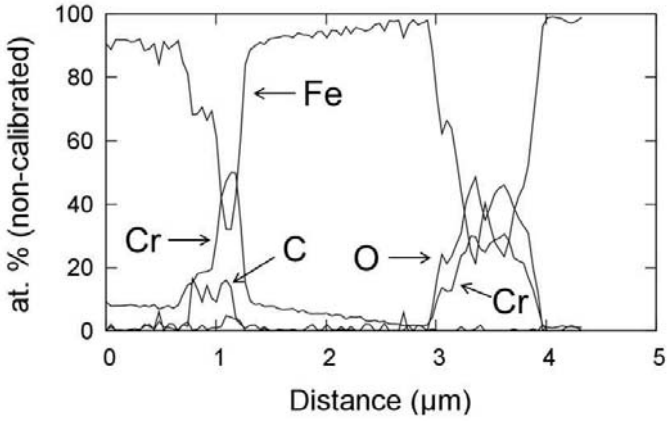

(b) EDS linescan

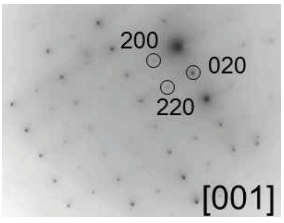

(c) SAD $(Fe,Cr)_{23}C_6$

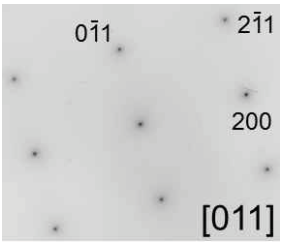

(d) SAD α-(Fe,Cr)

Figure 3.32 – TEM analyses at the interface between internal oxidation and carburisation zones in Fe-–9Cr after 20 h exposure to Ar–20CO_2 at 800 °C. The arrow in (a) indicates the location of the linescan in (b). The diffraction patterns in (c) and (d) correspond to the carbide particle marked by a star in (a) and the surrounding ferrite matrix, respectively.

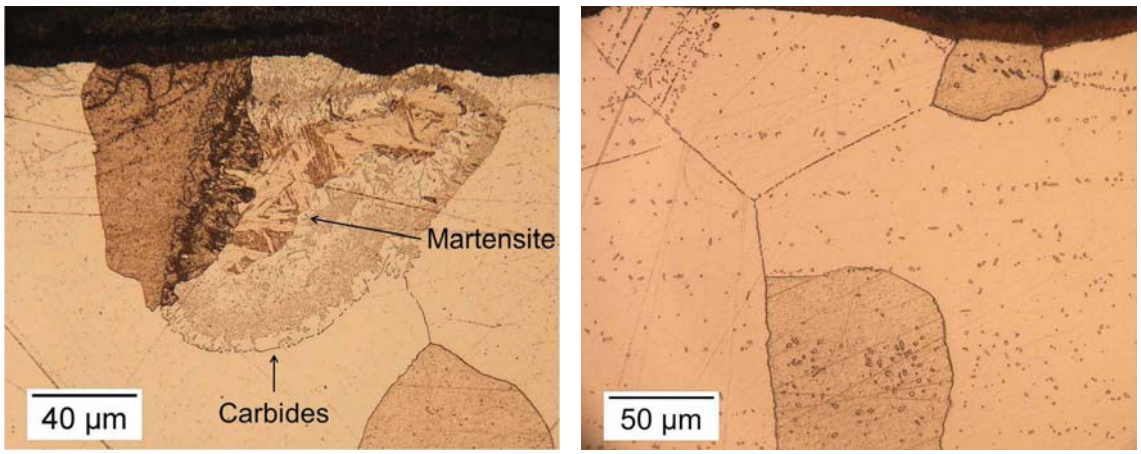

(a) Carbides surrounding martensite (b) Absence of martensite

Figure 3.33 – Optical micrographs showing exceptions to the carburisation morphology of Fe–9Cr, after (a) 30 h and (b) 48 h reaction in Ar–20CO_2–20H_2O at 800 °C. Specimens etched with Vilella's reagent.

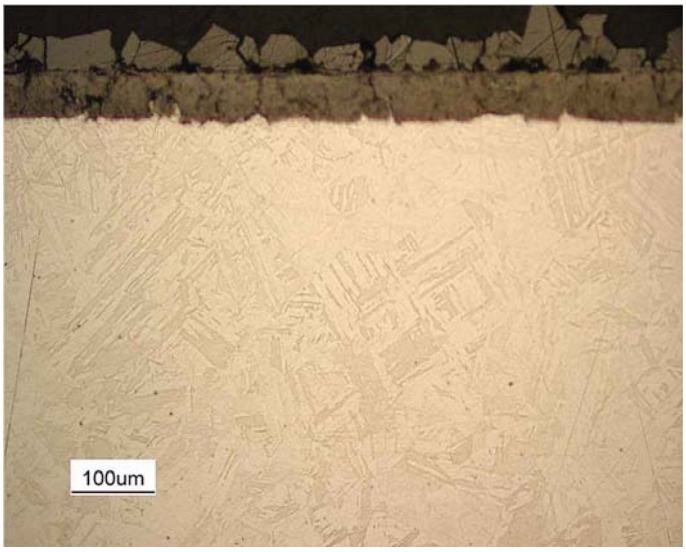

Figure 3.34 – Optical micrograph showing martensite formed in Fe–9Cr–10Ni after 30 h reaction in Ar–20CO_2 at 800 °C. Specimen etched with Vilella's reagent.

3.3 High chromium alloys at 650 °C

3.3.1 Surface appearance

Reaction of the high chromium alloys at 650 °C produced oxide surfaces of non-uniform appearance. The alloys formed a thin protective scale interrupted by thicker nodules, and the extent and distribution of nodule formation varied not only with alloy and gas composition, but also, for given compositions, from one specimen to another and even from one face to another of the same specimen. Of the 92 specimens reacted, a large number exhibited a unique surface appearance, and only the most relevant aspects are described here.

Analysis by XRD and Raman indicated that for all alloy and gas compositions, the protective scale was a Cr-rich corundum-type oxide, α-M_2O_3, which will be referred to as chromia. The nodules consisted of Fe-rich oxides, and are described in detail in Section 3.3.3.

Large differences in nodule development were clearly evident among the alloys, and three types of oxidation behaviour could be distinguished. The Fe–25Cr-10Ni and Fe–25Cr–20Ni alloys mainly formed Cr_2O_3. As seen in Fig. 3.35(a), the scale color changed from one substrate grain to another. Interference colors are generated

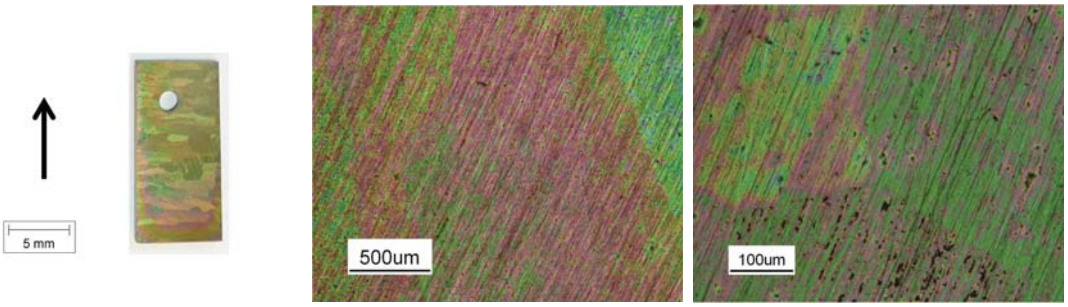

(a) Overview (b) Cr_2O_3 and nodules (c) Nodules on three grains

Figure 3.35 – Surface appearance of oxides formed on Fe–25Cr–20Ni after (a) 240 h and (b,c) 120 h reaction in Ar–20CO_2–20H_2O at 650 °C.

by thin films, and the variation of wavelength with oxide thickness [160] is commonly used in heat tinting (thermal etching) to reveal alloy microstructures. Clearly, the thickness of the Cr_2O_3 scale formed on the 25Cr ternaries varied with substrate orientation. Isolated nodules 1 to 30 µm large were formed in small quantities (Fig. 3.35(b)), to an extent varying with substrate orientation (Fig. 3.35(c)).

The binary alloys, Fe–20Cr and Fe–25Cr, suffered significant breakaway oxidation, characterised by high surface fractions of nodules. After short term reactions

in dry CO_2, most nodules were isolated and approximately circular in shape, and their distribution on the specimen surfaces was, if not uniform, more or less independent of grain orientation or gas flow direction (Fig. 3.36). The extent of nodule

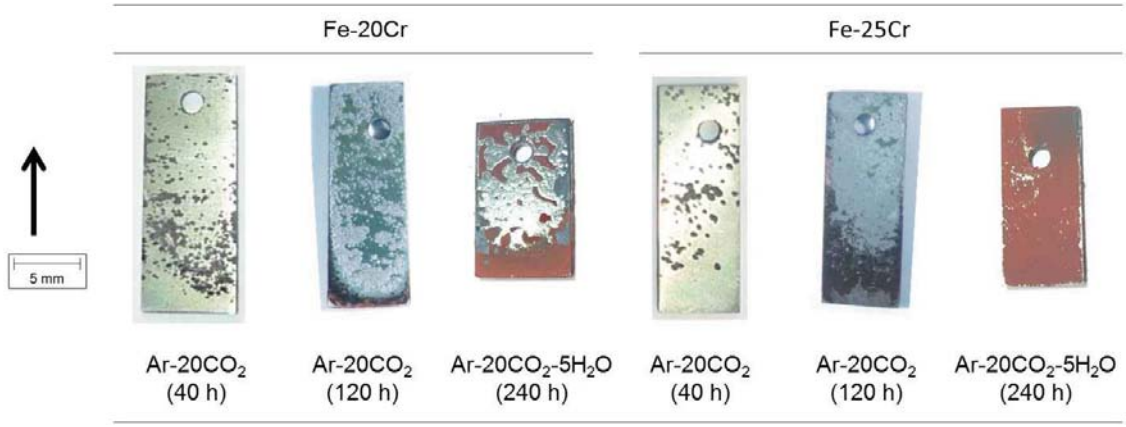

Figure 3.36 – Photographs showing surface appearance of oxides formed on Fe–20Cr and Fe–25Cr after reaction at 650 °C.

development was more advanced after exposure to wet CO_2, as nearly continuous scales of Fe-rich oxide covered the specimens. In addition, reaction in wet CO_2 produced Fe_2O_3 whiskers at the scale surface, which formed a loose powder and were readily detached from the scale. In Fig. 3.36, the surface of the scale formed on Fe–25Cr during exposure to Ar–20CO_2–5H_2O is uniform in appearance, while several types of iron oxide are visible on the surface of the Fe–20Cr specimen reacted in the same conditions. However, the contrary was also observed after other reaction times, for no apparent reason. In addition, both the extent of nodule formation and the surface morphology of the Fe-rich scale were, in some cases, dependent on the direction of the gas flow. This effect was mostly observed after long exposures to dry CO_2 (see Fig. 3.36).

The effect of H_2O(g) is clearly visible in Fig. 3.37: in dry CO_2, a small number of relatively large nodules were formed, which indicates that the nucleation rate was relatively low compared to the growth rate, whereas in wet CO_2, a large number of smaller nodules is visible, reflecting a relatively higher nucleation rate. If the influence of the gas flow is disregarded, nodule development on the binary alloys may be described as occurring by continuous, more or less uniform nucleation and growth of individual, circular nodules, and their coalescence into continuous scales. However, in a given reaction gas, the relative rates of nucleation and growth were variable. Although it did not produce very marked effects on nodule distribution, it

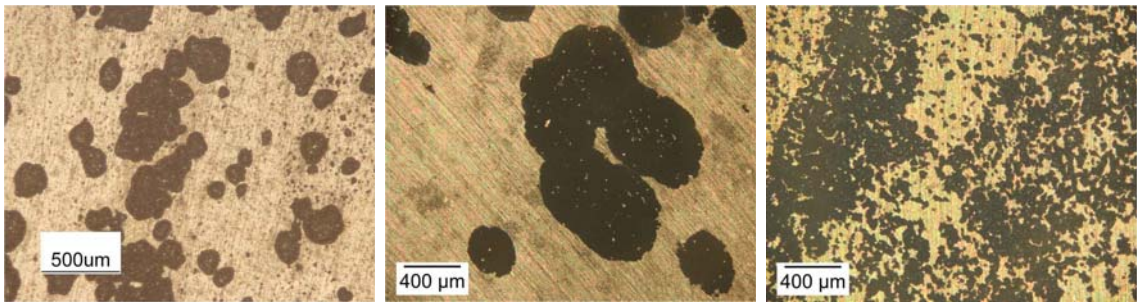

(a) Fe–20Cr, Ar–20CO_2 (b) Fe–25Cr, Ar–20CO_2 (c) Fe–25Cr, Ar–20CO_2–5H_2O

Figure 3.37 – Optical micrographs showing surface appearance of oxides formed on the binary alloys after reaction at 650 °C. Reaction times: (a) 120 h; (b,c) 40 h.

should be noted that the nucleation rate varied with substrate orientation, as seen for example in Fig. 3.37(c).

In addition to exposures in a classic vertical tube furnace (time-lapse experiments), specimens of the Fe–20Cr alloy were also reacted using a thermobalance (TGA experiments). Even though the gas velocity was kept constant, the fact that single specimens were oxidised, instead of 11 at a time, and that they were heated up progressively in contact with the reacting gas, could possibly induce changes in the reaction morphology, since breakaway is very sensitive to the exposure conditions. The surface appearance of specimens reacted in dry and wet CO_2 is shown in Fig. 3.38. The direction of the gas flow had no visible effect in dry CO_2, but clearly

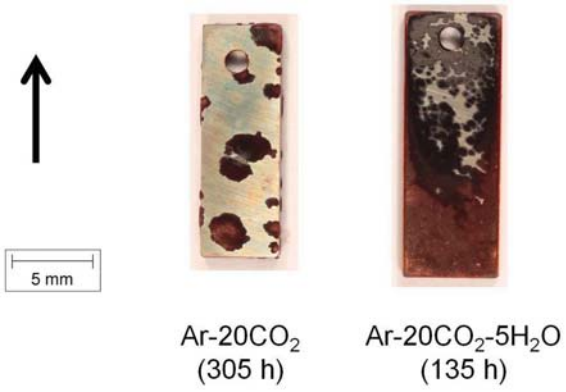

Figure 3.38 – Photographs showing surface appearance of oxides formed on Fe–20Cr after reaction in TGA furnace at 650 °C.

influenced nodule growth in wet CO_2. The presence of a small number of large nodules after reaction in dry CO_2 denotes a relatively lower nucleation rate than that observed on the time-lapse specimens. In contrast, the specimen reacted in wet CO_2

formed small, circular nodules, and its surface appearance was not different from that of specimens reacted in the vertical tube furnace.

The Fe–20Cr–10Ni and Fe–20Cr–20Ni alloys produced fewer nodules than the binary alloys. No significant difference was seen between dry and wet gases. The nodule distribution was not uniform, but mostly determined by the substrate orientation (Fig. 3.39(a)). Most grains were either fully passivated, forming only Cr_2O_3,

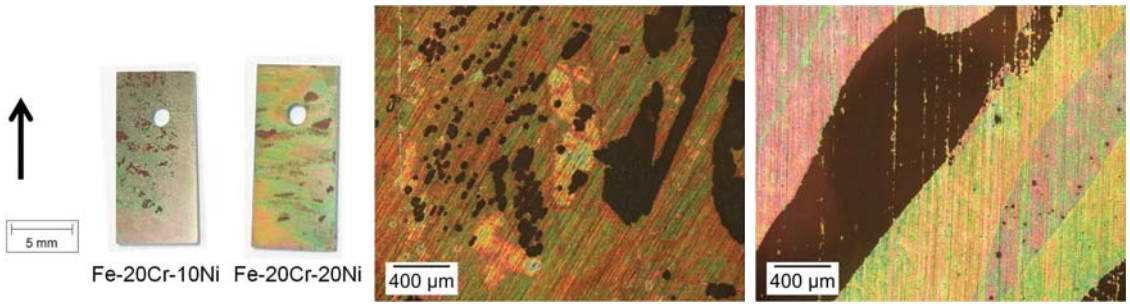

(a) Overview (b) Fe–20Cr–10Ni (c) Fe–20Cr–20Ni

Figure 3.39 – Surface appearance of oxides formed on the 20Cr ternary alloys after reaction at 650 °C. (a) 336 h, Ar–20CO_2–20H_2O; (b) 120 h, Ar–20CO_2–5H_2O; (c) 120 h, Ar–20CO_2–20H_2O.

or fully covered by iron-rich oxide. However, a whole range of behaviour was in fact produced, including grains where nodule growth was slow compared to nucleation, and individual, circular nodules could be observed (Fig. 3.39(b)). The effect of substrate orientation was visible for both alloys, but particularly marked in the case of Fe–20Cr–20Ni (Fig. 3.39(c)). Nevertheless, the process of nodule development was, even then, one of nucleation and growth of individual, circular nodules, as shown in Fig. 3.40.

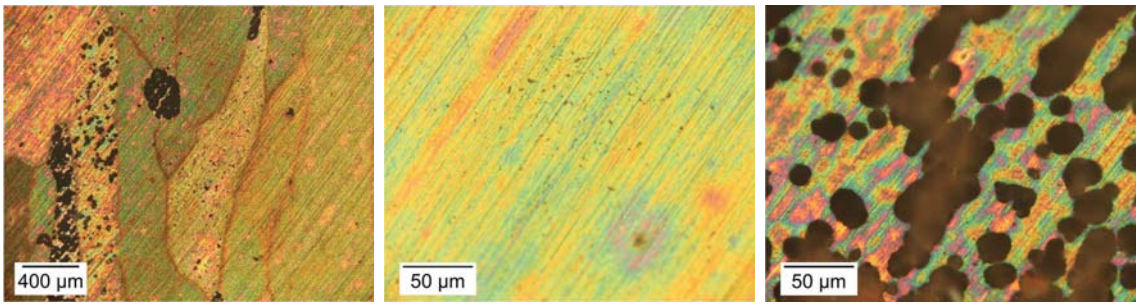

(a) Variable nodule formation (b) Early nodule growth (c) Circular growth

Figure 3.40 – Optical micrographs showing surface appearance of oxides formed on Fe–20Cr–20Ni after 120 h reaction in Ar–20CO_2–20H_2O at 650 °C.

3.3.2 Reaction kinetics

Surface area fractions of nodular oxide, θ, were measured by image analysis of reacted surfaces, using the ImageJ software [155]. Values of θ reflect the frequency of nodule formation and the rate at which they spread laterally, while weight gains also include the effects of oxide thickening and spallation (and the contribution of internal reaction, which is described subsequently). Spallation affected the Cr_2O_3 scale, the loose Fe_2O_3 whiskers and parts of the nodules, all to very variable extents. Net surface fractions and weight gains are shown in Figs. 3.41 and 3.42, respectively.

In many cases, the values of both θ and $\Delta m/A$ did not increase monotonically

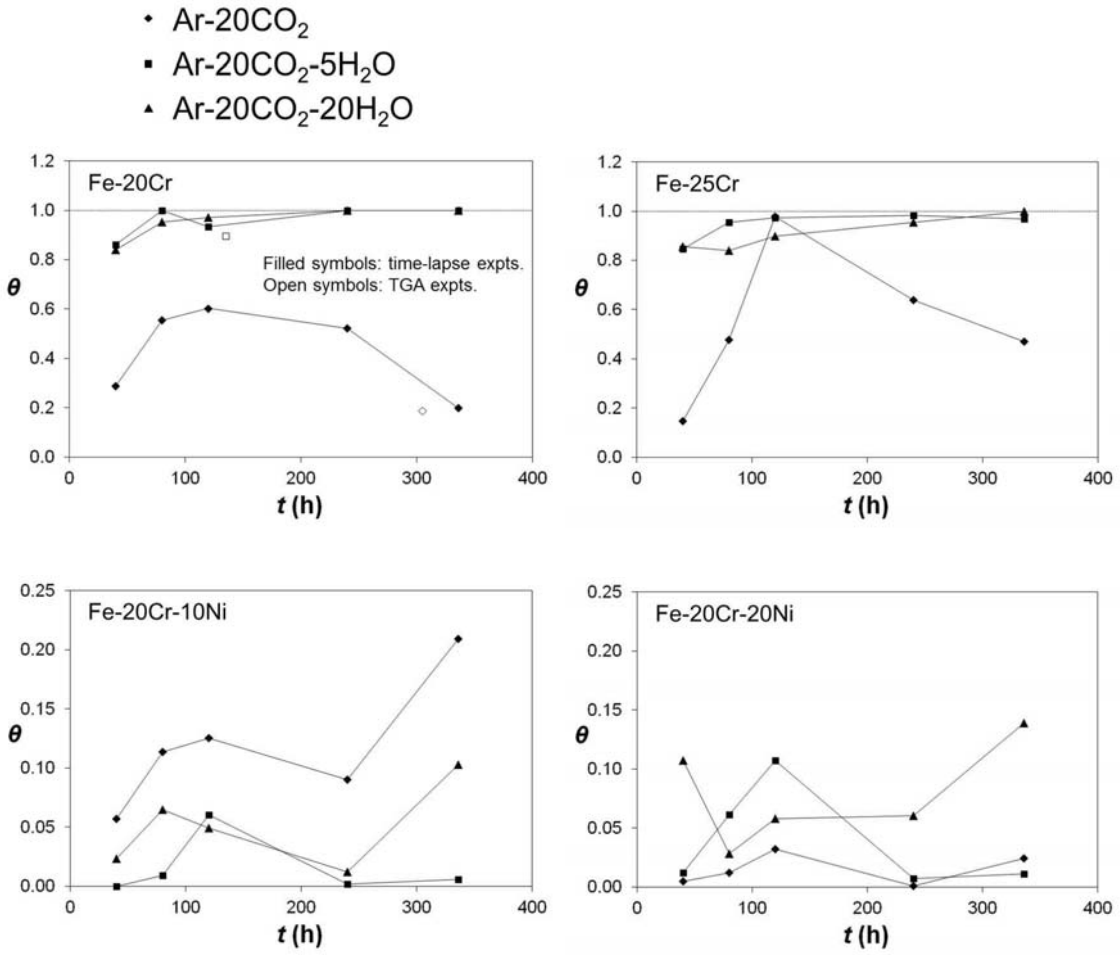

Figure 3.41 – Surface area fractions of nodules measured after reaction at 650 °C. Points are joined for clarity.

with time, reflecting the non-reproducibility of breakaway oxidation. The binary

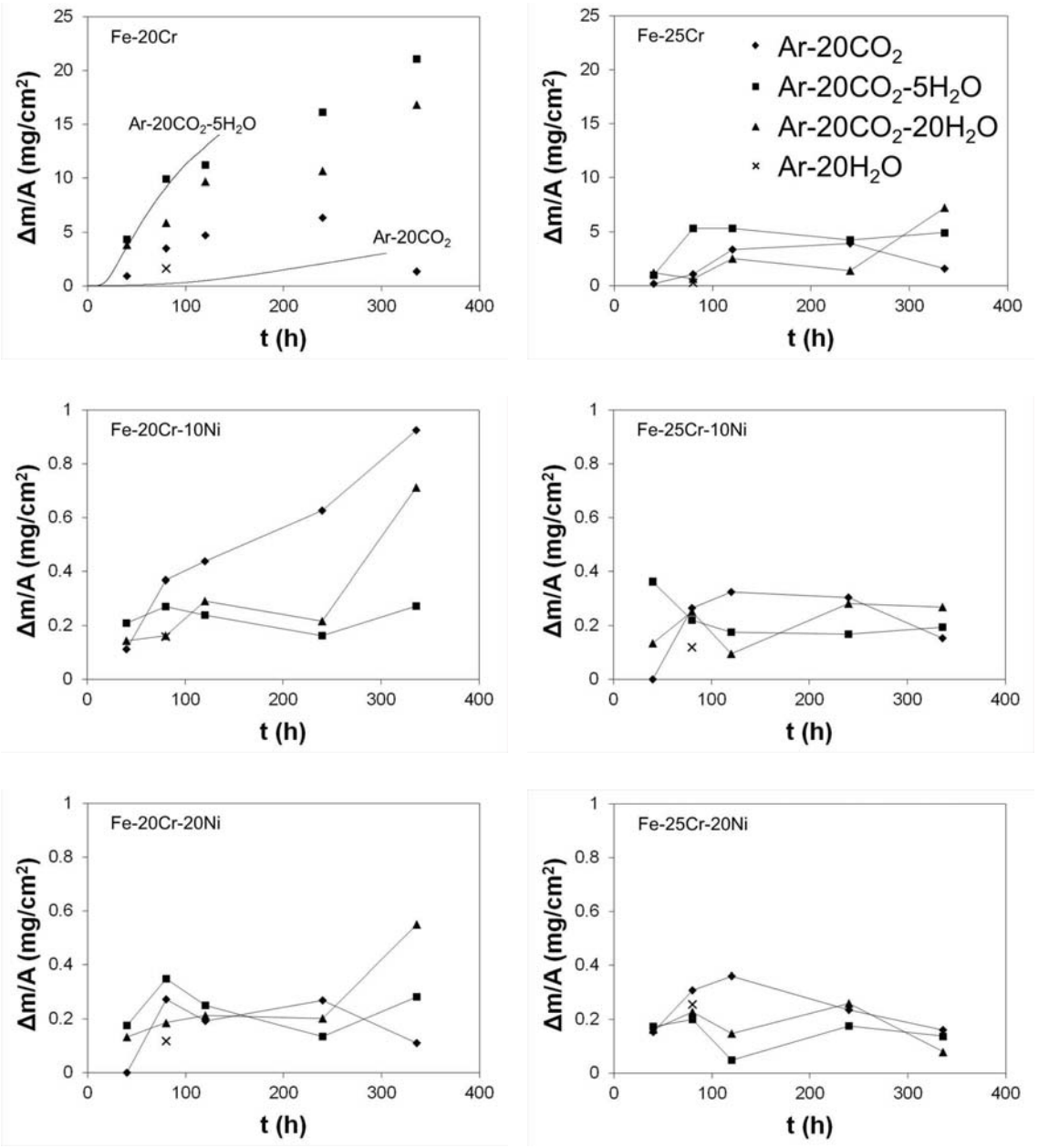

Figure 3.42 – Weight change kinetics of high chromium alloys at 650 °C. Solid lines in the Fe–20Cr graph are TGA data. Elsewhere, points are joined for clarity.

alloys underwent substantial breakaway, accumulating relatively high surface area fractions and weight gains. The θ values were similar, but weight gains were higher for Fe–20Cr than Fe–25Cr. The extent of breakaway was larger in wet CO_2 than in the dry gas, with nearly complete surface coverage by nodules in Ar–20CO_2–5H_2O and Ar–20CO_2–20H_2O. The extent of breakaway did not differ significantly between the two wet gases.

In order to obtain self-consistent kinetic information during breakaway of the Fe–20Cr alloy, the time-lapse experiments were complemented by TGA experiments conducted in Ar–20CO_2 and Ar–20CO_2–5H_2O. Continuous weight gain curves are plotted together with the discrete results in Fig. 3.42, and θ values measured after these isothermal exposures are included in Fig. 3.41. In the case of dry CO_2, the TGA specimen yielded results which fell within the large variability range defined by the time-lapse experiments. Reaction in Ar–20CO_2–5H_2O produced TGA results in agreement with the time-lapse measurements.

Early stage oxidation kinetics measured by TGA are shown in Fig. 3.43, together with those recorded during oxidation in dry air of an Fe–20Cr specimen taken from the same alloy batch. Short term reaction followed similar kinetics in all three gases.

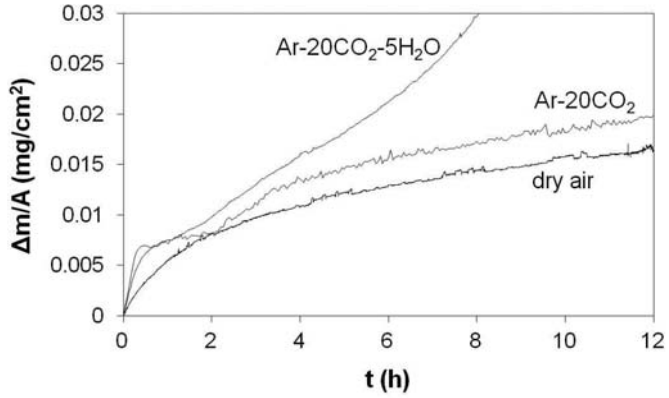

Figure 3.43 – Early stage weight gains (TGA) during oxidation of Fe–20Cr in dry and wet CO_2 and in dry air at 650 °C.

However, the rapid increase in weight gain after 2 hours reaction in Ar–20CO_2–5H_2O indicates that the presence of H_2O in the reacting atmosphere accelerated the appearance of breakaway oxidation.

The 20Cr ternary alloys also formed oxide nodules but θ and $\Delta m/A$ values were lower than those measured on the binary alloys. Furthermore, variability was very important in the three gases, and the presence or absence of H_2O did not appear to have an effect on the extent of breakaway. The 25Cr ternaries oxidised very slowly

in all gases. The term breakaway is used here to denote a rapid acceleration of the oxidation rate. On this basis, the 25Cr ternaries are seen in Fig. 3.42 to suffer no breakaway oxidation within the duration of the experiments. This corresponds to the fact that nodules were formed but never reached significant dimensions. However, given the low thickness of the Cr_2O_3 scale, the presence of nodules, even limited, did alter the weight gains, and Cr_2O_3 growth rates could not be properly measured using the time-lapse technique.

The influence of alloy and gas composition on θ and $\Delta m/A$ is summarised in Fig. 3.44, where values recorded after 336 h reaction are represented.

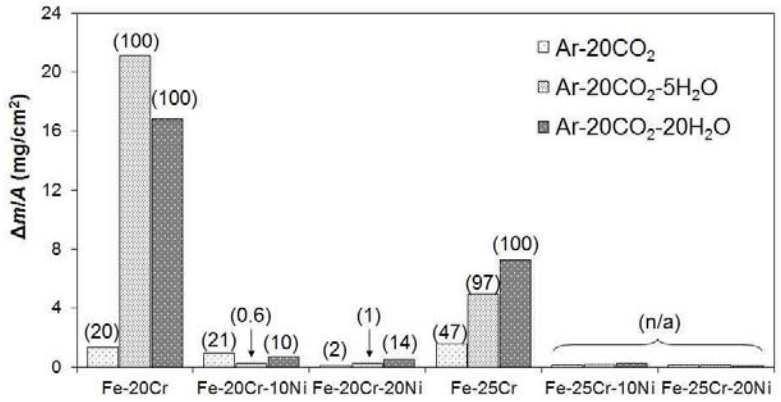

Figure 3.44 – Weight gains and associated nodule surface fractions (bracketed numbers, expressed in percent of the surface area) after 336 h reaction at 650 °C.

3.3.3 Reaction products

Analysis by XRD of entire oxidised specimen surfaces revealed the presence of Cr_2O_3 as the only oxide in the case of Fe–25Cr–10Ni and Fe–25Cr–20Ni. Small nodules formed (Fig. 3.35(c)), but none was seen by metallographic observation on cross-sections. For all other alloys, the characteristic patterns of Cr_2O_3, Fe_2O_3 and Fe_3O_4 were detected by XRD.

3.3.3.1 Fe–20Cr

The Fe–20Cr alloy formed thick, multilayer nodules, either isolated or coalesced into semi-continuous scales of uniform thickness (Fig. 3.45(a)). Individual nodules were approximately elliptical in section. The fact that uniform scales resulted from the coalescence of individual nodules is evident in Fig. 3.45(b), where the junction

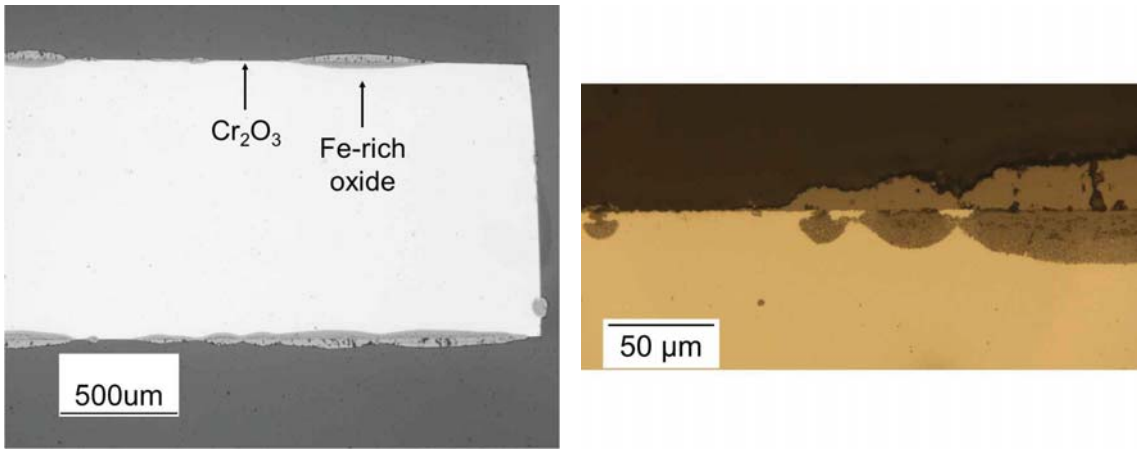

(a) Overview (b) Stages of nodule coalescence

Figure 3.45 – Optical micrographs of oxides formed on Fe–20Cr after reaction at 650 °C. (a) Ar–20CO_2, 80 h; (b) Ar–20CO_2–5H_2O, 40 h.

between the nodules is not yet complete. It is notable that the formerly protective Cr_2O_3 scale was never visibly disrupted by the iron-rich oxide: an intermediate layer is distinguished in all multilayer nodules, and was always continuous with the protective Cr_2O_3 scale surrounding the nodule, as is shown in Fig. 3.46. The only

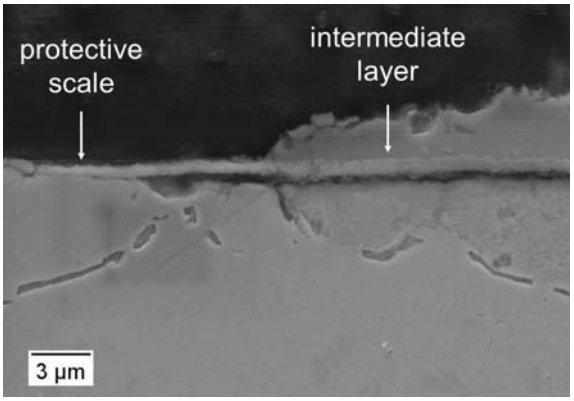

Figure 3.46 – Scanning electron micrograph (SE mode) showing the continuity between the protective Cr_2O_3 scale and the intermediate layer of a nodule grown on Fe–20Cr after 80 h reaction in Ar–20CO_2 at 650 °C. Specimen etched with Murakami's reagent.

difference observed between exposures to dry and wet CO_2 was that the extent of nodule formation was greater in the presence of H_2O, where a scale of uniform thickness covered a main part of the cross-sections (Fig. 3.41). Nodules appeared to be randomly distributed; in particular, nodule formation was not more important on the specimen corners or edges than on the faces (see Fig. 3.45(a)). On a given

specimen, that is, after a given reaction time, nodules of various dimensions were observed. However, large nodules and uniform scales all had the same morphology, regardless of reaction time or gas composition. The oxide morphology was very similar to that observed on the low chromium alloys, as it included a rather compact outer scale, a porous inner layer and an internal oxidation zone, where oxide particles were densely precipitated (Fig. 3.47).

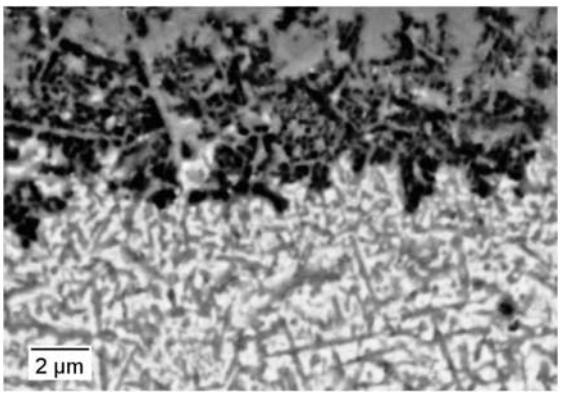

Figure 3.47 – Scanning electron micrograph (BSE mode) of interface between inner scale and internal oxidation zone in Fe–20Cr reacted 80 h in Ar–20CO_2–20H_2O at 650 °C.

The Fe-20Cr alloy also suffered carburisation. Internal precipitates were revealed by etching with Murakami's reagent, and identified as carbides by SEM–EDS. Raman signals were obtained from the carbides. However, as no reference data were found, these spectra could not be interpreted. The precipitate morphology and penetration depth varied with the nature of the overlying oxide. Intergranular carbides were found throughout reacted specimens, from the shortest exposure time (40 h). Underneath Cr_2O_3, intragranular carburisation was either absent or limited to a more or less continuous plate (Fig. 3.48(a)), parallel to the alloy surface at a shallow (< 20 µm) depth. The thickness of this plate was approximately constant with time between 40 and 120 h. Nodules were observed in both the presence and absence of intragranular carbides underneath the surrounding Cr_2O_3. Intragranular carbides were present beneath most, but not all, of the small nodules. Figure 3.48(b) shows the transition between Cr_2O_3 and a nodule. Underneath the nodule, carburisation consisted of a dense precipitation of both equiaxed and elongated particles, reaching substantial penetration depths. This precipitation extended sideways, but not to the metal strip separating the Cr_2O_3 scale from the preexisting array of carbides. Extensive carburisation generally occurred in a uniform manner once the nodules

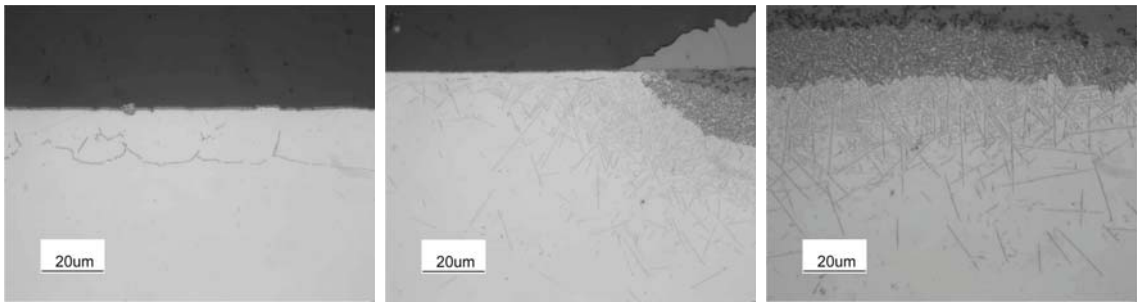

(a) Limited carburisation (b) Transition (c) Extensive carburisation

Figure 3.48 – Optical micrographs showing oxidation and carburisation morphology in Fe–20Cr after reaction at 650 °C. (a) Ar–20CO_2, 120 h; (b) Ar–20CO_2, 80 h; (c) Ar–20CO_2–20H_2O, 120 h.

formed uniformly thick scales (Fig. 3.48(c)).

Carbide penetration depths, X_c, measured from the interface between the internal oxidation and internal carburisation zones, increased according to a parabolic rate law (Eq. (3.3)). Values of k_c determined from the $X_c = f\left(t^{1/2}\right)$ plots shown in Fig. 3.49 are given in Table 3.7. The extent of overlapping between X_c values

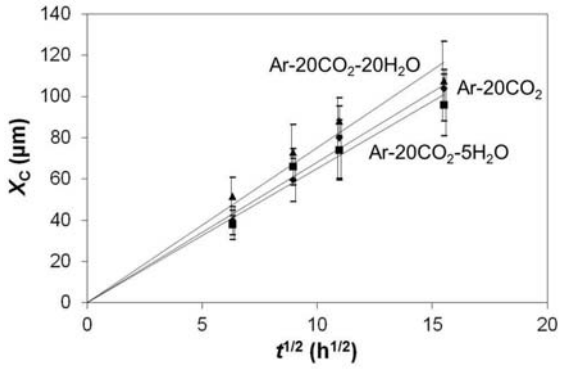

Figure 3.49 – Kinetics of intragranular carburisation beneath uniform Fe-rich oxide scale formed on Fe–20Cr at 650 °C. Mean values obtained from 10 or more measured values. Error bars indicate (X_C ± stdev), where stdev denotes standard deviation.

Table 3.7 – Carburisation rates beneath uniform Fe-rich oxide scale for Fe–20Cr at 650 °C, as defined in Eq. (3.3).

Gas	k_c (10^{-11} cm^2 s^{-1})
Ar–20CO_2	6.4
Ar–20CO_2–5H_2O	5.9
Ar–20CO_2–20H_2O	7.9

measured in the different gases is seen in Fig. 3.49 to be too large for any influence of the H_2O content to be distinguished on the basis of the rate constant.

The interplay between oxidation and carburisation was quite complex. As is seen in Fig. 3.48(c), internal oxide and carbide particles had a similar morphology, and a continuity existed between the two internal reaction zones. This was previously reported by Fujii and Meussner [112], who described the internal oxides as replicas of the carbides (see Section 1.5.2.4 for details). The volume fraction of the carbides formed in the Fe–20Cr alloy varied from one location to another in a given specimen, and the oxide volume fraction, f_{V-ox}, varied accordingly. Values of f_{V-ox} were relatively high, and did not change significantly with gas composition or reaction time; image analysis after reaction in dry and wet CO_2 yielded an average $f_{V-ox} = 0.7 \pm 0.1$. Secondary oxide particles occasionally precipitated in the metal matrix of the internal oxidation zone, such that its morphology tended toward that of a continuous external scale. Where this occurred, the carbide volume fraction decreased. A whole range of volume fractions was thus observed, up to the point where both internal oxidation and internal carburisation were suppressed. In particular, carburisation was absent beneath some of the smallest nodules. Examples of the typical precipitation morphology and of a denser oxide precipitation, both observed on the same specimen, are shown in Fig. 3.50.

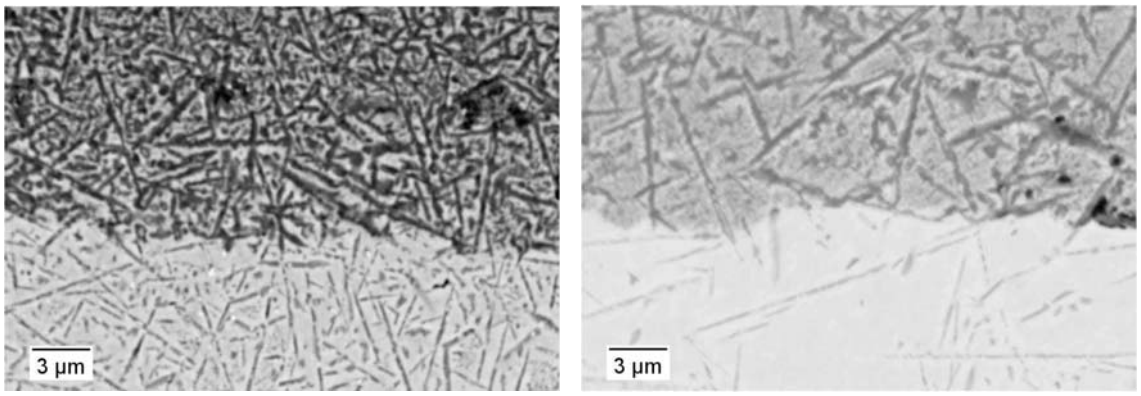

(a) Typical IOZ and ICZ (b) Dense IOZ and reduced carburisation

Figure 3.50 – Scanning electron micrographs (BSE mode) of the interface between internal oxidation zone (IOZ) and internal carburisation zone (ICZ) in Fe–20Cr after reaction 80 h reaction in Ar–20CO_2–20H_2O at 650 °C. Specimen etched with Murakami's reagent.

A small oxide nodule formed on Fe–20Cr after 80 h reaction in Ar–20CO_2 is shown in Fig. 3.51, along with an EDS profile recorded along the right hand arrow. The outer part of the nodule consists of iron oxide (zone 2), located above the

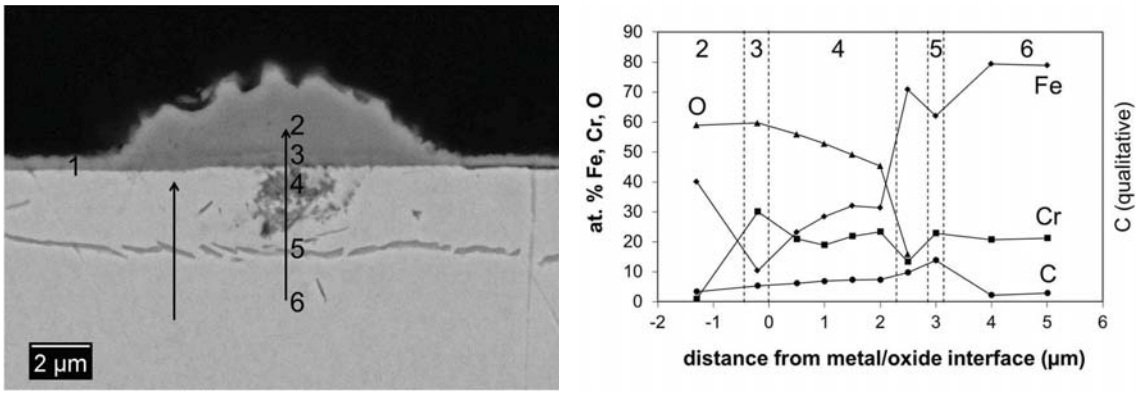

(a) BSE view (b) EDS profile

Figure 3.51 – SEM-EDS analysis of newly formed oxide nodule in Fe–20Cr reacted 80 h in Ar–20CO_2 at 650 °C. Specimen etched with Murakami's reagent. The right hand arrow and numbers in the BSE view (a) indicate the location of the profile in (b). The left hand arrow in (a) indicates the location of the profile marked by open square symbols (□) in Fig. 3.56.

originally protective scale; a chromium-rich oxide (zone 3) lies in a layer continuous with the protective scale surrounding the nodule; an internal oxidation zone with roughly equal concentrations of iron and chromium (zone 4) is found beneath the metal/oxide interface; and a more or less continuous plate of chromium-rich carbide (zone 5) lies parallel to the metal surface, under the internal oxides. Unreacted alloy (zone 6) lies beneath. The SEM–EDS results must be considered with caution: the analysis is quantitative only in the metal phase, and qualitative in oxide and carbide phases. Since the region probed is about 1 µm wide, when a point analysis is made on a smaller feature, part of the signal comes from the surrounding phase. In particular, for small Cr-rich features surrounded by Fe-rich environments, such as the oxide and carbide in zones 3 and 5, the Cr/Fe ratio is underestimated.

Raman spectra recorded on Fe–20Cr after 120 h reaction in Ar–20CO_2 from a similar nodule are shown in Fig. 3.52. Oxide phases were identified using the work of McCarty and Boehme [152], who studied Raman signatures of the spinel-($Fe_{3-x}Cr_xO_4$) and corundum-type ($Fe_{2-x}Cr_xO_3$) solid solutions. The protective scale (# 1) is Cr-rich M_2O_3, the nodule outer layer (# 2) Fe-rich M_2O_3, the layer which is continuous with the protective scale (# 3) is Cr-rich M_2O_3, and the internal oxide particles (# 4) Fe-Cr spinel. These phases are all consistent with the compositions determined with SEM–EDS. Data in Ref. [152] were used to construct the graph of Fig. 3.53, where the Raman shift of the A_{1g} symmetry (main band at 680–670 cm^{-1}) in the Fe–Cr spinel is plotted against the chromium content, expressed as x in $Fe_{3-x}Cr_xO_4$. A given Raman shift possibly corresponds to several compositions.

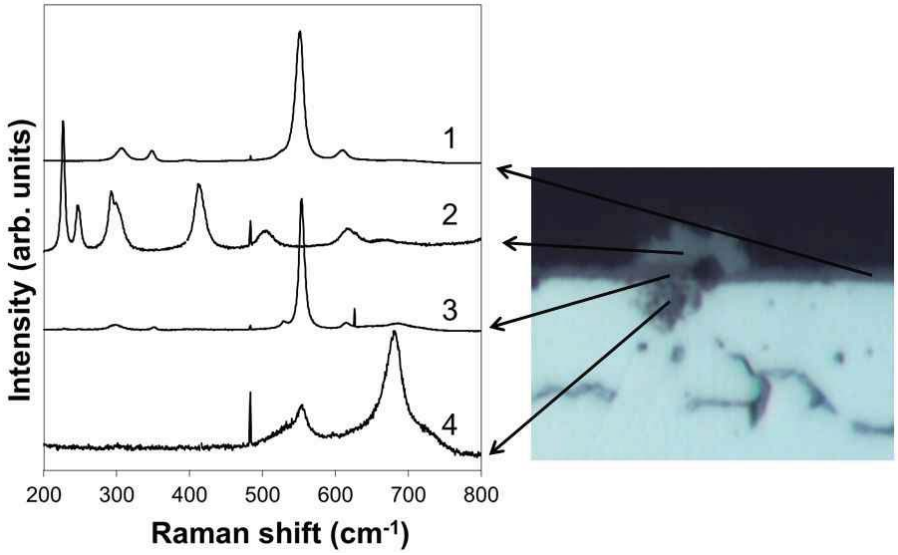

Figure 3.52 – Raman spectra of oxide phases in newly formed oxide nodule in Fe-20Cr reacted 120 h in Ar–20CO_2 at 650 °C. Note: the dark mark visible in the image is oxide "burnt" during a Raman analysis where the laser was not sufficiently filtered. The corresponding spectrum is not included in the chart, and was recorded after the spectra represented in the chart. The size of the mark denotes that of the analysed area.

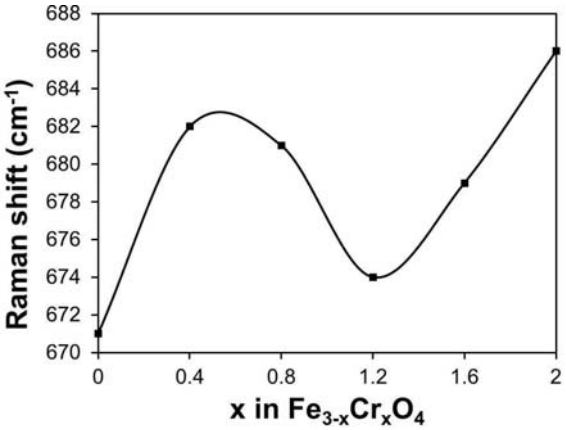

Figure 3.53 – Main Raman shift of Fe–Cr spinel oxide as a function of composition, after Ref. [152].

The internal oxides (# 4) present a Raman band at 680 cm^{-1}, which could correspond to x = 0.3, 0.9 or 1.6. On the basis of several EDS point measurements in the internal oxidation zone, the average Cr/Fe ratio yielded x = 1.3, which must be underestimated, as discussed previously. The internal oxides were therefore identified as $Fe_{1.4}Cr_{1.6}O_4$.

A typical uniform multilayer scale observed on Fe–20Cr after 80 h reaction in Ar–20CO_2 yielded the SEM images and the EDS profile shown in Fig. 3.54. Both

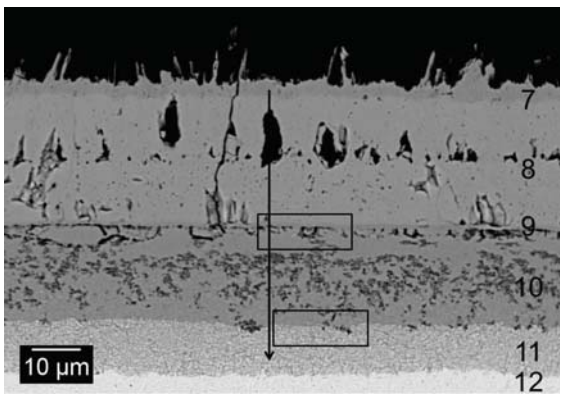

(a) Overview

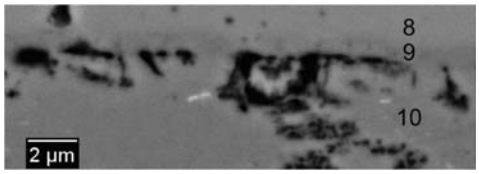

(b) Outer/inner scale interface

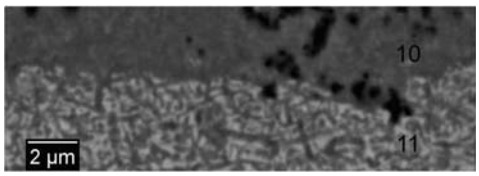

(c) Inner scale/IOZ interface

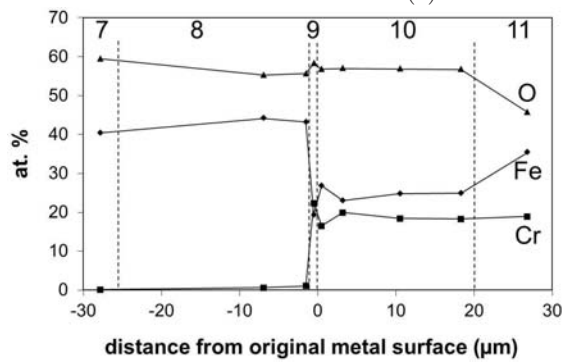

(d) EDS profile

Figure 3.54 – SEM–EDS analysis of Fe-rich oxide scale grown on Fe–20Cr reacted 80 h in Ar–20CO_2 at 650 °C. Specimen etched with Murakami's reagent. The boxes and arrow in (a) indicate the location of the images and profile in (b), (c) and (d).

outer layers (zones 7 and 8) consist of iron oxide. At the location of the original metal surface, a layer containing more chromium than the surrounding phases can still be distinguished (zone 9 in Fig. 3.54(b)). The inner layer is a two-phase mixture (zone 10 in Fig. 3.54(c)) containing iron and chromium. Beneath it lies the internal oxidation area (zone 11).

The Raman spectra in Fig. 3.55 were recorded in zones corresponding to those

described above, after 120 h reaction of Fe–20Cr in Ar–20CO_2. Using data in

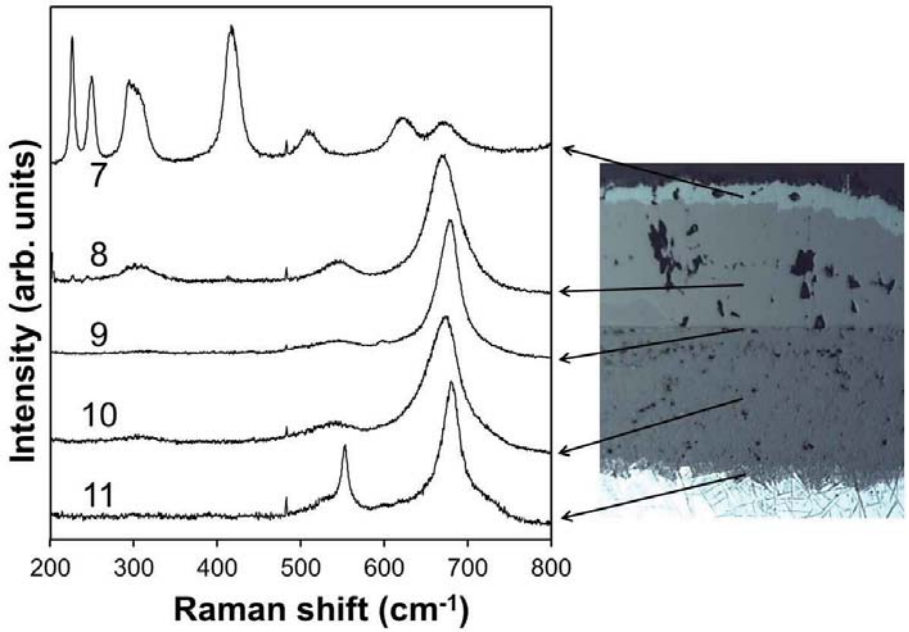

Figure 3.55 – Raman spectra of oxide phases in Fe-rich multilayer oxide grown on Fe–20Cr reacted 120 h in Ar–20CO_2 at 650 °C.

Ref. [152], the outermost layer was identified as Fe_2O_3, and all other oxides as spinel phases. In particular, it should be noted that the bands characteristic of FeO (at $\sim$ 280 and $\sim$ 400 cm^{-1} [153]) were not observed in the signal recorded in the inner layer. The outer spinel layer (# 8) featured a main band at 671 cm^{-1}, characteristic of pure Fe_3O_4. The thin intermediate layer (# 9) had a main band at 680 cm^{-1}, which could correspond to x = 0.3, 0.9 or 1.6. Since EDS provided x = 1.6, the phase was identified as $Fe_{1.4}Cr_{1.6}O_4$. The inner two-phase mixture (# 10) had a main Raman band at 674 cm^{-1}, corresponding to $Fe_{2.9}Cr_{0.1}O_4$ or $Fe_{1.8}Cr_{1.2}O_4$. These two compositions may well reflect the two spinel phases present in the inner layer. Indeed, the isothermal section of the Fe–Cr–O phase diagram at 627 °C calculated in Ref. [71] (see Fig. 1.10) predicts that the two coexisting spinels are $Fe_{2.7}Cr_{0.3}O_4$ and $Fe_{1.8}Cr_{1.2}O_4$. Chemical analysis in the inner layer yielded x = 1.3, implying that the iron-rich spinel was present in very small quantity. In the internal oxidation zone (# 11), three compositions are possible from the Raman spectrum, with x = 0.3, 0.8 or 1.7. At the low p_{O_2} of the internal oxidation zone, the highest chromium spinel $Fe_{1.3}Cr_{1.7}O_4$ is the only valid candidate (see Fig. 1.10).

Chromium depletion profiles underneath the protective Cr_2O_3 scale grown on the Fe–20Cr alloy after 80 h exposure to dry CO_2 were measured using SEM–EDS, in

carbide-free (Fig. 3.56(a)) and carbide-containing zones (Fig. 3.56(b)). The profiles

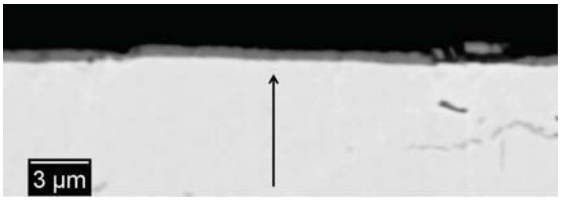

(a) BSE image, carbide-free zone

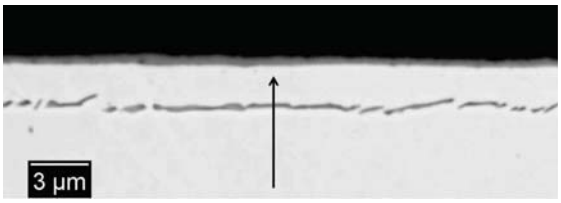

(b) BSE image, carbide-containing zone

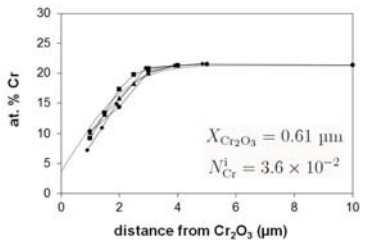

(c) Four profiles in carbide-free zones

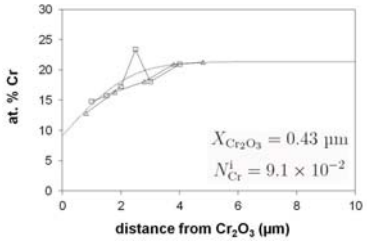

(d) Two profiles traversing carbides

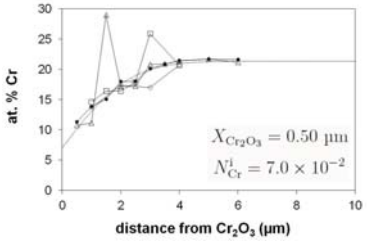

(e) Three profiles with carbides, one without

Figure 3.56 – SEM–EDS analysis of Cr depletion underneath Cr_2O_3 grown on Fe–20Cr reacted 80 h in Ar–20CO_2 at 650 °C. Specimen etched with Murakami's reagent. Points are experimental and dashed lines calculated from Eq. (1.66). Filled symbols: carbide-free locations, e.g. SEM view (a); open symbols: scans which traverse carbides as in (b). Open square symbols in (e): profile marked by the left hand arrow in Fig. 3.51(a).

thus recorded are grouped according to the local Cr_2O_3 thickness in Fig. 3.56(c-e), with results from carbide-free and carbide-containing regions represented by filled and open symbols, respectively. The same measurements were made after exposure of the Fe–20Cr alloy to Ar–20CO_2-20H_2O. No difference in chromium depletion could be seen between reaction in dry and wet gas, and similar Cr_2O_3 scale thicknesses were observed in both cases.

3.3.3.2 Fe–25Cr

The Fe–25Cr alloy formed oxide scales varying in thickness and constitution (Fig. 3.57), which can be classified in three morphological types, shown in Fig. 3.58: a thin protective scale, thick multilayer nodules and multilayer oxides of intermediate thick-

ness, referred to as "healed scale". The differentiation between healed scale and

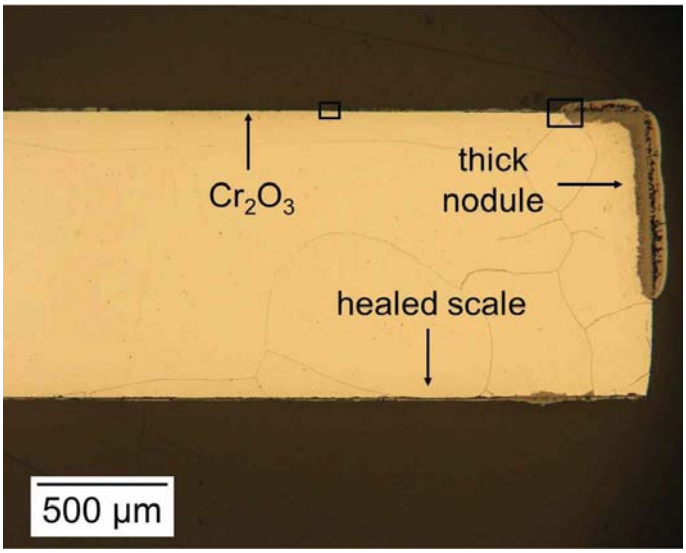

Figure 3.57 – Optical micrograph showing an overview of the oxides grown on Fe–25Cr, after 240 h reaction in Ar–20CO_2 at 650 °C. Specimen etched with Murakami's reagent.

thick nodules was made on the basis of the presence or absence of internal reaction, as is shown subsequently. Thicker nodules were observed to form preferentially on the specimen edges. The red, loose oxidation products visible in Fig. 3.58 are Fe_2O_3 whiskers, and were preferentially formed during reaction in wet CO_2 (see also surface views in Fig. 3.36). Apart from that, the only difference between reaction in dry and wet CO_2 was that the proportion of protective Cr_2O_3 scale was greater in the absence of H_2O(g) (Fig. 3.41).

The composition and symmetry of the oxide phases were investigated by SEM–EDS and Raman analysis. Raman spectra shown in Fig. 3.59(a) were recorded at the locations indicated in Figs. 3.59(b) and 3.59(c). The protective scale (# 1) is Cr-rich M_2O_3. On the healed scales (Fig. 3.59(b)), the outer layers are Fe-rich corundum (M_2O_3, # 2) and spinel type (M_3O_4, # 3). The inner layer (# 4) is a spinel, with a main band at 678 cm^{-1}, corresponding to x = 0.2, 1 or 1.5 in $Fe_{3-x}Cr_xO_4$. Chemical analysis using SEM–EDS was performed on several locations equivalent to zone # 4 (not shown). The results varied considerably with analysis location, with Cr/Fe ratios ranging from 1.76 to 12.3. While the lower value would correspond to $Fe_{1.1}Cr_{1.9}O_4$, the higher values indicate a Cr-rich corundum type oxide, $Fe_{2-x}Cr_xO_3$, with an average x = 1.8. Considering Raman and EDS results, it is concluded that the inner layer may be of spinel or corundum type, with varying

(a) Cr_2O_3 and early stage of breakaway

(b) Healed scale

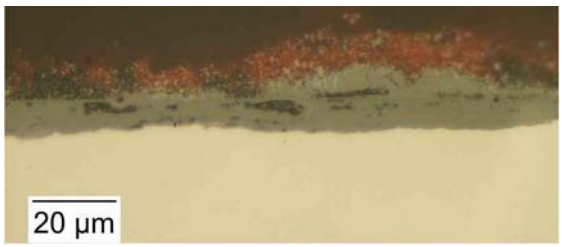

(c) Healed scale

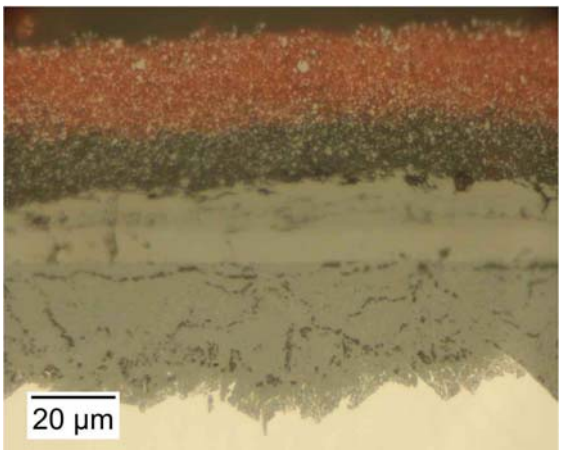

(d) Thick nodule

Figure 3.58 – Optical micrographs showing the three types of oxide grown on Fe–25Cr, after 240 h reaction in Ar–20CO_2–20H_2O at 650 °C.

composition, but always relatively rich in chromium. Internal oxidation was never observed underneath this type of scale. Analysis by SEM–EDS of the subscale region indicated that chromium depletion underneath the protective and healed types of scale were not different (Fig. 3.60).

In the thick nodules (Fig. 3.59(c)), the outer layers are also Fe_2O_3 (# 5) and Fe_3O_4 (# 6). The thin intermediate layer (# 7) is a spinel with a main Raman band at 680 cm^{-1}, corresponding to x = 0.3, 0.9 or 1.6. In view of the results presented before for Fe–20Cr, the Cr-richer composition is the most likely. Finally, the inner layer (# 8) is a spinel with a main band at 674 cm^{-1}, which again is interpreted as a $Fe_{2.9}Cr_{0.1}O_4$ + $Fe_{1.8}Cr_{1.2}O_4$ mixture. An oxide + metal mixture is apparent (# 9) below the inner layer, but it was not possible using metallographic observation to ascertain whether the oxide was detached from the inner layer (i.e. internal oxidation) or in continuous contact (i.e. protrusions of the inner layer into the metal). In either case, the volume fraction of oxide was very high.

After exposure to dry CO_2, intragranular carbides were found at scattered locations underneath the protective Cr_2O_3 scale and the healed scale, with a penetration depth less than 5 µm. Beneath the thick nodules, the alloy produced intragranular carburisation zones (Fig. 3.61), about 50–70 µm deep after 240 h, and intergran-

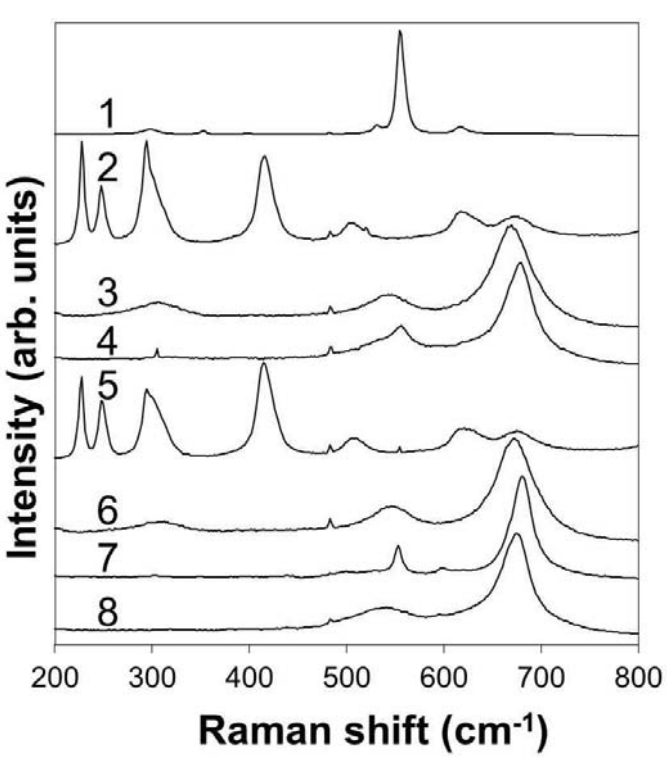

(a) Raman spectra

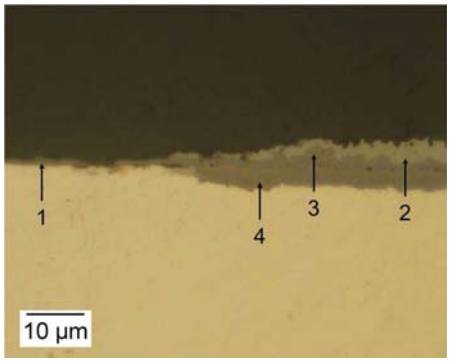

(b) Cr_2O_3 and healed scale

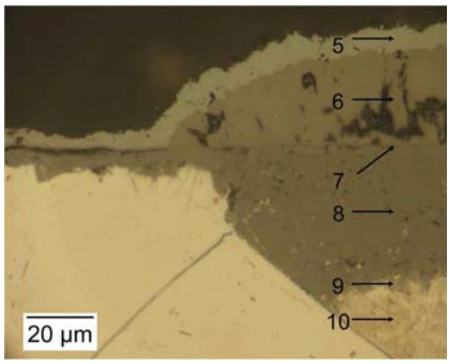

(c) Healed scale and thick nodule

Figure 3.59 – Raman analysis of the three types of oxide grown on Fe–25Cr, after 240 h reaction in Ar–20CO_2 at 650 °C. Specimen etched with Murakami's reagent.

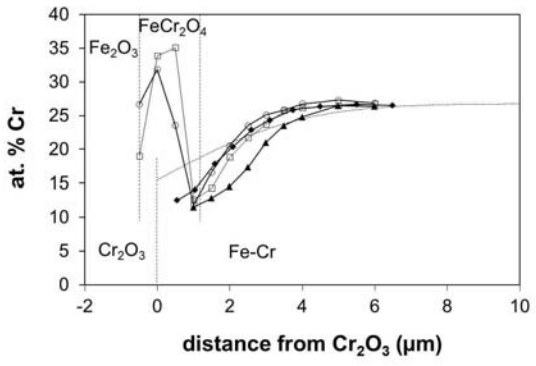

(a) Cr depletion profiles

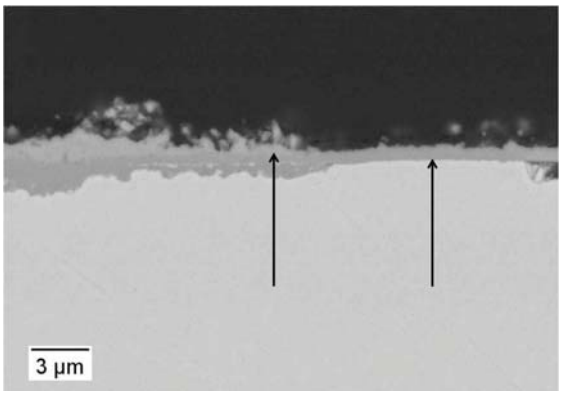

(b) BSE view

Figure 3.60 – SEM–EDS analysis of chromium depletion in Fe–25Cr reacted 240 h in Ar–20CO_2–20H_2O at 650 °C. Points are experimental and dashed line calculated from Eq. (1.66). Filled symbols: underneath Cr_2O_3, e.g. right hand arrow in (b); open symbols: underneath healed scale, e.g. left hand arrow in (b).

ular carbides were found to great depths (see Fig. 3.57). Thus, even though the

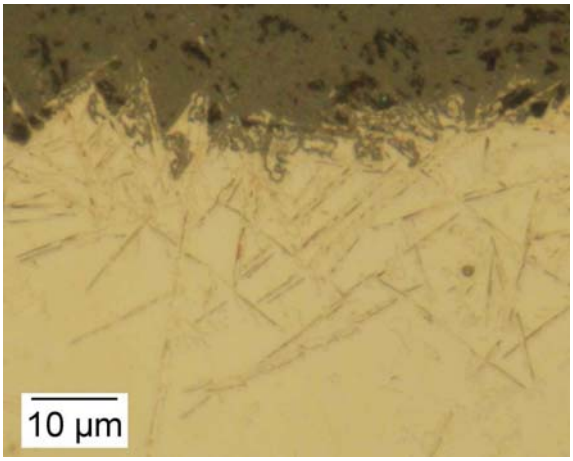

Figure 3.61 – Optical micrograph showing extensive intragranular carburisation underneath thick nodule grown in Fe–25Cr after 240 h reaction in Ar–20CO_2 at 650 °C.

healed type of scale existed with varying thickness (Fig. 3.58), the absence of internal reaction beneath it constitutes a qualitative distinction from the thick nodules. After exposure to Ar–20CO_2–20H_2O, carbides were absent below Cr_2O_3 and the healed scale. Underneath the thick nodules, intergranular carbides were sparsely distributed, and the intragranular carbide volume fractions and penetration depths (about 30–50 µm after 240 h) were lower than observed after exposure to the dry gas.

3.3.3.3 Fe–20Cr–10Ni and Fe–20Cr–20Ni

The Fe–20Cr–10Ni and Fe–20Cr–20Ni alloys formed a protective oxide scale and oxide nodules of varying dimensions. The nodules were on average thicker on the 10Ni alloy, but developed the same morphology on both alloys in both dry and wet CO_2. Figure 3.62 shows the reaction morphology observed on Fe–20Cr–20Ni.

The protective scales grown on the two alloys were identified as Cr_2O_3 by Raman analysis. Nodule constitution was studied on an Fe–20Cr–10Ni specimen using SEM imaging, EDS and Raman analysis (Figs. 3.63 and 3.64). The outer layers consisted of Fe_2O_3 (# 1) and Fe_3O_4 (# 2), with no significant amount of dissolved chromium or nickel. It was not possible to ascertain whether a thin intermediate Cr-rich layer was still present at the original metal surface. It was either too thin to be clearly distinguished, or sometimes apparent but disrupted. The inner layer (# 4) contained at least two phases, but might have contained three; this was difficult to

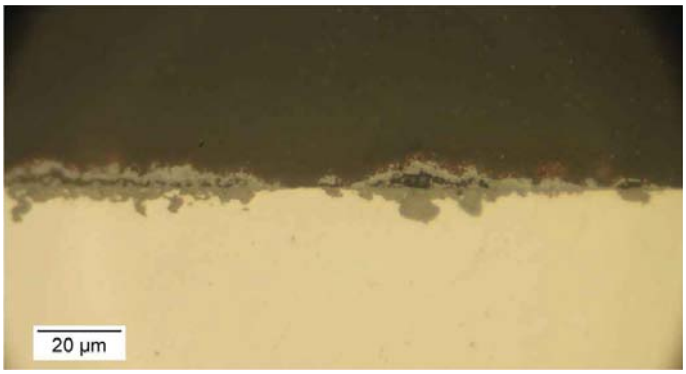

Figure 3.62 – Optical micrograph showing chromia scale and nodules grown on Fe–20Cr–20Ni after 40 h reaction in Ar–20CO_2–20H_2O at 650 °C. Specimen etched with Murakami's reagent.

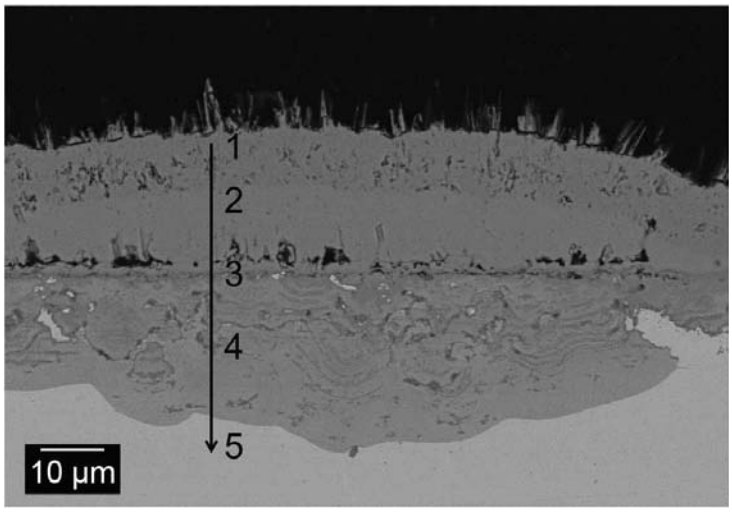

(a) Nodule

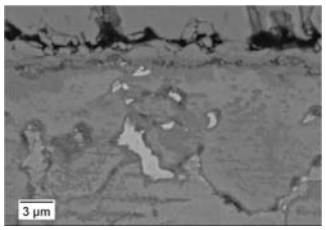

(b) Metal inclusions in inner layer

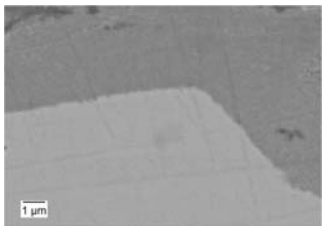

(c) Metal/oxide interface

Figure 3.63 – Scanning electron micrographs (BSE mode) of a nodule grown in Fe–20Cr–10Ni after 240 h reaction in Ar–20CO_2 at 650 °C. Specimen etched with Murakami's reagent.

determine using SEM, because of the extremely fine microstructure. The Raman spectrum (Fig. 3.64(b)) recorded in the inner layer shows a broad band which could be deconvoluted into two peaks at approximately 684 and 712 cm^{-1}. The former peak can be associated with either a Cr-rich Fe–Cr spinel [152] or $NiCr_2O_4$ [154], and the latter peak with $NiFe_2O_4$ [154]. This area was seen using EDS (Fig. 3.64(a)) to contain 24 at. % iron, 19 at. % chromium and 7 at. % nickel. Assuming that spinels of the precise stoichiometries $FeCr_2O_4$, $NiCr_2O_4$ and $NiFe_2O_4$ are present, then solving a simple 3 variable, 3 equation system yields the proportions of the spinel phases: 56.3, 0.5 and 43.2 mol %, respectively. Given the uncertainty in the Raman and EDS results, the inner layer may be approximated as a $NiFe_2O_4$–

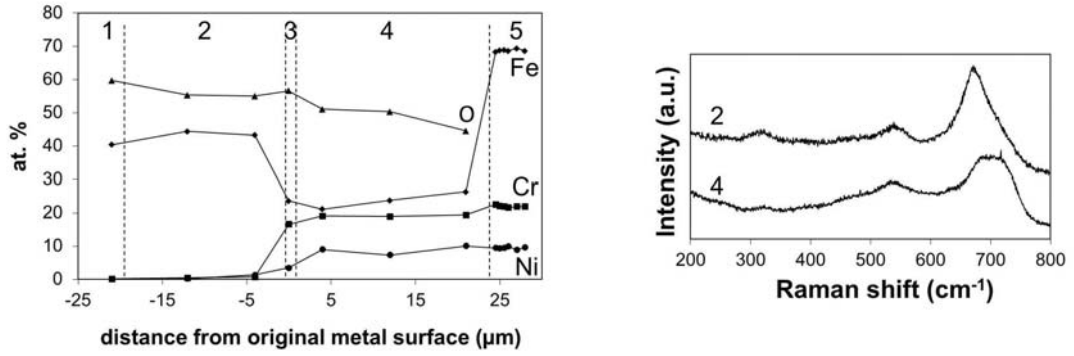

(a) EDS profile (b) Raman spectra

Figure 3.64 – EDS and Raman analysis of multilayer oxide grown on Fe–20Cr–10Ni after 240 h reaction in Ar–20CO_2 at 650 °C. Numbers refer to zones defined in Fig. 3.63.

$FeCr_2O_4$ mixture. Metal inclusions were present in the inner layer (Fig. 3.63(c)); their composition was found by EDS to be similar to that of the alloy. No apparent depletion or enrichment occurred beneath the scale (Fig. 3.64(a)).

The Fe–20Cr–10Ni and Fe–20Cr–20Ni alloys showed no internal oxidation. The Fe–20Cr–10Ni alloy occasionally developed intergranular carbides, but no intragranular carbides, after exposure to dry CO_2, and no carbides at all after exposure to wet CO_2. The Fe–20Cr–20Ni alloy formed no carbides in any of the gases.

3.3.4 Nodule growth kinetics

Maximum nodule thickness or average scale thickness measured after time-lapse exposure of Fe–20Cr to the dry and wet gases are reported in Fig. 3.65(a). The

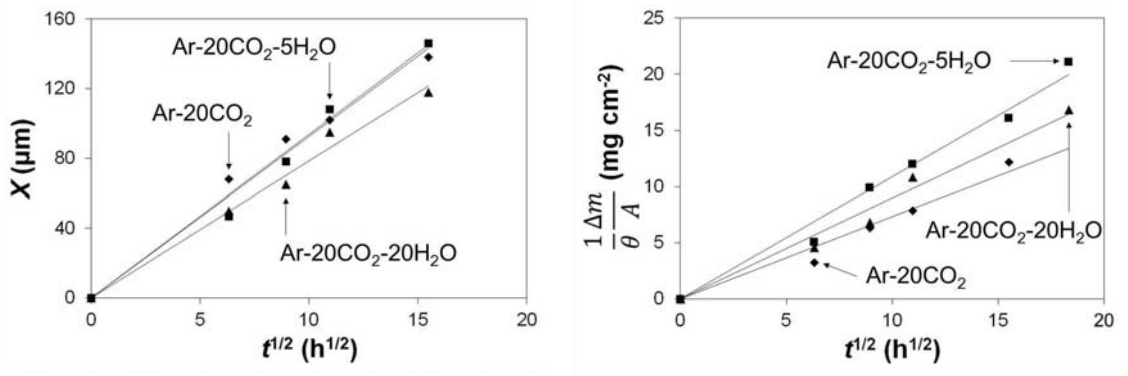

(a) Maximum thickness (b) Corrected weight gain, as defined in Eq. (3.8)

Figure 3.65 – Nodule growth kinetics measured on Fe–20Cr reacted at 650 °C.

data are seen to follow approximately parabolic kinetics. Error bars are not relevant here, at least in the case of reaction in dry CO_2, where X are maximum and not average values. More important are the implications of the fact that in principle, even the thickest nodules did not necessarily nucleate at $t = 0$. These aspects are discussed in Section 4.2.3. Parabolic constants $k_{\mathrm{p,Fe-ox}}$, as defined in Eq. (3.2), were determined by fitting the data in a $X = \mathrm{f}\left(t^{1/2}\right)$ plot. The poor reproducibility of breakaway did not allow any influence of gas composition to be distinguished on the basis of the $k_{\mathrm{p,Fe-ox}}$ values, which are given in Table 3.8. Rate constants were

Table 3.8 – Nodule thickening rate constants, $k_{\mathrm{p,Fe-ox}}$ (10^{-11} cm^2 s^{-1}), measured after reaction at 650 °C, as defined in Eq. (3.2).

Gas (Ar–20CO_2–)	0H_2O	5H_2O	20H_2O	average
Fe–20Cr	12	12	8.6	11
Fe–20Cr–10Ni	3.2			3.2
Fe–20Cr–20Ni			1.0	1.0
Fe–25Cr (thick nodules)	6.2		4.8	5.5
Fe–25Cr (healed scale)	0.083		0.087	0.085

determined in the same way for the three other alloys prone to breakaway oxidation, but using only two specimens per reacting gas; values are included in Table 3.8. In the case of Fe–25Cr, the kinetics were measured for both types of scale.

Since nodules grown on a given specimen have varying sizes, measuring the maximum thickness observed on a single cross-section may yield non-representative results. In the case of Fe–20Cr, these results were for this reason compared with rate constants obtained from weight gain measurements. Considering the fact that extensive carburisation did not occur below Cr_2O_3, the total weight gain may be expressed so as to reflect the contribution of Fe-rich oxide, carbides and Cr_2O_3

$$\frac{\Delta m}{A} = \theta \left[\left(\frac{\Delta m}{A} \right)_{\mathrm{Fe-ox}} + \left(\frac{\Delta m}{A} \right)_{\mathrm{MC}_\nu} \right] + (1-\theta) \left(\frac{\Delta m}{A} \right)_{\mathrm{Cr_2O_3}} \tag{3.7}$$

where $(\Delta m/A)_i$ is the average weight uptake per unit area of the indicated phase. In the present experiments, orders of magnitude of the weight uptakes are calculated to be 10, 1 and 0.1 mg cm^{-2} for Fe-rich oxide, carbides and Cr_2O_3, respectively. Consequently, the contribution of the carbides and Cr_2O_3 to the total weight gain may be neglected, and Eq. (3.7) is approximated to yield

$$\left(\frac{\Delta m}{A} \right)_{\mathrm{Fe-ox}} = \frac{1}{\theta} \frac{\Delta m}{A} \tag{3.8}$$

Assuming that nucleation of Fe-rich oxide occurs initially, at $t = 0$, and not subsequently, the values of $\Delta m/A$ and θ measured after time-lapse exposures may be used to estimate nodule growth kinetics. In view of the variety of nodule size on a given specimen (Fig. 3.45), the hypothesis of initial nucleation is not valid. However, it allows for a very simple quantitative treatment of weight gain kinetics, subsequently justified in Chapter 6 by a model taking into account continued nucleation throughout the exposure. The values of $(\Delta m/A)_{\mathrm{Fe-ox}}$ calculated from Eq. (3.8) are shown in Fig. 3.65(b), and confirm that nodule growth followed approximately parabolic kinetics. The variability associated with breakaway prevents any influence of gas H_2O content from being identified. Approximating the average oxide as dense Fe_3O_4, the average gravimetric rate constant obtained from Fig. 3.65(b), $k_{\mathrm{pm,Fe-ox}} = 1.2 \times 10^{-4}$ mg^2 cm^{-4} s^{-1}, is converted using Eq. (1.11) to a thickening constant $k_{\mathrm{p,Fe-ox}} = 5.8 \times 10^{-11}$ cm^2 s^{-1}, in reasonable agreement with the value given in Table 3.8 for Fe–20Cr. A difference between the two values must emerge from the fact that nodules are ellipsoid and not flat-topped. The error is maximum for small individual nodules, and decreases when nodules coalesce and form uniformly thick scales. Offsetting this error is the systematic underestimation of nodule thickness resulting from the fact that random cross-sections do not on average pass through nodule centres. These errors are estimated in Appendix B.

Iron-rich oxide growth kinetics on Fe–20Cr were estimated in a third independent way. The local fitting procedure described in Ref. [24] was applied to the TGA data recorded during reaction in Ar–20CO_2–5H_2O, in order to determine the instantaneous gravimetric rate constant as a function of time during the whole reaction. The rate constant is calculated according to a complete parabolic law

$$t = a + b\frac{\Delta m}{A} + c\left(\frac{\Delta m}{A}\right)^2 \tag{3.9}$$

where a and b are constants, and $c = \dfrac{1}{2\,k_{\mathrm{pm}}}$. The resulting curve $k_{\mathrm{pm}} = \mathrm{f}(t)$, shown in Fig. 3.66, is divided into three regions. Initially, as θ is low, the weight gain reflects Cr_2O_3 growth, and accordingly k_{pm} is very small. After a first inflection in the weight gain curve (visible at $t \simeq 2$ h in Fig. 3.43), and as θ and $\Delta m/A$ rapidly increase, k_{pm} is not defined (parabolic rate constants do not apply to convex weight gain curves). After a second inflection point, a second stage of parabolic kinetics is reached, and k_{pm} attains a constant, high value. Using the molar volume of Fe_3O_4, the gravimetric constant obtained this way is converted to $k_{\mathrm{p}} = 1.9 \times 10^{-10}$ cm^2 s^{-1}, a value consistent with that given in Table 3.8 for the directly measured rate constant of Fe-rich oxide grown on Fe–20Cr.

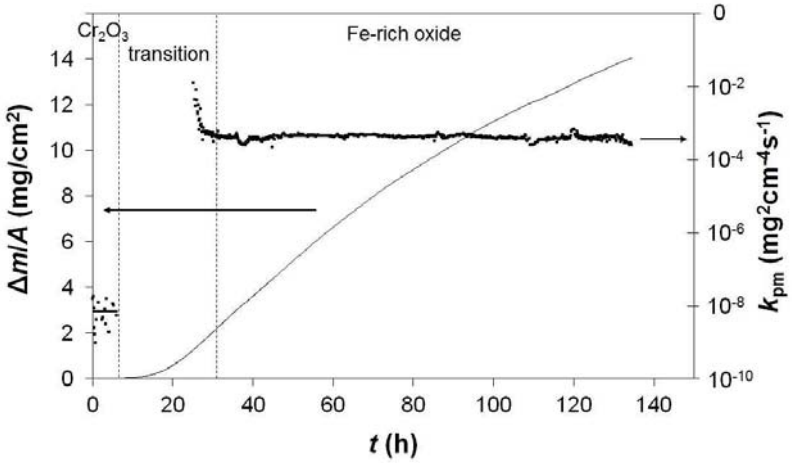

Figure 3.66 – Continuous weight gain (TGA) and local gravimetric rate constant (from fitting procedure in Ref. [24], see text) during oxidation of Fe–20Cr in Ar–20CO_2–5H_2O at 650 °C.

In Fig. 3.67, the thickness of individual nodules is plotted against their diameter. Diameter and thickness are seen to be proportional, and the proportionality constant

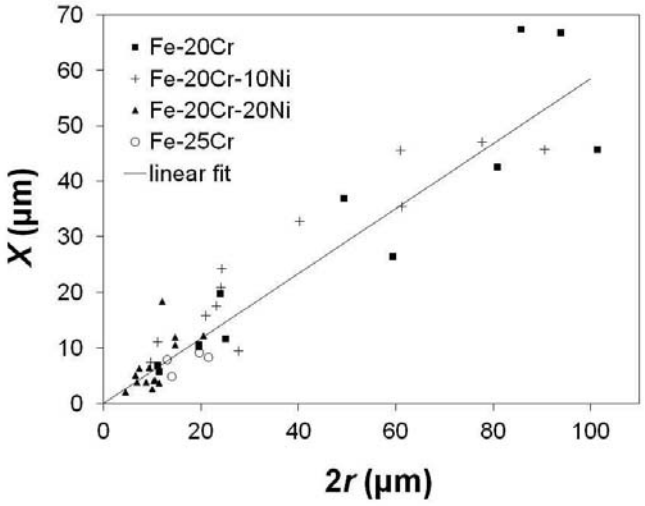

Figure 3.67 – Morphology of individual nodules grown on several alloys, regardless of the gas composition, at 650 °C.

characterising the nodule morphology is independent of gas and alloy composition. Lateral growth kinetics may thus be approximated as

$$r^2 = 2k_{\mathrm{r}}t \tag{3.10}$$

where r is the nodule radius and k_{r} the lateral growth rate constant ($k_{\mathrm{r}} = 0.73k_{\mathrm{p,Fe-ox}}$

for all alloys and gases).

3.4 High chromium alloys at 800 °C

3.4.1 Surface appearance

Reaction of Fe–20Cr and Fe–25Cr in dry CO_2 at 800 °C produced thin protective oxide scales (Fig. 3.68), identified by XRD analysis as Cr_2O_3. Partial scale

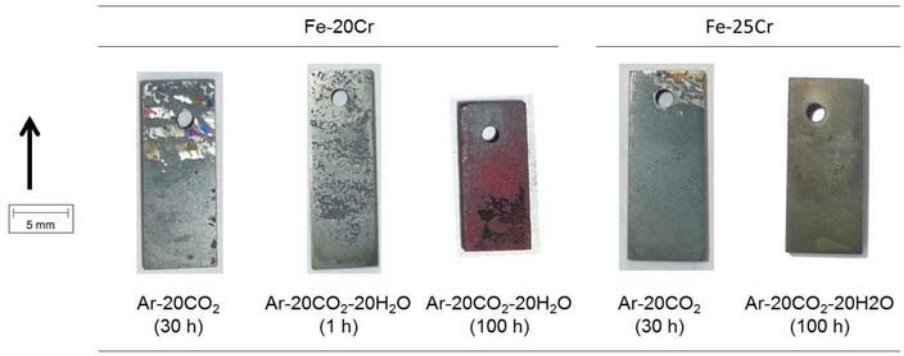

Figure 3.68 – Photographs showing surface appearance of oxides formed on Fe–20Cr and Fe–25Cr after reaction at 800 °C.

spallation was significant for both alloys. The Fe–20Cr alloy underwent breakaway oxidation in wet CO_2, with a reaction morphology similar to that observed during reaction at 650 °C: individual nodules partially covered the specimen surfaces after short reaction times, and coverage was complete after longer reactions. Reaction in Ar–20H_2O produced similar results. In contrast, the Fe–25Cr alloy maintained a protective behaviour in all atmospheres, and only thin Cr_2O_3 scales were formed within the duration of the experiments ($\leqslant$ 100 h).

The Fe–20Cr–10Ni alloy underwent breakaway oxidation in all gases, exhibiting a great variability in nodule development. For instance, after 5 h reaction in dry CO_2, one face of the specimen mostly passivated, forming Cr_2O_3 and only a few nodules, whereas nodule coverage was nearly complete on the other face (Fig. 3.69). Longer reaction times produced a whole range of intermediate nodule surface fractions. Partial spallation of the outermost oxide layers was observed. Reaction in Ar–20CO_2–5H_2O and Ar–20H_2O consistently led to generalised breakaway oxidation, as surface coverage by Fe-rich oxide was nearly complete for short reaction times, and complete for t $\geqslant$ 20 h. Exposure to Ar–20CO_2–20H_2O yielded variable θ values from 1 to 20 h reaction, including close to 100 % for 10 h, but the specimens reacted for 30 and 100 h had a fully protective behaviour, forming only Cr_2O_3. In the case of Fe–20Cr–20Ni, the extent of nodule formation depended on grain orientation, as

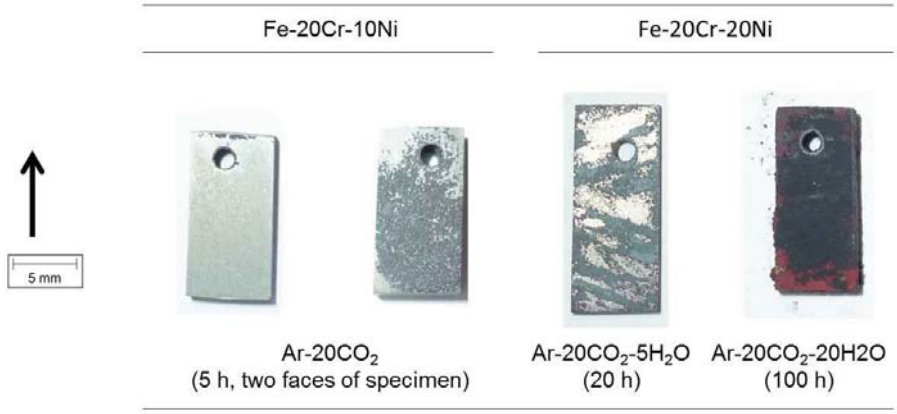

Figure 3.69 – Photographs showing surface appearance of oxides formed on Fe–20Cr–10Ni and Fe–20Cr–20Ni after reaction at 800 °C.

shown in Fig. 3.69. However, long exposures consistently resulted in nearly complete nodule surface coverage, in all atmospheres. A loose powder consisting of Fe_2O_3 whiskers was observed after long exposures to Ar–$20CO_2$–$20H_2O$ and Ar–$20H_2O$, as shown in Fig. 3.69.

Reaction of Fe–25Cr–10Ni mainly led to protective Cr_2O_3 formation in dry CO_2 and Ar–$20H_2O$, but significant scale spallation occurred during cooling. The alloy suffered breakaway oxidation in Ar–$20CO_2$–$5H_2O$ and Ar–$20CO_2$–$20H_2O$. The degree of nodule development was variable, and marked differences were sometimes observed between the two faces of a given specimen (Fig. 3.70). The Fe–25Cr–20Ni

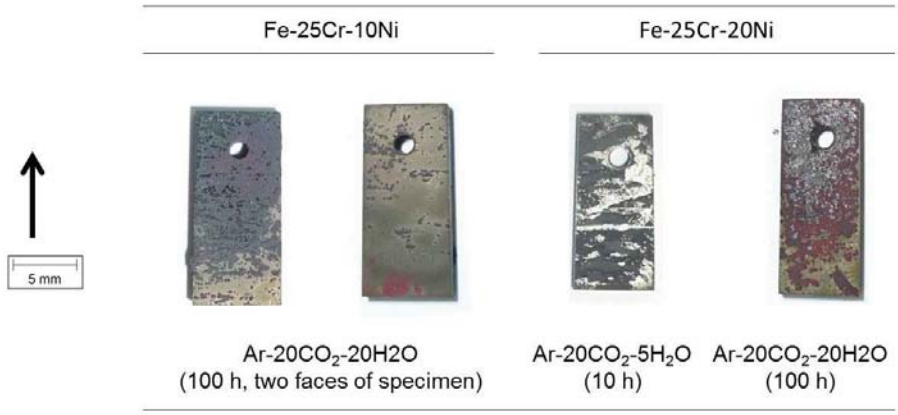

Figure 3.70 – Photographs showing surface appearance of oxides formed on Fe–25Cr–10Ni and Fe–25Cr–20Ni after reaction at 800 °C.

alloy produced Cr_2O_3 scales and Fe-rich oxide nodules, with no significant influence of gas composition. Short exposures resulted in variable nodule coverages accord-

ing to grain orientation, and long exposures consistently produced nearly complete surface coverage (Fig. 3.70).

3.4.2 Reaction kinetics

The weight gains recorded after reaction of the high chromium alloys at 800 °C are shown in Fig. 3.71. Only limited, semi-quantitative use can be made of the $\Delta m/A$ data, which reflect the non-reproducible nature of the breakaway reaction, and varying degrees of scale spallation. Reaction of the Fe–25Cr alloy resulted in small weight gains in all gases, due to exclusive Cr_2O_3 growth. However, spallation prevented proper determination of rate laws and rate constants, and a fortiori of the influence of gas composition. Nodule formation resulted in smaller weight gains for Fe–20Cr than for the 20Cr ternaries. In the case of Fe–25Cr–20Ni, weight gains were relatively small despite the substantial nodule surface coverage. This cannot be attributed to spallation only, and must instead reflect slow nodule growth.

The influence of alloy and gas composition on θ and $\Delta m/A$ is summarised in Fig. 3.72, where values recorded after 100 h reaction are represented.

3.4.3 Reaction products

3.4.3.1 Binary alloys

Reaction of Fe–20Cr in dry CO_2 produced only a thin protective oxide scale, identified as Cr_2O_3 by XRD and SEM–EDS. As is shown in Fig. 3.73, the scale contained cavities preferentially located at the metal/oxide interface. The presence of these cavities sometimes induced scale buckling, and spallation was significant (see Fig. 3.68).

After exposure to wet CO_2, the cavities at the Cr_2O_3/alloy interface were almost completely absent (Fig. 3.74(a)). Scale spalling and buckling were suppressed: the adherence of the metal/oxide interface was considerably improved. However, the presence of H_2O also caused breakaway oxidation. Several stages of nodule development observed on a single specimen reacted in Ar–20CO_2–20H_2O are shown in Fig. 3.74. In the zones of protective oxidation, the Cr_2O_3 scale was approximatively constant in thickness, and an extremely thin Fe_2O_3 layer formed at the oxide/gas interface, barely visible in Fig. 3.74(a). Early nodule development was marked by the simultaneous increase in thickness of both the Fe_2O_3 and the underlying, formerly protective layer. Oxide composition in zones equivalent to those shown in Fig. 3.74(b) was investigated by SEM–EDS. While the protective scale contained

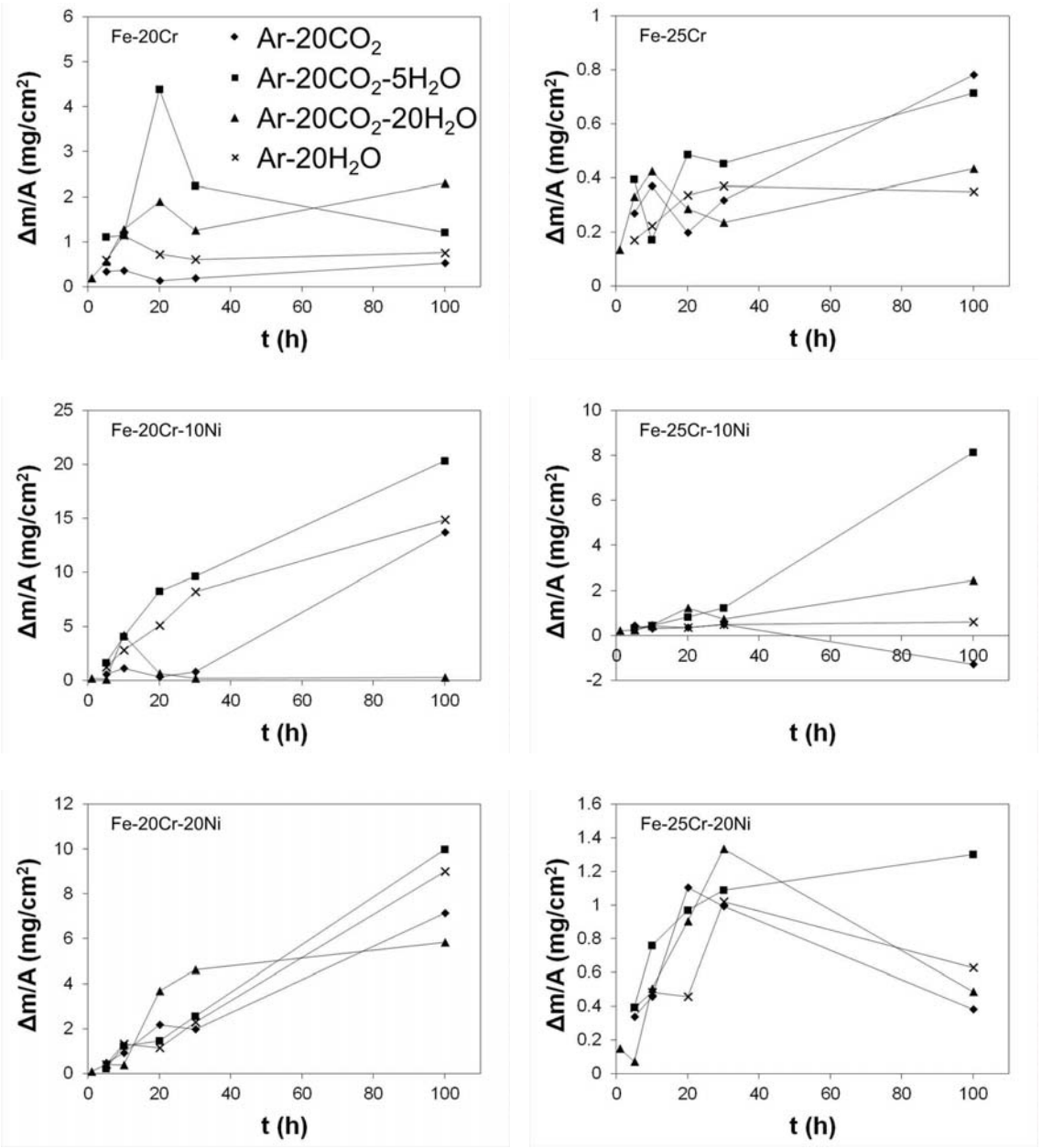

Figure 3.71 – Weight change kinetics of high chromium alloys at 800 °C. Points were joined for clarity.

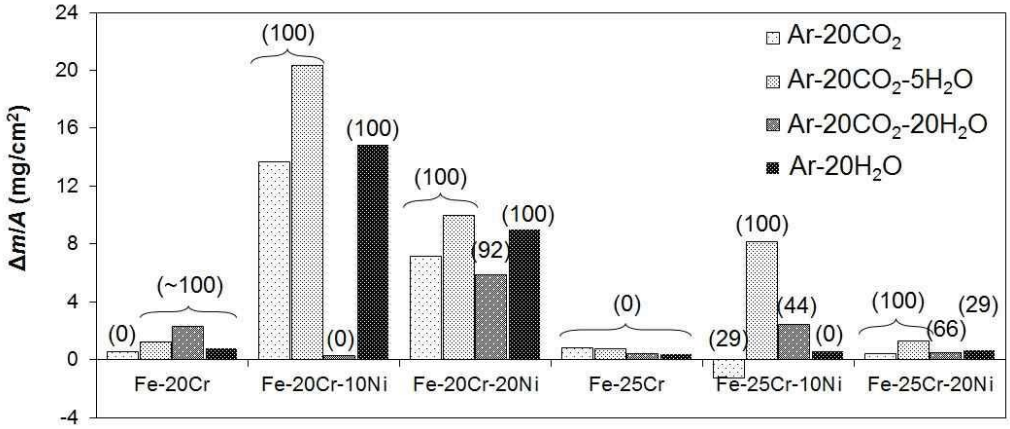

Figure 3.72 – Weight gains and associated nodule surface fractions (bracketed numbers, expressed in percent of the surface area) after 100 h reaction at 800 °C.

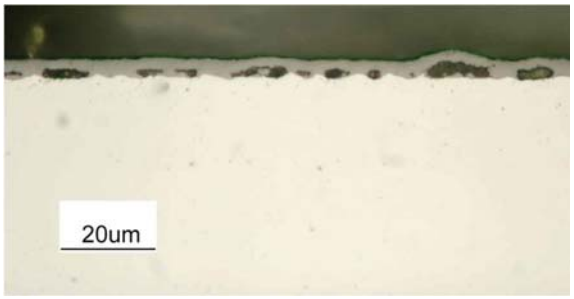

Figure 3.73 – Optical micrograph of Cr_2O_3 scale formed on Fe–20Cr after 100 h reaction in Ar–20CO_2 at 800 °C.

no measurable amount of iron ($\leqslant$ 1 at. %, which is the sensitivity of the analysis), the basal layer in early nodule development was seen to contain 1–2 at. % iron. Unfortunately, Raman analyses were not carried out, and no structural information is available. The light color of the outer layer is without doubt indicating Fe_2O_3, but the inner layer could be either corundum or spinel oxide. As nodule growth continued further, porosity developed at the inner/outer scale interface (Fig. 3.74(c)), a compact layer formed in the outer scale, most likely Fe_3O_4, and an extensively porous layer constituted the major part of the inner scale (Fig. 3.74(d)). The formerly protective layer was always present at the base of the scale, and no internal oxidation was observed.

Several concentration profiles were measured by EPMA in Fe–20Cr beneath the protective Cr_2O_3 scale formed in dry CO_2, yielding similar results. As shown in Fig. 3.75, chromium depletion extended to depths of about 50 µm, with interfacial contents of 15 wt. % (16 at. %).

(a) Cr_2O_3 and surface Fe_2O_3

(b) Early nodule growth

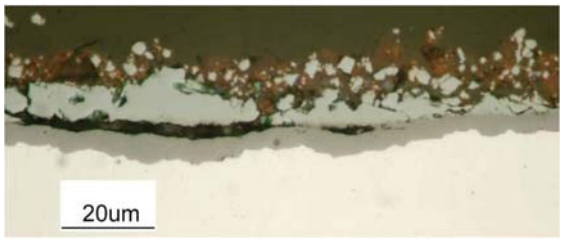

(c) Intermediate stage

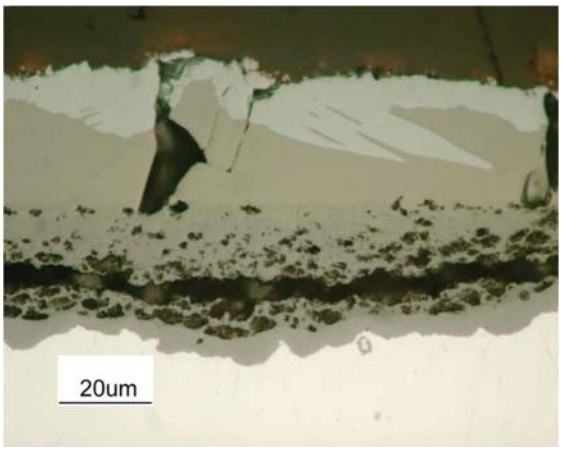

(d) Uniformly thick nodule

Figure 3.74 – Optical micrographs showing stages of nodule growth on Fe–20Cr after 100 h reaction in Ar–20CO_2–20H_2O at 800 °C.

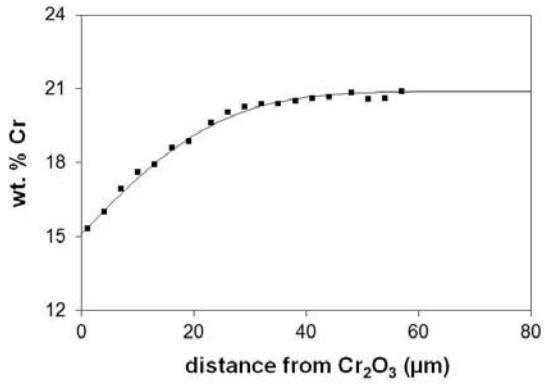

Figure 3.75 – Chromium depletion profile measured by EPMA underneath Cr_2O_3 grown on Fe–20Cr reacted 100 h in Ar–20CO_2 at 800 °C. Points are experimental and solid line calculated from Eq. (1.66).

The Fe–25Cr alloy formed only a protective scale, identified as Cr_2O_3 by XRD and SEM–EDS, after exposure to all gases. As for Fe–20Cr, buckling and spallation were important after exposure to dry CO_2, and suppressed in the presence of H_2O(g). The size and number of cavities were drastically reduced in wet CO_2, as shown in Fig. 3.76.

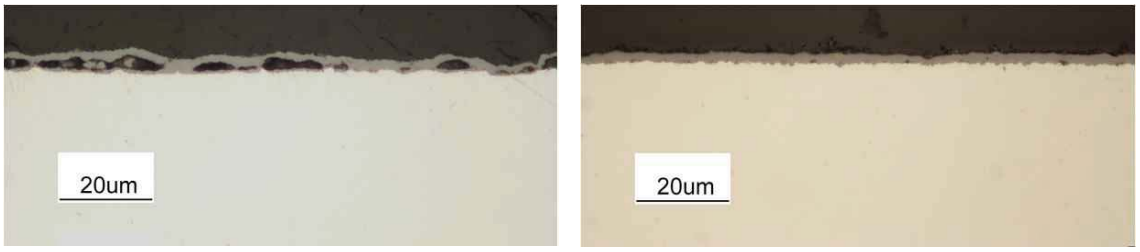

(a) Ar–20CO_2 (b) Ar–20CO_2–20H_2O

Figure 3.76 – Optical micrographs of Cr_2O_3 scale formed on Fe–25Cr after 100 h reaction at 800 °C.

3.4.3.2 Ternary alloys

As described in Section 3.4.1, the ternary alloys suffered breakaway oxidation, with varying nodule surface coverage. In the case of Fe–20Cr–10Ni, no growing nodule could be seen on the cross-sections prepared: most of the time, the oxide consisted of either a thick multilayer scale (Fig. 3.77(a)) or a protective Cr_2O_3 scale (Fig. 3.77(b)), and the transition between these two types of oxide was sharp. In

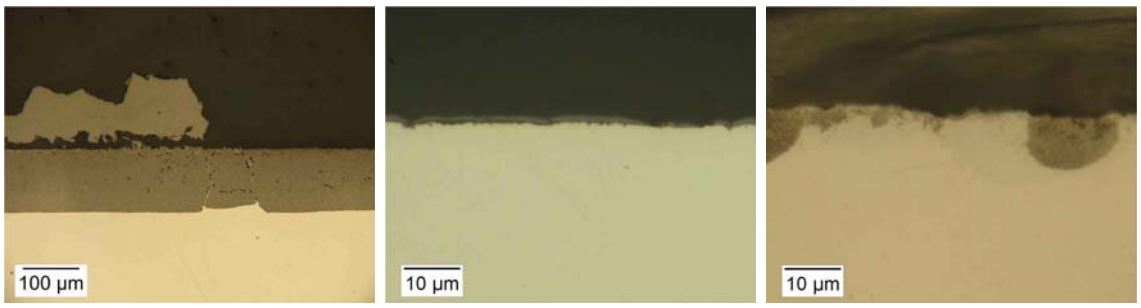

(a) Uniform Fe-rich scale (b) Cr_2O_3 scale (c) Early inner attack

Figure 3.77 – Optical micrographs of oxides formed on Fe–20Cr–10Ni after 100 h reaction at 800 °C. (a,c) Ar–20CO_2; (b) Ar–20CO_2–20H_2O.

Fig. 3.77(c), the early stage of breakaway oxidation is marked by internal attack, and no outer layer is seen. Examination of this zone and other equivalent zones did not allow determination of whether an outer layer had been formed and spalled, or

had not yet been formed. The oxide morphology below the original alloy surface consisted of small particles in a metal matrix, that is, internal oxidation. However, as the reaction progressed, oxide protrusions developed as continuous zones rather than internal precipitates. These inner reaction zones had the same morphology as inner layers of the thick scales. These were uniform, porous, and contained several finely dispersed phases. The number of phases could not be determined from optical micrographs, and electron microscopy was not used.

The thick scales formed on the Fe–20Cr–20Ni alloy had the same morphology after exposure to dry and wet CO_2. The outer layer contained many large cavities (Fig. 3.78(a)), and most of the time had spalled before any metallographic observation could be made (Fig. 3.78(b)). The inner layer was porous, and contained

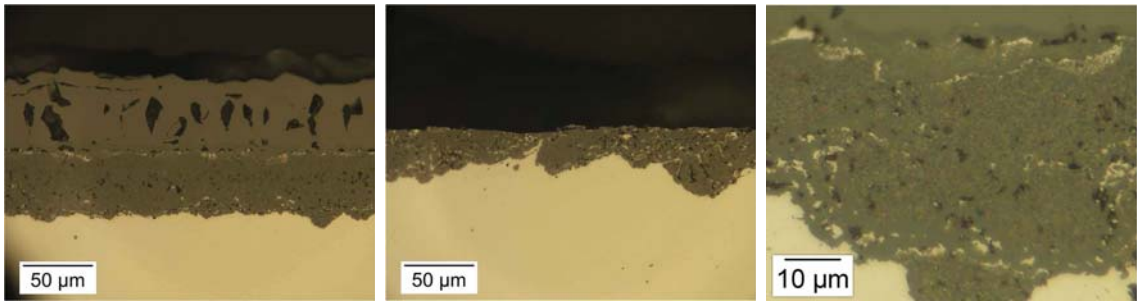

(a) Uniform multilayer scale (b) Convoluted inner layer (c) Inner layer morphology

Figure 3.78 – Optical micrographs of oxide scales formed on Fe–20Cr–20Ni after 100 h reaction in Ar–20CO_2 at 800 °C.

metal inclusions, in particular near the inner/outer scale interface. Its morphology varied with location in a given specimen. In Fig. 3.78(a) for instance, the layer is uniform in thickness, and mostly consists of a fine mixture of oxide particles. In Fig. 3.78(b), however, it is convoluted, contains much more metal inclusions, and continuous single-phase zones are seen around the metal inclusions. These different types of morphology are shown in Fig. 3.78(c).

Some individual nodules produced during exposure to Ar–20CO_2–20H_2O are shown in Fig. 3.79. The inner layer of the smallest nodule (a) was a dense and fine oxide mixture. However, in the two other nodules, significant amounts of metal were present both near the original metal surface, alongside continuous single-phase oxide zones, and deeper in the inner layer, associated with the fine oxide dispersion. These inner layers had a complex morphology, and cannot be accurately described either as external scales or as internal oxidation zones. The thickness of the outer layer varied (see Fig. 3.79(b) and (c)), although the Fe_2O_3 whiskers characteristic

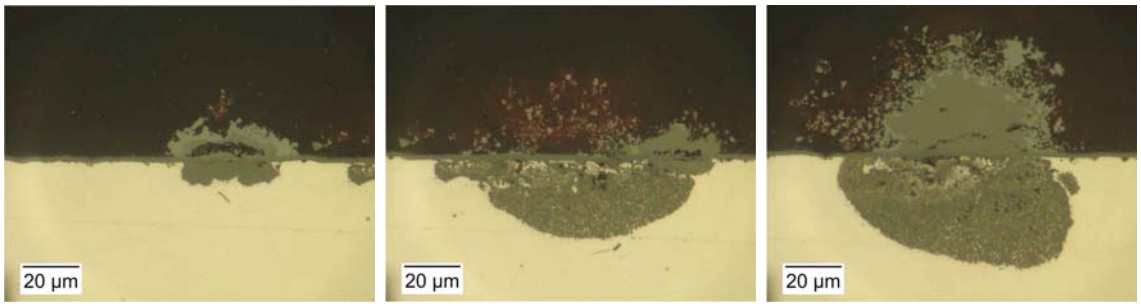

(a) Early nodule growth (b) Thin outer layer (c) Thick outer layer

Figure 3.79 – Optical micrographs of nodules formed on Fe–20Cr–20Ni after 100 h reaction in Ar–20CO_2–20H_2O at 800 °C.

of reaction in Ar–20CO_2–20H_2O were always formed.

The Cr_2O_3 scale formed on Fe–25Cr–10Ni was poorly adherent and prone to spallation after exposure to Ar–20CO_2 (Fig. 3.80(a)), but seemed perfectly adherent in the presence of H_2O(g). Nodules grown in dry and wet CO_2 had a morphology

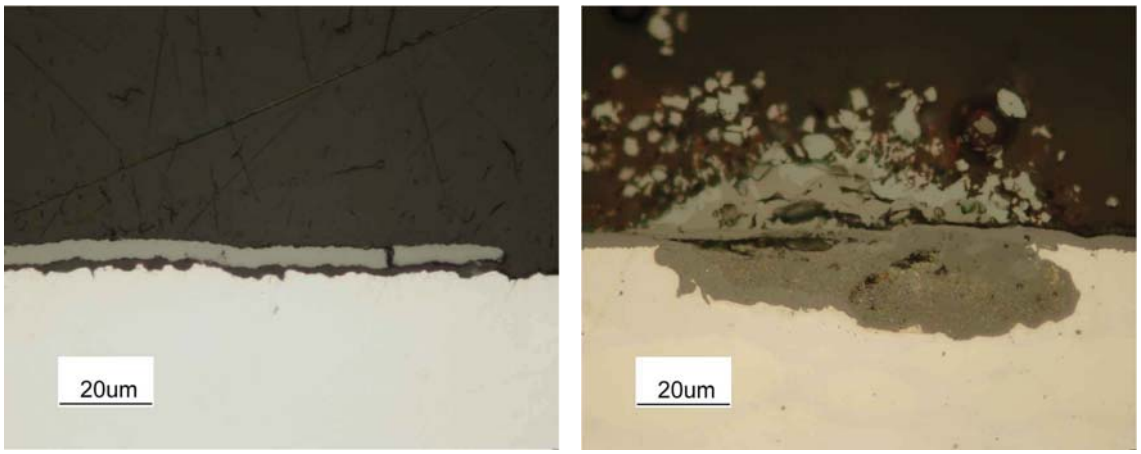

(a) Ar–20CO_2 (b) Ar–20CO_2–20H_2O

Figure 3.80 – Optical micrographs of oxides formed on Fe–25Cr–10Ni after 100 h reaction at 800 °C.

similar to those observed on Fe–20Cr–10Ni, except that a continuous oxide layer was always present at the base of the inner oxide (Fig. 3.80(b)).

This was also the case for Fe–25Cr–20Ni (Fig. 3.81). In nodules formed on both 25Cr ternaries, the outer layer was compact after exposure to Ar–20CO_2, but porous in Ar–20CO_2–20H_2O. The chemical composition of the nodule shown in Fig. 3.81(a) was investigated using SEM–EDS (Fig. 3.82). The outermost layer is iron oxide, as could be expected from its color, characteristic of Fe_2O_3. Immediately beneath lies a layer containing both iron and nickel, but no chromium. The inner layer contains all

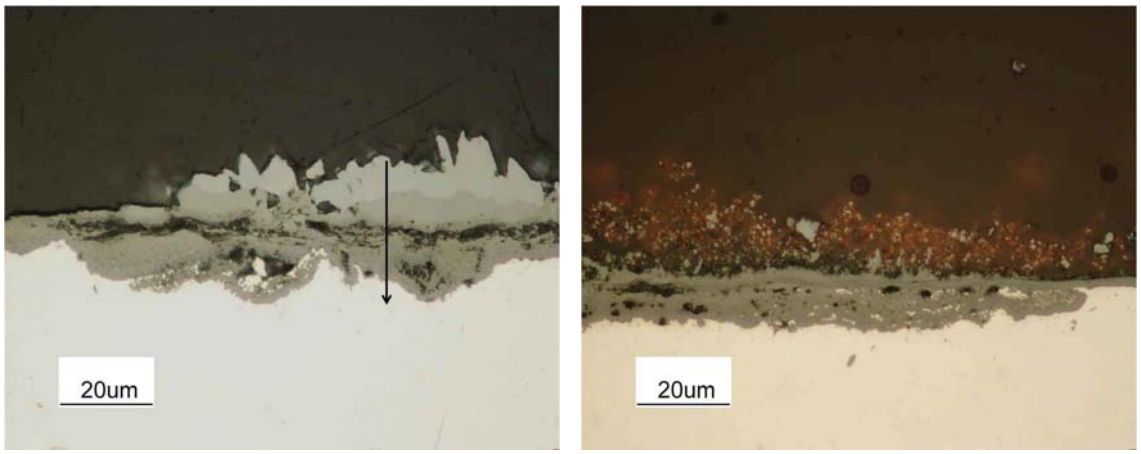

(a) Ar–20CO_2 (b) Ar–20CO_2–20H_2O

Figure 3.81 – Optical micrographs of oxides formed on Fe–25Cr–20Ni after 100 h reaction at 800 °C.

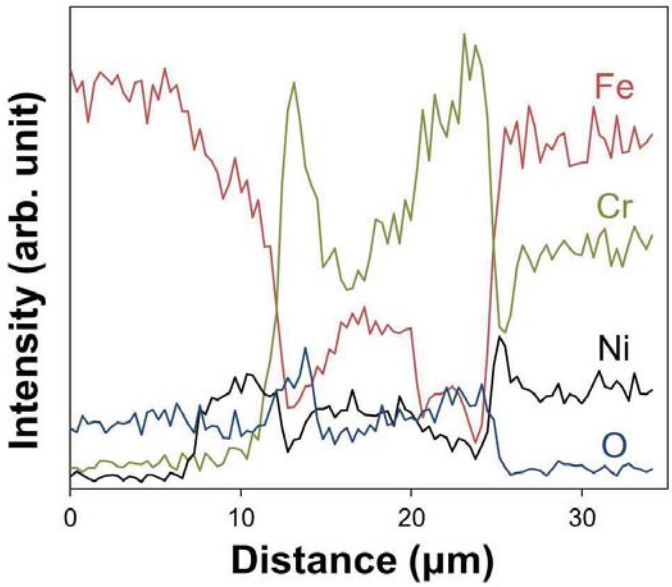

Figure 3.82 – SEM–EDS concentration profile in nodule formed on Fe–25Cr–20Ni after 100 h reaction in Ar–20CO_2 at 800 °C (location indicated by arrow in Fig. 3.81(a)). Information is qualitative only.

three elements. Chromium is significantly enriched in two zones: near the original alloy surface, and at the base of the scale. The two Cr peaks correspond to zones where a single-phase, continuous layer was present.

3.4.3.3 Nodule growth kinetics

Maximum nodule thickness or average scale thickness measured after 100 h reaction, when applicable, are given in Table 3.9. The values are discussed in Section 4.2.3.

Table 3.9 – Multilayer oxide thickness (µm) after 100 h reaction at 800 °C.

	$Ar–20CO_2$	$Ar–20CO_2–20H_2O$
Fe–20Cr	n/a	66
Fe–20Cr–10Ni	202	n/a
Fe–20Cr–20Ni	100	117
Fe–25Cr–10Ni	32	93
Fe–25Cr–20Ni	30	24

3.4.3.4 Carburisation

Carbide precipitation occurred in Fe–20Cr, in the form of coarse, isolated, extremely rare internal particles (less than 10 carbides per cross-section), as shown in Fig. 3.83. The precipitates were revealed by etching with Murakami's reagent, and EPMA

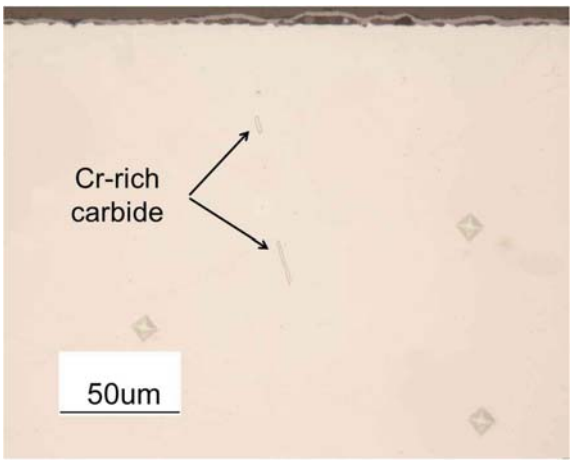

Figure 3.83 – Optical micrograph of carbides formed in Fe–20Cr after 100 h reaction in $Ar–20CO_2$ at 800 °C. Specimen etched with Murakami's reagent. The hardness indents were used to mark the location of the carbide (EPMA was carried out on polished cross-sections).

confirmed that they were Cr-rich carbides. No carbides were detected in any of the other alloys.

Chapter 4

Growth of iron-rich oxide

Uniformly thick multilayer oxide scales, formed at both 650 and 800 °C, were observed either from early reaction times (low chromium alloys), or as a result of the coalescence of individual nodules during the experimental time scale (high chromium alloys). They both consisted of two parts, located on either side of the original alloy surface; the outer part was made up of iron oxide layers, the inner part contained iron and the alloying elements.

This Chapter discusses the influence of alloy and gas composition on the growth rate of the iron-rich oxide scales. The simple case of iron is investigated first. The effect of chromium and nickel additions is studied by successive comparisons.

4.1 Oxidation of iron

Reaction of iron produced uniform scales of iron oxide, and no carburisation products were formed. This provides a simple way of investigating the role of the gas composition on external scaling, independently of selective oxidation, or of the interactions between oxidation and carburisation.

4.1.1 Reaction at 800 °C

Wüstite was the main constituent of the scales formed on iron at 800 °C (Fig. 3.19). Its large non-stoichiometry resulted in fast iron diffusion (see Section 1.1.3.1), accounting for the elevated scaling rates.

In dry CO_2, the reaction kinetics were linear (Fig. 3.16), and FeO was the only oxide formed, despite the fact that the gas p_{O_2} was high enough to stabilise all iron oxides (Section 2.2). The absence of Fe_3O_4 and Fe_2O_3 at the reaction temperature indicates that the scale/gas interface was not at thermodynamic equilibrium. A comparison of the rates of oxygen consumption from the oxidation reaction and oxygen supply from the gas phase to the specimen surface is presented in Appendix C, and shows that scaling could not be limited by gas phase transport. Hence, it is concluded that oxidation of iron in dry CO_2 was controlled by a surface reaction. As this reaction was relatively slow, a metastable state of high iron activity was maintained at the scale surface, such that FeO could not be converted to Fe_3O_4, as represented in Fig. 4.1. The activity of iron at the oxide/gas interface, $a_{FeO/gas}$, was then determined by the rate at which iron was consumed. This conclusion is supported by considering the surface morphology of the scale (Fig. 3.18(a)): the development of faceted crystals shows that oxide formation proceeded according to favoured crystallographic orientations, and was not limited by volume iron diffusion.

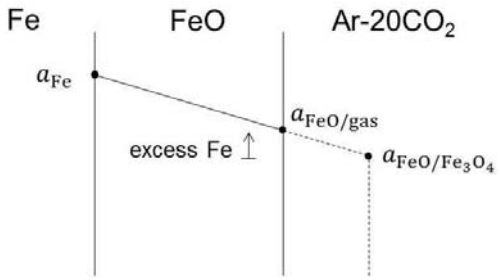

Figure 4.1 – Schematic representation of iron activity in oxide growing on iron in Ar–20CO_2 at 800 °C.

The present results are in agreement with previous studies of iron oxidation in CO–CO_2 mixtures in the temperature range 600–1100 °C. The rate-controlling step during the initial stage of linear kinetics was found to be the dissociation of CO_2 to CO and adsorbed oxygen ions on the oxide surface [110, 161, 162]. Mechanistic analyses, confirmed by experimental data, showed that under these conditions, the rate constant was a linear function of gas phase p_{CO_2} [110, 161–163]:

$$k_\ell = a\, p_{CO_2} + b \tag{4.1}$$

where a and b are constants. For iron oxidation in H_2–H_2O mixtures, oxidation rates were also found to be controlled by dissociation of H_2O on the FeO surface [164], and described by a similar relation [163, 164]:

$$k_\ell = a'\, p_{H_2O} + b' \tag{4.2}$$

In Ar–20CO_2–5H_2O, the oxidation kinetics were approximately linear, with a higher rate constant than in Ar–20CO_2 (Fig. 3.16): the addition of H_2O(g) caused the surface reaction to proceed at a faster rate. This conclusion is consistent with the results mentioned above: if oxidation rates in CO_2 and H_2O are linear functions of p_{CO_2} and p_{H_2O} via Eqs. 4.1 and 4.2, respectively, then the oxidation rate in Ar–CO_2–H_2O may be defined by a relation of the type

$$k_\ell = a''\, p_{CO_2} + a'''\, p_{H_2O} + b'' \tag{4.3}$$

The limited number of p_{CO_2} and p_{H_2O} values used in the present work does not allow the validity of Eq. (4.3) to be tested, or the values of the constants to be determined. However, the fact that k_ℓ increased in the presence of H_2O is readily understood.

When the gas H_2O level was raised to 20 %, the reaction proceeded according to parabolic kinetics after an initial linear stage (Fig. 3.16). The initial oxidation rate was higher than in Ar–20CO_2–5H_2O. It is concluded that the surface reaction rate

was further increased until it exceeded the rate of iron diffusion in FeO, causing a transition from surface to diffusion control. The morphology of the scale surface was then determined by the flux of iron across the scale, and uniform diffusion produced a flat surface, as seen in Fig. 3.18(c). Magnetite was found to form a continuous layer at the scale/gas interface after exposure to Ar–20CO_2–20H_2O (Fig. 3.19(b)). This layer could have been formed at the reaction temperature or by precipitation during cooling (because FeO is not stable under 570 °C, see Section 1.1.3.1), like the cuboid precipitates observed in the outer, oxygen-rich part of the FeO layer (Fig. 3.19(b)); this cannot be verified. Nonetheless, the presence of Fe_3O_4 undoubtedly shows that at its surface, the scale formed in Ar–20CO_2–20H_2O was richer in oxygen that those formed in Ar–20CO_2 and Ar–20CO_2–5H_2O. Faster iron consumption allowed the iron activity at the surface of the FeO layer to decrease to the value a_{FeO/Fe_3O_4}, as represented in Fig. 4.2.

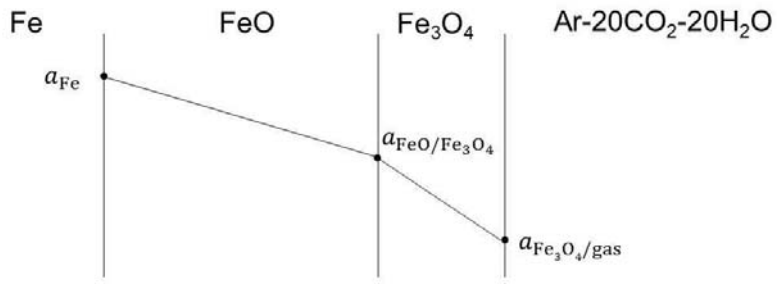

Figure 4.2 – Schematic representation of iron activity in oxide growing on iron in Ar–20CO_2–H_2O at 800 °C.

The initial oxidation rate observed in Ar–20H_2O was higher than that measured in Ar–20CO_2 (Fig. 3.16). Since the partial pressure of oxidant was the same in both cases, it appears that H_2O(g) inherently led to a faster surface reaction than CO_2(g). Comparing iron oxidation experiments performed in various H_2–H_2O and CO–CO_2 mixtures, Turkdogan et al. [164] also concluded that the reactivity of H_2O was higher than that of CO_2.

4.1.2 Effect of CO_2 and H_2O on diffusion in FeO

The question arises as to whether the diffusion process itself was altered by the presence of CO_2 and/or H_2O in the atmosphere, as compared to the situation of air for example. On the one hand, it has been suggested that the presence of H_2O leads to faster transport of oxygen-bearing species [145] and can eventually result in a change of the predominant oxidation process from outward to inward growth [146].

On the other hand, this is likely to apply only to oxides growing with a significant inward contribution in the absence of H_2O, which is not the case for FeO. Indeed, scaling rates of pure iron in O_2 were reported to be only slightly affected by the presence of H_2O [111, 131].

The parabolic rate constant k_{pm} (as defined in Eq. (3.1)) for oxidation of iron in air at 800 °C is calculated from the data of Paidassi [32] as 2.9×10^{-2} mg^2 cm^{-4} s^{-1}. This value is very close to that measured here for reaction in Ar–20CO_2–20H_2O at the same temperature, 2.3×10^{-2} mg^2 cm^{-4} s^{-1}. In air, scales grown on iron contain layers of FeO, Fe_3O_4 and Fe_2O_3. As shown by Gesmundo and Viani [34, 35], the growth rate of each layer depends on the fluxes of iron traversing all layers and reacting at the interfaces. Overall growth kinetics are thus determined by the rates of iron diffusion in all three layers. However, since iron diffusion in FeO is much faster than in Fe_3O_4 and Fe_2O_3, the FeO layer represents 95 % of the total thickness [32], and its growth rate represents, to a good approximation, that of the multilayered structure.

Similarly, when oxidation of iron proceeds according to parabolic kinetics (as in Ar–20CO_2–20H_2O, or in Ar–20CO_2 for longer exposures or higher temperatures than in the present study [110,162]), the oxidation rate is determined by iron vacancy diffusion in FeO [110]. The value of the parabolic constant is proportional to the iron vacancy concentration at the FeO/Fe_3O_4 interface, [V_{Fe}], which is related to the local oxygen activity by the relation

$$[V_{Fe}] \propto p_{O_2}{}^{\frac{1}{2(\alpha+1)}} \tag{4.4}$$

where α is the charge of the vacancies. Scales formed in Ar–20CO_2–20H_2O consisted of FeO, covered by a thin Fe_3O_4 layer. If a continuous FeO/Fe_3O_4 interface was established at the reaction temperature and local thermodynamic equilibrium prevailed, the value of p_{O_2} in FeO in the vicinity of the interface was set by the FeO/Fe_3O_4 equilibrium. It follows from Eq. (4.4) that the driving force for iron vacancy diffusion was the same as that in air. The oxygen potential in the gas–oxide–metal system is illustrated in Fig. 4.3 for both situations. This accounts for the fact that the k_{pm} values were close, even though the external p_{O_2} was 6 orders of magnitude lower in Ar–20CO_2–20H_2O than in air. In conclusion, the present results support the idea that neither the presence of CO_2(g) nor that of H_2O(g) affected the diffusion mechanism in FeO grown on pure iron, at least not to an extent which could be measured.

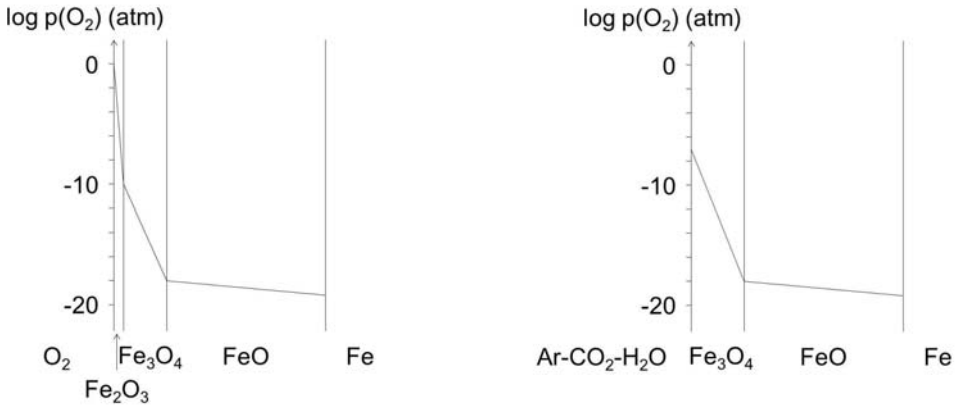

(a) Fe in O_2 (b) Fe in Ar–CO_2–H_2O

Figure 4.3 – Oxygen potentials associated with interfacial equilibria (numerical values at 800 °C).

4.1.3 Influence of oxidation temperature

In the absence of TGA data, the significant variability associated with the time-lapse experiments carried out at 650 °C limits the value of the gravimetric results. Reaction of iron in dry CO_2 initially proceeded according to a linear rate law (Fig. 3.1). The decrease in oxidation rate observed in a second stage may, perhaps, reflect a transition to parabolic kinetics. Additions of H_2O(g) led to an increase in the initial rate and to an earlier transition to approximately parabolic kinetics. No significative difference was seen between Ar–20CO_2–5H_2O and Ar–20CO_2–20H_2O reactions. Hematite was formed only in a narrow upstream region during exposure to Ar–20CO_2, but covered the entire specimens after reaction in both Ar–20CO_2–5H_2O and Ar–20CO_2–20H_2O (not shown). The presence of Fe_2O_3 as whiskers indicates that it was formed during reaction at 650 °C, and not during cooling. This shows that the scale/gas interface was in thermodynamic equilibrium, which is consistent with diffusion-controlled, parabolic oxidation kinetics.

Thus, with regard to the effect of H_2O(g), oxidation of iron at 650 °C is in qualitative agreement with the observations made for the 800 °C reaction (Section 4.1.1). The surface reaction was relatively slow in dry CO_2, and proceeded faster in the presence of H_2O. Faster iron consumption led to a decrease of the iron activity at the scale surface, allowing the formation of Fe_3O_4 and Fe_2O_3, and favouring the establishment of diffusion controlled kinetics. At 800 °C, iron diffusion in FeO was too fast, compared to the rate of the surface reaction, for equilibrium to be reached at the oxide/gas interface. The formation of Fe_2O_3 at 650 °C indicates that iron diffusion was relatively slower, compared to the rate of the surface reaction. It is

concluded that the activation energy for diffusion is higher than that of the surface reaction. No numerical estimates were attempted here because data were recorded for only two temperatures, and the 650 °C results were subject to significant experimental uncertainty.

4.2 Effect of alloy composition

4.2.1 Oxide constitution on low chromium alloys

Reaction of Fe–2.25Cr, Fe–9Cr, Fe–9Cr–10Ni and Fe–9Cr–20Ni in dry and wet CO_2 at both 650 and 800 °C produced external oxide scales and internal oxide precipitates typical of the oxidation of dilute alloys. Results of the present work, presented in Sections 3.1.3 and 3.2.3, are consistent with reports from other investigators, which were detailed in Sections 1.5.2 and 1.6.2. The oxide scales were multiphase, multilayered and could be divided into two parts. The inner part generally consisted of a mixture of FeO and spinel oxide containing iron and chromium, and nickel in the case of the ternary alloys. The outer part comprised layers of iron oxide, from FeO alone to $FeO/Fe_3O_4/Fe_2O_3$, depending on alloy composition, gas composition and temperature.

The case of the binary alloys is examined more closely with the help of an isothermal section of the Fe–Cr–O phase diagram [71] shown in Fig. 4.4. This

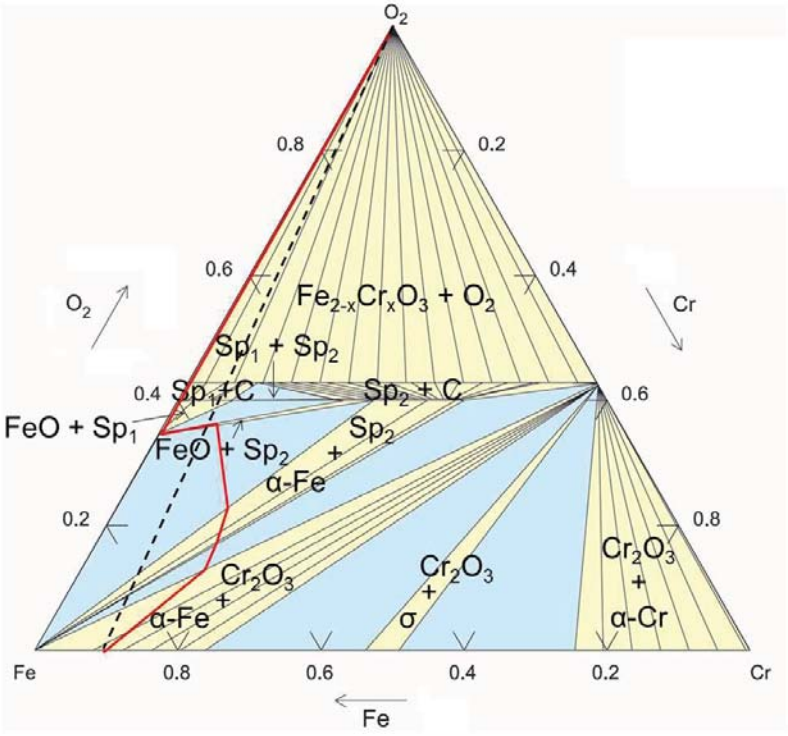

Figure 4.4 – Isothermal section of Fe–Cr–O phase diagram calculated at 627 °C (after Ref. [71]) and diffusion path typical of dilute alloy oxidation. C: corundum phase $Fe_{2-x}Cr_xO_3$; Sp_1 and Sp_2: Fe-rich and Cr-rich spinel phases $Fe_{3-x}Cr_xO_4$, respectively. The dashed line joins the oxygen corner to the unreacted alloy composition.

calculated diagram represents phase equilibria at 627 °C, which is quite close to the lower temperature of the present experiments, 650 °C. An isothermal section at $T = 900$ °C, published in Ref. [165], shows that the phase stability domains are essentially the same in this temperature range. For this reason, Fig. 4.4 is also used to discuss reaction at 800 °C.

The diffusion path shown as a red line was traced on the basis of the experimental results, and, in turn, defines the equilibrium scale constitution represented in Fig. 4.5. A dashed line joining the oxygen corner and the point representing the

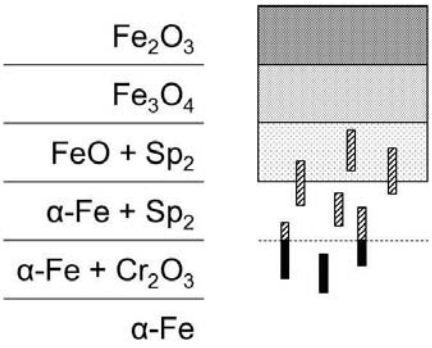

Figure 4.5 – Schematic representation of scale constitution along diffusion path shown in Fig. 4.4

unreacted alloy was traced in Fig. 4.4 in order to emphasise the mass balance in the reacting system. The part of the diffusion path located to the right of the alloy–O_2 line corresponds to the internal oxidation zone and inner scale, which are *globally* enriched in chromium with respect to the original alloy composition — that is, considering the matrix + precipitates system. In the α-Fe + Cr_2O_3 field, the diffusion path crosses tie-lines from the Cr-rich to the Fe-rich side, which reflects the fact that the metal matrix is enriched in iron as the chromium oxide precipitates. In the α-Fe + Sp_2 and FeO + Sp_2 fields, the diffusion path crosses tie-lines in the same direction, indicating that the composition of the solid-solution oxide, Sp_2, is shifting toward the iron-rich end. Subsequently, the diffusion path crosses the alloy–O_2 line and follows the three iron oxide phases to the oxygen corner; this corresponds to the outer scale layers.

Local thermodynamic equilibrium did not always prevail in the present experiments. The experimental study of phase constitution and composition was not exhaustive, but at least two non-equilibrium situations can be identified:

- Chromia is predicted to precipitate internally, but was never detected by XRD analysis or metallographic observation of the internal oxidation zones formed

in Fe–9Cr at both 650 and 800 °C. The chromium oxide could have been present in quantities too small to be detected, or not formed at all. Several reasons are possible for its absence: spinel oxide grows faster than Cr_2O_3, and a fast $Cr_2O_3 \rightarrow Sp_2$ conversion would make Cr_2O_3 short-lived. In some cases, as will be discussed in Chapter 5, internal oxides were produced by oxidation of preexisting carbides containing both iron and chromium, which could favour Sp_2 over Cr_2O_3 formation.

- In the case of reaction at 800 °C, the surface reaction was too slow, relative to iron diffusion in FeO, for equilibrium to be reached at the scale/gas interface, as discussed in Section 4.1.1, and Fe_2O_3 was not formed.

Nonetheless, the equilibrium description is useful to understand the local and global mass balances. Another use of the study of phase equilibria is the prediction of oxygen activity in the growing scale. Oxygen potentials are not apparent in a Gibbs triangle (Fig. 4.4), but are directly representated in predominance diagrams, $\log p_{O_2} - N_{Cr}$, as shown in Fig. 1.10. The essential outcome of this diagram, concerning scales grown on dilute Fe–Cr alloys, is that the oxygen activity at the α-$Fe + Sp_2/FeO + Sp_2$ interface is determined by the Fe/FeO equilibrium, as represented schematically in Fig. 4.6.

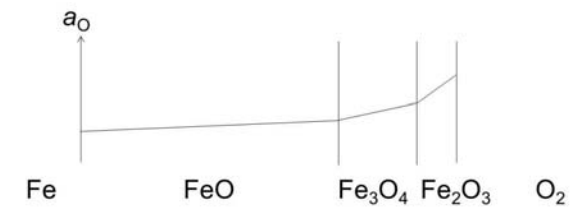

(a) Pure iron

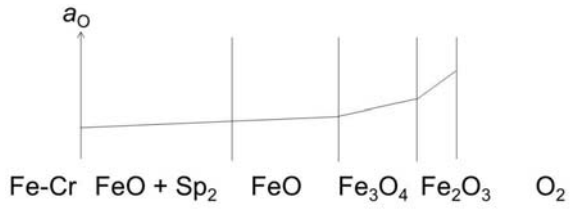

(b) Dilute Fe–Cr

Figure 4.6 – Schematic representation of oxygen activity in growing iron-rich oxide scale. Internal oxides are omitted for clarity.

4.2.2 Oxidation rate of low chromium alloys

The low chromium alloys were, in some cases, prone to carburisation. Weight gains due to carburisation, calculated in Appendix D, were found to be negligible compared to the total weights gains measured after reaction at both 650 and 800 °C. Thus experimental $\Delta m/A$ values may be used directly to discuss the effect of $H_2O(g)$ on the oxidation kinetics. Reaction at 800 °C, for which reliable gravimetric results are available, is examined first.

4.2.2.1 Reaction at 800 °C

After reaction of the low chromium alloys at 800 °C, the inner scale consisted of a mixture of FeO and spinel oxide containing iron and chromium, plus nickel in the case of the ternary alloys, and the outer scale contained an FeO and/or an Fe_3O_4 layer.

The formalism developed by Gesmundo and Viani [34,35] in describing diffusion-controlled scaling is used here to define a simple representation of the reacting system. Since FeO and Fe_3O_4 are cation diffusers [30], the scale is presumed to grow by outward iron diffusion only. This is investigated by considering the iron flux in the inner (j_1), FeO (j_2) and Fe_3O_4 (j_3) layers, as represented in Fig. 4.7. Magnetite is formed at the scale/gas interface, and consumed at the FeO/Fe_3O_4

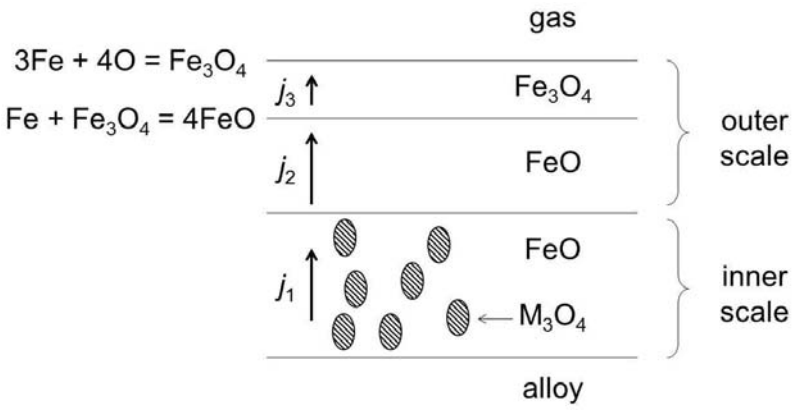

Figure 4.7 – Schematic representation of iron flux in growing multilayer scale. M denotes (Fe,Cr) or (Fe,Cr,Ni).

interface via [34, 35, 166]

$$\mathrm{Fe} + \mathrm{Fe_3O_4} = 4\mathrm{FeO} \tag{4.5}$$

A fraction j_2' of the flux crossing FeO reacts at the FeO/Fe_3O_4 interface, while the remaining part j_3 traverses the Fe_3O_4 layer to react at the scale surface: $j_2 = j_2' + j_3$.

While the growth rate of each individual layer depends on both j_2 and j_3, the outer scale as a whole can only grow by the amount allowed by j_2. As no reaction takes place at the FeO/FeO+spinel interface, $j_2 = j_1 = j$. Furthermore, because of a lower diffusivity in the spinel phase, the spinel precipitates in the inner layer reduce the effective diffusional cross-section [19]. It follows that j, and the overall scaling rate, are determined by j_1, and decrease with increasing volume fraction of spinel particles, $f_{V,sp}$.

It is recognised that iron diffusion in the inner scale could in principle be affected by chromium dissolution in the FeO matrix. However, unlike that of NiO, the inherent deviation from stoichiometry of FeO is so high that doping by chromium is thought to leave its defect structure, and the rate of iron diffusion, unaffected [20]. Under these conditions, the effect of doping, if there was any, would certainly be far less important than that related to the reduction of effective diffusional cross-section due to spinel precipitates [167]. It is also noted that the presence of low-diffusivity precipitates in a higher-diffusivity matrix could, in principle, cause an increase of the effective diffusivity, because of the contribution of matrix/precipitate interfacial diffusion. However, in the specific case of non-selective oxidation of dilute Fe–Cr alloys, there is overwhelming evidence supporting the fact that spinel precipitation in FeO effectively reduces iron diffusion, and the overall growth rate in situations of diffusion control [19, 20, 62].

As shown in Table 3.5, values of $f_{V,sp}$ were about 10 % and 30 % for Fe–2.25Cr and Fe–9Cr, respectively, after reaction in dry and wet CO_2. The evolution of $f_{V,sp}$ with alloy chromium concentration can be predicted using the lever rule in the FeO + Sp_2 field of a phase diagram at the appropriate temperature. Alternatively, it can be calculated from a mass balance for the entire alloy–scale system, taking into account all phase compositions, reaction zone thicknesses and the volume fraction of spinel particles (and pores) in the inner oxide layer, in the manner described, for instance, in Ref. [109]. No estimation is made here, because the chemical compositions were not determined quantitatively. However, the essential outcome of the mass balance is that the volume fraction of spinel particles in the inner layer is expected to increase with alloy chromium concentration, as observed experimentally. Accordingly, the outward iron flux is expected to decrease with chromium concentration.

Reaction of the binary alloys in Ar–20CO_2 proceeded according to linear kinetics (Fig. 3.16), with rate constants similar to that measured for iron (Table 3.4). The outer scale contained FeO, with some islands of Fe_3O_4 at the oxide/gas interface. The absence of Fe_3O_4 as a continuous layer, and of Fe_2O_3, reflects a metastable

state of high iron activity, and the argument made in Section 4.1.1 also applies to the binary alloys: linear oxidation kinetics in Ar–20CO_2 were determined by the relatively slow surface reaction. Thus, the flux of iron across the inner scale was limited by the surface reaction, and not affected by the presence of spinel precipitates.

Additions of 5 and 20 % H_2O to the reacting gas resulted in increased oxidation rates and led to a transition to parabolic kinetics (Fig. 3.16), with an Fe_3O_4 layer formed at the oxide/gas interface. These observations are consistent with the argument made earlier in the case of iron: H_2O(g) additions caused the rate of the surface reaction to increase until exceeding that of iron diffusion. In addition, faster iron consumption at the scale surface led to a decrease in the iron activity, favouring Fe_3O_4 precipitation. In Ar–20CO_2–20H_2O, kinetics were diffusion-controlled, and the parabolic rate constant decreased with increasing chromium content in the alloy (Table 3.4).

The validity of the simple description based on Fig. 4.7 can be tested by considering the effect of an increasing fraction of spinel oxide in the inner layer on the value of the parabolic rate constant, k_p. In Wagner's original treatment [21], the expression of the rate constant involves the integration of a term which is a function of oxide composition over the range of oxygen activity prevailing in the scale. A simplified treatment is considered here, where iron diffusion is described using an effective diffusion coefficient D_{eff}, and the simple relation $k_p \propto D_{eff}$ is arrived at (see Section 1.1.2.4). If, furthermore, the value of D_{eff} is assumed to be proportional to the diffusional cross-section, that is, to the volume fraction of FeO in the FeO + spinel layer, then the relation $k_p \propto (1 - f_{V,sp})$ should hold with the same proportionality constant for iron ($f_{V,sp} = 0$) and the binary alloys. This condition is quite restrictive, among other reasons because short-circuit diffusion along oxide grain boundaries and matrix/precipitate interfaces is neglected. Rate constants obtained from $\Delta m/A$ measurements, k_{pm}, are used rather than k_p values, because reliable thickness measurements were not available for Fe and Fe–2.2Cr. Values of k_{pm} to $(1 - f_{V,sp})$ ratios calculated from k_{pm} (Table 3.4) and average $f_{V,sp}$ (Table 3.5) are given in Table 4.1. The decrease in k_{pm} between Fe–2.25Cr and Fe–9Cr is seen to correlate well with the increase in $f_{V,sp}$. However, the large drop in k_{pm} between iron and the binary alloys cannot be attributed solely to a simple reduction of diffusional cross-section due to spinel particles. An additional factor must be at work, which could not be identified using the present results.

In the case of the 9Cr ternary alloys, the inner layer had a very fine microstructure and appeared to contain at least three phases (in addition to the pores), as

Table 4.1 – Parabolic rate constant (as defined in Eq. (3.1)) relative to volume fraction of FeO in inner layer at 800 °C.

	k_{pm} (10^{-3} mg^2 cm^{-4} s^{-1})	$f_{V,sp}$	$\frac{k_{pm}}{1-f_{V,sp}}$
Fe	28	0	28
Fe–2.25Cr	5.6	0.10	6.2
Fe–9Cr	4.3	0.32	6.3

shown in Figs. 3.25 and 3.26. The dark grey phase was seen by EDS to be chromium-rich, and its volume fraction was measured (by image analysis of micrographs such as those shown in Figs. 3.25(a) and 3.26(a)) as 0.55 and 0.22 for Fe–9Cr–10Ni and Fe–9Cr–20Ni, respectively, after exposure to dry CO_2. Here again, compositions and volume fractions are related through the mass balance. To proceed, additional information must be obtained either from a phase diagram of the Fe–Cr–Ni–O system, or from experimental, quantitative chemical analysis of the phases present in the inner layer, neither of which were available. Analysis by XRD showed that the inner layer contained both FeO and spinel oxides, and the presence of nickel in the light grey regions in Figs. 3.25 and 3.26 was evidenced by EDS analysis. It is reasonable to assume that nickel was contained in a ferrite-type spinel oxide of general formula $Ni_xFe_{3-x}O_4$.

In a study of Fe–Cr–Ni alloy oxidation in O_2 at 1000 °C, Croll and Wallwork [168] noted that the substitution of nickel for iron in the alloys at constant chromium levels resulted in reduced scaling rates. The major constituent of the scales was FeO at low nickel concentrations, $Ni_xFe_{3-x}O_4$ for alloys with more than 2 wt. % Ni, and stoichiometric $NiFe_2O_4$ for more than 40 wt. % Ni. The reduced oxidation rates were attributed to lower cation diffusivities with increasing Ni content in the oxide. Thus, it appears that in the present case, while FeO was always formed in the inner layer, diffusional blocking was provided by both Cr- and Ni-containing oxides. Accordingly, outward iron fluxes did not depend solely on Cr-rich oxide volume fractions, but also decreased with $Ni_xFe_{3-x}O_4$ volume fractions. The latter could not be measured, but are expected to increase with increasing alloy nickel concentration. It is also recognised that nickel dissolves, to some extent, in FeO — the solubility of nickel in FeO, in contact with Fe–Ni alloy and Fe–Ni spinel, has been measured to be less than one atom percent in the temperature range 800–1100 °C [169, 170]. The concentration of nickel in the FeO matrix of the inner scale formed on the 9Cr ternary alloys could not be measured, but the presence of nickel would affect the oxide diffusion properties [171].

Evidence for a reduction of the iron flux is available from a comparison of the 9Cr alloys oxidation behaviour. In dry CO_2, Fe_3O_4 was present as islands at the surface of the scale grown on Fe–9Cr, whereas it formed a continuous layer in the case of the ternary alloys (Fig. 3.22), reflecting an oxygen enrichment relative to iron, that is, a decrease in iron activity at the oxide/gas interface. Since the reacting gas was the same for all alloys, the surface reaction rate was also fixed, and the decrease in a_{Fe} must have resulted from a decrease in the iron flux. Despite the formation of a continuous Fe_3O_4 layer, the Fe–9Cr–10Ni alloy reacted according to linear kinetics in Ar–20CO_2, with a rate similar to that of iron and the binary alloys (Table 3.4). It is concluded that this alloy was in an intermediate situation, at the transition from surface to diffusion control. With 20Ni in the alloy, diffusion was further slowed, and parabolic kinetics were achieved (Fig. 3.16).

In the presence of H_2O(g), both ternary alloys reacted according to approximately parabolic kinetics (Fig. 3.16). Again, the transition from surface to diffusion control observed for Fe–9Cr–10Ni was most certainly due to an acceleration of the surface reaction, caused by H_2O additions. This could not affect the nature of the reaction kinetics of the Fe–9Cr–20Ni alloy, since diffusion was the rate-limiting step in all gases. Nevertheless, the faster surface reaction did have an effect for both alloys. The absence of Fe_2O_3, in both cases, reflects a metastable state of high iron activity at the Fe_3O_4/gas interface. As in the case of FeO grown on iron (see Section 4.1.1), a faster surface reaction results in a reduced surface iron activity, which then tends toward the value defined by the Fe_3O_4/Fe_2O_3 equilibrium. As shown in Fig. 4.8, since a_{Fe} is fixed by the FeO/Fe_3O_4 equilibrium at the bottom of the Fe_3O_4 layer, a decrease in a_{Fe} at its surface produces an increased iron activity gradient. For each of Fe–9Cr–10Ni and Fe–9Cr–20Ni, as a continuous Fe_3O_4 layer was formed, the flux of iron traversing the FeO layer, j_2, is determined by the a_{Fe} values at the inner scale/FeO and FeO/Fe_3O_4 interfaces. This flux is then expected not to vary from dry to wet CO_2. Instead, the increased iron activity gradient across Fe_3O_4 results in a faster growth rate of Fe_3O_4 *relative to that of FeO*: as j_3 increases but j_2 is fixed, the flux j_2' corresponding to the $FeO \rightarrow Fe_3O_4$ reaction must decrease, as represented in Fig. 4.8. Accordingly, for each alloy, the proportion of Fe_3O_4 increased from Ar–20CO_2 (Fig. 3.22) to Ar–20CO_2–H_2O (Fig. 3.23). In addition to the line of argument proposed here, which focuses on the influence of a faster surface reaction in wet CO_2, it is recognised that the presence of H_2O could also affect the transport properties of Fe_3O_4, as shown by Ueda et al. [49].

Values of the parabolic rate constants measured for the 9Cr alloys in Ar–20CO_2–20H_2O decreased with increasing alloy nickel concentration (Table 3.4), in agreement

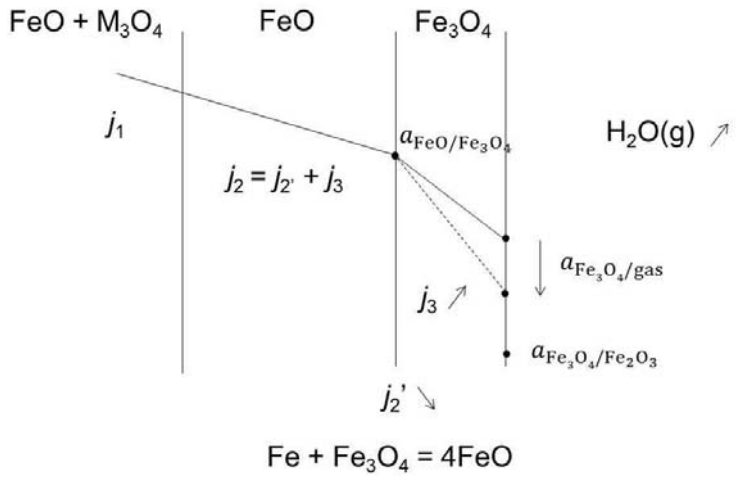

Figure 4.8 – Schematic representation of iron flux in scale growing under diffusion-control, with increasing surface reaction rate.

with the concept of diffusional blocking. This was accompanied by an increase in the proportion of Fe_3O_4 in the outer scale (Fig. 3.23), also indicative of a reduction of the iron flux. Here again, the absence of Fe_2O_3 at the scale surface reflects a metastably high iron activity, due to the slow surface reaction, relative to the iron flux j_3. With increasing nickel concentration in the inner scale, j_1, and therefore j_2, are reduced. This is accomodated by relative growth of the Fe_3O_4 layer, through reduced FeO growth at the FeO/Fe_3O_4 interface, which corresponds to a decrease in j_2'.

4.2.2.2 Reaction at 650 °C

The influence of alloy and gas composition on the oxidation behaviour of low chromium alloys at 650 °C can only be studied in an approximative manner. As already mentioned, experimental variability limits the use of weight gain kinetics. Furthermore, partial spallation of the outer layers was substantial at this temperature, and it was sometimes difficult to determine whether some oxide was absent because it had spalled, or because it had not been formed at all (see for example Fig. 3.4).

The gas H_2O content had no visible effect on the reaction at 650 °C, either in terms of oxidation kinetics (Fig. 3.1) or scale constitution (Fig. 3.4). In Ar–20CO_2, approximately parabolic kinetics together with the presence of a continuous Fe_2O_3 layer at the scale/gas interface indicate that diffusion was rate-limiting, and that the scale/gas interface was in thermodynamic equilibrium. Thus, a change in the surface reaction rate could not alter the boundary activities, and therefore the rate

of oxide formation.

Oxidation rates were seen to decrease with increasing chromium and nickel concentration in the alloys (Table 3.2), with one exception: Fe–2.25Cr reacted slower than did Fe–9Cr. The scale constitution was, for all alloys, similar to that represented in Fig. 4.7, except that Fe_2O_3 was formed at the scale surface, and FeO was suppressed in the case of the ternary alloys. Thus, it is tentatively concluded that the description proposed for reaction at 800 °C also applies to the lower temperature. The substitution of chromium and nickel for iron in the alloys led to an enrichment of these alloying elements in the inner scale, in the form of low diffusivity oxides, which in turn reduced the outward iron flux and led to a decrease in the oxidation rate. No explanation could be found for the abnormally slow reaction of Fe–2.25Cr.

4.2.3 Oxidation rate of high chromium alloys

The morphology of the oxides formed as a result of breakaway of the high chromium alloys was characterised by a greater diversity and a higher degree of complexity than that of the scales observed on dilute alloys. Both the transient and steady-state stages of nodule development (that is, stages preceding the establishment of a continuously thick oxide scale) have received little attention from other investigators, presumably because these stages are short-lived at high temperatures. The mechanism of nodule growth are examined in detail in Chapter 6.

After reaching a certain size, the nodules grown on the high chromium alloys assumed a steady-state morphology: the relative amounts of oxide phases did not vary with nodule size, and part of the nodules, near their centre, was flat-topped (see Figs. 3.45(a), 3.57, 3.63(a), 3.74(d)). The nodules then consisted of an outer region of iron oxides, and of an inner part containing mixed oxides. Oxide growth rates may therefore be viewed in light of inner nodule compositions, as in the case of the dilute alloys.

4.2.3.1 Reaction at 650 °C

During reaction at 650 °C, nodule development proceeded by continuous nucleation and growth, until the surface coverage was complete ($\theta = 1$). Consequently, as long as nodules observed on a given specimen had varying thicknesses, the kinetics of nodule thickening could not be established by considering average values. Instead, maximum thicknesses were measured. Given the large variability in nodule development, the degree to which measured values were representative was critically dependent on the sampling volume, that is, on the value of θ for a given speci-

men, and on the number of specimens considered (each corresponding to a different reaction time).

In the case of Fe–20Cr, thicknesses were obtained from four specimens reacted with each of the Ar–20CO_2, Ar–20CO_2–5H_2O and Ar–20CO_2–20H_2O atmospheres. Reaction in the wet gases almost exclusively produced uniformly thick Fe-rich scales, from the shortest reaction time ($t = 40$ h). In these conditions, average scale thickness provided a representative measure of the alloy scaling rate, and showed that growth kinetics were approximately parabolic (Fig. 3.65(a)).

As nodules do not necessarily nucleate at the beginning of the exposure, parabolic kinetics are best represented by the rate law

$$X^2 = 2k_\mathrm{p}\,(t - t_0) \tag{4.6}$$

where t_0 is the average time of nucleation, rather than Eq. (3.2) ($t_0 = 0$)[1]. For each specimen, only the thickest nodules were considered, which minimises the value of t_0. In fact, since nodules nucleate and spread continuously, the probability that the maximum thickness measured on a random cross-section is close to the maximum thickness for the entire specimen increases with increasing surface coverage. This absolute maximum includes nodules which nucleated earliest in the reaction, for which the error made in neglecting t_0 is minimum. For continuously thick scales, the error made in using a random cross-section vanishes. Accordingly, reaction of Fe–20Cr in wet CO_2 was well described using Eq. (3.2), that is, $t_0 = 0$ (Fig. 3.65(a)). Exposure of this alloy to dry CO_2 produced less favourable conditions, as the θ values were smaller. However, Eq. (3.2) was reasonably well adapted to the data, which shows that the surface coverage was sufficient for the average t_0 to be close to 0.

In addition to the effect of delayed nucleation, $t_0 > 0$, oxidation kinetics could, in principle, also be affected by the presence of a transient stage, characterised by a k_p value different from the steady-state one. Experimentally, the line of best fit to the $X = \mathrm{f}\left(t^{1/2}\right)$ plot crossed the X axis at either positive or negative, but always small values. This shows that experimental scatter prevailed over any systematic effect. For this reason, Eq. (3.2) was used rather than Eq. (4.6).

For the other alloys, thickness measurement were carried out on two specimens per reaction gas. Furthermore, for the 20Cr ternary alloys, variability in the breakaway reaction was more important, and the θ values smaller, than for Fe–20Cr. These factors all impair the statistical value of the thickness measurements, which

[1] In Section 3.3.4, parabolic rate constants relative to nodule growth were denoted $k_{\mathrm{p,Fe-ox}}$, in order to avoid confusion between nodules and Cr_2O_3. The present Section deals with nodules only, and parabolic rate constants are simply written as k_p.

consequently did not constitute a sound basis on which to investigate the nature of the rate law associated with nodule growth, or the effect of gas composition. Nevertheless, assumptions can be made on the basis of the arguments advanced earlier for iron and the dilute alloys.

An essential outcome of this analysis was that, provided that the inner scale contained a sufficient amount of slow diffusivity (chromium and/or nickel) oxides, the rate-limiting step was diffusion in the inner layer, and kinetics were approximately parabolic, with a rate constant independent of gas composition. Since this was the case for the Fe–20Cr alloy, and the nodules formed on the other high chromium alloys were always thinner than those formed on Fe–20Cr, the hypothesis of diffusion-control is adopted for the other alloys. Accordingly, k_p values were determined by fitting data in $X = f\left(t^{1/2}\right)$ plots. The differences obtained, for each alloy, between dry and wet CO_2, were small, and attributed to experimental scatter.

The average k_p value for the 20Cr alloys is seen in Table 3.8 to decrease with increasing alloy nickel concentration. This was accompanied by the partial substitution of Ni-containing spinel for Fe-rich $Fe_{3-x}Cr_xO_4$ in the inner part of the nodules (see Section 3.3.3.3). The volume fraction of Ni-containing spinel was only roughly estimated in the case of Fe–20Cr–10Ni, and not studied for Fe–20Cr–20Ni. However, the argument made earlier for the 9Cr alloys is thought to apply here: diffusion is faster in the Fe-rich spinel than in the Ni-rich spinel, whose volume fraction is expected to increase with increasing alloy nickel concentration. The corresponding reduction in outward iron flux is expected to lead to decreased oxidation rates in a situation of diffusion-control.

The thick nodules formed on Fe–25Cr were morphologically similar to those grown on Fe–20Cr, but yielded smaller k_p values. Again, the volume fraction of Cr-rich spinel was not measured, but is expected to be higher in Fe–25Cr, which would account for the reduced growth rate. In addition, the Fe–25Cr alloy also formed scales of intermediate thickness, containing a Cr-rich inner scale, either of corundum or spinel type. According to Töpfer et al. [72], at low p_{O_2}, the diffusion coefficient of both iron and chromium decreases with increasing chromium content in the Fe–Cr spinel oxide. Cation diffusivities in the corundum solid solution, $Fe_{2-x}Cr_xO_3$, do not seem to be available in the literature. However, diffusion in both Cr_2O_3 and Fe_2O_3 is relatively slow, as compared to spinel phases. Consequently, whether the Cr-rich layer present at the base of the scale was of corundum or spinel type, it provided a relatively good diffusion barrier, as compared to the inner layer of the thick nodules, which contained some Fe-rich spinel.

Although the 25Cr ternary alloys formed some oxide nodules in addition to

Cr_2O_3, their size and surface coverage were much lower than for the other alloys (Fig. 3.35). The constitution of these nodules was not studied, as none could be found in the cross-sections prepared. Nonetheless, as separate additions of chromium or nickel to the Fe-20Cr alloy each resulted in slower scale growth, it may be assumed that simultaneous additions of both caused further reductions in the growth rate, so that nodule development was drastically limited.

4.2.3.2 Reaction at 800 °C

The kinetics of nodule growth at 800 °C were not examined in detail. Growth rates on the different alloys are compared in a qualitative manner, using the maximum thicknesses measured after 100 h exposure, given in Table 3.9. As discussed earlier, the non-uniform nature of nodule development requires the results to be regarded with caution.

The case of Fe–20Cr reaction in Ar–$20CO_2$–$20H_2O$ is unique in the present set of results. Long term (100 h) exposure resulted in almost complete coverage of the specimen surface by Fe_2O_3, as shown in Fig. 3.68. However, this was accompanied by dramatic variations in oxide morphology, from Cr_2O_3 covered by an extremely thin Fe_2O_3 layer, to thick multilayer nodules (Fig. 3.74). As the fraction of thick nodules was quite small, the maximum thickness is only weakly correlated to the alloy scaling rate, and the relatively small value given in in Table 3.9 may lead to an underestimation of the actual rate.

In the case of the other alloys, chromium and nickel additions resulted in decreased nodule thicknesses. Nickel was seen to be included in the nodules formed on Fe–25Cr–20Ni, but the oxide composition was not examined for the other alloys. Nevertheless, the general nodule morphology was quite similar to that typical of reaction at 650 °C, and the observation of decreasing thicknesses with chromium and nickel additions is in agreement with the diffusional blocking description.

4.2.4 Overall comparison

A summary of the rate constants measured for the growth of multilayer Fe-rich oxide at 650 and 800 °C is presented in Fig. 4.9. The diagrams represent parabolic rate constants, k_p, reflecting the influence of alloy composition on cation diffusion in the scale, and were constructed using

- for low chromium alloys at 650 °C: the average of dry and wet CO_2 reaction rates, measured gravimetrically (Table 3.2);

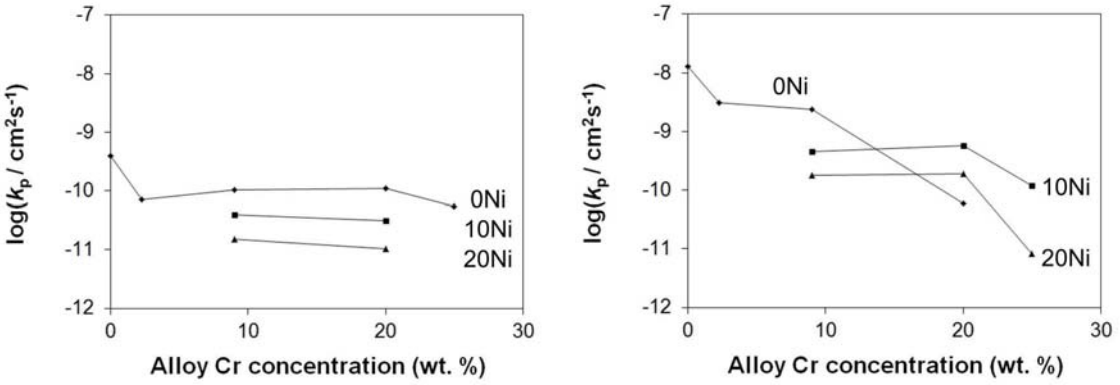

(a) 650 °C (b) 800 °C

Figure 4.9 – Growth rate of iron-rich multilayer oxide as a function of alloy composition (see text for details concerning the determination of k_p values).

- for low chromium alloys at 800 °C: gravimetric data for reaction in Ar–20CO_2–20H_2O (Table 3.6);
- for high chromium alloys at 650 °C: the average of dry and wet CO_2 reaction rates, determined from maximum thicknesses (Table 3.8);
- for high chromium alloys at 800 °C: the average of dry and wet CO_2 reaction rates, determined from maximum thicknesses (Table 3.9, maximum thicknesses were converted to k_p values assuming parabolic kinetics).

The overall evolution of the oxide growth rate was similar for both reaction temperatures. A remarkable observation is that at a given nickel concentration in the alloy, the rate constant of 20Cr alloys was not significantly different from that of 9Cr alloys (the k_p value for Fe–20Cr at 800 °C is likely underestimated, as discussed earlier). Overall, nickel proved more efficient than chromium in providing an effective diffusion barrier in the inner scale. Only when the chromium level was increased to 25 wt. % did a further reduction in rate become apparent. A similar observation was made by Croll and Wallwork [168], in a study of Fe–Cr–Ni alloys reaction in oxygen at 1000 °C. Of course, this concerns the post-breakaway oxidation rates only. A comparison of the general oxidation resistance also requires the kinetics of nodule nucleation to be considered; this is addressed in Chapter 6.

4.3 Summary

The main results obtained in the present Chapter are briefly recapitulated. The study of iron reaction provided a simple basis on which iron oxide growth in dry

and wet CO_2 could be examined. In particular, the role of the oxide/gas interfacial reaction and of iron diffusion in FeO in determining the reaction kinetics was highlighted. Iron diffusion in FeO was fast at the temperatures of interest, 650 and 800 °C. Consequently, in dry CO_2, the relatively slow surface reaction led to linear oxidation kinetics. The rate of the surface process (adsorption and oxide formation) was increased by H_2O(g) additions. This caused an increase of the oxidation rate, and a transition to diffusion controlled, parabolic kinetics. No influence of CO_2 and H_2O on iron diffusion in FeO was visible from the present results.

Uniformly thick oxide scales formed on the dilute alloys from early reaction times, and on high chromium alloys as a result of nodule development, had a morphology typical of non-selective oxidation of chromium in Fe-base alloys. The presence of chromium- and nickel-containing spinel oxides in the inner scale layer slowed down diffusion by reducing the effective diffusional cross-section, but not only. In particular, the large drop in oxidation rate observed between pure iron and the Fe–2.25Cr alloy at 800 °C could not be accounted for on the basis of this simple geometric argument, and must have instead involved another factor, yet to be determined. Nevertheless, the replacement of iron oxide by mixed spinel phases reduced the effective cation diffusivity in the inner scale layer, which favoured the transition to diffusion controlled kinetics. Once parabolic kinetics were achieved, increasing the alloy chromium and nickel contents resulted in decreased oxide growth rates.

Chapter 5

Carburisation

Exposure to dry and wet CO_2 was sometimes seen to result in carburisation of the metal substrate. Different reaction types were observed: extensive or limited carbide precipitation at 650 °C (Sections 3.1.5 and 3.3.3), carbide and martensite precipitation at 800 °C (Section 3.2.5); all providing evidence of carbon ingress in the alloy. The observation of attack by carbon in CO_2-rich atmospheres is consistent with results available in the literature, summarised in Section 1.5.2.4.

As noted in Section 1.5.1, CO_2–rich gas mixtures are not carburising with respect to iron and chromium. This statement emerges from a simple thermodynamic consideration: the equilibrium carbon activity in the gas, $(a_C)_{gas} \simeq 10^{-15}$ in the conditions of interest (see Section 2.2), is lower than that required to form carbides. The latter value varies with both temperature and alloy composition, but the order of magnitude 10^{-3}–10^{-4} is relevant to the present study (Fig. 1.17): the difference from $(a_C)_{gas}$ is very large. Hence, it appears that the carbon activity at the metal surface must have been much higher than that in the gas. As mentioned in Section 1.5.5, this apparent contradiction was identified by previous investigators, and explanations of different nature were proposed. In particular, it appears that the contradiction can be solved from simple thermodynamic considerations. Elaborating on this argument, a quantitative description of the conditions leading to carburisation is proposed in Section 5.1. This model is subsequently tested using experimental results.

5.1 Model for the establishment of carburising conditions

Several descriptions [13,14,19,20,129], which are thermodynamically equivalent but mechanistically different, have been proposed to account for the generation of a carburising environment within oxide scales grown in CO_2. However, a quantitative description of the carbon supersaturation developed in the alloy, relative to the gas, has been lacking.

5.1.1 Presentation of the model

As mentioned earlier, the conditions established within a growing oxide scale may differ markedly from those prevailing in the gas. Indeed, provided that the scale is (i) sufficiently compact and adherent to constitute a physical barrier separating the metal from the atmosphere, and (ii) thick enough to be considered in local thermodynamic equilibrium, then the oxygen activity within the scale varies between its

ambient value at the oxide/gas interface, and the dissociation pressure of the oxide at the metal/oxide interface (see Fig. 5.1). If, in addition, the scale transmits C-

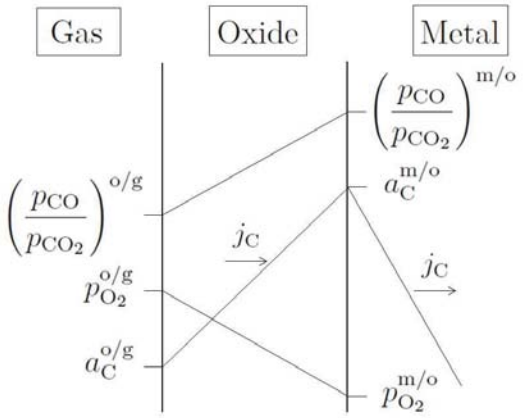

Figure 5.1 – Schematic representation of activities in a growing oxide scale. The superscripts o/g and m/o refer to the oxide/gas and metal/oxide interface, respectively, and j_C indicates a carbon flux.

bearing species (CO and CO_2), low values for p_{O_2} result in high values for p_{CO}/p_{CO_2}, and therefore for a_C, as is shown subsequently. The phase constitution and composition of the growing scale control the establishment of chemical potential gradients and resulting driving forces, while its transport properties limit the availability of the molecular species at the metal/oxide interface.

The driving force for carbon transport from the gas to the metal might appear unclear, as the carbon activity gradient across the scale is oriented in the opposite direction. However, the carbon activity may vary in the metal phase, between its surface and its interior. In situations where the bulk carbon concentration is such that $a_C^{m/o} > a_C^{bulk}$ — in particular when the alloy originally contains virtually no carbon, as it is the case here — the resulting gradient constitutes a driving force for carbon diffusion toward the interior of the metal phase, and consequently for "uphill" transport across the scale, as shown in Fig. 5.1.

5.1.2 Mechanistic description

A possible mechanistic description of the reacting system is proposed here. It is assumed that local thermodynamic equilibrium is achieved across the scale, and at the metal/oxide interface. Although large cracks are sometimes observed, it is assumed that these macroscopic defects do not constitute continuous pathways for gas access to the metal substrate — specific zones where a large crack is present or

spallation occurred are disregarded.

As discussed in Section 1.5.4, carbon transport in oxide scales has been subject to investigation by several authors, but the mechanism remains unclear. Solid-state diffusion is not possible, and carbon transport must instead involve molecular species, for example in nanochannels or along internal surfaces such as triple joints. In the present work, the external atmospheres contained Ar, O_2, CO, CO_2, H_2 and H_2O gas species. Since mass transport across growing scales is driven by electrochemical potential gradients, it is assumed that all species except the inert argon may migrate toward the metal/oxide interface. Let us then consider a system containing metal, oxide, and the molecular species O_2, CO, CO_2, H_2 and H_2O, where the oxygen activity is defined by the metal–oxide equilibrium.

In the conditions of interest, the oxide layer in contact with the metal substrate is always, to some degree, porous. Porosity was observed as part of the present work in Fe-rich and Cr-rich oxides, formed on the low and high chromium alloys, in dry and wet CO_2, at 650 and 800 °C. This is visible in many of the micrographs shown in Chapter 3; particular examples include Figs. 3.5, 3.24, 3.47 or 3.73. The degree of porosity observed from metallographic cross-sections, which was in many cases significant, could in fact have been underestimated, as polishing tends to fill the pores. It is then reasonable to consider that, whether connected or not, some pores were present at the metal/oxide interface. Interfacial porosity was also reported by previous investigators (see Sections 1.5.2.3 and 1.5.5).

As a consequence, the notional system introduced above may be taken to correspond, in practical terms, to an interfacial cavity, where the molecular species would form a gas phase. This conveniently justifies the use of gas phase equilibria to describe the system's thermodynamics. If both metal and oxide are instead strictly compact and adherent, it may be necessary to use different reactions to describe the interfacial equilibrium (thermodynamic states would have to be redefined), depending on the size of the oxide defects which contain the molecular species. In practical terms, a question of interest would be, *are the thermodynamics of a small number of molecules contained in a nanosized defect (e.g. triple joint) equivalent to those of a gas of the same composition ?* This question will not be addressed here.

In view of the assumptions made so far, a schematic representation of mass transport across the growing scale is proposed in Fig. 5.2. The molecular species first adsorb on the scale surface, then migrate across the scale in an adsorbed state, along an extended lattice defect such as a triple joint, and desorb in the interfacial cavity. The concentration of a component X in the adsorbed state at the scale surface is determined by its partial pressure in the external atmosphere, and by

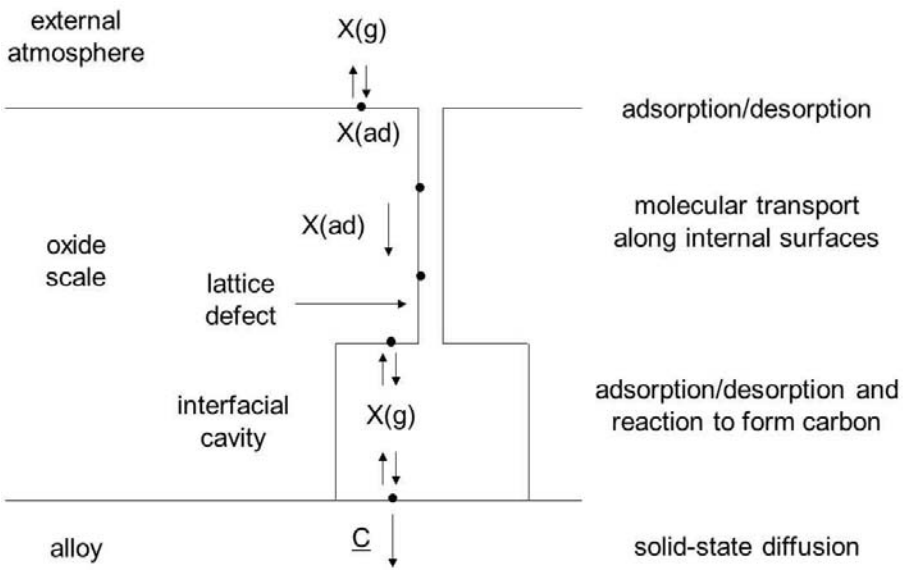

Figure 5.2 – Schematic representation of mass transport across a growing oxide scale, where X = O_2, CO, CO_2, H_2, H_2O. Emphasis is put on carbon, and the case of hydrogen is diregarded.

a selectivity coefficient [172]. Concentrations vary along the defect so as to reflect local equilibrium in the oxygen activity gradient, although it is questionable whether gas phase or another type of equilibria is to be considered, as mentioned above. Thermodynamic equilibrium in the interfacial cavity is now addressed.

5.1.3 Thermodynamic description

The thermodynamics of the metal–gas–oxide system defined above (interfacial cavity in equilibrium) are described as follows. Equilibrium between carbon and oxygen is represented by the reactions

$$CO_2 = CO + \frac{1}{2}O_2 \tag{5.1}$$

$$2\,CO = C + CO_2 \tag{5.2}$$

where O_2, CO and CO_2 are in a gas state. The case of carbon is different, since it does not form a pure gas. Let us examine practical situations. When the carbon potential is high (high p_{CO}/p_{CO_2} ratio and/or high pressure), as in metal dusting atmospheres, reaction (5.2) is often too slow for the flowing gas to reach equilibrium. Carbon is produced as a pure solid phase (graphite), but the gas remains "supersaturated in carbon", ie p_{CO}/p_{CO_2} remains higher than its equilibrium value. At low carbon potentials, carbon is produced as a dissolved species in the metal substrate. In order to define a carbon activity in these particular conditions, it is convenient

to introduce a virtual state of carbon, noted C(v), equivalent to a gas state. The symbol a_C is used to denote the activity of C(v) relative to carbon graphite (standard state, $a_{graphite} = 1$). The law of mass action of the Boudouard reaction is then written

$$K_{5.2} = \frac{a_C p_{CO_2}}{p_{CO}^2} \tag{5.3}$$

If, given the gas composition and pressure, Eq. (5.3) yields $a_C > 1$, then graphite precipitates

$$C(v) = C(graphite) \tag{5.4}$$

with, of course, $a_C = 1$ in the solid phase, but if the reaction is relatively slow, a_C possibly remains higher than unity: this is the sense of a "gas saturated in carbon". If the calculated value is lower than one, carbon dissolves in the metal phase

$$C(v) = \underline{C} \tag{5.5}$$

and, with the formalism introduced here, it is possible to describe this equilibrium using an equation equivalent to Sievert's law for gases

$$N_C = K_{5.5} a_C \tag{5.6}$$

where the symbols have their usual meaning.

The oxygen potential is defined by the metal–oxide equilibrium,

$$a\,M + \frac{b}{2}\,O_2 = M_aO_b \tag{5.7}$$

where M represents one or several oxide-forming elements. The p_{CO}/p_{CO_2} ratio is determined by the value of p_{O_2} (the dissociation pressure of the oxide),

$$\frac{p_{CO}}{p_{CO_2}} = \frac{K_{5.1}}{p_{O_2}^{1/2}} \tag{5.8}$$

where $K_{5.1}$ is the equilibrium constant for reaction (5.1). This ratio depends only on the nature of the oxide, alloy composition and temperature. The carbon activity can be determined from the Boudouard reaction equilibrium, as

$$\begin{aligned} a_C &= K_{5.2}\frac{p_{CO}^2}{p_{CO_2}} \\ &= K_{5.2}\frac{p_{CO}}{p_{CO_2}} p_{CO} \end{aligned} \tag{5.9}$$

It is important to note that describing the formation of carbon via the syngas reaction,

$$CO + H_2 = C + H_2O \tag{5.10}$$

yields an equivalent expression. Using the law of mass action for the syngas reaction, a_C is written

$$a_C = K_{5.10}\frac{p_{CO}p_{H_2}}{p_{H_2O}} \tag{5.11}$$

In the same way as for the carbon-bearing species, the p_{H_2}/p_{H_2O} ratio is determined by the oxygen activity, via

$$H_2O = H_2 + \frac{1}{2}O_2 \tag{5.12}$$

with

$$\frac{p_{H_2}}{p_{H_2O}} = \frac{K_{5.12}}{p_{O_2}^{1/2}} \tag{5.13}$$

which is rewritten, using Eq. (5.8),

$$\frac{p_{H_2}}{p_{H_2O}} = \frac{K_{5.12}}{K_{5.1}}\frac{p_{CO}}{p_{CO_2}} \tag{5.14}$$

Substituting Eq. (5.14) into Eq. (5.11), one obtains

$$a_C = \frac{K_{5.10}K_{5.12}}{K_{5.1}}\frac{p_{CO}^2}{p_{CO_2}} \tag{5.15}$$

Noting that the Boudouard reaction is equivalent to a linear combinaison of the syngas reaction and the reactions of decomposition of CO_2 and H_2O: (5.2) $\Leftrightarrow$ (5.10) + (5.12) − (5.1), it follows that

$$K_{5.2} = \frac{K_{5.10}K_{5.12}}{K_{5.1}} \tag{5.16}$$

and Eq. (5.11) is seen to be equivalent to Eq. (5.9).

The physical significance of these equations is twofold: (i) if the species O_2, CO, CO_2, H_2 and H_2O are present at the metal/oxide interface, the carbon activity may be defined in equivalent manners using two sets of variables, either $\{p_{CO}, p_{CO_2}\}$ with Eq. (5.9) or $\{p_{CO}, p_{H_2}, p_{H_2O}\}$ with Eq. (5.11); (ii) given that the metal–oxide equilibrium defines p_{O_2}, and, in turn, the p_{CO}/p_{CO_2} and p_{H_2}/p_{H_2O} ratios, one degree of freedom remains. This corresponds to the variable p_{CO} in Eqs. (5.9) and (5.11).

Given that Eq. (5.11) does not apply to dry CO_2 (that is, external atmospheres such as Ar–20CO_2), Eq. (5.9) is used here. Furthermore, in order to emphasise the physical reality of the system, it is convenient to rewrite Eq. (5.9) as

$$a_C = K_{5.2}\frac{b^2\beta}{1+b} \tag{5.17}$$

where $b = p_{CO}/p_{CO_2}$ is fixed, and $\beta = p_{CO} + p_{CO_2}$ now represents the degree of freedom. This parameter is a function of both the external gas composition and the

scale adsorption and transport properties. In the absence of any particular information, the value of β may be assumed to be equal to $p_{CO} + p_{CO_2}$ in the external gas: $\beta = (p_{CO} + p_{CO_2})_{ext} = 0.2$ atm for Ar–20CO_2, Ar–20CO_2–5H_2O and Ar–20CO_2–20H_2O. This simple choice reflects a neutral mass balance for carbon between the interfacial cavity and the external atmosphere. This hypothesis, together with the effect of selective adsorption is discussed in Section 5.2.1.1.

The value of b derives from the interfacial oxygen activity, which in turn is determined, for a given oxide constitution at the metal surface, from the thermodynamics of the metal–oxide system. The oxidation patterns observed in the present work are addressed separately in Section 5.1.4. As is shown in Section 5.2, determining interfacial carbon activities from experimental results (carburisation rates and carbide volume fractions) requires knowledge of the thermodynamics of the metal–carbide system. Both Fe–Cr–O and Fe–Cr–C phase diagrams were found to be available, while Fe–Cr–Ni–O and Fe–Cr–Ni–C could not be obtained. For this reason, the quantitative prediction of interfacial carbon activity is applied to the binary alloys only.

5.1.4 Calculation of the interfacial carbon activity

The oxide scales produced by reaction of the dilute Fe–Cr alloys (Fe–2.25Cr and Fe–9Cr), at both 650 and 800 °C, were equivalent with regard to metal/oxide equilibrium. In all cases, the layer in contact with the metal phase consisted of an $FeO + (Fe, Cr)_3O_4$ mixture. As mentioned in Chapter 4, $\log p_{O_2} - N_{Cr}$ diagrams in the Fe–Cr–O system calculated for $T = 627$ °C [71] (see Fig. 1.10) and 900 °C [165] indicate that the equilibrium p_{O_2} at the interface between such a mixture and the underlying alloy is the dissociation pressure of FeO on pure iron. In fact, p_{O_2} at the triple point α-(Fe,Cr)/FeO/$(Fe, Cr)_3O_4$ is slightly lower because dissolution of chromium in FeO stabilises the latter. However, this effect is neglected here and the p_{O_2} associated with the Fe−FeO equilibrium

$$Fe + \frac{1}{2} O_2 = FeO \tag{5.18}$$

is used to calculate the value of b for dilute alloys. Use of the equilibrium relationship

$$K_{5.18} = \frac{1}{p_{O_2}^{1/2}} \tag{5.19}$$

yields $b = K_{5.1} K_{5.18}$. Values of a_C calculated from Eq. (5.17) and thermochemical data tabulated in Ref. [74] are plotted in Fig. 5.3, along with a predominance diagram for Fe–9Cr. Phase boundaries in the Fe–9Cr–C system were calculated with

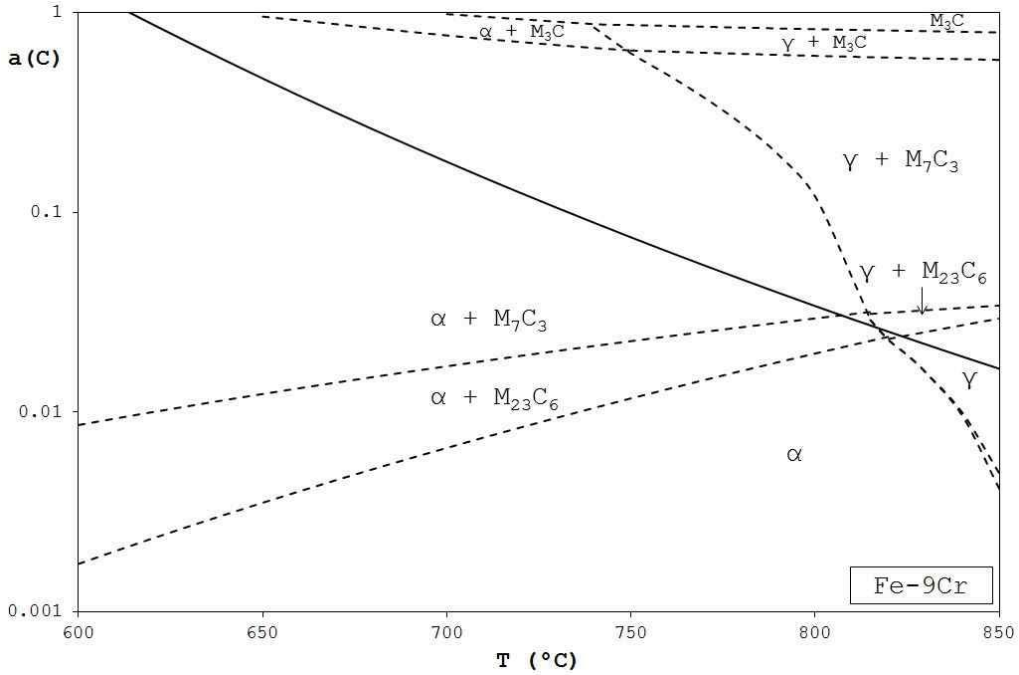

Figure 5.3 – Interfacial carbon activity from Eq. (5.17) (solid line) and predominance diagram from Thermo-Calc for Fe–9Cr (dashed lines).

the Thermo-Calc software and the TCFE4 database [58]. The calculated values are seen to exceed those required to form carbides at both 650 and 800 °C. Thus, if CO and CO_2 species can reach the metal/oxide interface in sufficient amounts for the condition $\beta = (p_{CO} + p_{CO_2})_{ext}$ to be met, the gas contained in the interfacial cavity is carburising with respect to Fe–9Cr.

During reaction at both 650 and 800 °C, the high chromium alloys, Fe–20Cr and Fe–25Cr, initially formed Cr_2O_3 according to

$$2\,Cr + \frac{3}{2}\,O_2 = Cr_2O_3 \tag{5.20}$$

with, at equilibrium,

$$K_{5.20} = \frac{1}{(\gamma_{Cr} N_{Cr})^2\, p_{O_2}^{3/2}} \tag{5.21}$$

In this case, $b = K_{5.1} K_{5.20} (\gamma_{Cr} N_{Cr})^2$. To proceed, the concentration and activity coefficient of chromium at the metal surface are required. As is evident from the a_C values eventually arrived at, rough approximations of N_{Cr} and γ_{Cr} are sufficient. Values of N_{Cr} measured by SEM-EDS after reaction at 650 °C were in the ranges (5–10) $\times 10^{-2}$ and (10–15) $\times 10^{-2}$ for Fe–20Cr and Fe–25Cr, respectively (see Section 3.3.3). For reaction at 800 °C, EPMA measurements were made in the case of Fe–20Cr only, yielding $N_{Cr} = 16 \times 10^{-2}$ (Fig. 3.75). Thus, the value $N_{Cr} = 10^{-1}$ is

chosen as representative of the metal/oxide interface for both alloys at both temperatures. Chromium activity coefficients were calculated as a function of alloy composition and temperature using Thermo-Calc. Values extrapolated to $N_{\mathrm{Cr}} = 0$ were found to be in reasonable agreement with reference data from Kubaschewski and Alcock [75] for γ_{Cr} in α-Fe (infinite dilution). Thus, the Thermo-Calc values for $N_{\mathrm{Cr}} = 10^{-1}$, $\gamma_{\mathrm{Cr}}\,(650) = 4.0$ and $\gamma_{\mathrm{Cr}}\,(800) = 2.7$, are used to calculate b. Finally, Eq. (5.17) yields $a_{\mathrm{C}} = 5.2 \times 10^4$ and 3.4×10^2 at 650 and 800 °C, respectively, both far above the activity required to stabilise graphite.

Following Cr_2O_3 failure, breakaway oxidation at both 650 and 800 °C produced multilayer Fe-rich oxide nodules and scales. Only steady-state stages of oxide development are considered here. In the case of reaction at 650 °C, the oxide constitution in contact with the metal phase was identified, for the thick nodules grown on Fe–20Cr and Fe–25Cr, as a mixture of Fe-rich and Cr-rich spinel phases, $Sp_1 + Sp_2$ (see Section 3.3.3). Again referring to the predominance diagram in the Fe–Cr–O system shown in Fig. 1.10, the phase boundary of interest is $\alpha + Sp_2/Sp_2$. The corresponding p_{O_2} depends on the metal and oxide interfacial compositions, and in order to calculate it, thermodynamic data are required for the temperature of interest, which were not found to be available. However, using the $\log p_{O_2} - N_{\mathrm{Cr}}$ diagram calculated for $T = 627$ °C [71] (Fig. 1.10), it is possible to find limiting values for p_{O_2} corresponding to stoichiometric compounds, for which equilibrium constants can be calculated for any temperature, from data in Ref. [74]. The oxygen activity is thus seen to vary between the values defined by the Fe−FeO and $Cr_2O_3 - FeCr_2O_4$ equilibria. In turn, these define limiting values for a_{C}: in the first case, a_{C} is the same as that calculated for the dilute alloys, and in the second case, the reaction of interest is

$$\mathrm{Fe} + \frac{1}{2}\,\mathrm{O_2} + \mathrm{Cr_2O_3} = \mathrm{FeCr_2O_4} \tag{5.22}$$

with

$$K_{5.22} = \frac{1}{\gamma_{\mathrm{Fe}} N_{\mathrm{Fe}} p_{\mathrm{O_2}}^{1/2}} \tag{5.23}$$

and $b = K_{5.1} K_{5.22} \gamma_{\mathrm{Fe}} N_{\mathrm{Fe}}$.

To proceed, it is necessary to know the concentration and activity coefficient of iron at the metal surface. The alloy composition was not measured experimentally, and it is quite difficult to predict, since it is affected by the composition of the scale, internal oxides and carbides, and the relative diffusivities in the metal phase (via chromium depletion). If N_{Fe} is taken to be that of the original alloy ($N_{\mathrm{Fe}} = 0.79$ for Fe–20Cr and 0.74 for Fe–25Cr), values of $\gamma_{\mathrm{Fe}} \simeq 1.1$ are calculated using Thermo-Calc. Finally, Eq. (5.17) yields $a_{\mathrm{C}} = 3 \times 10^2$ at 650 °C, again far above unity.

In the case of the thinner type of oxide formed on Fe–25Cr at 650 °C (termed healed scale in Section 3.3.3.2), and the thick nodules formed on Fe–20Cr at 800 °C, the oxide in contact with the metal phase was Cr-rich, either spinel or corundum type (composition and crystal structure varied with location). Although vague, this description can be used to define limiting conditions with the help of the predominance diagram, Fig. 1.10. If the oxide was a corundum type solid solution, $Fe_{2-x}Cr_xO_3$, it must have been almost pure Cr_2O_3 at the metal/oxide interface. Indeed, while a complete solid solution exists between Fe_2O_3 and Cr_2O_3 at relatively high p_{O_2}, the solubility of iron in the corundum oxide at the low p_{O_2} typical of metal–oxide equilibrium is very low, and should it be exceeded, $FeCr_2O_4$ would form. Thus the reaction of interest is given by Eq. (5.20), and leads to a_C values far above unity for both 650 and 800 °C.

Considering, instead, a Cr-rich spinel (Sp_2), the interfacial p_{O_2} could vary, depending on the local interfacial compositions, between the values defined by the Fe−FeO and $Cr_2O_3 - FeCr_2O_4$ equilibria, as detailed above. Carbon activities corresponding to the Fe–FeO equilibrium are the same as calculated for the dilute alloys (Fig. 5.3). In the case of the Cr_2O_3–$FeCr_2O_4$ equilibrium, the value $a_C = 3 \times 10^2$ was estimated above for reaction at 650 °C, and $a_C = 6.5$ is arrived at, making the same approximation for reaction at 800 °C.

The phase equilibria involving stoichiometric compounds and used to define limiting interfacial conditions, according to the different oxide morphological types observed, are summarised in Fig. 5.4. Corresponding values of a_C are given in Table 5.1. The validity of the proposed model is now tested against experimental

Table 5.1 – Interfacial carbon activities calculated from Eq. (5.17) and thermochemical data in Ref. [74].

Phase equilibrium	650 °C	800 °C
Fe−FeO	4.7×10^{-1}	3.4×10^{-2}
$Cr_2O_3 - FeCr_2O_4$	3.0×10^2	6.5
$Cr-Cr_2O_3$	5.2×10^4	3.4×10^2

results.

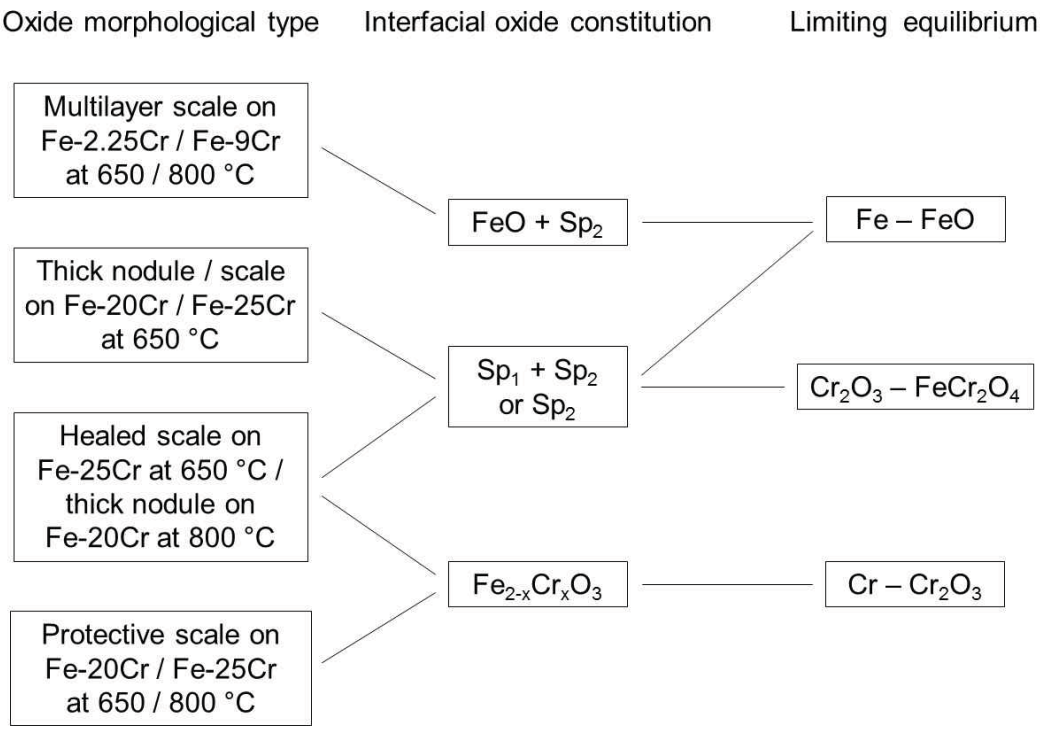

Figure 5.4 – Summary of limiting equilibria used to determine interfacial p_{O_2} according to the oxide morphological types observed on the binary alloys.

5.2 Reaction mechanism and interfacial carbon activity

The interfacial carbon activity is evaluated from experimental observations. In doing so, the carburisation mechanism corresponding to each particular reaction morphology is investigated. Carburisation rates and morphologies were seen in Chapter 3 to be drastically influenced by the nature of the oxide formed. A first distinction is made between Fe-rich oxide growth and protective scaling. In the former case, reactions at 650 °C and 800 °C are treated separately, as they led to different carburisation morphologies. The discussion is based on experimental results obtained for the Fe–9Cr and Fe–20Cr alloys, for which most information was available, and subsequently applied to the other alloys.

5.2.1 Extensive carburisation and Fe-rich oxide growth

5.2.1.1 Case of Fe–9Cr at 650 °C

According to the proposed model, Eq. (5.17) predicts carbon activities at the metal/oxide interface of oxidised alloys. However, the Fe–9Cr alloy produced both internal oxides and internal carbides, and the carburisation zone was not in contact with the metal/oxide interface (Fig. 3.11). Thus, predicted and experimental results apply to two distinct locations. In addition, the width of the carburisation zone is, a priori, affected by the inward movement of the oxidation front. Under certain conditions, the formalism developed by Meijering [19,173] to describe the simultaneous internal attack of dilute alloys by two oxidants may be used to overcome these difficulties.

The reaction morphology and schematic concentration profiles are depicted in Fig. 5.5. The two internal reaction zones are defined by the thermodynamic stability of the precipitates and the concentration of the oxidants. Essentially, as carbon diffusion in the metal is rapid, and carbon cannot react with the more stable chromium-rich oxide, the carbon concentration N_C in the metal matrix does not decrease significantly across the oxide precipitation zone. Thus, the value of a_C calculated for the metal/oxide interface can to a good approximation be applied at the interface between internal oxidation and internal carburisation zones (IOZ and ICZ). Furthermore, as the internal oxidation front advances, carbides are converted into oxides, and the carbon thus released diffuses inward to react with chromium at the carburisation front. Consequently, if the conversion is complete, the carburisation depth X_c can be defined from the interface between the IOZ and ICZ. The degree of carbide-to-oxide conversion increases along the p_{O_2} gradient, and at a given

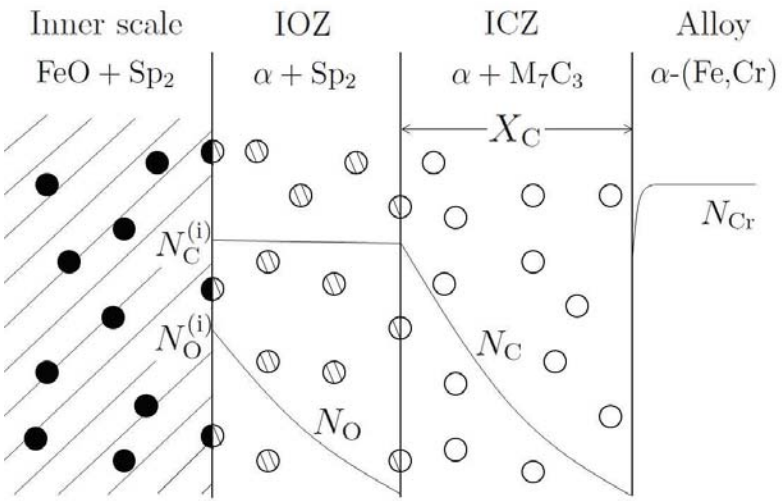

Figure 5.5 – Diffusion profiles during simultaneous reactions of oxygen and carbon with a dilute Fe–Cr alloy, after Ref. [19]. Symbols defined in text.

location in the reacting system, with increasing reaction temperature. In the case of Fe–Cr alloys reacted in CO_2, Fujii and Meussner [112] showed that conversion was complete at the IOZ/scale interface at 900 °C, and completed within the inner scale at 700 °C. Piron Abellan et al. [13] also reported an example of incomplete conversion within the inner scale after reaction at 550 °C. In the present case, TEM-EDS analysis after reaction at 800 °C (Fig. 3.32(b)) showed that the IOZ contained no carbon, and that the two precipitation zones were distinct. While no detailed result was obtained for reaction at 650 °C, it may be assumed that, whether in the IOZ or the inner scale, carbide conversion to oxide eventually reaches completion, and carbon is entirely released.

The carbon activity predicted from equilibrium at the Fe–9Cr metal/oxide interface is seen in Fig. 5.3 to exceed the value required to form M_7C_3 at 650 °C, thus qualitatively accounting for the observed carburisation. The quantitative success of the model is now tested by examining the amount of carbide formed.

Provided that local thermodynamic equilibrium is achieved throughout the carburisation zone, a diffusion path on the phase diagram can be used to define the compositions of coexisting phases and their mass fractions. Mass and volume fractions, f_m and f_V, are related through the densities of the phases. Although both metal matrix and carbides contained, as shown later, both iron and chromium, densities of pure compounds (Table 5.2) are used here for the sake of simplicity, iron and chromium having similar atomic weights. Image analysis of specimens reacted in Ar–20CO_2 and Ar–20CO_2–20H_2O showed that f_V values decreased with increasing relative depth, according to a profile which was independent of reaction time

Table 5.2 – Density of α-Fe and chromium carbides.

	ρ (g cm^{-3})	Reference
α-Fe	7.87	[174]
Cr_7C_3	6.92	[175]
$Cr_{23}C_6$	6.97	[175]

(see Fig. 3.15). The steady-state distribution of phases within the precipitation zone supports the hypothesis of local thermodynamic equilibrium. Accordingly, the Fe–Cr–C phase diagram shown in Fig. 5.6, constructed using Thermo–Calc and the TCFE4 database, is used to examine the local mass balance. In this isothermal

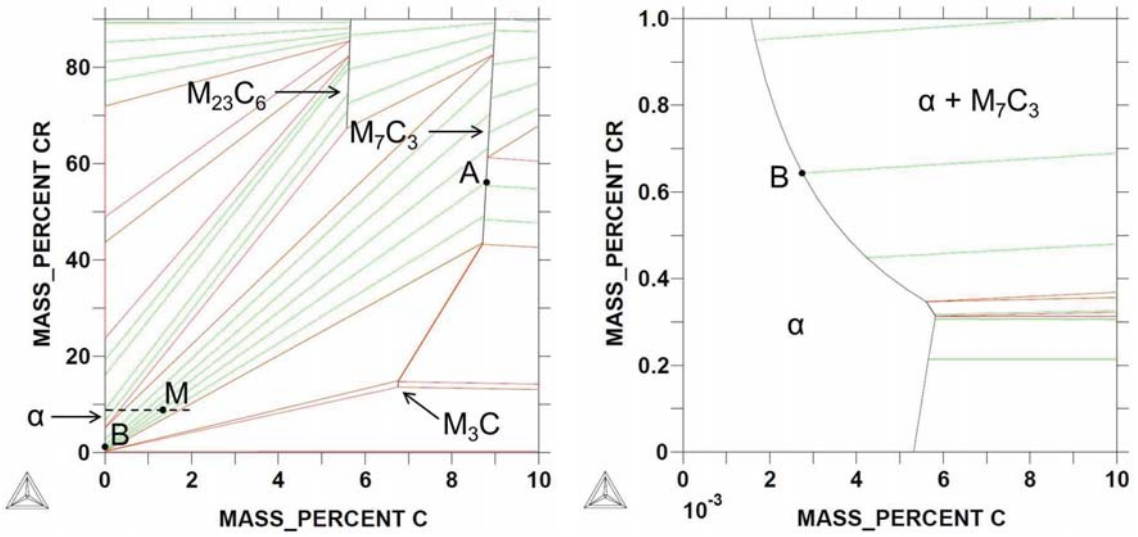

(a) Overall view (b) Fe-rich corner

Figure 5.6 – Isothermal section of the Fe–Cr–C phase diagram at 650 °C, calculated using Thermo-Calc. Points A, B and M are defined in text.

section, the points M, A and B represent the composition of the global metal + carbide mixture, the carbide precipitates and the metal matrix, respectively.

At 650 °C, the diffusion coefficients D_C [89,90] and D_{Cr} [81] in α-Fe are estimated as 2.4×10^{-7} and 5.6×10^{-14} cm^2 s^{-1}, respectively. Since $D_C \gg D_{Cr}$, chromium is assumed not to diffuse on a macroscopic scale, and the diffusion path lies along the dotted line in Fig. 5.6(a). This path cuts tie-lines at points corresponding to different f_m values. Expressed in terms of volume fraction, f_V, these range from 0 to 0.07 in the $\alpha + M_{23}C_6$ field and from 0.06 to 0.2 in the $\alpha + M_7C_3$ field. Experimental f_V values, shown in Fig. 3.15, thus indicate that the near interface region corresponds to M_7C_3 precipitation in ferrite, and the deeper region to $\alpha + M_{23}C_6$. Measured

volume fractions and XRD data (Fig. 3.12) are consistent and in agreement with the predicted reaction products.

Using the lever rule, a tie-line in the $\alpha + M_7C_3$ field corresponding to the volume fraction measured at the IOZ/ICZ interface is selected. This defines the carbon content of the metal matrix $N_C^{(i)}$. Thermodynamic data for the dissolution of carbon in α-(Fe,Cr), obtained from Thermo-Calc, are then used to calculate the local equilibrium carbon activity. The amount of carbide formed during reaction with Ar–20CO_2 and Ar–20CO_2–20H_2O is found in this way to correspond to $a_C = 0.43$ and 0.21, respectively. These values are to be compared with that calculated from metal/oxide equilibrium using Eq. (5.17), $a_C = 0.47$. This good agreement provides support for the validity of the proposed model.

Further confirmation is available from the carburisation rates. The observed parabolic kinetics (Fig. 3.14) indicate diffusion control, and the rate constant k_c is related to carbon permeability according to Wagner's equation [67]

$$k_c = \frac{N_C^{(s)} D_C}{\nu N_{Cr}^0} \tag{5.24}$$

where $N_C^{(s)}$ is the surface concentration of carbon in the metal matrix, ν the C/Cr ratio in the carbides, and N_{Cr}^0 the initial Cr mole fraction in the alloy. Diffusional blocking by the small equiaxed precipitates is ignored. In the presence of an external oxide scale, the surface concentration of carbon, $N_C^{(s)}$, is replaced by the interfacial value, $N_C^{(i)}$. For Eq. (5.24) to hold, (i) the condition $N_C^{(i)} D_C \gg N_{Cr}^0 D_{Cr}$ must be met, (ii) carbon must react with chromium but not iron, and (iii) the carbides must be sufficiently stable for both chromium and carbon concentrations in the metal matrix to be negligible throughout the precipitation zone. These conditions are now examined in light of the volume fraction measurements presented in Fig. 3.15.

Using an average value of 0.15 for f_V at x = 0 and the phase diagram of Fig. 5.6 yields $N_C^{(i)} = 8.6 \times 10^{-5}$. The carbon permeability is then calculated from D_C values in α-Fe [89, 90] as $N_C^{(i)} D_C = 4.0 \times 10^{-11}$ cm^2 s^{-1}. Standard data for D_{Cr} [81] lead to $N_{Cr}^0 D_{Cr} = 5.4 \times 10^{-15}$ cm^2 s^{-1}, and the condition $N_C^{(i)} D_C \gg N_{Cr}^0 D_{Cr}$ is satisfied. Volume fraction profiles together with the phase diagram indicate that both M_7C_3 carbides in the near-surface precipitation zone, and $M_{23}C_6$ carbides deeper in the alloy, contain large amounts of iron. Values of N_C range from 1.3×10^{-4} at $x = 0$ to 9.4×10^{-6} at $x = X_c$, while N_{Cr} ranges from 6.6×10^{-3} at $x = 0$ to 8.3×10^{-2} at $x = X_c$. The latter values are not negligible. Thus the conditions of pure chromium carbide formation and complete chromium precipitation are not met. Consequently Wagner's simplified Eq. (5.24), whilst providing good order of magnitude prediction of k_c, lacks the accuracy required for present purposes.

The present situation of partial precipitation is described by Ohriner and Morral [66], applying the lever rule to the matrix-precipitate two-phase field to more accurately reflect the mass balance underlying Eq. (5.24). This procedure was combined here with a numerical treatment of varying precipitate composition (defined in the phase diagram from f_V profiles), allowing $N_C^{(i)} D_C$ to be evaluated from k_c. Independently determined values of D_C [89, 90] then allow calculation of $N_C^{(i)}$, and a_C is determined from carbon dissolution equilibrium data using Thermo-Calc. The corresponding carbon activities are shown in Table 5.3, together with the values obtained from volume fraction measurements and those calculated from Eq. (5.17). Reasonable agreement between values obtained from the carburisation rate in Ar–

Table 5.3 – Interfacial carbon activities determined from experimental results for Fe–9Cr reaction at 650 °C.

	Experimental		Thermodynamic
Gas	from k_c	from f_V	equilibrium
Ar-20CO_2	0.25	0.43	0.47
Ar–20CO_2–5H_2O	0.16		
Ar–20CO_2–20H_2O	0.068	0.21	

$20CO_2$ and that calculated for metal/oxide equilibrium further supports the validity of the thermodynamic model.

Estimates of a_C arrived at from measurements of carburisation extent and rate are consistently lower than predicted from the local equilibrium model (Table 5.3). This may represent a systematic failure to image all carbide precipitates metallographically. The discrepancy is all the larger as the gas H_2O content is increased. This can be understood in terms of preferential uptake and/or transport of H-bearing molecules over C-bearing species. In Section 5.1.2, molecular transport across the scale was assumed to occur in an adsorbed state along internal oxide surfaces. Referring to this proposed mechanism, selective adsorption on the scale surface is expected to induce a composition in the adsorbed state, and at the metal/oxide interface, different from that prevailing in the gas. By partially excluding CO_2, the presence of H_2O would result in a decreased β value, and therefore in a decreased carbon activity. Qualitatively, the conclusion that selective uptake of H-bearing species decreases carbon penetration of an oxide is in agreement with suggestions of other investigators [13, 121, 125, 140] (see Section 1.7).

A quantitative evaluation of the H_2O ability to exclude carbon is made by rewrit-

ting Eq. (5.17)

$$a_{\mathrm{C}} = K_{5.2}\frac{b^2 p_{\mathrm{s}}}{(1+b)\left(1+\frac{\alpha}{\beta}\right)} \tag{5.25}$$

where $\alpha = p_{\mathrm{H_2}} + p_{\mathrm{H_2O}}$, and $p_{\mathrm{s}} = \alpha + \beta = p_{\mathrm{H_2}} + p_{\mathrm{H_2O}} + p_{\mathrm{CO}} + p_{\mathrm{CO_2}}$ (the small $p_{\mathrm{O_2}}$ value is neglected). The sum of partial pressures, p_{s}, is assumed to have the same value in the interfacial cavity as in the external gas. Thus selective adsorption is taken into account by considering its effect on the relative amounts of C- and H-bearing species, that is, on the α/β ratio. If α/β reflects the composition of the external atmosphere, the presence of H_2 and H_2O at the interface is compensated via a corresponding increase in p_{s}. If, on the other hand, α/β is higher than expected from the external gas composition, the a_{C} value is reduced, as compared to that obtained with a dry gas. An enrichment factor η is introduced as

$$\eta = \frac{\alpha/\beta}{\left(\frac{p_{\mathrm{H_2}} + p_{\mathrm{H_2O}}}{p_{\mathrm{CO}} + p_{\mathrm{CO_2}}}\right)_{\mathrm{ext}}} \tag{5.26}$$

where the subscript ext refers to the external atmosphere, to estimate the extent of selective adsorption. To avoid possible systematic experimental error while evaluating α/β, it is necessary to compare the a_{C} value obtained for Ar–20CO_2–5H_2O or Ar–20CO_2–20H_2O with that obtained for Ar–20CO_2 with the same method (f_{V} or k_{c}). Using the subscripts d and w to denote dry and wet CO_2, the ratio of a_{C} values is

$$\frac{(a_{\mathrm{C}})_{\mathrm{w}}}{(a_{\mathrm{C}})_{\mathrm{d}}} = \frac{(p_{\mathrm{s}})_{\mathrm{w}}}{(p_{\mathrm{s}})_{\mathrm{d}}}\frac{1+\left(\frac{\alpha}{\beta}\right)_{\mathrm{d}}}{1+\left(\frac{\alpha}{\beta}\right)_{\mathrm{w}}} \tag{5.27}$$

and since $\alpha = 0$ for dry CO_2, α/β for the wet gas is obtained from

$$\left(\frac{\alpha}{\beta}\right)_{\mathrm{w}} = \frac{(p_{\mathrm{s}})_{\mathrm{w}}}{(p_{\mathrm{s}})_{\mathrm{d}}}\frac{(a_{\mathrm{C}})_{\mathrm{d}}}{(a_{\mathrm{C}})_{\mathrm{w}}} - 1 \tag{5.28}$$

Values calculated from a_{C} given in Table 5.3 are plotted against $\left(\frac{p_{\mathrm{H_2}} + p_{\mathrm{H_2O}}}{p_{\mathrm{CO}} + p_{\mathrm{CO_2}}}\right)_{\mathrm{ext}}$ in Fig. 5.7. The enrichment ratio η is obtained as the slope of the curve, for each of the measurement method used to determine carbon activities (f_{V} or k_{c}). The agreement between the two methods is well within an order of magnitude, and values of $\eta \simeq 3 - 6$ are arrived at.

It must be recognised that the hypothesis made in estimating enrichment ratios, namely that H_2O additions result in constant p_{s} and varying α/β, is not only unverifiable, but also questionable. Indeed, with p_{s} equal to the sum of partial pressures in the external atmosphere, $\alpha/\beta > 1$ implies that $\alpha > (p_{\mathrm{H_2}} + p_{\mathrm{H_2O}})_{\mathrm{ext}}$. This represents not only an enrichment of H- over C-bearing species, but alo an enrichment of

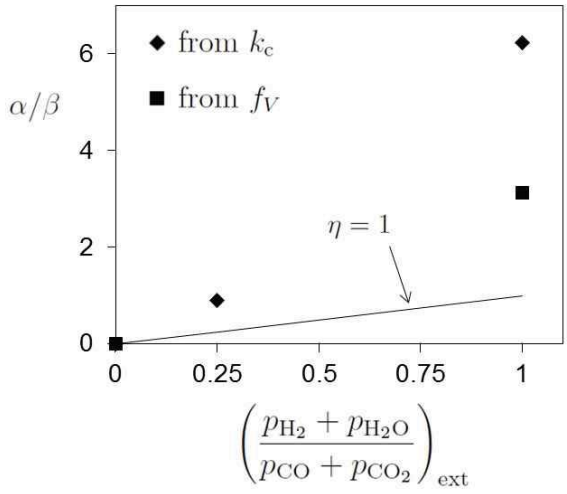

Figure 5.7 – Ratio of H-bearing species over C-bearing species at the metal/oxide interface against ratio in the external atmosphere, calculated from experimental carbon activities (variables defined in text).

H-bearing species at the interface, with respect to the external atmosphere. An alternative hypothesis would be that α is limited by the value of $(p_{H_2} + p_{H_2O})_{ext}$, and selective adsorption results in $p_s < (p_{H_2} + p_{H_2O} + p_{CO} + p_{CO_2})_{ext}$. An enrichment ratio would then be defined using the value of p_s obtained from a_C.

The difficulty of defining an enrichment ratio to estimate the effect of selective adsorption lies in the fact that, given the mechanistic description proposed here and summarised in Fig. 5.2, it is not possible to make a well-informed choice as to the additional condition needed to solve the degree of freedom problem contained in Eq. (5.17) or Eq. (5.25). Let us examine the two hypotheses made above, taking the example of a gas where $(p_{CO} + p_{CO_2})_{ext} = (p_{H_2} + p_{H_2O})_{ext} = 0.2$ atm, and enrichment of H-bearing species corresponds to $\alpha/\beta = 3$.

- $p_s = (p_{H_2} + p_{H_2O} + p_{CO} + p_{CO_2})_{ext}$. Here, $p_s = 0.4$ atm, and $\alpha/\beta = 3$ yields $\alpha = 0.3$ and $\beta = 0.1$. This condition corresponds to the replacement of some C (under the form of a CO–CO_2 mixture in proportions determined by the local p_{O_2}) with H (under the form of H_2–H_2O). In terms of adsorption, this would amount to a fixed number of adsorption sites, with a non-equivalent distribution of C-bearing and H-bearing species.
- $\alpha = (p_{H_2} + p_{H_2O})_{ext}$. Here, $\alpha = 0.2$ atm and $\alpha/\beta = 3$ yields $\beta = 0.067$ atm and $p_s = 0.267$ atm. This corresponds to a partial exclusion of CO/CO_2, with H_2/H_2O uptake maintained constant.

These two possible hypotheses are not consistent with each other, and neither can be considered satisfactory in the absence of a more precise mechanistic description

of the system. Defining an appropriate condition requires more information as to the scale physical and chemical properties with regard to adsorption, transport and saturation limtis (such as, for example, adsorption site densities) of the molecular species.

5.2.1.2 Application to reaction of other alloys at 650 °C

Fe–2.25Cr

Reaction of the Fe–2.25Cr alloy at 650 °C led to intergranular carburisation, but no intragranular carbides were observed (Fig. 3.10). The carbon activity calculated from thermodynamic equilibrium at the metal/oxide interface, $a_C = 0.47$ (Table 5.1), exceeds the value of 5.5×10^{-2} required to form M_7C_3 carbides in a Fe–2.25Cr alloy (calculated using Thermo-Calc). The driving force for carbide precipitation in this alloy is less than in Fe–9Cr, where a value of 1.2×10^{-2} is sufficient to stabilise M_7C_3 (see Fig. 5.3). The relatively low carbon supersaturation with respect to carbide formation is evident in preferential precipitate nucleation at grain boundaries. The qualitative implication of intergranular carburisation is nonetheless clear. Carbon enrichment at the metal/oxide interface relative to the gas has occurred, in agreement with the model.

Fe–20Cr

In regions covered by the multilayer, iron-rich oxide, intragranular carburisation of the Fe–20Cr alloy was extensive, and quite comparable to that observed in Fe–9Cr. The carbides formed in Fe–20Cr were elongated (Fig. 3.48), whereas those formed in the more dilute alloy were equiaxed. This morphological difference reflects the fact that a higher chromium content favours growth over nucleation of new precipitates. Similarly, carburisation depths were lower for Fe–20Cr, which could be expected from an elementary mass balance, as evident in Eq. (5.24). However, the reaction morphology and kinetics could also be affected by a change in carbon activity.

Carburisation rates were similar for reactions in dry and wet CO_2 (Fig. 3.49). Average values of $k_c = 8 \times 10^{-11}$ cm^2 s^{-1} and $f_V = 0.3$ yield $a_C = 0.01$ and 0.1, respectively, using the procedures described for the Fe–9Cr alloy. The difference between the two values is significant, although no evident reason for such a discrepancy is apparent. The value estimated via Eq. (5.24) from carburisation rates could possibly be in error. Indeed, the fact that extensive carburisation was never found in the absence of Fe-rich oxide, together with the observation that a number of early-stage nodules had no carbide beneath them, indicates that fast carbon ingress into the alloy started after protective scale breakdown, which did not necessarily

occur in the beginning of the reaction. The question as to how representative local carburisation kinetics might be therefore arises in exactly the same way as for local oxidation kinetics, which was discussed in Section 4.2.3.

After reaction in dry CO_2, carburisation depths were measured underneath the thickest nodules, in order to minimise the error. In the case of the wet gases, nodule coverage was nearly complete from short reaction times, which suggests that intense intragranular carburisation started not long after the beginning of the experiments. This view is supported by the fact that carburisation kinetics in all gases were well represented by a simple parabolic law (Fig. 3.49): if a rate law of the type $X_c^2 = 2k_c(t - t_0)$ had been used, the value of t_0 would have been found to be negligibly small, and thus the effect of this delay on the values of k_c insignificant in view of the experimental scatter.

The oxide constitution in contact with the metal was used in Section 5.1.4 to define a range of p_{O_2} values corresponding to the metal–oxide equilibrium (Fig. 5.4). Associated a_C values were found using Eq. (5.17) to lie between 0.47 and 3.0×10^2 (Table 5.1). Values of a_C obtained from both k_c and f_V measurements are lower than those predicted from metal–oxide equilibrium, and also from these obtained in the case of Fe–9Cr (Table 5.3). The assumption that CO_2 and CO access the metal/oxide interface at a sufficient rate for the condition $\beta = (p_{CO} + p_{CO_2})_{ext}$ to be satisfied, is therefore not quite verified in this case. Thus, the results indicate that some degree of protection against carbon ingress was obtained, as compared to the iron-rich oxide scale formed on Fe–9Cr.

Fe–25Cr

Reaction of the Fe–25Cr alloy at 650 °C produced three oxidation morphologies: protective scale, healing scale and thick nodules. In terms of internal reaction, the healing type of scale can be classified together with the protective type, since internal oxidation did not occur underneath it, and internal carburisation was absent or limited to narrow depths, typical to what was observed underneath Cr_2O_3. This situation is treated in Section 5.2.2.

Underneath the thick nodules, intragranular carbide precipitation occurred with a morphology similar to that of reaction in Fe–20Cr. Precipitates volume fractions and penetration depths varied greatly with location in a given specimen, indicating that the oxide properties with regard to carbon transport were not uniform. These variations were not studied quantitatively. The extent of reaction was only characterised from penetration depths measured after 240 h exposure to Ar–20CO_2 ($X_c \simeq$ 50–70 µm) and Ar–20CO_2–20H_2O ($X_c \simeq$ 30–50 µm), in regions where carburisation

was most important and more or less uniform. In the absence of more complete data, the discussion can only be qualitative; in particular, interfacial carbon activities are not calculated.

A first observation is that X_c values were lower after reaction in the wet gas, as compared to the dry gas. Qualitatively, lower volume fractions (not shown) also confirmed that the extent of carburisation was reduced in the presence of $H_2O(g)$. Although no such effect was apparent in the case of Fe–20Cr, it is consistent with the reduction of interfacial carbon activity observed for Fe–9Cr, which was attributed to selective adsorption of H-bearing species (see Section 5.2.1.1).

The oxide constitution in contact with the metal being the same for Fe–20Cr and Fe–25Cr, the same range of a_C values is arrived at using Eq. (5.17). If both inner scales were $Sp_1 + Sp_2$ mixtures, differing from their phase proportions but with the same individual phase compositions, then the same a_C value applies to both alloys. Conversely, if the Cr-rich spinel phase, Sp_2, contained more Cr when formed on Fe–25Cr, then the interfacial p_{O_2} is slightly lower, and a_C slightly higher for this alloy than for Fe–20Cr. Raman analysis in the bulk of the inner scale indicated that the Sp_2 spinel had the same composition on both alloys (Section 3.3.3), but no information is available as to local compositions at the metal/oxide interface. Any variation in p_{O_2} and a_C would be small, and is neglected here.

Carbide penetration depths in Fe–25Cr after 240 h reaction were lower than those measured for Fe–20Cr after the same reaction time, 100 µm in average. This was associated with lower volume fractions and more elongated carbide precipitates. As discussed earlier, the effect of a higher chromium content on the extent and morphology of the reaction is clear, but variations can also arise from changed a_C values. Although Eq. (5.24) is based on hypotheses which were shown earlier not to apply to the present situation (essentially because chromium carbides are not sufficiently stable), and was replaced in the case of Fe–9Cr and Fe–20Cr by a mass balance from experimental f_V values, it is used here for comparison purposes. Using the definition of k_c in Eq. (3.3), N_C is seen using Eq. (5.24) to be proportional, for a given reaction time, to the product $N_{Cr}^0 X_c^2$. Using an average X_c value of 60 µm for Fe–25Cr after 240 h reaction, a ratio

$$\frac{(N_C)_{Fe-25Cr}}{(N_C)_{Fe-20Cr}} = \frac{(N_{Cr}^0 X_c^2)_{Fe-25Cr}}{(N_{Cr}^0 X_c^2)_{Fe-20Cr}} = 0.43 \tag{5.29}$$

is calculated, indicating that during reaction in dry CO_2, the interfacial carbon activity was lower for Fe–25Cr than for Fe–20Cr. Thus, despite having a similar morphology, the oxide scale grown on Fe–25Cr was less permeable to carbon than that formed on Fe–20Cr.

5.2.1.3 Case of Fe–9Cr at 800 °C

Carburisation of Fe–9Cr at 800 °C produced martensite and chromium-rich $M_{23}C_6$ precipitates. Martensite is a metastable reaction product, formed by the $\gamma \rightarrow \alpha'$ transformation during rapid cooling, as diffusion is too slow for the equilibrium reaction products, ferrite and carbides, to form from the carbon supersaturated austenite according to the eutectoid transformation. Figure 5.3 shows that the a_C value predicted from metal–oxide equilibrium is sufficient to form $M_{23}C_6$, but too low to reach the $\gamma + M_7C_3$ phase field. Moreover, no single phase austenite field is available at this temperature and for the alloy chromium content. Thus the observed formation of martensite cannot be accounted for on this basis.

Several difficulties arise in trying to rationalise the reaction mechanism. A first difficulty is related to the distribution of martensite in the reacted specimens. The transformation affected entire prior α grains, instead of a continuous band of metal at the metal/oxide interface, as is usually observed. In addition, as shown in Fig. 3.30, some grains in contact with the oxide remained untransformed, while isolated martensite was found deep inside the alloy. Although preferential transformation at the alloy surface was sometimes evident, as after 48 h reaction in Ar–20CO_2 or 10 h reaction in Ar–20CO_2–20H_2O, martensite was more or less evenly distributed in the other specimens. Two limiting reaction morphologies can be defined:

- Preferential formation at the alloy surface (Fig. 5.8(a)). This corresponds to carbon diffusion being relatively rapid in the scale, and slow in the metal. A carbon activity gradient then exists within the alloy, and constitutes a driving force for carbon diffusion from the alloy surface to its interior. A transformation front is expected to progress into the alloy.
- Uniform distribution (Fig. 5.8(b)). This can be achieved if carbon diffusion is relatively slow in the scale, and rapid in the metal. In the absence of a carbon activity gradient, the reaction progresses via a uniform increase in the fraction of transformed grains.

In both cases, the carbon activity is expected to eventually reach a uniform value in the alloy (for $t \geqslant t_4$ in Figs. 5.8(a) and (b)). A state of macroscopic equilibrium then prevails, no carbon flux may exist, and phase proportions cannot evolve with time, unless the interfacial carbon activity subsequently varies.

In the present situation, it was, in general, not possible to ascertain whether a reaction front existed because the prior α grains were large, as compared to the specimen dimensions. However, total martensite volume fractions are readily measured from the images shown in Fig. 3.30, and these should increase with reaction

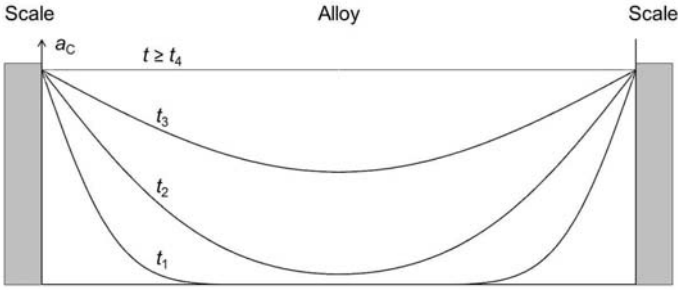

(a) Carbon diffusion relatively rapid in oxide and slow in metal

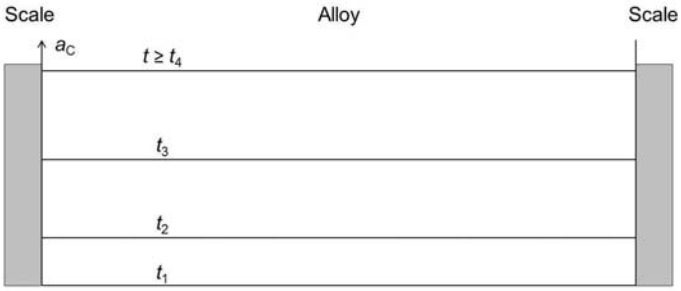

(b) Carbon diffusion relatively slow in oxide and rapid in metal

Figure 5.8 – Schematic representation of carbon activity profiles in alloy during carburisation, with increasing reaction time (see text for details).

time until global equilibrium is reached.

As shown in Fig. 3.33, the specimen reacted 100 h in Ar–20CO_2–20H_2O did not produce martensite, but developed intragranular carbides with a more or less uniform volume fraction. In order to compare this situation with that of martensite formation, let us consider the global mole fraction of carbon, N_C^g — that is, the overall mole fraction in either the α + martensite or α + carbides mixture. In doing so, the small amounts of $M_{23}C_6$ carbides occasionally associated with martensite precipitation are disregarded. Since the solubility limit of carbon in ferrite is very small, the carbon contained in the untransformed metal is neglected, and N_C^g is obtained from

$$N_C^g = f_{V,i}\, N_C^i\, \frac{V_{alloy}}{V_i} \tag{5.30}$$

where $f_{V,i}$, N_C^i and V_i are the volume fraction, carbon mole fraction and molar volume of phase i (i = martensite or carbide). In the case of martensite precipitation, since the weight fraction of carbon in martensite is small ($w_C^m = 2 \times 10^{-3}$), the mole fraction is calculated as

$$N_C^m = w_C^m\, \frac{M_{alloy}}{M_C} \tag{5.31}$$

and Eq. (5.30) is written

$$N_C^g = f_{V,m}\, w_C^m\, \frac{\rho_m}{M_C} V_{alloy} \tag{5.32}$$

Making the approximation $\rho_{\mathrm{m}} \simeq \rho_{\mathrm{alloy}} \simeq \rho_{\mathrm{Fe}}$, one obtains

$$N_{\mathrm{C}}^{\mathrm{g}} = f_{\mathrm{V,m}}\, w_{\mathrm{C}}^{\mathrm{m}}\, \frac{M_{\mathrm{Fe}}}{M_{\mathrm{C}}} \tag{5.33}$$

In the case of intergranular carbide precipitation, $N_{\mathrm{C}}^{\mathrm{g}}$ is calculated directly from Eq. (5.30), assuming that the carbides are Cr_7C_3 ($N_{\mathrm{C}}^{\mathrm{Cr_7C_3}} = 0.3$, and $V_{\mathrm{Cr_7C_3}}$ is obtained from $\rho_{\mathrm{Cr_7C_3}} = 6.92\ \mathrm{g\,cm^{-3}}$ [175] and $M_{\mathrm{Cr_7C_3}} = 400\ \mathrm{g\,mol^{-1}}$). Volume fractions of martensite and carbides measured by image analysis of entire cross-sections were used to construct the graph of Fig. 5.9. If the value obtained after

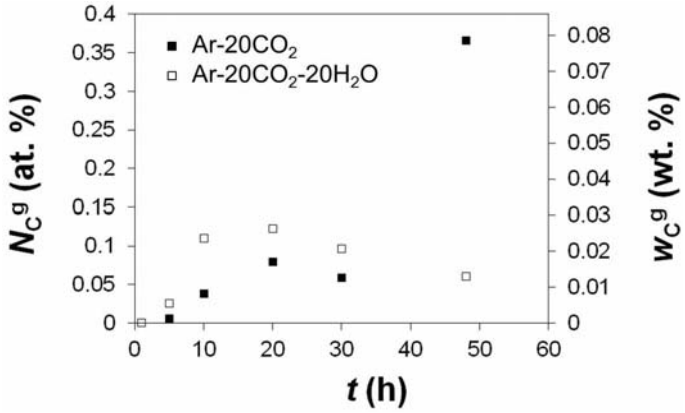

Figure 5.9 – Evolution of global carbon mole fraction (definition in text) during reaction of Fe–9Cr at 800 °C.

30 h reaction is dismissed, $N_{\mathrm{C}}^{\mathrm{g}}$ is found to increase with time during reaction in Ar–$20CO_2$. This indicates ongoing carburisation of the alloy. In the case of reaction in Ar–$20CO_2$–$20H_2O$, the evolution of $N_{\mathrm{C}}^{\mathrm{g}}$ is not monotonic. This suggests that after the initial stage, a macroscopic equilibrium was reached, and that the interfacial carbon activity subsequently decreased. Decarburisation could involve a preferential dissolution of martensite at the alloy surface, or a uniform dissolution. Again, this could not be verified (see Fig. 3.30). Alternatively, although this conclusion is puzzling, the shape of the $N_{\mathrm{C}}^{\mathrm{g}}$ curve might instead imply that the interfacial a_{C} varied *from one specimen to another* rather than *with time*, that is, that the reaction was not reproducible.

Whether the alloy reacted uniformly or according to a transformation front, and global equilibrium was reached or not during the experimental time frame, the carbon activity prevailing at the metal/oxide interface should be estimated by considering the fact that for martensite to form upon cooling, the $\alpha \rightarrow \gamma$ transformation had to occur during reaction at 800 °C. Another difficulty is met here, in that the phase constitution and composition determined experimentally are not consistent

with the thermodynamics of the Fe–Cr–C system. According to the phase diagram shown in Fig. 5.10, when an α phase containing 9 wt. % chromium is saturated in carbon, $M_{23}C_6$ carbides first precipitate. As the carbon content further increases,

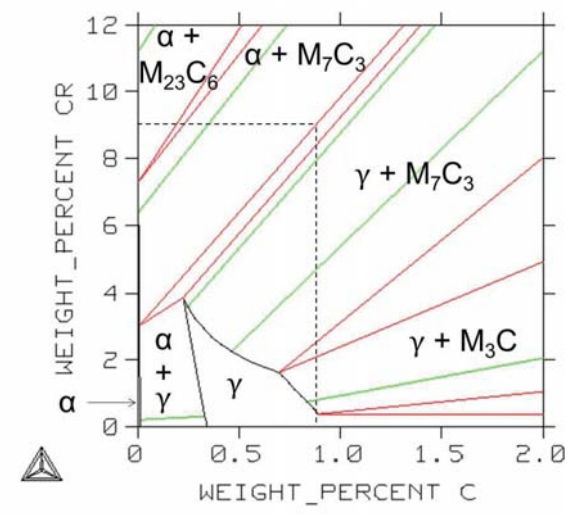

Figure 5.10 – Isothermal section of the Fe–Cr–C phase diagram at 800 °C, calculated using Thermo-Calc.

the nature of the carbides changes to M_7C_3, and ferrite eventually forms austenite when the global carbon content in the α+M_7C_3 mixture exceeds 0.9 wt. %. However, both types of carbide are chromium-rich, and their precipitation involves substantial chromium depletion in the metal matrix: when γ forms, it contains about 4 wt. % Cr, and this concentration can only decrease with further carbide precipitation. In the present case, no carbides were observed together with martensite, which was found by EPMA to contain 9 wt. % Cr.

Chromium depletion could possibly have occurred at the alloy surface, as a result of (partially) selective oxidation, but none was detected. The absence of visible chromium depletion in transformed zones suggests that carbides could not precipitate, or were too small to be detected metallographically and for the partition of chromium between carbide and metal to be detected by EPMA. The dimensions of carbide particles reflect the competition between nucleation and growth, whose outcome is determined by the ratio of chromium and carbon permeabilities. Thus, two possible obstacles to carbide growth may be thought of: slow chromium diffusion, or elevated carbon activity. However, both must be rejected, as (i) chromium diffusion is faster at 800 °C than at 650 °C, where carbides could grow, and (ii) given the values of a_C considered, a substantially higher activity would stabilise cementite, and

even graphite, whose formation does not require chromium diffusion. Furthermore, even if an equilibrium $\alpha + M_7C_3$ mixture existed, and the carbides were so small that only a global composition could be measured by EPMA, the carbon concentration would be 0.9 wt. %, considerably higher than the measured value, 0.2 wt. % (see Section 3.2.5).

Another difficulty arises from the location of the intragranular $M_{23}C_6$ carbides, occasionally found in a region comprised between martensite and the metal/oxide interface, when this strip was no more than a dozen µm wide. According to the phase diagram (Fig. 5.10), the $\alpha + M_{23}C_6$ corresponds to a relatively low carbon content. In particular, these regions located at the alloy surface would contain less carbon than the martensite. This suggests a state of decarburisation, which could not have occurred, at least up to 20 h reaction, as discussed earlier.

It is concluded that the reaction mechanism cannot be rationalised on an equilibrium basis. Nonetheless, the very formation of carburisation products beneath the oxide scale clearly demonstrates that carbon supersaturation was established at the metal/oxide interface, relative to the gas.

5.2.1.4 Application to the reaction of other alloys at 800 °C

Fe–2.25Cr

No carburisation product was observed in the Fe–2.25Cr alloy after reaction at 800 °C. This is in agreement with the proposed model, since Eq. (5.17) predicts a carbon activity of 3.4×10^{-2} (Table 5.1), below that required to form austenite (0.15) or M_7C_3 carbides (0.34) — for this composition, the phase transformations of interest, in increasing carbon activity, are $\alpha \rightarrow \alpha + \gamma$, $\alpha + \gamma \rightarrow \gamma$, $\gamma \rightarrow \gamma + M_7C_3$ (see Fig. 5.10); the equilibrium a_C values were calculated using Thermo-Calc.

Fe–20Cr

Reaction of Fe–20Cr in wet CO_2 at 800 °C produced, in addition to the protective Cr_2O_3 scale, thick multilayer Fe-rich nodules, whose constitution was similar to that observed on the dilute alloys. However, a Cr-rich layer was observed at the base of the scale. The interfacial oxygen activity corresponding to this reaction morphology was found in Section 5.1.4 to be in a range defined by the $Cr_2O_3 - FeCr_2O_4$ and $Cr - Cr_2O_3$ equilibria, both of which yielded a_C values higher than 1 using Eq. (5.17) (see Table 5.1). No carburisation product was observed underneath this type of oxide, indicating that it provided protection against carbon penetration.

5.2.2 Limited carburisation and protective scaling

5.2.2.1 Case of Fe–20Cr at 650 °C

Since the dissociation pressure of Cr_2O_3 is extremely low, a very high carbon activity is expected from thermodynamic equilibrium at the alloy/Cr_2O_3 interface. The value calculated from Eq. (5.17) exceeds 10^4 at 650 °C (Table 5.1). However, no graphite was observed, and carburisation of the Fe–20Cr alloy was either absent or limited to shallow depths (Fig. 3.48(a)). This indicates a low interfacial carbon activity. Thus, while carburisation did indeed occur beneath the Cr_2O_3 scale, the predicted carbon activity was not achieved. The assumption that CO_2 and CO access the metal/oxide interface at a sufficient rate for the condition $\beta = (p_{CO} + p_{CO_2})_{ext}$ to be satisfied, is incorrect in this case. It is therefore concluded that transport of carbonaceous species through Cr_2O_3 is much slower than in iron oxide, as has already been suggested [12, 13, 113, 116, 118] (see Section 1.5.2.4).

In order to estimate the extent to which the oxide transmitted carbon, and evaluate a carbon activity, from experimental observations, the reaction mechanism is now examined in more details. Carburisation underneath the Cr_2O_3 scale was either absent or limited to a thin, more or less continuous carbide plate parallel to the metal/oxide interface. The plate-like morphology indicates that when it formed early in the reaction, the inward carbon flux was small, allowing the relatively large chromium flux to favour precipitate growth and coalescence over new nucleation. Subsequently, the carbide plate was observed not to thicken (over 40–120 h, see Section 3.3.3.1), indicating that no further carbon uptake was occurring in the alloy. This observation is of particular interest in the implication it has for selective oxidation (discussed in Chapter 6), and therefore deserves close investigation.

Analysis of the subscale region by SEM–EDS (Fig. 3.56) showed that the carbide plate was located in the zone of oxidation-induced chromium depletion. This is represented in Fig. 5.11, where schematic depletion profiles corresponding to increasing reaction times are superimposed. The Fe–Cr–C phase diagram shown in Fig. 5.6(a) indicates that at the chromium concentrations of interest (10–20 at. %), carbon ingress into the alloy is expected to result first in $M_{23}C_6$ precipitation. As experimental measurements provided chromium concentrations, and not activities, it is convenient to consider carbide formation from dissolved species,

$$(23 - x)\,\underline{\mathrm{Cr}} + x\,\underline{\mathrm{Fe}} + 6\,\underline{\mathrm{C}} = \mathrm{Cr}_{23-\mathrm{x}}\mathrm{Fe}_{\mathrm{x}}\mathrm{C}_6 \tag{5.34}$$

and to study the metal/carbide equilibrium as

$$K_{sp} = N_{Cr}^{23-x} N_{Fe}^{x} N_{C}^{6} \tag{5.35}$$

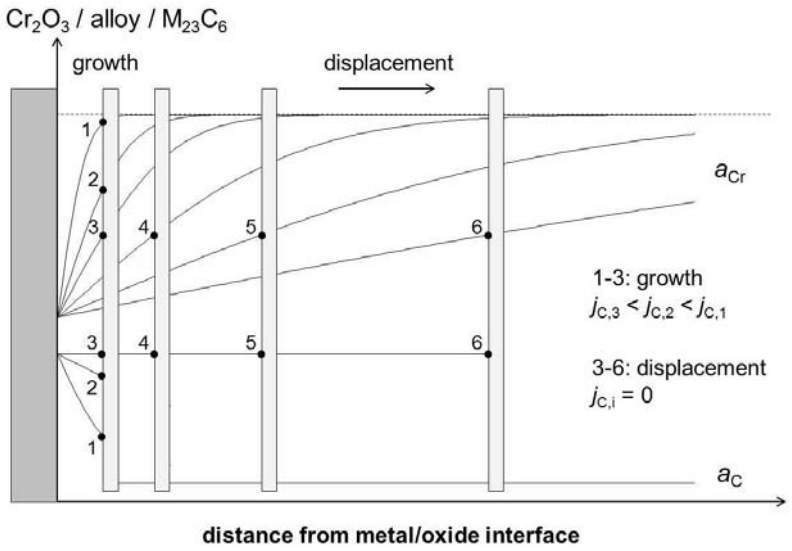

Figure 5.11 – Carbon and chromium activities in the metal matrix in the presence of a plate-like carbide precipitate underneath a protective scale. The symbol $j_{\mathrm{C,i}}$ denotes the carbon flux between the oxide and the carbide at time step i. Underneath the carbide plate, a_{C} falls to a negligibly small value.

where the solubility product K_{sp} is determined by the standard free energies for carbide formation and Fe, Cr and C dissolution. Noting that $N_{\mathrm{C}} \ll (N_{\mathrm{Cr}}, N_{\mathrm{Fe}})$, Eq. (5.35) is rewritten

$$K_{\mathrm{sp}} = N_{\mathrm{Cr}}^{23-x} \left(1 - N_{\mathrm{Cr}}\right)^{x} N_{\mathrm{C}}^{6} \tag{5.36}$$

Carbide precipitation occurs when K_{sp} is exceeded. However, as visible in Fig. 5.6(a), the composition of $\mathrm{M_{23}C_6}$ in equilibrium with the metal shifts toward an iron enrichment as N_{Cr} decreases. With a varying x, the mathematics of Eq. (5.36) are not straightforward. Furthermore, the influence of alloy composition on the activity coefficients adds to the complexity of Eq. (5.36), and render it inappropriate for a study of carbide stability. As shown in Fig. 5.12(a), the relationship between N_{Cr} and N_{C} at the $\alpha/\alpha + \mathrm{M_{23}C_6}$ phase boundary implied by Eq. (5.36) is misleading: when N_{Cr} decreases from 0.25 to 0.1, less carbon is needed to maintain carbide stability. In order to overcome the alloy solid-solution effect, let us consider the formation reaction

$$(23 - x)\,\mathrm{Cr} + x\,\mathrm{Fe} + 6\,\mathrm{C} = \mathrm{Cr_{23-x}Fe_xC_6} \tag{5.37}$$

where the species are in their reference state (pure bcc metal for Fe and Cr, graphite for C), and the law of mass action

$$K_{5.37} = \left[a_{\mathrm{Cr}}^{23-x} a_{\mathrm{Fe}}^{x} a_{\mathrm{C}}^{6}\right]^{-1} \tag{5.38}$$

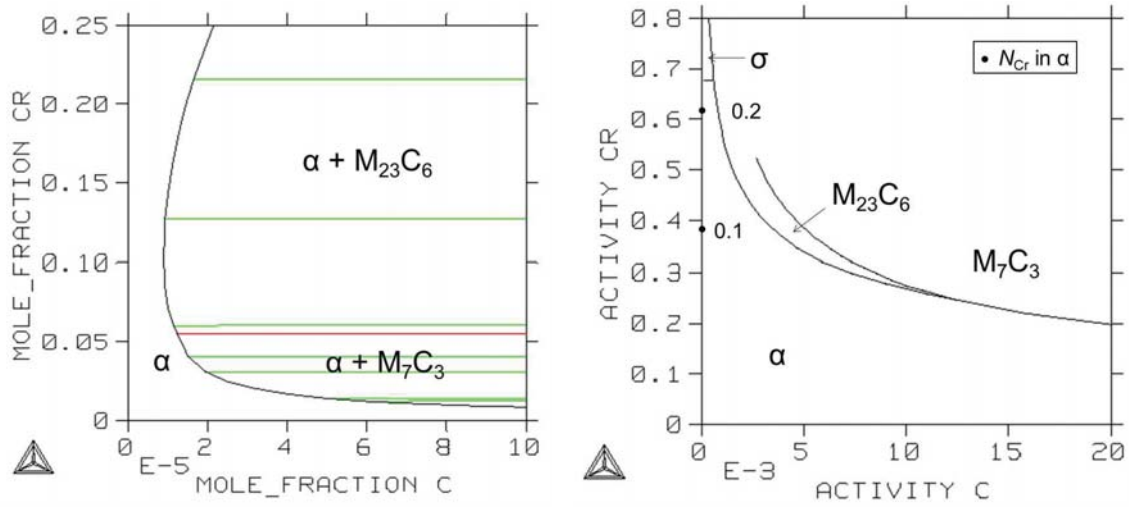

(a) Mole fractions (b) Activities

Figure 5.12 – Isothermal sections of the Fe–Cr–C phase diagram at 650 °C, calculated using Thermo-Calc, and showing the metal/carbide equilibrium.

where $K_{5.37}$ is the equilibrium constant for carbide formation. Then, the condition for carbide stability is seen in Fig. 5.12(b) to conform to what could be expected for the formation of a Cr-rich compound: a_C increases when a_{Cr} decrease. The reaction mechanism is now studied on the basis of chromium and carbon activities in the metal matrix.

Initially, a_{Cr} is close to the bulk chromium activity. The carbon activity at the metal/oxide interface, $a_C^{m/o}$, is sufficient to allow carbide precipitation to occur. Furthermore, as a result of the a_C gradient between the oxide and the carbide, a carbon flux is established, allowing the carbide to grow (step 1 in Fig. 5.11). As mentioned earlier, the plate-like morphology of the carbide indicates that this supersaturation was limited, and that carbon was rapidly exhausted. As the reaction proceeds further and Cr_2O_3 growth consumes chromium, a_{Cr} at the metal/carbide interface decreases (steps 2 and 3 in Fig. 5.11). Metal–carbide equilibrium then requires a_C to raise by virtue of Eq. (5.38). In this simplified model, the effect of the chromium activity gradient on the carbon flux is neglected. If $a_C^{m/o}$ is assumed to be constant, the increase in a_C at the metal/carbide interface is expected to decrease the carbon activity gradient, until the carbon flux vanishes and carbide growth ceases (step 3 in Fig. 5.11). With a fixed a_C value at the metal/carbide interface, but a decreasing a_{Cr}, Eq. (5.38) requires that the carbide dissolve. In doing so, carbon is made available to diffuse across the carbide toward the alloy interior, where a_{Cr} is sufficient to stabilise the carbide. Dissolution-reformation would thus result in the inward displacement of the carbide plate (steps 3–6 in

Fig. 5.11).

The fact that carbide growth stopped after a transient stage is supported by the experimental observation that its thickness did not increase over 40–120 h reaction. The conclusion that the carbide plate subsequently moved inward as chromium depletion progressed into the alloy is now investigated. The chromium concentrations measured in subsurface zones of Fe–20Cr in regions of protective oxidation (Fig. 3.56) were sensitive to the thickness of the Cr_2O_3 scale located directly above, and this varied with location. In order to rationalise the results, chromium concentrations are calculated using the classical one-dimensional diffusion analysis of the depletion problem.

Chromium depletion was limited to about 5 µm, whereas the specimens were more than 1 mm thick. Clearly, at the low experimental temperature, Cr_2O_3 growth is too slow for the depletion profiles generated on the opposed faces of a specimen to overlap in the time frame considered. Interfacial chromium mole fractions $N_{Cr}^{m/o}$ are calculated on the assumption that the scale is pure Cr_2O_3, using the steady-state equation given by Wagner [78]

$$\frac{N_{Cr}^{0} - N_{Cr}^{m/o}}{1 - N_{Cr}^{m/o}} = F\left[\frac{2V_a}{V_{Cr_2O_3}}\sqrt{\frac{k_{p,Cr_2O_3}}{2D_{Cr}}}\right] \tag{5.39}$$

where N_{Cr}^{0} is the initial chromium mole fraction, V_a and $V_{Cr_2O_3}$ the molar volume of alloy and oxide ($V_a = 7.1\ cm^3\,mol^{-1}$ and $V_{Cr_2O_3} = 29\ cm^3\,mol^{-1}$), D_{Cr} the diffusion coefficient of chromium in the alloy ($D_{Cr} = 5.61 \times 10^{-14}\ cm^2\,s^{-1}$ at 650 °C, extrapolated from data in Ref. [81]), and F a function defined by

$$F(u) = \pi^{1/2} u\,(1 - \operatorname{erf} u)\exp u^2 \tag{5.40}$$

Oxide growth is described by the rate law

$$X_{Cr_2O_3}^2 = 2\,k_{p,Cr_2O_3}\,t \tag{5.41}$$

using k_{p,Cr_2O_3} to denote the Cr_2O_3 rate constant. Molar volumes and diffusion coefficient are assumed not to vary with alloy composition. Since the experimental values were sensitive to the thickness of the oxide located directly above, k_{p,Cr_2O_3} values were estimated for each location using the measured oxide thickness and reaction time. Values of $N_{Cr}^{m/o}$ deduced from Eq. (5.39) were then used to calculate depletion profiles using the appropriate solution of Fick's second law of diffusion for a semi-infinite solid [176]

$$\frac{N_{Cr}(x,t) - N_{Cr}^{m/o}}{N_{Cr}^{0} - N_{Cr}^{m/o}} = \operatorname{erf}\left(\frac{x}{2\sqrt{D_{Cr}t}}\right) \tag{5.42}$$

where x is the distance from the metal/oxide interface. The calculated profiles, shown as dashed lines in Fig. 3.56(c-e), match very well the experimental data, whether carbide precipitation occurred or not. This observation is discussed in detail in Chapter 6.

Carbide precipitation occurs where the solubility product is exceeded. This condition defines a distance x_{carb} from the metal/oxide interface, below and above which no carbide is found: for $x < x_{\mathrm{carb}}$, N_{Cr} is too low because of oxidation-induced depletion, and for $x > x_{\mathrm{carb}}$, N_{C} is too low because carbon is almost entirely precipitated. The critical chromium mole fraction for carburisation, $N_{\mathrm{Cr}}^{\mathrm{m/c}}$ is determined by the carbon activity and carbide composition. In the absence of carbon activity data, $N_{\mathrm{Cr}}^{\mathrm{m/c}}$ is estimated to be 0.2 from the experimental profiles of Fig. 3.56.

Combining Eqs. (5.39), (5.41) and (5.42), $N_{\mathrm{Cr}}^{\mathrm{m/c}}$ is written

$$N_{\mathrm{Cr}}^{\mathrm{m/c}}(t) = \frac{N_{\mathrm{Cr}}^{0} - f(X_{\mathrm{Cr_2O_3}}, t)}{1 - f(X_{\mathrm{Cr_2O_3}}, t)} \left[1 - g(x_{\mathrm{carb}}, t)\right] + N_{\mathrm{Cr}}^{0}\, g(x_{\mathrm{carb}}, t) \tag{5.43}$$

where

$$g(x,t) = \mathrm{erf}\left(\frac{x}{2\sqrt{D_{\mathrm{Cr}} t}}\right) \tag{5.44}$$

$$f(X,t) = F\left[\frac{V_{\mathrm{a}}}{V_{\mathrm{Cr_2O_3}}} \frac{X}{\sqrt{D_{\mathrm{Cr}} t}}\right] \tag{5.45}$$

and F is the function defined in Eq. (5.40). In order to obtain x_{carb} as a function of $X_{\mathrm{Cr_2O_3}}$ and t, Eq. (5.43) was solved numerically. The result is shown in Fig. 5.13, together with experimental values measured after reaction in Ar–20CO_2. Reasonable agreement between predicted and measured values, for short reaction

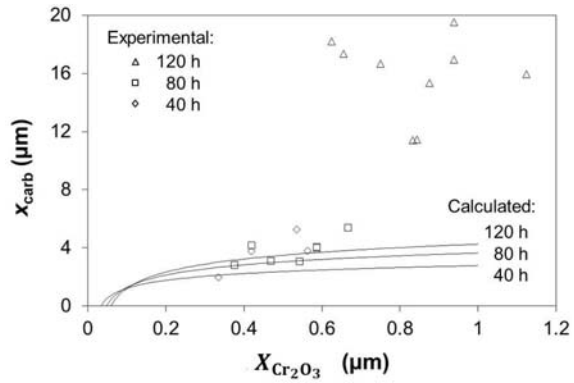

Figure 5.13 – Distance of carbide plate from alloy/Cr_2O_3 interface in Fe–20Cr after exposure to Ar–20CO_2 at 650 °C. Solid lines obtained from numerical solution of Eq. 5.43.

times, supports the mechanistic description of Fig. 5.11: at steady-state, as Cr_2O_3

grows and chromium depletion extends into the alloy, formation-dissolution of the carbide plate is responsible for its inward displacement. However, this model fails to describe the data after 120 h reaction, where the carbide plate is formed deeper within the alloy, beneath the chromium depletion zone. This is quite surprising, as no apparent driving force for carbide displacement could possibly exist in a zone of uniform alloy composition.

If this contradiction is diregarded and the model of Fig. 5.11 applied, the carbon activity is found to be constant everywhere between the oxide and the carbide, during the steady-state stage of the reaction. In particular, $a_C^{m/o}$ can then be determined, as it is the value corresponding to metal/carbide equilibrium for $N_{Cr} \simeq 0.2$. More precisely, since the $\alpha/M_{23}C_6$ interface did not extend to varying depths (no extended $\alpha + M_{23}C_6$ region was formed), the value of interest is that corresponding to the $\alpha/\alpha + M_{23}C_6$ phase boundary. Using Thermo–Calc, this value is found to be 8×10^{-4} (see Fig. 5.12(b)). This is much lower than the value expected from thermodynamic equilibrium at the metal/oxide interface (Table 5.1), confirming that the scale provides a partial barrier to carbon entry. Moreover, complete protection was achieved locally, as carbide-free regions were also observed.

5.2.2.2 Application to other alloy and reaction temperature

Fe–25Cr at 650 °C

During reaction of Fe–25Cr in Ar–20CO_2 at 650 °C, carburisation underneath the protective and healing scales was mostly absent, as carbides were found only at scattered locations, with shallow penetration depths. For both types of oxide, Eq. (5.17) predicts a_C values higher than 1 (see Fig. 5.4 and Table 5.1). It is concluded that these oxides generally constituted effective barriers against carbon penetration, and only transmitted carbon locally and to a limited extent.

No carbides were found underneath either type of scale after exposure to Ar–20CO_2–20H_2O. In addition to the oxides being efficient in blocking carbon, local failure to do so was avoided in the presence of H_2O(g). This can be understood in terms of selective adsorption of H_2O(g), as discussed in Section 5.2.1.1.

When carbides were formed, the precipitation morphology was quite similar to that observed underneath Cr_2O_3 in Fe–20Cr. Even though no quantitative measurements (carbide plate thickness and location in the chromium depletion zone) were made in the case of Fe–25Cr, it seems likely that a similar reaction mechanism was operating. The proportion of zones affected by carburisation was not measured for either of the two alloys. Qualitatively, carburisation was the exception rather than

the rule in Fe–25Cr, whereas it was more prevalent in Fe–20Cr.

This observation is to be related to the work of Young [126] on Cr_2O_3 permeability to carbon. During reaction in $CO/CO_2/N_2$ at 900 °C, Cr_2O_3 scales grown on pure chromium transmitted carbon, while those formed on Fe–Cr and Ni–Cr alloys did not. Analysis of the thermodynamics of carbide formation in each material demonstrated that the absence of carbides in the binary alloys was indeed due to the scale's suppressed permeability to carbon. The only apparent difference between the oxide formed on the three materials was that it contained low levels of iron or nickel when grown on the alloys ($N_{Fe}/N_{Cr} = 0.025$ and $N_{Ni}/N_{Cr} = 0.014$). The author suggested that segregation of the second metal to internal oxide surfaces blocked carbon transport by chemisorbing CO.

In the present case, the thermodynamics of carbide formation in Fe–20Cr and Fe–25Cr are quite similar. The only difference between the two alloys is that chromium depletion profiles underneath both healed and protective scales in Fe–25Cr (Fig. 3.60) were shifted toward high concentrations, as compared to Fe–20Cr (Fig. 3.56). Thus, carbide precipitation is expected to occur for lower carbon activities in Fe–25Cr — or, if a_C is fixed, at a closer distance to the metal/oxide interface. As a consequence, the prevailing absence of carbides in Fe–25Cr must reflect enhanced ability of the oxide to exclude carbon. Referring to the work of Young [126], this could be due to a higher iron concentration in the oxide. Analysis by SEM-EDS of the Cr_2O_3 scales did not allow any distinction to be made between the Fe–20Cr and Fe–25Cr reactions, since the iron concentration fell below the detection limit in both cases. The iron concentration in Cr_2O_3 is expected to be only slightly higher for Fe–25Cr, on the basis of metal/oxide equilibrium. From this perspective, the present results would indicate that permeability of Cr_2O_3 to carbon is very sensitive to its composition. In the case of the healed type of scale, however, the situation is clear: the inner layer was either spinel or corundum type, with N_{Fe}/N_{Cr} ratios in the range 0.081 to 0.57, much higher than in protective Cr_2O_3 scales.

Fe–20Cr and Fe–25Cr at 800 °C

As discussed for reactions at 650 °C, Eq. (5.17) results in very high carbon activities below Cr_2O_3 scales, provided that they transmit the CO and CO_2 species. The very occasional presence of internal carbides in Fe–20Cr after reaction at 800 °C suggests that the oxide was, in general, impervious to CO and CO_2, but that microscopic failure occurred locally. Furthermore, no carbides were observed at all in Fe–25Cr, confirming that the Cr_2O_3 scale formed on this alloy was inherently superior to that grown on Fe–20Cr, in that it was not prone to local failure.

5.3 Factors affecting oxide permeability to carbon

Carbon supersaturation at the metal/oxide interface of oxidised alloys, with respect to the external atmosphere, was evaluated using a model based on interfacial equilibrium. Essentially, the model allows the interfacial carbon activity to be calculated, given the nature of the oxide in contact with the metal, which determines the local oxygen activity. This calculation involves a degree of freedom in the system, which amounts to the quantity of carbon transferred from the external atmosphere to the metal/oxide interface. The thermodynamics of metal–carbide equilibrium were used to determine interfacial carbon activities from the observed morphology and rate of the carburisation reaction. This procedure served as a basis on which the effect of oxide and gas composition on carbon transport could be determined. The major outcomes of this analysis are now summarised.

5.3.1 Assessment of the model

Using the principle of local equilibrium to relate elevated carbon activities to low oxygen potentials prevailing at the metal/oxide interface has been proposed by previous investigators. This argument was significantly extended here to yield an analytical expression for the carbon activity. In most cases studied, calculated values were found to exceed those required to form carbides, and carburisation was indeed observed to occur. Qualitatively, this shows that the local equilibrium approach is indeed suitable to describe the establishment of carburising conditions during oxidation in a low a_C atmosphere.

In the case of the Fe–9Cr reaction in dry CO_2 at 650 °C, interfacial carbon activities determined from two independently measured quantities (volume fraction of carbides and carburisation rate) were found to be in good agreement with the calculated value. This quantitative success constitutes strong support for the proposed model.

Under two conditions, the extent of carburisation was less than that predicted from the hypothesis that the scale can transmit carbon unhindered: the presence of H_2O in the reacting gas, and the formation of Cr-rich oxide. These divergences were shown to be compatible with the model, and interpreted in terms of reduced carbon uptake and transport in the oxide. The formalism introduced here allowed the effect of gas and oxide compostion to be discussed.

5.3.2 Effect of water vapour on carbon uptake

The extent of carburisation in Fe–9Cr at 650 °C was seen to decrease with increasing H_2O content in the external atmosphere. This effect was attributed to selective adsorption of H_2O over CO_2 at the scale surface, and the ability of H_2O to partially exclude carbon was quantified by defining and calculating an enrichment ratio of H-bearing species over C-bearing species at the metal/oxide interface, with respect to the external gas. Qualitatively, the H_2O effect was confirmed by the results obtained for Fe–25Cr at the same temperature. This alloy formed different types of scale, which resulted in either extensive or limited carburisation. The reduced carbon uptake in wet CO_2 was characterised, in the case where carburisation was extensive, by a lower penetration rate and interfacial volume fraction of carbides, and in the case where protection against carbon ingress was generally achieved, by a lower propensity for local failure.

Carburisation of the ternary alloys could not be analysed according to the procedure used for the binary alloys, because thermodynamic data for the Fe–Cr–Ni–O and Fe–Cr–Ni–C systems could not be obtained. However, for a given alloy, reactions in dry and wet CO_2 can be compared. In the case of Fe–9Cr–10Ni and Fe–20Cr–20Ni at 650 °C, carbides were formed during exposure to Ar–20CO_2, but none were found after reaction in Ar–20CO_2–20H_2O (see Fig. 3.13 and Section 3.3.3.3). This provides further confirmation for the role of H_2O in excluding carbon.

For all the other alloys, a direct comparison between dry and wet CO_2 could not be made, for example because carburisation did not occur in any of the gases. The presence of H_2O was never found to cause enhanced carburisation, and only in one case, that of extensive carburisation underneath the Fe-rich oxide nodules formed on Fe–20Cr at 650 °C, was it seen to leave the carburisation rate unaffected. In this specific situation, the experimental scatter was substantial, and could possibly have masked the effect of H_2O, if it did operate.

5.3.3 Effect of oxide composition on carbon transport

The thick Fe-rich oxide scales formed on the Fe–9Cr, Fe–20Cr and Fe–25Cr alloys during reaction at 650 °C were morphologically similar. Carburisation was extensive beneath these scales, and the reaction rate and morphology were comparable for the three alloys. Taking into account the variation of carburisation rate inherently due to alloy composition, the rate of carbon transport in the oxide was shown to be gradually reduced with increasing alloy chromium concentration. The only distinction which could be drawn between the oxide scales grown on the three alloys

is the constitution of the inner layer. In the case of Fe–9Cr, it contained a mixture of FeO and Cr-rich spinel, whereas for the high chromium alloys, FeO was replaced by an Fe-rich spinel. Volume fractions of phases were not measured, but the mass balance requires that the proportion of Cr-rich oxide increase with increasing alloy chromium concentration. The present results therefore suggest that carbon transport was slower in the Cr-rich spinel than in the Fe-rich spinel or FeO, and that the overall transport rate was therefore affected by the phase proportions.

Carburisation of the higher chromium alloys was either absent or limited beneath the protective Cr_2O_3 scales, but also when a Cr-rich layer was present at the base of the multilayer scales. It is concluded that the formation of continuous layers of Cr-rich oxide resulted in drastically reduced rates of carbon transport. This confirms that Cr-rich oxide, either spinel or corundum type, is less permeable to carbon than iron oxide.

However, the propensity for local failure to block carbon ingress was shown to be reduced when these Cr-rich layers contained some dissolved iron, as compared to relatively pure Cr_2O_3 scales. This may be related to the work of Young [126], who suggested that molecular transport of carbon is hampered by iron segregation at the oxide grain boundaries.

Chapter 6

Breakaway oxidation

Although the high chromium alloys contained a sufficient amount of chromium for slow-growing Cr_2O_3 scales to be formed initially, this protective behaviour was, in most cases, not maintained for the duration of the experiments. Understanding the transition from selective to non-selective oxidation and the kinetics of breakaway oxidation is of decisive importance, since oxidation rates characterising the formation of Fe-rich oxides are considerably higher than those typical of Cr_2O_3.

Section 6.1 is aimed at investigating the local mechanism of Cr_2O_3 failure and nodule development. The kinetics of nodule nucleation and growth at the scale of the specimen are addressed in Section 6.2. The way in which alloy and gas composition affect the overall oxidation resistance, and the influence of reaction temperature on the factors controlling breakaway oxidation, are discussed in Section 6.3.

6.1 Mechanism of breakaway oxidation

The evolution of oxide morphology during breakaway can be summarised as follows. Initially, a protective Cr_2O_3 scale is formed on the alloy surface. At certain locations, the alloy fails to maintain selective oxidation, and Fe-rich oxide is formed. Individual nodules thicken and spread laterally, and then coalesce to form continuously thick oxide scales.

The conditions underlying Cr_2O_3 failure and nodule development are examined here. This discussion focuses on reaction at 650 °C, for which most information is available. Sections 6.1.1, 6.1.2 and 6.1.3 are based on the the results obtained at this temperature, while reaction at 800 °C is briefly discussed in Section 6.1.4.

6.1.1 Chromium depletion and influence of carburisation on breakaway

Chromium concentration profiles measured in Fe–20Cr underneath the protective Cr_2O_3 scale are shown in Fig. 3.56. In Section 5.2.2.1, it was noted that these profiles were affected by the thickness of the oxide located directly above, which varied with location. The procedure used to rationalise these results in Section 5.2.2.1 is recapitulated here.

The zone affected by chromium depletion was about 5 µm deep, whereas specimens were more than 1 mm thick. In this situation of relatively slow oxide growth, a steady-state description applies, and the interfacial chromium mole fraction $N_{Cr}^{m/o}$ is constant in the time frame considered. Local values of $N_{Cr}^{m/o}$ are calculated on the

assumption that the scale is pure Cr_2O_3, according to Wagner's expression [78]

$$\frac{N_{Cr}^0 - N_{Cr}^{m/o}}{1 - N_{Cr}^{m/o}} = F\left[\frac{2V_a}{V_{Cr_2O_3}}\sqrt{\frac{k_{p,Cr_2O_3}}{2D_{Cr}}}\right] \tag{6.1}$$

where N_{Cr}^0 is the initial chromium mole fraction, V_a and $V_{Cr_2O_3}$ the molar volume of alloy and oxide ($V_a = 7.1\ cm^3\,mol^{-1}$ and $V_{Cr_2O_3} = 29\ cm^3\,mol^{-1}$), D_{Cr} the diffusion coefficient of chromium in the alloy ($D_{Cr} = 5.61 \times 10^{-14}\ cm^2\,s^{-1}$ at 650 °C, extrapolated from data in Ref. [81]), and F a function defined by

$$F(u) = \pi^{1/2} u\,(1 - \mathrm{erf}\,u)\exp u^2 \tag{6.2}$$

Oxide growth is described by the rate law

$$X_{Cr_2O_3}^2 = 2\,k_{p,Cr_2O_3}\,t \tag{6.3}$$

using k_{p,Cr_2O_3} to denote the Cr_2O_3 rate constant. Molar volumes and diffusion coefficient are assumed not to vary with alloy composition. Since the experimental values were sensitive to the thickness of the oxide located directly above, k_{p,Cr_2O_3} values were estimated for each location considering the measured oxide thickness and reaction time. Values of $N_{Cr}^{m/o}$ deduced from Eq. (6.1) were then used to calculate depletion profiles according to the appropriate solution of Fick's second law of diffusion for semi-infinite solids [176]

$$\frac{N_{Cr}(x,t) - N_{Cr}^{m/o}}{N_{Cr}^0 - N_{Cr}^{m/o}} = \mathrm{erf}\left(\frac{x}{2\sqrt{D_{Cr}t}}\right) \tag{6.4}$$

where x is the distance from the metal/oxide interface. The calculated profiles are shown as dashed lines in Fig. 3.56(c-e).

Chromium depletion profiles recorded in carbide-free zones (filled symbols in Fig. 3.56(c-e)) are seen to match very well the calculated profiles. Significant changes in $N_{Cr}^{m/o}$ accompany local variations in scale thickness on the same specimen. The need to use local k_{p,Cr_2O_3} values in the calculation is clear. The success of Eq. (6.1) in relating chromium depletion to chromia scaling rate, despite local variations in the two quantities, demonstrates that the underlying mass balance is correct. In other words, the composition of the protective scale does not change significantly, and variations in its growth rate have some other cause. As diffusion in chromia scales at this temperature is predominantly via grain boundaries [25], it seems likely that local variations in oxide grain size and/or shape are responsible for altered scaling rates. However, no information is available from the present work.

The observed variations in $X_{Cr_2O_3}$ and $N_{Cr}^{m/o}$ along the scale interface are significant. Although the steady-state analysis of Eqs. (6.1–6.4) succeeds when applied locally, the alloy-scale system as a whole is characterised by a boundary condition which varies with lateral position. Thus the system is not in a uniform steady state. Rather, it should be thought of as subject to fluctuations which are not quickly removed. The process for their removal — lateral diffusion of alloy chromium parallel to the scale interface — is slow compared to chromium diffusion toward the scale, because the concentration gradients involved are smaller.

Carburisation affects the concentration profiles in that whenever it occurred, the chromium concentration was higher than the predicted value in the carbide, and slightly lower in the surrounding matrix. This merely reflects the fact that the carbides are chromium-rich. However, away from the carbides, the depletion profiles are entirely determined by the thickness of the overlaying Cr_2O_3 scale. Depletion profiles recorded after exposure to Ar–20CO_2–20H_2O (not shown here) were equivalent: $N_{Cr}^{m/o}$ values were similar, and related in the same way to $X_{Cr_2O_3}$, independently of whether or not carbide precipitated.

The results demonstrate that in the conditions of interest, the limited carbide precipitation which occurs in Fe–20Cr below a protective Cr_2O_3 scale does not affect chromium depletion. In particular, the interfacial concentration, which is critical to the resistance of the alloy to breakaway, remains unchanged. The reason for this lies in the fact that the Cr_2O_3 scale is a rather good (but not perfect) barrier to carbon entry into the alloy. As shown in Section 5.2.2.1, the plate-like morphology of the carbides indicates a low interfacial carbon activity, and the fact their thickness did not increase with time reflects the absence of an inward carbon flux. The essential implication of the analysis presented in Section 5.2.2.1 is that at steady-state, as Cr_2O_3 grows and chromium depletion extends into the alloy, formation-dissolution of the carbide plate results in its inward displacement and enables the global outward chromium flux to remain unaltered, thus accounting for the fact that $N_{Cr}^{m/o}$ is the same in the presence and absence of carburisation. This situation is depicted in Fig. 6.1. In the absence of precipitation beneath the carbide plate, the chromium concentration in the matrix, and therefore the driving force for outward chromium diffusion, are globally unaffected by carburisation. As a consequence, the flux of chromium available at the metal/oxide interface is also unchanged.

As noted in Section 5.2.2.1, the Fe-rich oxide formed as a result of Cr_2O_3 failure is significantly more permeable to carbon than is Cr_2O_3. The fact that extensive carburisation was never found in the absence of Fe-rich oxide, together with the observation that a number of early-stage nodules had no carbide beneath them,

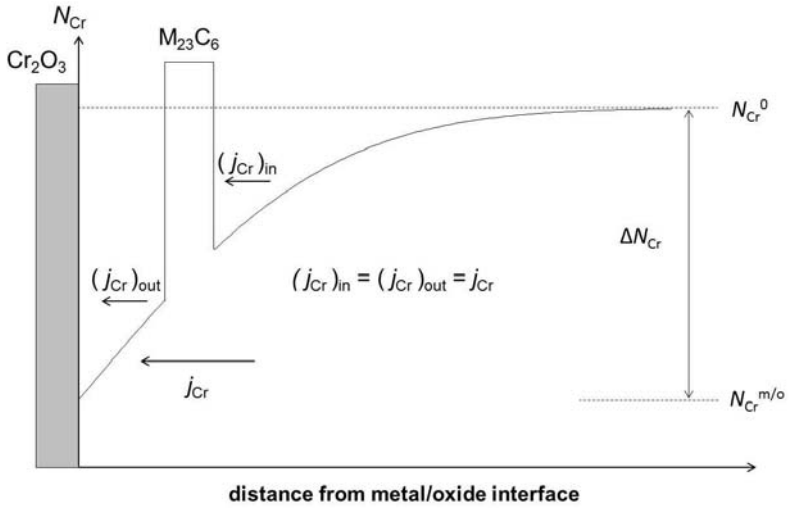

Figure 6.1 – Chromium mole fraction in the presence of a plate-like carbide precipitate underneath a protective oxide scale. The symbols $(j_{Cr})_{in}$ and $(j_{Cr})_{out}$ denote the chromium fluxes entering and departing the carbide, while j_{Cr} is the globally unaffected flux.

indicates that fast carbon ingress into the alloy is a consequence of breakaway oxidation, rather than a precursor.

Freshly formed nodules were observed in regions of the Fe–20Cr surface where carburisation did not occur beneath the surrounding Cr_2O_3 scale. Similarly, in the case of Fe–25Cr, Fe–20Cr–10Ni and Fe–20Cr–20Ni, carburisation was almost completely absent below the protective Cr_2O_3 scale, but the alloys formed Fe-rich oxide nodules (see Section 3.3.3). Thus chromium-rich carbide precipitation is not a necessary condition for breakaway.

Giggins and Pettit [12] found that at 900 °C, a model Fe–15Cr alloy formed a protective oxide scale in O_2, but produced a rapidly growing Fe-rich oxide scale and internal carbides in CO_2. Furthermore, precarburisation and subsequent exposure to O_2 also resulted in breakaway, with the same rate and morphology as in CO_2. The authors concluded that carbide precipitation lessened the outward chromium flux and prevented external Cr_2O_3 growth. However, their precarburisation experiment produced a situation of massive internal carbide precipitation and a heavily depleted alloy matrix.

In contrast, Fe–20Cr reaction in CO_2 at 650 °C is found here initially to lead to Cr_2O_3 formation and only limited carburisation, leaving an outward chromium flux sufficient to sustain the scale growth. This protective behaviour is thus expected to be maintained under steady-state conditions, that is, as long as the scale permeability to oxygen and carbon is unaltered, and as long as it remains mechanically intact.

Nonetheless, the alloy ultimately went into breakaway. An Fe–20Cr specimen from the same alloy batch used for CO_2 reaction was reacted in dry air at 650 °C for 336 h, resulting in exclusive Cr_2O_3 formation. Clearly then, breakaway in CO_2 must be accelerated by carbon, although carbide precipitation beneath Cr_2O_3 is not of itself a sufficient condition. Further discussion requires the conditions for Cr_2O_3 failure to be defined.

6.1.2 Mode of Cr_2O_3 failure

Breakaway follows from the alloy's inability to maintain growth of the protective scale. The case of Cr_2O_3-forming alloys has been extensively discussed, for example in Refs. [65, 85, 86]. Chemical failure occurs when the oxygen activity at the metal/oxide interface exceeds the value required for iron to react with Cr_2O_3 to form $FeCr_2O_4$ according to

$$\underline{\mathrm{Fe}} + \underline{\mathrm{O}} + \mathrm{Cr_2O_3} = \mathrm{FeCr_2O_4} \tag{6.5}$$

where underlining denotes solid solution in the metal matrix. The critical oxygen activity is reached when a_{Cr} falls below the value defined by the equilibrium between Cr_2O_3 and chromium in the alloy

$$2\,\underline{\mathrm{Cr}} + 3\,\underline{\mathrm{O}} = \mathrm{Cr_2O_3} \tag{6.6}$$

Thus, assuming that the oxygen necessary for the formation of $FeCr_2O_4$ comes only from the dissociation of Cr_2O_3, the competition reaction is

$$\underline{\mathrm{Fe}} + \frac{4}{3}\,\mathrm{Cr_2O_3} = \frac{2}{3}\,\underline{\mathrm{Cr}} + \mathrm{FeCr_2O_4} \tag{6.7}$$

Since the chromium concentration involved is small, the solvent iron is approximated as pure ($a_{\mathrm{Fe}} = N_{\mathrm{Fe}} = 1$), and the law of mass action for reaction (6.7) is written

$$K_{6.7} = \exp\left(\frac{-\Delta_{\mathrm{f}}G^0_{\mathrm{FeCr_2O_4}} + \frac{4}{3}\Delta_{\mathrm{f}}G^0_{\mathrm{Cr_2O_3}} - \frac{2}{3}\Delta\bar{G}^{\mathrm{xs}}_{\mathrm{Cr}}}{RT}\right) = N^{2/3}_{\mathrm{Cr}} \tag{6.8}$$

where $\Delta_{\mathrm{f}}G^0_{\mathrm{i}}$ is the standard free energy of formation of oxide i, and $\Delta\bar{G}^{\mathrm{xs}}_{\mathrm{Cr}}$ the excess free energy of mixing for chromium solution in the metal matrix. The critical chromium atom fraction for Cr_2O_3 stability, N^*_{Cr}, is thus calculated from standard free energies [74] and dissolution data [75] to be 1.2×10^{-5} at $T = 650$ °C.

To sustain selective chromia formation, it is necessary that Cr_2O_3 be both thermodynamically and kinetically stable. Wagner [78] showed that the condition for an alloy chromium flux sufficient to maintain exclusive chromia growth is met if

application of Eq. (6.1) yields values of $N_{Cr}^{m/o} \geqslant 0$. Thermodynamic stability further requires that $N_{Cr}^{m/o} \geqslant N_{Cr}^{*}$; these requirements are essentially the same, given the value of N_{Cr}^{*}. In all cases where a protective chromia scale is retained, then by definition the condition is met. Evaluation of $N_{Cr}^{m/o}$ is nonetheless useful, as it provides a guide as to how close an alloy might be to breakaway.

In the case of Fe–20Cr reacted in dry CO_2, Eq. (6.1) yields $N_{Cr}^{m/o} = (6.9 \pm 4.6) \times 10^{-2}$, where the average and standard deviation were calculated from a large number (84) of experimental $X_{Cr_2O_3}$ values, measured after 40–240 h of reaction. The surplus of chromium over the N_{Cr}^{*} requirement is variable and sometimes small. Similar values were obtained from specimens reacted in wet CO_2. In the case of Fe–25Cr exposed to both dry and wet CO_2, values of $N_{Cr}^{m/o}$ calculated from local $X_{Cr_2O_3}$ and Eq. (6.1) were about 10–15 at. %, in reasonable agreement with EDS measurements (Fig. 3.60), and far above the critical value, N_{Cr}^{*}. In the case of the ternary alloys, meaningful values of D_{Cr} are not available, because short-circuit (grain boundary and dislocation) diffusion prevails at the low reaction temperature of 650 °C [19]. Indeed, the 10Ni alloys possess a fine $\alpha+\gamma$ structure, and in the fully austenitic 20Ni alloys, the effects of cold working in the subscale region are likely to be still present at 650 °C [177]. In the absence of D_{Cr} values, no estimate of $N_{Cr}^{m/o}$ is possible.

Under steady-state conditions then, the Fe–20Cr alloy is in some locations heavily depleted, but the Fe–25Cr alloy only moderately so. Nonetheless, both alloys suffered short-term breakaway. It is recognised that the diffusional steady-state described by Eqs. (6.1–6.4), and experimentally observed in Fe–20Cr (Fig. 3.56) and Fe–25Cr (Fig. 3.60) is predicted to endure until depletion reaches the specimen center. As depletion zones were very shallow, such an outcome was remote under the conditions considered here. Thus steady-state chromia scale growth, once established, is predicted to remain in effect within the experimental time frame. Clearly, this prediction failed for the alloys examined.

Scale cracking or spallation can expose the depleted alloy to the reacting gas. Reformation of chromia at the relatively fast rate typical of initial growth causes an increase in the outward chromium flux, and $N_{Cr}^{m/o}$ first decreases before returning to the steady-state value (see Fig. 1.15). If $N_{Cr}^{m/o}$ falls below N_{Cr}^{*} during the transient stage, chemical failure occurs. As shown in Section 1.3.4, Whittle's analysis [83] allows the minimum chromium content required to reform Cr_2O_3 after one or several spallation events to be approximated, on the basis of a number of more or less restrictive assumptions. Limits of this treatment, along with those of other treatments derived from it, were discussed by Nesbitt [178] in the context of cyclic oxidation with repeated spallation. In the present case, where chromium depletion

profiles were rather steep (Fig. 3.56), it is unclear whether Whittle's neglect of the recession of the metal/oxide interface is acceptable. This assumption amounts to making the approximation $F(u) \simeq \sqrt{\pi}u$ (valid for $u \ll 1$) in Eq. (6.1). The size of the resulting error is estimated using the average scale thickness for the reaction of Fe–20Cr in Ar–20CO_2 at 650 °C. If $(N^0_{Cr})_I$ is defined as the minimum alloy chromium concentration to sustain Cr_2O_3 kinetic stability, obtained for $N^{m/o}_{Cr} = N^*_{Cr}$, the approximate expression obtained by Whittle in place of Eq. (6.1) (see Section 1.3.4) yields $(N^0_{Cr})_I = 0.18$, whereas the exact solution Eq. (6.1) leads to $(N^0_{Cr})_I = 0.16$. The difference is small, which allows Whittle's calculation [83] to be used in order to estimate the minimum alloy chromium concentration needed for the alloy to reform Cr_2O_3 after mechanical failure

$$\left(N^0_{Cr}\right)_{II} = \phi(2 - \phi) \tag{6.9}$$

where $\phi = \dfrac{2V_a}{V_{Cr_2O_3}}\sqrt{\dfrac{\pi k_{p,Cr_2O_3}}{2D_{Cr}}}$. Using the values of $X_{Cr_2O_3}$ measured on Fe–20Cr after reaction in Ar–20CO_2, one obtains $(N^0_{Cr})_{II} = 0.31 \pm 0.08$ (standard deviation obtained from 84 $(N^0_{Cr})_{II}$ values), which exceeds the alloy chromium concentration. The implication is clear: while the Fe–20Cr alloy may form Cr_2O_3 initially, it would fail to reform Cr_2O_3 if the initial scale sustained mechanical failure.

No steady-state description can encompass the onset of breakaway. However, examination of Eq. (6.1) reveals that the steady-state description loses applicability if k_{p,Cr_2O_3} changes, leading to a change in the boundary value and, by definition, a change in the reaction state. As discussed already, k_{p,Cr_2O_3} varied with position on the same specimen, and fluctuations in chromia growth rate must therefore be considered. Although the origins of these fluctuations are obscure, their consequences can be anticipated. Locally increased scaling rates can accelerate mechanical failure of the scale as growth stresses rise with increasing scale thickness. The lower value of $N^{m/o}_{Cr}$ induced by faster scaling means that scale cracking or spallation can allow gas access to a more heavily depleted alloy surface which cannot then repassivate. More simply, a sufficient increase in k_{p,Cr_2O_3} will render the scale kinetically unstable, because of limited alloy diffusion. In the case of Fe–20Cr, the $N^{m/o}_{Cr}$ values calculated from Eq. (6.1), $(6.9 \pm 4.6) \times 10^{-2}$, are close to the critical value. It is concluded that fluctuations in scaling rate can lead to breakaway, either through exceeding the alloy's capacity to supply chromium to the scale or by accelerating mechanical failure.

The effect of carbon on the breakaway process is obviously of interest. As already established, limited carbide precipitation beneath Cr_2O_3 does not affect the

kinetic stability of the protective scale during steady-state growth, because carbide dissolution releases chromium. During the transient stage following Cr_2O_3 failure, while the demand for chromium is increased, the presence of a carbide plate in the depletion zone may reduce the chromium flux to the alloy surface if carbide dissolution is not instantaneous. However, in most cases examined here, carburisation of the alloy was seen not to be a necessary condition for breakaway. Nevertheless, since the onset of breakaway in CO_2 is greatly accelerated compared with the process in dry air, carbon must play some part in changing scale properties and/or k_{p,Cr_2O_3}.

No direct information is available from the present work for the mechanism of carbon entry into growing chromia scales. It is known [122] that the solubility of carbon in Cr_2O_3 is negligible. In light of this, the observation of carbide formation beneath chromia scales grown on both pure chromium and Fe–Cr alloys led to the proposal [121,125] that carbon penetrated the scales as molecular species (CO/CO_2) along internal surfaces. As scale growth is supported by grain boundary diffusion, alterations to k_{p,Cr_2O_3} can result from direct diffusional interactions, or indirectly from changed grain size and/or shape. In addition, the presence of carbon-bearing species on grain boundaries could affect the scale mechanical properties, rendering it more susceptible to fracture. Information on the form and location of carbon is lacking, and these possibilities cannot be explored further at this time.

6.1.3 Morphological evolution during breakaway

6.1.3.1 Fe–20Cr

An early stage of Fe-rich oxide growth on Fe–20Cr is shown in Fig. 3.51. Beneath the nodule lies a Cr-rich oxide layer which appears to be continuous with the surrounding, protective Cr_2O_3 scale. In fact, this layer evidences quite different behaviour at the nodule centre and its periphery. The depletion profile recorded below the outer part of the small nodule, marked by the left hand arrow in Fig. 3.51(a), is shown in Fig. 3.56(e). No significant difference is seen between it and other profiles plotted in the same graph, which were recorded underneath the protective Cr_2O_3 scale, away from any Fe-rich nodule. Thus, the concentration profile is not affected by the presence of the nodule; in particular, the chromium concentration is low below the metal/oxide interface, despite the fact that the outer layer located directly above is pure iron oxide (Fe_2O_3). This apparent contradiction with local mass balance shows that the morphology of the small nodule is transient, of course, and that outward iron diffusion across the metal/oxide interface to form Fe_2O_3 occurred only in the centre of the nodule, at a location where the chromia layer had lost its protective

character. Furthermore, internal Cr-rich spinel particles were found below the centre of the nodule, although a Cr_2O_3 layer appeared to be present at the metal surface (zone 3 in Fig. 3.52). Since Cr_2O_3 is inherently more stable than the spinel oxide, local thermodynamic equilibrium along a p_{O_2} gradient would preclude internal spinel precipitation underneath a true Cr_2O_3 layer. This observation also reflects the transient nature of the nodule, and shows that inward oxygen diffusion to form the internal oxide occurred only beneath the nodule centre, where the Cr-rich layer was no longer protective, and the local oxygen activity had increased.

Halvarsson et al. [179] made very similar observations in a study of 304L steel (18.5 wt. % Cr) oxidation in O_2–H_2O at 600 °C, and their TEM observations coupled with chemical analysis and diffraction studies allowed a more precise characterisation of the oxide phases. Away from the nodules, the protective scale was a Cr-rich corundum type oxide. In regions of breakaway oxidation, the intermediate oxide layer continuous with the protective scale also had a corundum structure, and contained more chromium than the surrounding inner and outer scales. Its chromium content abruptly dropped along the original metal/oxide interface, toward the nodule centre (from 80–85 wt. % to 55–60 wt. % Cr, in terms of cation content, over a 100 nm distance). At the nodule centre, in a 1–2 µm wide region, the chromium content was as low as 40 wt. %, and the oxide had a spinel structure.

The mechanism of breakaway oxidation may then be understood as follows: initially, the alloy surface is covered by a protective Cr_2O_3 scale, the growth of which generates a subsurface chromium-depleted zone. Failure of the Cr_2O_3 scale occurs locally, either in a mechanical way such as cracking, or by fluctuations in k_{p,Cr_2O_3}, leading to chemical failure. The chromium-depleted alloy is exposed to the atmosphere and, unable to reform Cr_2O_3, produces spinel oxide. Töpfer et al. [72] showed that the iron tracer diffusion coefficient was about 3 orders of magnitude higher than that of chromium over a range of oxygen activity in $Fe_{3-x}Cr_xO_4$ spinels, with $0 < x < 0.4$, at 1200 °C. This observation is likely to hold, at least qualitatively, at the lower temperature of the present work. Thus, the outward cation flux across the newly formed spinel oxide comprises mainly iron, and an outer Fe_2O_3 layer is formed. As a further consequence of spinel formation, the interfacial oxygen activity rises locally, and oxygen permeability in the metal reaches a value where outward chromium diffusion from the depleted alloy is not sufficient to prevent internal precipitation of Cr-rich spinel.

At first, the counterflows of iron and oxygen are located in the centre of the nodule, and the nearby alloy is not affected. The processes described above produce a subscale alloy matrix at local equilibrium with the spinel precipitates. Conse-

quently, the interfacial chromium activity is too low to stabilise Cr_2O_3. As oxygen diffusion into the alloy is inward but also lateral, internal precipitation and conversion of the Cr_2O_3 layer to spinel oxide spread laterally. Since fast iron and oxygen diffusion across the originally protective layer is limited to a central region, whereas the inner and outer parts may grow in all directions, the nodule assumes an elliptical shape. Then, as oxygen diffuses inward into the alloy, the depth of the internal oxidation front increases, while the metal matrix surrounding the internal Cr-rich spinel particles is subsequently oxidised into an Fe-rich spinel, forming the two-phase inner oxide layer. Fast outward iron diffusion results in the formation of Fe_3O_4 beneath the first formed Fe_2O_3. As iron diffuses faster than chromium in the spinel phases [72], kinetic demixing [180–182] maintains the observed structure, with an outer scale consisting of pure iron oxides, and an inner scale containing both iron and chromium.

Continued nodule growth is proposed to occur by outward iron diffusion along a_{Fe} gradients, which are defined by the iso-a_{Fe} lines, themselves determined by the nodule shape. On this basis, the protective Cr_2O_3 scale is expected to be enveloped by the laterally growing nodule, as shown in Fig. 6.2. The high iron activity in the

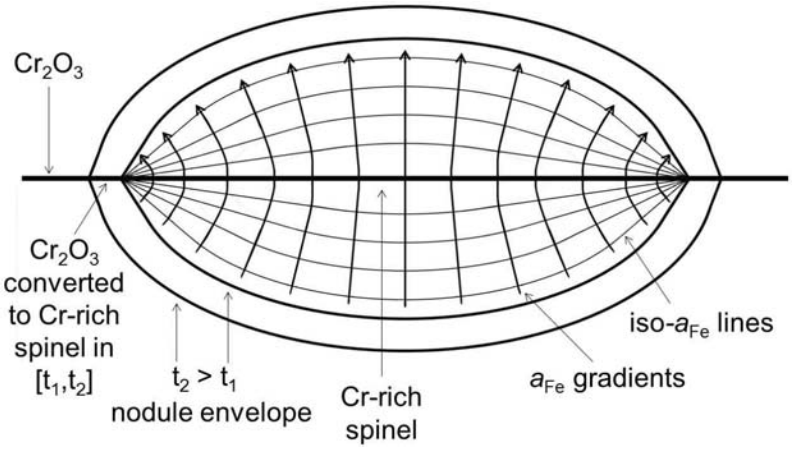

Figure 6.2 – Schematic representation of nodular oxide growth.

outer and inner oxides destabilises the chromia, which is converted to Cr-rich spinel. A steady-state is thus arrived at, where the elliptical shape is maintained. Describing lateral and vertical growth with the same solid-state diffusion process qualitatively accounts for the fact that lateral growth is parabolic, with a rate proportional to the thickening rate (Fig. 3.67). Nodule growth and overlapping eventually results in the uniformly thick scales typified by Fig. 3.54(a).

The volume fraction of internal oxides was very high ($f_{V-ox} = 0.7 \pm 0.1$, see

Section 3.3.3.1). In particular, it exceeded the value measured by Rapp [183] for the transition from internal to external oxidation of Ag–In alloys at 550 °C, $f^*_{V-ox} = 0.3$. The oxides form such a dense precipitation zone rather than a continuous layer because they are produced by in situ oxidation of preexisting internal carbides [13, 112], as discussed in Section 5.2.1.1. Extensive carburisation beneath the Fe-rich oxide nodules and scales causes massive chromium depletion in the alloy matrix, and carbide dissolution cannot sustain the chromium flux required to reform a Cr-rich layer at the base of the scale [12]. Thus whilst internal carburisation is a consequence, not a cause, of the onset of breakaway, subsequent oxidation of the carbides permanently immobilises the chromium, making repassivation impossible. Iron-rich oxide formation, together with in situ oxidation of chromium (in the form of internal carbides, internal oxides and Cr-rich oxide particles in the inner scale), are thus maintained in a fast steady-state reaction.

Following on the approach used for the dilute alloys in Section 4.2.1, the two steady-states characterising the reaction of Fe–20Cr at 650 °C are represented by diffusion paths on the Fe–Cr–O phase diagram in Fig. 6.3, and the corresponding oxide constitutions are depicted in Fig. 6.4. The case of protective scaling is straightforward: formation of Cr_2O_3 leads to chromium depletion in the alloy, represented by a horizontal segment on the Fe–Cr binary. Subsequently, the diffusion path follows a tie-line in the $\alpha + Cr_2O_3$ field, reflecting the alloy/scale phase boundary. The multilayer, Fe-rich scale formed as a result of breakaway oxidation of Fe–20Cr is quite similar to that grown on the dilute alloys. As discussed in Section 5.2.1, the permeability of carbon in the alloy, defined as the $N_C^{(i)} D_C$ product, is much higher than that of chromium. Carburisation proceeds without large scale chromium diffusion, and the global chromium concentration in the internal carburisation zone equals that in the bulk alloy. Thus the internal oxidation front advances into a material globally containing as much chromium as the bulk alloy, but where chromium mobility is reduced. As in the case of dilute alloys, the diffusion path in the Fe–Cr–O diagram (Fig. 6.3) first traverses a chromium-enriched region (inner scale), crosses the alloy–O_2 line, and follows the Fe–O binary (outer scale). The relatively high chromium content allows FeO formation to be avoided in the inner scale, although some FeO was occasionally observed at the base of the outer scale. However, as pointed out in Section 4.2.4, the suppression of FeO had no significant effect on the overall diffusivity of the inner scale, and scaling rates were found to be similar for Fe–9Cr and Fe–20Cr.

Finally, it is noted that the chromium enrichment in the internal oxidation zone and in the inner scale layer is not the result of alloy diffusion and selective oxidation

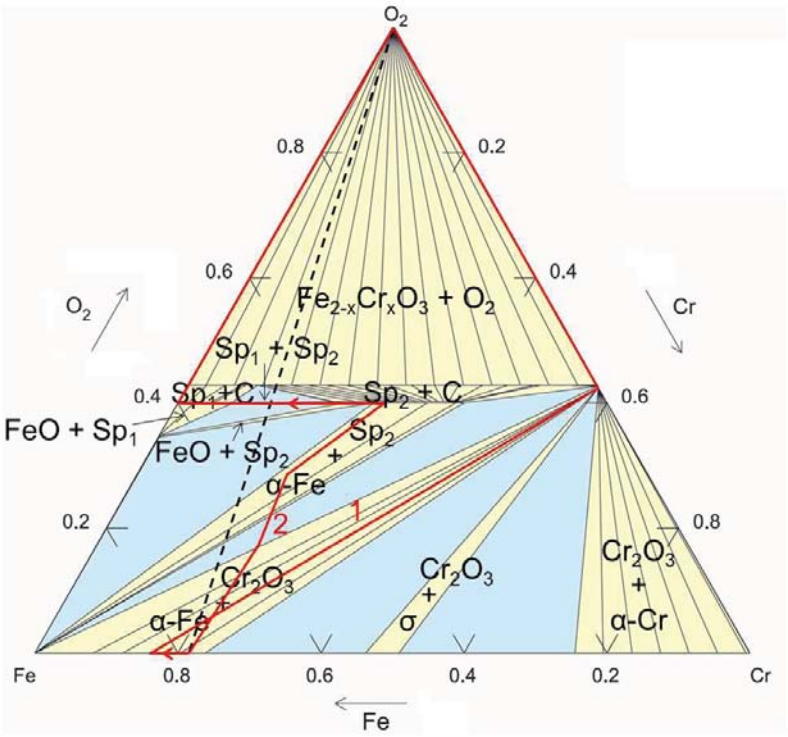

Figure 6.3 – Isothermal section of Fe–Cr–O phase diagram calculated at 627 °C (after Ref. [71]) and diffusion paths representing protective and non-protective oxidation of Fe–20Cr at 650 °C. C: corundum phase $Fe_{2-x}Cr_xO_3$; Sp_1 and Sp_2: Fe-rich and Cr-rich spinel phases $Fe_{3-x}Cr_xO_4$, respectively. The dashed line joins the oxygen corner to the unreacted alloy composition.

(a) Protective oxidation (b) Non-protective oxidation

Figure 6.4 – Schematic representation of scale constitution along diffusion paths shown in Fig. 6.3

of chromium. Rather, it is the consequence of iron removal via rapid growth of the outer iron oxide layers.

6.1.3.2 Fe–20Cr–10Ni and Fe–20Cr–20Ni

Nodules grown on Fe–20Cr–10Ni and Fe–20Cr–20Ni were morphologically similar to those found on Fe–20Cr. The composition of the inner layer was different, as it contained nickel, and internal oxidation was suppressed. A reaction mechanism similar to that discussed above for Fe–20Cr is thought to apply for the 20Cr ternaries. After the protective Cr_2O_3 scale fails and oxygen starts diffusing inward in the alloy, the most stable spinel $FeCr_2O_4$ is first formed. The surrounding Cr-depleted matrix is then oxidised, producing a nickel-containing spinel, $Ni_xFe_{3-x}O_4$, instead of Fe_3O_4 (see Section 3.3.3.3).

No specification on the composition of the nickel-containing spinel could be obtained from Raman or EDS analysis, and the lack of thermodynamic data for the quaternary Fe–Cr–Ni–O system[1] further hinders a quantitative discussion of the reaction morphology. Assuming that the stoichiometric compound $NiFe_2O_4$ was formed, the competition reaction with pure Fe_3O_4 is written

$$Ni + Fe_3O_4 = Fe + NiFe_2O_4 \tag{6.10}$$

with, at equilibrium between the two spinel phases,

$$K_{6.10} = \exp\left(\frac{-\Delta_f G^0_{NiFe_2O_4} + \Delta_f G^0_{Fe_3O_4}}{RT}\right) = \frac{a_{Fe}}{a_{Ni}} \tag{6.11}$$

Nickel ferrite is inherently less stable than magnetite, and standard free energies of formation, $\Delta_f G^0_i$, calculated from data tabulated in Ref. [74] yield $a_{Fe}/a_{Ni} = 3 \times 10^{-4}$. Therefore, the formation of $NiFe_2O_4$ instead of Fe_3O_4 indicates a substantial increase of the Ni/Fe ratio at the metal/oxide interface, relative to the bulk alloy. This nickel enrichment can be understood as a consequence of outward iron diffusion to form the outer oxide layers. It was, however, too shallow to be detected by SEM-EDS (Fig. 3.64(a)).

The presence of isolated metal islands in the inner scale formed on Fe–20Cr–10Ni (Fig. 3.63) reflects a non-equilibrium situation. As the oxidation front initially moves inward into the alloy of bulk composition, the thermodynamics of reaction (6.10) require that nickel stays unoxidised, and accumulate at the metal/oxide interface until local nickel enrichment allows $NiFe_2O_4$ formation to proceed. If the relative inward displacement of the metal/oxide interface is rapid in comparison to nickel

[1] These data exist, but were not available to the present author.

diffusion in the alloy and $NiFe_2O_4$ formation, it is then possible that a nickel-rich metal phase is incorporated into the growing scale. However, SEM-EDS analysis of the metal island showed in Fig. 3.63(b) indicated that its composition was close to that of the bulk alloy. This observation, together with the apparent absence of any depletion/enrichment zone in the metal substrate beneath the scale, supports the view that because diffusion in the alloy was slow compared to the scaling rate, compositional changes in the metal phase were not rapid enough for local equilibrium to be achieved as the oxidation front progressed inward.

Another difference between the binary and ternary 20Cr alloys is that nickel additions suppressed internal oxidation. Again, no quantitative argument can be made in the absence of a proper description of the system's thermodynamics. For comparison purposes then, local equlibrium at the metal/oxide interface of the binary and ternary 20Cr alloys is represented by the reactions

$$3\,\mathrm{Fe} + 2\,\mathrm{O_2} = \mathrm{Fe_3O_4} \tag{6.12}$$

$$\mathrm{Ni} + 2\,\mathrm{Fe} + 2\,\mathrm{O_2} = \mathrm{NiFe_2O_4} \tag{6.13}$$

for which the laws of mass action yield

$$p_{\mathrm{O_2}}(\mathrm{alloy}/\mathrm{Fe_3O_4}) = \left[a_{\mathrm{Fe}}^3 \exp\left(\frac{-\Delta_\mathrm{f} G^0_{\mathrm{Fe_3O_4}}}{RT}\right)\right]^{-1/2} \tag{6.14}$$

$$p_{\mathrm{O_2}}(\mathrm{alloy}/\mathrm{NiFe_2O_4}) = \left[a_{\mathrm{Ni}} a_{\mathrm{Fe}}^2 \exp\left(\frac{-\Delta_\mathrm{f} G^0_{\mathrm{NiFe_2O_4}}}{RT}\right)\right]^{-1/2} \tag{6.15}$$

Activities are approximated to be mole fractions. In the case of Fe–20Cr, the alloy composition at the interface with the scale was not measured, and is difficult to estimate, as it depends on the volume fraction and composition of internal oxides and carbides. The bulk alloy composition is considered for simplicity. As discussed above, in the case of the ternary alloys, it is not clear whether nickel enrichment expected from local equilibrium prevailed or not. The alloy composition may then be described using two limiting situations: non-equilibrium, where the interfacial composition is that of the bulk alloy, and equilibrium, where the $a_{\mathrm{Fe}}/a_{\mathrm{Ni}}$ ratio is determined by Eq. (6.11). In the latter case, a_{Fe} and a_{Ni} are approximated as 10^{-4} and 1, respectively. Values of $p_{\mathrm{O_2}}$ shown in Table 6.1 indicate that in any case, $p_{\mathrm{O_2}}(\mathrm{Fe–20Cr}/\mathrm{Fe_3O_4}) < p_{\mathrm{O_2}}(\mathrm{Fe–20Cr–10Ni}/\mathrm{NiFe_2O_4})$, because Fe_3O_4 is inherently more stable than $NiFe_2O_4$. On this basis, the presence of a Ni-containing spinel instead of Fe_3O_4 in the ternary alloys is expected to favour internal oxidation.

Table 6.1 – Values of p_{O_2} (atm) at the metal/oxide interface of nodules grown on Fe–20Cr and Fe–20Cr–10Ni at 650 °C calculated from oxide standard free energies of formation in Ref. [74] (details given in text).

Metal composition	$Fe–20Cr/Fe_3O_4$ Eq. (6.14)	$Fe–20Cr–10Ni/NiFe_2O_4$ Eq. (6.15)
bulk alloy	1.3×10^{-23}	2.3×10^{-21}
$a_{Fe} = 10^{-4}$; $a_{Ni} = 1$		4.8×10^{-18}

The minimum bulk alloy chromium concentration required for the transition from internal to external oxidation is usually evaluated using Wagner's expression [67]

$$N_{Cr}^{0} = \left(\frac{\pi g^{*}}{2\nu} \frac{V_{alloy}}{V_{oxide}} \frac{N_{O}^{(s)} D_{O}}{D_{Cr}} \right)^{1/2} \tag{6.16}$$

where the symbols have their usual meaning. This relation is valid only when a number of conditions are met (see Section 1.2.3). In particular, it applies to pure chromium oxide, in situations where the chromium permeability is far greater than that of oxygen, and the chromium outward flux is substantial ($\frac{N_{O}^{(s)}}{N_{Cr}^{0}} \ll \frac{D_{Cr}}{D_{O}} \ll 1$). In the present case, the oxide of interest is a Cr-rich $Fe_{3-x}Cr_xO_4$ spinel, and the presence of an outer scale of pure iron oxides further complicates the mass balance underlying Eq. (6.16). Furthermore, the condition $N_{O}^{(s)} D_{O} \ll N_{Cr}^{0} D_{Cr}$ is not met, as is shown subsequently. Values of N_{Cr}^{0} cannot then be calculated using Eq. (6.16). The analysis was extended to less restrictive conditions by several investigators (in Ref. [184] for instance), but the lack of precision for a number of parameters (oxide composition, diffusivities in the metal phase) render any quantitative attempt irrelevant in the present situation. However, the essence of the calculation can be used, at least qualitatively. The analysis is based on the relative fluxes of chromium (outward) and oxygen (inward) at the alloy surface when the volume fraction of oxide precipitates reaches a critical value. Assuming that this critical value is the same for Fe–20Cr and Fe–20Cr–10/20Ni, an approximate comparison of the relative propensities of the alloys for internal oxidation is made here on the basis of the $\frac{N_{O}^{(s)} D_{O}}{D_{Cr}}$ ratio.

The oxygen solubility at the alloy surface, $N_{O}^{(s)}$, is taken to be the oxygen mole fraction at the metal/oxide interface, calculated from the oxide dissociation pressure according to Sievert's law

$$N_{O}^{(s)} = \exp\left(\frac{-\Delta \bar{G}_{O}^{xs}}{RT} \right) p_{O_2}^{1/2} \tag{6.17}$$

The phase constitution of the Fe–20Cr, Fe–20Cr–10Ni and Fe–20Cr–20Ni alloys was α, $\alpha + \gamma$ and γ, respectively (Section 2.1). For simplicity, standard free energies of dissolution of oxygen [185] in α-Fe and γ-Fe are used for the binary and ternary alloys, respectively. It is noted that describing the alloy γ phase as pure γ-Ni (data in Ref. [186]) yields very similar results. Values of $N_O^{(s)}$ are then estimated using p_{O_2} corresponding to the equilibrium of spinel oxide with alloys of the bulk composition, as given in Table 6.1. Oxygen diffusion coefficients [185] in α-Fe and γ-Fe are used for the binary and ternary alloys, respectively.

Chromium diffusion coefficients in α-Fe or ferritic Fe–Cr alloys with 0 to 25Cr, calculated from diffusion data obtain by various investigators [81,187,188], all fall in the range $10^{-14}-10^{-13}$ cm^2 s^{-1} at $T = 650$ °C. The median value 5.6×10^{-14} cm^2 s^{-1}, corresponding to chromium diffusion in α-Fe [81], is used here, as in the rest of this document. In the case of the γ phase, considerable scatter exists between results available in the literature. Values of D_{Cr} in γ-Fe and various austenitic Fe–Cr–Ni alloys, extrapolated to $T = 650$ °C, are found to be, for example, 2.7×10^{-17} cm^2 s^{-1} [189], 2.5×10^{-16} cm^2 s^{-1} [81], or 2.3×10^{-15} cm^2 s^{-1} [190] — these variations do not reflect any alloy composition effect, but rather disagreement between the sources. Furthermore, as discussed in Section 6.1.2, short-circuit diffusion prevails at the low reaction temperature of 650 °C.

The value of $\dfrac{N_O^{(s)} D_O}{D_{Cr}}$ is thus found to be 0.25 for the ferritic alloy, and, allowing for the discrepancy in D_{Cr}, from 2 to 2×10^2 for the austenitic alloys. The effective diffusion coefficient, D_{Cr}^{eff}, taking into account short-circuit diffusion and the fact that the Fe–20Cr–10Ni alloy has an $\alpha + \gamma$ structure, is difficult to predict. Values of D_{Cr}^{eff} for the ternary alloys could be several orders of magnitude higher than the lattice coefficient, but likely not above D_{Cr}^{eff} for the binary alloy. It is concluded that the $\dfrac{N_O^{(s)} D_O}{D_{Cr}}$ ratio is, in any case, not smaller for the ternary alloys than it is for Fe–20Cr. Thus, the absence of internal oxidation associated with alloy nickel additions cannot be accounted for on this basis.

However, the results can be rationalised by considering the effect of carburisation. No intragranular carbides were formed in the ternary alloys beneath the Fe-rich nodules, probably reflecting the fact that the inner layer, consisting of $FeCr_2O_4 + NiFe_2O_4$, was a better barrier to carbon than the Fe-rich + Cr-rich $Fe_{3-x}Cr_xO_4$ mixture formed in Fe–20Cr. A direct comparison of carbon permeability cannot be made because the carbon solubility differs between the binary and ternary alloys (see Section 5.3). Nonetheless, it is clear that carburisation of Fe–20Cr reduced the possibility of satisfying the criterion of Eq. (6.16), whereas the

absence of carbides in the ternary alloys favoured external over internal oxidation.

As noted in Section 4.2.3, the oxide growth rate decreased with increasing alloy nickel concentration, reflecting the substitution of nickel-containing spinel for the faster diffusing Fe-rich spinel in the inner scale.

6.1.3.3 Fe–25Cr

The different types of oxide observed during steady-state reaction of Fe–25Cr at 650 °C are represented by diffusion paths in the Fe–Cr–O phase diagram in Fig. 6.5. Protective Cr_2O_3 growth is represented by diffusion path # 1. Its failure resulted

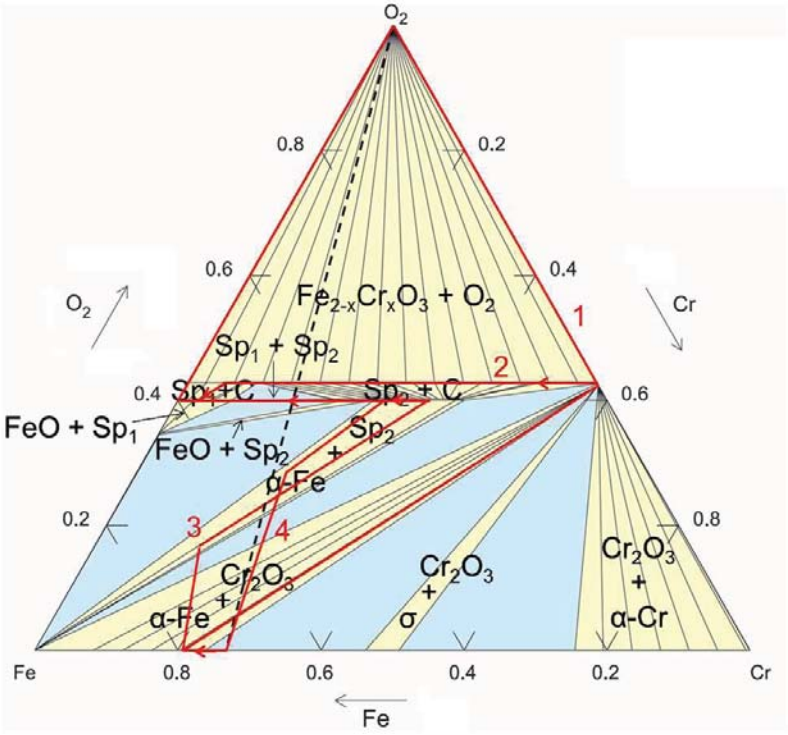

Figure 6.5 – Isothermal section of Fe–Cr–O phase diagram calculated at 627 °C (after Ref. [71]) and diffusion paths representing protective and non-protective oxidation of Fe–25Cr at 650 °C. C: corundum phase $Fe_{2-x}Cr_xO_3$; Sp_1 and Sp_2: Fe-rich and Cr-rich spinel phases $Fe_{3-x}Cr_xO_4$, respectively. The dashed line joins the oxygen corner to the unreacted alloy composition.

in two types of oxide morphology: healed scales on the specimen faces, containing a Cr-rich inner layer, of either corundun (# 2) or spinel type (# 3), and thick Fe-rich nodules (# 4) near the edges of the specimens. The formation, after Cr_2O_3 failure, of two types of scale morphologically equivalent to those observed in the present work, at different locations of a given specimen, has been documented and

discussed by previous investigators. This was the case, for example, after exposure to high pressure CO_2 (41 bar, containing 1–3 % CO and 200–700 ppm H_2O) of 9Cr1Mo steels in the temperature range 450–650 °C [105], and of 18/8 steels at 650 °C [117], and was also reported to occur for an Fe–18Cr alloy at 800–1200 °C in air [86]. The views expressed by the authors as to the processes leading to two different post-failure oxide structures are consistent with each other. These are applied to the present results in the following paragraphs.

Near the specimen edges, the high surface to volume ratio, and/or significant spallation, resulted in severe chromium depletion and formation of the thick Fe-rich nodules. In these regions, the external oxide constitution ($Sp_1 + Sp_2/Fe_3O_4/Fe_2O_3$) and the internal reaction zones (dense oxide and carbide precipitation) were equivalent to the reaction morphology observed for the Fe–20Cr alloy. It is likely then that a similar reaction mechanism prevailed. Essentially, the external scale, by virtue of its low chromium content, grows rapidly and is relatively permeable to carbon, which allows internal reaction to occur. This in turn immobilises chromium, and fast scaling is further maintained. As noted in Section 4.2.3, oxide growth was slower on Fe–25Cr than on Fe–20Cr, most likely reflecting a higher volume fraction of slow diffusing, Cr-rich spinel Sp_2 in the inner scale.

Away from the edges, the chromium concentration at the Cr_2O_3/alloy interface was quite high (10–15 at. % as determined from Eq. (6.1) and SEM-EDS), which enabled the formation of a Cr-rich oxide after localised Cr_2O_3 failure. This reaction morphology corresponds to the diffusion paths # 2 and 3 in Fig. 6.5, and schematic oxide constitutions are represented in Fig. 6.6. As discussed in Section 4.2.3, whether

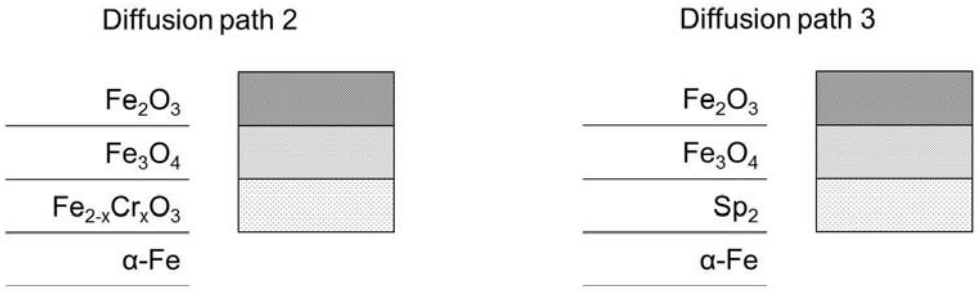

(a) Corundum type Cr-rich layer (b) Spinel type Cr-rich layer

Figure 6.6 – Schematic representation of scale constitution along the two diffusion paths corresponding to the healed type of scale shown in Fig. 6.5

the Cr-rich layer present at the base of the scale was of corundum or spinel type, its diffusivity was relatively low, which accounts for the low growth rate, as compared

to that of the Fe-rich thick nodules. Furthermore, the healed scale was seen to be a relatively good barrier to carbon, preventing carburisation (see Section 5.2.2.2). For these two reasons, chromium diffusion in the alloy toward the metal/oxide interface was substantial, and the relatively protective morphology was maintained. Accordingly, a chromium depletion profile was generated in these regions (Fig. 3.60), which is represented in the diffusion path by the horizontal segment on the Fe–Cr binary in Fig. 6.5. It is noted that Cr_2O_3 and Cr-rich, Sp_2 spinel particles are expected to precipitate internally beneath the external Sp_2 layer, on thermodynamic grounds (see path # 3 in Fig. 6.5). Their absence must then be kinetic in nature. The reduction of the depth of the internal oxidation zone, to the point where it was not visible, reflects the fact that oxygen inward diffusion in the alloy was counteracted by a substantial outward chromium flux. As discussed in Section 6.1.3.2, the relative complexity of the external oxide scales precludes a verification of this kinetic argument using the existing criteria for the transition from internal to external oxidation. It is noted that a convoluted alloy/Sp_2 interface would satisfy the diffusion path, without the need for internal oxidation.

The nature and composition of the oxide formed after Cr_2O_3 failure depends on the local alloy chromium content. The latter must have varied along the metal/oxide interface, since the oxide composition measured by SEM-EDS varied considerably with analysis location, sometimes indicating a spinel structure (as observed by Raman analysis), and sometimes corresponding to a corundum structure (see Section 3.3.3.2). Although the relationship between alloy and oxide composition at the phase boundary is uniquely defined by local thermodynamic equilibrium, it is not clear which alloy chromium content corresponds to the transition from a Cr-rich corundum oxide to a Cr-rich spinel oxide. As discussed in Section 6.1.2, when the alloy chromium concentration at the alloy/Cr_2O_3 interface decreases, the local oxygen activity rises until $FeCr_2O_4$ is stabilised and forms according to reaction (6.7). Whittle et al. [77] pointed out that this reaction was thermodynamically favoured, as compared to the formation of Fe_2O_3

$$Cr_2O_3 + 2\,\underline{Fe} = Fe_2O_3 + 2\,\underline{Cr} \tag{6.18}$$

Accordingly, $FeCr_2O_4$ is expected to form *before* Fe_2O_3, that is, for a higher chromium concentration. The authors claimed that the free energy change corresponding to the dissolution of Fe_2O_3 in Cr_2O_3 would be small, and the corresponding increase in the critical N_{Cr} value negligible. However, since Fe_2O_3 and Cr_2O_3 form a complete solid-solution, the corresponding dissociation pressures continuously decrease from values typical of the Fe_3O_4/Fe_2O_3 equilibrium, to that corresponding to the

$Cr_2O_3/FeCr_2O_4$ equilibrium. This is illustrated in Fig. 1.10; for lower p_{O_2} values, the corundum oxide contains very little iron and is termed Cr_2O_3. Thus, provided that the chromium content is high enough, the solid solution $Fe_{2-x}Cr_xO_4$ may be as stable as $FeCr_2O_4$. Indeed, it was sometimes observed to form as an inner scale instead of the spinel oxide, as suggested by the high Cr/Fe ratios measured by SEM-EDS for Fe–25Cr (Section 3.3.3.2). It is interesting to note that in a study of a commercial chromia-forming steel reaction in O_2 and O_2–H_2O at 600 °C [191], the inner scale of an early stage nodule was shown by TEM-CBED[1] to have a cubic structure, but TEM-EDS analysis at the same location indicated a Cr content of 80 % (expressed as cation ratio Cr/Fe+Cr), too high for a spinel oxide. The authors suggested that either small grains of both spinel and corundum oxide were present, or that the oxide was a metastable Cr-rich spinel.

The question arises as to whether the state of relatively protective oxidation provided by the healing type scale can actually be sustained for long reaction times. As shown in Fig. 3.60, the alloy underlying the healing scale is chromium depleted. If local equilibrium with the metal substrate prevails, its composition is determined by the value of $N_{Cr}^{m/o}$. It might then be argued that the oxide can remain Cr-rich so long as the outward chromium flux in the alloy is sufficient. However, the condition for the healing scale structure to be maintained is in fact different from that determining the stability of Cr_2O_3, for a reason related to the iron solubility in the different oxides. At the low p_{O_2} typical of alloy/Cr_2O_3 interface, the solubility of iron in Cr_2O_3 is very low (Fig. 1.10). As p_{O_2} increases, however, the corundum solid-solution can dissolve unlimited amounts of iron. In the case of the spinel oxide, Fe_3O_4 and $FeCr_2O_4$ are not completely miscible, but the Cr-rich phase can dissolve significant amounts of iron (Fig. 1.10).

As a consequence, as Sabioni et al. [42] pointed out, the stability of chromia is not determined by the relative diffusivities of iron and chromium in the oxide, but by the thermodynamics of the metal/oxide interface: in a true steady-state, once Cr_2O_3 is formed, it is expected to remain stable for long reaction times, because it maintains a p_{O_2} too low for iron to oxidise. The diffusion coefficients of iron and chromium in Cr_2O_3 are similar [42, 192]. Nevertheless, the iron activity in a Cr-depleted alloy is much higher than that of chromium. If, then, the interfacial chromium activity decreases and allows the solubility of iron in the oxide at the interface with the alloy to become substantial, the outward flux of iron in the oxide is expected to rise and eventually exceed that of chromium. Accordingly, an unstable situation of continued iron enrichment will prevail, eventually leading to $FeCr_2O_4$ precipitation.

[1] Convergent Beam Electron Diffraction

In the case of an original Cr_2O_3 scale then, the phase transformation to $FeCr_2O_4$ needs to be triggered by a sufficient instability in alloy chromium content. In contrast, iron diffuses much faster than chromium in the spinel phase (D_{Fe} was measured to be three orders of magnitude higher than D_{Cr} at 1200 °C over a range of oxide composition and oxygen activity [72]). As iron is soluble in the spinel, any instability in oxide growth rate or composition will be self-sustained. In the absence of thermodynamic or kinetic obstacles to iron enrichment in the oxide, and since instabilities are expected in any actual system, the Cr-rich spinel phase cannot be maintained in the long term. Kinetic demixing will favour the precipitation of iron-rich oxides in the outer part of the spinel phase, but eventually Fe-rich spinel particles will form as a connected phase throughout the oxide thickness, and the relatively protective character of the scale will be lost. As, moreover, the Fe-rich spinel is more permeable to carbon than the Cr-rich spinel is (see Section 5.3), dense intragranular precipitation will follow and prevent subsequent rehealing.

The healed type scale is clearly distinguished from the thick iron-rich nodules, in that it had a distinctively lower growth rate and prevented internal reaction. Moreover, it covered a large part of the Fe–25Cr alloy (Fig. 3.57), indicating that the transition from protective to non-protective oxidation was not instantaneous. Despite its inherent instability, the healed structure was maintained over a substantial period of time, as compared to the experimental time frame. On the other hand, on a given specimen, the thickness of this type of scale was observed to vary with location (Fig. 3.58), indicating that several stages in the morphological evolution from protective to non-protective oxidation coexisted. This resulted from the fact that Cr_2O_3 failure occurred at different moments and/or at locations characterised by different interfacial alloy compositions. This observation also supports the conclusion that the protective nature of the healed structure was limited in its extent and in its duration.

6.1.4 Reaction at 800 °C

Apart from some very occasional carbide precipitation in Fe–20Cr (Fig. 3.83), reaction at 800 °C did not cause carburisation of any of the alloys, either in regions of protective oxidation or where nodules had formed. Carbide precipitation is therefore concluded to play no part in Cr_2O_3 failure or nodule development at this temperature.

6.1.4.1 Binary alloys

Exposure of Fe–20Cr to wet CO_2 resulted in breakaway oxidation. Several stages of nodule development were visible on the same specimen (Fig. 3.74). In the most advanced stage, the oxide was uniformly thick, and contained several layers of Fe-rich oxide. A Cr-rich layer was present at the base of the scale, and internal oxidation did not occur. In regions of protective oxidation, the chromium content at the metal/oxide interface was measured by EPMA to be 15 wt. % (Fig. 3.75), far above the minimum concentration required for Cr_2O_3 thermodynamic stability (at 800 °C, Eq. (6.8) yields $N_{Cr}^{*} = 8.3 \times 10^{-5}$). Chromia failure must then have involved severe local instabilities in oxide growth rate or properties, possibly including mechanical damage. It is noted, however, that Cr_2O_3 scales grown in wet CO_2 were closely adherent to the metal substrate, and apparently free from macroscopic defects (Fig. 3.74(a)).

The relatively high value of $N_{Cr}^{m/o}$ allowed renewed formation of a Cr-rich layer after local Cr_2O_3 failure. In the early stage of nodule development, this layer contained 1–2 at. % iron, and the overall oxide structure resembled the healed scales formed on Fe–25Cr at 650 °C. However, at the higher temperature, no intermediate state of relatively protective oxidation was identified. Instead, the transition from Cr_2O_3 to thick multilayer oxide growth was continuous. Although it maintained an interfacial oxygen activity too low for the alloy to be oxidised internally, the Cr-rich oxide layer did not constitute a good barrier to cation diffusion, not even in a transient manner. Nonetheless, this layer contained more chromium than that, for example, formed on Fe–20Cr at 650 °C, indicating that the alloy was close to repassivation at 800 °C.

Increasing the alloy chromium content to 25 wt. % allowed protective oxidation to be maintained in all atmospheres. The value of $N_{Cr}^{m/o}$ in the case of Fe–25Cr was not measured experimentally, but can be estimated from the average scale thickness. Application of Eq. (6.1) yields $N_{Cr}^{m/o} = 0.22$. This chromium concentration was sufficient for Cr_2O_3 to reform after local failure, if it occurred.

In addition to altering the performance as a diffusion barrier of the Cr-rich layer formed after Cr_2O_3 failure, increasing the reaction temperature qualitatively affected the oxide morphology during breakaway, indicating a different reaction mechanism. At 650 °C, the onset of non-delective oxidation was characterised by the formation of new oxide layers above and below the initially protective scale, which then lay at the initial metal surface, surrounded by the inner and outer scales. In contrast, breakaway oxidation of Fe–20Cr at 800 °C involved the formation of new oxide layers

above the initially protective scale, which then lay at the base of the multilayer scale (Fig. 3.74). In the early stage of breakaway (Fig. 3.74(b)), this oxide layer was found to be considerably thicker than the surrounding protective scale, and to contain 1–2 at. % iron, while the protective scale contained no measurable iron. Since the relatively small composition difference cannot account, by itself, for the significantly increased thickness, it is concluded that iron dissolution in Cr_2O_3 to form either a corundum $Fe_{2-x}Cr_xO_3$ or a spinel $Fe_{3-x}Cr_xO_4$ solid solution caused an increase in oxide growth rate, due to enhanced cation diffusivity in either of the non-stoichiometric oxides. The difference, then, from reaction at 650 °C, is that the outward alloy chromium flux was in this case sufficient to prevent the formation of a new phase at the metal/oxide interface, and the reaction proceeded rather by continued thickening of the preexisting base layer. The observation of iron-rich oxide precipitation at the outer surface of this formerly protective layer indicates that iron diffusion across it was fast, compared to chromium diffusion.

6.1.4.2 Ternary alloys

While the binary alloys exhibited protective oxidation (only in dry CO_2 for Fe–20Cr), the ternary alloys suffered breakaway in all atmospheres, forming Fe-rich oxide in large proportions (Section 3.4.1). Enhanced Cr_2O_3 failure might possibly reflect a deleterious influence of nickel on the scale mechanical properties: after exposure to dry CO_2, the alloy/Cr_2O_3 adherence was seen to be poor for all alloys, but complete spallation was particularly marked for the ternary alloys (see for example Fig. 3.80(a)), while buckling was prevalent in the case of the binary alloys (see Figs. 3.73 and 3.76(a)). However, after reaction in wet CO_2, the Cr_2O_3 scales grown on all alloys showed good adherence to the metal substrate, and this did not prevent local scale failure in the case of the 25Cr ternaries. In contrast, the Fe–25Cr alloy maintained its protective behaviour within the experiment time-frame.

The chromium concentrations at the metal/oxide interface in regions of protective oxidation was not measured for any of the ternary alloys. The thickness of the Cr_2O_3 scale was not significantly affected by the alloy composition. It may then be argued that since chromium diffusion is slower in austenitic materials than in ferritic ones, the value of $N_{Cr}^{m/o}$ is expected to be lower for the alloys containing 20Ni than for their binary counterparts. This in turn would increase the probability for local instabilities to result in scale failure, and qualitatively account for the detrimental effect of nickel. The question of chromium diffusion is further addressed in Section 6.3.3. It should be noted that the Fe–20Cr–10Ni and Fe–25Cr–10Ni alloys

had, both before and after reaction, a mixed $\alpha + \gamma$ phase constitution. As shown in Fig. 6.7, the Cr-rich α phase was dissolved near the metal/oxide interface, which is expected as Cr_2O_3 growth consumes chromium. Although the phase in contact with

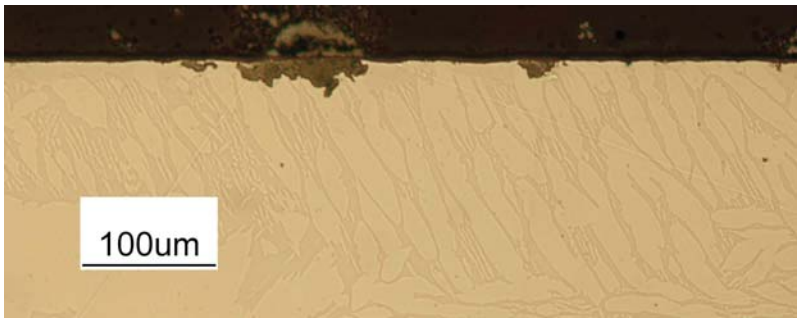

Figure 6.7 – Optical micrograph of an Fe–25Cr–10Ni specimen after 100 h reaction in Ar–20CO_2–20H_2O at 800 °C. The contrast between the α (dark) and γ (bright) phases was obtained by polishing with a basic (pH = 9.8) solution of 0.04 µm silica particles.

the oxide was always γ, the depth of the dissolution zone, $\sim$ 10 µm, was smaller than that of the depletion zone for a fully ferritic alloy at this temperature ($\sim$ 40 µm, see Fig. 3.75). Thus the chromium depletion profile must have varied locally, according to whether the phase directly beneath the dissolution zone was α or γ. It is noted, however, that the presence or absence of oxide nodules was not apparently related to the underlying phase constitution.

The early stage of breakaway oxidation involved, in the case of Fe–20Cr–10Ni and Fe–20Cr–20Ni, internal oxidation underneath the initially protective oxide (Figs. 3.77(c) and 3.79). As mentioned in Section 3.4.3.2, the oxide volume fraction in these internal reaction zones was very high, and certainly higher than that required to form an external scale. This situation was only transient, and the internal reaction zones subsequently evolved to form dense oxide layers (Figs 3.77(a) and 3.78). However, even once this transformation was achieved, numerous unoxidised metal islands remained present in the inner scale, preferentially near the metal/oxide interface and directly underneath the originally protective oxide layer, marking the initial metal surface. Metal islands were particularly prevalent in the case of Fe–20Cr–20Ni — for Fe–20Cr–10Ni, this is not visible in Fig. 3.77(a), but was observed in higher magnification views. As discussed earlier for reaction at 650 °C (Section 6.1.3.2), this reflects a non-equilibrium situation. Since Fe_3O_4 is inherently more stable than $NiFe_2O_4$, nickel is initially rejected from the growing oxide. Some metal may then be incorporated as a separate phase if the scale growth is fast as compared to diffusion

in the alloy and $NiFe_2O_4$ formation.

Although the inner scale formed on Fe–20Cr–20Ni mostly consisted of a fine mixture of oxide particles, continuous single-phase zones were seen around the metal inclusions (Fig. 3.79(c)). The composition of these particular oxide regions was not determined, but these bear some morphological similarity to oxides observed in the inner scale formed on the 9Cr ternaries and on Fe–25Cr–20Ni, which were identified by EDS to be chromium-rich (see Sections 3.2.3 and 3.4.3.2). It may then be possible that if the continuous single-phase oxide present on Fe–20Cr–20Ni was sufficiently rich in chromium, it imposed a p_{O_2} too low for Fe- and Ni-rich spinels to form, which would leave some iron and nickel unoxidised. Of course the prevalence of such a low oxygen potential in the middle of a growing oxide scale contradicts local equilibrium. Eventually, a monotonic p_{O_2} gradient must be established, such that at a given vertical position within the scale, no metal is present, and the different oxide phases have the same oxygen activity. This might not be the case with more noble alloying elements or a lower p_{O_2} atmosphere, but in the present conditions, nickel is to be oxidised. Nevertheless, the presence of metal inclusions indicates that this state of non-equilibrium was not short-lived, as compared to the experimental time-frame.

The nodules formed on Fe–25Cr–10Ni (Fig. 3.80) and Fe–25Cr–20Ni (Fig. 3.81) were morphologically similar to those observed during the early stages of breakaway on Fe–20Cr–10Ni and Fe–20Cr–20Ni, respectively. However, in the case of the 25Cr ternaries, the nodules were not seen to coalesce into uniformly thick scales. This is most likely due to their slower growth rate, in turn related to the higher chromium content (see Section 4.2.3), and the fact that more time was required to reach this more advanced morphological stage. In addition, although the inner scale contained, for both 25Cr ternaries, a fine mixture of oxides and some metal inclusions, a continuous layer was always present at the metal/oxide interface. This oxide layer and that located at the original alloy surface were both continuous with the protective scale present in zones adjacent to the nodules, and were both found by EDS to be Cr-rich (Fig. 3.82). This situation is thus seen to combine morphological features observed on the other alloys, and reflects a complex reaction mechanism. The oxide first formed as a result of Cr_2O_3 failure caused the oxygen activity to rise to such a level that, given the local chromium flux, the alloy oxidised internally. However, the chromium flux was, later on, sufficient for a continuous chromium-rich layer to be formed. These apparently conflicting deductions, together with the observation of alternate single-phase oxide zones, mixed oxide particles and metal inclusions ((Fig. 3.81(b)), indicate a non-equilibrium situation.

6.1.5 Influence of water vapour

The influence of water vapour on the oxidation behaviour of Fe–20Cr and Fe–25Cr was straightforward. At 650 °C, H_2O(g) additions resulted, for both binary alloys, in increased surface area fractions of Fe-rich oxide (Fig. 3.41), and in increased weight gains (Fig. 3.42). At 800 °C, the Fe–20Cr alloy oxidised protectively in dry CO_2, and H_2O(g) caused breakaway (Fig. 3.72). No effect was visible on Fe–25Cr, as this alloy formed only Cr_2O_3 in all gases. Reaction of the ternary alloys appeared not to be significantly affected by the presence or not of H_2O in the reacting gas. The 25Cr ternary alloys formed some nodules at 650 °C, but did not suffer breakaway, in that nodule development was too slow to cause any visible effect on the overall weight gains. The weight gains were similar after exposure to dry and wet CO_2 (Fig. 3.42). In the case of Fe–20Cr–10Ni and Fe–20Cr–20Ni at 650 °C, and of the 20Cr and 25Cr ternary alloys at 800 °C (Fig. 3.71), breakaway occurred to varying extents, but again, with no visible influence of the gas composition.

The results concerning the effect of H_2O on carburisation were summarised in Section 5.3.2. Except in the case of Fe–20Cr at 650 °C, where no effect was apparent, the presence of H_2O(g) was found to cause a decrease in the extent of carbide formation. Water vapour affected all types of carburisation: intergranular precipitation, formation of plate-like carbides beneath Cr_2O_3 and dense intragranular precipitation beneath iron-rich nodules and scales. Since carburisation was not enhanced by H_2O(g) additions, the reason for accelerated breakaway in wet CO_2 appears to be unrelated to carbide precipitation. Analysis of nodule development kinetics is needed in order to gain insight into the influence of H_2O on breakaway oxidation. This subject is addressed in Section 6.2.

6.2 Kinetics of breakaway oxidation

As Fe-rich oxide nodules thicken and spread laterally on the alloy surface, a transition occurs from a stage of low oxidation rate, characterising Cr_2O_3 growth, to a stage of fast reaction, typical of thick Fe-rich oxide. While this transition is local in essence, it is important to understand how it affects oxidation kinetics as measured for the entire specimen. The kinetics of breakaway oxidation are investigated here in terms of nodule nucleation and growth. This analysis is restricted to reaction at 650 °C, for which most results were available.

6.2.1 Analytical model for nucleation-spreading of oxide nodules

The surface area fraction of Fe-rich oxide, θ, reflects both the frequency of nodule nucleation, and the rate at which they spread laterally. Nucleation rates, which represent lack of permanent resistance of the initially formed Cr_2O_3 scale, are estimated from nodule surface fractions and growth rates measured after reaction at 650 °C, according to the procedure outlined below.

6.2.1.1 Theory

Evans [193] proposed a simple mathematical treatment of the problem of a surface covered by films spreading out as expanding circles. In the present case, individual nodules were approximately circular in plan. As nodules observed on a given specimen surface had varying sizes (see Section 3.3.1), it is assumed that nucleation occurs continuously until complete surface coverage is reached. In the case of the 20Cr ternary alloys, the nodule surface coverage varied greatly according to grain orientation (Fig. 3.39). However, since the experimental data available (values of θ and weight gains) are measures of nodule development on entire specimens, nucleation-growth kinetics can only be described in an overall way, reflecting average behaviour. Similarly, the influence of specimen edges and suspention holes is disregarded. It is thus assumed that nucleation occurs on the still uncovered portion with an average frequency which is independent of the time since the last nucleus appeared, and of the distance to the location of other nucleii. This is a particular case of the Poisson distribution [194].

Consider a random point P on the sample surface (already covered by Cr_2O_3), and an annulus of breadth $\mathrm{d}x$ situated around P at radial distance x. The annulus possesses the area $\mathrm{d}A = 2\pi\, x\, \mathrm{d}x$. The rate law for lateral nodule growth was deter-

mined in Section 3.3.4, Eq. (3.10): $r^2 = 2k_r t$. The growth kinetics of any nodule i, nucleated at $t = t_i$, are thus described by the relation

$$r_i^2 = 2k_r\,(t - t_i) \tag{6.19}$$

Hence, during a period equal to $(t - x^2/2k_r)$, any point within the annulus will be capable of growing a nodule which will reach P before time t, as represented in Fig. 6.8. The expected number of nodules reaching P from the annulus is

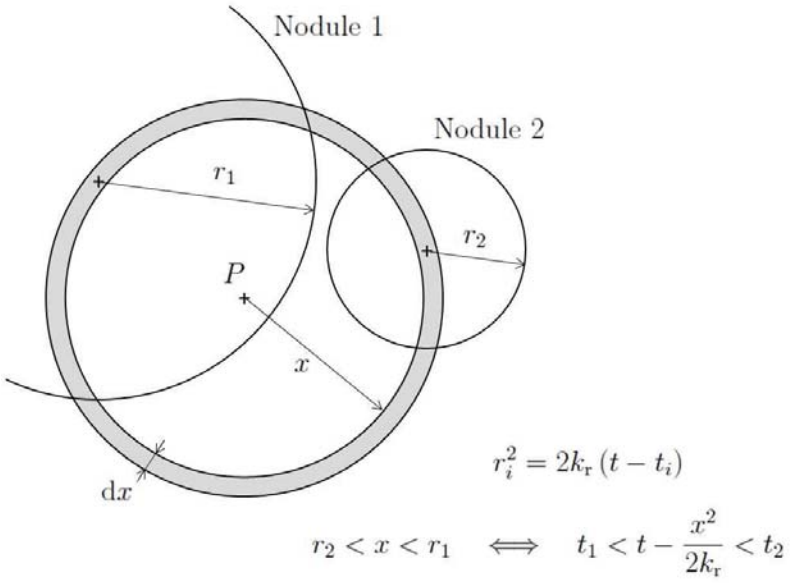

Figure 6.8 – Scheme of the geometric construction underlying Eq. (6.22), after Evans' nucleation-growth model [193]. Nodules 1 and 2 nucleated at times t_1 and t_2, respectively, such that nodule 1 reached P before time t, but nodule 2 did not.

$$\mathrm{d}E = \Omega\, 2\pi\, x\, \mathrm{d}x \left(t - \frac{x^2}{2k_r}\right) \tag{6.20}$$

where Ω is the two-dimensional nucleation rate, i.e. the number of nucleation events per unit of time and surface area. The expected number of nodules originating from the whole surface is calculated by integrating $\mathrm{d}E$ over the area in which nodules can reach P in time t:

$$\begin{aligned} E &= \int_0^{\sqrt{2k_r t}} \mathrm{d}E \\ &= \pi \Omega k_r t^2 \end{aligned} \tag{6.21}$$

Finally, the surface area fraction of nodules, θ, is calculated as the probability that point P is covered by any of the expanding nodules which formed after $t = 0$, equal

to $1 - \exp(-E)$, which yields

$$\theta = 1 - \exp\left(-\pi \Omega k_{\mathrm{r}} t^2\right) \tag{6.22}$$

It is noted that Eq. (6.22) is a particular case of Avrami (or KJMA, for Kolmogorov–Johnson–Mehl–Avrami) kinetics [195–200]. In particular, the fact that expanding nodules eventually overlap is accounted for.

6.2.1.2 Application

For each alloy, k_{r} is derived from the relationship $k_{\mathrm{r}} = 0.73 k_{\mathrm{p,Fe-ox}}$ (see Section 3.3.4), using $k_{\mathrm{p,Fe-ox}}$ values obtained from thickness measurements, and given in Table 3.8. The nucleation rate Ω is then determined as the arithmetic average of values obtained from Eq. (6.22), using θ measured after varying reaction times. The cases where $\theta = 1$ cannot be taken into account using Eq. (6.22), and are dismissed. The statistical bias thus introduced is significant, since only five values of θ were measured for each alloy and gas composition. However, precisely because the number of experimental values is low, and also because the results are poorly reproducible, it is not possible to include the cases for which $\theta = 1$ without making unreasonable assumptions.

Calculated θ curves are shown in Fig. 6.9 for the Fe–20Cr alloy. Reaction in

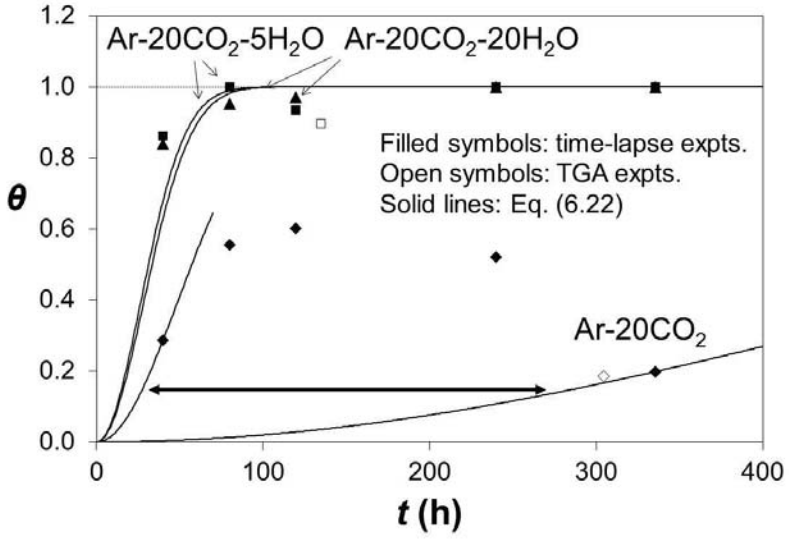

Figure 6.9 – Experimental and calculated (Eq. (6.22)) values of θ for reaction of Fe–20Cr at 650 °C.

the wet gases is reasonably well described by the model. In contrast, the results

obtained after exposure to dry CO_2 cannot be represented using a single nucleation rate. Extreme curves are plotted rather than the average, and the arrow represents the variability range. Lack of reproducibility between specimens of the same composition reacted under apparently the same experimental conditions has been reported by previous investigators, e.g. in Refs [85, 115]. The variable behaviour of the Fe–20Cr specimens in Ar–20CO_2 seen in Fig. 6.9 is puzzling; it presumably reflects differences in the specimen surfaces. As is discussed later, grain orientation had a critical effect on nodule nucleation for the ternary alloys (Figs 3.39 and 3.40). Since the grains were large relative to the specimen sizes, the influence of grain orientation could induce a statistical bias and account for the lack of reproducibility. However, such an effect existed but was not marked in the case of the binary alloys (Figs 3.36 and 3.37).

Exposure of both Fe–20Cr and Fe–25Cr alloys to wet CO_2 consistently resulted in extensive breakaway oxidation. The surface area fraction of Fe-rich oxide was high (> 80 %) for all specimen of both compositions. However Fig. 6.10 shows that, in the case of Fe–25Cr, complete coverage was not reached as fast as predicted by Evans' analysis: the last 5 % or so of the specimen surfaces resisted coverage to an unexpected degree. The same observation may also apply to Fe–20Cr (Fig. 6.10),

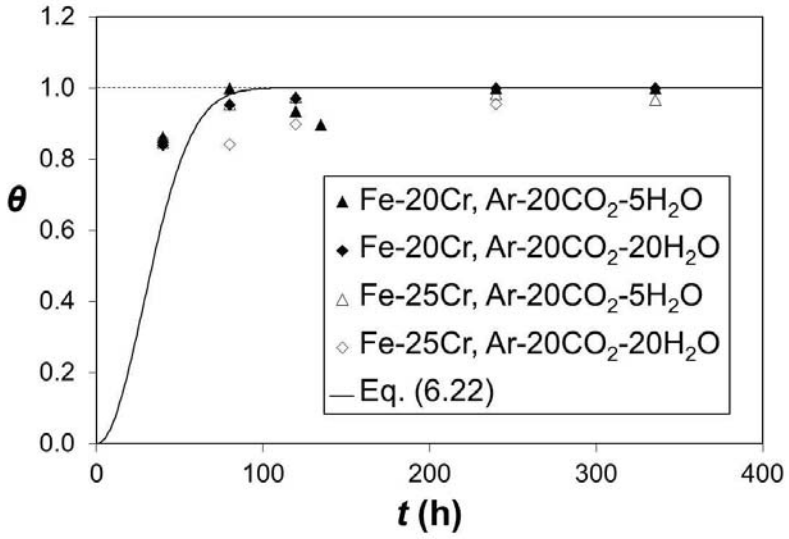

Figure 6.10 – Experimental and calculated (Eq. (6.22)) values of θ for reaction of Fe–20Cr and Fe–25Cr in wet CO_2 at 650 °C.

although the effect is less evident because of the inherent variability of breakaway. In order to overcome the lack of reproducibility among different specimens and further investigate this apparent delay in surface coverage, continuous weight gain kinetics

measured by TGA during exposure of Fe–20Cr to Ar–20CO_2–5H_2O (see Fig. 3.42) are used to estimate θ throughout the reaction.

Neglecting the small contributions of carbides and Cr_2O_3, the total weight gain recorded at any given reaction time is written

$$\frac{\Delta m}{A} = \theta \left(\frac{\Delta m}{A} \right)_{\mathrm{Fe-ox}} \tag{6.23}$$

This relation was used to construct the graph of Fig. 3.65, according to which nodule weight gain kinetics are reasonably well described by the rate law

$$\left(\frac{\Delta m}{A} \right)^2_{\mathrm{Fe-ox}} = 2k_{\mathrm{pm,Fe-ox}}t \tag{6.24}$$

It is important to note that, while Eq. (6.23) is applicable at any given reaction time, and Eq. (6.24) might well reflect intrinsic nodule growth kinetics, the relation obtained from their combination,

$$\frac{\Delta m}{A} = \theta\sqrt{2k_{\mathrm{pm,Fe-ox}}t} \tag{6.25}$$

is only valid under the condition of exclusive initial nucleation, that is, provided that nucleation occurs at $t = 0$ and not subsequently. This condition is not met in the present situation, as argued earlier. The fact that experimentally, the quantity $\frac{1}{\theta}\frac{\Delta m}{A}$ is well represented by the expression $\sqrt{2k_{\mathrm{pm,Fe-ox}}t}$, merely reflects the fact that the number of new nucleation events decreases as the available surface decreases. This effect is all the more marked when the nucleation rate is high — which was indeed the case here, in particular during reaction in wet CO_2. This was discussed at length in Section 4.2.3, when addressing the nodule thickness measurements. However, the present case is slightly different, as specimen weight changes include the contribution of all nodules, and not only those which had nucleated earliest, which were selected for thickness measurements. Thus the discrepancy observed between experimental data and the ideal parabolic law should be more important in the case of the weight gain measurements. Here again, the fact that Eq. (6.24) applied reasonably well shows that systematic deviations from the initial nucleation scenario and from the ideal rate law are negligible compared with the experimental scatter.

Recognising that it is not applicable in principle, but acceptable in practice, Eq. (6.25) is now used to calculate θ from TGA data recorded during exposure of Fe–20Cr to Ar–20CO_2–5H_2O. To proceed, the rate constant $k_{\mathrm{pm,Fe-ox}}$ is adjusted so that the calculated value of θ for $t = 135$ h equals the value measured experimentally at

the end of the TGA experiment. This yields $k_{\mathrm{pm,Fe-ox}} = 2.5 \times 10^{-4}$ mg^2 cm^{-4} s^{-1} or, again using the molar volume of Fe_3O_4, $k_{\mathrm{p,Fe-ox}} = 1.2 \times 10^{-10}$ cm^2 s^{-1}, in agreement with the value determined from thickness measurements (Table 3.8). The resulting θ curve, plotted as a solid line in Fig. 6.11, follows an S-shape, as predicted by Evans' analysis (Eq. (6.22)). However, toward the end of the experiment, θ reaches

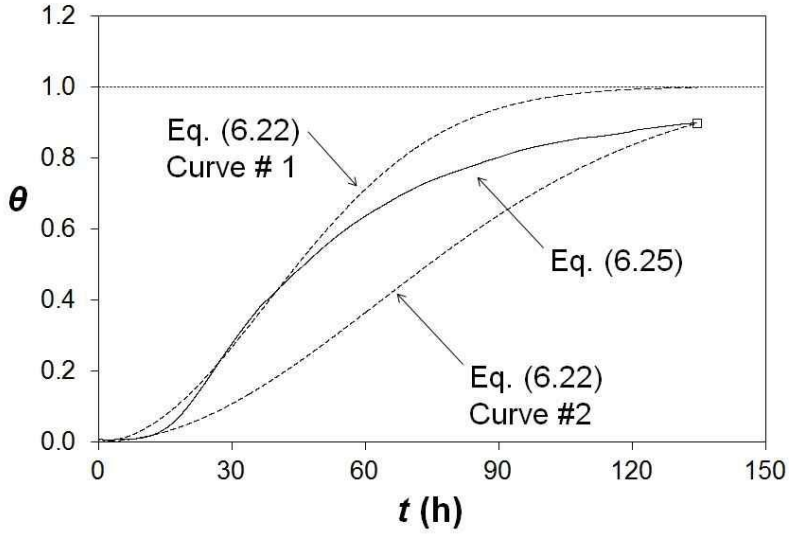

Figure 6.11 – Surface are fraction of nodules, θ, during exposure of Fe–20Cr to Ar–20CO_2–5H_2O at 650 °C, obtained from TGA data and Eq. (6.25), and θ curves calculated using Eq. (6.22). Curve # 1 was obtained by adjusting the nucleation rate to fit the θ curve from TGA data, while curve # 2 was obtained considering the final θ value only.

a nearly constant level, despite the fact that coverage is not complete. Thus, the fact that θ values recorded after time-lapse exposures of Fe–20Cr and Fe–25Cr to wet CO_2 are not perfectly represented by Eq. (6.22) is not only due to experimental scatter, but also to an actual deviation from uniform nucleation-spreading kinetics.

The overall evolution of θ is best described by considering Eq. (6.22) for most of the reaction, and recognising that past a certain stage, nodule coverage is delayed with respect to the ideal situation. This delay amounts to the nucleation rate Ω being either not constant with time, or, more likely, not uniform in space. The latter situation could originate from regions of the specimens exhibiting preferential resistance to breakaway, such as grain boundaries or grains with particular orientations. Accelerated chromium supply at the alloy grain boundaries is to be expected for austenitic materials at low temperatures, and was indeed observed to prevent (or at least delay) breakaway in the case of a 304 steel reacted at 600 °C [179].

It is questionable whether such an effect would be important for ferritic alloys reacted at 650 °C, and it was not observed in the present study. Grain orientation has been shown to affect the nature of the oxide formed on Fe–Cr alloys reacted in CO_2–1%CO at 600 °C [201]. During reaction of Fe–10Cr and Fe–20Cr single crystals in low pressure O_2 at 900 K [202], (110) surfaces formed Cr-rich α-$Fe_xCr_{2-x}O_3$, whereas (100) surfaces formed spinel oxides, regardless of the alloy composition. In both Refs. [201] and [202], epitaxial relationships were invoked by the authors to explain the stabilisation of either rhomboedral or cubic oxide during the initial stage of oxidation. If substrate-oxide orientation relationships can determine the nature of the oxide initially formed, they might also affect the protective scale growth rate, or propensity to suffer mechanical failure. In the present work, variations in nodule density according to grain orientation were prevalent on the ternary alloys, but also existed in the case of the ferritic Fe–20Cr and Fe–25Cr (see Section 3.3.1).

When using time-lapse results to calculate a value of the nucleation rate Ω, the deviation from uniform nucleation-spreading kinetics leads to an error, which is now estimated. In Fig. 6.11, curve # 1 is a plot of Eq. (6.22), where the product Ωk_r has been adjusted to represent, as well as possible, the evolution of θ as determined from the TGA data. Curve # 2 was also obtained from Eq. (6.22), but Ωk_r was adjusted to fit the value of θ measured at the end of the TGA experiment (square symbol), repeating the procedure used for time-lapse experiments. When compared to curve #1, this procedure leads to an underestimation of Ω by a factor 3. This error is not significant in relation to the Ω values presented subsequently.

In the case of the Fe–25Cr alloy, θ values arise from two sorts of nucleation events, corresponding to the two types of scale formed after Cr_2O_3 failure, which cannot be distinguished when measuring θ on the specimen surfaces. However, metallographic observations of cross-sections showed that the thinner type of scale (healed scale) represented a major proportion of the post-failure oxide products. The corresponding growth rate was used to determine nucleation rates. The extent to which Fe-rich oxide nodules developed varied from one grain to another of a given specimen. The influence of grain orientation on nodule nucleation was particularly marked in the case of the 20Cr ternaries (Fig. 3.39). Therefore, the value of Ω obtained from Eq. (6.22) for each specimen is an average of the values corresponding to each individual grain.

6.2.1.3 Discussion of the results

Average nucleation rates for all alloys and gases are shown in Fig. 6.12, where the error bars indicate minimum and maximum values, reflecting the poor reproducibility of breakaway oxidation.

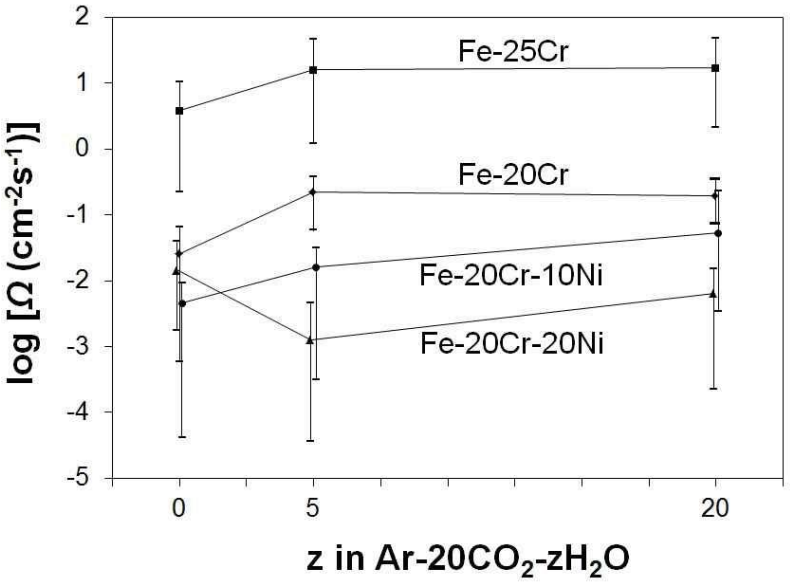

Figure 6.12 – Nucleation rates resulting from the nucleation-spreading analysis (Eq. (6.22) applied to the time-lapse θ values) for reaction at 650 °C.

If the large variability is disregarded, water vapour is generally seen to cause an increase in nucleation rates. Thus, while no effect was seen in terms of nodule growth rate (Fig. 3.65), the fact that $H_2O(g)$ triggers or accelerates breakaway oxidation is clearly related to the more frequent nucleation of Fe-rich oxide nodules. This is evident from the appearance of the reacted surfaces in the case of the binary alloys. In Fig. 3.37 for example, the Fe–25Cr specimen reacted in dry CO_2 exhibits a small number of relatively large nodules, which indicates that the nucleation rate was relatively low compared to the growth rate, whereas in wet CO_2, a large number of smaller nodules is visible (Fig. 3.37(c)), reflecting a higher nucleation rate. The interest of the present analysis lies in the quantification of the H_2O effect, and of the associated variability.

Chromia scales are known to grow faster in the presence of $H_2O(g)$ (see Refs. [18, 141–143] and Section 1.6.4.1). A higher growth rate would indeed enhance chromium depletion, and favour non-selective oxidation after failure of the initial Cr_2O_3 scale. This could not be verified in the present work, as differences in Cr_2O_3 scale thickness

between dry and wet CO_2 were not more important than local variations on a given specimen. The early stage oxidation kinetics measured by TGA in the case of Fe–20Cr (Fig. 3.43) did not indicate any difference in Cr_2O_3 growth rate between dry and wet CO_2. The presence of H_2O(g) must then have affected Cr_2O_3 growth without significantly altering the early stage kinetics. The influence of H_2O(g) in accelerating breakaway has been subject to a large amount of investigation, and possible explanations were reviewed in Section 1.6.4. No further insight in the reaction mechanism can be gained from the present results.

The Fe–25Cr alloy is seen in Fig. 6.12 to present higher nucleation rates than the 20Cr alloys. Thus, while the higher chromium content enables a temporary stage of relative protection to be reached after Cr_2O_3 failure, through the formation of a slow-growing, healed scale, it also leads to more frequent Cr_2O_3 failure. This finding is of interest, and its causes are investigated here.

No effect of alloy composition on Cr_2O_3 growth kinetics could be identified in the present study, because Cr_2O_3 thicknesses varied on a given specimen as much as they did among specimens of different compositions. However, studies conducted by previous investigators [73, 167, 203] on series of Fe–Cr alloys in dry or wet O_2 indicated that a minimum in Cr_2O_3 growth rate occurred for alloys containing about 15–20 wt. % Cr, a composition range apparently valid for all temperatures tested, which lied between 650 and 1000 °C. According to these data, Cr_2O_3 growth would thus be faster on Fe–25Cr than on Fe–20Cr. This is expected to result in higher scale failure frequency, and would account for the higher nucleation rates obtained for Fe–25Cr.

Possible reasons underlying these variations in oxide growth rate are now discussed. Chromia scales grown on the Fe–20Cr and Fe–25Cr alloys presumably differed in their iron content. This could not be verified using SEM–EDS in the present work, but such variations are expected from local metal–oxide equilibrium, and were observed by other investigators [73, 204]. Chromium concentrations in the metal at the interface with Cr_2O_3, $N_{Cr}^{m/o}$, were determined using Eq. (6.1) to be (6.9 ± 4.6) at. % and about 10–15 at. % for Fe–20Cr and Fe–25Cr, respectively, in agreement with SEM–EDS measurements (see Section 6.1.2). Thus the activity of chromium in the oxide at the interface with the metal is expected to be higher for Fe–25Cr. This would result in an increased chromium activity gradient in Cr_2O_3, which in turn would enhance the chromium flux, and lead to a higher oxide growth rate on Fe–25Cr.

An alternative explanation has been proposed by previous investigators, based on the oxide defect structure and transport properties. Electrical conductivity mea-

surements were carried out on synthetic Cr_2O_3, Fe_2O_3 and $Fe_{2-x}Cr_xO_3$ using different techniques, either in the temperature range 600–1100 °C [73, 205] or at room temperature after deposition at 600 °C [204]. These measurements showed that Cr_2O_3 and Fe_2O_3 had *p*-type and *n*-type properties, respectively, while the solid solution oxides exhibited, according to their composition, either of these two types of behaviour or intrinsic conductivity. This indicates that a change of predominant defect type occurs in the solid solution, although the critical concentration, which depends on temperature, is not known with precision. This change in electric properties was accompanied by a minimum conductivity [73, 205]. Observing that the composition of the $Fe_{2-x}Cr_xO_3$ compact exhibiting a minimum conductivity was similar to that of the thermally grown oxide of minimum growth rate, Footner et al. [73] concluded that alloy composition and oxidation rate could be directly related via the oxide composition and associated defect structure. While this conclusion is qualitatively evident, the validity of the quantitative implication can be doubted, since defect and transport properties vary along the p_{O_2} gradient established in a growing oxide, a condition not present in electric conductivity measurements carried out on oxide compacts. Furthermore, the $Fe_{2-x}Cr_xO_3$ composition corresponding to a change in defect type significantly varied between the different studies referred to here [73, 204, 205], which were based on different techniques and experimental conditions. It is noted that in the most recent study [204], electrochemical impedance measurements carried out at room temperature after oxidation of two different steels showed that the properties of the thermally grown oxides were comparable to those measured on oxide compacts. The scale grown on an X20 (11Cr) steel was seen to contain more iron than that grown on 310 (25Cr/20Ni) steel, and to grow faster. The difference in oxidation rate was attributed by the authors to a variation in the oxide defect structure with composition, which was also observed on the oxide compacts.

It is not clear whether the arguments invoked in Refs. [73, 204] apply to the present results. Nevertheless, the possibility of faster Cr_2O_3 growth on Fe–25Cr compared to Fe–20Cr, expected from the data in Refs. [73, 167, 203], must be considered in accounting for the increased nucleation rates on the higher chromium alloy.

Adding nickel to the Fe–20Cr alloy proved beneficial, as it reduced the average nucleation rate. However, this average result encompasses values which varied greatly with grain orientation. A complete range of oxidation behaviour was observed depending on grain orientation (see Section 3.3.1), from seemingly exclusive Cr_2O_3 formation to complete coverage by Fe-rich oxide, from short reaction times.

The nodule growth rate being, for both ternary alloys, inherently lower than that measured for Fe–20Cr (Table 3.8), it is concluded that the nucleation rate locally reached very elevated values, in particular much higher than those typical of Fe–20Cr. The fact that the influence of grain orientation was drastically enhanced for the ternary alloys is of interest, but could not be investigated from the present experimental results.

6.2.2 Statistical model for nucleation-spreading-thickening kinetics of oxide nodules

The model developed by Evans [193] enables surface area fractions to be calculated, but does not extend to a prediction of weight gain kinetics arising from nucleation and growth of oxide nodules during breakaway oxidation. These kinetics have been approximated using a relation equivalent to Eq. (6.25) in the past [115]. However, this relation holds only if nucleation occurs initially, at $t = 0$, and not subsequently. Accordingly, it is desirable to develop a more accurate description of weight gain kinetics during a process of continuous nucleation and growth.

In the present situation, the observation of nodules of significantly different sizes at a given time clearly shows that nucleation continues throughout the reaction until surface coverage is complete. As represented schematically in Fig. 6.13, the total weight gain then depends on the nodule "age" (or size) distribution. The Fe-rich oxide thickness at any given point on the surface is determined by the time elapsed since an expanding nodule reached this point. In order to calculate the total weight gain, a statistical approach is presented, based on the probability that any given point is covered by Fe-rich oxide in a given time interval. This analysis is constructed using the statistical model for oxide scale spallation during thermal cycling presented in Ref. [206].

In the present model, both Cr_2O_3 and Fe-rich oxide growth are described using a simple parabolic law. The assumption is reasonable in view of the results presented in Fig. 3.43 and Fig. 3.65, as discussed earlier. Furthermore, the probability of nodule nucleation is assumed to be independent of time and location. This hypothesis requires that the contributions of the different grain orientations be gathered into an average nucleation rate.

The rate law for uniform Fe-rich oxide growth kinetics is written

$$M(t) = \sqrt{2k_{\mathrm{pm,Fe-ox}}t} \tag{6.26}$$

where $M(t) = (\Delta m/A)_{\mathrm{Fe-ox}}$. In the following equations, time is described as a

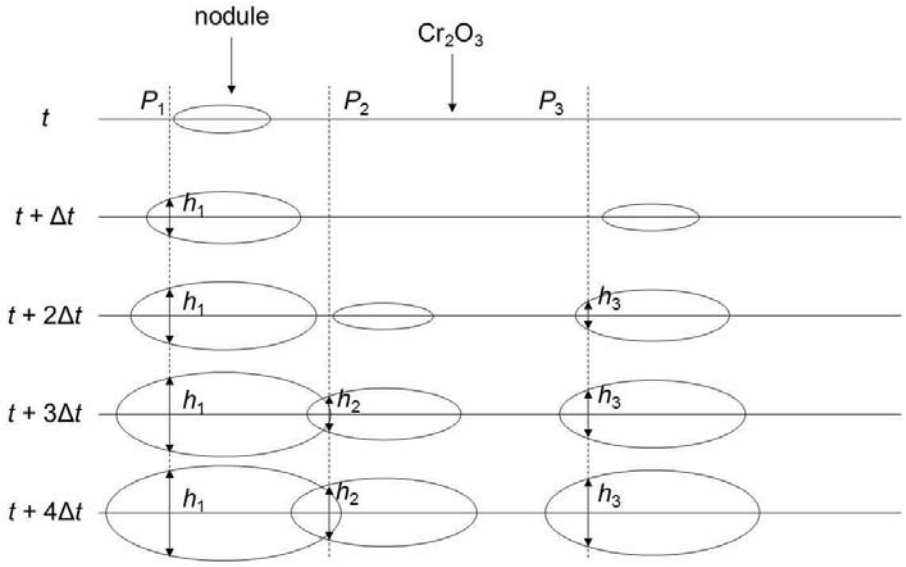

Figure 6.13 – Scheme representing a specimen cross-section during a continuous nucleation-growth process. A nodule reached P_1 between t and $t + \Delta t$, while P_3 was covered between $t + \Delta t$ and $t + 2\Delta t$, and P_2 between $t + 2\Delta t$ and $t + 3\Delta t$. The relation $h_i^2 = 2k_{\mathrm{p,Fe-ox}}(t - t_i)$ applies to all three points, and at any given time $h_1 > h_3 > h_2$.

discrete quantity: $t = n\Delta t$, where n is an integer and Δt a fixed time step. The rate law is then written

$$M_n = M_1\sqrt{n}, \quad \text{for } n \geqslant 1 \tag{6.27}$$

with $M_1 = \sqrt{2k_{\mathrm{pm,Fe-ox}}\Delta t}$. Let us consider a point P on the surface. The weight gain due to carbides and Cr_2O_3 is neglected at this stage. If P was covered by a nodule at the beginning of the high temperature exposure, i.e. during the first time step, the "local" weight gain at point P during the nth time step is

$$\Delta M_{1n} = M_1\left(\sqrt{n} - \sqrt{n-1}\right), \quad \text{for } n \geqslant 1 \tag{6.28}$$

The surface area fraction of Fe-rich oxide, $\theta(t)$, is the cumulative distribution function for surface coverage. Hence the probability that point P is reached by a nodule before time step i is $\theta(i\Delta t)$, denoted by θ_i. Therefore, the probability that point P is covered during time step i, that is to say between $t = (i-1)\Delta t$ and $t = i\Delta t$, is $\theta_i - \theta_{i-1}$, for $i \geqslant 1$. In this case, the weight gain at point P during the nth time step is

$$\Delta M_{in} = M_1\left(\sqrt{n-i+1} - \sqrt{n-i}\right), \quad \text{for } n \geqslant i \tag{6.29}$$

The total sample weight gain during time step n is then calculated by adding, for every step i, the product of the probability that P was reached by a nodule during

step i and the associated weight gain:

$$\begin{aligned}\Delta M_n = {} & \theta_1 M_1 \left(\sqrt{n} - \sqrt{n-1}\right) \\ & + (\theta_2 - \theta_1) M_1 \left(\sqrt{n-1} - \sqrt{n-2}\right) \\ & + \cdots + (\theta_i - \theta_{i-1}) M_1 \left(\sqrt{n-i+1} - \sqrt{n-i}\right) \\ & + \cdots + (\theta_n - \theta_{n-1}) M_1, \quad \text{for } n \geqslant 1\end{aligned} \tag{6.30}$$

The first term is related to areas covered by nodules during the first time step, leading to a minimum weight gain during time step n; the last term represents areas covered by nodules during time step n. The probability that point P has not yet been covered by any nodule at time step n is $1 - \theta_n$. The corresponding weight gain is zero, as the contribution of Cr_2O_3 is neglected at this stage. Thus, provided that $\theta_0 = 0$, the fact that

$$\sum_{i=1}^{n} (\theta_i - \theta_{i-1}) + 1 - \theta_n = 1, \quad \text{for } n \geqslant 1 \tag{6.31}$$

proves that all possible events have been taken into account in Eq. (6.30).

The relative contribution of Cr_2O_3 to the total weight gain is significant in early reaction times, where the surface covered by nodules is relatively small. Since $k_{\mathrm{pm,Fe-ox}}$ is four orders of magnitude larger than $k_{\mathrm{pm,Cr_2O_3}}$, this contribution becomes negligible quite rapidly after breakaway has started. Thus, the accumulated weight gain at time step N, which is the quantity measured experimentally, may be written

$$\begin{aligned}m_N = \sqrt{2 k_{\mathrm{pm,Cr_2O_3}} N \Delta t} + \sum_{n=1}^{N} \sum_{i=1}^{n} \Big[& (\theta_i - \theta_{i-1}) \sqrt{2 k_{\mathrm{pm,Fe-ox}} \Delta t} \\ & \cdot \left(\sqrt{n-i+1} - \sqrt{n-i}\right) \Big], \quad \text{for } N \geqslant 1\end{aligned} \tag{6.32}$$

with

$$\theta_i = 1 - \exp\left(-0.73 \pi \Omega k_{\mathrm{p,Fe-ox}} i^2 \Delta t^2\right) \tag{6.33}$$

where the empirical relationship $k_{\mathrm{r}} = 0.73 k_{\mathrm{p,Fe-ox}}$ (see Section 3.3.4) has been used.

Equation 6.32 was fitted to the TGA data recorded during exposure of Fe–20Cr to Ar–20CO_2 and Ar–20CO_2–5H_2O by adjusting the nucleation and growth parameters Ω and $k_{\mathrm{pm,Fe-ox}}$. The computation was performed with Mathematica version 8.0 [82]. A time step $\Delta t = 1$ h was used; this value was verified to be sufficiently small to have no effect on the results. The rate constants for Cr_2O_3 growth were determined from the early stage reaction kinetics measured by TGA (Fig. 3.43). In both cases the fit of Eq. (6.32) to experimental data is seen in Fig. 6.14 to be very good. After converting the gravimetric constants $k_{\mathrm{pm,Fe-ox}}$ into

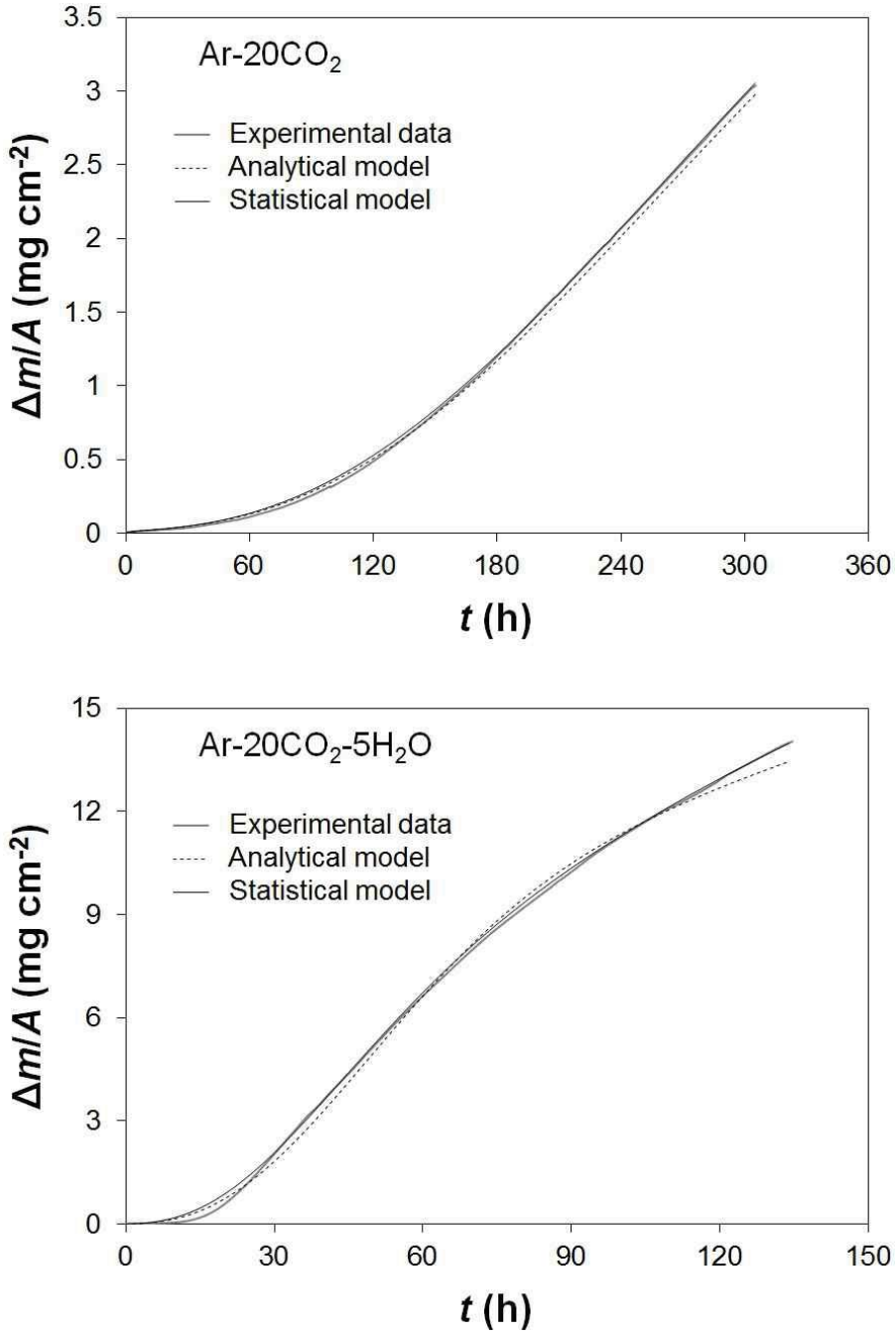

Figure 6.14 – Weight gain kinetics during breakaway oxidation of Fe–20Cr at 650 °C. Comparison of experimental data (TGA) with results of statistical (Eq. (6.32)) and analytical (Eq. (6.34)) models.

thickening constants $k_{\mathrm{p,Fe-ox}}$ (describing the Fe-rich oxide as Fe_3O_4), the parameters obtained are $k_{\mathrm{p,Fe-ox}} = 6.8 \times 10^{-12}$ cm^2 s^{-1}, $\Omega = 6.0 \times 10^{-3}$ cm^{-2} s^{-1} and $k_{\mathrm{p,Fe-ox}} = 1.3 \times 10^{-10}$ cm^2 s^{-1}, $\Omega = 2.1 \times 10^{-1}$ cm^{-2} s^{-1} for the dry and wet gas, respectively. These values are in reasonable agreement with those measured directly from time lapse experiments (see Table 3.8 for growth rates and Fig. 6.12 for nucleation rates).

The results of this statistical approach are now compared with those obtained from the simpler analytical model. Again neglecting the contribution of carburisation to the total weight gain, the relation

$$\frac{\Delta m}{A} = (1 - \theta(t)) \sqrt{2 k_{\mathrm{pm,Cr_2O_3}} t} + \theta(t) \sqrt{2 k_{\mathrm{pm,Fe-ox}} t} \tag{6.34}$$

where

$$\theta(t) = 1 - \exp\left(-0.73 \pi \Omega k_{\mathrm{p,Fe-ox}} t^2\right) \tag{6.35}$$

was fitted to the TGA data by adjusting the values of Ω and $k_{\mathrm{pm,Fe-ox}}$, using the Gnuplot software [207] version 4.4. The results obtained from Eq. (6.34) are shown as dashed lines in Fig. 6.14. Two observations emerge from the comparison of the two models. First, the statistical model is inherently better adapted than the analytical model. It allows a more accurate fitting of the experimental data, while using the same number of adjustable parameters, and yielding reasonable values for these parameters. In particular, the TGA curve obtained for reaction in Ar–20CO_2–5H_2O is well fitted using the statistical model, whereas some deviation is observed toward the end of the experiment when using the analytical model. This renders Eq. (6.34) unsuitable for extrapolation purposes. Nevertheless, and although it is not, strictly speaking, applicable to a situation of continuous nucleation, the analytical model provides a reasonable approximation of the experimental data. This justifies the use of the simple Eq. (6.25) for qualitative treatment of the experimental results. In particular, the fact that actual surface area fractions do not evolve strictly according to uniform nucleation-growth kinetics (Figs. 6.10 and 6.11) explains why the parameters obtained with the statistical model (Eq. (6.32)) could not perfectly match those resulting from direct experimental measurements.

The weight gains due to carbides and Cr_2O_3 are calculated to be one and two orders of magnitude lower than that corresponding to the Fe-rich oxide, respectively. It might then appear contradictory to have included the contribution of Cr_2O_3, but not that of the carbides, in the equations representing the statistical (Eq. (6.32)) and analytical (Eq. (6.34)) models. The reason is that since the carbides were predominantly found beneath the oxide nodules, neglecting these amounts to making a small error in the determination of $k_{\mathrm{pm,Fe-ox}}$. Conversely, the contribution of Cr_2O_3 is involved in the shape of the $\Delta m/A$ curve, during the early stage of the breakaway

reaction. While, again, this cannot affect the values of Ω and $k_{\mathrm{pm,Fe-ox}}$ determined by curve-fitting significantly, it was desirable to include the contribution of Cr_2O_3 in order to compare the ability of the models to reproduce the shape of breakaway oxidation kinetics.

6.3 Factors affecting breakaway oxidation

The oxidation behaviour of the high chromium alloys at 650 and 800 °C is summarised in Table 6.2. The comparison is made on the basis of a single criterion,

Table 6.2 – Summary of oxidation behaviour as a function of alloy composition and constitution, gas composition and reaction temperature.

	Gas composition	Protective ox.	Breakaway ox.
Key	$Ar–20CO_2$	◇	◆
	$Ar–20CO_2–5H_2O$ $Ar–20CO_2–20H_2O$	△	▲
	$Ar–20H_2O$	○	●

	650 °C (336 h)				800 °C (100 h)			
	Fe–20Cr		Fe–25Cr		Fe–20Cr		Fe–25Cr	
0Ni	α	◆ ▲ ●	α	◆ ▲ ●	α	◇ ▲ ●	α	◇ △ ○
10Ni	$\gamma-\alpha$	◆ ▲ ●	$\gamma-\alpha$	◇ △ ○	$\gamma-\alpha$	◆ ▲ ●	$\gamma-\alpha$	◆ ▲ ●
20Ni	γ	◆ ▲ ●	γ	◇ △ ○	γ	◆ ▲ ●	γ	◆ ▲ ●

according to whether breakaway oxidation was observed (filled symbols) or not (open symbols). Breakaway oxidation is defined here as the substantial development of Fe-rich oxide nodules, giving rise to weight gains significantly higher than those corresponding to exclusive Cr_2O_3 formation. The results obtained after reaction in $Ar–20H_2O$ were not described in this thesis, but the oxidation behaviour of the alloys (protective versus breakaway oxidation) is included in Table 6.2 for comparison purposes. This was determined by considering the surface appearance of the reacted specimens, using micrographs such as those shown in Sections 3.3.1 and 3.4.1, and weight changes, which are included in Figs. 3.42 and 3.71. Finally, it is noted that for each of the temperatures of interest, reaction in the two gas mixtures contain-

ing both CO_2 and H_2O led to equivalent results, and they are grouped together in Table 6.2.

A first observation emerges from Table 6.2, which applies to both reaction temperatures. With the exception of Fe–20Cr reaction at 800 °C, which is addressed subsequently, the composition of the gases used in the present study had no influence on the general alloy oxidation behaviour. Although it was not determined with precision, the minimum chromium concentration required to maintain protective oxidation did not vary greatly between gas mixtures containing CO_2 and/or H_2O as the reacting species. A very similar observation was made by Pirón Abellán et al. [13] and Meier et al. [14], in the case of commercial Cr steels at 550 °C and model Fe–Cr alloys at 650 °C, respectively. In each of these studies, expositions to Ar–CO_2, Ar–H_2O and CO_2–H_2O mixtures led to a transition from protective to breakaway oxidation for alloy chromium concentrations under the same critical value.

It is noted that although the experimental conditions used in the present work and in Ref. [14] were equivalent in terms of alloy and gas composition, the results disagree. At 650 °C, Meier et al. [14] found the critical Cr content to lie between 13.5 and 22 wt. % in the three atmospheres — the range was narrowed down to 15–16 wt. % in the case of Ar–H_2O — whereas in the present study, breakaway oxidation was observed for up to 25 wt. % chromium at this same temperature. The discrepancy is substantial, and all the more difficult to explain as specimen surface preparation, which is likely to alter the oxidation behaviour, was similar in these two studies, and reaction times were comparable.

In order to have a larger basis for comparison, the simple criterion used in Table 6.2 (protective versus breakaway oxidation) was applied to the results reported in 24 articles, most of which were referred to in Chapter 1. Only binary Fe–Cr alloys containing 5 to 40 wt. % Cr were taken into account, with reaction temperatures in the range 500–1200 °C. The atmospheres were divided into the following categories: dry oxygen (O_2, air, Ar–O_2 and N_2–O_2), wet oxygen (O_2–H_2O, air–H_2O, Ar–O_2–H_2O and N_2–O_2–H_2O), water vapour (Ar–H_2O), carbon dioxide (CO_2 and Ar–CO_2) and CO_2–H_2O. A chart was produced, containing 178 (N_{Cr}, gas, T) triplets (not shown here). Breakaway was always observed for the condition ($N_{Cr} \leqslant 0.25$, $T \geqslant 1050$ °C). Apart from this straightforward situation, the most critical condition in determining the minimum chromium content to maintain protective oxidation was seen not to be the gas composition or temperature, but the source of the data. This confirms that breakaway is extremely sensitive to the exposure conditions, as observed in the present study and noted by other investigators (for example in Refs [85, 115]). Direct, quantitative comparisons with literature data can only be made with the

greatest caution, if at all.

6.3.1 Alloy performance at 650 °C

As discussed in Section 6.2.1.3, nickel additions to Fe–20Cr caused considerable variations in the extent of nodule development according to grain orientation. In these conditions, the analysis of reaction kinetics in terms of an average nucleation rate is of limited use. On the other hand, the nodule growth rate was significantly reduced by nickel additions (see Section 4.2.3). Overall, as breakaway oxidation was not avoided for any of the 20Cr alloys, nickel additions proved beneficial, as evident from the lower weight gains (Fig. 3.42).

Nucleation rates determined for Fe–25Cr reaction in dry and wet CO_2 were significantly higher than those measured for Fe–20Cr (Fig. 6.12), but the higher chromium content allowed a relatively protective, "healed" type of scale to be formed, in a transient manner, after Cr_2O_3 failure. More importantly, it caused a decrease in the thick nodule growth rate (see Section 4.2.3). Since, again, breakaway was not avoided and prolonged exposures would eventually lead to complete surface coverage by thick Fe-rich oxide for both binary alloys, the overall effect of the higher chromium content is beneficial. This is also reflected in the total weight gains (Fig. 3.42).

Exclusive Cr_2O_3 growth was not maintained in the case of the 25Cr ternaries, and oxide nodules formed (Fig. 3.35). No information was obtained as to nodule development. However, as discussed in Section 4.2.3, the nodule growth rate was certainly lower than those measured for the other alloys, as a result of combined chromium and nickel additions. Whatever the nucleation rate might have been, limited nodule growth allowed the total weight gains to remain typical of Cr_2O_3 formation (Fig. 3.42).

It is concluded that the propensity for Cr_2O_3 failure was less critical than the rate of nodule growth in determining the overall alloy performance during reaction at 650 °C. In these conditions, only increasing chromium and nickel concentrations proved an effective way of mitigating metal loss, and the alloy phase constitution (ferritic versus austenitic) was unimportant.

6.3.2 Alloy performance at 800 °C

The transition from selective to non-selective oxidation at 800 °C was highly non-reproducible, even more so than during reaction at 650 °C. Nodule coverage varied greatly for specimens of the same composition, and also, in some cases, on the two faces of the same specimen (see Figs. 3.69 and 3.70). This is also visible in

the weight gains given in Fig. 3.71. In addition, the morphology and size of the oxides formed as a result of Cr_2O_3 failure varied considerably, which further limited the use of surface area fractions in analysing the reaction kinetics. It also caused inconsistencies between θ and $\Delta m/A$ values (Fig. 3.72), scale spallation being an additional source of scatter. For instance, the surface of Fe–20Cr specimens reacted in H_2O-containing gases was mostly covered by Fe_2O_3 whiskers (Fig. 3.68), but this corresponded to a wide range of oxide structures, from a submicrometric Fe_2O_3 layer overlaying Cr_2O_3, to 100 µm thick multilayer scales (Fig. 3.74).

As discussed in Section 6.1.4, reaction of Fe–20Cr in dry CO_2, and of Fe–25Cr in all gases, resulted in exclusive Cr_2O_3 formation, and nickel additions proved detrimental in that they triggered nodule nucleation. Conversely, Fe–20Cr suffered breakaway oxidation in the H_2O-containing gases, but a higher alloy chromium content allowed nodule formation to be avoided. In these gases, the weight gains measured for the 20Cr ternaries were significantly higher than those measured for Fe–20Cr, despite the fact that nodule coverage was about 100 % for all three alloys (see Fig. 3.72). It is also noted that nodule growth rates are expected to decrease with alloy nickel content, because of the relatively low diffusivity of Ni-containing oxides, as compared to Fe-rich oxides (see Section 4.2.3). The reason for these apparent contradictions lies in the fact that the scale grown on Fe–20Cr after Cr_2O_3 failure contained a Cr-rich layer in contact with the metal. This layer did not prove an efficient diffusion barrier in the long term, as shown in Section 6.1.4, but nonetheless exhibited a lower diffusivity than the Fe- and Ni-rich oxides formed on the 20Cr ternaries, which were not as close to repassivation.

It is concluded that the critical parameter in determining the overall alloy performance during reaction at 800 °C was the alloy's ability to maintain exclusive Cr_2O_3 formation, or to reform a Cr-rich oxide after Cr_2O_3 failure. A condition for selective oxidation to be favoured is that the outward chromium flux in the alloy must be sufficient compared to the rate of Cr_2O_3 growth, which controls Cr_2O_3 stability. Also, in view of the rates of Fe-rich oxide growth and oxygen diffusion into the alloy following Cr_2O_3 failure, which affect the degree of chromium enrichment at the base of the oxide, the chromium flux is critical to the alloy's ability to repassivate. This constitutes an essential difference from reaction at 650 °C, where nodule nucleation affected all alloys, and the overall oxidation rate was determined by the oxide composition. This in turn was in most cases directly determined by the alloy bulk composition, in that chromium was oxidised in situ and chromium diffusion thus played no important part. The reason why the general oxidation behaviour was controlled by different processes at 650 and 800 °C is discussed in Section 6.3.3.

It is noted that because it involves local instabilities, nodule nucleation is inherently more subject to variability than nodule growth. Thus, the fact that the degree of non-reproducibility was more important at 800 °C than at 650 °C is a simple consequence of the fact that nucleation became relatively more important in controlling the overall oxidation process. Similarly, steady-state growth of thick Fe-rich scales, if controlled by solid-state diffusion, is expected to be unaffected by changes in gas composition. This was indeed observed in the present study, in particular in the case of the low Cr alloys (see Chapter 4). In contrast, the propensity for Cr_2O_3 failure and the nature of the oxide subsequently formed, that is, the tendency for chromium to be oxidised selectively, involve processes (Cr_2O_3 growth, oxygen permeability in the alloy) which are likely to be influenced by the gas composition, and in particular by the presence of water vapour.

Selective oxidation is sensitive to the gas composition. It became apparent from the results of reaction at 800 °C that CO_2 and H_2O species were not strictly equivalent in the degree to which they are aggressive to the alloys of interest — as represented, for example, by the minimum chromium concentration required to maintain protective oxidation. Indeed, addition of 5 vol. % H_2O to Ar–20CO_2 triggered breakaway oxidation of the Fe–20Cr alloy, and exposure of this alloy to Ar–20H_2O also resulted in breakaway oxidation. Thus the transition from protective to breakaway oxidation in the presence of both CO_2 and H_2O was not merely due to the higher concentration of reacting species in the gas. Instead, it is concluded that H_2O(g) is inherently more aggressive than CO_2(g).

The observation that H_2O(g) affects selective oxidation has been made by several investigators, who proposed various explanations (see Section 1.6.4). The present results did not allow the existing theories to be tested, nor did they reveal any novel explanation. It should nonetheless be noted that during reaction at 800 °C, alloy/Cr_2O_3 adherence was significantly improved by H_2O additions to CO_2. This was observed for all alloys investigated, as shown in the micrographs of Sections 3.4.3.1 and 3.4.3.2. Thus, in the present case, enhanced nodule formation in wet CO_2 is likely unrelated to Cr_2O_3 mechanical resistance.

6.3.3 Temperature dependence

Comparison of the oxidation behaviour in Table 6.2 reveals that relative alloy performance varied with reaction temperature. At 650 °C, only the ternary alloys containing 25Cr oxidised protectively, whereas at 800 °C, breakaway was avoided only by the binary alloys. As shown in the precedent sections, the overall oxidation

behaviour is determined by two types of processes, related to selective oxidation or to nodule growth, whose relative importance depends on the reaction temperature.

The same temperature dependence on breakaway was reported by Peraldi and Pint [208], in a study of the cyclic oxidation of various model Fe–Cr and Fe–Cr–Ni alloys, containing 10–20 wt. % Cr and 0–30 wt. % Ni, in air–H_2O at 650 and 800 °C. Their results were equivalent to those presented in Table 6.2, in that protective oxidation was observed only for ternary alloys with high Cr and Ni contents at 650 °C, and only for binary alloys with high Cr contents at 800 °C. The authors discussed the temperature dependance in terms of relative chromium diffusivities in the ferritic and austenitic materials. Using a set of diffusion data [209] including volume and grain boundary diffusion coefficients in 9–20 wt. % chromium steels, Peraldi and Pint [208] noted that while chromium diffusion was one to two orders of magnitude faster in ferritic alloys than in austenitic ones at 800 °C, values of D_{Cr} all fell within the same order of magnitude at 650 °C. The authors concluded that higher chromium diffusivity in ferritic alloys explained their better oxidation resistance at 800 °C, but that no advantage over austenitic alloys was gained during reaction at 650 °C.

Although the role of chromium diffusivity in maintaining a Cr_2O_3 scale is clear, a practical limitation of the argument made in Ref. [208] is that values of D_{Cr} can differ significantly between sources, and in particular for austenitic materials. This was discussed in Section 6.1.3.2, where values of D_{Cr} obtained from three studies were seen to differ by two orders of magnitude at 650 °C. Short-circuit diffusion is an additional source of discrepancy, and its influence is particularly marked in situations of low volume diffusivity, such as chromium in austenitic materials at low temperatures. In the absence of a complete set of diffusion data for the alloys of interest — in terms of effective diffusion coefficients, including the effects of grain size and specimen preparation (cold working) — the applicability of a quantitative argument can be questioned, given that the interfacial chromium concentration, as determined from Eq. (6.1), is quite sensitive to the value of D_{Cr}. The difficulty of using a quantitative analysis of chromium depletion, without experimental concentration profiles, to discuss the relative oxidation behaviour of different alloys at different temperatures is further increased when considering two-phase alloys, with subsurface α dissolution.

Growth rates of Fe-rich multilayer oxide scales formed as a result of non-selective oxidation of chromium steels in H_2O-containing environments have been found by several authors [13, 210–212] to follow a complex temperature dependence in the range 550–650 °C. The so-called "bell-shaped temperature dependence" was always

associated with a morphological evolution of the scale, which tended to form a layer of increasing chromium concentration at the metal/oxide interface as the temperature increased. This was also accompanied by a progressive suppression of internal oxidation, and the establishment of a chromium depletion profile. These observations were interpreted by the authors as indicating a transition from non-selective to selective oxidation, which is consistent with the interpretations made in the present study. The explanations provided by the authors can be expressed in the following terms. The possibility for chromium to be selectively oxidised results from the outcome of a competition between outward chromium diffusion in the alloy and inward progress of the oxidation front. In the temperature range 600–650 °C — and the present results suggest that it can be extended to 800 °C — the rate of chromium diffusion in the alloy increases faster than that of Fe-rich oxide formation. As a result, marginal chromia-formers exhibit a transition toward selective oxidation with increasing temperature. Even if exclusive Cr_2O_3 formation is not achieved, this leads to reduced weight gains.

Making a similar argument, Meier et al. [14] showed that the critical chromium concentrations for the transition from internal to external oxidation (Eq. (6.16)) and for maintained external Cr_2O_3 formation (obtained for $N_{Cr}^{m/o} = 0$ in Eq. (6.1)) had opposed variations with temperature. The authors concluded that depending on the particular alloy composition and Cr_2O_3 growth rate, which, in turn, may be affected by the presence of water vapour, the tendency for protective oxidation could be characterised by a complex temperature dependence.

In the absence of precise and complete sets of diffusion and oxide growth rate data, no quantitative argument is made here. Qualitatively then, the present results are interpreted in the following terms. At 650 °C, the difference in chromium diffusivity between the ferritic and austenitic alloys may have been relatively small, especially taking into account short-circuit diffusion, resulting in similar propensity for Cr_2O_3 failure. Nickel additions had a beneficial influence in maintaining relatively low nodule growth rates. It is noted that even in this case, no chromium depletion was observed beneath the nodules grown on Fe–20Cr–10Ni (Fig. 3.64(a)): this alloy was not in a situation of near repassivation. However, this might have been the case for Fe–20Cr–20Ni and for the 25Cr ternaries. In any case, nodule growth rate was the decisive parameter.

In contrast, at 800 °C, volume diffusion of chromium in the alloys was faster, which limited the influence of short-circuit diffusion. The difference between ferritic and austenitic alloys might also have been enhanced because of volume diffusion itself, if the data of Tökei et al. [209] are considered. Accordingly, ferritic and

austenitic alloys differed in their tendency for selective oxidation, which was then critical in determining the overall oxidation behaviour. This, in turn, enhanced the influence of gas composition. The nodules formed on Fe–20Cr contained a Cr-rich layer in contact with the alloy, which was not the case after reaction at 650 °C. This reflects an evolution toward selective oxidation, as mentioned earlier and accounted for in Ref. [210] on the basis of relative alloy and oxide diffusivities. In the dynamic situation prevailing after local Cr_2O_3 failure, repassivation was relatively favoured over fast scaling, as compared to reaction at 650 °C. Statistically, this can be expressed in terms of a reduced probability of nodule nucleation, and for nodule evolution toward fast growing Fe-rich scales.

It is noted that a further increase in temperature would at some point cause the binary alloys to suffer breakaway in all gases, because of the overwhelming influence of faster Cr_2O_3 growth.

The interpretation of temperature effects provided in the preceding paragraphs on the basis of other investigators's work [14, 210] allows the general reaction morphology and kinetics to be rationalised. At 650 °C, where nodule nucleation was unavoidable, and their growth was decisive, development of individual nodules could be observed and led to a relatively slow (as compared to the experimental time frame) transition from the initial state of protective oxidation to complete surface coverage by Fe-rich oxide. The reaction was poorly reproducible and nucleation rates depended on grain orientation. However, on a given alloy grain, nucleation could be considered as a continuous and uniform process. Accordingly, weight gain kinetics were successfully represented using a uniform nucleation-growth model (Fig. 6.14). It is noted that Avrami-type kinetics have been used by previous investigators to describe various processes involving nucleation-growth at moderate temperatures. examples include growth of Fe_2O_3 on Fe–Cr at 200–500 °C [213], of metastable Al_2O_3 on Al–Zn at 500 °C [214], of sulfides on Ni–Al at 700 °C [215], Fe_3O_4 and Fe_2O_3 on Fe at 350–500 °C [216], or, as mentioned earlier, breakaway oxidation of Fe–Cr in CO_2–1%CO at 600 °C [115].

At 800 °C, however, nodule nucleation could be avoided by appropriate alloying. The ability to maintain selective chromium oxidation was thus decisive in determining the alloy oxidation resistance. Nucleation was so sensitive to local instabilities that it could not be described as a uniform and continuous process. Instead, the reaction proceeded according to a sharp transition from exclusive Cr_2O_3 formation to large-scale non-selective oxidation. This is suggested from the variety of oxidation morphologies observed in cross-sections (Sections 3.4.3.1 and 3.4.3.2), and in particular from the fact that entire regions of either Fe-rich oxide or Cr_2O_3 were ob-

served rather than individual nodules: the stage of individual nodule development was short lived. Continuous weight gain kinetics for single specimens were not available, but TGA results obtained by other investigators at temperatures of 900 °C and higher, for example in Refs. [16, 84, 136], confirm that the transition is highly irreproducible and sharper than that observed in the present work for $T = 650$ °C. In these conditions, alloy performance is characterised in terms of "incubation time" or "time to failure", rather than nucleation rate.

Conclusions

This work was aimed at examining the factors controlling the oxidation of Cr_2O_3-forming alloys in CO_2–H_2O atmospheres at moderately high temperatures. Protection of these alloys against oxidation is provided through the slow growth of Cr-rich oxide scales, which can only be achieved above a critical alloy chromium content. The literature survey conducted in Chapter 1 showed that non-selective oxidation of dilute alloys in either CO_2(g) or H_2O(g) was well documented. The principles underlying the influence of alloy chromium concentration on the stability of Cr_2O_3 are also well known. However, these have been mostly applied to reaction in air, and a detailed description of the effects of CO_2 and H_2O has been lacking. Of particular interest is carburisation and its interactions with selective oxidation. The evolution of reaction product morphology accompanying the development of Fe-rich oxide nodules from a previously existing Cr_2O_3 scale have been described for reaction in air, but little has been published as to the specific influence of CO_2 and H_2O, and concerning the kinetics of this transformation.

Model Fe–Cr and Fe–Cr–Ni alloys were exposed to Ar–CO_2–H_2O gas mixtures at 650 and 800 °C. Reaction of the alloys containing 2.25 and 9 wt. % Cr produced uniformly thick multilayer Fe-rich oxide scales. While the 20 and 25Cr alloys initially formed Cr_2O_3 scales, nucleation and growth of Fe-rich oxides were observed in most cases, eventually resulting in scales morphologically equivalent to those grown on the dilute alloys. These scales consisted of outer layers of iron oxides, and an inner part containing iron and chromium, plus nickel in the case of the ternary alloys.

Growth of Fe-rich oxide

Steady-state growth of the multilayer Fe-rich oxide scales was studied in Chapter 4. Substitution of chromium and nickel for iron in the alloy led to the replacement of iron oxides, either FeO or Fe-rich spinel, by Cr- and Ni-rich spinel phases in the inner scale. Owing to the elevated cation diffusivity in iron oxides, the presence of chromium and nickel oxide precipitates reduced the effective diffusional cross-section in the inner scale. As a consequence, increasing the alloy chromium and nickel contents had the effect of decreasing the rate of outward cation diffusion in the multilayer scales.

Surface reactions (adsorption and oxide formation) were relatively slow in dry CO_2, as compared to the rate of iron diffusion in iron oxides. Accordingly, the oxidation kinetics of dilute alloys were controlled by the surface process in dry CO_2. The reactivity of oxide surfaces with H_2O(g) was higher than with CO_2(g). Additions of water vapour to the reacting gas led to increased surface reaction rates, favouring the establishment of diffusion-controlled kinetics. In these conditions, diffusional

blocking was effective, and chromium and nickel additions caused reductions of the oxidation rate.

Carburisation

Carburisation of the alloys in dry and wet CO_2 occurred to variable extents. The reaction was affected by the alloy and gas composition, the reaction temperature, and most importantly by the nature of the overlying oxide. This was the subject of Chapter 5.

As noted earlier, carbon dioxide is not carburising to the alloys of interest. Previous investigators proposed that the gradient of oxygen potential established across growing oxide scales would result in elevated carbon activities at the metal surface if the scale transmitted carbon. This thermodynamic argument was extended here to yield a quantitative evaluation of the carbon supersaturation at the metal/oxide interface of oxidised alloys, with respect to the external atmosphere. In this model, the interfacial carbon activity is calculated from the local oxygen potential, allowing for a degree of freedom, which is related to the degree to which carbon is transmitted by the oxide scale.

Experimental results obtained after reaction of the Fe–Cr alloys — morphology of the carburisation products, and, when available, carbide volume fractions and penetration depth kinetics — were used together with the thermodynamics of the Fe–Cr–C system to estimate interfacial carbon activities. In the case of Fe–9Cr exposed to dry CO_2 at 650 °C, good quantitative agreement was obtained, providing support for the validity of the proposed model. In other instances, the experimental carbon activity was found to be lower than that predicted on the assumption that the scale could transmit carbon unhindered. Reduced carbon activities do not contradict the concept underlying the thermodynamic description, but were instead interpreted, within the same formalism, as indicative of decreased carbon accessibility to the metal. This led to the conclusions that water vapour partially excluded carbon by altering CO_2 access to the oxide scale in a process of competitive adsorption, and that Cr-rich oxides were less permeable to carbon than Fe-rich oxides were.

In early studies of carburisation in CO_2 [103, 112, 113], the establishment of carburising conditions at the metal/oxide interface was interpreted in terms of a CO build-up, produced by the reaction of iron with CO_2 to form the oxide. Carbon deposition was then argued to proceed, via to the Boudouard reaction, to an extent determined by the amount of CO generated by the oxidation reaction. Similarly, arguments based on the stoichiometry and kinetics of chemical reactions were made

very recently [128] to account for the carburisation of a 9Cr steel in CO_2. The present work is in contradiction with this kinetic interpretation. It was shown here that high a_C values and ensuing alloy carburisation could be rationalised without the need to introduce successive reaction steps and debate their individual rate, but rather by considering the state of local thermodynamic equilibrium imposed by the coexistence of the metal and oxide phases at the interface. This approach proved quantitatively successful in predicting experimental results.

Breakaway

Upon exposure to dry and wet CO_2, alloys containing 20 and 25Cr initially produced Cr_2O_3 scales, but this protective reaction state was, in most cases, short-lived, as Fe-rich oxide nodules were subsequently formed. The conditions leading to Cr_2O_3 failure, the morphological evolutions accompanying nodule development and the kinetics of this transition to non-selective oxidation were discussed in Chapter 6.

The present results indicate that dense carbide precipitation in the metal matrix is not necessary for breakaway to occur in CO_2, and that fast carbon ingress in the metal is a consequence, rather than a cause, of Fe-rich oxide formation. In particular, limited carburisation beneath Cr_2O_3 scales was shown to have no significant influence on chromium supply to the metal/oxide interface, and, consequently, on the oxide stability. Once Fe-rich oxide is formed and dense carburisation of the alloy prevails, however, repassivation is not possible, an observation in agreement with the early work of Giggins and Pettit [12].

Chromia scale growth is accompanied by chromium depletion in the metal substrate. Measured interfacial chromium concentrations, $N_{Cr}^{m/o}$, were found to be locally in agreement with predictions of Wagner's theory, confirming the establishment of a kinetic steady-state. Recognising that Cr_2O_3 growth was, in view of the specimen thickness, sufficiently slow for this steady-state to be maintained over the experimental time-frame, it was concluded that Cr_2O_3 failure must result from local instabilities in the oxide properties. In particular, scale thicknesses and values of $N_{Cr}^{m/o}$ were found to vary on a given specimen, reflecting fluctuations in local Cr_2O_3 scaling rate. These fluctuations can cause breakaway through exceeding the alloy's capacity to supply chromium, by accelerating mechanical failure of the scale, or by allowing gas access to a more heavily depleted alloy. Comparison of reaction of Fe–20Cr in air and Ar–20CO_2 showed that the presence of carbon accelerates the onset of breakaway. This effect may be attributed to carbon entry into the chromia scale, probably along its grain boundaries, where it can affect grain growth, boundary diffusion and scale mechanical properties.

The protective character of Cr_2O_3 is related to the low p_{O_2} imposed at the metal/oxide interface, which partially prevents iron oxidation — the solubility of iron in Cr_2O_3 at the p_{O_2} characteristic of metal–oxide equilibrium is small. Chromia failure and its conversion to spinel oxide lead to an increase in the local oxygen activity, and allow outward iron diffusion to proceed at a substantial rate, producing iron oxide. The subsequent morphological evolution of the newly formed nodule is determined by the concentration and diffusivity of chromium in the alloy. Limited chromium fluxes result in internal oxidation and formation of an iron-rich inner scale (case of Fe–20Cr at 650 °C and the 20Cr ternaries at 800 °C). Greater chromium fluxes favour the reformation of a Cr-rich layer at the base of the scale (case of Fe–25Cr at 650 °C, Fe–20Cr and 25Cr ternaries at 800 °C). This distinction is made clearer in CO_2-containing atmospheres by the fact that the scale permeability to carbon is affected by the oxide constitution and composition. Iron-rich oxides allowed fast carbon ingress and dense carbide precipitation in the alloy. As chromium was oxidised in situ, its outward diffusion and selective oxidation were prevented. Conversely, continuous Cr-rich oxide layers proved effective barriers to carbon entry. The absence of internal precipitation allowed chromium to diffuse, favouring selective oxidation. However, whenever such repassivation occurred, the relative degree of protection it provided was short-lived, and a transition to rapid Fe-rich oxide growth was subsequently observed.

The morphological changes following local Cr_2O_3 failure spread laterally from the initiation site. Once oxide development achieved a steaty-state, individual nodules maintained an elliptical shape until their coalescence produced uniformly thick scales. Both lateral and vertical nodule growth followed approximately parabolic kinetics, reflecting rate-control by diffusion along iron activity gradients.

The extent of nodule development was, in general, characterised by poor reproducibility. This was attributed to the fact that breakaway originates from local instabilities. Grain orientation was found to be an additional cause of variability, especially for the ternary alloys. In the case of reaction at 650 °C, the kinetics of breakaway oxidation were analysed according to an approach based on nodule nucleation and growth. A simple geometric model was used to relate surface area fractions of nodules, θ, to nucleation rates, Ω, making the assumption of uniform nucleation. As an average statistical measure of Cr_2O_3 failure frequency, nucleation rates constitute a quantitative indicator of Cr_2O_3 resistance.

Comparison of calculated and experimental $\theta = f(t)$ plots revealed that in addition to the inherent variability associated with breakaway, reaction of the binary alloys did not, on a macroscopic scale, strictly conform to the uniform nucleation

assumption. Past a certain stage, surface coverages did not increase as fast as predicted, probably reflecting the existence of zones of enhanced Cr_2O_3 resistance. However, the error due to deviations from uniform nucleation was shown to be negligible. Thus, the nucleation-growth analysis proved useful in evaluating the influence of alloy and gas composition on Cr_2O_3 resistance. In particular, the presence of water vapour was found in this way to promote Cr_2O_3 failure, as observed by previous investigators. Nucleation rates obtained for Fe–25Cr in all gases were higher than those corresponding to Fe–20Cr. The enhanced propensity for Cr_2O_3 failure on Fe–25Cr can possibly be attributed to faster oxide growth. Adding nickel to the Fe–20Cr alloy proved beneficial, in that it reduced the average nucleation rate. However, a critical observation is that the influence of grain orientation on Cr_2O_3 resistance was drastically enhanced for the ternary alloys.

Under the hypothesis of exclusive initial nucleation, two-dimensional nucleation-growth kinetics readily yield an analytical expression for the weight gain accumulated during nodule development. However, this condition was not met in the present situation. A numerical model based on a statistical approach was developed to allow for continuous nucleation in predicting weight gain kinetics. Leading to more accurate fitting of the experimental data, the statistical model was shown to be inherently better suited than the analytical model. Nonetheless, although strictly not applicable to a situation of continuous nucleation, the analytical model provided a reasonable approximation to the experimental results.

Reaction of all alloys in dry and wet CO_2 at 650 °C produced Fe-rich oxide nodules. In these conditions, the overall alloy performance was controlled by the nodule growth rate rather than by the tendency for Cr_2O_3 failure. Hence, chromium and nickel additions not only proved beneficial, but also represented the only viable strategy to achieve long-term protective behaviour. Conversely, during reaction at 800 °C, faster chromium diffusion allowed the binary alloys to maintain exclusive Cr_2O_3 formation. This was achieved only in dry CO_2 for Fe–20Cr, but in all gases for Fe–25Cr. Thus, the oxidation resistance was mostly controlled by alloy propensity for selective oxidation, and was therefore critically influenced by the diffusivity of chromium in the alloy, relative to the oxide growth rate and alloy oxygen permeability. This provided a decisive advantage to the ferritic, binary alloys over the austenitic, Ni-containing alloys, and also emphasised the detrimental effect of water vapour.

Practical implications

Constraints imposed on materials derive from a number of requirements, such as those related to mechanical properties, functional properties or formability, as well as corrosion resistance. Alloy design therefore results from an optimisation process guided by possibly conflicting requirements. For instance, it may be necessary to limit the chromium concentration in order to avoid the presence of the brittle σ phase. Some applications may require an austenitic structure if a certain creep resistance has to be achieved. It is noted that the scope of this study, in terms of alloy design possibilities, was very limited. Secondary alloying elements such as molybdenum, manganese or silicon are known to affect corrosion resistance. More generally, materials properties are determined not only by their chemical composition but also by their phase constitution and microstructure, which are adjusted via thermomechanical treatments.

Although the present results are not transposable into alloy design guidelines, some observations may be useful *in principle*, in that they provide information as to the way in which the general alloy performance in CO_2–H_2O atmospheres is affected by chromium and nickel contents and service temperature. It is recognised that the necessary compromise associated with alloy design must take into account the specific constraints imposed by a material function in terms of corrosion resistance. For example, if the only design requirement is that of not exceeding a certain metal loss, in that it defines the effective load-bearing section of a component, the formation of Fe-rich nodules at a low rate might be acceptable. Referring to the present results, this criterion would allow austenitic materials to be used at moderate temperatures, provided that the chromium and nickel contents are sufficient. Conversely, if Cr_2O_3 is the only acceptable oxide, for instance because of heat or electrical conductivity concerns, a higher service temperature would be conceivable for ferritic, high Cr materials.

Defining requirements in terms of oxidation behaviour involves the choice of criteria and associated tools to assess alloy performance in given exposure conditions. Considering the case of reaction at relatively high temperature, if nodule growth is unacceptably fast and the regime of exclusive Cr_2O_3 growth is used to define a service lifetime, then the concept of incubation time (or time-to-failure) constitutes a relevant criterion, and weight gain kinetics or even simple surface observation of a reacted specimen might be sufficient to determine a lifetime. Conversely, if nodule formation cannot be avoided but can be limited, as observed here in the case of reaction at 650 °C, the concept of nucleation rate and the methods introduced here to analyse reaction kinetics may prove useful. Such an analysis can be based

on surface area fractions of nodules or on weight gains, using either the analytical nucleation-spreading model or the statistical nucleation-spreading-thickening model.

Bibliography

[1] World Energy Outlook 2008, International Energy Agency.

[2] Recommendations by the COORETEC advisory council on support for research and development for low-CO_2 emission power plant technologies and carbon capture and storage technologies, Federal Ministry of Economics and Technology (BMWi), 2009.

[3] http://www.netl.doe.gov/keyissues/clean_power.html, National Energy Technology Laboratory, accessed 2012.

[4] http://www.ccsd.biz/index.cfm, Cooperative Research Center for Coal in Sustainable Development, accessed 2012.

[5] http://www.co2crc.com.au, Cooperative Research Centre for Greenhouse Gas Technologies, accessed 2012.

[6] http://www.asiapacificpartnership.org/english/tf_fossil_energy.aspx, Asia-Pacific Partnership on Clean Development and Climate, accessed 2012.

[7] http://www.newgencoal.com.au, Australian Coal Association, accessed 2012.

[8] K Jordal, M. Anheden, J. Yan, and L. Stroemberg. Oxyfuel combustion for coal-fired power generation with CO_2 capture-opportunities and challenges. In *7th International Conference on Greenhouse Gas Control Technologies*, pages 201–209, Vancouver, Canada, 2004.

[9] B. J. P. Buhre, L. K. Elliott, C. D. Sheng, R. P. Gupta, and T. F. Wall. Oxy-fuel combustion technology for coal-fired power generation. *Progress in Energy and Combustion Science*, 31(4):283–307, 2005.

[10] T. Wall, Y. Liu, C. Spero, L. Elliott, S. Khare, R. Rathnam, F. Zeenathal, B. Moghtaderi, B. Buhre, C. Sheng, R. Gupta, T. Yamada, K. Makino, and J. Yu. An overview on oxyfuel coal combustion-state of the art research and technology development. *Chemical Engineering Research & Design*, 87(8A):1003–1016, 2009.

[11] S. Sridhar, P. Rozzelle, B. Morreale, and D. Alman. Materials challenges for advanced combustion and gasification fossil energy systems. *Metallurgical and Materials Transactions A*, 42A(4):871–877, 2011.

[12] C. S. Giggins and F. S. Pettit. Corrosion of metals and alloys in mixed gas environments at elevated-temperatures. *Oxidation of Metals*, 14(5):363–413, 1980.

[13] J. Piron Abellan, T Olszewski, H. J. Penkalla, G. H. Meier, L. Singheiser, and W. J. Quadakkers. Scale formation mechanisms of martensitic steels in high CO_2/H_2O-containing gases simulating oxyfuel environments. *Materials at High Temperatures*, 26(1):63–72, 2009.

[14] G. H. Meier, K. Jung, N. Mu, N. Yanar, F. Pettit, J. Piron Abellan, T. Olszewski, L. Nieto Hierro, W. J. Quadakkers, and G. R. Holcomb. Effect of alloy composition and exposure conditions on the selective oxidation behavior of ferritic Fe-Cr and Fe-Cr-X alloys. *Oxidation of Metals*, 74(5):319–340, 2010.

[15] Y. Ikeda and K. Nii. Mechanism of accelerated oxidation of Fe-Cr alloys in water-vapor containing atmosphere. *Transactions of National Research Institute for Metals*, 26(1):52–62, 1984.

[16] S. Henry, A. Galerie, and L. Antoni. Abnormal oxidation of stabilized ferritic stainless steels in water vapor. In R. Streiff, Wright I. G., Krutenat R. C., Caillet M., and Galerie A., editors, *High Temperature Corrosion and Protection of Materials 5, Pts 1 and 2*, volume 369-3 of *Materials Science Forum*, pages 353–360, 2001.

[17] J. Ehlers, D. J. Young, E. J. Smaardijk, A. K. Tyagi, H. J. Penkalla, L. Singheiser, and W. J. Quadakkers. Enhanced oxidation of the 9%Cr steel P91 in water vapour containing environments. *Corrosion Science*, 48(11):3428–3454, 2006.

[18] N. K. Othman, J. Q. Zhang, and D. J. Young. Water vapour effects on Fe-Cr alloy oxidation. *Oxidation of Metals*, 73(1-2):337–352, 2010.

[19] D. J. Young. *High temperature oxidation and corrosion of metals*. Elsevier Corrosion Series. Elsevier, Amsterdam, 2008.

[20] N. Birks and G. H. Meier. *Introduction to High Temperature Oxidation of Metals*. Edward Arnold, 1st edition, 1983.

[21] C. Wagner. The theory of the warm-up process. *Zeitschrift Fur Physikalische Chemie-Abteilung B-Chemie Der Elementarprozesse Aufbau Der Materie*, 21(1/2):25–41, 1933.

[22] P. Moulin, A. M. Huntz, and P. Lacombe. Effect of diffusional phenomena on oxidation mechanism of Ni-Cr alloys. *Acta Metallurgica*, 28(6):745–756, 1980.

[23] B. Pieraggi. Calculations of parabolic reaction rate constants. *Oxidation of Metals*, 27(3-4):177–185, 1987.

[24] D. Monceau and B. Pieraggi. Determination of parabolic rate constants from a local analysis of mass-gain curves. *Oxidation of Metals*, 50(5-6):477–493, 1998.

[25] P. Kofstad. *High Temperature Corrosion*. Elsevier, London, 1988.

[26] F. A. Kroger and H. J. Vink. Relations between the concentrations of imperfections in crystalline solids. *Solid State Physics-Advances in Research and Applications*, 3:307–435, 1956.

[27] C. Gleitzer. Electrical properties of anhydrous iron oxides. *Electrical Properties of Oxide Materials*, 125-:355–417, 1997.

[28] R. Dieckmann and H. Schmalzried. Defects and cation diffusion in magnetite (I). *Berichte Der Bunsen-Gesellschaft-Physical Chemistry Chemical Physics*, 81(3):344–347, 1977.

[29] R. Dieckmann and H. Schmalzried. Defects and cation diffusion in magnetite (II). *Berichte Der Bunsen-Gesellschaft-Physical Chemistry Chemical Physics*, 81(4):414–419, 1977.

[30] L. Himmel, R. F. Mehl, and C. E. Birchenall. Self-diffusion of iron in iron oxides and the Wagner theory of oxidation. *Transactions of the American Institute of Mining and Metallurgical Engineers*, 197(6):827–843, 1953.

[31] W. K. Chen and N. L. Peterson. Effect of deviation from stoichiometry on cation self-diffusion and isotope-effect in wustite, $Fe_{1-x}O$. *Journal of Physics and Chemistry of Solids*, 36(10):1097–1103, 1975.

[32] J. Paidassi. The kinetics of the air oxidation of iron in the range 700-1250-degrees-C. *Acta Metallurgica*, 6(3):184–194, 1958.

[33] M. H. Davies, M. T. Simnad, and C. E. Birchenall. On the mechanism and kinetics of the scaling of iron. *Transactions of the American Institute of Mining and Metallurgical Engineers*, 191(10):889–896, 1951.

[34] F. Gesmundo and F. Viani. Formation of multilayer scales in parabolic oxidation of pure metals - (I). Relationships between different rate constants. *Corrosion Science*, 18(3):217–230, 1978.

[35] F. Gesmundo and F. Viani. Formation of multilayer scales in parabolic oxidation of pure metals - (II). Temperature and pressure-dependence of different rate constants. *Corrosion Science*, 18(3):231–243, 1978.

[36] K. P. Lillerud and P. Kofstad. On high-temperature oxidation of chromium.(I). Oxidation of annealed, thermally etched chromium at 800-degrees-1100-degrees-C. *Journal of the Electrochemical Society*, 127(11):2397–2410, 1980.

[37] D. Caplan and G. I. Sproule. Effect of oxide grain structure on high-temperature oxidation of Cr. *Oxidation of Metals*, 9(5):459–472, 1975.

[38] A. C. S. Sabioni, B. Lesage, A. M. Huntz, J. C. Pivin, and C. Monty. Self-diffusion in Cr_2O_3. (I). Chromium diffusion in single-crystals. *Philosophical Magazine A-Physics of Condensed Matter Structure Defects and Mechanical Properties*, 66(3):333–350, 1992.

[39] A. C. S. Sabioni, A. M. Huntz, F. Millot, and C. Monty. Self-diffusion in Cr_2O_3. (II). Oxygen diffusion in single-crystals. *Philosophical Magazine A-Physics of Condensed Matter Structure Defects and Mechanical Properties*, 66(3):351–360, 1992.

[40] A. C. S. Sabioni, A. M. Huntz, F. Millot, and C. Monty. Self-diffusion in Cr_2O_3. (III). Chromium and oxygen grain-boundary diffusion in polycrystals. *Philosophical Magazine A-Physics of Condensed Matter Structure Defects and Mechanical Properties*, 66(3):361–374, 1992.

[41] A. C. S. Sabioni, A. M. Huntz, J. Philibert, B. Lesage, and C. Monty. Relation between the oxidation growth-rate of chromia scales and self-diffusion in Cr_2O_3. *Journal of Materials Science*, 27(17):4782–4790, 1992.

[42] A. C. S. Sabioni, A. M. Huntz, F. Silva, and F. Jomard. Diffusion of iron in Cr_2O_3: polycrystals and thin films. *Materials Science and Engineering A-Structural Materials Properties Microstructure and Processing*, 392(1-2):254–261, 2005.

[43] P. Kofstad. On the formation of porosity and microchannels in growing scales. *Oxidation of Metals*, 24(5-6):265–276, 1985.

[44] D. J. Srolovitz and T. A. Ramanarayanan. An elastic analysis of growth stresses during oxidation. *Oxidation of Metals*, 22(3-4):133–146, 1984.

[45] J. Stringer. Stress generation and relief in growing oxide films. *Corrosion Science*, 10(7):513, 1970.

[46] G. B. Gibbs and R. Hales. Influence of metal lattice vacancies on oxidation of high-temperature materials. *Corrosion Science*, 17(6):487–507, 1977.

[47] B. Pieraggi and R. A. Rapp. Stress generation and vacancy annihilation during scale growth limited by cation vacancy diffusion. *Acta Metallurgica*, 36(5):1281–1289, 1988.

[48] T. Maruyama, N. Fukagai, M. Ueda, and K. Kawamura. Chemical potential distribution and void formation in magnetite scale formed in oxidation of iron at 823 K. In P Steinmetz, IG Wright, G Meier, A Galerie, B Pieraggi, and R Podor, editors, *6th International Symposium on High Temperature Corrosion and Protection of Materials*, volume 461-464, pages 807–813, Les Embiez, FRANCE, 2004.

[49] M. Ueda, K. Kawamura, and T. Maruyama. Void formation in magnetite scale formed on iron at 823 K - Elucidation by chemical potential distribution. *Materials Science Forum*, 522-523:37–44, 2006.

[50] A. W. Funkenbusch, J. G. Smeggil, and N. S. Bornstein. Reactive element - sulfur interaction and oxide scale adherence. *Metallurgical Transactions A-Physical Metallurgy and Materials Science*, 16(6):1164–1166, 1985.

[51] W. Y. Lee, Y. Zhang, I. G. Wright, B. A. Pint, and P. K. Liaw. Effects of sulfur impurity on the scale adhesion behavior of a desulfurized Ni-based superalloy aluminized by chemical vapor deposition. *Metallurgical and Materials Transactions A-Physical Metallurgy and Materials Science*, 29(3):833–841, 1998.

[52] J. L. Smialek. Adherent Al_2O_3 scales formed on undoped NiCrAl alloys. *Metallurgical Transactions A-Physical Metallurgy and Materials Science*, 18(1):164–167, 1987.

[53] P. Y. Hou and J. Stringer. Oxide scale adhesion and impurity segregation at the scale metal interface. *Oxidation of Metals*, 38(5-6):323–345, 1992.

[54] V. K. Tolpygo and H. Viefhaus. Segregation at the Al_2O_3–FeCrAl interface during high-temperature oxidation. *Oxidation of Metals*, 52(1-2):1–29, 1999.

[55] H. J. Grabke, D. Wiemer, and H. Viefhaus. Segregation of sulfur during growth of oxide scales. *Applied Surface Science*, 47(3):243–250, 1991.

[56] H. J. Grabke, G. Kurbatov, and H. J. Schmutzler. Segregation beneath oxide scales. *Oxidation of Metals*, 43(1-2):97–114, 1995.

[57] S. Mrowec. On mechanism of high temperature oxidation of metals and alloys. *Corrosion Science*, 7(9):563, 1967.

[58] B. Sundman, B. Jansson, and J. O. Andersson. The Thermo-Calc databank system. *Calphad-Computer Coupling of Phase Diagrams and Thermochemistry*, 9(2):153–190, 1985.

[59] C. Bale, P. Chartrand, S. A. Degterov, G. Eriksson, K. Hack, R. Ben Mahfoud, J. Melancon, A. D. Pelton, and S. Petersen. FactSage thermochemical software and databases. *Calphad-Computer Coupling of Phase Diagrams and Thermochemistry*, 26(2):189–228, 2002.

[60] J.B. Clark and F.N. Rhines. *Trans. ASM*, 51:199, 1959.

[61] J.S. Kirkaldy and L.C. Brown. Diffusion behaviour in ternary, multiphase systems. *Can. Met. Quart.*, 2:89, 1963.

[62] A. D. Dalvi and D. E. Coates. Review of diffusion path concept and its application to high-temperature oxidation of binary-alloys. *Oxidation of Metals*, 5(2):113–135, 1972.

[63] A. Atkinson. A theoretical analysis of the oxidation of Fe-Si alloys. *Corrosion Science*, 22(2):87–102, 1982.

[64] B. D. Bastow, G. C. Wood, and D. P. Whittle. Morphologies of uniform adherent scales on binary-alloys. *Oxidation of Metals*, 16(1-2):1–28, 1981.

[65] H. E. Evans, A. T. Donaldson, and T. C. Gilmour. Mechanisms of breakaway oxidation and application to a chromia-forming steel. *Oxidation of Metals*, 52(5-6):379–402, 1999.

[66] E. K. Ohriner and J. E. Morral. Precipitate distribution in sub-scales. *Scripta Metallurgica*, 13(1):7–10, 1979.

[67] C. Wagner. Reaktionstypen bei der oxydation von legierungen. *Zeitschrift Fur Elektrochemie*, 63(7):772–790, 1959.

[68] R. A. Rapp. Kinetics microstructures and mechanism of internal oxidation - its effect and prevention in high temperature alloy oxidation. *Corrosion*, 21(12):382, 1965.

[69] C. Wagner. Formation of composite scales consisting of oxides of different metals. *Journal of the Electrochemical Society*, 103(11):627–633, 1956.

[70] F. Gesmundo, F. Viani, and Y. Niu. The possible scaling modes in the high-temperature oxidation of 2-phase binary alloys. Part 1: High oxidant pressures. *Oxidation of Metals*, 42(5-6):409–429, 1994.

[71] H. Davies and A. Dinsdale. Theoretical study of steam grown oxides as a function of temperature, pressure and p_{O_2}. *Materials at High Temperatures*, 22(1-2):15–25, 2005.

[72] J. Töpfer, S. Aggarwal, and R. Dieckmann. Point-defects and cation tracer diffusion in $(Cr_xFe_{1-x})_{(3-\delta)}O_4$ spinels. *Solid State Ionics*, 81(3-4):251–266, 1995.

[73] P. K. Footner, D. R. Holmes, and D. Mortimer. Oxidation of iron-chromium binary alloys. *Nature*, 216(5110):54, 1967.

[74] I. Barin. *Thermochemical Data of Pure Substances*. VCH, Weinheim, second edition, 1993.

[75] O. Kubaschewski and C.B. Alcock. *Metallurgical Thermochemistry*. Pergamon Press, Oxford, 5th edition, 1979.

[76] D. P. Whittle, D. J. Evans, D. B. Scully, and G. C. Wood. Compositional changes in underlying alloy during protective oxidation of alloys. *Acta Metallurgica*, 15(9):1421–, 1967.

[77] D. P. Whittle, G. C. Wood, D. J. Evans, and D. B. Scully. Concentration profiles in the underlying alloy during the oxidation of iron-chromium alloys. *Acta Metallurgica*, 15(11):1747–1755, 1967.

[78] C. Wagner. Theoretical analysis of the diffusion processes determining the oxidation rate of alloys. *Journal of the Electrochemical Society*, 99(10):369–380, 1952.

[79] D. P. Whittle. Oxidation of finite samples of heat-resistant alloys. *Corrosion Science*, 12(11):869, 1972.

[80] H.C. Cowen and S.J. Webster. Chromium depletion during oxidation of stainless steel foils. In D.R. Holmes, R.B. Hill, and L.M. Wyatt, editors, *B.N.E.S. International Conference on Corrosion of Steels in CO_2*, pages 349–358, Reading, U.K., 1974.

[81] A.W. Bowen and G.M. Leak. Solute diffusion in alpha- and gamma-iron. *Metallurgical Transactions*, 1(6):1695–1700, 1970.

[82] Inc. Wolfram Research. Mathematica version 8.0, 2010.

[83] D. P. Whittle. Spalling of protective oxide scales. *Oxidation of Metals*, 4(3):171–179, 1972.

[84] G. C. Wood and D. P. Whittle. On the mechanism of oxidation of iron-16.4% chromium at high temperature. *Corrosion Science*, 4(1-4):263–292, 1964.

[85] G. C. Wood and D. P. Whittle. The mechanism of breakthrough of protective chromium oxide scales on Fe-Cr alloys. *Corrosion Science*, 7(11):763–782, 1967.

[86] D. P. Whittle and G. C. Wood. Complex scale formation on an iron-18 percent chromium alloy. *Journal of the Electrochemical Society*, 114(10):986, 1967.

[87] R. Benz, J. F. Elliott, and J. Chipman. Thermodynamics of carbides in system Fe-Cr-C. *Metallurgical Transactions*, 5(10):2235–2240, 1974.

[88] J. A. Lobo and G. H. Geiger. Thermodynamics and solubility of carbon in ferrite and ferritic Fe-Mo alloys. *Metallurgical Transactions A-Physical Metallurgy and Materials Science*, 7(9):1347–1357, 1976.

[89] E. Budke, C. Herzig, and H. Wever. Volume and grain-boundary diffusion of C-14 in alpha-Fe. *Physica Status Solidi A-Applied Research*, 127(1):87–101, 1991.

[90] K. Tapasa, A. V. Barashev, D. J. Bacon, and Y. N. Osetsky. Computer simulation of carbon diffusion and vacancy-carbon interaction in alpha-iron. *Acta Materialia*, 55(1):1–11, 2007.

[91] O. Ahmed and D. J. Young. Precipitate distributions in internally carburised and oxidised Fe-Cr alloys. In M McNallan, E Opila, T Maruyama, and T Narita, editors, *Per Kofstad Memorial Symposium on High Temperature Corrosion and Materials Chemistry at the 1999 Joint Int Meeting of the Electrochem-Soc/Electrochem-Soc-of-Japan*, volume 99, pages 77–92, HONOLULU, HI, 2000.

[92] D. J. Young and O. Ahmed. Kinetic and morphological development of internal precipitates in iron-chromium alloys. In R Streiff, IG Wright, RC Krutenat, M Caillet, and A Galerie, editors, *5th International Symposium on High Temperature Corrosion and Protection of Materials*, volume 369-3, pages 93–100, LES EMBIEZ, FRANCE, 2001.

[93] A. Schnaas and H. J. Grabke. Changes in material properties of austenitic CrNiFe-alloys by carburization. *Werkstoffe Und Korrosion-Materials and Corrosion*, 29(10):635–644, 1978.

[94] C.P. Haigh. Opening address. In D.R. Holmes, R.B. Hill, and L.M. Wyatt, editors, *B.N.E.S. International Conference on Corrosion of Steels in CO_2*, pages viii–x, Reading, U.K., 1974.

[95] G. B. Gibbs and L. A. Popple. Oxidation of structural-steels in CO_2 cooled reactors. *Nuclear Energy-Journal of the British Nuclear Energy Society*, 21(1):51–55, 1982.

[96] F. S. Pettit, J. A. Goebel, and G. W. Goward. Thermodynamic analysis of simultaneous attack of some metals and alloys by 2 oxidants. *Corrosion Science*, 9(12):903, 1969.

[97] P.A. German and A.C. Littlejohn. Oxidation kinetics of carbon steels in pressurised CO_2-based atmospheres at elevated temperatures. In D.R. Holmes, R.B. Hill, and L.M. Wyatt, editors, *B.N.E.S. International Conference on Corrosion of Steels in CO_2*, pages 1–14, Reading, U.K., 1974.

[98] J.R. Donati and J. Garaud. "Electricité de France" work on the mild steel CO_2 corrosion problem. In D.R. Holmes, R.B. Hill, and L.M. Wyatt, editors, *B.N.E.S. International Conference on Corrosion of Steels in CO_2*, pages 28–41, Reading, U.K., 1974.

[99] J.S.L. Leach, A.Y. Nehru, D.E. Taylor, and M.F. Taylor. The high temperature oxidation of structural steels. In D.R. Holmes, R.B. Hill, and L.M. Wyatt, editors, *B.N.E.S. International Conference on Corrosion of Steels in CO_2*, pages 97–105, Reading, U.K., 1974.

[100] G. B. Gibbs, R.E. Pendlebury, and M. R. Wootton. Protective and breakaway corrosion of mild steel in CO_2. In D.R. Holmes, R.B. Hill, and L.M. Wyatt, editors, *B.N.E.S. International Conference on Corrosion of Steels in CO_2*, pages 59–72, 1974.

[101] J.M. Ferguson, J.C.P. Garrett, and B. Lloyd. A multivariable investigation of the kinetics of oxidation of mild steels in high temperature CO_2. In D.R. Holmes, R.B. Hill, and L.M. Wyatt, editors, *B.N.E.S. International Conference on Corrosion of Steels in CO_2*, pages 15–27, Reading, U.K., 1974.

[102] P. L. Surman. Oxidation of iron at controlled oxygen partial pressures - (II). Carbon monoxide carbon dioxide. *Corrosion Science*, 13(11):825, 1973.

[103] J. E. Antill, K. A. Peakall, and Warburton.Jb. Oxidation of mild and low-alloy steels in CO_2 based atmospheres. *Corrosion Science*, 8(9):689, 1968.

[104] G. B. Gibbs. Model for mild-steel oxidation in CO_2. *Oxidation of Metals*, 7(3):173–184, 1973.

[105] P.L. Harrison, R.B. Dooley, S.K. Lister, D. B. Meadowcroft, P.J. Nolan, R.E. Pendlebury, P. L. Surman, and M. R. Wootton. The oxidation of 9Cr 1Mo steels in carbon dioxide - A discussion of possible mechanisms. In D.R. Holmes, R.B. Hill, and L.M. Wyatt, editors, *B.N.E.S. International Conference on Corrosion of Steels in CO_2*, pages 220–233, 1974.

[106] A. M. Pritchard and A. E. Truswell. Mechanistic experiments on the oxidation of 9% Cr steels in CO_2 at 550 °C. In D.R. Holmes, R.B. Hill, and L.M. Wyatt, editors, *B.N.E.S. International Conference on Corrosion of Steels in CO_2*, pages 234–246, 1974.

[107] M. R. Taylor, J. M. Calvert, D. G. Lees, and D. B. Meadowcroft. The mechanism of corrosion of Fe-9% Cr alloys in carbon dioxide. *Oxidation of Metals*, 14(6):499–516, 1980.

[108] A. M. Pritchard, N. E. W. Hartley, J. F. Singleton, and A. E. Truswell. O-18 and deuterium profiling in thick-films on Fe-9-percent Cr alloys by 3 MeV nuclear microprobe. *Corrosion Science*, 20(1):1, 1980.

[109] F. Rouillard, G. Moine, L. Martinelli, and J. C. Ruiz. Corrosion of 9Cr steel in CO_2 at intermediate temperature I: Mechanism of void-induced duplex oxide formation. *Oxidation of Metals*, 77(1-2):27–55, 2012.

[110] W. W. Smeltzer. The kinetics of wustite scale formation on iron. *Acta Metallurgica*, 8(6):377–383, 1960.

[111] A. Rahmel and J. Tobolski. Einfluss von wasserdampf und kohlendioxyd auf die oxydation von eisen in sauerstoff bei hohen temperaturen. *Corrosion Science*, 5(5):333–346, 1965.

[112] C. T. Fujii and R. A. Meussner. Carburization of Fe-Cr alloys during oxidation in dry carbon dioxide. *Journal of the Electrochemical Society*, 114(5):435, 1967.

[113] H. E. McCoy. Type 304 stainless steel vs flowing CO_2 at atmospheric pressure and 1100-1800F. *Corrosion*, 21(3):84, 1965.

[114] M. G. C. Cox, B. McEnaney, and V. D. Scott. Vacancy condensation and void formation in duplex oxide scales on alloys. *Philosophical Magazine*, 28(2):309–319, 1973.

[115] M. G. C. Cox, B. McEnaney, and V. D. Scott. Kinetics of initial oxide-growth on Fe-Cr alloys and role of vacancies in film breakdown. *Philosophical Magazine*, 31(2):331–338, 1975.

[116] S.J. Allan, J.F. Norton, and L. A. Popple. A survey of the oxidation behaviour of stainless steels in CO_2 environments. In D.R. Holmes, R.B. Hill, and L.M. Wyatt, editors, *B.N.E.S. International Conference on Corrosion of Steels in CO_2*, pages 284–297, 1974.

[117] J.C.P. Garrett, S.K. Lister, P.J. Nolan, and J.T. Crook. Some factors in the oxidation of austenitic stainless steels. In D.R. Holmes, R.B. Hill, and L.M. Wyatt, editors, *B.N.E.S. International Conference on Corrosion of Steels in CO_2*, pages 298–310, 1974.

[118] G. H. Meier, W. C. Coons, and R. A. Perkins. Corrosion of iron-base, nickel-base, and cobalt-base alloys in atmospheres containing carbon and oxygen. *Oxidation of Metals*, 17(3-4):235–262, 1982.

[119] M.R. Taylor, J.M. Calvert, K.A. Hay, D.G. Lees, and D.B. Meadowcroft. Tracer movement in growing oxide scales on an Fe-8.5wt% Cr binary alloy. In D.R. Holmes, R.B. Hill, and L.M. Wyatt, editors, *B.N.E.S. International Conference on Corrosion of Steels in CO_2*, pages 272–274, 1974.

[120] J. Robertson and M. I. Manning. Criteria for formation of single layer, duplex, and breakaway scales on steels. *Materials Science and Technology*, 4(12):1064–1071, 1988.

[121] X. G. Zheng and D. J. Young. High-temperature corrosion of Cr_2O_3-forming alloys in CO–CO_2–N_2 atmospheres. *Oxidation of Metals*, 42(3-4):163–190, 1994.

[122] I. Wolf and H. J. Grabke. A study on the solubility and distribution of carbon in oxides. *Solid State Communications*, 54(1):5–10, 1985.

[123] A. Bruckman. Mechanism of transport of matter through scales during oxidation of metals and alloys. *Corrosion Science*, 7(1):51, 1967.

[124] A. Bruckman, R. Emmerich, and S. Mrowec. Investigation of high-temperature oxidation of Fe-Cr alloys by means of isotope O-18. *Oxidation of Metals*, 5(2):137–147, 1972.

[125] X. G. Zheng and D. J. Young. High-temperature corrosion of pure chromium in CO–CO_2–SO_2–N_2 atmospheres. *Corrosion Science*, 36(12):1999–2015, 1994.

[126] D. J. Young. Simultaneous oxidation and carburisation of chromia forming alloys. *International Journal of Hydrogen Energy*, 32(16):3763–3769, 2007.

[127] M. F. Taylor. The application of thermodynamics to the oxidation behavior of mild steels in carbon dioxide-based atmospheres. *Oxidation of Metals*, 16(1-2):133–146, 1981.

[128] F. Rouillard, G. Moine, M. Tabarant, and J. C. Ruiz. Corrosion of 9Cr steel in CO_2 at intermediate temperature II: Mechanism of carburization. *Oxidation of Metals*, 77(1-2):57–70, 2012.

[129] N Birks. In Z. A. Foroulis and F. S. Pettit, editors, *Corrosion of High Temperature Alloys in Multicomponent Oxidative Environments*, page 215, Electrochem. Soc., Las Vegas, 1976.

[130] S. R. J. Saunders, M. Monteiro, and F. Rizzo. The oxidation behaviour of metals and alloys at high temperatures in atmospheres containing water vapour: A review. *Progress in Materials Science*, 53(5):775–837, 2008.

[131] C. W. Tuck, M. Odgers, and K. Sachs. Oxidation of iron at 950 degrees C in oxygen/water vapour mixtures. *Corrosion Science*, 9(4):271, 1969.

[132] C. T. Fujii and R. A. Meussner. Oxide structures produced on iron-chromium alloys by a dissociative mechanism. *Journal of the Electrochemical Society*, 110(12):1195–1204, 1963.

[133] C. T. Fujii and R. A. Meussner. The mechanism of the high-temperature oxidation of iron-chromium alloys in water vapor. *Journal of the Electrochemical Society*, 111(11):1215–1221, 1964.

[134] E. Essuman, G. H. Meier, J. Zurek, M. Hansel, and W. J. Quadakkers. The effect of water vapor on selective oxidation of Fe-Cr alloys. *Oxidation of Metals*, 69(3-4):143–162, 2008.

[135] A. Galerie, S. Henry, Y. Wouters, M. Mermoux, J. P. Petit, and L. Antoni. Mechanisms of chromia scale failure during the course of 15-18Cr ferritic stainless steel oxidation in water vapour. In *Workshop on Scale Growth and Exfoliation in Steam Plant*, volume 22, pages 105–112, Teddington, ENGLAND, 2003, 2005.

[136] J. Shen, L. J. Zhou, and T. F. Li. High-temperature oxidation of Fe-Cr alloys in wet oxygen. *Oxidation of Metals*, 48(3-4):347–356, 1997.

[137] T. Ericsson. Stratified oxide scale growth on two Cr-Ni steels oxidized in high-pressure steam at 800 °C. *Oxidation of Metals*, 2(2):173–205, 1970.

[138] J. E. Castle and P. L. Surman. Self-diffusion of oxygen in magnetite . techniques for sampling and isotopic analysis of micro quantities of water. *Journal of Physical Chemistry*, 71(13):4255, 1967.

[139] I. Kvernes, M. Oliveira, and P. Kofstad. High-temperature oxidation of Fe-13Cr-xAl alloys in air–H_2O vapor mixtures. *Corrosion Science*, 17(3):237–252, 1977.

[140] D. J. Young. Effects of water vapour on the oxidation of chromia formers. In P. Steinmetz, I.G. Wright, A. Galerie, D. Monceau, and S. Mathieu, editors, *7th International Symposium on High Temperature Corrosion and Protection of Materials*, volume 595-598, pages 1189–1197, Les Embiez, FRANCE, 2008.

[141] G. Hultquist, B. Tveten, and E. Hornlund. Hydrogen in chromium: Influence on the high-temperature oxidation kinetics in H_2O, oxide-growth mechanisms, and scale adherence. *Oxidation of Metals*, 54(1-2):1–10, 2000.

[142] S. Henry, J. Mougin, Y. Wouters, J. P. Petit, and A. Galerie. Characterization of chromia scales grown on pure chromium in different oxidizing atmospheres. *Materials at High Temperatures*, 17(2):231–234, 2000.

[143] M. Michalik, M. Hansel, J. Zurek, L. Singheiser, and W. J. Quadakkers. Effect of water vapour on growth and adherence of chromia scales formed on Cr in high and low p_{O_2}-environments at 1000 and 1050 degrees C. *Materials at High Temperatures*, 22(3-4):213–221, 2005.

[144] T. Norby. Protonic defects in oxides and their possible role in high-temperature oxidation. In *3rd International Symposium on High Temperature Corrosion and Protection of Materials*, volume 3, pages 99–106, LES EMBIEZ, FRANCE, 1993.

[145] A. Galerie, Y. Wouters, and M. Caillet. The kinetic behaviour of metals in water vapour at high temperatures: Can general rules be proposed? In R. Streiff, I.G. Wright, R.C. Krutenat, M. Caillet, and A. Galerie, editors, *5th International Symposium on High Temperature Corrosion and Protection of Materials*, volume 369-3, pages 231–238, LES EMBIEZ, FRANCE, 2001.

[146] J. Zurek, D. J. Young, E. Essuman, M. Hansel, H. J. Penkalla, L. Niewolak, and W. J. Quadakkers. Growth and adherence of chromia based surface scales on Ni-base alloys in high- and low p_{O_2} gases. *Materials Science and Engineering a-Structural Materials Properties Microstructure and Processing*, 477(1-2):259–270, 2008.

[147] M. H. B. Ani, T. Kodama, M. Ueda, K. Kawamura, and T. Maruyama. The effect of water vapor on high temperature oxidation of Fe-Cr alloys at 1073 K. *Materials Transactions*, 50(11):2656–2663, 2009.

[148] C. S. Tedmon. Effect of oxide volatilization on oxidation kinetics of Cr and Fe-Cr alloys. *Journal of the Electrochemical Society*, 113(8):766, 1966.

[149] D. J. Young and B. A. Pint. Chromium volatilization rates from Cr_2O_3 scales into flowing gases containing water vapor. *Oxidation of Metals*, 66(3-4):137–153, 2006.

[150] H. Asteman, J. E. Svensson, L. G. Johansson, and M. Norell. Indication of chromium oxide hydroxide evaporation during oxidation of 304L at 873 K in the presence of 10% water vapor. *Oxidation of Metals*, 52(1-2):95–111, 1999.

[151] H. Asteman, J. E. Svensson, M. Norell, and L. G. Johansson. Influence of water vapor and flow rate on the high-temperature oxidation of 304L; effect of chromium oxide hydroxide evaporation. *Oxidation of Metals*, 54(1-2):11–26, 2000.

[152] K. F. McCarty and D. R. Boehme. A raman study of the systems $Fe_{3-x}Cr_xO_4$ and $Fe_{2-x}Cr_xO_3$. *Journal of Solid State Chemistry*, 79(1):19–27, 1989.

[153] B. Gleeson, S. M. M. Hadavi, and D. J. Young. Isothermal transformation behavior of thermally-grown wustite. *Materials at High Temperatures*, 17(2):311–318, 2000.

[154] M. D. Belo, M. Walls, N. E. Hakiki, J. Corset, E. Picquenard, G. Sagon, and D. Noel. Composition, structure and properties of the oxide films formed on the stainless steel 316L in a primary type PWR environment. *Corrosion Science*, 40(2-3):447–463, 1998.

[155] Tony J. Collins. Imagej for microscopy. *Biotechniques*, 43(1):25–30, 2007.

[156] E.C. Bain and H.W. Paxton. *Alloying elements in steel*. ASM, Metals Park, OH, USA, 2nd edition, 1961.

[157] R. A. Grange, C. R. Hribal, and L. F. Porter. Hardness of tempered martensite in carbon and low-alloy steels. *Metallurgical Transactions A-Physical Metallurgy and Materials Science*, 8(11):1775–1785, 1977.

[158] M. Cohen. The strengthening of steel. *Transactions of the Metallurgical Society of AIME*, 224:638–657, 1962.

[159] CaRIne Crystallography version 3.1, C. Boudias and D. Monceau, 1989-2012, Divergent SA, Compiègne, France.

[160] U. R. Evans. The colours due to thin films on metals. *Proceedings of the Royal Society of London Series A-Containing Papers of a Mathematical and Physical Character*, 107(742):228–237, 1925.

[161] F. S. Pettit, R. Yinger, and J. B. Wagner. The mechanism of oxidation of iron in carbon monoxide-carbon dioxide mixtures. *Acta Metallurgica*, 8(9):617–623, 1960.

[162] F. S. Pettit and J. B. Wagner. Transition from linear to parabolic rate law during oxidation of iron to wustite in CO-CO_2 mixtures. *Acta Metallurgica*, 12(1):35–40, 1964.

[163] H. T. Abuluwefa, R. I. L. Guthrie, and F. Ajersch. Oxidation of low carbon steel in multicomponent gases .1. reaction mechanisms during isothermal oxidation. *Metallurgical and Materials Transactions a-Physical Metallurgy and Materials Science*, 28(8):1633–1641, 1997.

[164] E.T. Turkdogan, W. M. McKewan, and L. Zwell. Rate of oxidation of iron to wustite in water-hydrogen gas mixtures. *Journal of Physical Chemistry*, 69(1):327–334, 1965.

[165] A. D. Pelton, H. Schmalzried, and J. Sticher. Computer-assisted analysis and calculation of phase-diagrams of the Fe-Cr-O, Fe-Ni-O and Cr-Ni-O systems. *Journal of Physics and Chemistry of Solids*, 40(12):1103–1122, 1979.

[166] A. Bruckman and Simkovic.G. Concerning the mechanism of scale growth due to cation diffusion in Fe_2O_3 and CuS. *Corrosion Science*, 12(7):595–601, 1972.

[167] G. C. Wood, I. G. Wright, T. Hodgkiess, and D. P. Whittle. A comparison of the oxidation of Fe-Cr, Ni-Cr and Co-Cr alloys in oxygen and water vapour. *Materials and Corrosion*, 21(11):900–910, 1970.

[168] J. E. Croll and G. R. Wallwork. The high-temperature oxidation of iron-chromium-nickel alloys containing 0-30 % chromium. *Oxidation of Metals*, 4(3):121–140, 1972.

[169] A. D. Dalvi and W. W. Smeltzer. Thermodynamics of iron-nickel-oxygen system at 1000 °C. *Journal of the Electrochemical Society*, 117(11):1431–1436, 1970.

[170] A. D. Dalvi and R. Sridhar. Thermodynamics of Fe-Ni-O and Fe-Ni systems at 1065 K to 1380 K. *Canadian Metallurgical Quarterly*, 15(4):349–357, 1976.

[171] A. D. Dalvi and W. W. Smeltzer. Diffusion-model for oxidation of nickel-iron alloys at 1000 °C. *Journal of the Electrochemical Society*, 121(3):386–394, 1974.

[172] A. L. Myers and J. M. Prausnitz. Thermodynamics of mixed-gas adsorption. *A.I.Ch.E. Journal*, 11(1):121–127, 1965.

[173] J. L. Meijering. In H. Herman, editor, *Advances in Materials Research*, pages 1–81, Wiley-Interscience, New York, 1971.
[174] "Physical Constants of Inorganic Compounds," in CRC Handbook of Chemistry and Physics, 91st Edition (Internet Version 2011), W. M. Haynes, ed., CRC Press/Taylor and Francis, Boca Raton, FL.
[175] H. J. Goldschmidt. *Interstitial Alloys*. Butterworths, London, 1967.
[176] J. Crank. *The mathematics of diffusion*. Oxford University Press, Oxford, 2nd edition, 1975.
[177] R. A. Holm and H. E. Evans. The resistance of 20Cr/25Ni steels to carbon deposition. iii. Cold work and selective preoxidation. *Werkstoffe Und Korrosion-Materials and Corrosion*, 38(5):219–224, 1987.
[178] J. A. Nesbitt. Predicting minimum aluminum concentrations for protective scale formation on ni-base alloys.ii. Cyclic oxidation. *Journal of the Electrochemical Society*, 136(5):1518–1527, 1989.
[179] M. Halvarsson, J. E. Tang, H. Asteman, J. E. Svensson, and L. G. Johansson. Microstructural investigation of the breakdown of the protective oxide scale on a 304 steel in the presence of oxygen and water vapour at 600 °C. *Corrosion Science*, 48(8):2014–2035, 2006.
[180] C. Wagner. Distribution of cations in metal oxide and metal sulphide solid solutions formed during oxidation of alloys. *Corrosion Science*, 9(2):91–109, 1969.
[181] D. J. Young, T. Narita, and W. W. Smeltzer. Diffusional analysis for growth of the monosulfide scale on cobalt-iron alloys. *Journal of the Electrochemical Society*, 127(3):679–686, 1980.
[182] H. Schmalzried and W. Laqua. Multicomponent oxides in oxygen potential gradients. *Oxidation of Metals*, 15(3-4):339–353, 1981.
[183] R. A. Rapp. The transition from internal to external oxidation and the formation of interruption bands in silver-indium alloys. *Acta Metallurgica*, 9(8):730–741, 1961.
[184] F. Gesmundo and F. Viani. Transition from internal to external oxidation for binary alloys in the presence of an outer scale. *Oxidation of Metals*, 25(5-6):269–282, 1986.
[185] J. H. Swisher and E.T. Turkdogan. Solubility permeability and diffusivity of oxygen in solid iron. *Transactions of the Metallurgical Society of Aime*, 239(4):426, 1967.
[186] J. W. Park and C. J. Altstetter. The diffusion and solubility of oxygen in solid nickel. *Metallurgical Transactions a-Physical Metallurgy and Materials Science*, 18(1):43–50, 1987.
[187] A.W. Bowen and G.M. Leak. Diffusion in bcc iron base alloys. *Metallurgical and Materials Transactions B*, 1(10):2767–2773, 1970.
[188] R. Braun and M. Fellerkniepmeier. Diffusion of chromium in alpha-iron. *Physica Status Solidi A - Applied Research*, 90(2):553–561, 1985.
[189] S. J. Rothman, L. J. Nowicki, and G. E. Murch. Self-diffusion in austenitic Fe-Cr-Ni alloys. *Journal of Physics F-Metal Physics*, 10(3):383–398, 1980.
[190] A. F. Smith and G. B. Gibbs. *Metals Science Journal*, 3:93–94, 1969.

[191] L. Intiso, L. G. Johansson, S. Canovic, S. Bellini, J. E. Svensson, and M. Halvarsson. Oxidation behaviour of Sanicro 25 (42Fe22Cr25NiWCuNbN) in O_2/H_2O mixture at 600 °C. *Oxidation of Metals*, 77:209–235, 2012.

[192] R. E. Lobnig, H. P. Schmidt, K. Hennesen, and H. J. Grabke. Diffusion of cations in chromia layers grown on iron-base alloys. *Oxidation of Metals*, 37(1-2):81–93, 1992.

[193] U. R. Evans. The laws of expanding circles and spheres in relation to the lateral growth of surface films and the grain-size of metals. *Transactions of the Faraday Society*, 41(7):365–374, 1945.

[194] S.D. Poisson. *Recherches sur la probabilité des jugements en matière criminelle et en matière civile, précédées des règles générales du calcul des probabilités*. Bachelier, Paris, 1837.

[195] A. N. Kolmogorov. On statistical theory of metal crystallisation. *Izvestiya Akademii Nauk SSSR, Ser. Fiz.*, 3:355–359, 1937.

[196] W. A. Johnson and R. F. Mehl. Reaction kinetics in processes of nucleation and growth. *Transactions of the American Institute of Mining and Metallurgical Engineers*, 135:416–442, 1939.

[197] M. Avrami. Kinetics of phase change i - general theory. *Journal of Chemical Physics*, 7(12):1103–1112, 1939.

[198] M. Avrami. Kinetics of phase change. ii transformation-time relations for random distribution of nuclei. *Journal of Chemical Physics*, 8(2):212–224, 1940.

[199] M. Avrami. Granulation, phase change, and microstructure - kinetics of phase change. iii. *Journal of Chemical Physics*, 9(2):177–184, 1941.

[200] J. W. Christian. *The theory of transformation in metals and alloys*. Pergamon Press, Oxford, 2002.

[201] M. G. C. Cox, B. McEnaney, and V. D. Scott. Phase interactions in growth of thin oxide-films on iron-chromium alloys. *Philosophical Magazine*, 29(3):585–600, 1974.

[202] C. Leygraf and G. Hultquist. Initial oxidation stages on Fe-Cr(100) and Fe-Cr(110) surfaces. *Surface Science*, 61(1):69–84, 1976.

[203] J. Webber. Oxidation of Fe-Cr alloys in O_2/3 % H_2O. *Corrosion Science*, 16(8):499–506, 1976.

[204] H. Asteman, E. Ahlberg, and J. E. Svensson. *Electric properties of* α-Fe_2O_3, Cr_2O_3 *and* α-$(Cr, Fe)_2O_3$ *and their relevance to corrosion*, volume 99 of *High Temperature Corrosion and Materials Chemistry*. Electrochemical Society Inc, Pennington, 2000.

[205] F. G. Hicks, D. R. Holmes, and D. B. Meadowcroft. In *4th International Congress on Metallic Corrosion*, Amsterdam, 1969.

[206] D. Poquillon and D. Monceau. Application of a simple statistical spalling model for the analysis of high-temperature, cyclic-oxidation kinetics data. *Oxidation of Metals*, 59(3-4):409–431, 2003.

[207] J. Racine. gnuplot 4.0: A portable interactive plotting utility. *Journal of Applied Econometrics*, 21(1):133–141, 2006.

[208] R. Peraldi and B. A. Pint. Effect of Cr and Ni contents on the oxidation behavior of ferritic and austenitic model alloys in air with water vapor. *Oxidation of Metals*, 61(5-6):463–483, 2004.

[209] Z. Tokei, K. Hennesen, H. Viefhaus, and J. Grabke. Diffusion of chromium in ferritic and austenitic 9-20 wt % chromium steels. *Materials Science and Technology*, 16(10):1129–1138, 2000.

[210] J. Ehlers, E. J. Smaardijk, H. J. Penkalla, A. K. Tyagi, L. Singheiser, and W. J. Quadakkers. Effect of steel composition on the bell-shape temperature dependance of oxidation in water vapour containing environments. In *14th International Corrosion Congress*, 1999.

[211] J. Zurek, E. Wessel, L. Niewolak, F. Schmitz, T. U. Kern, L. Singheiser, and W. J. Quadakkers. Anomalous temperature dependence of oxidation kinetics during steam oxidation of ferritic steels in the temperature range 550-650 °C. *Corrosion Science*, 46(9):2301–2317, 2004.

[212] W. J. Quadakkers, P. J. Ennis, J. Zurek, and M. Michalik. Steam oxidation of ferritic steels - laboratory test kinetic data. *Materials at High Temperatures*, 22(1-2):47–60, 2005.

[213] D. J. Young and D. F. Mitchell. Low-temperature oxidation of Fe-24 wt% Cr. *Oxidation of Metals*, 13(5):437–456, 1979.

[214] A. J. Brock, G. R. Irani, and M. J. Pryor. The kinetics of the oxidation of aluminum-zinc alloys in oxygen at high temperature. *Oxidation of Metals*, 15(1-2):77–100, 1981.

[215] V. S. Bhide and W. W. Smeltzer. The sulfidation kinetics of nickel-aluminum alloys at 700 °C in hydrogen sulfide-hydrogen atmospheres. *Journal of the Electrochemical Society*, 128(4):902–908, 1981.

[216] C. I. Howe, B. McEnaney, and V. D. Scott. A new kinetic-model for nucleation and growth of duplex oxide scales on iron between 350 and 500 °C. *Corrosion Science*, 25(3):195–207, 1985.

[217] N. G. Sjostrand. What is the average chord length? *Annals of Nuclear Energy*, 29(13):1607–1608, 2002.

[218] R. Sanchez. On the use of the average chord length. *Annals of Nuclear Energy*, 31(18):2211–2216, 2004.

[219] W. J. M. de Kruijf and J. L. Kloosterman. On the average chord length in reactor physics. *Annals of Nuclear Energy*, 30(5):549–553, 2003.

[220] D.R. Gaskell. *An introduction to transport phenomena in materials engineering*. Macmillan, New York, 1992.

[221] J. Zurek, M. Michalik, F. Schmitz, T. U. Kern, L. Singheiser, and W. J. Quadakkers. The effect of water-vapor content and gas flow rate on the oxidation mechanism of a 10%Cr-ferritic steel in Ar-H_2O mixtures. *Oxidation of Metals*, 63(5-6):401–422, 2005.

[222] L. Cheng, A. Bottger, T. H. Dekeijser, and E. J. Mittemeijer. Lattice-parameters of iron-carbon and iron-nitrogen martensites and austenites. *Scripta Metallurgica Et Materialia*, 24(3):509–514, 1990.

Appendix A

Gas phase equilibrium

The equilibrium activities of oxygen and carbon in the reacting gases were calculated in the following manner. Let us consider a gaseous Ar–CO_2–H_2O system, at a total pressure P, initially composed of y moles carbon dioxide, z moles water vapour (y and $z \neq 0$), and $1 - y - z$ moles argon. Oxygen is produced by the decomposition of CO_2 and H_2O:

$$CO_2\ (g) = CO\ (g) + \frac{1}{2}\,O_2\ (g) \tag{A.1}$$

$$H_2O\ (g) = H_2\ (g) + \frac{1}{2}\,O_2\ (g) \tag{A.2}$$

The laws of mass action are written

$$K_{A.1} = \frac{p_{CO} p_{O_2}^{1/2}}{p_{CO_2}} \tag{A.3}$$

$$K_{A.2} = \frac{p_{H_2} p_{O_2}^{1/2}}{p_{H_2O}} \tag{A.4}$$

Let the corresponding extents of reaction at equilibrium be called x_1 and x_2, respectively. The amounts of substances in the gas system are then given by

	CO_2	=	CO	+	$\frac{1}{2}\,O_2$	and	H_2O	=	H_2	+	$\frac{1}{2}\,O_2$
Initial stage	y		0		0		z		0		0
Equilibrium	$y - x_1$		x_1		$\frac{1}{2}\,x_1$		$z - x_2$		x_2		$\frac{1}{2}\,x_2$

The partial pressure p_i of a gas constituent i is

$$p_i = \frac{n_i}{\sum_j n_j} P \tag{A.5}$$

where n_i is the amount of substance of i, and

$$\sum_j n_j = 1 + \frac{1}{2}\,(x_1 + x_2) \tag{A.6}$$

In particular,

$$p_{O_2} = \frac{\frac{1}{2}(x_1 + x_2)}{1 + \frac{1}{2}(x_1 + x_2)} P \tag{A.7}$$

Equations (A.3) and (A.4) can then be expressed as

$$K_{A.1}^2 = \frac{P}{1 + \frac{1}{2}(x_1 + x_2)} \frac{\frac{1}{2}(x_1 + x_2) x_1^2}{(y - x_1)^2} \tag{A.8}$$

and

$$K_{A.2}^2 = \frac{P}{1 + \frac{1}{2}(x_1 + x_2)} \frac{\frac{1}{2}(x_1 + x_2) x_2^2}{(z - x_2)^2} \tag{A.9}$$

respectively. At the temperatures of interest, both $K_{A.1}$ and $K_{A.2}$ have relatively small values, in the range $10^{-12} - 10^{-9}$: $K_{A.1}, K_{A.2} \ll 1$. It follows that reactions (A.1) and (A.2) do not produce much O_2, CO and H_2, and in the equilibrium mixture CO_2 and H_2O largely predominate over the other species. This can be expressed as $x_1, x_2 \ll 1$, and as a consequence Eqs. (A.8) and (A.9) may be approximated as

$$K_{A.1}^2 = \frac{P}{2} \frac{x_1^2 (x_1 + x_2)}{y^2} \tag{A.10}$$

and

$$K_{A.2}^2 = \frac{P}{2} \frac{x_2^2 (x_1 + x_2)}{z^2} \tag{A.11}$$

respectively. The values of x_1 and x_2 are obtained by solving this 2-equation, 2-variable system as

$$x_1 = \left(\frac{2y^2 K_{A.1}^2}{P\left(1 + \frac{zK_{A.2}}{yK_{A.1}}\right)} \right)^{\frac{1}{3}} \tag{A.12}$$

and

$$x_2 = \left(\frac{2z^2 K_{A.2}^2}{P\left(1 + \frac{yK_{A.1}}{zK_{A.2}}\right)} \right)^{\frac{1}{3}} \tag{A.13}$$

Values of the equilibrium constants were calculated from thermodynamic data in Ref. [74], and Eq. (A.7) was used to yield the p_{O_2} values given in Table 2.2.

Carbon is produced by the Boudouard and syngas reactions,

$$2\,CO\ (g) = C\ (s) + CO_2\ (g) \tag{A.14}$$

and

$$CO\ (g) + H_2\ (g) = C\ (s) + H_2O\ (g) \tag{A.15}$$

with, at equilibrium,

$$K_{A.14} = \frac{a_C p_{CO_2}}{p_{CO}^2} \tag{A.16}$$

$$K_{A.15} = \frac{a_C p_{H_2O}}{p_{CO} p_{H_2}} \tag{A.17}$$

These competitive reactions yield, in principle, two different values for a_C. The common practice is to consider the fastest reaction, depending on the temperature. In the present case, Eqs. (A.16) and (A.17) lead to very close results. The amount of carbon monoxide produced by reaction (A.1) is relatively low, and results in $\frac{p_{CO}}{p_{CO_2}} \ll 1$. Accordingly, the carbon activity generated by the reaction of carbon monoxide does not reach unity: the gas is "under-saturated" with respect to carbon graphite, which does not precipitate. It follows that as carbon monoxide does not actually react, the gas composition is not altered by the equilibria involving carbon, reactions (A.14) and (A.15). Thus, the values of p_{CO} and p_{CO_2} calculated from the equilibrium of reaction (A.1) (see previous paragraph) were used in Eq. (A.16) to calculate the carbon activity of the gaseous mixtures, which denotes the carburising potential of the gas phase. The figures obtained this way are reported in Table 2.2.

Appendix B

Measurement of nodule dimensions

B.1 Error made in measurements from cross-sections

Individual nodules are approximately circular-shaped when observed on a specimen surface (see Section 3.3.1). When a specimen is cut, the cross-section does not necessarily pass through the middle of the nodule, where the width is maximum and equal to the diameter d. As the specimen is cut in a random manner, what is measured instead of the diameter is the length of a random chord ℓ. The length ℓ can be expressed as a function of the diameter d in several ways, two of which are representated in Fig. B.1.

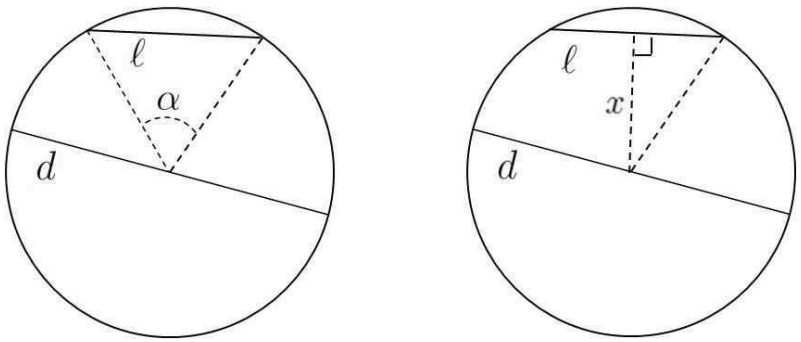

Figure B.1 – Schemes showing two different ways of calculating the length of a chord in a circle.

Using the angle α, ℓ is calculated as

$$\ell = d \sin\left(\frac{\alpha}{2}\right) \tag{B.1}$$

and the average length $\bar{\ell}$ is

$$\begin{aligned} \bar{\ell} &= \frac{1}{\pi}\int_0^{\pi} d \sin\left(\frac{\alpha}{2}\right) \mathrm{d}\alpha \\ &= \frac{2\,d}{\pi} \end{aligned} \tag{B.2}$$

Using the height x, ℓ is calculated as

$$\ell = 2\sqrt{\frac{d^2}{4} - x^2} \tag{B.3}$$

and the average $\bar{\ell}$ is

$$\begin{aligned} \bar{\ell} &= \frac{1}{d}\int_{-d/2}^{d/2} 2\sqrt{\frac{d^2}{4} - x^2}\,\mathrm{d}x \\ &= \frac{\pi\,d}{4} \end{aligned} \tag{B.4}$$

The results given by Eqs. (B.2) and (B.4) are different. The reason for this discrepancy is that the average $\bar{\ell}$ is calculated from the same values, but using different weight distributions. This is evident in Fig. B.2, where the evolution of ℓ is plotted as a function of α and x according to the two methods.

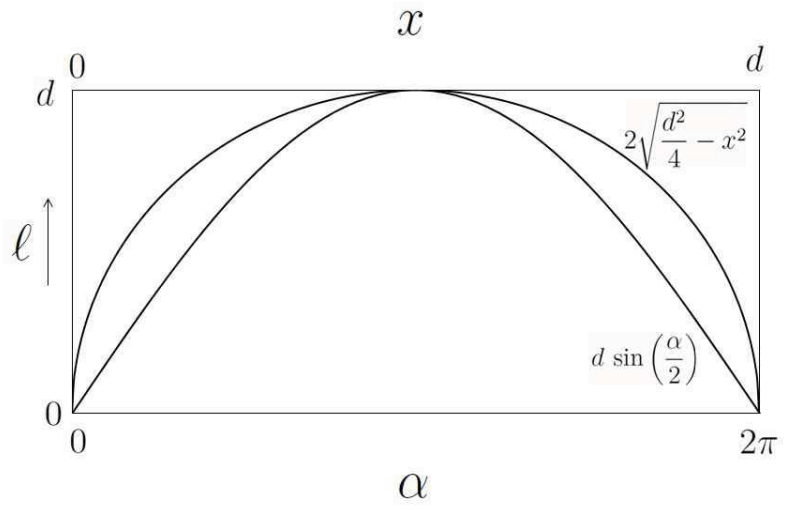

Figure B.2 – Length of a chord in a circle calculated according to the two methods defined in text.

Other formulas for ℓ as a function of d can be derived, resulting in either Eq. (B.2) or (B.4), depending on whether the chords are described as issued from a single

source on the circle perimeter (using the chord angle α), or all parallel to each other (using the angle between the chords and the normal). For a reason which has not been investigated here, this question seems to be of some importance in nuclear reactor physics, where average chord lengths are used to calculate "escape probabilities" [217, 218]. The use of Eqs. (B.2) and (B.4) is discussed, in particular, in Ref. [219]. In the present case, as the nodule size distribution is not known, the average chord length cannot be calculated. The relative error between the measured width and the actual nodule diameter is calculated, according to Eq. (B.2) and (B.4), to be $\frac{d-\bar{\ell}}{d} = 1 - \frac{2}{\pi} \simeq 36\ \%$ and $\frac{d-\bar{\ell}}{d} = 1 - \frac{\pi}{4} \simeq 21\ \%$, respectively. In either case, the error is not significant in view of the differences seen in nodule growth rate as a function of alloy composition, and does not significantly affect the application of the lateral spreading rate as described in Chapter 6.

Similarly, an error is made when measuring the maximum thickness X. It can be estimated with the same reasoning, given that when observed in cross section, nodules are not circles but ellipses. Since their maximum height is smaller than their width, the error is less than that calculated in the case of a circle.

B.2 Comparison between growth rates obtained from thickness and gravimetric data

A difference between the growth rates determined from thickness and gravimetric data must emerge from the fact that nodules are ellipsoid and not flat-topped. Indeed, in applying Eq. (3.8), nodules are assumed to be of constant height, while they actually are ellipsoid. The rate constant determined from thickness measurements is calculated from the evolution of X, the maximum thickness. In contrast, the weight uptake generated by a nodule depends on its volume, itself related to the area of the ellipse observed in a cross-section, as shown in Fig. B.3. When calculating growth rate constants from weight gain measurements, the nodules are implicitely assumed to be flat-topped, covering a rectangular surface, whose height is lower than the maximum nodule thickness. The height h is calculated as the solution of

$$\begin{aligned} \mathcal{A}_{\text{ellipse}} = \mathcal{A}_{\text{rectangle}} &\Leftrightarrow \frac{\pi X r}{2} = 2\,h\,r \\ &\Leftrightarrow h = \frac{X\pi}{4} \end{aligned} \tag{B.5}$$

where $\mathcal{A}$ stands for area. If the thickening rate law is written $X^2 = 2k_{\text{p,Fe-ox}}t$, the rate constant determined from weight gain measurements is underestimated,

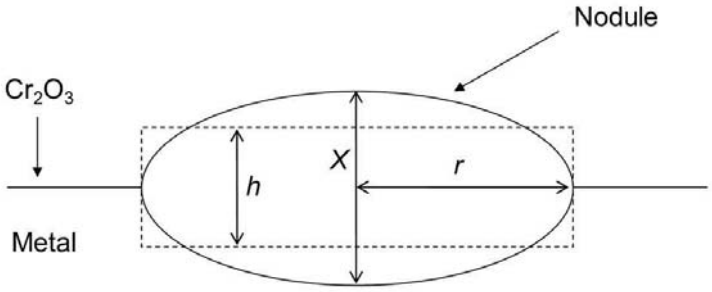

Figure B.3 – Schematic cross section of a breakaway oxide nodule

with a relative error by a factor of $\frac{X-h}{X} = 1 - \frac{\pi}{4} \simeq 21\ \%$. This difference is a maximum, and only applies to small nodules, originating from individual nuclei. Big nodules originate from several nuclei and are flat-topped over a large distance, tending toward a continuous layer. This explains why the difference is small in the case of wet gas reactions, where the nodule surface fractions are high.

Appendix C

Mass transport in gas phase

In this Appendix, the rate of oxygen consumption due to the oxidation reaction is compared with the flux of oxygen supplied by the gas to the surface of a reacting specimen. The underlying aim is to determine, in the present experimental conditions, (i) whether (linear) oxidation kinetics can be limited by the oxygen supply from the gas, and (ii) which of O_2 or CO_2 is the predominant reacting species.

The calculation is applied to the reaction of iron in Ar–20CO_2 at 800 °C, for which linear oxidation kinetics were observed. Since the reaction produced a single phase FeO scale, and no other reaction product was formed, the rate of oxygen consumption can readily be calculated from the recorded weight gains. Furthermore, this situation represents the maximum oxygen consumption rate recorded in the present study.

C.1 Oxygen consumption from the oxidation reaction

Non-stoichiometry of wustite is neglected, and the oxidation reaction is written

$$\mathrm{Fe} + \frac{1}{2}\,\mathrm{O_2} = \mathrm{FeO} \tag{C.1}$$

Accordingly, the amount of oxygen consumed is related to the amount of oxide formed by

$$\Delta n_{\mathrm{O}} = \Delta n_{\mathrm{FeO}} \tag{C.2}$$

The specimen surface area, A, is considered constant. The experimental weight change, $\Delta m/A$, is due to oxygen uptake, and may be expressed

$$\frac{\Delta m}{A} = \frac{\Delta m_{\mathrm{O}}}{A} = M_{\mathrm{O}}\frac{\Delta n_{\mathrm{O}}}{A} \tag{C.3}$$

where M_O is the molar mass of oxygen. The linear rate low is written

$$\frac{\Delta m}{A} = 2k_\ell t \tag{C.4}$$

Hence, the rate of oxygen consumption, j_O, is given by

$$j_O = \frac{\mathrm{d}\,(\Delta n_O/A)}{\mathrm{d}t} = \frac{2k_\ell}{M_O} \tag{C.5}$$

Using the value of k_ℓ given in Table 3.4, j_O is calculated to be 7.3×10^{-9} mol cm^{-2} s^{-1}. The value holds for time-lapse and TGA experiments, and is also representative of the high linear rates measured for Fe–2.25Cr and Fe–9Cr at 800 °C. The maximum reaction rates measured for reaction at 650 °C were of the same order of magnitude (see Fig. 3.1).

C.2 Oxygen supply from the gas to the specimen surface

Calculating the flux of oxygen reaching the surface of a specimen is complex, as various elements must be taken into account: gas phase velocity, composition, physical properties (interdiffusion rate, viscosity), thermodynamics, and of course the effect of the oxidation reaction on the gas composition. Only rough estimates will be attempted here.

The amount of oxygen available in the whole gas flow is easily estimated. Oxygen is transferred from the gas to the specimen via O_2 and CO_2 species. Since the formation of one mole FeO requires 0.5 mole O_2 or 1 mole CO_2, the molar flux of oxygen due to either of these is

$$J_{O,i} = \delta_i\, y_i\, \frac{F}{V_m} \tag{C.6}$$

where $\delta_i = 2$ for $i = O_2$ and 1 for $i = CO_2$, y_i is the volume fraction of O_2 or CO_2, F the total volume flow rate and V_m the gas molar volume. The flux available per unit of specimen surface area is simply obtained by dividing $J_{O,i}$ by the total specimen surface area, A_t:

$$j_{O,i} = \delta_i\, y_i\, \frac{F}{V_m A_t} \tag{C.7}$$

In time-lapse experiments, 11 specimens of average surface area $A = 2.5$ cm^2 were reacted at the same time, hence $A_t \simeq 27$ cm^2. The equilibrium partial pressure of O_2 in the gas is quite low, 1.6×10^{-7} atm in dry CO_2 at 800 °C (see Appendix A and Table 2.2). Since the amount of oxygen as an impurity in Ar and CO_2 gas

bottles is higher, the maximum O_2 volume fraction specified by the manufacturer, 5 ppm, will be used for the calculation. Oxygen fluxes given in Table C.1 were calculated from the gas molar volume at 25 °C and 1 atm, 24.5 L mol^{-1}, and a total flow rate $F = 450$ mL min^{-1}. The oxygen supply rate via O_2 molecules is two orders

Table C.1 – Calculated oxygen supply rates, j_O (mol cm^{-2} s^{-1})

	CO_2	O_2 (5 ppm)
from Eq. (C.7)	2.2×10^{-6}	1.1×10^{-10}
from Eq. (C.8)	2.2×10^{-6}	1.2×10^{-10}

of magnitude lower than the oxygen consumption rate. It is concluded that p_{O_2} is too low for O_2(g) to keep pace with the oxidation reaction, and that the reacting species is CO_2. The oxygen flux generated by the CO_2 flow would be sufficient to sustain the fast reaction of 11 iron specimens.

It should be pointed out that the above calculation is very approximative, as it disregards the influence of the reaction on the gas composition, and the gas physical properties. The formation of a boundary layer in the specimens viscinity can be taken into account by adapting the method described in Ref. [220] for the determination of a mass transfer coefficient in the case of a flat plate of a solid dissolving in a flowing fluid. Let us consider a specimen exposed to a gas flow, as represented in Fig. C.1. The specimen is oriented with its longer dimension (L) in

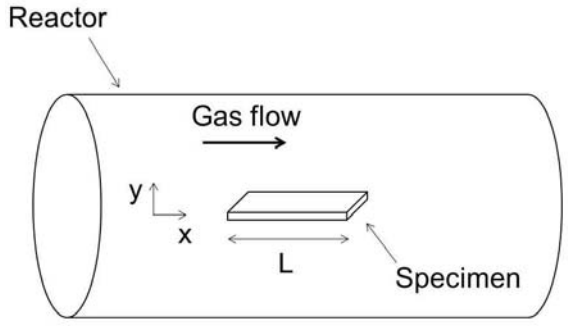

Figure C.1 – Schematic representation of a specimen in a gas flow.

the direction of the gas flow, x, like in an oxidation experiment. The problem is assumed to be symmetric in the direction parallel to the specimen width, and one considers the flux of gas species in the direction normal to the specimen face, y.

The problem treated in Ref. [220] is the following: as the solid A dissolves in

the gas, a concentration boundary layer is generated in the viscinity of the flat plate. In Fig. C.2, the boundary layer is represented by the coordinate $delta_c$, defined as the isoconcentration line for which $\frac{\rho_{A,s} - \rho_A}{\rho_{A,s} - \rho_{A,\infty}} = 0.99$, where ρ is the mass concentration, and the subscripts s and ∞ denote the surface of the plate and the bulk gas, respectively. As A dissolves in the flowing gas, the concentration

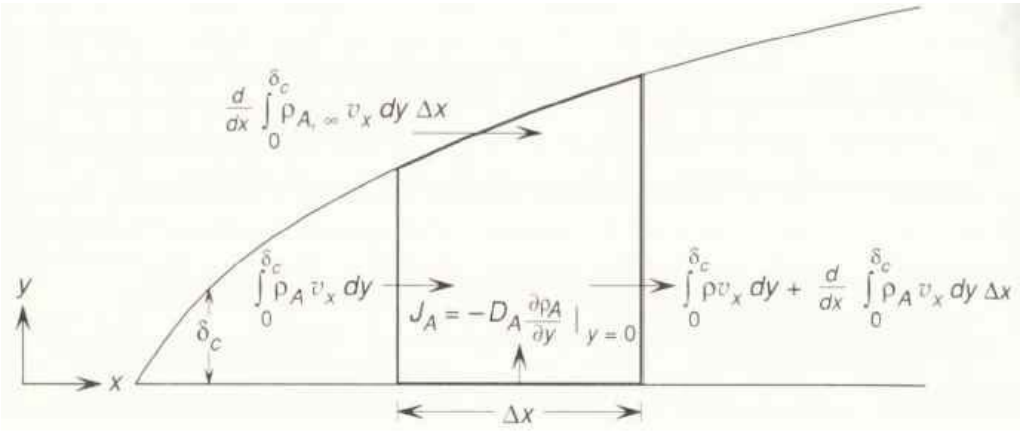

Figure C.2 – Control volume considered in the approximate integral method of determining the properties of the concentration boundary layer, after Ref. [220].

of A inside the boundary layer at any given y increases with increasing x. As a consequence, the gradient of A concentration, the local rate of mass transport of A in the direction y, and the local mass transfer coefficient decrease with x. The local mass balance is represented in Fig. C.2, and a similar approach can readily be used, by choosing appropriate boundary conditions, to determine the flux of CO_2 or O_2 reaching the surface of a reacting specimen. The maximum flux of oxygen due to species $i = CO_2$ or O_2 is obtained in the case where species i is entirely consumed by the reaction, that is, by setting the concentration of i as zero at the specimen surface, and is expressed as

$$j_{O,i} = \delta_i \frac{h_{m,L}(i) p_i}{RT} \tag{C.8}$$

where p_i is the partial pressure of species i in the bulk gas. The global mass transfer coefficient $h_{m,L}(i)$ is obtained by integrating the local values $h_{m,x}(i)$ over the length of the specimen, that is, for $x = 0$ to L, and is given by [220]

$$h_{m,L}(i) = 0.662 \left(\frac{D_i^4}{\nu_i}\right)^{1/6} \left(\frac{v_x}{L}\right)^{1/2} \tag{C.9}$$

where D_i is the diffusion coefficient, ν_i the kinematic viscosity and v_x the gas linear velocity. Values of ν_i at 800 °C for CO_2 and O_2 were calculated from data tabulated

in Ref. [220]. Diffusion coefficients were determined from the Chapman–Enskog expression for interdiffusion coefficient in ideal i–Ar mixtures, that is, the influence of CO_2 was neglected. Thus [220]

$$D_{i-Ar} = 1.8583 \times 10^{-3} \frac{\sqrt{T^3 \left(\frac{1}{M_i} + \frac{1}{M_{\mathrm{Ar}}}\right)}}{P\sigma_{i-\mathrm{Ar}}^2 \Omega_D} \tag{C.10}$$

where P is the total gas pressure, $\sigma_{i-\mathrm{Ar}}$ is the collision diameter (calculated as the arithmetic average of the individual collision diameters, $\sigma_{i-\mathrm{Ar}} = (\sigma_i + \sigma_i)/2$), and Ω_D is a dimensionless function of the interaction potential between i and Ar, taken here as being that given by the Lennard–Jones function [220]. All parameters were determined according the the methods and data tabulated in Ref. [220].

The values obtained from Eq. (C.8) are seen in Table C.1 to be very close to those calculated from Eq. (C.7). Since the two methods are completely different in nature and reflect different limiting conditions, the proximity of the numerical results can only be a mere coincidence, and by no means constitues a validation of either method. Qualitatively, the values obtained from Eq. (C.8) also indicate that CO_2 is the predominant reacting species, and further suggest that the reaction kinetics cannot be limited by mass transport in the gas phase.

C.3 Note on the non-uniformity of reacted surfaces

However, gas phase mass transport does, in some cases, have an influence on the oxidation reaction. The occasional presence of so-called "flow patterns" after reaction at 650 °C, as shown in Fig. 3.2, indicates that the conditions prevailing at the specimen surfaces may vary with location along the direction of the gas flow. In particular, despite the fact that the gas equilibrium p_{O_2} (and impurity oxygen content) is high enough to stabilise all iron oxides, Fe_2O_3 is sometimes present in upstream regions only. The absence of Fe_2O_3 in downstream regions indicates that reducing species CO and/or H_2 generated by the oxidation reaction upstream were not totally evacuated, and caused a decrease in p_{O_2} along the direction of the gas flow. Other investigators observed the same phenomenon in similar conditions, and, using different methods to estimate gas phase concentrations, showed that oxidation-induced CO [109] and H_2 [221] species could indeed lower p_{O_2} at the specimen surface below the value corresponding to the Fe_3O_4/Fe_2O_3 equilibrium. No numerical estimation will be attempted here.

Appendix D

Weight gains due to carburisation

This Appendix is aimed at estimating the contribution of carburisation products to measured weight gains. The total weight gain is written

$$\frac{\Delta m}{A} = \left(\frac{\Delta m}{A}\right)_{\text{ox}} + \left(\frac{\Delta m}{A}\right)_{\text{carb}} \tag{D.1}$$

The contribution of carburisation is due to carbon uptake:

$$\left(\frac{\Delta m}{A}\right)_{\text{carb}} = \frac{\Delta m_{\text{C}}}{A} \tag{D.2}$$

which is calculated in different manners if the carburisation products are carbides, formed during reaction at 650 °C, or martensite, observed after reaction at 800 °C.

D.1 Weight gains due to carbide formation at 650 °C

Carbides are formed according to

$$a\,\text{Cr} + b\,\text{C} = \text{Cr}_\text{a}\text{C}_\text{b} \tag{D.3}$$

Hence, the carbon weight uptake is

$$\frac{\Delta m_{\text{C}}}{A} = b\,M_{\text{C}}\,\frac{\Delta n_{\text{carb}}}{A} \tag{D.4}$$

with the usual notations. The carbide mole uptake is obtained from

$$\frac{\Delta n_{\text{carb}}}{A} = X_{\text{c}}\,f_{\text{V,carb}}\,\rho_{\text{carb}}\,\frac{1}{M_{\text{carb}}} \tag{D.5}$$

where X_c is the carburisation depth and $f_{V,carb}$ the average volume fraction of carbides. If carburisation kinetics are described by Eq. (3.3), $X_c^2 = 2k_c t$, one obtains

$$\left(\frac{\Delta m}{A}\right)^2_{carb} = 2k_{w,c}t \tag{D.6}$$

with

$$k_{w,c} = \left(b\, f_{V,carb}\, \frac{M_C}{M_{carb}}\, \rho_{carb}\right)^2 k_c \tag{D.7}$$

The carburisation depths were maximum for the Fe–9Cr alloy. As the precipitates were identified to be Cr_7C_3, it follows that $b = 3$, $M_{carb} = 400\ g\,mol^{-1}$, and $\rho_{carb} = 6.92\ g\,cm^{-3}$ [175]. The carburisation rate and average volume fraction were $X_c = 6.5 \times 10^{-10}\ cm^{-2}\,s^{-1}$ and $f_{V,carb} = 0.1$ (see Section 3.1.5). The gravimetric carburisation rate is thus calculated to be $k_{w,c} = 2.5 \times 10^{-6}\ mg^2\,cm^{-4}\,s^{-1}$, which represents weight gains two orders of magnitude lower than the values measured for overall (oxidation plus carburisation) reaction.

D.2 Weight gains due to martensite formation at 800 °C

The calculation is slightly different in the case of martensite formation: since martensite did not precipitate *from the metal/oxide interface to a given depth*, but rather *in the whole substrate with a given volume fraction*, the weight uptake due to carbon is not an intensive variable, but depends on each specimen's dimension. Thus, the contribution of martensite is written

$$\left(\frac{\Delta m}{A}\right)_{carb} = w_{C,m}\, f_{V,m}\, \rho_m\, \frac{V_{sp}}{A} \tag{D.8}$$

where the subscript m denotes martensite, and V_{sp} is the specimen volume. The weight fraction of carbon in martensite, $w_{C,m}$, was seen to be 2×10^{-3} in Fe–9Cr (see Section 3.2.5). Using this value, the lattice parameters of the martensite bct unit cell were calculated from data in Ref. [222]. Considering the volume and number of atoms in a bct unit cell, the theoretical density was calculated to be $\rho_m = 7.84\ g\,cm^{-3}$ — as the carbon content is relatively low, it is only slightly lower than that of pure iron, $7.88\ g\,cm^{-3}$. Carburisation was the most important in Fe–9Cr–10Ni, as the whole specimens were converted to martensite upon cooling. Using average specimen dimensions to calculate V_{sp} and A, the volume fraction $f_{V,m} = 1$ yields $(\Delta m/A)_{carb} = 1.0\ mg\,cm^{-2}$. This value is negligible in view of the total weight gains measured for reaction at 800 °C.

Publications and oral communications

- Peer-reviewed journals

Carburisation of ferritic Fe–Cr alloys in low carbon activity gases
T. Gheno, D. Monceau, J. Zhang, D.J. Young
Corrosion Science 53 (2011) 2767–2777

Mechanism of breakaway oxidation of Fe–Cr and Fe–Cr–Ni alloys in carbon dioxide
T. Gheno, D. Monceau, D.J. Young
Accepted for publication in Corrosion Science

Kinetics of breakaway oxidation of Fe–Cr and Fe–Cr–Ni alloys in carbon dioxide
T. Gheno, D. Monceau, D.J. Young
To be submitted

- Peer-reviewed conference proceedings

High temperature corrosion of Fe–Cr, Fe–Al, Fe–Si and Fe–Si–Al alloys in CO_2–H_2O gases
T. Gheno, H. Li, J. Zhang, D.J. Young
Materials Science Forum, 654–656 (2010) 1948–1951
7th Pacific Rim International Conference on Advanced Materials and Processing, August 2–6, 2010, Cairns, Australia

- Conference proceedings

High temperature corrosion of Fe–Cr alloys in CO_2–H_2O gas atmospheres
T. Gheno, J. Zhang, D.J. Young
Corrosion & Prevention 2009 (Australasian Corrosion Association), Paper 092, November 16–18, 2009, Coffs Harbour, Australia
Marshall Fordham Best Research Paper Award

High temperature corrosion resistance of Fe–Cr–Ni alloys in CO_2–H_2O
T. Gheno, J. Zhang, D.J. Young
Corrosion & Prevention 2010 (Australasian Corrosion Association), Paper 042, November 15–17, 2010, Adelaide, Australia

High temperature corrosion of chromia-forming alloys under oxyfuel firing conditions
T. Gheno, J. Zhang, D.J. Young
18th International Corrosion Congress, Paper 313, November 20–24, 2011, Perth, Australia

- Oral communications without proceedings

Influence de la vapeur d'eau sur l'oxydation d'alliages Fe–Cr–Ni dans le dioxyde de carbone à haute température
T. Gheno, D. Monceau
Groupement de Recherche "Vapeur d'eau", February 1, 2011, Dijon, France

Carburation d'alliages Fe–Cr par des gaz à basse activité en carbone
T. Gheno, D. Monceau, D.J. Young
42$^{\text{èmes}}$ Journées d'Étude sur la Cinétique Hétérogène, March 30–31, 2011, La Rochelle, France

Simultaneous oxidation and carburisation of Fe–Cr–Ni alloys in hot CO_2–H_2O atmospheres
T. Gheno, D. Monceau, D.J. Young
Gordon Research Seminar on High Temperature Corrosion, July 23–24, 2011, New London, USA

Carburation et oxydation catastrophique d'alliages Fe–Cr exposés à des mélanges CO_2–H_2O à haute température
T. Gheno, D. Monceau, D.J. Young
Commission Corrosion Haute Température et Protection du CEFRACOR, December 9, 2011, Paris, France

- Posters

Simultaneous oxidation and carburisation of Fe–Cr–Ni alloys in hot CO_2–H_2O atmospheres
T. Gheno, D. Monceau, D.J. Young
Gordon Research Conference on High Temperature Corrosion, July 24–29, 2011, New London, USA
Runner-up Award for the best student/post-doc poster

Résumé étendu en français

1 Introduction

L'oxycombustion est un procédé actuellement en développement dans le cadre de la réduction des émissions de dioxyde de carbone issu des centrales thermiques à charbon. Il consiste à brûler le charbon dans un mélange d'oxygène et de gaz de combustion recyclé plutôt que dans l'air. En l'absence d'azote, le gaz de sortie est principalement composé de CO_2 et H_2O, ce qui permet une séparation du dioxyde de carbone plus aisée, en vue de sa séquestration géologique. Cependant, il importe d'étudier les effets en termes d'oxydation de l'exposition des composants en acier à ces mélanges gazeux.

La résistance à l'oxydation des aciers au chrome repose sur la croissance lente d'une couche d'oxyde riche en chrome. Ce régime d'oxydation protectrice nécessite une quantité minimum de chrome à l'interface métal/oxyde. Si l'alliage ne peut pas fournir suffisamment de chrome à sa surface, des oxydes de fer à croissance rapide sont formés. La transition vers ce régime d'oxydation non-sélective, associée à une accélération importante de la vitesse d'oxydation, est appelée *breakaway*.

Le comportement en oxydation des aciers au chrome dans des environnements riches en CO_2 a été longuement étudié, notamment parce que le dioxyde de carbone a été utilisé comme fluide caloporteur dans certains types de réacteurs nucléaires. Il apparait que nombre d'alliages qui s'oxydent de manière protectrice dans l'air subissent une oxydation de type rapide dans le CO_2 [12–14]. D'un point de vue thermodynamique, le dioxyde de carbone est oxydant, mais non-carburant, vis à vis des alliages conventionnels. Cependant, les résultats disponibles dans la litérature indiquent que ces alliages sont sujets à la carburation quand ils sont exposés au CO_2. Il semble que la précipitation interne de carbures riches en chrome, réduisant la capacité du chrome à diffuser vers l'interface métal/oxyde, soit à l'origine du phénomène de breakaway [12].

La corrosion par H_2O est elle aussi bien documentée, parce que beaucoup de procédés industriels utilisent la vapeur d'eau, par exemple comme fluide caloporteur pour la production d'énergie électrique, ou comme un réactif ou produit de réaction dans les piles à combustible à oxyde solide. Il apparait que l'ajout d'H_2O à un mélange gazeux, ou le remplacement de O_2 par H_2O, déclenche le breakaway d'alliages Fe–Cr [15–18]. Diverses explications de cet effet ont été proposées, et sont détaillées dans le Chapitre 1.

Si les mécanismes sous-tendant les effets néfastes de CO_2 et H_2O sont peut-être différents, il reste que maintenir un régime d'oxydation protectrice en présence de chacune de ces espèces gaseuses nécessite des concentrations en chrome relativement

élévées, et en particulier plus élevées que lors d'une exposition à l'air [13,14]. Ainsi, comme les environnements riches en CO_2 et riches en H_2O sont particulièrement corrosifs, il est nécessaire d'examiner le comportement en oxydation d'alliages exposés à des mélanges gazeux contenant les deux espèces en concentration importante, une situation qui a jusqu'ici reçu peu d'attention.

Ce travail de thèse est axé sur les aspects fondamentaux plutôt que sur des problématiques d'application en conditions de service industrielles. Des alliages modèles Fe–Cr et Fe–Cr–Ni sont considérés à la place des aciers au chrome ferritiques et austénitiques, respectivement. De la même manière, les gaz employés sont des mélanges Ar–CO_2–H_2O. Le fait de s'affranchir des éléments d'alliages secondaires, qui sont indispensables à la formabilité et aux propriétés mécaniques de ces matériaux, et des composants gaseux suplémentaires, qui sont inévitables dans des conditions de service réelles, permet une étude simplifiée des effets combinés de CO_2 et H_2O sur le comportement en oxydation.

Le premier Chapitre consiste en une revue bibliographique, établissant un cadre général pour l'étude de l'oxydation à haute température, et détaillant les questions spécifiquement liées à la réaction sous CO_2–H_2O. Les procédures expérimentales et méthodes de caractérisation sont décrites dans le Chapitre 2, et les résultats expérimentaux sont rassemblés dans le Chapitre 3. La discussion est organisée en trois parties de complexité croissante. Le Chapitre 4 s'intéresse à la façon dont la croissance des couches d'oxydes riches en fer est affectée par la composition du gaz et des alliages. Le Chapitre 5 adresse la question de la carburation. L'attention est d'abord portée sur les conditions thermodynamiques prévalant à la surface des alliages oxydés et sur le mécanisme de formation des carbures internes, la finalité étant de définir les conditions dans lesquelles la carburation peut affecter l'oxydation sélective. Le mécanisme et la cinétique du breakaway sont étudiés dans le Chapitre 6. La transition du régime d'oxydation protectrice à celui d'oxydation rapide est par essence un phénomène localisé, mais ses conséquences sont mesurées à l'échelle de l'échantillon de laboratoire. Ce dernier Chapitre a pour but d'analyser les facteurs contrôlant l'oxydation sélective du chrome, tant du point de vue des mécanismes de réaction à l'échelle locale que de la performance générale des alliages. Par ailleurs, les techniques expérimentales et les méthodes de traitement des résultats employées pour mettre en relation descriptions micro et macroscopiques sont évaluées.

Ce résumé étendu reprend les principaux éléments de discussion mis en œuvre aux Chapitres 4, 5 et 6 pour interpréter les résultats expérimentaux, et les principales conclusions.

2 Croissance des oxydes riches en fer

2.1 Oxydation du fer: effet de la composition du gaz

La réaction du fer dans les mélanges Ar–CO_2 et Ar–CO_2–H_2O, à 650 et 800 °C, produit des couches uniformes d'oxyde de fer, mais n'entraîne pas de carburation. Ainsi, ces résultats fournissent une manière simple d'examiner le rôle de la composition du gaz sur la formation de couches d'oxyde externes, indépendamment des questions liées à l'oxydation sélective ou aux interactions entre oxydation et carburation.

L'effet de la composition de l'atmosphère est le plus marqué dans le cas de la réaction à 800 °C. À cette température et sous CO_2 sec, la cinétique d'oxydation du fer est linéaire, et seule une couche de FeO est formée, malgré le fait que la pression partielle d'oxygène dans le gaz soit suffisante pour stabiliser Fe_2O_3. L'absence de Fe_3O_4 et Fe_2O_3 indique que la diffusion dans FeO est rapide par rapport aux réactions interfaciales, si bien qu'un état métastable de haute activité en fer est maintenu à l'interface oxyde/gaz, empêchant l'oxydation de Fe (II) en Fe (III). En accord avec de précédentes études [110,161,162], on conclut que dans ces conditions, la cinétique d'oxydation du fer est contrôlée par une réaction de surface relativement lente.

Les ajouts de 5 puis 20 vol. % H_2O dans le gaz provoquent des augmentations successives de la vitesse d'oxydation. Dans le cas de Ar–20CO_2–20H_2O, le régime linéaire est suivi par un régime parabolique. On en déduit que la vitesse de la réaction de surface est augmentée par l'addition de vapeur d'eau, jusqu'à ce qu'elle excède la vitesse de diffusion du fer dans FeO, causant une transition d'un contrôle surfacique à un contrôle diffusionnel.

Il apparait aussi, d'après la cinétique d'oxydation du fer sous Ar–20H_2O à 800 °C, que la réactivité de la vapeur d'eau vis-à-vis des surfaces de fer oxydées est intrinsèquement supérieure à celle du dioxyde de carbone, en accord avec les conclusions de Turkdogan et al [164].

La question se pose alors de savoir si la présence de CO_2 et/ou H_2O dans le gaz affecte le processus de diffusion lui-même, en comparaison avec la réaction dans l'air par exemple. Dans l'air, l'oxydation du fer produit trois couches successives de FeO, Fe_3O_4 and Fe_2O_3 [32]. La couche de FeO croît beaucoup plus rapidement que les autres, si bien qu'elle forme la majeur partie de l'épaisseur totale, et que sa croissance représente, à une bonne approximation, celle de l'ensemble des trois couches. La constante parabolique d'oxydation est alors déterminée par le gradient d'activité du fer (ou de l'oxygène, de façon équivalente) à travers FeO, défini par les

équilibres Fe–FeO et FeO–Fe_3O_4. Ainsi, dès lors qu'une couche continue de Fe_3O_4 est formée sur FeO, ce qui est la cas ici pendant la réaction sous Ar–20CO_2–20H_2O, la force motrice pour la diffusion du fer dans FeO est fixée, et la constante parabolique d'oxydation k_{pm} ne peut varier que si la diffusivité du fer dans l'oxyde varie. La valeur de k_{pm} mesurée ici à partir de données gravimétriques lors de la réaction sous Ar–20CO_2–20H_2O à 800 °C, $2{,}3 \times 10^{-2}$ $mg^2\,cm^{-4}\,s^{-1}$, est très proche de celle obtenue par Paidassi [32] sous air à la même température, $2{,}9 \times 10^{-2}$ $mg^2\,cm^{-4}\,s^{-1}$. En conclusion, les résultats présents supportent l'idée selon laquelle ni la présence de CO_2 ni celle de H_2O n'affecte le mécanisme de croissance de FeO sur le fer pur de façon significative.

2.2 Effet de la composition des alliages

L'exposition des alliages binaires Fe–Cr et ternaires Fe–Cr–Ni aux mélanges Ar–CO_2 et Ar–CO_2–H_2O à 650 et 800 °C produit des structures multicouches d'oxydes riches en fer et d'épaisseur uniforme. Elles sont formées soit à partir de temps de réaction courts pour les alliages bas chrome (2,25 et 9 % m. Cr), soit en résultat de la coalescence de nodules individuels dans l'échelle de temps expérimentale pour les alliages haut chrome (20 et 25 % m. Cr). Ces produits de corrosion sont constitués de deux parties, situées de part et d'autre de la surface originale de l'alliage. La partie externe comprend des couches d'oxyde de fer, tandis que la partie interne contient du fer mais aussi du chrome, et du nickel dans le cas des alliages ternaires.

L'effet de la composition des alliages sur la cinétique de croissance de ces structures multicouches est analysé en détail dans le Chapitre 4, en considérant la relation entre le flux de fer traversant les couches d'oxyde et leur constitution. À 800 °C, la partie interne des oxydes formés sur les alliages bas chrome est composée de précipités de spinelle mixte, $(Fe, Cr)_3O_4$ ou $(Fe, Cr, Ni)_3O_4$, dans une matrice de FeO. La diffusivité étant bien moins importante dans la phase spinelle que dans FeO, les précipités de spinelle dans la couche interne réduisent la section efficace pour la diffusion.

La formation de spinelle n'a aucun effet sur la cinétique d'oxydation lorsque celle-ci est contrôlée par la réaction de surface. C'est le cas de la réaction des alliages binaires Fe–2,25Cr et Fe–9Cr dans Ar–20CO_2 à 800 °C, pour lequel la cinétique d'oxydation est linéaire, avec une constante de réaction similaire à celle mesurée pour le fer pur. En revanche, dans des conditions de contrôle diffusionnel, comme pour ces alliages durant l'exposition à Ar–20CO_2–20H_2O, la présence d'oxyde spinelle provoque une réduction du flux de fer à travers la couche FeO + $(Fe, Cr)_3O_4$, et par

conséquent une baisse de la vitesse de croissance de l'ensemble de la structure multicouche. Cette diminution de la vitesse d'oxydation entre les alliages Fe–2,25Cr et Fe–9Cr peut être liée, directement et de façon quantitative, aux fractions volumiques d'oxyde spinelle mesurées expérimentalement. Par contre, on montre que la chûte de k_{pm} entre Fe et Fe–2,25Cr est trop importante pour être seulement attribuée au bloquage diffusionnel, et que par conséquent une autre cause doit être recherchée.

Alors que les alliages Fe–9Cr et Fe–9Cr–10Ni suivent une cinétique d'oxydation linéaire sous Ar–20CO_2, la substitution de FeO par un spinelle mixte $(\mathrm{Fe,Cr,Ni})_3\mathrm{O}_4$ atteint pour l'alliage Fe–9Cr–20Ni une proportion telle que la partie interne de l'oxyde ne peut maintenir le flux de fer nécessaire à la réaction de surface. Ainsi, la cinétique de réaction de cet alliage est contrôlée par la diffusion, et suit une loi parabolique. Lors de l'exposition à Ar–20CO_2–20H_2O, les trois alliages contenant 9 % en masse de chrome s'oxydent selon une cinétique parabolique, et la valeur de k_{pm} décroît quand la concentration en nickel dans l'alliage augmente, en accord avec le concept de bloquage diffusionnel.

Comme dans le cas du fer, l'influence de la composition du gaz sur la cinétique d'oxydation des alliages bas chrome est beaucoup moins marquée lors de la réaction à 650 °C. En revanche, l'effet de la composition de l'alliage sur la constante parabolique d'oxydation est, qualitativement, en accord avec les conclusions tirées d'après les résultats obtenus à 800 °C.

La morphologie des oxydes produits à la suite de la rupture de la couche de chromine initialement formée sur les alliages haut chrome est caractérisée par une plus grande diversité et un degré de complexité plus élevé que celle des oxydes observés sur les alliages bas chrome. Le mécanisme de croissance des nodules pendant les régimes transitoire et stationnaire de leur développement (c'est à dire, les étapes précédant l'établissement d'une structure d'épaisseur uniforme) est examiné en détail dans le Chapitre 6. On note qu'après avoir atteint une certaine taille, ces nodules adoptent une morphologie pseudo-stationnaire, en ce que les quantités relatives des phases d'oxyde présentes ne varient pas avec la taille des nodules, et que leur épaisseur est, dans une région centrale, uniforme. Dans ces conditions, la constitution de ces structures multicouches est similaire à celle correspondant aux alliages bas chrome, et on montre que le concept de bloquage diffusionnel s'applique de la même manière, aussi bien à 650 qu'à 800 °C. Ainsi, les additions de chrome et de nickel sont bénéfiques, puisqu'elles réduisent la vitesse de croissance des structures d'oxyde multicouches.

La surface des alliages haut chrome étant couverte par des oxydes d'épaisseur variable, une attention particulière est portée à la signification statistique des épais-

seurs mesurées en section transverse. En particulier, sur l'exemple de l'alliage Fe–20Cr oxydé à 650 °C, on montre que l'application d'une loi parabolique simple ($X^2 = 2k_\mathrm{p}t$) à des épaisseurs d'oxyde maximales permet d'obtenir une mesure représentative de la croissance de l'oxyde. La fiabilité des mesures réalisées sur une section transverse donnée augmente avec la fraction de surface couverte par des nodules.

3 Carburation

En plus de la croissance de couches d'oxyde, l'exposition aux mélanges Ar–CO_2 et Ar–CO_2–H_2O provoque, dans certains cas, la carburation du substrat métallique. Différents types de réaction sont observés: précipitation de carbures dense ou limitée à 650 °C, précipitation de carbures et de martensite à 800 °C.

Les mélanges gazeux riches en CO_2 ne sont pas carburants vis-à-vis des alliages considérés. Ceci tient à une simple considération thermodynamique: l'activité en carbone à l'équilibre dans le gaz, $(a_\mathrm{C})_\mathrm{gaz} \simeq 10^{-15}$ dans les conditions qui nous intéressent, est inférieure à l'activité requise pour stabiliser des carbures. Cette dernière varie avec la température et la composition de l'alliage, mais l'ordre de grandeur 10^{-3}–10^{-4} est adapté à la présente étude: l'écart avec $(a_\mathrm{C})_\mathrm{gaz}$ est considérable. Il apparait donc que l'activité en carbone à la surface du métal doit être en réalité beaucoup plus élevée que celle prévalant dans le gaz. Élaborant sur la base du principe d'équilibre thermodynamique local, une méthode de calcul de l'activité en carbone à l'interface métal/oxyde est proposée au Chapitre 5. Ce modèle est ensuite confronté aux résultats expérimentaux.

3.1 Modèle pour l'établissement de conditions carburantes

L'activité en carbone à l'interface métal/oxyde d'alliages oxydés est calculée selon le principe suivant. À condition que la couche d'oxyde soit (i) suffisamment compacte et adhérente pour constituer une barrière physique séparant le métal de l'atmosphère, et (ii) assez épaisse pour qu'un équilibre thermodynamique local soit atteint, alors l'activité en oxygène dans cette couche varie entre sa valeur ambiante à l'interface oxyde/gaz, et la pression de dissociation de l'oxyde à l'interface métal/oxyde. Si, par ailleurs, l'oxyde transmet les espèces CO et CO_2, la faible p_{O_2} à la surface du métal produit de fortes valeurs pour le ratio p_CO/p_{CO_2}, et par conséquent pour l'activité en carbone.

L'augmentation de l'activité en carbone à travers la couche d'oxyde n'est possible que si un équilibre thermodynamique local prévaut. Ceci exclut les zones où d'éventuels défauts macroscopiques (fissures, écaillage) donnent au gaz un accès direct au métal. Sur la base de résultats publiés dans la litérature, il est supposé que les espèces CO, CO_2, H_2 et H_2O atteignent la surface du métal sous forme moléculaire, adsorbées le long de nanocannaux ou de surfaces internes telles que les joints triples de l'oxyde. Par ailleurs, pour simplifier la modélisation et en accord avec les observations expérimentales, nous considérons que ces espèces moléculaires se désorbent et forment un gaz à l'interface métal/oxyde, dans des cavités préexistentes.

L'hypothèse fondamentale sur laquelle est basé le modèle est que l'activité en oxygène dans ce système interfacial est contrôlée par l'équilibre métal–oxyde. Les ratios p_{CO}/p_{CO_2} et p_{H_2}/p_{H_2O} sont alors déterminés de manière unique, pour un couple alliage–oxyde et une température donnée, via la loi d'action de masse des réactions de dissociation de CO_2 et H_2O. L'activité en carbone est ensuite calculée, de manière équivalente, en considérant l'équilibre de l'une ou l'autre des réactions suivantes:

$$2\,CO = C + CO_2 \tag{1}$$

ou

$$CO + H_2 = C + H_2O \tag{2}$$

On note que ce calcul fait intervenir un degré de liberté, qui peut être représenté par le paramètre $\beta = p_{CO} + p_{CO_2}$. Cette somme de pressions partielles à l'interface est fonction de la composition de l'atmosphère extérieure et des propriétés d'adsorption et de transport de l'oxyde. On suppose a priori que la valeur de β est celle de la somme $p_{CO} + p_{CO_2}$ dans l'atmosphère extérieure, 0,2 atm pour les mélanges utilisés ici.

L'activité interfaciale en oxygène est déterminée par la composition des phases métal et oxyde en contact. Pour des raisons liées à la disponibilité des données thermodynamiques, seul le cas des alliages binaires est traité dans cette étude. Pour chaque type morphologique d'oxyde observé (structures multicouches riches en fer, couches protectrices de Cr_2O_3, structures contenant une couche basale riche en chrome formées après rupture de Cr_2O_3 et repassivation partielle), le potentiel d'oxygène est déduit de la constitution de l'oxyde directement en contact avec le métal via un diagramme de type $\log p_{O_2} - N_{Cr}$ pour le système Fe–Cr–O.

L'utilisation de diagrammes de prédominance de type $a_C - T$ dans le système Fe–Cr–C permet de comparer les activités en carbone calculées à celles requises pour former des carbures dans les alliages binaires. Ainsi, on montre que dans la

plupart des cas, si les espèces CO et CO_2 peuvent atteindre l'interface métal/oxyde en quantité suffisante (ce qui peut se traduire en termes de valeur du paramètre $\beta = p_{CO} + p_{CO_2}$), le gaz contenu dans la cavité interfaciale est carburant vis-à-vis de l'alliage considéré. En particulier, compte tenu des faibles potentiels d'oxygène, les valeurs de a_C calculées dans le cas des oxydes riches en chrome sont extrêmement élevées, nettement supérieures à 1.

3.2 Mécanisme de réaction et activité interfaciale en carbone

Les valeurs d'a_C effectivement atteintes sous les couches d'oxyde formées sur les alliages binaires sont évaluées à partir des observations expérimentales, et comparées aux valeurs calculées à l'aide du modèle d'équilibre local. Ce faisant, le mécanisme de carburation correspondant à chaque morphologie de réaction est examiné. L'étendue de la réaction de carburation dépend de manière décisive de la nature de l'oxyde formé. En particulier, une différence est faite entre les couches d'oxyde riches en fer et les couches de Cr_2O_3. Pour illustrer ces deux situations, les principaux éléments de discussion tenant au mécanisme de carburation des alliages Fe–9Cr et Fe–20Cr à 650 °C sont résumés ici.

3.2.1 Carburation importante et croissance d'oxydes riches en fer

La réaction de l'alliage Fe–9Cr à 650 °C produit une structure multicouche d'oxydes riches en fer, une zone d'oxydation interne (ZOI) et une zone de carburation interne (ZCI). Les carbures forment une précipitation dense et uniformément profonde dans la matrice ferritique.

On montre par analyse d'image que l'évolution de la fraction volumique de carbures, f_V, en fonction de la profondeur relative (c'est à dire selon une coordonnée de type $x/\sqrt{t}$), suit un profil indépendant de la durée de réaction. Le caractère pseudo-stationnaire de la répartition des phases métal et carbure indique qu'un équilibre thermodynamique local est établi. Ceci justifie l'utilisation du diagramme de phase Fe–Cr–C pour mettre en relation les compositions chimiques de la matrice et des précipités avec les fractions volumiques.

Afin de pouvoir réaliser ce bilan de matière, on note d'abord qu'à 650 °C, le carbone diffuse beaucoup plus vite que le chrome dans la matrice ferritique. On fait donc l'hypothèse que le chrome est immobile à l'échelle macroscopique (la diffusion à courte distance pour former les carbures n'intervient pas dans le bilan de masse), et que la concentration globale en chrome dans le système matrice + précipités

est constante et égale à la valeur à cœur. En utilisant la règle du levier dans le champ biphasé $\alpha + M_7C_3$, une connode correspondant à la valeur de f_V à l'interface ZOI/ZCI est sélectionnée. Ceci définit la concentration en carbone dans la matrice métallique, N_C, à la surface de la zone de carburation. Finalement, l'activité en carbone est calculée à partir de N_C à l'aide de données thermodynamiques pour la dissolution du carbone dans Fe–Cr. La valeur d'a_C obtenue de cette manière pour la carburation sous Ar–20CO_2 est en excellent accord avec la valeur calculée par le modèle.

Ce résultat est confirmé par une autre méthode. Sur la base d'un bilan de matière appliqué au front de carburation, la constante parabolique de carburation est utilisée pour déterminer N_C, et par la suite a_C. Ce faisant, nous prenons soin d'étudier les conditions d'application de l'équation simplifiée donnée par Wagner [67] pour la modélisation de l'oxydation interne. Il apparait alors que les carbures de chrome ne sont pas assez stables pour que les hypothèses faites par Wagner soient vérifiées. La situation de précipitation incomplète est décrite par Ohriner and Morral [66], qui appliquent la règle du levier au champ biphasé matrice-précipités pour une application plus précise du bilan de matière. Cette procédure est combinée ici avec un traitement numérique des compositions de la matrice et des précipités (définies dans le diagramme de phase par les profils de f_V), permettant d'évaluer N_C avec une précision adaptée. Un bon accord est obtenu avec la valeur d'a_C prévue par le modèle.

On remarque que les activités en carbone évaluées à partir des deux méthodes exposées ci-dessus sont légèrement plus faibles que celle calculée par le modèle en faisant l'hypothèse que la couche d'oxyde transmet le carbone sans entrave. Cet écart est d'autant plus marqué que la pression partielle de vapeur d'eau dans le gaz de réaction est importante. Ceci peut être interprété en termes d'adsorption préférentielle de H_2O par rapport à CO_2 à la surface de la couche d'oxyde. En accord avec des suggestions faites par d'autres dans la litérature, nous proposons que la baisse de l'activité interfaciale en carbone est dûe à l'exclusion partielle du dioxyde de carbone par la vapeur d'eau. Une méthode est proposée pour quantifier l'enrichissement en espèces hydrogénées H_2 et H_2O par rapport aux espèces carbonées CO et CO_2 à l'interface métal/oxyde.

3.2.2 Carburation limitée et oxydation protectrice

Dans les régions où la couche de Cr_2O_3 formée initialement sur l'alliage Fe–20Cr à 650 °C subsiste, la carburation est soit absente, soit limitée à une plaque de carbure

fine et plus ou moins continue, parallèle à l'interface métal/oxyde.

Étant donné que la pression de dissociation de la chromine est extrèmement faible, le modèle d'équilibre thermodynamique prévoit une activité en carbone très élevée à l'interface alliage/Cr_2O_3 — on obtient une valeur supérieure à 10^4 à 650 °C. Cependant, aucune précipitation de graphite n'est observée, et la faible amplitude de la réaction de carburation suggère au contraire une activité en carbone basse. Ainsi, l'hypothèse que CO_2 et CO accèdent à la surface du métal avec un flux suffisant pour que la condition $\beta = (p_{CO} + p_{CO_2})_{ext}$ soit vérifiée, est incorrecte dans ce cas. On conclut donc que la chromine est considérablement moins perméable aux espèces carbonées que ne le sont les oxydes riches en fer, en accord avec les travaux disponibles dans la litérature [12, 13, 113, 116, 118].

La morphologie des carbures, arrangés selon un plan de faible épaisseur sous la couche d'oxyde, indique que quand ils sont formés en début de réaction, le flux de carbone est faible, ce qui favorise la croissance et la coalescence des précipités par rapport à leur germination. On note que par la suite, l'épaisseur de la plaque de carbure n'augmente pas, ce qui indique que la diffusion du carbone dans l'alliage a cessé.

La plaque de carbure est située dans la zone d'appauvrissement en chrome induite par la formation de la chromine. En considérant l'évolution du profil de déplétion, on montre comment, sur la base de l'équilibre thermodynamique entre métal et carbure, une sursaturation limitée en carbone vis-à-vis des carbures implique nécessairement l'arrêt de la croissance de la plaque. De surcroît, alors que la déplétion en chrome progresse dans l'alliage, l'équilibre impose la dissociation de la plaque du côté de l'oxyde et sa reformation du côté du cœur de l'alliage. Ce processus explique le déplacement de la plaque de carbure vers l'intérieur de l'alliage, qui est observé expérimentalement.

3.3 Facteurs affectant la perméabilité des oxydes au carbone

3.3.1 Effet de la vapeur d'eau sur la prise de carbone

L'ampleur de la réaction de carburation de l'alliage Fe–9Cr à 650 °C diminue à mesure que la pression partielle d'eau dans le gaz de réaction augmente. De manière qualitative, cet effet est confirmé par les résultats obtenus avec l'alliage Fe–25Cr à la même température. Cet alliage forme différents types d'oxydes, qui entrainent une carburation soit limitée soit importante. La réduction de la prise de carbone en présence de vapeur d'eau est caractérisée, dans le cas où la carburation est im-

portante, par une précipitation de carbures moins rapide et moins dense, et dans le cas où l'oxyde fournit une protection efficace vis-à-vis de la pénétration du carbone, par une plus faible propension à la perte locale de ce caractère protecteur.

La carburation des alliages ternaires n'a pas pu être analysée suivant la procédure utilisée pour les alliages binaires, parce que les données thermodynamiques pour les systèmes Fe–Cr–Ni–O et Fe–Cr–Ni–C n'ont pu être obtenues. Cependant, pour un alliage donné, il est possible de comparer les réactions dans les gaz avec et sans vapeur d'eau. Dans le cas des alliages Fe–9Cr–10Ni et Fe–20Cr–20Ni à 650 °C, des carbures sont formés à la suite de l'exposition à Ar–20CO_2, mais aucune précipitation n'est observée après réaction sous Ar–20CO_2–20H_2O. Ceci fournit une confirmation supplémentaire de la capacité de H_2O à exclure le carbone.

Pour tous les autres alliages, une comparaison directe entre Ar–CO_2 et Ar–CO_2–H_2O n'a pas pu être effectuée, par exemple lorsque des carbures n'ont été formés dans aucun des gaz. On observe cependant que la présence de vapeur d'eau ne provoque jamais d'amplification de la carburation.

3.3.2 Effet de la composition de l'oxyde sur le transport du carbone

Les structures multicouches d'oxydes riches en fer formées sur les alliages Fe–9Cr, Fe–20Cr et Fe–25Cr durant la réaction à 650 °C sont morphologiquement similaires. La carburation est importante dans le métal sous-jacent, et les morphologie et vitesse de réaction sont comparables pour ces trois alliages. Suivant le principe du bilan de matière appliqué au front de carburation, on montre que le flux de carbone traversant la couche d'oxyde est graduellement réduit quand la concentration en chrome dans l'alliage augmente. Il apparait alors, au vu de la constitution de la partie interne des couches d'oxydes formées sur ces trois alliages, que la perméabilité au carbone des oxydes spinelles riches en chrome est moins importante que celle des spinelles riches en fer et de FeO, et que la vitesse globale de transport du carbone est sensible aux proportions de ces phases.

La carburation des alliages haut chrome est soit absente soit limitée sous la chromine, mais aussi lorsque qu'un oxyde riche en chrome est présent à la base d'une structure multicouche. On en déduit que la formation d'une couche continue d'oxyde riche en chrome permet de réduire de manière drastique le flux de carbone. Ceci confirme que les oxydes riches en chrome, que ce soit de type spinelle ou corindon, sont moins perméables au carbone que les oxydes riches en fer.

Pourtant, la propension à la perte locale de la capacité à bloquer le carbone est réduite lorsque ces oxydes riches en chrome dissolvent une faible quantité de fer

(de l'ordre de 1 % at.), en comparaison avec la chromine relativement pure. Ceci peut être mis en relation avec le travail de Young [126], qui suggère que le transport moléculaire du carbone peut être entravé par la ségrégation de fer aux joints de grain de l'oxyde.

4 Transition vers l'oxydation non-protectrice

Bien que les alliages haut chrome (20 et 25 % m. Cr) contiennent suffisamment de chrome pour que des couches de Cr_2O_3 à croissance lente soient formées initialement, ce régime d'oxydation protectrice n'est, dans la plupart des cas, pas maintenu dans l'échelle de temps expérimentale. La transition vers un régime d'oxydation rapide s'effectue par le biais de l'apparition et du développement de nodules d'oxydes riches en fer. Les aspects mécanistiques et cinétiques de cette transformation sont étudiés au Chapitre 6.

4.1 Mécanisme de la transition

L'évolution morphologique accompagnant le développement des nodules peut être résumé comme suit. Initialement, une couche de Cr_2O_3 est formée à la surface de l'alliage. À certains endroits, l'oxydation sélective ne peut être maintenue, et l'alliage produit des oxydes riches en fer. Les nodules individuels s'épaississent et s'étendent latéralement, et finalement coalescent pour former des couches d'oxydes d'épaisseur uniforme. Les conditions sous-tendant la rupture des couches de Cr_2O_3 et le développement des nodules sont examinées, en particulier dans le cas des alliages binaires à 650 °C.

4.1.1 Appauvrissement en chrome et influence de la carburation

L'appauvrissement en chrome dans le métal dû à la croissance de Cr_2O_3 sur l'alliage Fe–20Cr à 650 °C est étudié par microscopie électronique à balayage. La composition de l'alliage est affectée dans une zone de profondeur inférieure à 5 µm, alors que l'épaisseur des échantillons est supérieure au millimètre. Par conséquent, la croissance de la chromine s'effectue, a priori, dans un régime pseudo-stationnaire, où la fraction molaire en chrome dans le métal à l'interface avec l'oxyde, $N_{Cr}^{m/o}$, est constante dans l'échelle de temps considérée. On montre que les profils de déplétion peuvent être directement liés à l'épaisseur locale de la chromine par l'intermédiaire de l'analyse de Wagner [78] et du traitement classique du problème de diffusion à une dimension.

Les profils calculés sont en très bon accord avec les valeurs expérimentales, et ce indépendamment de la présence ou de l'absence de carbures dans la zone de déplétion. Ceci démontre que dans ces conditions, la précipitation limitée de carbures dans l'alliage Fe–20Cr sous une couche de chromine n'affecte pas l'appauvrissement en chrome. En particulier, la concentration interfaciale, qui est déterminante pour l'oxydation sélective, n'est pas altérée. Ceci tient au fait que la couche de chromine est une barrière relativement efficace à l'entrée du carbone. L'implication essentielle de l'analyse du mécanisme de carburation menée au Chapitre 5 est que dans un régime pseudo-stationnaire, alors que la chromine croît et que la zone de déplétion progresse dans l'alliage, la dissolution-reformation de la plaque de carbure provoque son déplacement vers le cœur de l'alliage et permet au flux global de chrome en direction de l'interface métal/oxyde de ne pas être altéré. En l'absence de précipitation au delà de la plaque, la concentration en chrome dans la matrice métallique, et par conséquent la force motrice pour la diffusion du chrome, sont globalement inchangés.

Par ailleurs, on montre que la diffusion rapide du carbone dans l'alliage, qui produit une précipitation dense de carbures dans les régions couvertes par des oxydes riches en fer, est une conséquence plutôt qu'une cause de la transition vers l'oxydation non-sélective. Il apparait aussi que la carburation limitée sous la chromine n'est pas une condition nécessaire à cette transition.

4.1.2 Mode de rupture de la chromine

Afin d'examiner la cause de la rupture des couches de chromine, les critères de stabilité thermodynamique et cinétique de Cr_2O_3 sont exprimés en termes de concentration interfaciale en chrome, $N_{Cr}^{m/o}$. L'analyse des profils de déplétion montre que, après réaction à 650 °C, le surplus de chrome à l'interface est variable et parfois réduit dans le cas de l'alliage Fe–20Cr, mais qu'il est considérable pour Fe–25Cr.

Dans les deux cas, étant donné l'épaisseur importante des échantillons au vu de la vitesse de réaction, le régime pseudo-stationnaire d'oxydation sélective devrait a priori perdurer dans l'échelle de temps expérimentale. Ainsi, l'échec des alliages à maintenir la croissance exclusive de la chromine est attribué à des instabilités locales, comme en témoigne d'ailleurs le développement non-uniforme des nodules à la surface des échantillons. Puisque des variations spatiales de l'épaisseur de Cr_2O_3 sont observées, la possibilité de variations temporelles de la constante de croissance k_{p,Cr_2O_3} doit être considérée.

Bien que les origines de telles fluctuations ne soient pas clairement identifiées,

leurs conséquences peuvent être anticipées. Une augmentation locale de la vitesse d'oxydation peut accélérer la génération de contraintes de croissance, et donc la rupture mécanique de la couche de chromine. La réduction de la valeur de $N_{\mathrm{Cr}}^{\mathrm{m/o}}$ liée à une oxydation plus rapide implique que l'écaillage ou l'apparition de fissure peuvent permettre au gaz d'accéder à un alliage plus sévèrement appauvri en chrome, qui alors ne parvient pas à reformer Cr_2O_3. Plus simplement, une augmentation suffisante de k_{p,Cr_2O_3} peut rendre l'oxyde instable cinétiquement, à cause d'un flux de chrome depuis l'alliage limité.

4.1.3 Développement des nodules

Les évolutions morphologiques qui suivent la perte locale du caractère protecteur de la couche d'oxyde initialement formée sont étudiées au moyen d'observations en microscopie électronique à balayage et en spectroscopie Raman, en particulier dans le cas de l'alliage Fe–20Cr à 650 °C. Pour cet alliage, le développement des nodules implique la diffusion rapide du fer à travers la phase spinelle qui remplace la chromine pour former une couche externe d'hématite. Simultanément, la perméabilité de l'oxygène dans le métal augmente, provoquant la précipitation interne de spinelle riche en chrome. La matrice métallique entourant ces précipités est à son tour oxydée en un spinelle riche en fer.

La diffusion rapide du fer à travers la couche d'oxyde initialement protectrice est limitée à une région centrale, alors que la croissance des parties externe et interne du nodule s'effectue dans toutes les directions des demi-espaces externe et interne. Ce faisant, le nodule adopte une forme elliptique. Il s'ensuit aussi que dans les régions adjacentes au site de germination, la chromine est entourée par les lobes d'oxyde externe et interne, et destabilisée par l'augmentation de l'activité en oxygène associée à la présence d'oxydes contenant du fer. La zone de conversion de Cr_2O_3 en spinelle s'étend alors latéralement. La diffusion du fer dans le nodule en croissance s'effectue le long des gradient d'activité, perpendiculairement aux lignes d'isoactivité définies par la forme du nodule. Ainsi, cette forme elliptique est maintenue dans le temps. Décrire les composantes latérale et verticale de la croissance des nodules selon le même processus de diffusion à l'état solide permet d'expliquer pourquoi des cinétiques paraboliques sont observées dans chacune des deux directions.

Le processus de coalescence des nodules individuels finit par engendrer les structures multicouches d'épaisseur uniforme caractéristiques de l'oxydation non-sélective rencontrée sur les alliages bas chrome. Par ailleurs, la formation d'une précipitation dense de carbures internes riches en chrome empêche la diffusion du chrome vers

l'interface métal/oxyde, rendant la repassivation impossible. Un régime pseudo-stationnaire d'oxydation rapide est ainsi maintenu.

Dans le cas de la réaction de l'alliage Fe–25Cr à 650 °C, deux types d'oxydes sont formés à la suite de la rupture de Cr_2O_3. Près des arêtes des échantillons, là où l'appauvrissement en chrome et la probabilité d'écaillage sont les plus marqués, l'alliage produit des nodules multicouches tout à fait similaires à ceux observés pour l'alliage Fe–20Cr. Loin des arêtes, en revanche, la concentration en chrome est suffisante pour qu'une forme de repassivation ait lieu: une couche d'oxyde de type spinelle ou corindon suivant les emplacements, mais toujours riche en chrome, est formée dans la partie interne des nodules, à l'interface avec le métal. La croissance de cette structure est considérablement ralentie par rapport aux nodules d'oxyde riches en fer. Cependant, bien que la couche d'oxyde riche en chrome soit une barrière efficace au transport du carbone et empêche la carburation du substrat, le degré de protection associé à cette structure d'oxyde n'est pas maintenu dans le long terme.

Lors de la réaction à 800 °C, l'alliage Fe–25Cr produit exclusivement de la chromine. Ce régime d'oxydation protecteur est aussi observé pour l'alliage Fe–20Cr exposé au CO_2 sec, mais la présence de vapeur d'eau dans l'atmosphère provoque le breakaway. Comme dans le cas de Fe–25Cr à 650 °C, la concentration en chrome dans le substrat est suffisante pour qu'une couche d'oxyde riche en chrome soit formée à la base de la structure multicouche. Cependant, cette couche ne constitue pas une barrière à la diffusion du fer efficace, et sa présence n'empêche pas la croissance rapide de couches externes d'oxydes de fer. On note que le mécanisme de développement des nodules évolue avec la température: à 800 °C, le flux de chrome est suffisant pour empêcher la formation d'une nouvelle phase à l'interface métal/oxyde, et la réaction procède plutôt par une dissolution du fer dans la couche de chromine preéxistente, et par la croissance continuée de cette couche basale et des couches externes.

Le cas des alliages ternaires est plus complexe. À 650 °C, les alliages Fe–20Cr–10Ni et Fe–20Cr–20Ni forment des nodules d'oxydes riches en fer similaires à ceux formés par Fe–20Cr. L'oxydation interne est supprimée en présence de nickel. On montre que la transition vers une oxydation exclusivement externe ne peut être expliquée sur la base d'une simple comparaison des perméabilités de l'oxygène et du chrome dans le métal. Qualitativement, l'absence de carbures internes dans les alliages ternaires, dans les régions couvertes par des nodules, favorise la diffusion du chrome par rapport à son oxydation interne.

Par ailleurs, dans la partie interne des nodules formés sur les alliages ternaires,

le spinelle riche en fer observé dans le cas de Fe–20Cr est remplacé par un spinelle contenant du nickel, dans lequel la diffusivité des cations est inférieure. Cette substitution s'accompagne d'une baisse de la vitesse de croissance des nodules. La réduction est encore plus marquée pour les alliages Fe–25Cr–10Ni et Fe–25Cr–20Ni, si bien que la croissance est considérablement limitée, et le comportement en oxydation de ces deux alliages peut être qualifié de protecteur.

Au contraire, l'exposition de tous les alliages ternaires à 800 °C produit des nodules à croissance relativement rapide. La microstructure de ces nodules est complexe, et témoigne d'une situation hors-équilibre. Des zones d'oxydation interne sont initialement formées, puis évoluent pour constituer des couches d'oxyde multiphase finement divisées, dans lesquelles subsistent des régions métalliques en proportion importante.

4.2 Cinétique de la transition

Lorsque des nodules d'oxydes riches en fer se développent à la surface d'un alliage, une transition s'opère entre un régime d'oxydation lente, caractéristique de la croissance de Cr_2O_3, et un régime d'oxydation rapide, typique des structures multicouches d'oxydes riches en fer. Alors que le changement de mécanisme de réaction est par nature local, la cinétique de réaction est mesurée à l'échelle de l'échantillon. La cinétique associée à cette transition est étudiée ici selon une approche basée sur la prise en compte des processus de germination et de croissance des nodules. Cette analyse est appliquée aux résultats obtenus après réaction à 650 °C uniquement.

4.2.1 Modèle analytique de germination-croissance des nodules

La fraction de surface d'oxyde riche en fer, θ, reflète la fréquence de germination des nodules, et la vitesse à laquelle ils s'étendent latéralement. La fréquence de germination, qui représente le manque de résistance de la couche de chromine initialement formée, est estimé à partir de fractions de surface de nodules et de vitesses de croissance mesurées après réaction à 650 °C.

Un modèle analytique, basé sur les travaux d'Evans [193], est construit à partir de simples considérations géométriques. Ce modèle repose sur les hypothèses suivantes:

1. la germination est continue sur les régions encore non couvertes d'oxyde riche en fer,
2. la germination est uniforme dans l'espace et dans le temps, et
3. la loi de croissance latérale est de la forme $r^2 = 2k_{\mathrm{r}}t$.

On obtient alors une équation donnant la fraction de surface de nodules en fonction du temps de réaction, de la fréquence de germination Ω et de la constante de croissance latérale k_r:

$$\theta = 1 - \exp\left(-\pi \Omega k_r t^2\right) \tag{3}$$

Cette équation est un cas particulier de cinétique d'Avrami (ou KJMA, pour Kolmogorov–Johnson–Mehl–Avrami) [195–200]. En particulier, le fait que les nodules finissent par se chevaucher est pris en compte.

Le modèle est d'abord appliqué aux résultats obtenus après réaction des alliages binaires, Fe–20Cr et Fe–25Cr. Les fractions de surface mesurées après exposition au CO_2 sec sont caractérisées par une variabilité importante, et ne peuvent être décrites à l'aide d'une fréquence de germination unique. En revanche, l'exposition aux mélanges Ar–CO_2–H_2O mène, pour les deux alliages, à des valeurs de θ systématiquement élevées. À l'aide du signal de gain de masse mesuré de façon continue lors de la réaction d'un échantillon de Fe–20Cr sous Ar–20CO_2–5H_2O, et en faisant l'approximation d'une germination uniquement initiale, on montre que l'évolution de θ avec le temps suit effectivement une courbe en S, mais qu'il existe une déviation par rapport à la situation de germination uniforme à la fin de la transition, où la progression de θ est moins rapide qu'attendu. Cela indique que certaines parties de l'échantillon, probablement correspondant à des grains d'orientation cristallographique particulière, présentent une résistance à la germination notablement supérieure à celle prévalant, en moyenne, dans le reste de l'échantillon.

Dans un deuxième temps, le modèle est utilisé pour quantifier les effets de la composition de l'atmosphère et des alliages sur la germination. Malgré une variabilité importante des résultats expérimentaux, cette analyse met en évidence une augmentation de Ω pour les mélanges gazeux contenant de la vapeur d'eau. Les fréquences de germination maximales sont atteintes pour l'alliage Fe–25Cr. Ainsi, alors que pour cet alliage ferritique la concentration en chrome relativement élevée permet, après la rupture de la couche de Cr_2O_3, une repassivation partielle et temporaire, elle provoque aussi une réduction de la résistance de la chromine. Cette observation est discutée à l'aide de considérations sur la structure et les propriétés de transport de Cr_2O_3. Finalement, on note que l'addition de nickel à l'alliage Fe–20Cr permet de réduire les valeurs moyennes de Ω, mais surtout provoque une augmentation considérable de l'influence de l'orientation cristalline sur la germination.

4.2.2 Modèle statistique de germination-croissance-épaississement des nodules

Le modèle développé par Evans [193] permet de calculer la fraction de surface, mais ne s'étend pas à une prédiction de l'évolution du gain de masse associée avec la germination et la croissance de nodules. Cette cinétique a été modélisée dans le passé [115], sur la base d'une relation qui n'est valable que lorsque la germination a lieu initialement, à $t = 0$, et pas par la suite. Dans la situation présente, la germination a lieu de manière continue jusqu'à ce que la surface soit entièrement recouverte d'oxyde riche en fer. Le gain de masse total dépend alors de la distribution en âge (ou en taille, de manière équivalente) des nodules. Une approche statistique est développée pour calculer ce gain de masse, sur la base d'un modèle d'écaillage en cyclage thermique [206].

Par ailleurs, on évalue aussi la capacité d'un modèle analytique plus simple, mais faisant l'hypothèse de la germination initiale, à simuler les données obtenues par thermogravimétrie lors de l'oxydation de Fe–20Cr sous Ar–20CO_2 et Ar–20CO_2–5H_2O. La comparaison montre que le modèle statistique est intrinsèquement mieux adapté. Il permet de rendre compte des valeurs expérimentales de manière plus précise, en utilisant le même nombre de paramètres d'ajustement, et en produisant des valeurs physiquement cohérentes pour ces paramètres. On note que le modèle analytique, bien que non-applicable, en toute rigueur, à une situation de germination continue, fournit une approximation raisonnable des valeurs expérimentales. Cela justifie les approximations faites plus tôt pour une discussion qualitative des données expérimentales. En particulier, le fait que la fraction de surface d'oxyde riche en fer n'évolue pas strictement selon une cinétique de germination-croissance uniforme explique pourquoi les paramètres de germination et de croissance obtenus à l'aide du modèle statistique et des gains de masse ne peuvent pas correspondre de manière précise à ceux obtenus à partir de mesures directes.

4.3 Facteurs affectant la transition

Une comparaison du comportement en oxydation des alliages haut chrome à 650 et 800 °C est effectuée, sur la base d'un critère simple: oxydation protectrice (croissance exclusive de chromine ou développement limité de nodules, sans influence significative sur le gain de masse total) contre oxydation non-protectrice (croissance significative de nodules, en termes de fraction de surface et/ou gain de masse).

Au vu de l'ensemble des résultats, on conclut que la propension à la rupture de la chromine est moins importante que la vitesse de croissance des nodules pour

déterminer la performance générale des alliages lors de la réaction à 650 °C. Dans ces conditions, augmenter les concentrations de chrome et de nickel est une façon efficace de limiter la perte de métal, et la constitution des alliages (ferritique/austénitique) n'est pas un paramètre déterminant.

Au contraire, lors de la réaction à 800 °C, le facteur décisif pour la performance générale des alliages est leur capacité à maintenir la formation exclusive de chromine, ou à reformer une couche d'oxyde riche en chrome après rupture de la couche initalement formée. L'oxydation sélective est favorisée lorsque le flux de chrome dans l'alliage est suffisant par rapport à la vitesse de croissance de la chromine; ceci conditionne la stabilité de Cr_2O_3. Par ailleurs, au vu de la vitesse de croissance de l'oxyde riche en fer et de la perméabilité de l'oxygène dans l'alliage après la rupture de Cr_2O_3, qui affectent le degré d'enrichissement en chrome à la base de l'oxyde, le flux de chrome est déterminant quant à la capacité de l'alliage à repassiver. Ceci constitue une distinction essentielle par rapport à la réaction à 650 °C, où la nucléation de nodules concerne tous les alliages, et la vitesse d'oxydation est déterminée par la composition de l'oxyde. Cette dernière est elle-même directement déterminée par la composition à cœur des alliages, en ce que le chrome est oxydé in situ, et sa diffusion ne joue pas de rôle important.

On note que parce qu'elle implique des instabilités locales, la germination des nodules est caractérisée par une variabilité plus grande que la croissance des nodules. Ainsi, le fait que le degré de non-reproductibilité soit plus important à 800 °C qu'à 650 °C est une simple conséquence du fait que le rôle de la germination dans le contrôle du comportement en oxydation est plus important à 800 °C. De la même manière, le régime de croissance pseudo-stationnaire des structures multicouches d'oxydes riches en fer, cinétiquement limité par la diffusion du fer à l'état solide, n'est pas affecté par la composition du gaz. Au contraire, la propension à la rupture des couches de Cr_2O_3 et la nature de l'oxyde formé à la suite de cette rupture, c'est à dire, la tendance pour le chrome à être oxydé sélectivement, impliquent des processus qui sont sujets à l'influence de la composition du gaz. En conséquence, la composition du gaz n'a qu'une influence quantitative à 650 °C, mais est davantage déterminante à 800 °C. En particulier, les résultats obtenus pour l'alliage Fe–20Cr à cette température montrent que l'ajout de H_2O à un mélange Ar–CO_2 est susceptible de déclencher le breakaway, et que le caractère néfaste de la vapeur d'eau vis-à-vis de l'oxydation sélective est plus marqué que celui du dioxyde de carbone.

Le changement de nature des processus contrôlant la performance des alliages avec la température est interprété, sur la base de travaux publiés par d'autres [14, 210], en considérant l'évolution de la diffusivité du chrome dans l'alliage et de la

vitesse de croissance des oxydes. À 650 °C, la diffusion dans le métal est relativement lente, si bien que le rôle des court-circuits de diffusion (joints de grain) est important, et la différence entre alliages ferritiques et alliages austénitiques peu marquée. En conséquence, la propension à la rupture de la chromine est similaire pour tous les alliages, et les ajouts de chrome et de nickel sont bénéfiques en ce qu'ils permettent de ralentir la croissance des nodules. Les phénomènes de germination et croissance sont suffisamment lents et, malgré le manque de reproductibilité, suffisamment uniformes pour que le développement des nodules soit observable dans l'échelle de temps expérimentale.

L'augmentation de la température réduit l'influence relative de la diffusion aux joints de grains dans le métal, et amplifie la différence, en termes de coefficient de diffusion effectif, entre alliages ferritiques et austéniques. De plus, le coefficient de diffusion du chrome dans le métal augmente plus vite, avec la température, que la vitesse de croissance des structures multicouches d'oxydes riches en fer, ce qui favorise la repassivation aux températures élevées. Cela confère un avantage déterminant aux alliages ferritiques, par rapport aux alliages austénitiques, lors de la réaction à 800 °C. Par ailleurs, puisque l'étape de germination est déterminante à cette température, la transition du régime d'oxydation protectrice au régime d'oxydation rapide est relativement brutale, et l'étape de développement individuel des nodules de courte durée.

5 Implications pratiques

Le cahier des charges d'un matériau est formé de contraintes d'origines diverses, telles que celles liées aux propriétés mécaniques, aux propriétés fonctionnelles ou à la formabilité, et au comportement en oxydation. La conception d'un alliage est donc le résultat d'un processus d'optimisation guidé par des contraintes potentiellement conflictuelles. Par exemple, il peut être nécessaire de limiter la concentration en chrome pour éviter la présence de la phase σ, qui est fragile. Certaines applications peuvent nécessiter une structure austénitique si une certaine résistance au fluage est attendue. On note que la portée de cette étude, en termes de possibilités de conception, est très limitée. Les éléments d'alliages secondaires, tels le molybdène, le manganèse ou le silicium peuvent affecter la résistance à l'oxydation. Plus généralement, les propriétés des matériaux sont déterminées non seulement par leur composition chimique mais aussi par leur microstructure, qui est ajustée par des traitements mécaniques.

Bien que les résultats de cette étude ne soient pas directement transposable en recommandations pour la conception d'alliages, certaines observations peuvent être utiles en principe, en ce qu'elles renseignent sur la façon dont la performance générale des alliages dans des atmosphères de type CO_2–H_2O est affectée par les concentrations en chrome et en nickel et par la température de service. On note que le compromis nécessaire associé à la conception d'un alliage doit prendre en compte les contraintes spécifiques imposées par la fonction du matériau sur le comportement en corrosion. Par exemple, si la seule contrainte est celle de ne pas dépasser une certaine perte de métal, en ce qu'elle définit la section porteuse efficace d'une pièce, la croissance de nodules à une vitesse faible pourrait être acceptable. En référence aux présents résultats, ce critère permettrait l'utilisation d'alliages austénitiques à des températures modérées, sous réserve que les concentrations en chrome et en nickel soient suffisantes. Au contraire, si la chromine est le seul oxyde acceptable, par exemple pour des raisons liées à la conductivité thermique ou électrique d'une pièce, une température de service plus élevée serait concevable pour des alliages ferritiques à haute teneur en chrome.

Définir des contraintes en termes de comportement en oxydation nécessite de se doter de critères et d'outils pour évaluer la performance des alliages dans des conditions d'exposition données. Si l'on considère le cas d'une utilisation à une température relativement élevée, où la croissance de nodules est trop rapide pour être acceptable et la durée de vie est définie par le régime de croissance exclusive de Cr_2O_3, alors le concept de temps d'incubation constitue un critère pertinent, et le gain de masse ou simplement l'observation de la surface d'un échantillon peuvent être suffisants pour déterminer cette durée de vie. Au contraire, si la formation de nodules ne peut pas être évitée mais peut être limitée, comme ici dans le cas de la réaction à 650 °C, le concept de fréquence de germination et les méthodes développées ici pour analyser les cinétiques de réaction peuvent se révéler utiles. Un telle analyse peut être basée sur la fraction de surface de nodules ou sur le gain de masse, en utilisant le modèle analytique de germination-croissance ou le modèle statistique de germination-croissance-épaississement.